

RESEARCH AND TECHNOLOGY 1994



RESEARCH AND TECHNOLOGY 1994

Dedicated to the memory of Anne Wilson
for her years of superb editorial oversight
of the Research and Technology Report.

National Aeronautics
and Space Administration

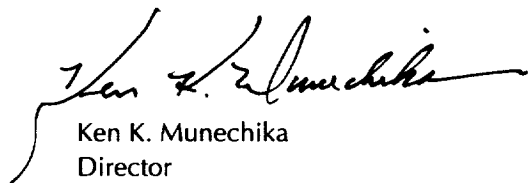
Ames Research Center

Foreword

Each year, brief summaries of selected achievements at Ames Research Center are compiled as a NASA Technical Memorandum.

This year's report, Research and Technology 1994, presents some of the challenging work recently accomplished in the areas of Aerospace Systems, Information Systems, and Space Research. Here, you can sample the scope and diversity of the research that is now being conducted and obtain a view of the stimulating research challenges of the future.

If you would like further information on any of the Ames research and technology programs, please call the contact person(s) at the end of each article.



Ken K. Munechika
Director

Aerospace Systems

Applied Aerodynamics Division

UH-60 Airloads Program 1
William G. Bousman, Robert M. Kufeld

Prediction of Nonlinear Maneuver Aerodynamics 2
Neal M. Chaderjian, Lewis B. Schiff

Parallel Optimization with Computational Aerodynamics 3
Samson H. Cheung

Inlet Bleed Simulation 6
Wei J. Chyu, Daniel P. Bencze

Navier–Stokes Solutions of Helicopter Rotor Flow Fields in Forward Flight 7
Earl P. N. Duque

Business Jet Optimization 8
John W. Gallman, Michael D. Madson, David A. Saunders, Robert A. Kennelly, Jr.

Linear Stability Transition Prediction in Supersonic Flow 9
Joseph A. Garcia, Eugene L. Tu

Tangential Slot Blowing on Rounded and Chined Forebodies 11
Ken Gee, Roxana M. Greenman, Lewis B. Schiff

HSCT Wing-Body Aeroelasticity Computations Using Parallel Computers 12
Guru P. Guruswamy, Chansup Byun

Transonic Flutter Boundary Computation for an AST Wing 13
Guru P. Guruswamy

Separation and Hysteresis of Overexpanded Nozzle Flows 14
Ching-mao Hung

Reduction of Helicopter BVI Noise, Vibration, and Power Consumption Through Individual Blade Control 16
Steven A. Jacklin, Stephen M. Swanson

Oblique All-Wing Supersonic Transport 18
Robert A. Kennelly, Jr.

Optimum Design of High-Speed Proprotors 19
Sesi Kottapalli, Thomas R. McCarthy, Aditi Chattopadhyay, Sen Zhang

Rotor Hub Loads Research: Dynamically Tuned Blade Pitch Links 20
Sesi Kottapalli, Judah Milgram, Inderjit Chopra

Code Validation for Supersonic Flows 21
Scott L. Lawrence

Higher Harmonic Optimal Controller to Minimize Helicopter Vibration 22
Jane Anne Leyland

Tiltrotor Aeroacoustic Model Research Program 24
Paul Loschke

Software Utilities for Surface Modeling 25
Catherine M. Maksymiuk

Triangular Surface Grids 26
Catherine M. Maksymiuk

Aerospace Systems (continued)

Applied Aerodynamics Division (continued)

Magnetic Flight of a Vehicle	27
<i>Unmeel Mehta, Goetz Klopfer</i>	
Application and Development of Three-Dimensional Cartesian CFD Technology	28
<i>John E. Melton, Michael J. Aftosmis, Michael D. Wong</i>	
Aeroelastic Stability of Modern Bearingless Rotors	30
<i>Khanh Q. Nguyen</i>	
Correlation of Loads on a Bearingless Rotor	31
<i>Khanh Q. Nguyen</i>	
Dynamics of the MDART Rotor Test Rig	32
<i>Khanh Q. Nguyen</i>	
Turbulence Modeling Enhancement for Overflow Code	32
<i>Yehia Rizk</i>	
Maneuver Performance Enhancement for an Advanced Fighter/Attack Aircraft	33
<i>Jeffrey Samuels</i>	
Flight and Wind Tunnel Investigations of Blade-Vortex Interaction Noise	34
<i>David B. Signor, Gloria K. Yamauchi, C. W. Acree</i>	
Noise-Suppression Nozzle Testing	36
<i>Brian E. Smith</i>	
Axial Mixer Ejector Nozzle (AMEN) Performance	37
<i>Paul T. Soderman</i>	
Phased Microphone Arrays for Wind Tunnels	38
<i>Paul T. Soderman</i>	
Computation of Helicopter Rotor Acoustics in Forward Flight	39
<i>Roger C. Strawn, Rupak Biswas</i>	
Airfoil Drag Reduction	40
<i>Paul Michael Stremel</i>	
TRAM Rotating Amplifier System	41
<i>Alexandra Swanson</i>	
Effect of Canard on Dynamic Stability	42
<i>Eugene Tu</i>	

Aeronautical Technologies Division

Compressibility Corrections for Turbulence Models	44
<i>Thomas J. Coakley, P. George Huang, Jorge E. Bardina</i>	
Computations of Multistage Turbine Flows	45
<i>Karen L. Gundy-Burlet</i>	
Remote-Access Wind Tunnel	46
<i>Dennis J. Koga, Anthony J. Lisotta, Bruce L. Gilbaugh</i>	
Commissioning of the Laminar Flow Supersonic Wind Tunnel	47
<i>James A. Laub, Stephen W. D. Wolf, and Lyndell S. King</i>	
Pressure Sensitive Paint System Development	49
<i>Blair G. McLachlan, James H. Bell, John A. Schreiner, Jose M. Espina</i>	

Aerospace Systems (continued)

Aeronautical Technologies Division (continued)

Measurement of Surface Shear Stress Distributions Using Liquid Crystal Coatings 50
Daniel C. Reda

Effects of Two-Dimensional Forcing on Free Shear Layers 51
Michael M. Rogers, Robert D. Moser

Convergence Acceleration for Simulation of High-Lift-Airfoil Turbulent Flow Problems 53
Stuart E. Rogers

Instabilities Originating from Suction Holes Used for Laminar Flow Control 54
Jonathan H. Watmuff

Advanced Navier–Stokes Solver 55
Seokkwan Yoon

Flight Management and Human Factors Division

Head-Up Spatial Auditory Displays for Aeronautics 57
Durand R. Begault

The Box: A Free-Play Multimedia Learning Environment for the Boeing 737-300 Flight Management System 58
Steven M. Casner

Terminal Area Productivity: Air Traffic Management 59
Victor Cheng, Rhonda Slattery

Interviews with Apollo Astronauts 60
Mary M. Connors, Dean B. Eppler, Daniel G. Morrow

Final Approach Spacing Tool 61
Tom Davis, Ken Krzeczowski

Civil Tiltrotor Terminal Area Operations 61
William A. Decker

Rotorcraft Modeling Using Flight Test Data 62
Jay W. Fletcher, Mark B. Tischler

V/STOL Systems Research Aircraft 64
John D. Foster, Ernesto Morales III, Delamar M. Watson

ASTOVL Lift Fan Simulation 65
James A. Franklin, William W. Y. Chung, Paul F. Borchers

Preliminary Field/Flight Testing of Descent Advisor (DA) at Denver 66
Steven Green

RASCAL Noise-Abatement Flight Tests 68
William S. Hindson, Robert T. N. Chen

Enhancing Situation Displays 69
James C. Johnston

Dynamic Eye-Point Displays 70
Mary K. Kaiser

Effects of Automation on Crew Communication and Coordination 71
Barbara G. Kanki, Elizabeth Veinott, Cheryl Irwin, Kimberly Jobe

Aerospace Systems (continued)

Flight Management and Human Factors Division (continued)

New Metric for Domain Analysis	72
<i>Michael W. McGreevy</i>	
Aeronautical Team Decision Making	73
<i>Judith Orasanu, Ute Fischer, Michelle Rodvold</i>	
Computational Modeling of Team Communications Demands	75
<i>Roger W. Remington</i>	
High-Speed Research Piloted Simulations	76
<i>Jeffery A. Schroeder, Shawn A. Engelland, Dan W. Dorr, Charles S. Hynes</i>	
Precision Approaches to Closely Spaced Parallel Runways	77
<i>Rhonda Slattery</i>	
Real-Time Passive Ranging	78
<i>Banavar Sridhar, Ray Suorsa</i>	
Traffic Management Advisor Adaptation for Denver International Airport	79
<i>Harry N. Swenson, Laurie Engle</i>	
Advanced Rotorcraft Flight Control Design	79
<i>Marc D. Takahashi, Mark B. Tischler</i>	
Real-Time Facility for Safety Monitor Concept Evaluation	80
<i>Marc D. Takahashi, Mohammadreza H. Mansur</i>	
Limited Operational Assessment of the Traffic Management Advisor	81
<i>Leonard Tobias</i>	
Characterizing the Human Visual Motion Filter	82
<i>Andrew B. Watson, Kathleen Turano</i>	
Perceptual Consequences of Engineering Compromises During Spatial Sound Synthesis	83
<i>Elizabeth M. Wenzel</i>	
New Dynamic Planner for CTAS	84
<i>Gregory Wong, Heinz Erzberger</i>	
Helicopter Guidance System with Obstacle Avoidance Capability	85
<i>Rick Zelenka</i>	
Takeoff Trajectory Optimization for Category-A Helicopters	86
<i>Yiyuan Zhao, Robert T. N. Chen, William S. Hindson</i>	

Aerospace Systems (continued)

Aeronautical Projects and Programs Office

Variable-Complexity Genetic Algorithm for Topological Design	88
<i>Peter Gage, Ilan Kroo, Hirokazu Miura</i>	
Conceptual Aircraft Geometry Modeling Program	89
<i>James R. Gloudemans, Paul Gelhausen</i>	
Oblique All-Wing Aircraft First Flight	91
<i>Tom Gregory</i>	
Aircraft Concepts for High-Altitude Remotely Piloted Vehicle Missions	92
<i>Andrew S. Hahn</i>	
Internal Layout Module for ACSYNT	93
<i>Shahab Hasan</i>	
Detailed Aerodynamic Information from Conceptual Aircraft Geometry	94
<i>David Kinney, James R. Gloudemans, Paul Gelhausen</i>	
New Approximation of Frequency Responses for Structural Optimization	96
<i>Hirokazu Miura, Mladen Chargin</i>	
Minimum-Weight Structural Design of an Axisymmetric Inlet	97
<i>Shari-Beth Nadell</i>	
Oblique All-Wing Control Surface Design	98
<i>James D. Phillips</i>	
Validation and Application of a Conical Viscous Flow Solver	100
<i>David R. Schleicher</i>	

Information Systems

Computational Sciences Division

Portable Computer Technology Project	101
<i>Rick Alena</i>	
Super-Resolution Imaging from Multiple Images	102
<i>Peter Cheeseman, Bob Kanefsky, Richard Kraft</i>	
Anechoic Chamber Evaluation of Fiber-Optic Aeroacoustic Transducers	103
<i>Young C. Cho, Maria Bualat</i>	
Prototype Electronic Purchase Request System	104
<i>Michael Compton, Shawn Wolfe</i>	
Bacteriorhodopsin Films for Optical Processing and Sensing Applications	105
<i>John Downie</i>	
Efficient Scheduling of Automatic Telescopes	106
<i>Mark E. Drummond</i>	
Optical Matrix Processors for Structural Control and Plume Analysis	107
<i>Charles Gary, Maria Bualat</i>	
Payload Data Systems Engineering and Analysis	108
<i>Terry L. Grant</i>	
Principal Investigator in a Box	109
<i>Nick Groleau</i>	
Dante II at Mt. Spurr, Alaska	110
<i>Butler Hine</i>	
Application of Neural-Network Technology to Wind Tunnel Testing	111
<i>Charles Jorgensen, James Ross</i>	
Intelligent Aircraft Control System	112
<i>Charles Jorgensen, James Urness</i>	
Mars Atlas on the World-Wide Web	112
<i>Bob Kanefsky, John Stutz</i>	
Human Exploration Demonstration Project (HEDP)	113
<i>David J. Korsmeyer</i>	
Pattern Recognition Tool Kit for Mission Control	115
<i>Philip Laird</i>	
Amphion: Real-World Automatic Programming	116
<i>Michael Lowry, Andrew Philpot, Thomas Pressburger</i>	
Advanced Interactive Media	117
<i>Nathalie Mathé, Joshua Rabinowitz, James Chen</i>	
Science Planning and Sequencing for Space-Based Observatories	118
<i>Nicola Muscettola, Sunil Mohan</i>	
DMS Advanced Monitoring and Diagnosis Application (DMS AMDA)	119
<i>Ann Patterson-Hine, David Iverson</i>	
Phased-Array Microphone for Noise Measurement in Wind Tunnels	120
<i>Michael Watts, Paul Soderman</i>	

Space Research

Space Projects Division

Solid State PhotoMultiplier (SSPM)	121
<i>John H. Goebel</i>	
Multiline Si(Li) Gamma-Ray Spectrometer	121
<i>G. Scott Hubbard, Robert E. McMurray, Jr., Robert G. Keller, Paul F. Wercinski</i>	
2-Kelvin Magnetic Cooler	123
<i>Ali Kashani, Ben Helvensteijn</i>	
Modeling the Pulse Tube Refrigerator	125
<i>Jeffrey M. Lee, Peter Kittel</i>	
Detectors for IR Astronomy	126
<i>Mark McKelvey, Robert E. McMurray, Jr., Craig R. McCreight</i>	

Earth System Science Division

Boreal Ecosystem–Atmosphere Study (BOREAS) Aircraft Data Processing	128
<i>Gary Angelici, Lidia Popovici, Steve Klooster</i>	
Grapevine Remote-Sensing Analysis of Phylloxera Early Stress (GRAPES) Project	129
<i>Cindy Bell, Kathleen Dammann, Liane Guild, Christine Hlavka, Lee Johnson, Brad Lobitz, Joan Salute</i>	
Satellite Sensing of Fires and Estimation of Resultant Emissions in Brazil	130
<i>James A. Brass, Christine A. Hlavka, Robert B. Chatfield, Liane S. Guild, Susan Alexander</i>	
ER-2 Meteorological Measurement System	131
<i>K. Roland Chan, T. Paul Bui, Stuart W. Bowen, Leonhard Pfister</i>	
Simulating the Lower-Atmosphere Ozone Buildup	132
<i>Robert B. Chatfield, John A. Vastano</i>	
Spectral Reflectance and Leaf Chemistry	133
<i>Jennifer Dungan, Lee Johnson, Vern Vanderbilt</i>	
Human-Induced Land Transformations	134
<i>Leonard Gaydos, William Acevedo, Cindy Bell</i>	
Terrestrial Remote Sensing Using Imaging Interferometry	135
<i>Philip D. Hammer, David L. Peterson, William H. Smith</i>	
Stratospheric Dehydration by Thin Cirrus Clouds	136
<i>Eric J. Jensen, Owen B. Toon, Leonhard Pfister, Henry B. Selkirk</i>	
ERS-1 SAR Investigations of High-Latitude Wetlands	138
<i>Leslie A. Morrissey, Gerald P. Livingston</i>	
NASA Science User Networks Working Group	139
<i>Leslie A. Morrissey</i>	
Polar Stratospheric Cloud Detection Using Advanced Very-High-Resolution Radiometer Satellite Imagery	140
<i>Kathy L. Pagan, R. Stephen Hipskind, Steven E. Gaines</i>	
Ozone Power Spectra and Deposition	141
<i>Richard Pearson, Jr.</i>	
Analysis of Stratosphere–Troposphere Exchange	143
<i>Leonhard Pfister, Henry B. Selkirk</i>	

Space Research (continued)

Earth System Science Division (continued)

Satellite Weather Data for Stratospheric Science	144
<i>Leonhard Pfister, Henry B. Selkirk, Steven Hipskind, Steven Gaines</i>	
Stratospheric Ice	145
<i>Rudolf F. Pueschel, Jindra Goodman, Guy Ferry</i>	
Aerosols and Their Radiative/Climatic Effects: Space, Air, and Ground Measurements and Analyses	146
<i>Philip B. Russell, Rudolf F. Pueschel</i>	
Airborne Autotracking Sunphotometry	147
<i>Philip B. Russell, Robert Wrigley, David Bergner, Damon Ried, Danelle Ketner, Rudolf F. Pueschel</i>	
Environmental Research Aircraft and Sensor Technology	148
<i>Philip B. Russell, Steven Wegener</i>	
Composition of the Atmosphere over the Pacific	149
<i>Hanwant B. Singh</i>	
Improved Measurement of Terrestrial (Infrared) Radiation	150
<i>Francisco P. J. Valero, Anthony W. Strawa, Warren J. Y. Gore</i>	
Measurement of Atmospheric Radiation Using an Unmanned Airborne Vehicle	151
<i>Francisco P. J. Valero, Warren J. Y. Gore, Shelly K. Pope, Larry Pezzolo, Neil Heather</i>	
Cloud Modeling for the Study of Climate Change	152
<i>Douglas L. Westphal, Eric J. Jensen, Stefan A. Kinne, Annette L. Walker</i>	
Global Monitoring and Human Health	153
<i>Byron Wood, Louisa Beck, Sheri Dister, Mike Spanner</i>	
Aerosol Measurements for the Boreal Ecosystem–Atmosphere Study (BOREAS)	154
<i>Robert Wrigley, Philip Russell, John Livingston, Brad Lobitz</i>	

Life Science Division

Calcium Balance in a Spaceflight Model	155
<i>Sara B. Arnaud, Meena Navidi</i>	
Noninvasive Test of Bone Strength	156
<i>Sara B. Arnaud, Teresa Hutchinson</i>	
Intramuscular Pressure During Treadmill Walking	157
<i>Richard E. Ballard, Donald E. Watenpugh, Gregory A. Breit, Gita Murthy, Robert T. Whalen, Alan R. Hargens</i>	
Cardiovascular Responses to Real and Artificial Gravity	158
<i>Gregory A. Breit, Donald E. Watenpugh, Theresa M. Buckley, Richard E. Ballard, Gita Murthy, Alan R. Hargens</i>	
Cyclic Skeletal Forces During Daily Activity	161
<i>Gregory A. Breit, Robert T. Whalen</i>	
Spaceflight and Hindlimb Suspension Affect the Posture and Gait of Rats	163
<i>Meryl L. Corcoran, Robert A. Fox, Nancy G. Daunton, Emily Morey-Holton</i>	
Effects of Autonomic Conditioning on Motion Sickness and Physiology	164
<i>Patricia S. Cowings, William B. Toscano, Neal E. Miller, S. Sekiguchi</i>	

Space Research (continued)

Life Science Division (continued)

Effects of Promethazine on Performance, Motion Sickness, and Physiology	166
<i>Patricia S. Cowings, Cynthia S. Stout, William B. Toscano, Samuel M. Reynoso, Charles W. DeRoshia, Neal E. Miller</i>	
Potential Treatment for Postflight Low Blood Pressure in Astronauts: Autogenic-Feedback Training	168
<i>Patricia S. Cowings, William B. Toscano, Neal E. Miller, Thomas G. Pickering, David Shapiro, David Robertson</i>	
Technology Transfer from Spaceflight Research	169
<i>Philip Davies</i>	
Hyperhydration Fluids for Astronauts	171
<i>John E. Greenleaf, R. Looft-Wilson, C. D. Jensen, James H. Whittam</i>	
Force and Mammalian Cells	172
<i>Rosalind A. Grymes</i>	
Small Payloads Flown on Space Shuttle Missions	175
<i>Joellen Jarvi</i>	
Evaluation of Structural and Material Properties of Long Bones	176
<i>BethAnn Katz, Tammy M. Cleek, Robert T. Whalen</i>	
Cardiovascular Responses of Snakes to Hypergravity	178
<i>Harvey B. Lillywhite, Richard E. Ballard, Alan R. Hargens</i>	
International Microgravity Laboratory-2 Mission	179
<i>Chris Maese</i>	
From Neurons to Robots	180
<i>Muriel D. Ross</i>	
Space Life Sciences-2 Mission	182
<i>Paul D. Savage</i>	
Effective Presentation of Motion Information in Aerospace Display Systems	183
<i>Leland S. Stone, Preeti Verghese</i>	
Noninvasive Measurement of Human Eye Movements	184
<i>Leland S. Stone, Brent R. Beutter, Philippe A. Stassart</i>	
Spinal Lengthening in Simulated Microgravity	185
<i>Jorma R. Styf, Richard E. Ballard, Donald E. Watenpaugh, Klaus P. Fechner, Alan R. Hargens</i>	
Autonomic Responses to Microgravity	186
<i>William B. Toscano, Patricia S. Cowings, Neal E. Miller</i>	
Heart Rate Variability During Early Adaptation to Space	188
<i>William B. Toscano, Patricia S. Cowings, Neal E. Miller</i>	
Gravity Simulation and Redistribution of Body Fluids	189
<i>Donald E. Watenpaugh, Gregory A. Breit, Richard E. Ballard, Gita Murthy, Alan R. Hargens</i>	

Space Research (continued)

Space Science Division

Outer Heliosphere and Termination Shock	191
<i>Aaron Barnes</i>	
Production of Organic Molecules in Cometary and Interstellar Ice Analogs	192
<i>Max P. Bernstein, Scott A. Sandford, Louis J. Allamandola, Sherwood Chang</i>	
New Structural Forms of Water Ice and Their Possible Role in the Processing and Delivery of Prebiotic Organic Materials to Early Earth	193
<i>David Blake, Peter Jenniskens</i>	
Spectral Imaging from the Kuiper Airborne Observatory	195
<i>Jesse D. Bregman</i>	
Significance of Fullerenes in Nature	196
<i>Ted Bunch, Luann Becker</i>	
Particle–Gas Dynamics in the Protoplanetary Nebula	197
<i>Jeffrey Cuzzi</i>	
Planetary Ring Dynamics and Morphology	199
<i>Jeffrey Cuzzi</i>	
Earth’s Atmospheric Oxygen Supply is Linked to the Evolution of Its Crust	200
<i>David J. Des Marais</i>	
Refinement of Planetary Protection Policy for Mars Missions	201
<i>Donald L. DeVincenzi, Pericles D. Stabekis, Jack Barengoltz</i>	
Airborne Astronomy	201
<i>Edward W. Dunham, Edwin F. Erickson, Jacqueline A. Davidson</i>	
Stellar Occultation Study of Chiron	203
<i>Edward W. Dunham</i>	
Exploring for an Ancient Martian Biosphere	204
<i>Jack D. Farmer, David J. Des Marais</i>	
Carbonaceous Components in Comet Halley Dust	206
<i>Marina N. Fomenkova, Sherwood Chang</i>	
Mars Soil Oxidant—A Science Puzzle	207
<i>Minoru M. Freund, John J. Plombon, Steven J. Butow, Friedemann Freund</i>	
Accurate Evaluation of Quantum Integrals	209
<i>David C. Galant, David Goorvitch</i>	
Halite Crystals as an Exobiological Resource	210
<i>Lawrence I. Hochstein, Harold Morowitz</i>	
Center for Star Formation Studies	211
<i>David J. Hollenbach, Patrick M. Cassen</i>	
Simulations of the Martian Water Cycle	212
<i>Howard C. Houben, Robert M. Haberle, Aaron P. Zent</i>	
Evolution of Bacterial Symbiosis at Deep-Sea Methane Vents	213
<i>Linda L. Jahnke</i>	
Exobiology Science Strategy for Mars Exploration	214
<i>Harold P. Klein, Donald L. DeVincenzi</i>	

Space Research (continued)

Space Science Division (continued)

FOSTER: The Flight Opportunities for Science Teacher Enrichment Project 215
David G. Koch, Garth Hull, Carl Gillespie

Light Transmission and Reflection in Perennially Ice-Covered Lakes on Earth and on Mars 216
Christopher P. McKay

Extragalactic, Galactic, and Solar System Organics 217
Yvonne J. Pendleton

Mechanism of Unassisted Ion Transport Across Membranes 218
Andrew Pohorille, Michael A. Wilson

Isotopic Ratios of Carbon and Oxygen 219
Todd B. Sauke, Joseph F. Becker, Clayton G. Bratton

Star Formation in Colliding Galaxies 220
Bruce F. Smith, Richard A. Gerber

Telepresence for Planetary Exploration 221
Carol Stoker

Nitrogen Fixation for the Origins of Life 223
David P. Summers

Interstellar Dust Destruction 224
Alexander G. G. M. Tielens, Anthony P. Jones

Infrared Spectroscopy of the Impact of Comet P/Shoemaker-Levy 9 on Jupiter 225
Fred C. Witteborn, Diane H. Wooden

Simulation of the Mt. Pinatubo Volcanic Aerosol Cloud in the Stratosphere 227
Richard E. Young, Howard C. Houben, Brian Toon

Collision of Comet P/Shoemaker-Levy 9 with Jupiter 228
Kevin Zahnle

Space Technology Division

Spectroscopic Determination of Enthalpy in an Arc-Jet Wind Tunnel 230
Dikran S. Babikian, Chul Park, George A. Raiche

Simulations of Collisional–Radiative Nonequilibrium Plasmas 232
Jean-Luc Cambier

Rotational Relaxation Rate Models in Rarefied, Expanding Nitrogen Flows 234
Lawrence A. Gochberg, Brian L. Haas

Simulation of Galileo Probe Aerobraking 235
Brian L. Haas, Frank S. Milos

Simulation of Polymer Properties 237
Richard L. Jaffe

Durable Flexible Insulation 238
Demetrius Kourtides

Heating Analysis of a Single-Stage-to-Orbit Vehicle 239
Grant Palmer, Bill Henline, David Olynick

Space Research (continued)

Space Technology Division (continued)

Stagnation-Point Vacuum-Ultraviolet-to-Infrared Radiation in an Arc-Jet Wind Tunnel	240
<i>Giuseppe Palumbo, Chul Park, Roger Craig</i>	
Computing the Flow about the Venus Composition Descent Module	242
<i>Periklis Papadopoulos, Paul Wercinski</i>	
NASA Ames 16-Inch Shock Tunnel Simulation and Experimental Comparison	244
<i>Periklis Papadopoulos, S. Tokarcik-Polsky, Ethiraj Venkatapathy, George S. Deiwert</i>	
Reactive Intermediates in Soot Formation	245
<i>Stephen P. Walch</i>	

Appendix

Color Plates	249
--------------------	-----

UH-60 Airloads Program

William G. Bousman, Robert M. Kufeld

Flight testing of a UH-60A helicopter with a highly instrumented rotor has been completed at Ames Research Center. The aircraft, shown in the figure, had 242 pressure transducers installed on the blade, making the test program the most extensive ever performed. From August 1993 to February 1994 31 flights were flown and data were obtained for over 860 test conditions. The flight test data are being installed in an electronic data base for use by industry and academia; at the close of the fiscal year, 60% of the data had been installed.

The flight test program focused on five areas: steady flight, maneuvering flight, in-flight acoustics, ground acoustics, and handling qualities. The steady-flight data were obtained at six weight coefficients for all flight speeds within the power limit of the aircraft. These data will be useful for the validation of both CFD and conventional analyses. Maneuvering-flight data were obtained for classical maneuvers such as pull-ups, banked turns, and diving rolling pullouts. These maneuvers tend to size the rotor and the flight controls. The data set will provide insight into the aerodynamic sources of these high loads. In-flight measurements of rotor acoustics were obtained by flying the UH-60A in formation with a YO-3A quiet aircraft that had microphones installed on its wings and tail. Ground-acoustics test data were obtained in

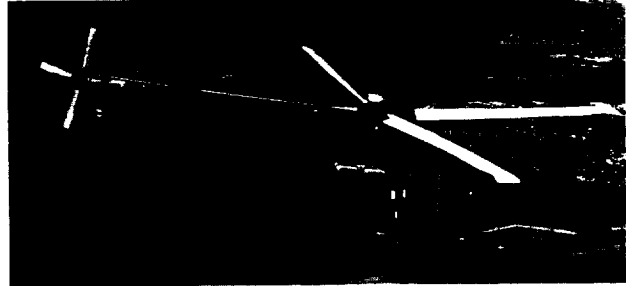


Fig. 1. Highly instrumented UH-60A in flight over the Livermore Valley, California.

cooperation with Langley Research Center by flying the test aircraft in precision approaches and maneuvers relative to a ground-based array of microphones. Finally, the handling qualities investigations focused on different maneuvers that can be used for system identification and, with the measured blade pressures, provide a unique resource for understanding rotorcraft dynamic behavior.

**Ames-Moffett contact: W. Bousman
(415) 604-3748**

Headquarters program office: OA

Prediction of Nonlinear Maneuver Aerodynamics

Neal M. Chaderjian, Lewis B. Schiff

Fighter aircraft can obtain improved maneuver and agility performance by flying at high angles of attack. This performance gain is a result of the nonlinear lift obtained from vortices that form on the leeward side of the aircraft. If the angle of attack is sufficiently large, vortex asymmetries can form and cause a sustained roll oscillation known as wing rock. This phenomenon can be dangerous and can restrict the aircraft's useful flight envelope.

Our goal is to provide an experimentally validated computational tool to compute wing rock and other aircraft motions. The approach adopted here is to utilize the Navier-Stokes Simulation (NSS) code to numerically integrate the time-dependent, three-dimensional, Reynolds-averaged Navier-Stokes equations. This work supports the NASA High-Alpha Technology Program and experimental investigations at Wright Aeronautical Laboratory.

Previous investigations focused on a delta wing with a wing sweep of 65 degrees under conditions of subsonic turbulent flow and a single degree of freedom in roll. Computed and experimental forces and moments for static and forced roll motions were in good agreement at 15 degrees angle of attack, where no vortex breakdown occurs. A follow-on study was carried out at 30 degrees angle of attack, where vortex breakdown does occur. There was good

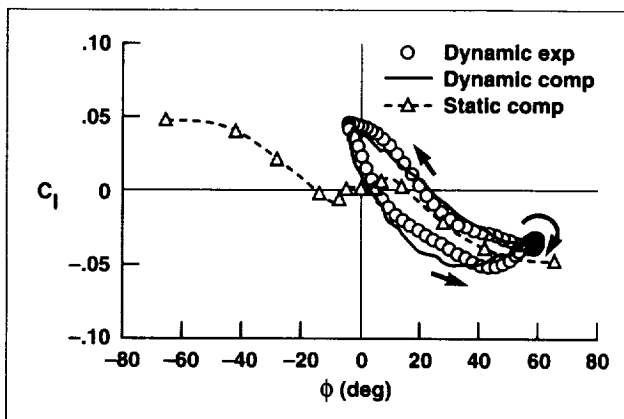


Fig. 1. Comparison of computed and experimental rolling moment coefficients.

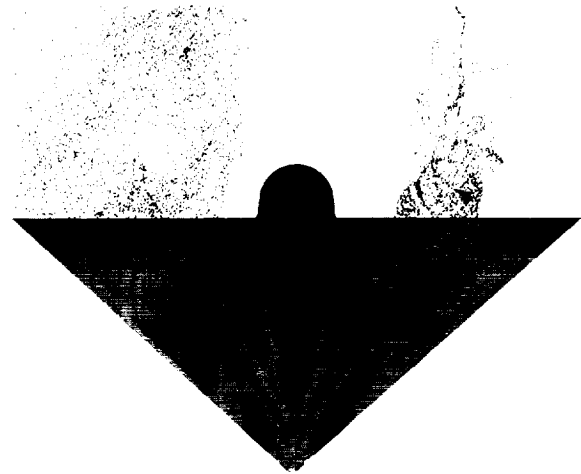


Fig. 2. Numerical flow visualization of surface pressures and nonsteady leeward-side vortices. (See color plate 1 in Appendix)

agreement between computed and experimental forces and moments, and breakdown locations for static roll angles through 65 degrees of roll.

Our current research builds upon the previous results by computing two forced roll motions and a damped free-to-roll motion for the same delta wing at 30 degrees angle of attack. Once again, vortex breakdown is present. The first figure shows the computed and experimental rolling moment coefficients (C_l) for the delta wing undergoing a forced roll motion between -3.9 degrees and 59.9 degrees of roll, with a frequency of 10 cycles per second. The agreement is good. Arrows in the figure indicate how the C_l vary in time. The large counterclockwise loop indicates a damped portion of the flow, whereas the small clockwise loop represents the undamped portion. The computed static roll curve is included to show that there are large differences between the static and dynamic cases. These differences are caused by time lags associated with the nonlinear motion of vortex breakdown over the delta wing.

Numerical flow visualization of this case has been produced in a VHS video format. The second

figure is a single frame from the video. Blue colors indicate low surface pressures; reds indicate high surface pressures. The nonsteady vortices are also shown. Vortex breakdown occurs on both sides of the delta wing as indicated by the rapid growth of the vortex core diameters. The low pressures (blue) underneath the vortices provide nonlinear lift, which is greatly diminished downwind of vortex breakdown. Vortex breakdown has been numerically observed to move off the wing (downwind of the trailing edge) and completely disappear, only to re-form at a later time over the wing. It is usually thought that vortex breakdown simply moves off the

wing and then back onto it again. The validity of this numerical observation is supported by recent water tunnel experiments. The computed nonsteady flow topology of the vortex core was found to be very different from the same nonsteady flow examined at an instant of time with "steady streamlines," a method used by many investigators. Further examination of these phenomena will be the subject of a follow-on study next year.

**Ames-Moffett contact: N. Chaderjian
(415) 604-4472
Headquarters program office: OA**

Parallel Optimization with Computational Aerodynamics

Samson H. Cheung

In order to enhance the competitiveness of the nation's airframe industry, the three design-cycle criteria of speed, low cost, and reliability must be addressed. A fast design cycle allows early entry into the market; a low-cost design cycle allows more iterations in the design process to produce higher-performance aircraft; a reliable design reduces the differences between the design expectation and the actual performance, allowing an accurate pricing strategy. Unlike large mainframe computers such as the Cray-C90, which are typically saturated with jobs waiting to be executed, most personal workstations are idle after normal office hours. These computers represent a significant computational resource with low maintenance cost compared to the Cray-C90. The objective of this exercise is to develop a parallel optimization procedure utilizing computational fluid dynamics (CFD) on a cluster of workstations to reduce the cost and time associated with the airplane design process.

A cluster of engineering workstations are connected by the communication software Parallel Virtual Machine (PVM) to form a virtual parallel computer. A mathematical optimization routine based on the Quasi-Newton method for solving unconstrained optimization problems has been

developed on PVM such that the gradient evaluations and the expensive line-search routines are executed in parallel fashion. This optimization routine is called *IOWA* (Parallel Optimization With Aerodynamics).

To test the optimization routine, a problem of minimizing aerodynamic drag by changing the fuselage of an arrow wing-body configuration is used. The aerodynamic analysis is performed by an inviscid space-marching CFD flow solver. The first figure shows 7% drag reduction obtained from *IOWA* on a cluster of four SGI workstations. The lower left diagram shows the fuselage area of the original and optimized configurations. The adjacent diagram shows the convergence history of the optimization which indicates the quadratic convergence of the quasi-Newton method. A similar result was obtained from a popular serial optimization routine, NPSOL, on the Cray-C90.

This parallel optimization routine has been integrated with a validated parallel CFD flow solver, MEDUSA, supported by PVM. The combination of a parallel flow solver and the optimization routine on a cluster of workstations enhances the parallelism of the design process, thereby reducing the time and cost of the airplane design cycle.

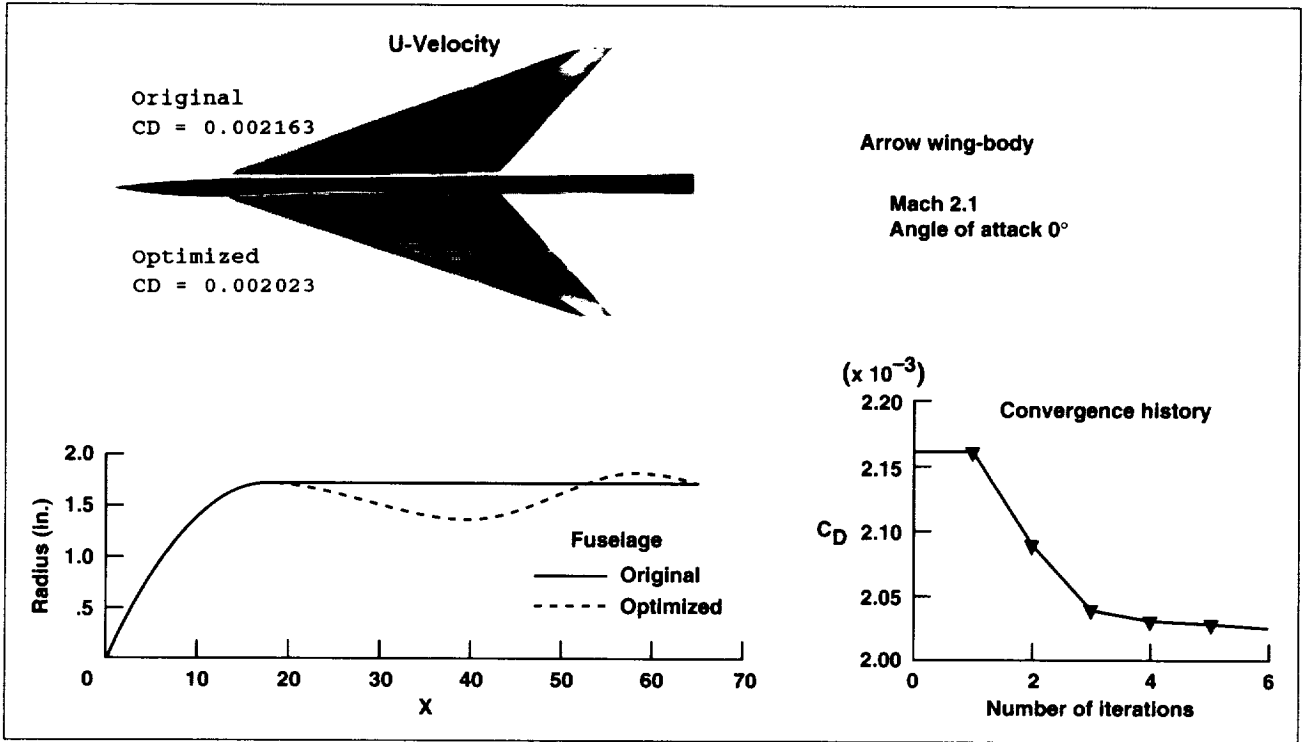


Fig. 1. Drag minimization of an arrow wing-body.

The described procedure has been applied to optimize the aerodynamic performance of an airfoil to demonstrate the parallel capability of the optimization procedure. An intuitively (by hand) optimized two-dimensional NACA airfoil, with available wind tunnel data, is considered. Multiple overset grids represent the airfoil/wind tunnel geometry. In this exercise, five SGI R4000 and five SGI R3000 central processing units are employed; a total of 25 processes are spread over the virtual machine. The second figure shows the result of this optimization. The aerodynamic lift of the airfoil is increased by

1.43% within 10.5 clock hours. The optimization process performs at a rate of about 40 MFLOPS.

This optimization process, which makes use of a parallel optimization routine and CFD code based on a set of low-priced engineering workstations, and performs high-order CFD calculations, meets the three criteria of speed, low cost, and reliability for U.S. aerospace industry.

**Ames-Moffett contact: S. Cheung
(415) 604-4462**

Headquarters program office: OA

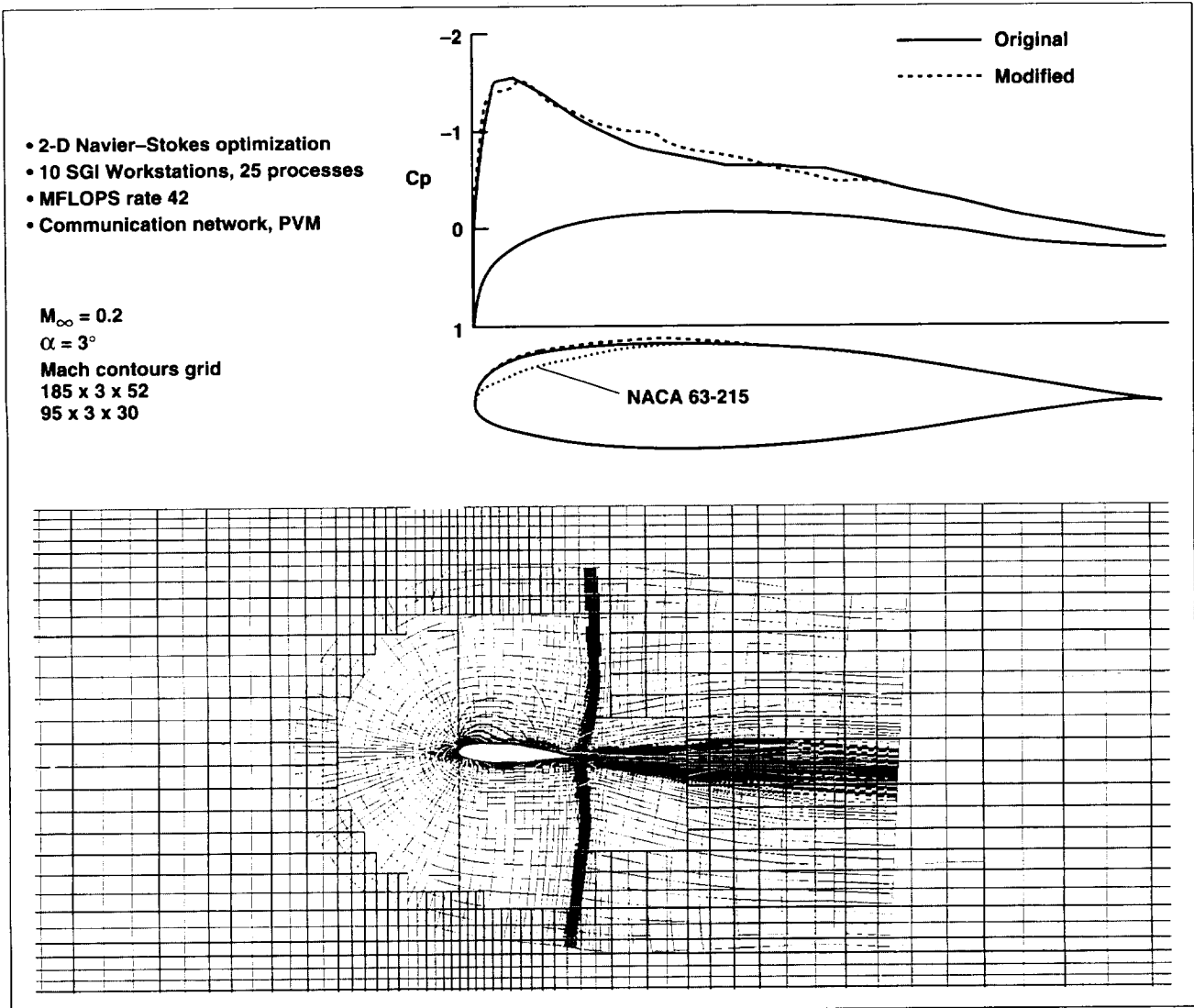


Fig. 2. Fully parallel, multiple-zone viscous aerodynamic optimization. (See color plate 2 in Appendix)

Inlet Bleed Simulation

Wei J. Chyu, Daniel P. Bencze

Effective control of shock-wave-induced boundary layer separation with bleed plays an important role in the operation of inlets for supersonic aircraft. In addition, porous bleed surfaces are used extensively in transonic wind tunnels to relieve blockage effects.

In this study, numerical simulations were performed to investigate the shock-wave/boundary-layer interactions on a flat plate with bleed through one or more circular holes that vent into a plenum. The bleed-hole patterns considered for the study included a single hole; in-line (normal and slanted) multiple holes; and staggered, multiple-row holes that are configured to simulate the patterns used in inlet bleed systems of high-performance aircraft. A typical diagram of the staggered multiple-row holes is shown in the upper portion of the first figure. Also shown in the figure is the computational domain, enclosed by dotted lines. It consists of a supersonic flow field over a flat plate where the air in the

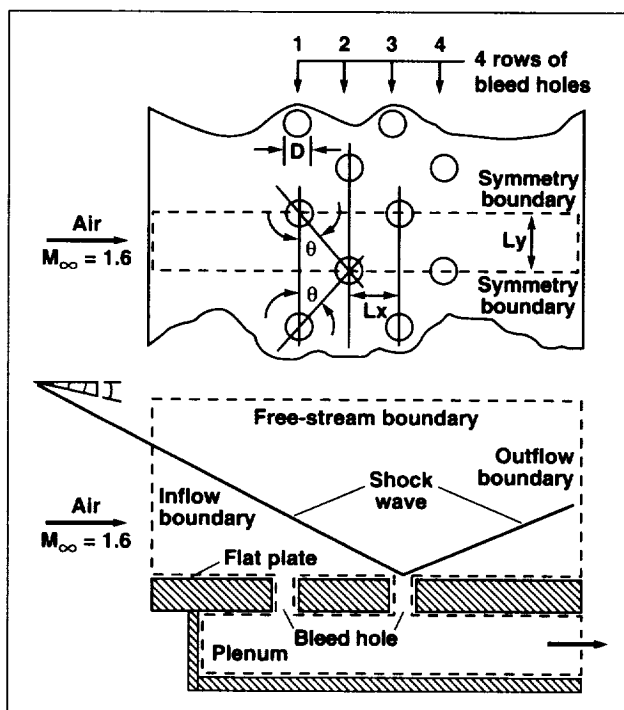


Fig. 1. Schematic of the bleed-hole problem.

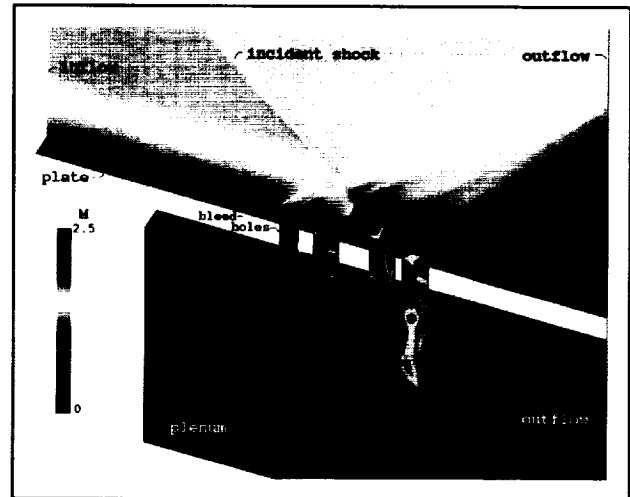


Fig. 2. Mach contours of bleed flow field. (See color plate 3 in Appendix)

boundary layer is ducted through four rows of staggered circular holes into a plenum. Incident and reflected shock waves are simulated which would cause boundary layer separation on the plate without bleed holes.

The study covers the physics of bleed flow affected by parameters related to bleed-hole geometry and flow conditions. The parameters investigated are (1) the structure of the incoming boundary layer and free-stream Mach number, (2) the presence of an incident shock wave, (3) the location of the shock wave relative to the holes, (4) the spacing between bleed holes, (5) the diameter and the length of the bleed holes, (6) hole angles relative to the free stream, (7) multiple-row in-line and staggered hole arrangement, and (8) the pressure ratio across the holes. The second figure shows the typical Mach contours for staggered multiple-row bleed holes at Mach = 1.6.

The calculated results show that the bleed rate is a strong function of hole angle; for instance, the rate for the holes slanted at 30 degrees to the free stream is about two times higher than for those at 90 degrees. The bleed rate is also dependent on the hole location relative to the incident shock; the bleed

rate for holes downstream of the shock wave is significantly higher than for holes upstream of the shock. This is primarily due to the significantly higher pressures downstream of the incident shock wave. The results show that a "barrier" shock is formed in and on the downstream edge of each bleed hole. This barrier shock can prevent downstream disturbance from propagating upstream. It was further noted that the barrier shock also increases mixing in the spanwise direction because it disrupts the flow locally by slowing it down and increasing its static pressure. The increased mixing is still another mechanism that

can be utilized to control flow separation. The results also give the pressure ratio across the bleed holes at which the flow in the holes is choked. The new knowledge gained of the physics of bleed and the related computational techniques developed in this study are directly applicable to the design or performance evaluation of inlet bleed systems.

Ames-Moffett contact: W. Chyu

(415) 604-6208

Headquarters program office: OA

Navier–Stokes Solutions of Helicopter Rotor Flow Fields in Forward Flight

Earl P. N. Duque

The accurate computation of a helicopter flow field is essential for proper and efficient airload and acoustic predictions in forward flight and hover. The constantly changing aerodynamic environment and loads are important features of rotorcraft aerodynamics. Strong tip vortices in the rotor wakes dominate the flow field to produce a highly unsteady and nonuniform induced velocity field at the rotor disk. This work presents a numerical method that computes the unsteady flow field of a helicopter rotor in forward flight or hover. The method solves the thin-layer Navier–Stokes equations on a system of moving overset grids and uses the blade harmonics measured in flight to prescribe the blade motions.

An overset grid thin-layer Navier–Stokes code has been extended to include dynamic motion of helicopter rotor blades through relative grid motion. The unsteady flow field and airloads on an AH-1G rotor in forward flight was computed to verify the methodology and to demonstrate the method's potential usefulness for comprehensive helicopter codes. In addition, the method uses the blade's first harmonics measured in the flight test to prescribe the blade motion. The solution was impulsively started and became periodic in less than three rotor revolutions, as shown in the first figure. Detailed unsteady

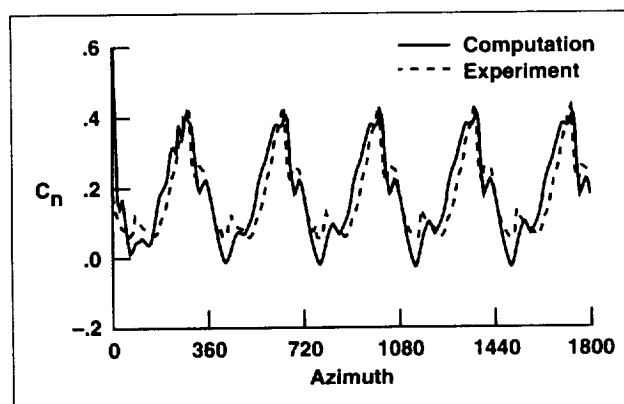


Fig. 1. Normal force coefficient at radial location = 0.97.

numerical flow visualization techniques were applied to the entire unsteady data set of five rotor revolutions, and exhibited flow-field features such as blade–vortex interaction and wake roll-up, as shown in the second figure. The results of this work were presented at the AIAA Applied Aerodynamics Meeting in July 1994. Overall, given the blade dynamics, this method can compute the unsteady flow field of a general helicopter rotor in forward flight.

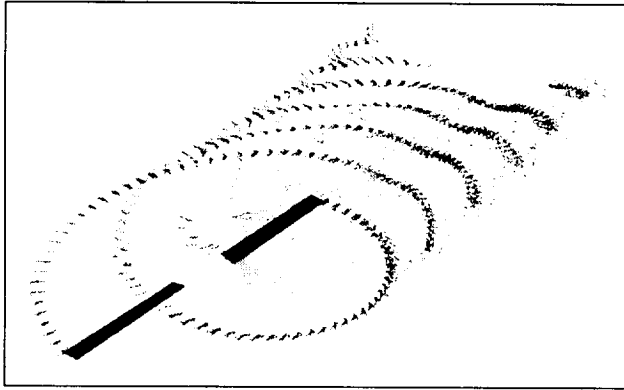


Fig. 2. Unsteady streaklines for five rotor revolutions.

Although the rotor was only partially trimmed, these results demonstrate the method's capabilities. Future plans include loosely coupling a dynamics analysis for helicopter rotors with the current aerodynamics method. A properly coupled dynamics method will include trimmed rotor calculations that include aeroelastic effects such as torsion and bending.

**Ames-Moffett contact: E. Duque
(415) 604-4489
Headquarters program office: OA**

Business Jet Optimization

John W. Gallman, Michael D. Madson, David A. Saunders, Robert A. Kennelly, Jr.

As the technology for high subsonic flight has matured, many business jet manufacturers have started developing faster aircraft with significant increases in range. Development of these advanced business jets requires the application of transonic wing technology commonly used on larger transport aircraft. Addressing detailed aerodynamic design issues without undertaking a large number of costly wind tunnel tests presents a unique challenge for the business jet community. The work described here addresses this challenge by assessing the application of modern aircraft optimization tools and computational fluid dynamics to the development of an advanced transonic wing.

A cooperative design effort between NASA Ames Research Center and Learjet Inc. focused on the evolution of a Mach-0.75–0.78 business jet that carries six passengers for 2,800 nautical miles into a configuration capable of carrying eight passengers at Mach numbers up to 0.85. Because of the higher cruise speed and a requirement for a 10% shorter runway, an entirely new wing was required to satisfy the design specifications.

Conceptual aircraft optimization studies were performed using two aircraft synthesis codes coupled



Fig. 1. Learjet model installed in the Ames 11-foot Transonic Wind Tunnel.

with numerical optimization algorithms. These advanced aircraft design tools enabled the development of an entire family of optimum business jets in a couple of months. This family of aircraft illustrated the sensitivity of the aircraft performance and purchase price to changes in the wing shape and the aircraft cruising speed. These optimum sensitivity results enabled the selection of a final configuration

on the basis of a compromise between aircraft performance and development risk. The final configuration selected for transonic testing had a wing sweep of 35 degrees, an average wing thickness-to-chord ratio of 0.10, and a gross wing area of 396 square feet.

A new wing was designed in this study, using numerical optimization and computational fluid dynamics. A quasi-Newton optimization package coupled with a wing-alone full-potential flow solver (R22OPT) was used to design a Mach-0.85 wing with supercritical pressure distributions. Wing-alone optimization results were augmented with trial-and-error design modifications based on full-potential analyses (TranAir) of a wing, fuselage, nacelle, and pylon model. The analyses of this complete aircraft model captured the impact on the wing pressures of nacelles that were located near the wing's trailing edge. In addition to the cruise design condition, constraints on maximum lift, shock-induced separation during high-speed maneuvers, and geometric constraints for ease of manufacturing were considered. An active maximum lift constraint led to a slight

compromise in the wing's cruise performance. The optimization procedure was used to produce a uniform supercritical pressure distribution along the outer 60% of the semispan with just two wing defining sections. This simplifies the manufacturing process without compromising performance.

Both the conceptual and detailed design studies described were completed in less than a year and were used to build the transonic wind tunnel model shown in the figure. Test results from the Ames 11- by 11-Foot Transonic Wind Tunnel are in good agreement with the predicted wing pressure distributions. However, interference drag caused by fuselage, nacelle, pylon, and wind tunnel mounting remains an issue for this concept. These results demonstrate the success of the wing-alone optimization used in this study and the need to develop an aerodynamic optimization tool that is capable of considering a model of an entire airplane.

**Ames-Moffett contact: J. Gallman/M. Madson
(415) 604-6266/3621**

Headquarters program office: OA

Linear Stability Transition Prediction in Supersonic Flow

Joseph A. Garcia, Eugene L. Tu

The Supersonic Laminar Flow Control (SLFC) Program is one of the key elements in the development of the next generation of high-speed civil transports. Extending the region of laminar flow over an aircraft will increase range, payload, and altitude capabilities as well as lower fuel requirements, skin temperature, and overall cost.

Increasing the extent of laminar flow is equivalent to delaying boundary layer transition, which can be done by passive or active techniques. Passive techniques are those means of altering the boundary layer flow through normal aerodynamic control parameters (e.g., angle of attack or Reynolds number). Active techniques involve alteration of the flow through outside, applied means such as wall suction and heat transfer.

The compressible stability analysis code (COSAL), which uses linear stability, was used to measure the disturbances in the boundary layer in order to predict transition. The mean flow is predicted using computational fluid dynamics and then processed through a boundary layer code to produce the needed velocity profiles. Using this methodology, a parametric study was conducted on a generic swept wing (NACA 64A010 airfoil section) at supersonic speed to investigate the effects of Reynolds number, angle of attack, and wing sweep. Results of the parametric study show that an increase in angle of attack, for specific Reynolds numbers, can actually delay transition, as shown in the first figure. Therefore, higher lift capability caused by the

increased angle of attack, as well as a reduction in viscous drag because of the delay in transition, is possible for certain flight conditions.

These results can be correlated with the maximum crossflow velocity inside the boundary layer. The second figure shows a plot of the maximum crossflow versus chordwise location (x/c) for angles of attack of 0, 5, and 10 degrees at a Reynolds number of 6.8 million. Note that for the 0-degree case the transition location in the first figure is predicted at approximately 12% chord. The second figure indicates that near an x/c of 12%, the 0-degree case has a maximum crossflow that is higher than at the angles of attack of 5 and 10 degrees. The correlation here is that as angle of attack increases the maximum crossflow decreases and, therefore, the boundary layer is stabilized and transition moves aft,

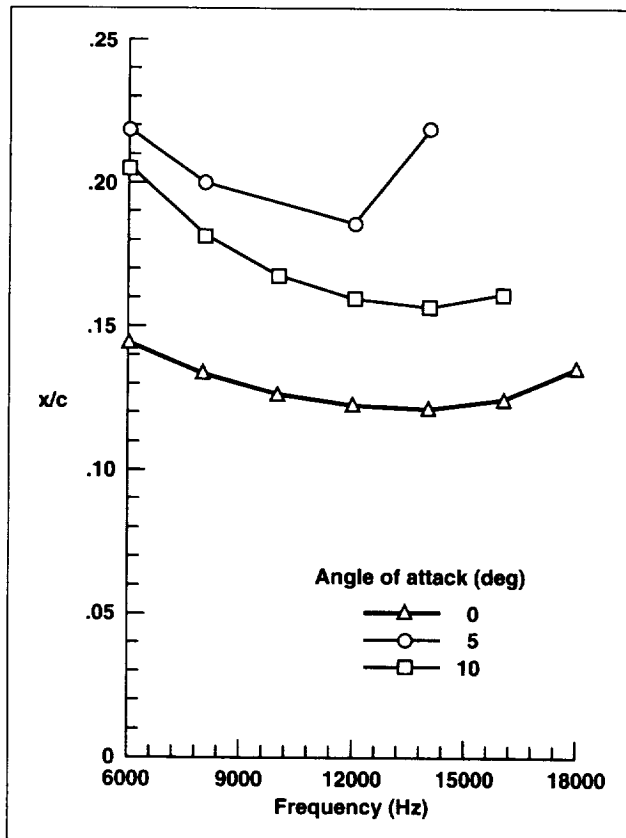


Fig. 1. Effect of angle of attack on transition prediction at 48% semispan for $Re = 6.34$ million and 45-degree sweep.

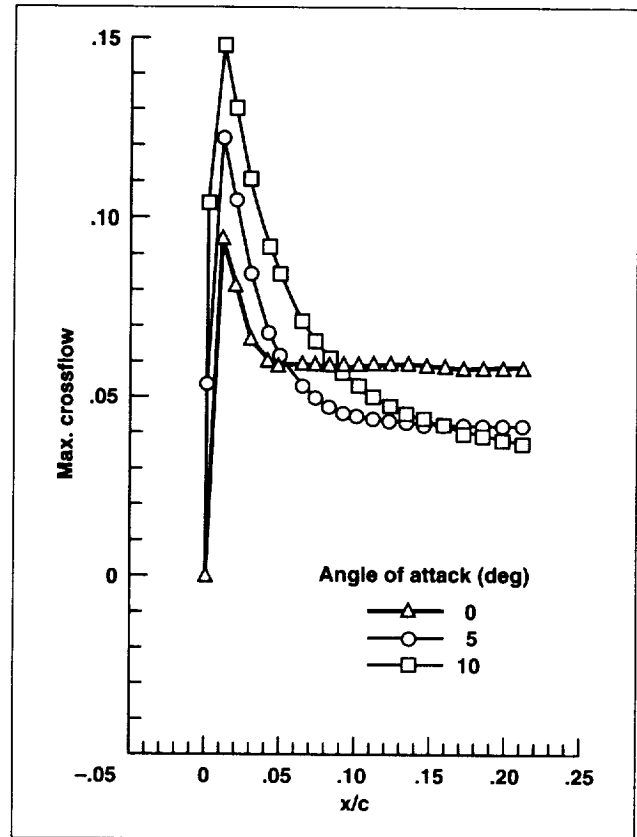


Fig. 2. Maximum crossflow effect due to angle of attack at 48% semispan for $Re = 6.34$ million and 45-degree sweep.

as shown in the first figure. Finally, the opposite trends were found for a 12.7-million-Reynolds-number flow over the same geometry, since the transition at 0 degrees now occurred at an x/c of 3% where the maximum crossflow (second figure) is lower for the 0-degree case and increases with increasing angle of attack. This increase in maximum crossflow results in a destabilization of the boundary layer and a forward movement in the predicted transition location.

Ames-Moffett contact: J. Garcia
 (415) 604-0614
 Headquarters program office: OA

Tangential Slot Blowing on Rounded and Chined Forebodies

Ken Gee, Roxana M. Greenman, Lewis B. Schiff

Flying in the high-angle-of-attack regime increases the maneuverability of high-performance aircraft. The vortices that form over the forebody and fuselage of an aircraft at high angle of attack create additional lift. However, the vortices can become asymmetrical, differing in strength and position on the forebody, leading to loss of control of the aircraft. In order to take advantage of high-angle-of-attack flight, methods need to be developed to control the flow asymmetries that develop. One such method is tangential slot blowing.

Tangential slot blowing ejects air into the flow field tangential to the surface through a thin slot located on the nose of an aircraft. The thin jet of air alters the flow field over the forebody, creating a side force and yawing moment that can be used to control the aircraft. The asymmetries in the flow field can be controlled by altering the amount of air ejected through the slot. However, for such a system to be used effectively, the effects of tangential slot blowing on the flow field must be thoroughly understood.

Computational fluid dynamics is used to study forebody tangential slot blowing on both rounded and chined forebodies. Rounded forebodies are used in current-generation high-performance aircraft, whereas chined forebodies are being studied for use in future aircraft designs. Over the past year, a numerical study has been carried out to understand the effects of free-stream Mach number and blowing rate on the amount of yawing moment produced on a rounded forebody. A second study investigated the application of blowing on chined forebodies at various angles of attack, blowing rates, and slot locations.

Since high-performance aircraft can maneuver over a range of free-stream Mach numbers, any system providing yawing moment to control the aircraft must also operate throughout this Mach number range. The first figure compares the yawing moment obtained at various mass flow ratios (the ratio of the mass flow rate of the jet and a reference mass flow rate based on free-stream values) for three free-stream Mach numbers. The data indicate

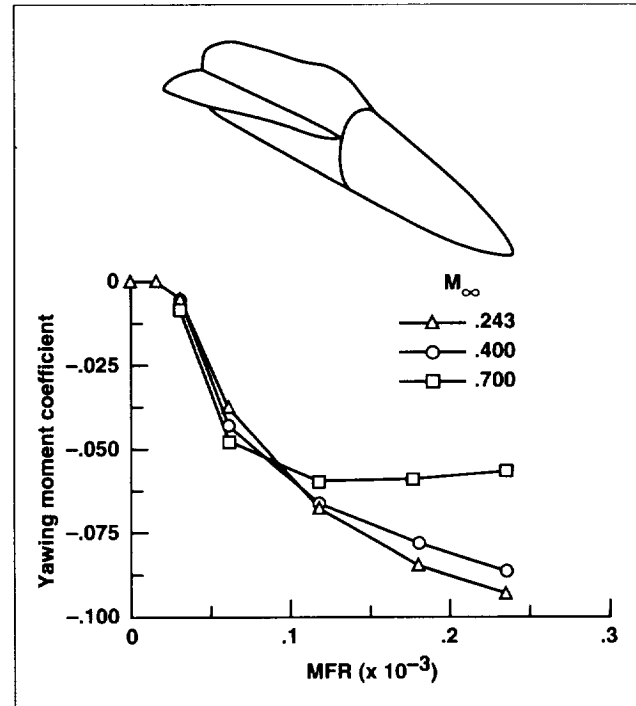


Fig. 1. Comparison of yawing moment and mass flow ratio at three free-stream Mach numbers on a rounded forebody.

that tangential slot blowing remains effective over this Mach number range and that significant levels of yawing moment can be obtained at low blowing rates.

The sharp corners of a chined forebody fix the separation location of the shear layer which forms the vortices over the forebody. Since forebody tangential slot blowing alters the separation line and the vortex location, the effects of blowing on a chined forebody will differ from those on a rounded forebody, where the separation location can vary. The second figure shows a comparison of the computational and experimental data obtained from the investigation of blowing on a chined forebody. The computational results agree well with the experimental data, and

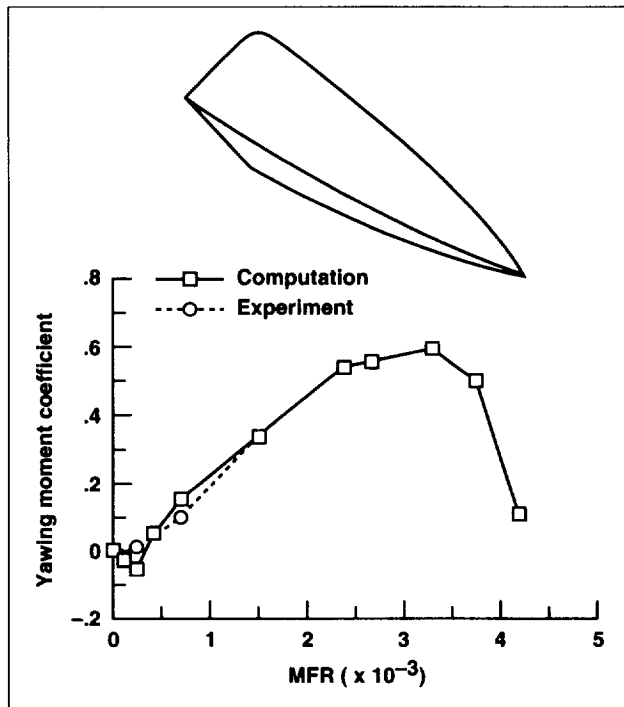


Fig. 2. Comparison of computational and experimental yawing moment and mass flow ratio on a chined forebody.

indicate that blowing is effective on chined forebodies in generating yawing moment. As was the case with the rounded forebody, high blowing rates lead to a reduction of the yawing moment as a result of early separation of the jet.

These are two examples of the data obtained from the computational investigations. Additional information has been obtained concerning the behavior of the flow field, the effect of blowing on top of and below the chine, and the effect of the location of the slot along the forebody. The results of these investigations will prove useful to aircraft designers who are developing aircraft to fly in the high-angle-of-attack regime. The data bases generated by the computational studies indicate that forebody tangential slot blowing can be successfully applied to current and future aircraft designs.

Ames-Moffett contact: K. Gee
 (415) 604-4491
 Headquarters program office: OA

HSCT Wing-Body Aeroelasticity Computations Using Parallel Computers

Guru P. Guruswamy, Chansup Byun

This work is being done in connection with the development of efficient computational aeroelastic tools for high-speed civil transport (HSCT) and advanced subsonic transport (AST) using state-of-the-art parallel computers. The finite-difference-based three-dimensional Euler equations of motion coupled with the finite-element plate/shell structural equations of motion are solved by using a time-accurate numerical integration scheme with configuration-adaptive dynamic grids. A domain decomposition method suitable for parallel computers is used. In this method, the computational domain is divided into fluids and structural domains. The information

between domains is communicated using a robust grid-point (fluid) to element (structural) approach. The fluid domain is solved in parallel with the structural domain in separate cubes (groups of processors). Within each domain (cube), computations are also performed in parallel.

Using the above approach, a new version of the computer code ENSAERO that solves the Euler equations simultaneously with the finite-element structural equations of motion has been developed on the Intel iPSC/860 computer and demonstrated for the Boeing HSCT-1807 wing-body model shown in

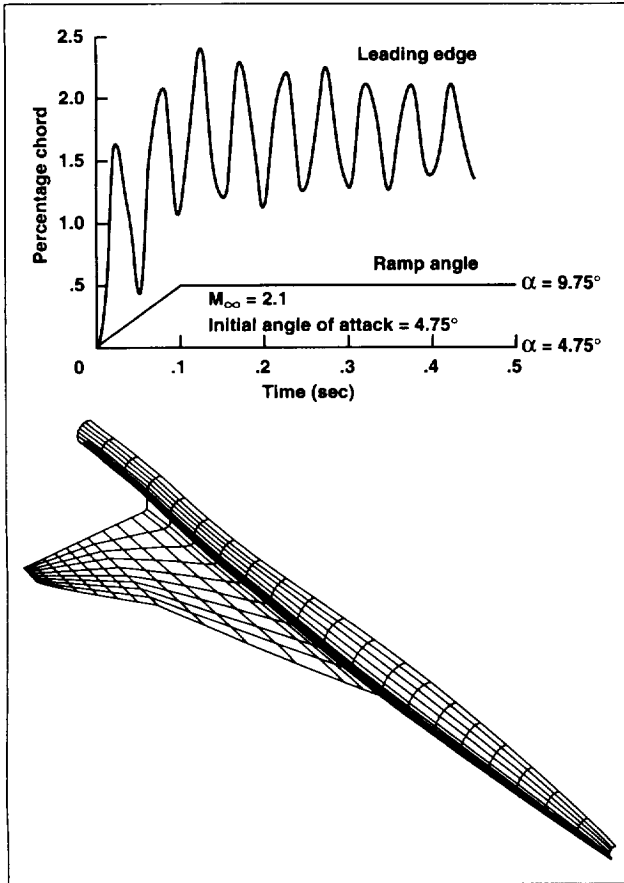


Fig. 1. Aeroelastic response for Boeing HSCT-1807 model.

the figure. The flow is modeled using H-O-type grid topology using 250,000 grid points. The structures of the wing and body are modeled using plate and shell elements. This results in a structural matrix equation with 1,641 degrees of freedom. The fluids part of ENSAERO, including the moving grid, is computed in a cube of 32 processors; the finite-element structural domain is computed in a cube using 8 processors. A typical aeroelastic response, shown in the figure, required about 20 CPU hours. The same computation requires 8 hours on the Cray-C90 computer. The Intel iPSC/860 computer performed at an efficiency of about 10% for this practical problem.

The successful implementation of ENSAERO with finite-element structures on the Intel is a major stepping-stone in the development of general-purpose computer codes to solve fluid/structure interaction problems of HSCT and AST configurations on parallel computers.

Ames-Moffett contact: G. Guruswamy
(415) 604-6329
Headquarters program office: OA

Transonic Flutter Boundary Computation for an AST Wing

Guru P. Guruswamy

There is a continuous effort to improve the performance of subsonic transport aircraft. An attempt is being made to improve the fuel efficiency by extending the flight regime to high subtransonic Mach numbers in order to increase lift-to-drag ratios and flight speeds. To avoid the high drag associated with strong shock waves, advanced subsonic transports (ASTs) require modern wing sections such as supercritical wings that delay the shock wave formation. Early experiments have shown that these advanced wings experience an undesirable reduction

in flutter speed in the transonic regime. This phenomenon, commonly known as "transonic dip," is more pronounced for wings with supercritical airfoils. In order to accurately predict the flutter characteristics, it is necessary to model viscous flows using the Navier-Stokes equations.

Conventional time integration approaches for computing flutter boundary are computationally expensive, particularly when high-fidelity flow equations are used such as the Euler/Navier-Stokes

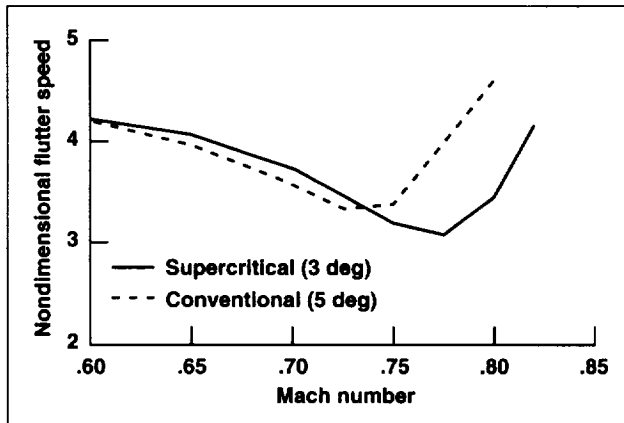


Fig. 1. Comparison of transonic flutter boundaries of supercritical and conventional wings.

equations. Faster methods that can give useful results for preliminary design were investigated with the Ames aeroelastic code ENSAERO. A time-linearized procedure based on the indicial method was developed and incorporated in ENSAERO code to

compute flutter boundaries of wings by using the Navier–Stokes-based unsteady flow computations. The indicial method assumes that the nonlinear aerodynamic forces can be linearly superimposed under small modal perturbations. This assumption is valid in predicting the onset of flutter which is a small perturbation phenomenon. The figure shows the transonic flutter boundary of a Lockheed–Air-Force–NASA–NLR (LANN) wing designed for AST configurations. The LANN wing shows better aerodynamic properties (i.e., higher lift for a given angle of attack) but less desirable aeroelastic properties (lower flutter speed) than the equivalent conventional wing (NACA 64A012). The computation time required is about ten times less than with the previously used time-integration approach. This work will be extended for wing-body-tail configurations and will be useful in the design of AST configurations.

Ames-Moffett contact: G. Guruswamy
(415) 604-6329
Headquarters program office: OA

Separation and Hysteresis of Overexpanded Nozzle Flows

Ching-mao Hung

The objective of this investigation was to numerically study the separation and hysteresis phenomenon of overexpanded nozzle flows. In the testing of the Space Shuttle main engine it was observed that, during the startup and throttle-down processes, a nozzle might lose performance and/or experience tremendous side loads. These problems also frequently occurred during the first or second stage of a launch when the nozzle flow was at the overexpanded condition, i.e., when the ambient pressure was higher than the ideal exit pressure. Ideally, the overexpanded nozzle flow would be supersonic within the entire portion of the nozzle downstream of the throat, and the exit-plane pressure would be uniformly lower than the ambient pressure. However, in the actual flight, complicated shock

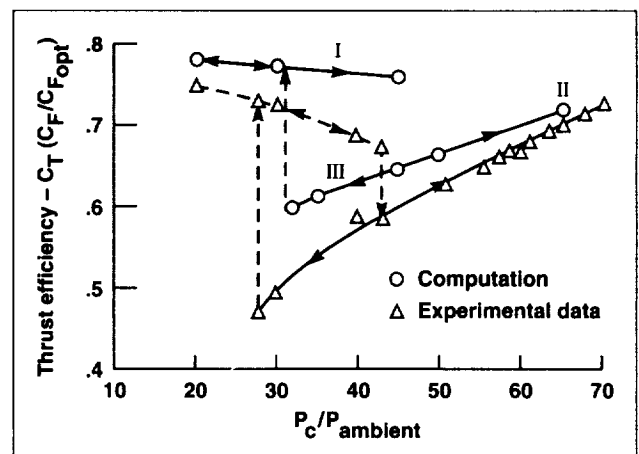


Fig. 1. Thrust efficiency vs. chamber pressure.

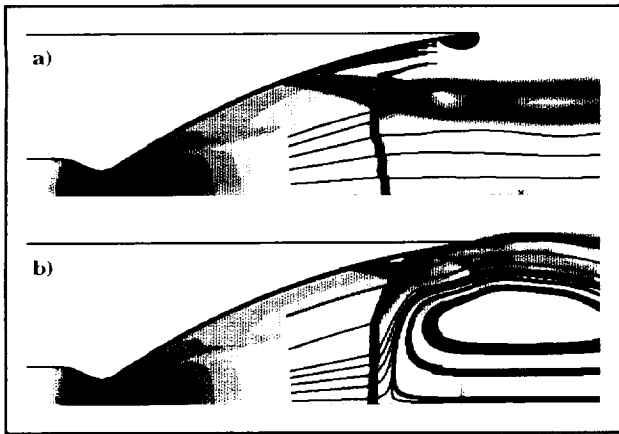


Fig. 2. Instantaneous streamlines and pressure field for $PR = 45$. (a) Startup; (b) throttle-down.

wave and boundary layer interaction could lead to flow separation on the nozzle wall and result in a highly nonuniform flow at the nozzle exit plane. The flow separation could not only affect nozzle performance, but could cause severe damage to the structure.

The equations solved were the unsteady, axisymmetric, Reynolds-averaged, compressible Navier–Stokes equations, with an algebraic turbulence model used for closure. A time-accurate Navier–Stokes solver was employed to compute the flows through a 1/16-scale nozzle of a J-2S rocket engine with an area ratio of 39.6, a nozzle length of 87.72 inches, and a throat radius of 6.1 inches. (The J-2S rocket engine was a precursor of the Space Shuttle main engine.) The ratio of the chamber total pressure to ambient pressure (PR) was at various levels between 20 and 65. Based on the inviscid one-dimensional nozzle analysis for an area ratio of 39.6, the so-called overexpanded nozzle flow ranged from $PR = 1030$ at the design condition to $PR = 28$ at which an internal shock is standing right at the exit plane. The flow structures of the startup and throttle-down processes were investigated. During the impulsive startup process, features of the Mach disk, separation shock, Mach stem, vortex core, contact surface, slipstream, initial shock front, and shocklet were observed. The overall computed wall pressure agreed well with the experimental data, and the

points of separation were well predicted for all of the cases studied.

Three types of flow structures have been observed in the computation, based on different pressure ratios and processes. The first type (Type I) is a fully separated flow without a vortex behind the Mach disk. The second type (Type II) is a fully separated flow with a vortex behind the Mach disk (but the separated region is very small). The third type (Type III) is a separated flow reattached to the nozzle wall with a vortex behind the Mach disk. The computed thrust efficiency varying with the pressure ratio was compared with the experimental measurements (see first figure). The three types of flow structures were also identified in the corresponding computational results. The overall agreement was encouraging, despite the exact process not being known and despite the use of a simple Baldwin-Lomax turbulence model. The hysteresis phenomenon was observed and two stable solution branches existed. (The upper-end turning point was not well resolved in the computation because of the small jump in thrust efficiency and the possible lack of grid resolution to preserve the vortical structure.) The existence of two quite different solutions at the same pressure ratio is clearly demonstrated in the second figure, which shows the instantaneous streamlines and gray-shaded pressure field for the startup and the throttle-down processes at $PR = 45$. After the startup process, the flow was fully separated and there was no reversed flow behind the Mach disk (Type 1). In the throttle-down processes, the flow was reattached to the nozzle wall, and there was a reversed flow behind the Mach disk (Type III). The reattachment of the flow to the nozzle led to a high-pressure peak on the wall, and the existence of a large reversed-flow region with a trapped vortical structure behind the Mach disk reduced thrust efficiency more than 12%. A continuation of the present work will be an investigation of the more realistic three-dimensional flow structure.

Ames-Moffett contact: C. Hung

(415) 604-5072

Headquarters program office: OA

Reduction of Helicopter BVI Noise, Vibration, and Power Consumption Through Individual Blade Control

Steven A. Jacklin, Stephen M. Swanson

A fundamental limitation of conventional helicopter control systems for rotors with four (or more) blades is that the fixed-frame control system cannot be used to independently control the pitch of each blade. This shortcoming limits the degrees of freedom available for improving rotor performance and reducing rotorcraft vibrations and noise.

For this reason, ZF Luftfahrttechnik, GmbH (Germany), developed the first set of high-bandwidth servo-actuators for the rotating system.

These servo-actuators were designed to replace the conventional pitchlinks of the rotor system so that the pitch of each blade could be controlled independently. The general arrangement of the individual blade control (IBC) actuators in the rotor hub is shown in the first figure.

Two wind tunnel tests were conducted in the NASA Ames 40- by 80-Foot Wind Tunnel to evaluate the potential of this IBC system to improve rotor performance, to reduce blade-vortex interaction (BVI) noise, and to alleviate helicopter vibrations. The wind tunnel test was an international collaborative effort between the NASA/U.S. Army Aeroflight-dynamics Directorate at Ames Research Center; ZF Luftfahrttechnik, GmbH; Eurocopter Deutschland, GmbH; and the German Aerospace Laboratory (DLR). It was conducted under the auspices of the U.S./German Memorandum of Understanding on Rotorcraft Aeromechanics. The rotor system used for the test was a full-scale MBB BO 105 rotor system and was tested on the Ames Rotor Test Apparatus (RTA). An extensive amount of measurement information was acquired for each IBC data point. These data include rotor performance, static and dynamic hub forces and moments, rotor loads, control loads, inboard and outboard blade pitch motion, and BVI noise.

The data indicated that significant (80%) simultaneous reductions in both BVI noise and hub vibrations could be obtained using multiharmonic IBC inputs at the critical descent (terminal approach) condition. Although the wind tunnel data showed the remarkable result that nearly all single-frequency

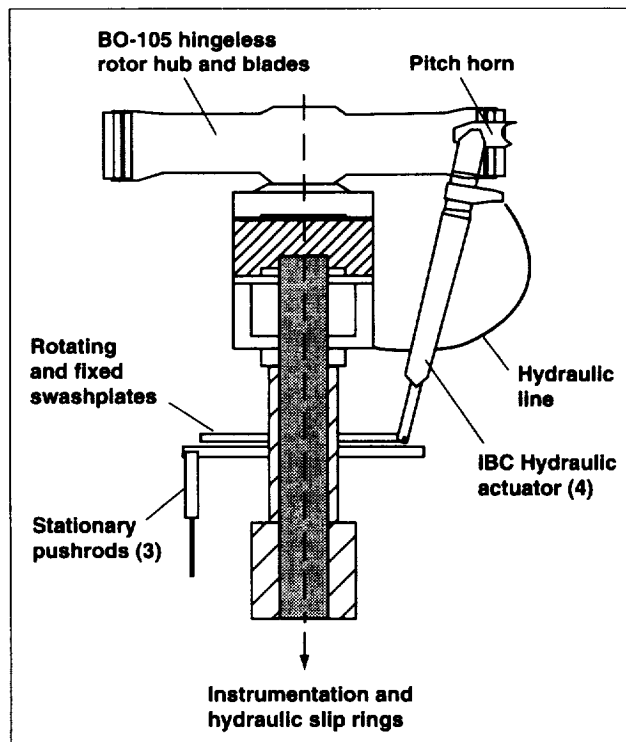


Fig. 1. General placement of IBC actuators in the rotor hub.

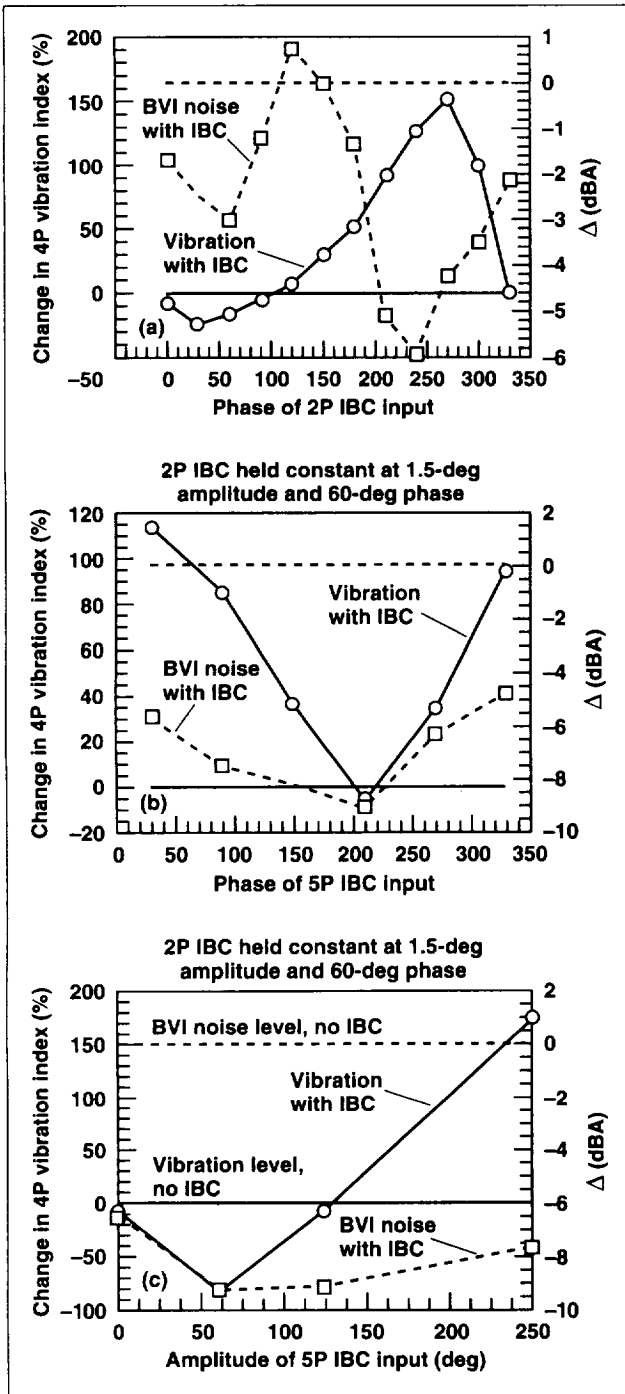


Fig. 2. Changes in vibration and BVI noise with IBC at the 43-knot terminal approach descent condition. (a) Effect of 1.5-degree 2/rev IBC; (b) effect of adding 0.5-degree 5/rev IBC; (c) effect of 5/rev IBC amplitude at 210-degree phase angle.

(sinusoidal) IBC inputs (up to six/revolution, or 6/rev) were capable of reducing BVI noise, only a few IBC inputs could significantly reduce both noise and vibration at the same time. The best results were obtained using multiharmonic IBC input. The second figure shows that for 1.5-degree amplitude of 2/rev IBC input, there were two phase angles of IBC input that yielded BVI noise reduction minima. In the first plot, the percent change in vibration and the change in BVI noise are plotted together as a function of the IBC input phase angle. One of these phase angles increased the 4/rev hub vibrations, the other phase angle decreased them. As shown in the second plot, if the 2/rev IBC input is held at the phase angle that reduces vibrations, the noise especially, and also the vibration, can be somewhat further reduced by adding 0.5-degree 5/rev input phased at about 120 degrees. The third plot shows that by reducing the amplitude of the 5/rev input to 0.25 degree, the 4/rev hub vibrations were reduced by 83%, and that the BVI noise was reduced by 9 decibels. The noise reduction caused the BVI noise pressure to drop by about 80%. Simultaneous noise and vibration reductions of this magnitude have never before been achieved in a flight or wind tunnel test program.

The data also showed that performance improvements could be obtained using 2/rev input at high-speed forward flight conditions. At 170 and 190 knots, ± 2.5 -degree-amplitude, 2/rev IBC was shown to reduce the required shaft power as much as 7% at the most favorable IBC input phase angle. No performance improvement was observed at airspeeds of 130 knots and below using IBC.

Ames-Moffett contact: S. Jacklin
 (415) 604-4567
 Headquarters program office: OA

Oblique All-Wing Supersonic Transport

Robert A. Kennelly, Jr.

The oblique all-wing, a radical alternative to conventional supersonic transport concepts, has been proposed on several occasions but never subjected to detailed scrutiny. The work described here is the final step of an interdisciplinary study of the concept which sought to determine the trimmed cruise lift-to-drag ratio obtainable for a complete airplane configuration. The research team, from NASA Ames Research Center, Boeing Commercial Airplane Group, and McDonnell Douglas Aircraft, studied passenger accommodations, airport compatibility, structures, weight and balance, stability and control, propulsion, and aerodynamics. In the case of such a novel configuration, it is understood that the team's conclusions are tentative, but the resulting design was felt to be of sufficient validity and interest to warrant a wind tunnel test program and detailed computational analysis.

A 1.8%-scale, blade-mounted model of the oblique all-wing concept was constructed and tested in the Ames 9- by 7-Foot Supersonic Wind Tunnel during June and July 1994. An impressionistic view of the wind tunnel model is shown in the figure. The test conditions included Mach numbers of 1.56 to 1.80, unit Reynolds numbers of 1.0 to 4.5 million/foot, and angles of attack of 0 to 6 degrees. Because this work was concerned primarily with cruise performance, only a single sweep angle of 68 degrees was tested. Force and moment data were obtained from a specially designed "flat" balance, and surface pressure data were obtained using pressure sensitive paint. A coordinated series of Navier-Stokes calculations for the bare wing and full configuration, with and without blade support, was performed prior to the test. The quality of agreement obtained between the calculations and the test results, observed in both surface pressure comparisons and in the force and moment data, was excellent.

A new scheme for interacting with wind tunnel users is under development at Ames, and a prototype



Fig. 1. Wind tunnel model of the supersonic oblique all-wing configuration.

application of this digital-network-based technology was successfully demonstrated during the test. A three-way video teleconference was established among the interested parties at Ames, Boeing Commercial Airplane Company (in Seattle, Washington), and McDonnell Douglas (in Long Beach, California) to keep each other apprised of test progress and to allow feedback on results. The conferencing software ("InPerson," Silicon Graphics Computer Systems, Mountain View, California) featured "live" audio, video, and shared access to a whiteboard, and was supplemented by near-real-time transfers of reduced data in a format suitable for plotting. Although some network isolation safeguards were required, the network connection employed already-existing NASA links to the two companies. This form of remote collaboration shows great promise; it was convenient, effective, and inexpensive.

**Ames-Moffett contact: R. Kennelly
(415) 604-5860
Headquarters program office: OA**

Optimum Design of High-Speed Proprotors

Sesi Kottapalli, Thomas R. McCarthy, Aditi Chattopadhyay, Sen Zhang

High-speed proprotor aircraft have continued to receive substantial attention. These rotorcraft are capable of operating with fixed-wing-like efficiencies in high-speed cruise flight while maintaining the lifting capabilities of the helicopter in hovering flight. The design of such rotorcraft involves conflicting requirements. For example, in high-speed cruise

(350 to 450 knots) the tip Mach number is an important parameter which can be addressed through a reduction in the rotor tip speed and/or blade thickness and the introduction of blade sweep. These design considerations may affect hover performance, aeroelastic stability of the blade, and other characteristics.

Proprotor research has involved formal numerical optimization techniques in the analytical treatment of the design trade-offs associated with the optimization of such high-speed rotorcraft. This research has included the selection of blade aerodynamic characteristics in order to improve the hover figure of merit (FM) and the high-speed cruise propulsive efficiency (η). The following blade aerodynamic parameters are currently included in this optimization procedure: chord, twist, thickness, and camber. The figure shows a sample of the optimization results obtained within the present analytical framework. The optimization was performed for the following flight modes: hover only, cruise only, and hover and cruise simultaneously. The figure shows that a single objective function formulation results in significant performance improvements: 9.2% in FM and 8.7% in η . In the multilevel objective formulation, the improvements are also significant (7.7% in FM and 3.7% in η), although not as large as in the single-objective function formulation.

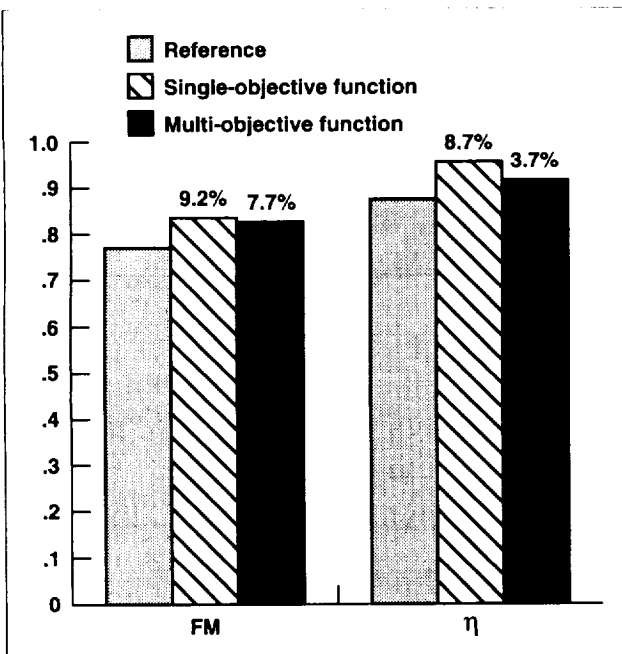


Fig. 1. Summary results from proprotor optimization study. FM is the figure of merit; η is the propulsive efficiency. (XV-15 configuration, blade radius = 12.5 feet, cruise speed = 300 knots, cruise thrust = 774 pounds, cruise rotational speed = 421 rpm, aircraft weight = 13,000 pounds, hover thrust = 7,280 pounds, hover rotational speed = 570 rpm.)

Thomas R. McCarthy, Aditi Chattopadhyay, and Sen Zhang are at Arizona State University, Tempe, Arizona.

Ames-Moffett contact: S. Kottapalli
(415) 604-3092
Headquarters program office: OA

Rotor Hub Loads Research: Dynamically Tuned Blade Pitch Links

Sesi Kottapalli, Judah Milgram, Inderjit Chopra

The dynamically tuned blade pitch link is a passive vibration device in which the main rotor blade pitch link (also commonly referred to as a push rod) is replaced by a spring/damper element. A sample study was conducted using an articulated rotor blade, the S-76. This research was performed using the analytical rotorcraft code UMARC (University of Maryland Advanced Rotor Code).

It was found after extensive study that pushrod damping in combination with reduced pushrod stiffness resulted in significant reductions in 4/rev fixed-system hub loads (for example, 25% for the longitudinal inplane shear (see figure)). At the same time, the 1/rev pushrod loads increased by about 50%. Note that the pushrod must be redesigned in any case to

accommodate the additional damping. This design process will have to include resizing, keeping in mind fatigue considerations that account for the increased 1/rev loads. In general, the results show that a combination of damping and reduced stiffness was required to yield any improvements in hub loads.

The reductions in hub loads signify that the dynamically tuned blade pitch link is a promising concept.

Judah Milgram and Inderjit Chopra are at the University of Maryland, College Park, Maryland.

Ames-Moffett contact: S. Kottapalli
(415) 604-3092

Headquarters program office: Funded by DDF

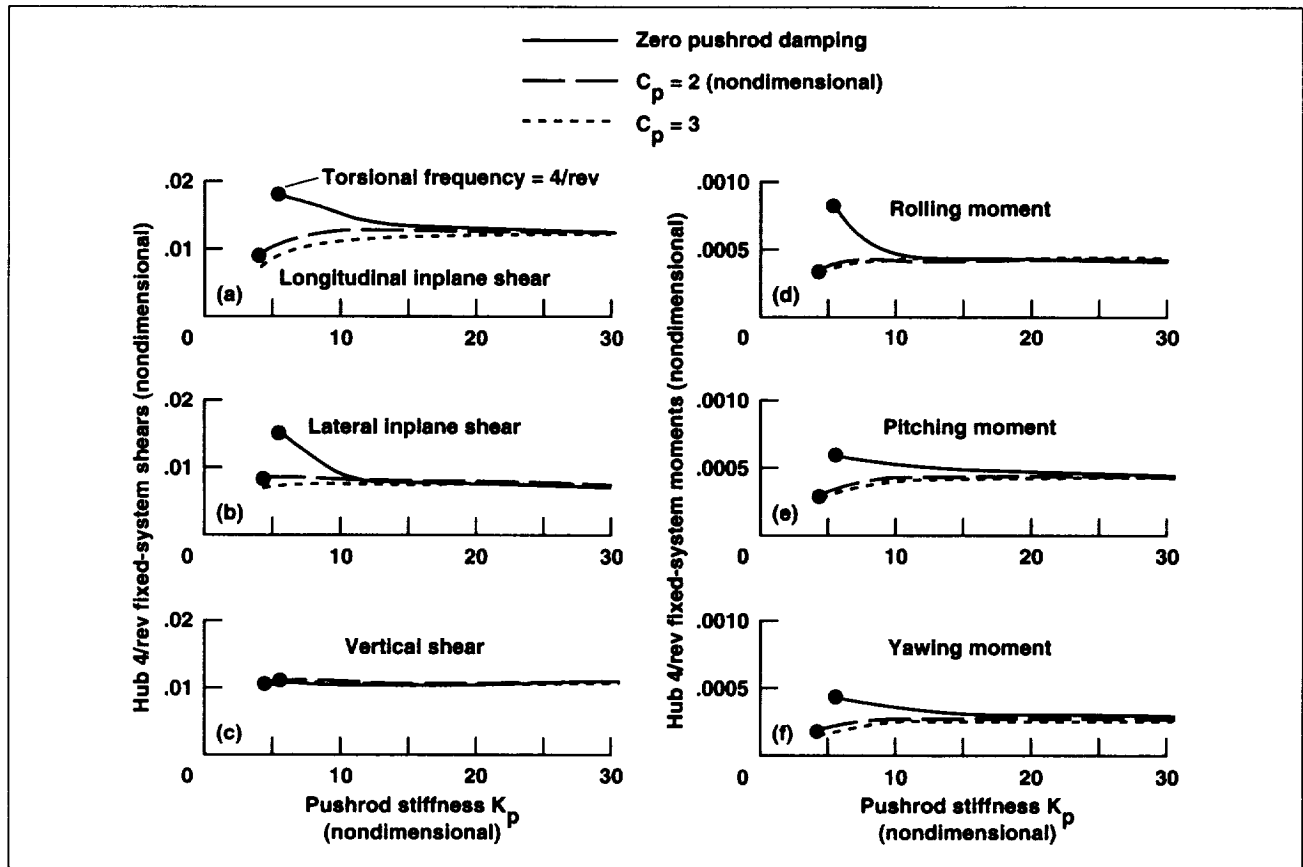


Fig. 1. Variations in fixed-system hub loads resulting from parametric changes in pushrod stiffness and damping; advance ratio = 0.38, thrust coefficient divided by solidity = 0.80, shaft angle = 5 deg. Pushrod stiffness and damping are nondimensionalized by a reference mass, rotor speed, and blade radius.

Code Validation for Supersonic Flows

Scott L. Lawrence

To support industry feasibility studies and technology development for the High-Speed-Civil Transport (HSCT), NASA has undertaken the High-Speed Research Program (HSRP), a two-phase, ten-year program. The first phase (1989–1995) addresses environmental issues such as community noise, ozone depletion, and sonic boom. The second phase (1994–1999) emphasizes technology development and design studies.

Included in the second phase is the development and validation of computational tools to include nonlinear effects in the aerodynamic design of the vehicle shape. Euler (inviscid) methods are currently being developed which, when coupled with standard optimization methods, are proving successful at improving aerodynamic characteristics of typical supersonic transport configurations. In these methods, viscous boundary layer effects are included through a simple flat-plate skin friction model. Navier–Stokes codes, in which the viscous terms are included, are therefore valuable tools in the verification of improvements predicted by the optimization methods, but only if their accuracy has been well established. In order to establish the necessary

confidence in these numerical flow simulations, prospective codes must be applied to realistic configurations, and results must be compared with experimental data.

The objective of this effort is to demonstrate the utility of sophisticated Navier–Stokes solution methods in understanding the fluid dynamics issues involved in mated wing/body/nacelle/diverter configurations. The emphasis of the research is on understanding the Reynolds number scaling effects at supersonic cruise conditions. For the present objectives, emphasis is on flow solver accuracy and geometric fidelity. Ultimately, however, the validated codes and processes are to be employed within an optimization framework to guide the design of improved propulsion–airframe systems. For this purpose, efficiency is a primary concern.

Parabolized Navier–Stokes solutions for flow over a supersonic wing-body configuration at several angles of attack were computed using the upwind parabolized Navier–Stokes flow solver code (UPS). In the figure, computed pressure levels on the surface at supersonic cruise conditions are shown in comparison with wind tunnel data. Predicted drag was

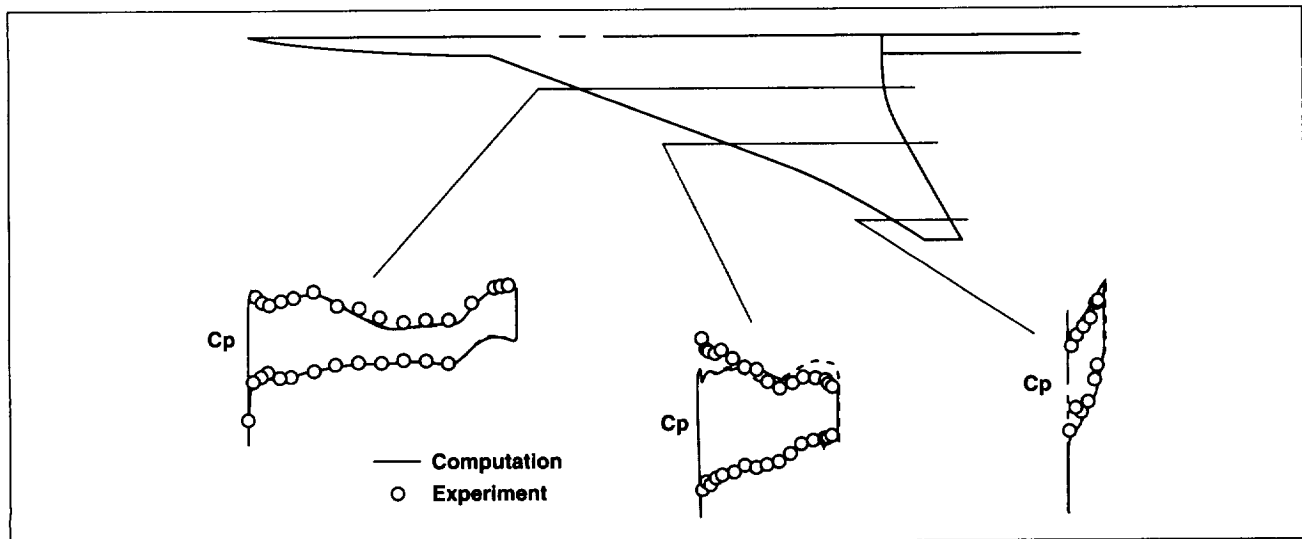


Fig. 1. Comparison of computed surface pressures with those obtained by experiment.

obtained through surface pressure and skin friction integration. At each angle of attack, predicted drag agrees with measured drag to within 0.0002.

The full Navier–Stokes code, OVERFLOW, is in the process of being validated for integrated propulsion/airframe flow fields. Initially, flow past a flat plate/nacelle/diverter configuration at supersonic cruise conditions will be simulated. The purpose of this study is to establish computational grid and

turbulence model requirements for accurate simulation of this type of flow field. The results will also be useful in determining the suitability of the more efficient parabolized Navier–Stokes approach for these flows.

Ames-Moffett contact: S. Lawrence
(415) 604-4050
Headquarters program office: OA

Higher Harmonic Optimal Controller to Minimize Helicopter Vibration

Jane Anne Leyland

Three methods to solve the helicopter vibration control problem were identified and implemented in a stand-alone code. These methods determine the optimal control vector which minimizes the vibration metric subject to constraints at discrete time points. The methods differ from the commonly used non-optimal constraint penalty methods such as those employed by conventional controllers (e.g., the Deterministic, Cautious, and Dual Controllers) in that the constraints are handled as actual constraints to an optimization problem rather than just as additional terms in the performance index. The first method is to use a nonlinear programming algorithm to solve the problem directly. The second method is to solve the full set of nonlinear equations that define the necessary conditions for optimality. The third method is to solve each of the possible reduced sets of equations defining the necessary conditions for optimality when the constraints are preselected to be either active or inactive, and then to simply select the best solution. The effects of maneuvers and aeroelasticity on the systems matrix are modeled by using a “proportional navigation” type pseudo-random, pseudo-row-dependency scheme to define the systems matrix.

Cases run to date indicate that the first method of solution (direct optimization of the control vector subject to constraints, here referred to as the Optimal Controller) is reliable, robust, and the easiest to use. The algorithm employed for direct optimization is particularly suitable for this problem since, although

it is designed to solve the general nonlinear programming problem, it employs a successive quadratic programming method to solve this more general problem. Because this method initially estimates the Hessian and then updates it successively as the quadratic solutions are updated, and because the only difference between the problem of interest and the standard quadratic programming problem is that the constraints are quadratic rather than linear, the Hessian is invariant to the optimization process and is analytically known. Correspondingly, modifications to this successive quadratic programming

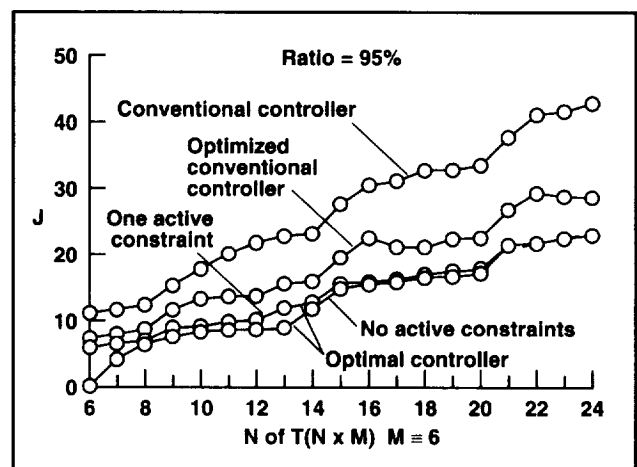


Fig. 1. Performance index (J) vs. number of measurements (N) for 95% row duplication.

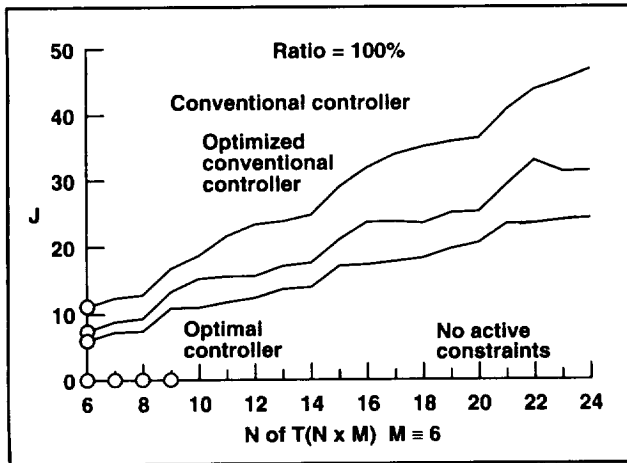


Fig. 2. Performance index (J) vs. number of measurements (N) for 100% row duplication.

method that will enhance its reliability, overall robustness, and speed appear feasible for this particular problem.

The second and third methods successfully solved systems of nonlinear equations that define the necessary conditions for optimality. These methods do not appear practical for use by themselves, however, because there exist perhaps an infinite number of solutions to these equations and there is no real way to recognize the solution yielding the global minimum or to even guarantee convergence to this solution if it were known. The second method can, however, be used to verify that the necessary conditions are satisfied when the first method is employed. The use of the second method for verification after the first method obtains a solution was made an option in the stand-alone code.

The Deterministic Controller was added to the stand-alone code to provide a convenient means of comparison. Options to directly optimize the weighting coefficients of the Deterministic Controller either

in a specified ratio to one another (the option used by the controller referred to here as the Conventional Controller) or individually (the option used by the controller referred to here as the Optimized Conventional Controller) while satisfying the constraints were provided as a means to obtain a more representative and meaningful comparison of controllers and to help access the relative merit of solving the actual optimization problem. Occasionally a mathematical conditioning problem occurs with the direct optimization of the individual weighting coefficients of the Optimized Conventional Controller which causes a numerical overflow and subsequent termination caused by error. This occurs when the optimization process converges to a "solution" that has a harmonic phase angle with an $n\pi/2$ value. In this case, the value of one of the associated harmonic coefficients approaches zero whereas the value of the associated weighting coefficient has no finite upper bound.

Cases run to date (see figures) indicate that the performance (that is, the reduction of the vibration metric) of the Optimal Controller was superior to that of both the Conventional and the Optimized Conventional Controllers. In accordance with theory, the Optimal Controller yielded a zero vibration metric for square nonsingular T-Matrices (the case when the number of measurements equals the number of controls with no redundancy). As expected, the Optimized Conventional Controller was superior to the Conventional Controller in performance, but inferior to the Optimal Controller for nearly all cases. The performance gap was widest for square nonsingular T-Matrices.

**Ames-Moffett contact: J. Leyland
(415) 604-4750**

Headquarters program office: OA

Tiltrotor Aeroacoustic Model Research Program

Paul Loschke

Predicting and improving the aeroacoustic characteristics of tiltrotor aircraft is critical to their successful introduction as short-haul civil transport. To accomplish this, moderate- to large-scale wind tunnel testing of current-generation tiltrotor technology is required. This testing will provide the data necessary to verify aeroacoustic prediction methodologies and to demonstrate advanced tiltrotor technologies.

NASA Ames and Langley and the U.S. Army have been jointly conducting a tiltrotor aeroacoustic research program. The cornerstone of this research program is the development of an approximately 1/4-scale V-22 Tiltrotor Aeroacoustic Model (TRAM). This model is to be used as a testbed for wind tunnel testing at several research facilities, including the Duits-Nederlandse Windtunnel (DNW) in The Netherlands, the National Full-Scale Aerodynamics Complex (NFAC) at Ames Research Center, and the 14- by 22-Foot Subsonic Wind Tunnel at Langley Research Center.

The TRAM will have the capability of being configured as two different test installations: an isolated rotor test stand and the full-span, dual-rotor model. The TRAM Isolated Rotor configuration Critical Design Review (CDR) was conducted in June 1994. In addition to the Ames TRAM project team, a broad-based group of industry and government

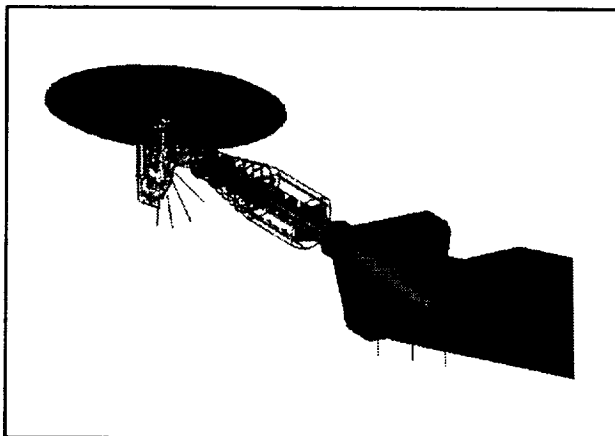


Fig. 1. Computer-generated view of TRAM isolated rotor in the Duits-Nederlandse Windtunnel.

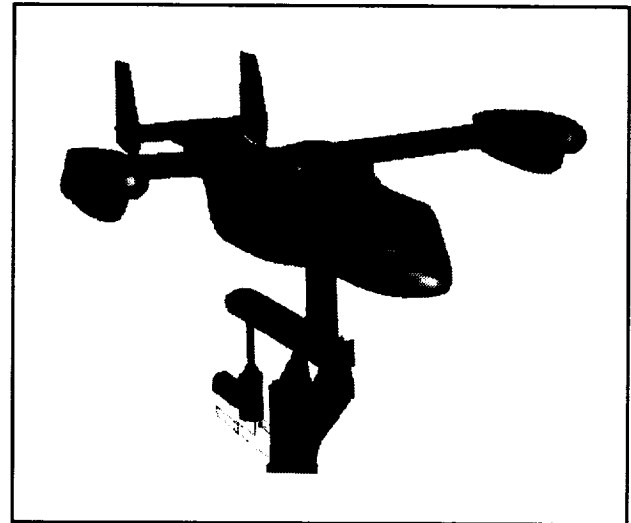


Fig. 2. Computer-generated view of TRAM full-span model in the Ames National Full-Scale Aerodynamics Complex.

reviewers participated in the CDR. Fabrication of the isolated rotor configuration began in July 1994 and will be completed by January 1995. The current plan for the joint research program calls for isolated rotor testing in the NFAC in April 1995 and in the DNW by October 1995 (see first figure). Full-span testing in the NFAC is currently planned for fiscal year 1997 (see second figure).

The TRAM test stand is also a key test platform for the Short-Haul, Civil Tiltrotor (SHCT) element of the NASA Advanced Subsonic Transport initiative. Current plans for the SHCT program include the separate testing of advanced, quiet, efficient propellers from Boeing and Sikorsky on both the isolated and the full-span model test stands. Advanced propeller testing on the isolated rotor test stand will begin in fiscal year 1996. Discussions are under way with industry to insure compatibility of their small-scale rotor designs with the TRAM hardware.

Ames-Moffett contact: P. Loschke
(415) 604-6576

Headquarters program office: OA

Software Utilities for Surface Modeling

Catherine M. Maksymiuk

Computational Fluid Dynamics (CFD) is the computer simulation of airflow. It has become an effective tool for aircraft design because computer-based analysis is much cheaper and faster than flight testing of full-size airplanes or wind tunnel testing of smaller-scale models. The first step in any computer simulation is to obtain an accurate representation of the aircraft; this activity is known as "surface modeling." Surface models are typically created using Computer-Aided Design (CAD) software. To resolve the problem of surface models being represented in many different ways, the CAD industry established the Initial Graphics Exchange Specification (IGES) as a standard format.

IGES is far more complicated than is necessary for CFD models. It contains entities such as labels and tolerances that are irrelevant to CFD analysis. It also contains many redundant geometric entities. To simplify IGES models, a NASA-wide committee recently established a format specifically for CFD. The NASA-IGES format is a subset of IGES that retains less than 10% of the IGES entities. Further geometric redundancy can be eliminated by requiring that all curves and surfaces be represented as nonuniform rational B-splines (NURBS). The NASA-IGES-NURBS-only format thus becomes a compact standard for use by CFD software packages.

Software that takes input in NASA-IGES-NURBS-only format already exists, but CAD packages continue to use only the more unwieldy IGES format. NASA Ames developers created two computer programs to bridge the gap between the two standards. The figure illustrates the flow of data through these programs. The NASA-IGES Translator program

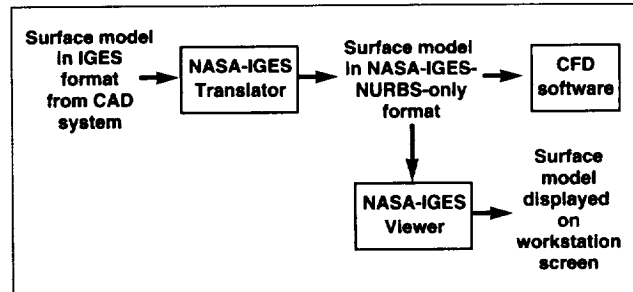


Fig. 1. Data flow through NASA-IGES surface modeling utilities.

deletes irrelevant entries from an IGES file and converts all non-NURB geometric entities to NURBS. Sometimes the conversion can be done so that the NURB entity is an exact representation of the non-NURB entity. In other cases, the conversion is not exact, and the Translator estimates the error incurred. When the deletions and conversions are completed, the Translator produces a surface model in NASA-IGES-NURBS-only format. The NASA-IGES Viewer allows a user to display the model as a graphical image on a workstation. Additional capabilities include displaying multiple models at once; copying, pasting, or deleting entities from and between models; and merging models together.

**Ames-Moffett contact: J. Chou/M. Logan
(415) 604-4351/4494**

Headquarters program office: OA

Triangular Surface Grids

Catherine M. Maksymiuk

Grid generation is an important step in the process of computer simulation of airflow. A grid is a set of points and connecting lines on the surface of an aircraft model and in the space of interest around the model. Generating a grid about a complex aircraft model can be difficult and labor-intensive. One promising technique for automating the grid generation process begins with creating a grid of triangles on the surface of the model. Software has been developed at NASA Ames that improves the generation of triangular surface grids. The USHAGG (Unstructured Shape-Adaptive Grid Generator) computer program uses an automatic method to determine grid point location and has a graphical user interface which makes it easy for nonspecialists to use.

It is of vital importance that a surface grid be an accurate representation of the original model. The automatic method used by the USHAGG program addresses that need directly. Grid points always lie exactly on the original surface, but when the points are connected to form triangles, the triangles do not always conform to the original surface. USHAGG estimates how well the triangle conforms to the surface and adds additional points until the user-specified level of accuracy is achieved. The ultimate accuracy of the simulation also depends on the shape

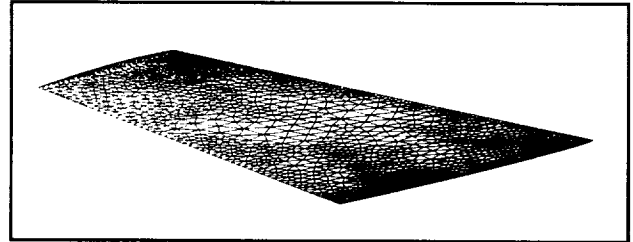


Fig. 1. Triangular surface grid on an airplane wing.

of the triangles; USHAGG can add grid points to improve that aspect of the grid. The figure shows an airplane wing grid generated by USHAGG.

Grid generation software must be easy to use. USHAGG incorporates a graphical user interface that guides a user through the grid generation process. The impact of changes in parameters is immediately evident in the graphical display. The combined grid generator and user interface can serve as a platform for developing enhancements to the basic method.

**Ames-Moffett contact: C. Maksymiuk
(415) 604-3972
Headquarters program office: OA**

Magnetic Flight of a Vehicle

Unmeel Mehta, Goetz Klopfer

A magnetically propelled system that “flies” may lead to revolutionary progress in transportation. The system is off the ground—that is, it flies—because of magnetic lift. This levitation technique requires the system to fly very close to the ground. High-speed magnetic flight (magflight) vehicles glide above their guideways suspended, guided, and propelled by magnetic forces. The possible rationales for magflight studies at NASA are the following: (1) space opportunities are offered through launching Earth-to-orbit systems with magflight-based catapults; (2) aeronautics opportunities for hypersonic research are provided through launching research vehicles with magflight catapults and through the use of magflight test tracks; and (3) commercial opportunity is provided in the possibility of a high-speed, magflight ground transportation system.

Magflight has technical risks associated with vehicle/guideway interactions, guidance and control, and noise issues, which can be addressed only by aerospace technologies. These interaction issues and adverse effects of aerodynamic forces and moments

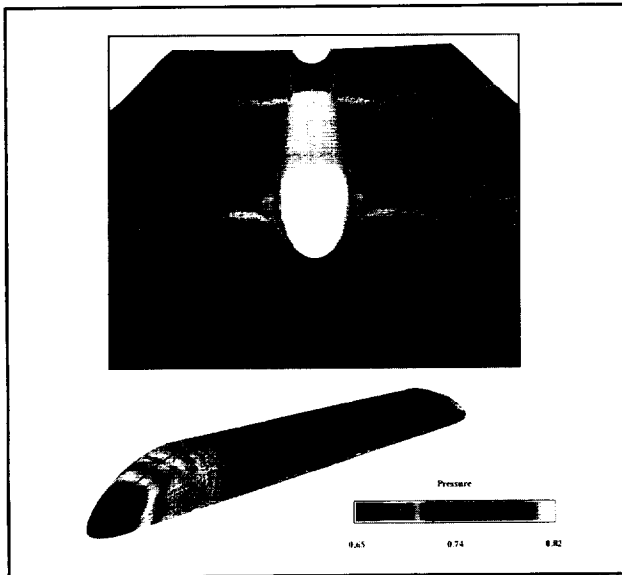


Fig. 1. Pressure contours on the surfaces of guideway and vehicle. (See color plate 4 in Appendix)

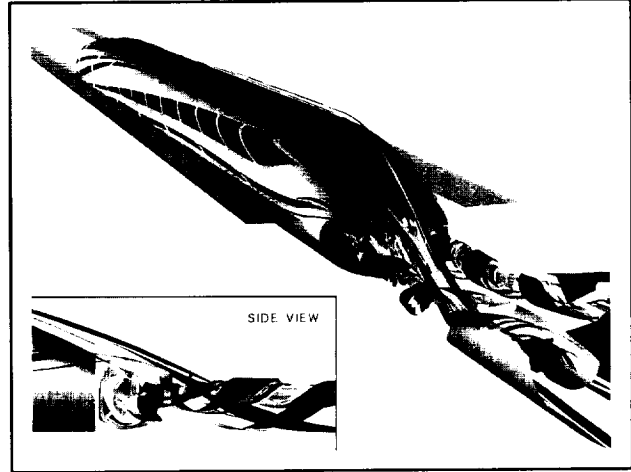


Fig. 2. Stream surfaces emanating from the nose region manifest large streamwise vortices at the base of the vehicle. (See color plate 5 in Appendix)

require state-of-the-art computational fluid dynamics (CFD) tools.

After the completion of the system-concept-definition studies for developing high-speed magnetic levitation (maglev) trains, conducted under the National Maglev Initiative, the Federal Railroad Administration requested that NASA provide aeronautical expertise.

A conceptual magflight vehicle traveling at 300 miles per hour is being considered. It uses a trough-shaped guideway for guidance. A newly developed CFD code is used to solve three-dimensional, Reynolds-averaged, thin-layer Navier–Stokes equations. The first figure shows complex pressure fields on the vehicle surface and the guideway surface. A finding of this study is that the shaping of the base region and of the nose region are equally important in lowering the vehicle drag. The base region of the model investigated contributes the most to drag, because of flow separation and the complex streamwise vortex pattern, as shown in the second figure.

The Headquarters Offices of Aeronautics and of Space Access and Technology are in the process of identifying a compelling need for NASA to become involved with magflight technology. If this need is found to exist, the current study will lead

to a comprehensive investigation of magflight aeronautical issues.

Ames-Moffett contact: U. Mehta

(415) 604-6744

Headquarters program office: OA

Application and Development of Three-Dimensional Cartesian CFD Technology

All aspects of computational fluid dynamics (CFD) are being scrutinized because of the urgent need for dramatic reductions in aircraft design cycle time. Dramatic reductions in the computational aerodynamics portion of the design cycle time will

John E. Melton, Michael J. Aftosmis, Michael D. Wong

most likely come not from increased reliance on user-interactive (and therefore time-expensive) methods, but instead from the use of methods that can be fully automated and incorporated into "black box" solutions. Although tremendous progress has been and is being made with the use of unstructured tetrahedral methods, other unstructured grid approaches are also worthy of investigation. In comparison with tetrahedral methods, three-dimensional (3-D) Cartesian grid approaches are in their infancy, but initial experiences with Cartesian techniques are promising. The goal of this research is the further development of Cartesian methods so that they can become key elements of an automated grid-generation/flow-solution procedure applicable to the Euler analysis of complex aircraft geometries.

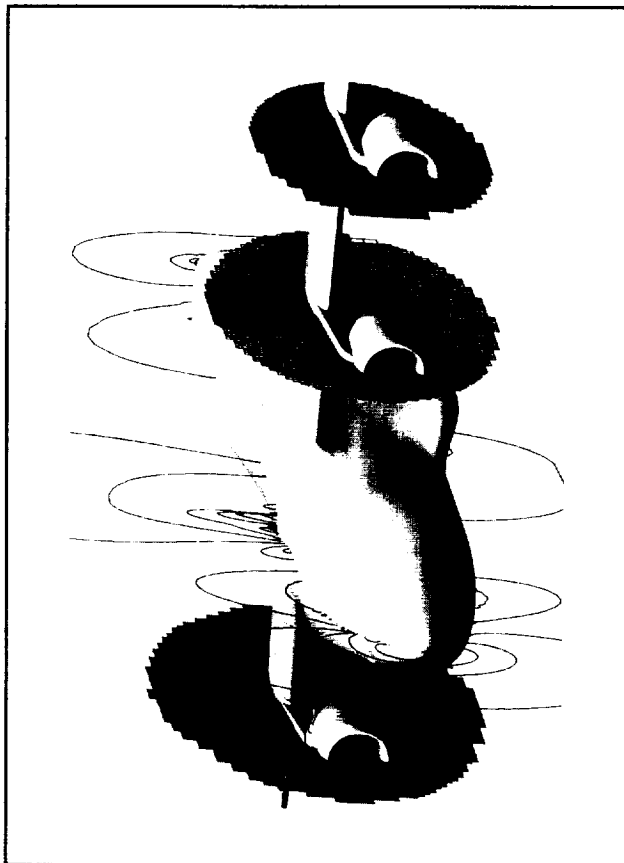


Fig. 1(a). Cartesian CFD solution for advanced transonic transport. (See color plate 6 in Appendix)

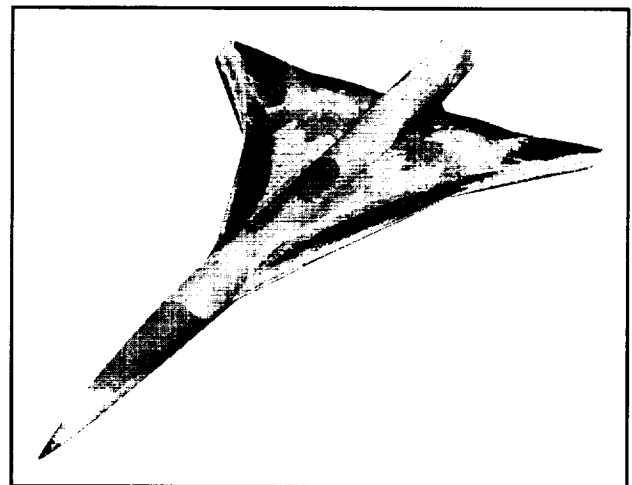


Fig. 1(b). Cartesian CFD solution for advanced supersonic transport. (See color plate 7 in Appendix)

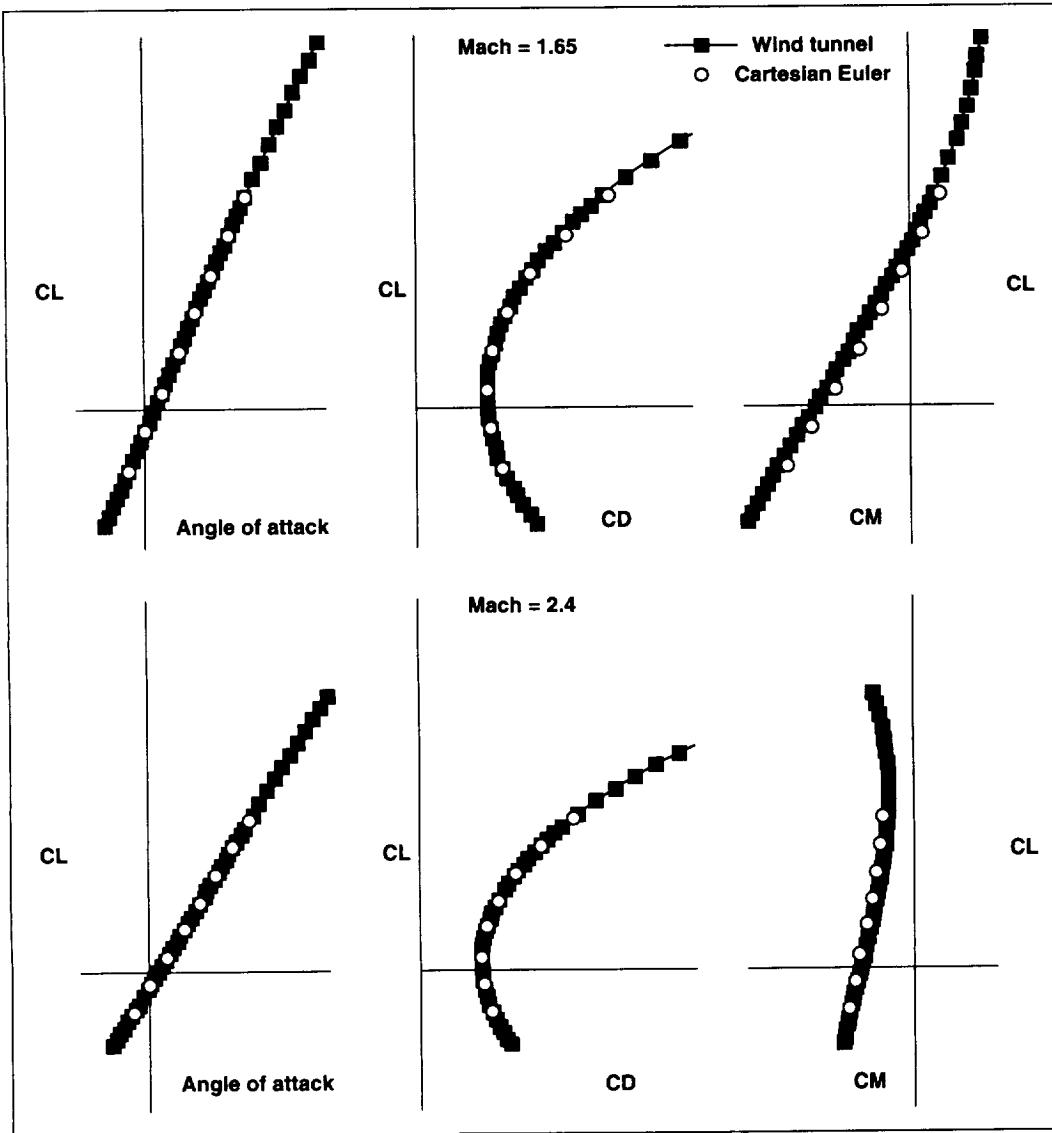


Fig. 2. Comparison of Cartesian CFD and wind tunnel data for advanced supersonic transport.

Cartesian approaches are beset with unique and interesting difficulties. Removal of the body-fitted-grid constraint allows the Cartesian hexahedra used to discretize the flow field to intersect the surface in an arbitrary manner. Successful research into the development of robust procedures for the efficient creation and distribution of the hexahedra has produced an automatic, "hands-off" procedure for Cartesian grid generation. Additional efficiency gains have resulted from the adoption of a component-based approach to surface modeling. This approach streamlines the labor-intensive computer-aided design and manufacturing (CAD/CAM) process of

creating the input surface discretizations and eliminates the need to regenerate new surface grids containing updated intersection information when individual components are translated or rotated. New intersections between components are automatically recognized and captured by the grid generation procedures, significantly improving the usefulness of the code in a design effort. This capability dramatically accelerates the analysis of complicated 3-D multibody geometries, such as multicomponent high-lift systems or configurations involving arbitrary control-surface deflections. Current research is

focused on the modeling of extremely thin components. The accurate implementation of the surface boundary conditions is crucial to the success of any flow-field simulation procedure. Research in this challenging area has produced improved boundary condition routines with increased accuracy.

Demonstrations of some successful 3-D applications of the resultant Cartesian CFD technology are illustrated in the figures. All of the applications were performed on the CRAY C-90 at the Numerical Aerodynamics Simulation facility at Ames. In part (a) of the first figure, a portion of the Cartesian grid for an advanced transonic transport is displayed along with some selected planes of the flow field painted by the pressure distribution. A curvature-sensitive grid refinement algorithm was used to initially refine the flow-field grid about the nacelles and pylons, at the fuselage nose, and around the leading and trailing

edges of the wing. Additional automatic refinements were performed to increase the resolution of shocks and large gradient regions in the flow field. Part (b) of the first figure shows the surface pressure distribution for a supersonic civil transport aircraft. In the second figure, selected comparisons of the supersonic lift, drag, and pitching moment characteristics of the supersonic transport are compared with wind tunnel data. Current efforts to further improve the efficiency and accuracy of the Cartesian-grid-generation and flow-solution procedures will soon provide the capability to rapidly and automatically produce high-resolution, 3-D flow-field simulations for arbitrarily shaped vehicles.

Ames-Moffett contact: J. Melton
(415) 604-1461
Headquarters program office: OA

Aeroelastic Stability of Modern Bearingless Rotors

Khanh Q. Nguyen

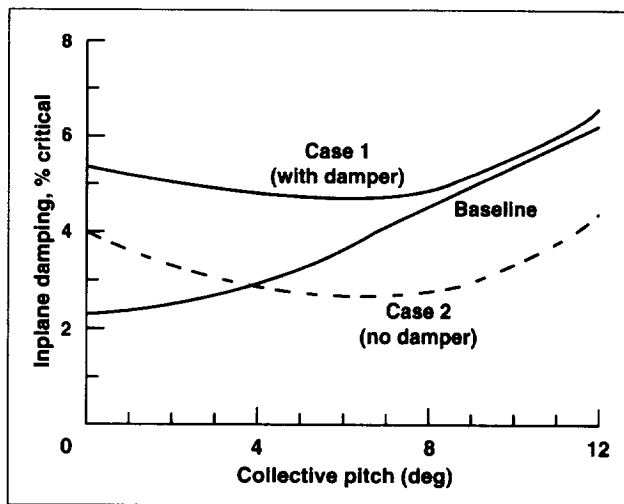


Fig. 1. Effects of combined parameters on inplane damping of bearingless rotors.

The University of Maryland Advanced Rotorcraft Code (UMARC) was utilized to study the effects of blade design parameters on the aeroelastic stability of an isolated modern bearingless rotor blade in hover. The McDonnell Douglas Advanced Rotor Technology (MDART) Rotor was the baseline rotor investigated. Results indicate that the hover inplane damping of the baseline rotor blade is strongly affected by (1) kinematic pitch-lag coupling introduced through the control system geometry and (2) the damping levels of the shear lag dampers. The hub precone, pitchcase chordwise stiffness and the blade fundamental torsion frequency have small to moderate influence on the inplane damping, whereas blade pretwist and placements of blade fundamental

flapwise and chordwise frequencies have negligible effects. A damperless configuration, shown as case 2 in the figure, with a leading-edge pitch link, 15 degrees of pitch-link cant angle, and reduced pitch-link stiffness, is shown to be stable with an inplane damping level in excess of 2.7% critical at

the full hover tip speed. In the figure, case 1 is similar to case 2 but has an elastomeric damper added.

Ames-Moffett contact: K. Nguyen
(415) 604-5043
Headquarters program office: OA

Correlation of Loads on a Bearingless Rotor

Khanh Q. Nguyen

Computed results of analyses by the University of Maryland Advanced Rotorcraft Code (UMARC) and Dynamics Analysis Research Tools (DART), a McDonnell Douglas code, were compared with the blade bending moments and vibratory hub loads data obtained from a full-scale wind tunnel test of the McDonnell Douglas five-bladed advanced bearingless rotor. The 5/rev vibratory hub loads data were corrected with results obtained from a dynamic calibration of the rotor balance. The agreement between UMACR-computed blade bending moments at different flight conditions is poor to fair, whereas the DART results are fair to good. The figure shows the comparison between UMACR- and DART-computed blade bending moments with wind tunnel data. Using the free-wake module, UMACR adequately computes the 5/rev vibratory hub loads for this rotor, capturing both magnitude and variations with forward speed. DART employs a uniform inflow wake model and does not adequately compute the 5/rev vibratory hub loads for this rotor.

Ames-Moffett contact: K. Nguyen
(415) 604-5043
Headquarters program office: OA

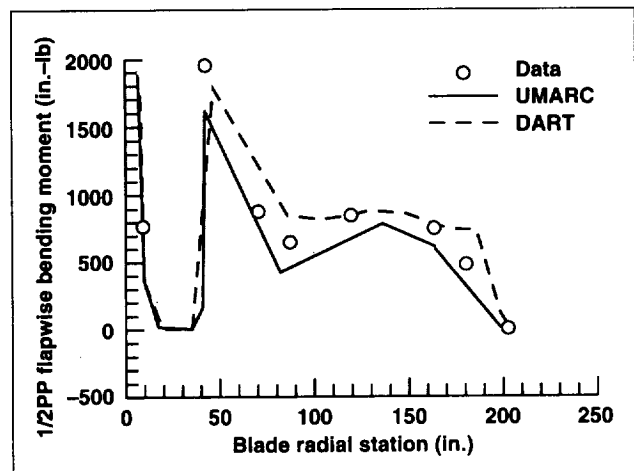


Fig. 1. Comparison of measured and computed half-peak-to-peak blade flapwise bending moment (blade loading = 0.076, advance rotor = 0.37).

Dynamics of the MDART Rotor Test Rig

Khanh Q. Nguyen

A shake test was performed on the Large-Scale Dynamic Rig in the Ames 40- by 80-Foot Wind Tunnel in support of the McDonnell Douglas Advanced Rotor Technology (MDART) Test Program. The shake test identified the hub modes and the dynamic calibration of the rotor balance. For hub mode identification, three configurations were tested:

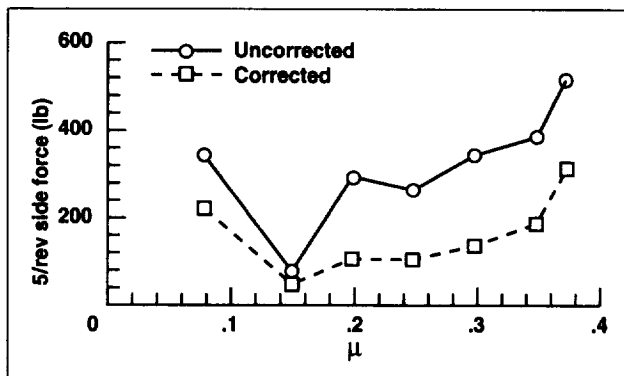


Fig. 1. Effects of dynamic calibration of the 5/rev side force of the MDART rotor.

wind tunnel scale unlocked with dampers engaged and disengaged, and wind tunnel scale locked. Test data were analyzed with a multi-degree-of-freedom time domain algorithm to identify the modal mass, damping, and stiffness of the inplane hub modes. The damping of the low-frequency hub modes (ground resonance modes) increased significantly with the wind tunnel dampers engaged. For dynamic calibration of the rotor balance, the shake test was performed only with the wind tunnel dampers engaged. The dynamic calibration matrix, computed from the shake test data using a least squares error method, is used to correct the 5/rev vibratory balance readings. The corrections were large for the side force (see figure), moderate for the axial force and inplane hub moments, and small for the normal force.

Ames-Moffett contact: K. Nguyen
(415) 604-5043

Headquarters program office: OA

Turbulence Modeling Enhancement for Overflow Code

Yehia Rizk

The objective of this work is to improve the accuracy and efficiency of predicting turbulent flow fields by the zonal Navier-Stokes code OVERFLOW.

The first task was to study the accuracy and stability of available one-equation turbulence models. These include the Baldwin-Barth (BB) and Spalart-Allmaras (SA) models and the one-equation version of the shear stress transport (SST) model. Since OVERFLOW already contained the BB model, the code was modified to include the SA and SST models by generalizing the formulation of the BB

models and adding only the needed modifications to account for the differences in the source term in the transport equation for the turbulent viscosity.

Results were obtained for the NACA 0012 airfoil at a Mach number of 0.799 and an angle of attack of 2.26 degrees. The pressure coefficient comparison shown in the figure indicates that the one-equation SA model predicts the shock location more accurately than the algebraic Baldwin-Lomax (BL) model does. Similar results were obtained with the BB and

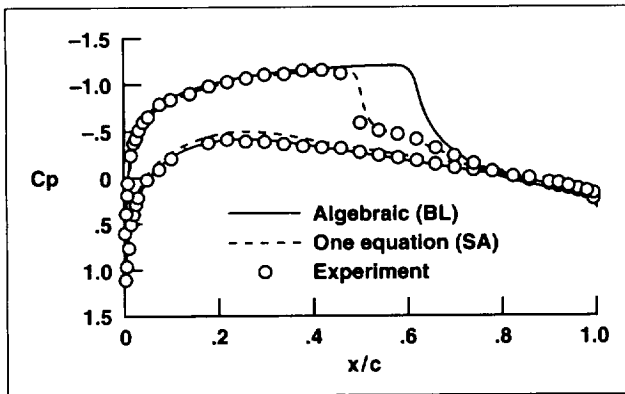


Fig. 1. Comparison between surface pressure prediction by algebraic and one-equation turbulence models using OVERFLOW.

the one-equation SST model; however, the SST model is currently less stable than the BB and SA models. Future work will include possible improvement in the stability of the SST models through implicit treatment of the source term.

These results indicate that the one-equation turbulence models are more accurate than the algebraic models without the addition of a significant computer requirement. The one-equation models are also more suitable for complex configurations which mandate zonal calculations.

Ames-Moffett contact: Y. Rizk
(415) 604-4466
Headquarters program office: OA

Maneuver Performance Enhancement for an Advanced Fighter/Attack Aircraft

Jeffrey Samuels

Aircraft designs that emphasize survivability incorporate low-observability features. Advanced aircraft geometries and control concepts may be fundamentally different from those of older aircraft. The joint NASA-U.S. Air Force Fighter Lift and Control (FLAC) research program was established to enhance the maneuver and control capability of next-generation Air Force multirole fighter aircraft with "low-observables" geometries. This effort involves both small- and large-scale wind tunnel testing and computational analysis of mechanical and pneumatic lift augmentation and control concepts. The model studied in this program (first figure) is a realistic, near-term-technology, low-observables multirole fighter derivative concept developed by the Innovative Concepts Branch at Wright-Patterson Air Force Base.

As part of this program, a 10%-scale wind tunnel test of the FLAC model has been completed in the NASA Ames 7- by 10-Foot Wind Tunnel. The principal objective of this test was to use passive mechanical boundary-layer-control devices to improve maneuvering performance (i.e., increase the lift-to-drag ratio (L/D) over the range of lift coefficients from 0.3 to 1.0). Roughly 200 configurations of vortex

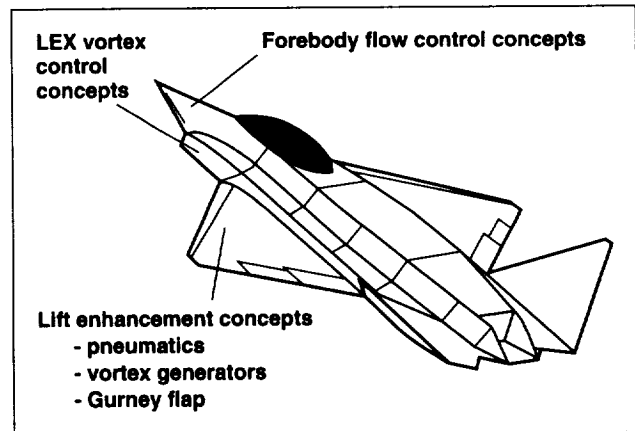


Fig. 1. FLAC model concept.

generators (VGs) were tested to energize the boundary layer to prevent or delay flow separation. Principal test parameters were leading- and trailing-edge flap deflections as well as the location, size, spacing, and orientation for each of three VG types (corotating vanes, counterrotating vanes, and Wheeler Wishbone VGs).

All VG types were evaluated on the two best flap configurations, and it was found that VG performance was dependent on flap setting. VGs improved maneuver L/D with flaps at leading-edge deflection (δ_{LE}) = 20 degrees and trailing-edge deflection (δ_{TE}) = 0 degrees (second figure) but not, except in a few cases, with flaps at δ_{LE} = 15 degrees and δ_{TE} = 10 degrees. In general, corotating-vane VGs performed better than the Wheeler Wishbone VGs or counterrotating-vane VGs. The influence of VG parameters such as height and spacing depended on VG location. Gurney flaps were also tested and showed an increase in C_L across the range of angle of attack, and improved L/D for C_L values above maximum L/D. Further research with these devices will be conducted on a 55%-scale model in the NASA Ames 40- by 80-Foot Wind Tunnel.

Ames-Moffett contact: J. Samuels
(415) 604-4235
Headquarters program office: OA

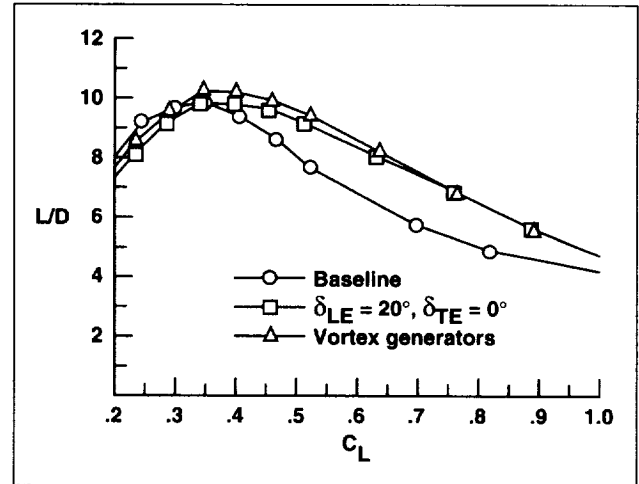


Fig. 2. Maneuver performance improvement with flaps and vortex generators.

Flight and Wind Tunnel Investigations of Blade–Vortex Interaction Noise

David B. Signor, Gloria K. Yamauchi, C. W. Acree

As part of the continuing In-Flight Rotorcraft Acoustics Program, test programs are currently in progress for the UH-60 and BO-105 helicopters. Both programs include flight testing and full-scale and small-scale testing of the helicopter rotors. The program objectives are (1) to use the NASA Ames YO-3A acoustic research aircraft to measure noise from rotorcraft in flight and make comparisons with similar wind tunnel measurements, (2) to use these comparisons to better understand blade–vortex interaction (BVI) noise, and (3) to determine how to minimize BVI noise on rotorcraft.

Measurement of UH-60 BVI Noise

During the flight testing, the NASA Ames YO-3A fixed-wing aircraft used a wingtip-mounted microphone to pick up BVI noise generated by the UH-60

Airloads helicopter. The simultaneous acquisition of both acoustic and airloads data in flight will allow the BVI noise to be examined in great detail. Six flights were performed with the YO-3A and UH-60 flying in close formation. The figure shows a side view of the flight formation. The starboard wingtip microphone of the YO-3A was positioned 22 degrees below the rotor hub at a rotor azimuth of 150 degrees. The distance between the starboard wingtip microphone and the rotor hub was 1.5 rotor diameters (80.5 feet). Target flight conditions included advance ratios from 0.175 to 0.250, tip Mach numbers of 0.636 and 0.66, rotor thrust coefficients of 0.0058 and 0.0071, and descent rates of 200–900 feet/minute. A subset of these flight

conditions matches conditions tested previously in the Deutsch-Niederlandischer Windkanal (DNW). During the DNW test, acoustic and blade pressure data from a 1:5.73-scale model of the UH-60 rotor were acquired. In an effort to eliminate any errors caused by different data reduction techniques, the data from the DNW test were processed using the same equipment and procedures used to reduce the flight acoustic data. To complete the acoustic data base of the UH-60 rotor, preparations are under way to test the UH-60 Airloads blades in the NASA Ames 80- by 120-Foot Wind Tunnel. Acoustic and blade pressure data will be acquired for conditions matching the flight and DNW tests. Because the rotor was heavily instrumented in flight, the in-flight rotor state can be accurately duplicated in the wind tunnel.

Measurement of BO-105 BVI Noise

Acoustic measurements of a Messerschmitt-Bolkow-Blohm (MBB) BO-105 helicopter acquired in flight have been compared with similar data acquired in a full-scale test of a BO-105 rotor in the NASA Ames 40- by 80-Foot Wind Tunnel and a small-scale BO-105 rotor test in the DNW. Significant differences (in amplitude and shape) were observed between the in-flight and the 40-by-80-foot-wind-tunnel BVI noise time histories.

A concern arising from this initial comparison between flight and wind tunnel data was whether the differences in rotor trim were a major contributor to differences in the BVI noise waveforms. During the test in the 40- by 80-Foot Wind Tunnel, the rotor was trimmed to zero flapping; during the flight test, the rotor was trimmed in order to balance moments on the helicopter.

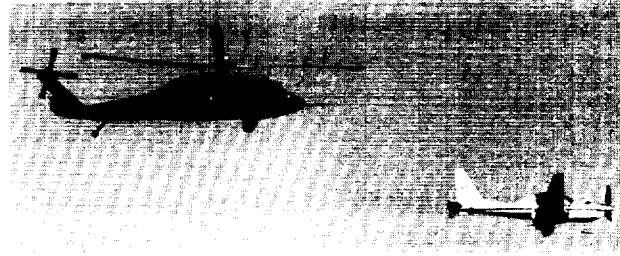


Fig. 1. YO-3A and UH-60 formation, side view.

The effect of rotor trim on BVI noise was investigated in a subsequent test of the BO-105 rotor in the 40- by 80-Foot Wind Tunnel by duplicating flight trim conditions. Also, small longitudinal and lateral cyclic excursions about the flight trim condition were input to the rotor to account for small trim variations that occur in flight. No significant effects on measured BVI noise were observed. During the latest testing of the small-scale BO-105 rotor in the DNW, the measured BVI noise time histories were similar to those acquired in the 40- by 80-Foot Wind Tunnel. Trim variations performed during this test showed no observable effect of trim on BVI noise.

The differences between the BVI noise measured in the wind tunnel and that measured in flight for the BO-105 rotor cannot be attributed to differences in rotor trim.

**Ames-Moffett contact: G. Yamauchi
(415) 604-6719
Headquarters program office: OA**

Noise-Suppression Nozzle Testing

Brian E. Smith

A critical part of the NASA High-Speed Research (HSR) program is the demonstration of satisfactory suppression of the jet noise present at low airspeeds. One scheme for reducing jet exhaust noise generated by a future high-speed civil transport (HSCT) is the use of a mixer/ejector system which would entrain large quantities of ambient air into the exhaust flow from the power plant in order to cool and slow the jet exhaust before it leaves the tailpipe. Of the variety of factors that can affect the noise-suppression characteristics of the mixer/ejector system, the influence of the wing flow field and high-lift devices is not well understood. The effectiveness of the noise-suppression device must be evaluated in the presence of the wing/high-lift system before definitive assessments can be made concerning HSCT noise. Of nearly equal importance is the evaluation of the performance of the high-lift system(s) in the presence of realistic propulsion units that feature high ambient flow entrainment rates. The noise suppressors must provide the required acoustic attenuation while not overly degrading the thrust efficiency of the propulsion system or the lift enhancement of the high-lift devices on the wing. The overall objective of the NASA High-Lift Engine Aeroacoustics Technology

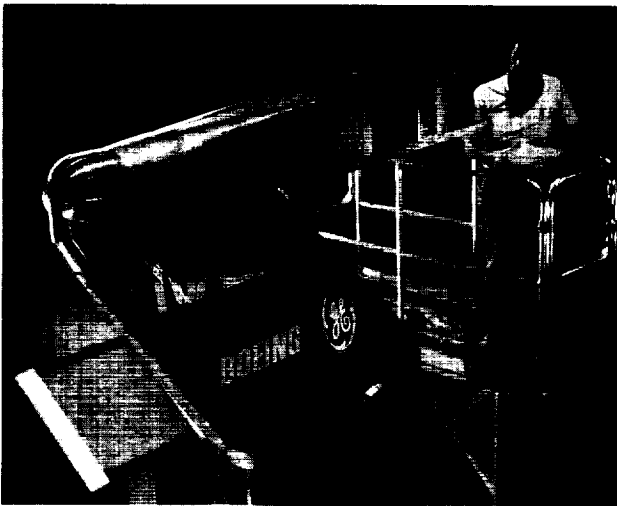


Fig. 1. General Electric mixer/ejector noise suppressor nozzle in the Ames 40- by 80-Foot Wind Tunnel.

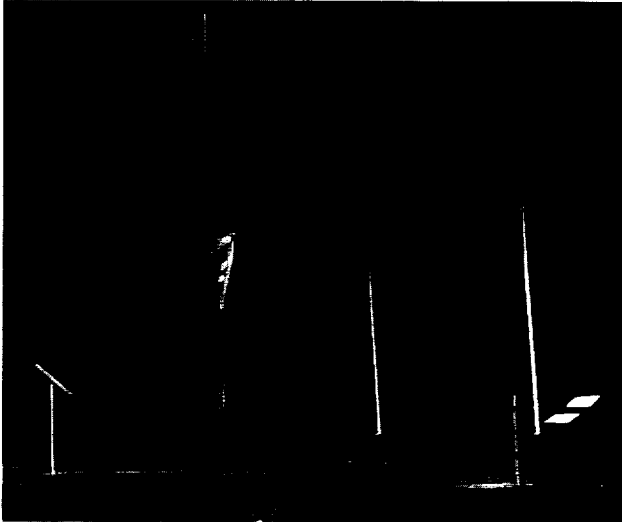


Fig. 2. Noise suppressor nozzle and acoustic measurement hardware in the Ames 40- by 80-Foot Wind Tunnel.

program is to demonstrate satisfactory interaction between the jet noise suppressor and the high-lift system at airspeeds and angles of attack consistent with takeoff, climb, approach, and landing.

In support of this program, an aeroacoustic test of 13.5%-scale candidate mixer/ejector nozzles was performed in the Ames 40- by 80-Foot Wind Tunnel. The nozzles were provided by General Electric Aircraft Engines under contract to Lewis Research Center. The first figure shows a close-up of one of the rectangular nozzles; the second figure shows the nozzle and acoustic measurement hardware in the 40- by 80-foot test section. The purpose of the test was to measure the baseline aeroacoustic performance characteristics of these nozzles in isolation from the aerodynamic flow field induced by the airframe. The test documented the acoustic signature of the nozzles with treated and hardwall ejector surfaces and with changes in the ratio of ejector duct to jet area over a wide range of nozzle pressure ratios and free-stream Mach numbers. The test also measured thrust performance, ambient-flow aspiration

ratio, and internal and external static pressures on the nozzles. The isolated nozzle test was a cooperative effort between NASA Ames, NASA Lewis, Boeing, General Electric, and McDonnell Douglas. The isolated aeroacoustic performance data will be compared with results obtained when these nozzles are installed on a 13.5%-scale Boeing Reference H HSCT configuration, semispan model scheduled for testing in 1995. The semispan model test will document the first-order effects of the airframe flow field

on the acoustic performance of the nozzles and the effect of the nozzle secondary inlet flows on the aerodynamic performance of the wing high-lift systems. This investigation is critical to understanding the mutual installation effects of mixer/ejector nozzles and wing high-lift systems.

**Ames-Moffett contact: B. Smith
(415) 604-6669**

Headquarters program office: OA

Axial Mixer Ejector Nozzle (AMEN) Performance

Paul T. Soderman

The Axial Mixer Ejector Nozzle (AMEN), designed by General Electric for the suppression of supersonic jet noise, was tested for acoustic and aerodynamic performance in the Ames 40- by 80-Foot Wind Tunnel. This test was one of a series of suppressor tests at various facilities around the country which are part of the High-Speed Research Program dealing with the control of landing and takeoff noise from the high-speed civil transport (HPCT). The suppressor nozzle was tested using a Boeing propane-fueled, high-pressure air jet simulator to generate a supersonic hot jet plume at approximately 10% scale of the proposed HSCT engine. Noise and thrust loss with the AMEN were compared to those with a baseline round, convergent calibration nozzle. The jet simulator with the baseline calibration nozzle is shown in the figure, mounted in the wind tunnel. Another goal of this study was to compare the acoustic measurements taken in the large, closed test section of the 40- by 80-foot wind tunnel with similar data acquired in smaller, open-jet wind tunnels in order to evaluate the test techniques.

Data reduction and analysis are ongoing. Preliminary results indicate that data quality is good. Far-field acoustic directivity patterns of the baseline and suppressor nozzles have been documented up to a flight Mach number of 0.32 for frequencies from



Fig. 1. Baseline nozzle mounted on jet simulator in the Ames 40- by 80-Foot Wind Tunnel.

400 hertz to 80 kilohertz. A range of engine cycle points, both on and off design, was simulated. Nozzle pressure ratios up to 4.0 and jet temperatures up to 1840°R were achieved, and suppressor-nozzle thrust loss was measured. Data will be scaled to a representative aircraft flyover condition for

computation of expected “effective perceived noise level” (EPNL).

**Ames-Moffett contact: P. Soderman
(415) 604-6675
Headquarters program office: OA**

Phased Microphone Arrays for Wind Tunnels

Paul T. Soderman

Phased arrays of microphones are being developed for inflow acoustic measurements in the wind tunnels of the National Full-Scale Aerodynamics Complex. Phased microphone arrays or antennas are used to remotely detect localized noise sources on aircraft models as well as to increase the signal-to-noise ratio by eliminating part of the wind tunnel background noise. The latter is an important consideration when working with relatively small-scale, quiet aircraft models or aircraft components. By scanning the aircraft model with an antenna beam, it is possible to identify and quantify the various noise sources and evaluate new noise reduction concepts. This technique is superior to the use of individual microphones, which record the total radiated sound of the model but cannot discriminate among the various aeroacoustic sources.

The use of phased arrays in wind tunnels requires the development of several technologies such as beam-forming algorithms, digital signal processing, microphone patterns, aerodynamics of installed arrays, and flow noise reduction. Some of these technologies can be adapted from electromagnetic or acoustic antenna systems that have been well developed for other purposes. The figure shows a prototype array installed in the test section of the 40- by 80-foot wind tunnel for the measurement of airframe noise. This design incorporates 15 microphones embedded in the flat surface of a rectangular plate with a simple airfoil cross-sectional shape. The surface of the array plate is aimed at the aircraft model, and beam scanning over the model surface is accomplished electronically. Array performance is being evaluated with regard to acoustic frequency, source strength, source distribution, and wind speed.



Fig. 1. Prototype microphone array installed in the Ames 40- by 80-Foot Wind Tunnel.

More advanced arrays with many more elements and improved sensor technology are being developed for future wind tunnel tests.

**Ames-Moffett contact: P. Soderman
(415) 604-6675
Headquarters program office: OA**

Computation of Helicopter Rotor Acoustics in Forward Flight

Roger C. Strawn, Rupak Biswas

Noise reduction is a major objective of the designers of future civilian and military rotorcraft. This is particularly true for aircraft that operate in urban areas. Accurate prediction of helicopter noise is the first step in its reduction and control.

Helicopter aerodynamic and acoustic simulations present several challenges for conventional computational fluid dynamics (CFD) methods. One major difficulty is that rotor wakes and acoustic waves require high resolution in localized regions that extend far out from the rotor blades. It is difficult to create computational grids to resolve these phenomena without exceeding the capacity of even the largest supercomputers. This work presents innovative solutions to this problem by using combinations of CFD simulations and Kirchhoff integral methods to predict helicopter rotor noise. The CFD methods are used to compute the nonlinear acoustic signals close to the rotor blades. This flow-field solution is then interpolated onto a cylindrical Kirchhoff surface that completely encloses the rotor and hub. A Kirchhoff integration over this surface is then used to propagate the acoustic signals to the far field. A portion of a Kirchhoff surface around a rotor blade is shown in the figure. Corresponding contours of interpolated acoustic pressure are also shown.

Kirchhoff theory says that if the acoustic pressure and its derivatives are known for a surface that completely encloses a source of noise, then an integration over that surface can be used to determine the acoustic signal at any observer location in the far field. This Kirchhoff integration is computationally more efficient than its CFD counterpart and can propagate acoustic signals over large distances without numerical dissipation. The only drawback to the Kirchhoff formulation is that it lacks the ability to capture nonlinear acoustic phenomena.

The combination of CFD simulations in the near field and Kirchhoff integrations for the far field is an excellent compromise for predicting helicopter noise. The CFD method accurately captures the

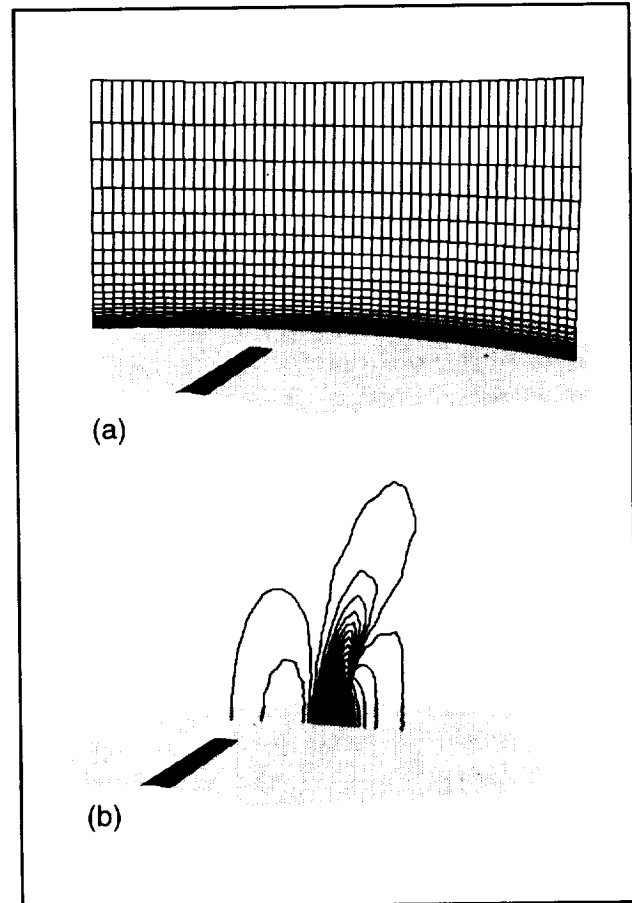


Fig. 1. Portion of Kirchhoff surface (a) and interpolated nondimensional pressure contours (b) for an Army UH-1H helicopter rotor with a hover tip Mach number of 0.95.

near-field transonic flow nonlinearities, whereas the Kirchhoff integration is computationally efficient over large distances.

A new CFD/Kirchhoff method has been developed in this project. The CFD model solves the Euler/Navier–Stokes equations for rotating helicopter

blades. The Kirchhoff scheme uses an innovative nonrotating, translational surface for the acoustic integral evaluation. Computed values for high-speed, impulsive noise in hover and forward flight show excellent agreement with experimental data. The combined CFD/Kirchhoff method offers high

accuracy with reasonable computer resource requirements.

Ames-Moffett contact: R. Strawn
(415) 604-4510
Headquarters program office: Army

Airfoil Drag Reduction

Paul Michael Stremel

A parametric study has been conducted on the effect of fences on the flow about an airfoil normal to the free-stream flow. A validated two-dimensional computational method has been applied to accurately calculate the viscous flow about an XV-15 wing airfoil with an upper- or lower-surface fence. This investigation includes the effect of fence location, for both upper and lower surfaces, and fence height on airfoil loading. Comparisons of steady lift and pitching moment, the ratio of steady drag for the fence case to that for the basic airfoil, and average surface pressure distributions are made to evaluate the effectiveness of each airfoil/fence configuration.

The results indicate that (1) the steady airfoil loading is highly dependent on the fence chordwise location, ranging from a 15% increase in drag for an upper-surface fence to a 35% decrease in drag for a lower-surface fence with respect to the basic airfoil value; (2) the average airfoil loading is also dependent on the fence height, with a drag reduction of 25% for a lower-surface fence of 35% chord height located at 15% chord; and (3) the reduction in drag is the direct result of increased suction on the airfoil upper surface near the leading edge and an increase in the airfoil base pressure over the entire airfoil chord. Sample results are shown in the figures.

In the first figure, the airfoil lift, the ratio of drag to the basic airfoil drag, and the airfoil pitching moment are shown as functions of fence chordwise location. Results are shown for an upper- and a lower-surface fence of height 30% of airfoil chord.

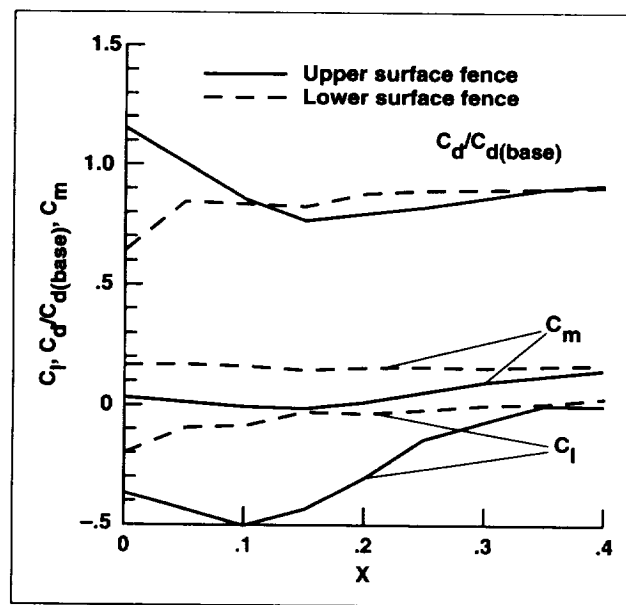


Fig. 1. Effect of fence location on steady airfoil loading: upper- or lower-surface fence; fence height = 0.3 chord.

The figure shows the significant reduction in airfoil drag for a lower-surface fence located at the airfoil leading edge and an increase in drag for an upper-surface fence positioned at the same location. Also shown are the significant variations in lift and pitching moment as functions of fence location.

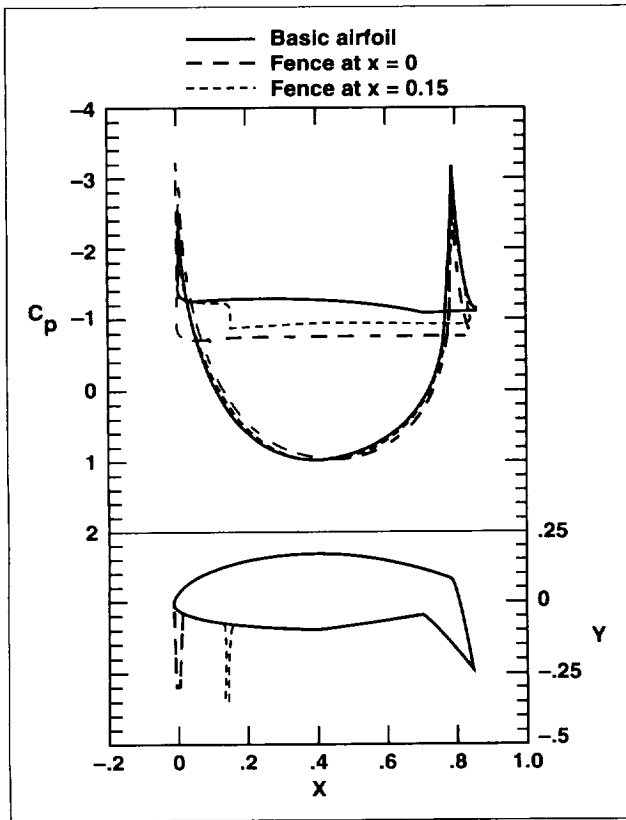


Fig. 2. Effect of fence location on airfoil average surface pressure: lower-surface fence; fence height = 0.3 chord.

The second figure depicts the dependence of airfoil surface pressure as a function of fence location for a lower-surface fence. When the fence is located at the airfoil leading edge, a significant increase in the airfoil base pressure is shown across the entire airfoil chord and an increase in the upper-surface suction near the leading edge is present. It is this increase in the base pressure and the increased upper-surface suction that contribute to the significant reduction in airfoil drag shown in the first figure. As the lower-surface fence is moved aft on the airfoil, as shown in the second figure, the effect of the fence on the airfoil base pressure and upper-surface suction are diminished with respect to the results shown for a fence located at the leading edge, resulting in less drag reduction.

Ames-Moffett contact: P. Stremel
(415) 604-4563
Headquarters program office: OA

TRAM Rotating Amplifier System

A specially designed rotating amplifier system (RAS) is being developed through a cooperative effort between NASA Ames Research Center, the Army's Aeroflightdynamics Directorate (AFDD), and the National Aerospace Laboratory (NLR) in The Netherlands. The RAS was specifically designed to satisfy both NASA's and the AFDD's highly instrumented wind tunnel test models. The RAS is able to accommodate the large number of rotating instrumentation signal requirements for the first wind tunnel entry of the Tiltrotor Aeroacoustic Model (TRAM).

Alexandra Swanson

The RAS technology is based on previous wind tunnel instrumentation and amplifier system development work performed by the Dutch-German Wind Tunnel in The Netherlands. The amplifiers are made up of hybrid circuit technology which consists of very small printed circuit boards. The first figure shows three of these hybrid circuits beside a module that is composed of 16 hybrid circuits (or channels). The RAS will be used to preamplify low-level signals that are generated by 150 dynamic pressure transducers which are mounted on the surface of the TRAM's

tiltrotor blades. The RAS will also amplify other rotating instrumentation signals. The signals will be transmitted by a 300-channel slip-ring system to a data acquisition system. The low-level signals must be amplified between the transducer and the slip ring in order to guarantee a sufficient signal-to-noise ratio. This means that the RAS must be mounted between the TRAM's drive system and the slip ring.

The primary functions of the RAS are to provide amplification for up to 256 input signals, supply excitation voltage for each transducer, perform calibration functions, and pass through an additional 128 nonamplified signals. The settings for each amplifier channel will be set and downloaded by means of a PC via a serial data link with the RAS unit. The RAS unit is composed of 16 pie-shaped modules.

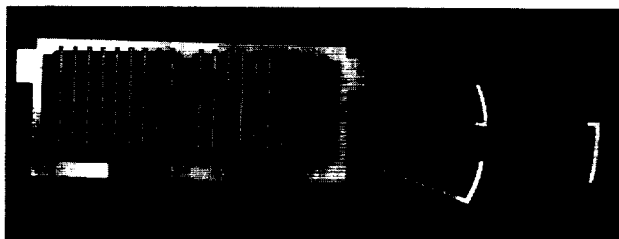


Fig. 1. RAS module and three hybrid circuits.

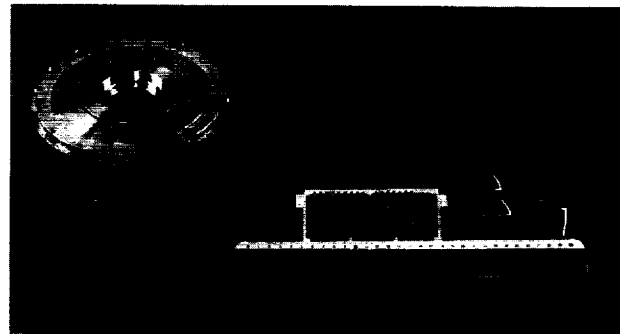


Fig. 2. Metric ruler illustrates compact features of assembled RAS unit, module, and hybrid circuits.

Each of these modules contains 16 amplified channels, 8 pass-through channels, a choice of 4 gain settings, and a choice of 3 calibration settings. The RAS is very compact (7.1 inches in diameter by 5.6 inches long). In the second figure, a metric ruler illustrates the compact features of one of the modules beside the assembled RAS unit. This unit was specifically designed to fit within the compact space of the TRAM's nacelle.

**Ames-Moffett contact: A. Swanson
(415) 604-6856
Headquarters program office: OA**

Effect of Canard on Dynamic Stability

Eugene Tu

In comparison with conventional aft tail designs, canard-configured aircraft have unique stability characteristics. These characteristics are particularly pronounced in the highly nonlinear aerodynamic regime that results from maneuvers or other such dynamic unsteady conditions. The ability to predict the effects of canards on dynamic stability is required for the optimal designing of future advanced canard-configured aircraft. The current work seeks to improve the understanding of the canard configurations associated with dynamic stability. In particular,

an assessment is made of advanced computational fluid dynamics (CFD) techniques in predicting dynamic stability.

Using a CFD solver, the time-accurate Navier-Stokes equations are solved for a canard-wing-body configuration undergoing pitch oscillations about various angles of attack. Computations are made at the high subsonic Mach number of 0.70, mean angles of attack from 0 to 12 degrees, pitch amplitude of 1 degree, and various frequencies of

oscillation. By performing Fourier analyses on the time-history responses of lift and pitching moment, an assessment of the aerodynamic damping and oscillatory stability can be obtained.

The first figure shows the effect of the canard on the lift and pitching moment coefficients during a typical pitch oscillation simulation. The horizontal axis represents the change in angle of attack from the mean during the oscillations. The lift and moment coefficients shown on the vertical axes are normalized about their respective mean values. The lift coefficient results show that the presence of the canard increases the lift amplitude without significant changes in the phase. On the other hand, the moment curves show that the canard causes a phase shift in the pitching moment response while producing little change in moment amplitude.

The changes in lift and moment responses shown in the first figure have direct effects on the dynamic

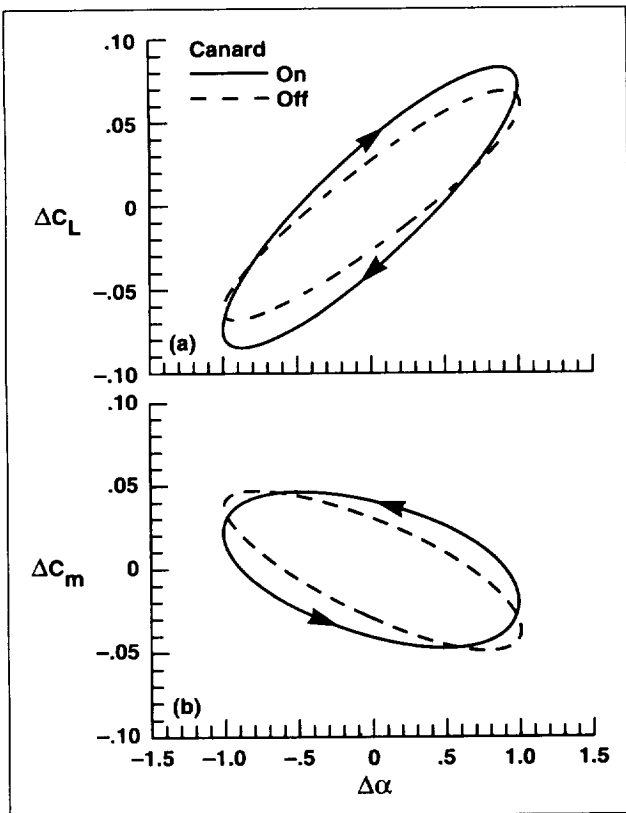


Fig. 1. Effect of canard on lift and moment curves.

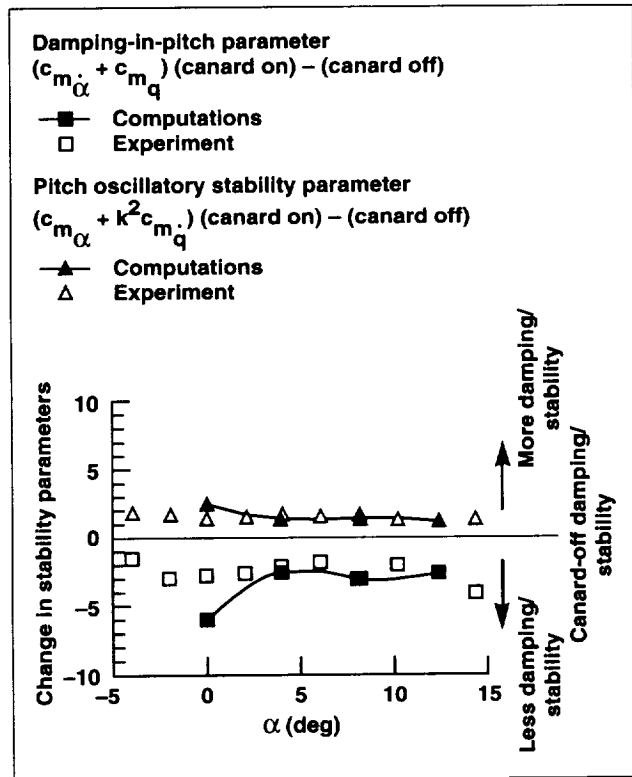


Fig. 2. Effect of canard on pitching-moment dynamic stability parameters (differences between canard-on and canard-off values shown).

stability of the configuration. For example, the second figure illustrates the effect of the canard on damping and oscillatory stability. For reference, comparisons with experimental data measured in a wind tunnel are shown as well. Both the computational simulation and the experimental results in the second figure show that the canard increases the aerodynamic damping of the configuration while decreasing the oscillatory stability. The capability to predict such dynamic effects using CFD will serve to enhance the design of future canard-configured aircraft.

Ames-Moffett contact: E. Tu
 (415) 604-4486
 Headquarters program office: OA

Compressibility Corrections for Turbulence Models

Thomas J. Coakley, P. George Huang, Jorge E. Bardina

The overall goal of this research was to identify, test, develop, and recommend turbulence models that can be incorporated into computational-fluid-dynamics codes used in the design of hypersonic aerospace vehicles. A literature survey was done to identify a well documented data base on high-speed compressible fluid flows, including supersonic and hypersonic flows that could be used to validate turbulence models. Since it was anticipated that this data base would be incomplete, additional experiments were performed in the NASA Ames 3.5-Foot Hypersonic Wind Tunnel.

The objective of the current (theoretical) effort was to identify promising turbulence models through their application to simple flows such as flat plate flows, and then to investigate the application of these models to more complex flows. The complex flows were to be selected from the data base developed in the first phase of the study. For these flows it was anticipated that model performance would not be entirely satisfactory, so model corrections would be required.

Calculations were undertaken for a wide variety of flows, including flat plates, mixing layers, and shock-wave/boundary layer interactions in two and three dimensions. A major requirement of the work was to develop model corrections that could be incorporated into standard or baseline turbulence models that have been used successfully on simpler flows or at lower speeds.

The baseline turbulence models selected were the $k-\epsilon$ model of Jones and Launder and the $k-\omega$ model of Wilcox. These models were modified to include corrections to improve predictions of characteristics of complex flows, including (1) separation extent and location, (2) heat transfer at reattachment location, and (3) the spreading rate of free shear layers.

An example of the models' ability to improve predictions is shown in the figure. Comparisons are shown of experimental and computed surface

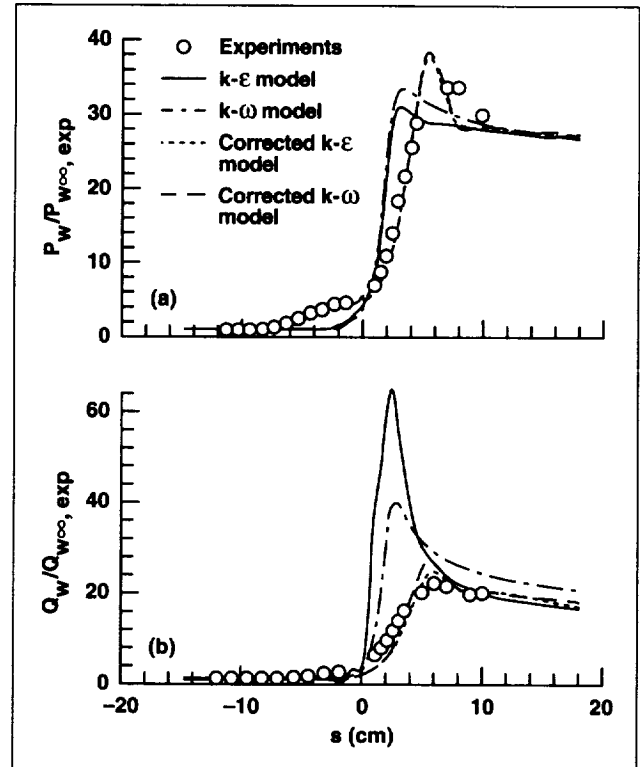


Fig. 1. Surface pressure (a) and heat transfer (b) for the flow over a cylinder flare configuration.

pressure and heat transfer for the flow over a cylinder flare configuration at Mach 7. The predictions of the baseline and corrected $k-\epsilon$ and $k-\omega$ models are shown. It can be seen that the baseline models fail to predict both extent of separation (pressure) and level of heat transfer on the flare downstream of reattachment. The model corrections give dramatically improved predictions of separation and heat transfer.

Ames-Moffett contact: T. Coakley
(415) 604-6451

Headquarters program office: OA

Computations of Multistage Turbine Flows

Karen L. Gundy-Burlet

A three-dimensional, unsteady, thin-layer Navier–Stokes zonal code (STAGE-3) has been developed to analyze flows within multistage turbomachines. The unsteady Navier–Stokes equations are cast in the strong conservative form. A fully implicit, finite-difference approximation is then applied to the governing equations. Convective fluxes are evaluated by a third-order-accurate, upwind-biased Roe scheme. The viscous fluxes are evaluated using second-order-accurate central differences. The nonlinear finite-difference equations are solved iteratively at each time level using a Newton–Raphson scheme.

A zonal grid approach has been employed in order to model the relative motion between rotors and stators inherent in an axial turbomachine. Two grids are used to discretize the flow around each airfoil. An inner “O” grid is used to resolve the viscous effects around the airfoil. This “O” grid is overlaid on an outer “H” mesh which resolves the flow in the passages between the airfoils. The “H” meshes are allowed to slip with respect to one another in order to simulate the relative motion between rotors and stators.

A fine-grid, three-dimensional calculation of a 1-1/2-stage turbine was completed. Results from the

code agree well with experimental data for time-averaged surface and cross-flow pressure distributions and time-averaged surface streamlines. The code requires 93 megawords of main memory for the 2.7-million-point grid. This 1-1/2-stage turbine calculation required approximately 500 CRAY-C90 hours for the time-averaged solution to converge. The figure shows the turbine geometry, time-averaged surface pressures, and instantaneous entropy contours within the turbine.

Unsteady turbomachinery flow fields are extremely complex, especially in the latter stages of

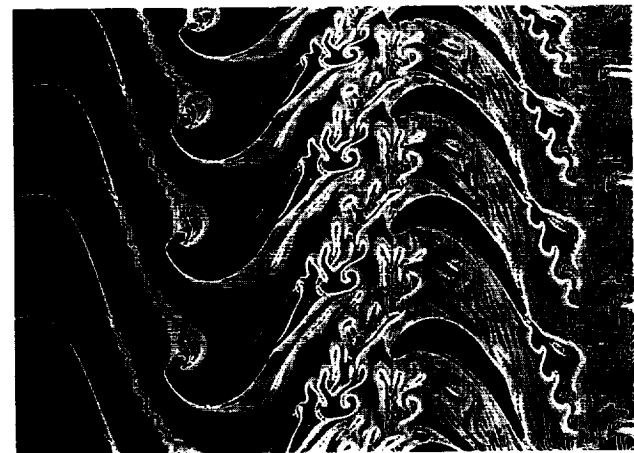


Fig. 1. The turbine geometry, time-averaged surface pressures, and instantaneous entropy contours within a 1-1/2-stage turbine. (See color plate 8 in Appendix)

multistage turbomachines. Wake/wake and wake/airfoil interactions cause complex time-varying forces on the downstream airfoils. It is important to understand these interactions in order to design turbomachines that are light and compact as well as reliable and efficient.

Investigations of hot-streak migration in multistage turbines are currently under way. In addition,

the effect of turbulence modeling on the flow in a multistage compressor will be studied.

**Ames-Moffett contact: K. Gundy-Burlet
(415) 604-4475**

Headquarters program office: OA

Remote-Access Wind Tunnel

A new advance in the way customers can interact with NASA Ames in experiments is provided by the Remote Access Wind Tunnel (RAWT), which allows interactive connectivity to remote customer sites. The benefits are substantial; wind tunnel customers can save \$50,000 per week in travel and associated costs by reducing the size of the teams sent to carry out wind tunnel tests.

Dennis J. Koga, Anthony J. Lisotta, Bruce L. Gilbaugh

The RAWT is a new development of the Ames Integration of Numerical and Experimental Wind Tunnels (I_of_NEWT) program. It produces real-time comparisons of wind tunnel data and numerical calculations. I_of_NEWT relies heavily on information technology and computer networking to provide communication links via AEROnet to aeronautical customers throughout the country. The RAWT system

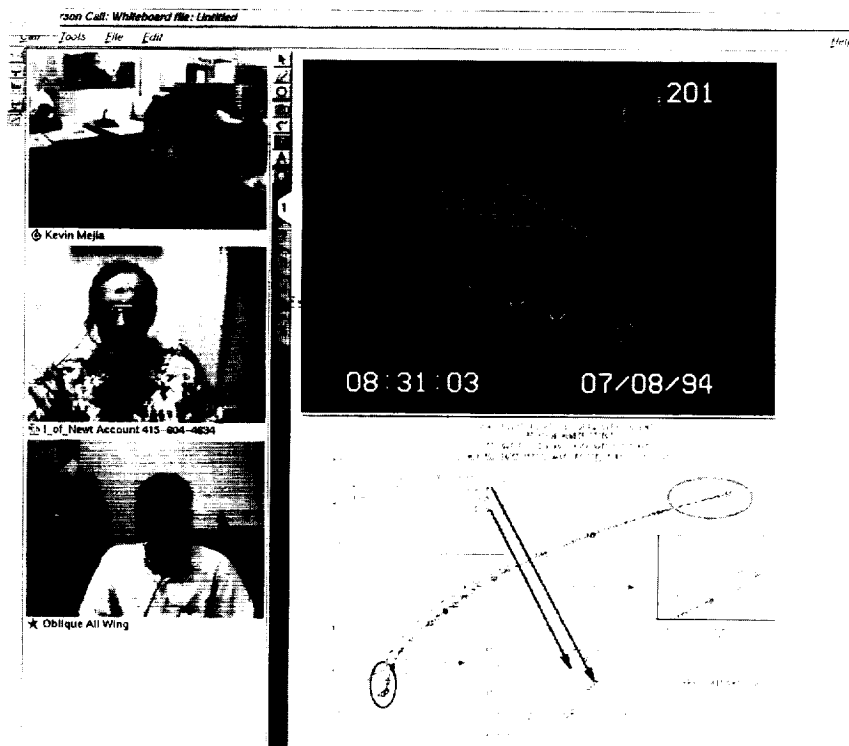


Fig. 1. Remote Access Wind Tunnel screen display.

provides interactive communication of the I_of_NEWT information by means of videoconferencing. This information consists of computational and wind tunnel test data and scanned photographs, live video images, and other forms of data.

The RAWT system implementation consisted of Silicon Graphics Computer Systems Indy workstations running their InPerson software at both the wind tunnel and remote customer sites. Multiple simultaneous customers can be linked to the system. Such a link occurred in recent test programs at Ames in cooperation with Boeing in Seattle, Washington, and McDonnell Douglas in Long Beach, California.

The figure shows a sample screen of the RAWT system; the three images on the left side are small, full-motion video images from the three sites using the RAWT system. These video images may be images of the personnel as recorded by the Indy-supplied camera, or they can be video feeds from inside the wind tunnel itself. The right side of the

screen is dedicated to a "whiteboard" to display multiple pages of information. Each remote site has the capability of viewing data shared on the whiteboard; interaction between the sites takes place via audio exchanges and drawing tools available on the whiteboard. Users are identified by different colors used for drawing.

The RAWT system is a successful implementation and enhancement of the I_of_NEWT program. It saves customers time and money, and allows shared information from remote sites to reach more customers. This system will have a significant impact on how testing is done in an interactive mode with the design cycle. The basic technology is commercially available and can be applied to areas other than wind tunnel testing for similar benefits.

Ames-Moffett contact: D. Koga

(415) 604-6285

Headquarters program office: OA

Commissioning of the Laminar Flow Supersonic Wind Tunnel

James A. Laub, Stephen W. D. Wolf, and Lyndell S. King

The Fluid Mechanics Laboratory (FML) at Ames developed and built the Laminar Flow Supersonic Wind Tunnel (LFSWT), the first low-supersonic wind tunnel designed to look at low-disturbance flow. Low-disturbance or "quiet" wind tunnels are recognized as an essential part of meaningful transition research. In conventional supersonic wind tunnels, settling-chamber disturbance levels are relatively high, and significantly alter the transition phenomena under investigation. Furthermore, the boundary layers of the nozzle and test section walls are turbulent, radiating noise that does not exist in flight, which impacts transition research on models mounted in the test section. Before this tunnel was built, transition research at low supersonic speeds was performed only in high-risk, high-cost flight programs.

The unit Reynolds number range of the LFSWT is 2.6 to 3.8 million per foot, which matches high-speed civil transport flight conditions at Mach 1.6.

The LFSWT is a continuously operating research tunnel with an 8- by 16-inch test section. Unique features of the wind tunnel include vibration isolation of the settling chamber, nozzle, and test section. The highly polished nozzle and test section walls promote laminar boundary layers. The first figure illustrates that visual access in the test section is possible from all four sides. The LFSWT operates at unusually low stagnation pressures with compression ratios (ratios of stagnation pressures upstream and downstream of the test section) of less than unity. This is achieved through the use of a unique dual-stage ambient injector drive system, shown in the second figure. Design and construction costs of the LFSWT were held to a minimum through the use of the existing FML high-mass-flow and low-compression-ratio (1.8:1) compressor and Ames Research Center's high-pressure dry air supply system. The low compression

ratio of the compressor was offset by the injector drive system.

Flow characteristics of the new tunnel have been investigated using a full array of measurement techniques. Preliminary measurements along the nozzle and test section walls indicate that the boundary layers are indeed laminar. We have also measured low disturbance levels in the settling chamber flow with pressure fluctuations of less than 0.2% and velocity fluctuations of less than 1%. The combination of laminar boundary layers and a low-disturbance settling-chamber flow field have made possible "quiet" (low-disturbance) flow in the test section (pressure fluctuations less than 0.1%). However, much more mapping of the test-section flow field is needed to quantify the extent of the quiet test core. To accomplish a detailed profile of the nozzle and test-section flow fields, we designed a three-axis traversing mechanism. The new traversing mechanism is scheduled for tunnel installation in November 1994.



Fig. 1. The LFSWT test section with visual access on all four sides.

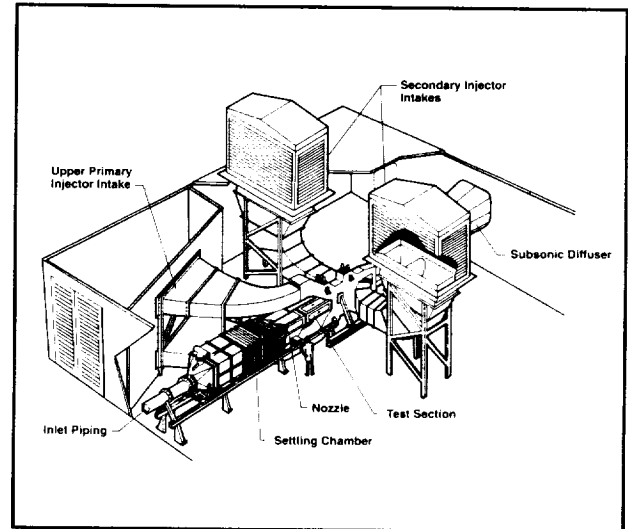


Fig. 2. The LFSWT drive system with primary and secondary ambient injectors.

Commissioning of the tunnel in June 1994 was signified by the testing of LFSWT's first model—a full-scale portion of a 70-degree swept wing. Data acquisition at different angles of attack (from -2.0 to 8.0 degrees) included oil-flow, liquid-crystal, and shadowgraph/video observations. Surface-pressure and temperature data were also taken. Good comparisons between computations and experimental data at 0 degrees angle of attack were obtained. The commissioning of the LFSWT is the culmination of a 4-year joint experimental and computational-fluid-dynamics research effort.

**Ames-Moffett contact: J. Laub
(415) 604-4136**

Headquarters program office: OA

Pressure Sensitive Paint System Development

Blair G. McLachlan, James H. Bell, John A. Schreiner, Jose M. Espina

An automated, production-level pressure sensitive paint (PSP) system was developed by NASA Ames Research Center and applied in a series of wind tunnel tests. The PSP is a mixture of an oxygen-permeable binder with a properly selected luminescent molecule. It is used in wind tunnel tests to produce a surface pressure map. The system is capable of producing qualitative and quantitative surface pressures in a real-time production facility. Under a Joint Sponsored Research Agreement, the University of Washington and the Advanced Aerodynamic Concepts Branch at Ames were given the task of developing this technology for production facility use.

This past year, the development of a comprehensive set of PSP formulations for the Ames Unitary Plan Facility was begun and resulted in the production of first-generation polymer-variant PSP coatings and substrates for use in unitary facilities. These polymer coatings have been aerodynamically examined, validated, and employed in a number of tests in large-scale facilities at Ames and at other testing sites. These tests included Boeing's cooperative test in the Ames 11- by 11-Foot Transonic Wind Tunnel (TWT), and tests of the Stratospheric Observatory for Infrared Astronomy in the Ames 14-Foot TWT, the oblique all-wing (OAW) in the Ames 9- by 7-Foot Supersonic Wind Tunnel (SWT), the Boeing 737X and the Boeing 777 in the Boeing TWT, the Navy F-18 and Lockheed-THAAD at the Arnold Engineering Development Center, and the double delta in Langley Research Center's 8-Foot SWT.

The figure illustrates representative results from one of these tests, that of the OAW in the Ames 9- by 7-Foot SWT. Displayed is a false-color pressure map of the lower surface of the OAW model for

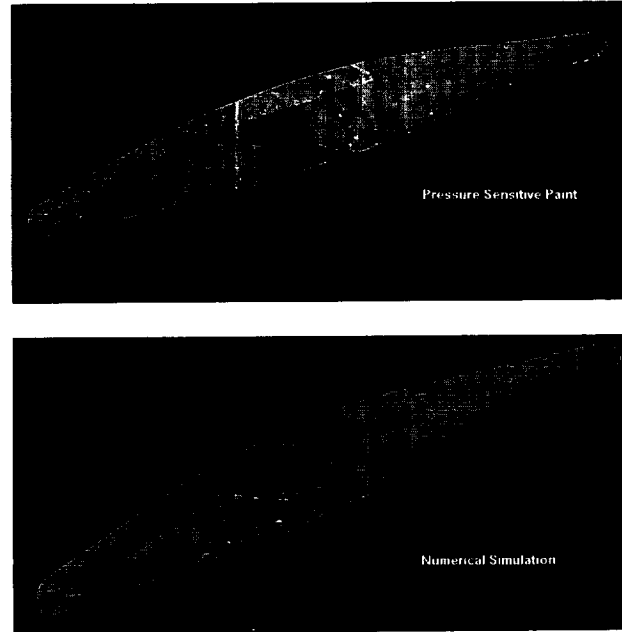


Fig. 1. Pressure maps of the oblique all-wing.
(See color plate 9 in Appendix)

supersonic flow conditions using both PSP and a numerical simulation. The fine detail provided by the PSP is apparent.

Future work will include the development of advanced-polymer pressure paints for high-pressure environments and the development of second-generation polymer-variant pressure paints for the unitary facilities.

**Ames-Moffett contact: B. McLachlan
(415) 604-0944
Headquarters program office: OA**

Measurement of Surface Shear Stress Distributions Using Liquid Crystal Coatings

Daniel C. Reda

The objective of the present research is to develop a technique for the full-surface measurement of the instantaneous shear stress distribution acting on any test surface immersed in a three-dimensional flow field.

The liquid crystal phase of matter is a highly nonuniform, fluidlike state that exists between the solid and uniform liquid phases of some organic compounds. Such materials can exhibit optical properties that are characteristic of solid, crystalline materials. If a thin film of liquid crystals is applied to a surface and the molecules within the coating are aligned by frictional forces into the required planar state, then this molecular structure selectively scatters incident white light as a spectrum of colors. Each color is oriented at a discrete angle relative to the surface. Liquid crystal coating (LCC) color-change response to shear depends both on the shear stress magnitude and on the direction of the applied shear relative to the observer's line of sight. This color-change response is rapid (as little as one

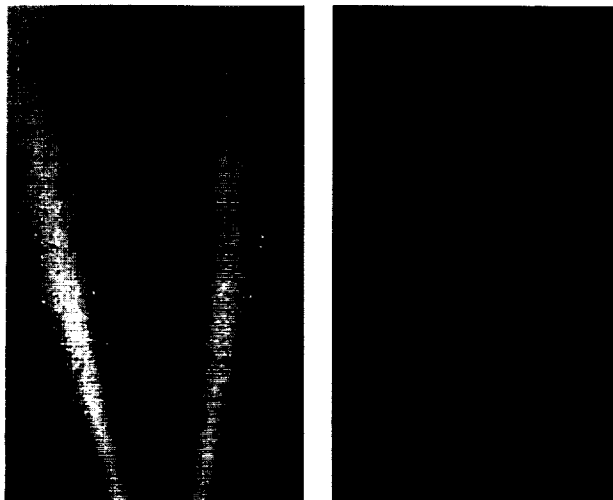


Fig. 1. Color-change response of liquid crystal coating to tangential jet flow: left-hand side, flow away from camera; right-hand side, flow toward camera. (See color plate 10 in Appendix)

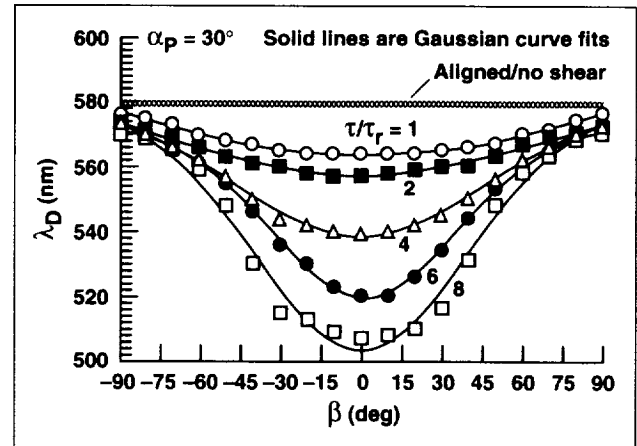


Fig. 2. Dominant wavelength versus relative in-plane view angle between observer and shear vector, with relative surface-shear-stress magnitude as the parameter.

millisecond), continuous (over entire test surface), and reversible (results are valid for dynamically changing flow conditions).

The first figure illustrates the color-change response of an LCC subjected to a tangential jet of air. In the figure, the white light was positioned normal to the test surface and the camera was oriented at an oblique view angle of 35 degrees above the surface. In the left-hand frame, flow is directed away from the camera; orange indicates no shear, whereas yellow through green to blue indicates increasing magnitudes of shear. In the right-hand frame, flow is directed toward the camera; under these conditions, the coating always takes on a rusty-brown appearance, independent of shear magnitude.

A fiber-optic probe, positioned at an above-plane view angle $\alpha_p = 30$ degrees, was used to obtain color measurements on the centerline of this jet-induced pattern. Results are shown in the second figure, in which dominant wavelength λ_D (nanometers) is plotted versus β (degrees). The term β is the in-plane

view angle between the shear stress direction and the observer's line of sight ($\beta = 0$ degrees corresponds to flow directly away from the observer). Relative shear stress magnitude (τ/τ_r) was varied over an eight-fold range. The maximum color change with reference to the no-shear color was always measured when the shear force was aligned with and directed away from the observer; changes in β to either side of this aligned position resulted in symmetric reductions in color change. It was also found that

color change scaled linearly with increasing shear stress magnitude for flow directly away from the sensor. Based on these results, a full-surface shear measurement method involving multiple, oblique views of the test surface was formulated and is currently being validated.

Ames-Moffett contact: D. Reda
(415) 604-6034
Headquarters program office: OA

Effects of Two-Dimensional Forcing on Free Shear Layers

Michael M. Rogers, Robert D. Moser

We have used direct numerical simulation to investigate the effects of two-dimensional (2-D) forcing on turbulent plane mixing layers and on wakes in order to develop improved turbulence models. It is well known that turbulent free shear layers, such as plane wakes and mixing layers, are sensitive to initial conditions. This makes it possible to control the layer spreading rate and mixing characteristics through the use of forcing.

The initial conditions for the computations consist of two realizations from a direct numerical simulation of a turbulent boundary layer done by P. Spalart. The initial conditions for the plane wake simulations consist of two turbulent boundary layers flowing in the same direction on opposite sides of a "splitter plate" which is removed at time zero to create the wake. The mixing layer is generated by removing the splitter plate when the boundary layers are flowing in opposite directions. Forcing is accomplished by artificially amplifying the existing 2-D modes in the initial conditions by a constant factor (five for "moderate" forcing and twenty for "strong" forcing). Similar 2-D forcing has been achieved in experiments by vibrating the tip of the splitter plate, and it is likely that some "natural" 2-D forcing occurs

even in unforced free shear flows as a result of the receptivity of the splitter-plate tip to disturbances originating elsewhere in the flow.

Once developed, both the unforced and the forced flows exhibit periods of at least approximate self-similarity during which the flow evolution can be characterized by single length and velocity scales. However, the self-similar states achieved by the forced and unforced flows are quite different, with different growth rates, turbulence statistics, mixing characteristics, and flow structure. The wake is more sensitive to forcing than the mixing layer. As a result of "strong" forcing, the growth rate of the wake increased by a factor of three, compared with a 20% increase in the mixing layer. "Moderate" forcing has little impact on the mixing-layer growth rate but increases the wake growth rate by about 35%.

The relative magnitude of the cross-stream turbulent fluctuation intensity is also increased as a result of the forcing. In the mixing layer (at the centerline), the increase is 3% for moderate and 50% for strong forcing; the corresponding increases in the wake flow are by factors of 2.1 and 5.4. In this respect, the wake is more sensitive to forcing than

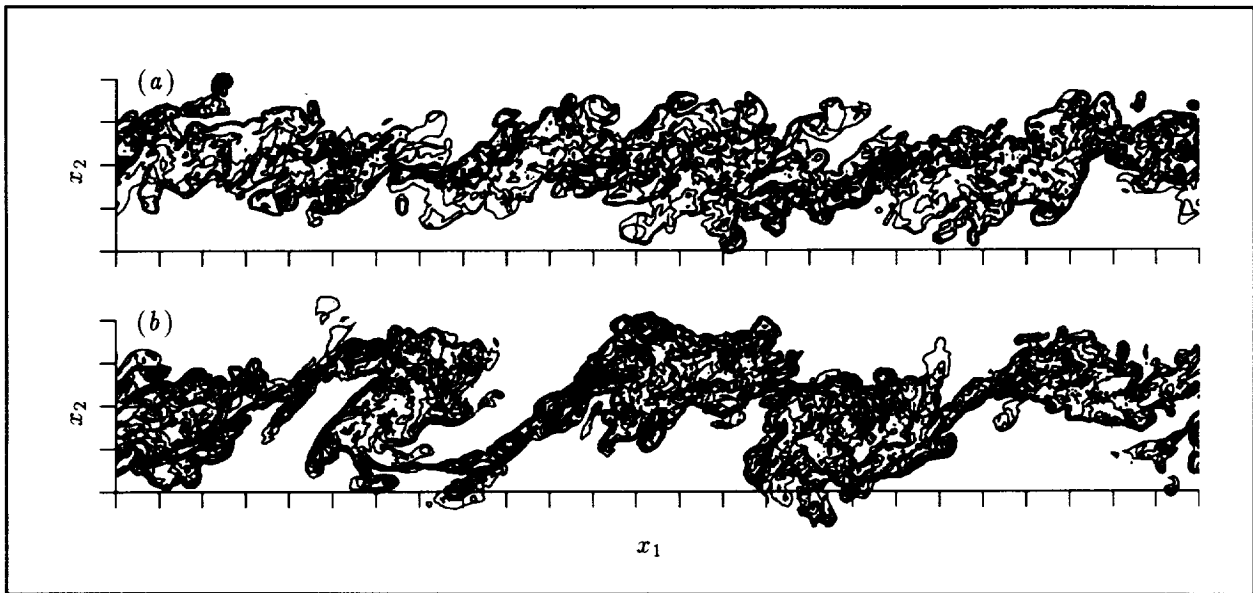


Fig. 1. Concentration contours of a passive scalar quantity marking the large-scale structure in (a) an unforced plane mixing layer and (b) a forced plane mixing layer.

the mixing layer. This and other turbulence statistics computed from the numerical simulations are being used to develop improved turbulence models.

Two-dimensional forcing promotes organized, large-scale flow structure. The figure contains a flow visualization of the turbulent eddies in the plane mixing layer. The first frame is a side view of the unforced flow; the second is the same view of the strongly forced layer. The organization of the forced flow into large-scale 2-D roller structures that undergo “pairings” similar to those observed in

transitional mixing layers is readily apparent. Similar large-scale organization is also observed in the forced-wake cases. This organized large-scale structure has a strong impact on mixing characteristics. This information can improve our understanding and control of chemical reactions in free shear layers.

Ames-Moffett contact: M. Rogers

(415) 604-4732

Headquarters program office: OA

Convergence Acceleration for Simulation of High-Lift-Airfoil Turbulent Flow Problems

Stuart E. Rogers

The INS2D flow solver has been extensively tested and used for solving high-lift-airfoil flow problems. Engineering analysis of high-lift devices using flow solvers for subsonic commercial transports has become a critical part of the design cycle. Changes in cruise wing cross sections and the need for cheaper and mechanically simpler systems require improvements in the high-lift designs. The original line-relaxation algorithm of the INS2D flow solver was found to work well for most flow problems, giving a converged solution in 200–400 iterations. However, for some fine-resolution overset grid cases, this algorithm took a long time to converge—up to several thousand iterations. Users of the code at Boeing asked that these cases of slow convergence be examined.

The incorporation and testing of a number of different algorithms into the INS2D flow solver has resulted in significant improvements through the use of a generalized minimum residual (GMRES) solver preconditioned with an incomplete lower-upper (ILU) factorization. The GMRES solver converges at least twice as fast as the line-relaxation solver for all cases tested thus far: it converges in 300–400 iterations for the cases that previously required thousands of iterations, at a slightly lower cost per iteration. The figures illustrate the convergence plots for a typical

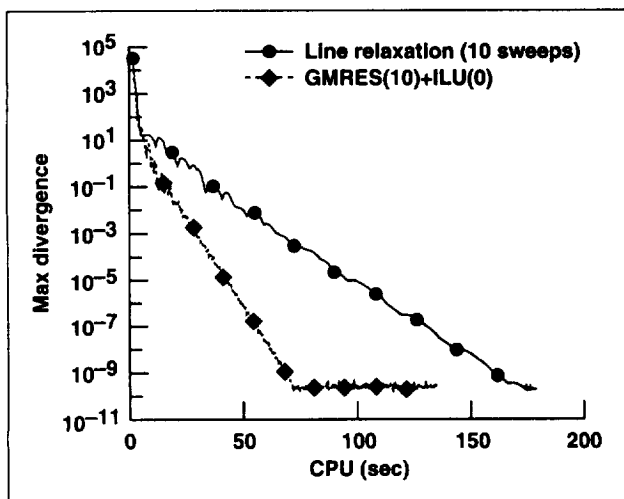


Fig. 1. Convergence for a typical airfoil flow case.

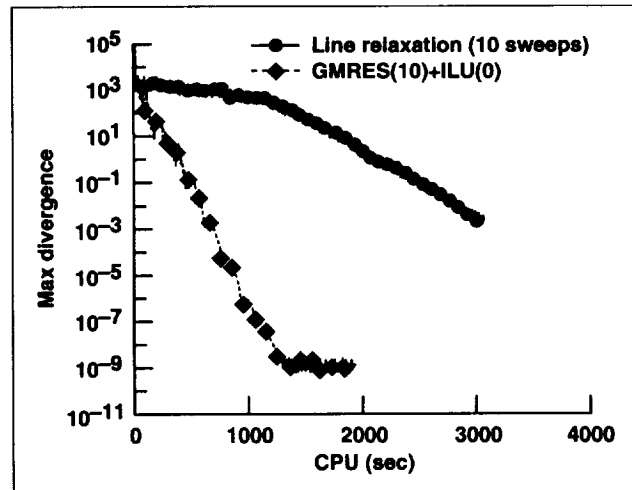


Fig. 2. Convergence for a difficult fine-grid case.

airfoil case and for a fine-grid case. The first figure plots the maximum divergence velocity versus CPU (central processing unit) seconds on a CRAY C-90 for a NACA 4412 airfoil at 14 degrees angle of attack. Symbols are plotted for every 50 iterations. The second figure shows a dramatic savings (greater than a factor of six) in the CPU time required for convergence for the flow over a McDonnell Douglas three-element airfoil at 8 degrees angle of attack. It is expected that NASA, Boeing, and McDonnell Douglas will save on the order of 1000 hours of CRAY C-90 CPU time over the next year as a result of the current improvement in the convergence rate.

The same improvement in convergence rate would be beneficial to the INS3D flow solver. Although the GMRES algorithm cannot be used in the same manner for this three-dimensional flow solver as it was in INS2D (because of memory limitations), a matrix-free version of the GMRES algorithm may be possible. This work will continue in an effort to implement a GMRES algorithm into the INS3D flow solver.

Ames-Moffett contact: S. Rogers
(415) 604-4481

Headquarters program office: OA

Instabilities Originating from Suction Holes Used for Laminar Flow Control

Jonathan H. Watmuff

Suction through porous surfaces may offer considerable fuel savings for aircraft because of the drag reduction obtained by maintaining laminar flow over a large portion of a wing's surface. However, local three-dimensional (3-D) disturbances (e.g., streamwise vortices) are generated by the discrete suction holes, and evidence suggests that interactions between these disturbances could defeat the purpose of the suction and even cause premature transition. The objective of this project is to determine the characteristics of disturbances generated by isolated suction holes and to explore the interactions between disturbances generated by multiple holes, which are aligned but displaced in the streamwise direction.

Detailed studies have been made using isolated holes under conditions of strong suction and without suction. Small sinusoidal perturbations are applied at

the hole, and hot-wire measurements are averaged on the basis of the phase of the disturbance. The experiment is completely automated and can be run continuously (24 hours/day) for weeks at a time. Data are measured using unprecedentedly large, spatially dense grids, and the results are examined using software tools developed for studying the results of numerical simulations on a graphics workstation.

In both cases, with and without suction, 3-D contour surfaces of the velocity perturbations in the vicinity of the hole show highly 3-D Tollmien-Schlichting (TS) waves that fan out away from the hole with streamwise distance. A plan view of the 3-D contours for both cases is shown in the figure. When suction is applied, the perturbations on the centerline are much stronger, and they decay less rapidly, whereas the TS waves in the far field are

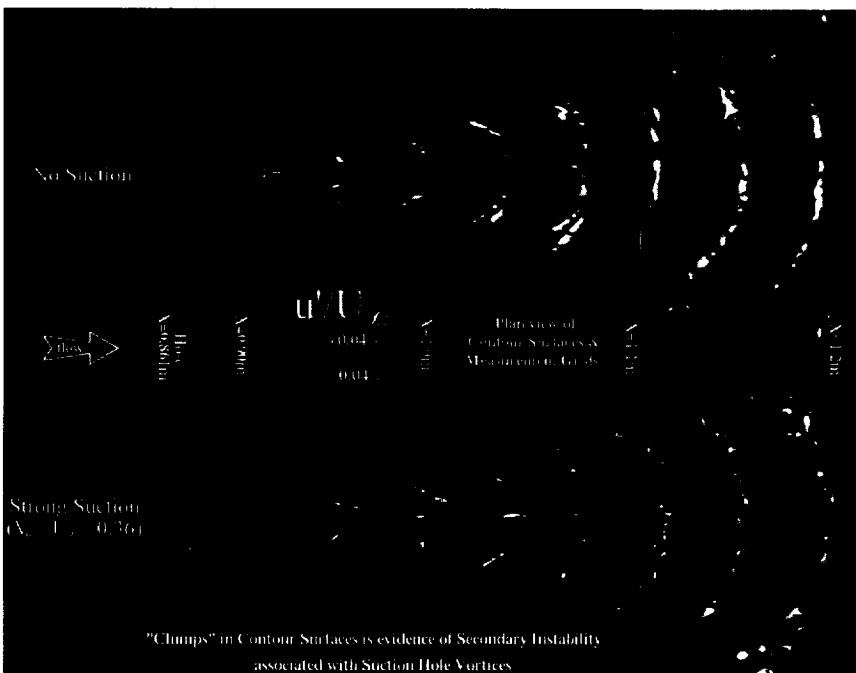


Fig. 1. A plan view of the 3-D contours under conditions of strong suction and without suction. (See color plate 11 in Appendix)

much the same as in the case without suction. The bow-shaped contour surfaces of the TS waves downstream of the hole develop spanwise irregularities which eventually form into clumps. The contours remain smooth when suction is not applied. The spanwise clumping observed in the contour surfaces is evidence of a secondary instability that could be associated with the suction vortices.

Results from using two holes aligned but displaced in the streamwise direction indicate that partial TS wave cancellation is possible, depending on the hole spacing and the disturbance frequency. This is an important consideration because it implies that an optimal streamwise spacing exists for cancellation of TS wave disturbances generated by suction holes. The optimal grid spacing would depend on the flight speed.

Even without suction, the harmonic point source problem is challenging for computational fluid dynamics, even for advanced and expensive direct

numerical simulations (DNS). With suction, grid resources are consumed by the hole, and this makes DNS even more expensive. Using DNS for streamwise interaction studies will be prohibitively expensive since linear superposition cannot be used for the multiple holes.

A 20:1 scale porous surface has been machined for improved spatial resolution with hot wires. The interactions between disturbances generated by multiple holes will be studied. Some potentially illustrative techniques will be used, including (1) perturbing the suction through a particular hole, (2) perturbing the suction through an entire group of holes, (3) using harmonic perturbations, and (4) using impulsive perturbations.

**Ames-Moffett contact: J. Watmuff
(415) 604-4150
Headquarters program office: OA**

Advanced Navier–Stokes Solver

Seokkwan Yoon

Recent advances in computational methods in aerodynamics have made the Navier–Stokes codes promising tools in the design process of advanced transport aircraft configurations. However, most existing three-dimensional (3-D) Navier–Stokes codes still need improvements in efficiency and robustness for routine aerodynamic design applications when high-resolution shock capturing is required.

It is known that non-oscillatory finite volume schemes can be constructed through the introduction of artificial diffusion, which produces an upwind bias. One approach to the construction is to blend low- and high-order diffusive terms using a switch with a pressure sensor, as in the Jameson–Schmidt–Turkel (JST) scheme. However, the JST scheme suffers from relatively poor resolution of discontinuities and unsightly oscillations near the edge of the boundary layer. Another approach to the construction of high-

resolution schemes that combines monotonicity and high-order accuracy is to add limited antidiffusive terms to a low-order scheme. A symmetric limited positive (SLIP) scheme with characteristic decomposition can produce highly accurate solutions.

Multigrid methods have been effective for accelerating the convergence of iterative schemes by taking large time steps and propagating waves quickly on coarse meshes. Although conventional implicit methods often achieve fast convergence rates, they require more computer time per iteration than explicit methods do. An unconditionally stable implicit algorithm based on lower–upper (LU) factorization, symmetric Gauss–Seidel (SGS) relaxation, and Newton-like iteration requires less computer time per iteration than the explicit Runge–Kutta scheme does.

Implementation of new algorithms has resulted in a highly efficient and accurate Navier–Stokes solver named CNS3D (Compressible Navier–Stokes solver in generalized 3-D coordinates), which requires an order-of-magnitude smaller number of user-provided input parameters than most existing codes do. In order to demonstrate the performance of the new code, transonic flow calculations have been carried out for an ONERA M6 wing using a $193 \times 49 \times 33$ C-O grid with high cell aspect ratios. The first figure shows pressure coefficients at the 44% semispan station for both experimental data and Euler solutions at Mach 0.84 and 3 degrees angle of attack. The SLIP scheme appears to be able to capture non-oscillatory shocks with a sharper resolution than the JST scheme can provide. The second figure shows

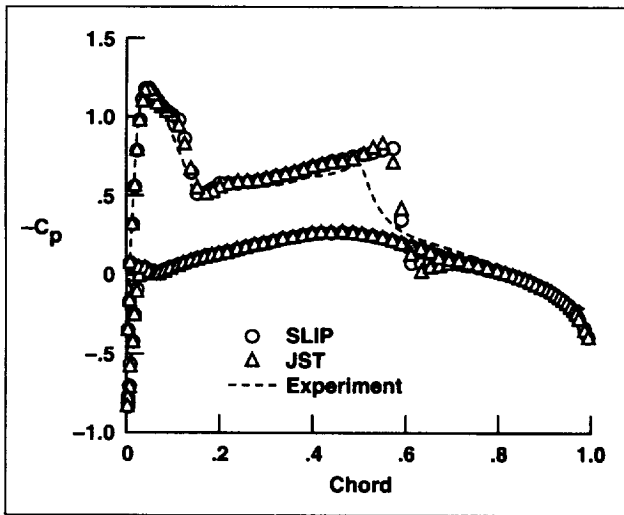


Fig. 1. Pressure distribution for an ONERA M6 wing.

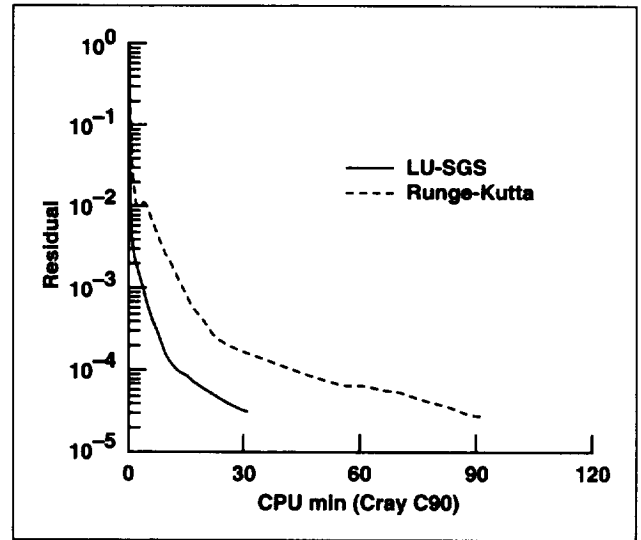


Fig. 2. Convergence histories using a SLIP scheme.

convergence histories of the implicit LU-SGS and explicit Runge–Kutta methods for a viscous turbulent separated flow at Mach 0.84 and 5 degrees angle of attack. The results show that the implicit LU-SGS scheme converges 3 times faster than the explicit Runge–Kutta scheme does on a CRAY C-90 computer.

Future plans include the development of a multiblock version with multiequation turbulence models. Work on further acceleration in convergence rates is in progress.

Ames-Moffett contact: S. Yoon
(415) 604-4482

Headquarters program office: OA

Head-Up Spatial Auditory Displays for Aeronautics

Durand R. Begault

The current implementation of the Traffic Alert and Collision Avoidance System (TCAS) uses both auditory and visual displays of information to supply flight crews with real-time information about proximate aircraft. However, only the visual component is delegated to convey spatial information about surrounding aircraft, whereas the auditory component is used as a redundant warning or, in the most critical scenarios, for issuing instructions for evasive action.

Within its standard implementation, three categories of visual–aural alerts are activated by TCAS, contingent on an intruding aircraft's distance. One category, a visual–aural cautionary alert, is known as a traffic advisory. The threshold for activating a traffic advisory is a potential for conflict within forty seconds; an amber filled circle is generated on a visual map display, and an auditory warning consisting of a single cycle of the spoken words "TRAFFIC, TRAFFIC" is given.

Work conducted through the Ames Spatial Auditory Display Laboratory has shown that spatially correlated information from an auditory source can substantially reduce visual search time (between 175 and 1200 milliseconds, depending on the target azimuth). In two studies, we evaluated the effectiveness of a three-dimensional (3-D) head-up auditory TCAS display by measuring target detection time. Pilots from a major air carrier flew a generic "glass cockpit" flight simulator. All crews used visual out-the-window search in response to a TCAS advisory, since no visual TCAS display was used. Half the crews heard the standard loudspeaker audio alert, and half heard an alert that was spatialized over headphones using 3-D sound techniques. The direction of the spatialization was linked to the target location's azimuth, but not to its elevation. In addition, the spatialized audio stimuli were exaggerated

by a factor of three in relationship to the visual angle in order to encourage head movement in the aurally guided visual search (e.g., visual targets at 10 degrees azimuth would correspond to spatialized stimuli at 30 degrees azimuth). Results of the study showed a significant reduction in visual detection time by using spatialized sound to guide head direction (4.7 versus 2.2 seconds).

A similar study by Begault and Pittman compared target detection time between a head-down visual display (standard TCAS) and a head-up audio display (3-D TCAS). Three-dimensional sound was used for aurally guided visual search, as in the previous study by Begault, but without inclusion of the exaggeration factor mentioned above. The mean detection time for the standard, head-down TCAS group was 2.63 seconds, whereas the mean for the 3-D audio head-up group was 2.13 seconds. The results imply that the presence of a spatial auditory cue can significantly reduce the time necessary for visual search in an operational setting.

Although 500 milliseconds may seem to be only a modest improvement, it does suggest that an aural 3-D TCAS display may be desirable in addition to a standard TCAS display: pilots can keep their head "out the window" looking for traffic without needing to move the head downward to the visual display and then back up. In other words, by accessing an alternative perceptual modality—sound—the visual perceptual modality is freed to concentrate on other tasks, if necessary. A patent application is pending for the application of several technologies related to this type of aurally guided visual search.

**Ames-Moffett contact: D. Begault
(415) 604-3920**

Headquarters program office: OA

The Box: A Free-Play Multimedia Learning Environment for the Boeing 737-300 Flight Management System

Steven M. Casner

The Box is a Macintosh-based multimedia learning environment for the Boeing 737-300 flight management system. A prototype of a next-generation computer-based learning environment that can be used in the home, The Box combines five important resources. First, The Box contains a reverse-engineered simulation of the Boeing 737-300 control/display unit and mode control panel together with significant portions of the flight management computing system, including simulated three-dimensional path-prediction, performance, and navigational databases. Second, The Box provides full multimedia presentation capabilities including video, still photography, sound, animation, text, and voice. Third, through extensive collaboration with avionics manufacturers and experienced airline pilots, The Box offers a library of instructional materials that can be accessed interactively by the pilot. These instructional materials provide the pilot with topical discussions, animated explanations of system features, informal advice collected from experienced pilots, or entire courses. Fourth, The Box provides three practice modes that allow pilots to exercise what they know. In Free Play mode, The Box allows pilots to explore the system at their leisure, experimenting with new techniques or brushing up on old ones. In Focused Practice mode, The Box challenges the pilot with problems relating to a specific topic, such as holds or cruise descents.

In Line Practice mode, The Box challenges the pilot to work through difficult departures and arrivals containing entire sequences of air traffic control clearances. The Line Practice mode allows The Box to be positioned at any location within the continental United States and configured with any flight plan. All of the Line Practice scenarios were collected during inflight observations of challenging departures and arrivals. Fifth, for purposes of research, The Box also serves as a data gathering tool. The Box provides a feature that allows all pilot interactions with The Box to be time-stamped and saved in a history file that can be inspected or analyzed later.

The Box is available in two versions, a CD-ROM version that contains the full variety of multimedia instructional materials described, and a text-only version that presents all instructional materials by text and thus does not require CD-ROM.

The Box will be distributed as a public-domain tool for university classrooms and ultimately for airline transport pilots. Ongoing research and development efforts are aimed at expanding the store of instructional materials through contributions made by airline and avionics industry partners.

**Ames-Moffett contact: S. Casner
(415) 604-6908**

Headquarters program office: OA

Terminal Area Productivity: Air Traffic Management

Victor Cheng, Rhonda Slattery

The Center/TRACON Automation System (CTAS) is an integrated package being developed for the extended terminal airspace to improve air traffic throughput with automated safety enhancement features. CTAS has three components: Traffic Management Advisor, Final Approach Spacing Tool (FAST), and Descent Advisor (DA). Prototypes of these three components have reached different levels of maturity and are being evaluated at selected airports.

The Terminal Area Productivity (TAP) project, an element of NASA's Advanced Subsonic Technology program, contains an air traffic management (ATM) effort to augment the CTAS development effort with parallel plans to enhance CTAS performance and extend CTAS functionalities.

The initial effort to enhance CTAS performance has been directed toward improving the efficiency and realism of the Trajectory Synthesis (TS) function. The TS function can be found in both DA and FAST, which provide traffic advisories for the Center and terminal environments, respectively. The differences in flight characteristics in these two environments are reflected in different TS implementations in DA and FAST. The TS methodology employed in FAST has been examined in detail, and conditions for specifying the final approach flight segments have been modified to more realistically reflect procedures used by air carriers in practice. The modifications are expected to provide more accurate trajectory and flight-time predictions. A parallel effort to improve TS performance in DA has led to the identification of all the capture conditions for the various deceleration and descent segments normally flown in the Center airspace. These capture conditions will be useful in developing more robust TS algorithms.

Two separate efforts have been initiated to extend CTAS functionalities beyond the current state

of the art. The first is a joint effort with Langley Research Center to establish a coordinated air-ground flight system between the flight management system (FMS) on the aircraft and CTAS. A flight experiment was performed in Denver with the B737 research aircraft from Langley flying DA descent profiles. Details of the flight test can be found in a companion report on the DA test. Results from this test will be useful in defining advanced CTAS/FMS integration concepts to be developed, implemented, and evaluated in the future.

The second effort to extend CTAS functionalities involves the exploitation of advanced navigation systems such as the Global Positioning System (GPS) to achieve more throughput in landing on closely spaced parallel runways under instrument meteorological conditions. A simulation with air traffic controllers serving as test subjects has been carried out as the first in a series of experiments to develop and evaluate advanced concepts to safely reduce spacing requirements. Preliminary results from the experiment are promising, and more details can be found in the report on "Precision Approaches to Closely Spaced Parallel Runways."

In addition to continuing the investigations described here, plans for the TAP-ATM project include the study of CTAS trajectory prediction sensitivity, which will strongly affect the confidence level in the conflict detection capability of CTAS, and the investigation of an additional CTAS functionality for performing rapid runway and airspace reconfiguration.

**Ames-Moffett contact: V. Cheng
(415) 604-5424**

Headquarters program office: OA

Interviews with Apollo Astronauts

Focused interviews were conducted with the astronauts who landed on the Moon during the Apollo program. The purpose of the interviews was to define extravehicular activity (EVA) system requirements that will be needed for a return to the lunar surface and for future planetary missions. Although more than 20 years have passed since these men walked on the Moon, they remain the only humans who have carried out operations on an extraterrestrial celestial body.

Information from the interviews was examined with particular attention to areas of consensus, since commonality of experience is necessary in order to inform the design of advanced systems. There were both general and specific findings. Among the general results were the following:

1. All subsystem designs should be based on principles of fundamental simplicity and reliability. Given a trade-off, simplicity and reliability are to be preferred over added functionality.
2. Emphasis should be put on the integration of crew, equipment, and facilities as a total system, not just on system components.
3. The EVA hardware-related areas most in need of improvement are the bulkiness and inflexibility of the suits and the awkwardness of the gloves.

Mary M. Connors, Dean B. Eppler, Daniel G. Morrow

4. Equipment design should be based on EVA task requirements, just as crew training should be on actual tasks and equipment.

5. Future missions will require increased crew autonomy. Crews will need greater flexibility in operations, particularly in daily scheduling.

6. The habitat crew will play an increasingly important role in supporting EVA crew operations, replacing many of the activities previously performed by ground control.

7. High levels of maintainability and repairability must be designed into experiments as well as into equipment and facilities.

8. Extended missions will require ways to achieve and sustain high levels of mental performance.

Specific results are presented in the study report in the following categories: mission approach; mission structure; suits; portable life support systems; dust control; gloves; automation; information, displays, and controls; rovers and remotes; tools; operations; and training. Research recommendations were also developed as a result of the interviews.

**Ames-Moffett contact: M. Connors
(415) 604-6114**

Headquarters program office: UL

Final Approach Spacing Tool

Tom Davis, Ken Krzczowski

The automated air traffic control system referred to as the Center/TRACON Automation System (CTAS) continues to be developed and evaluated. The development and field deployment of the terminal area component of the system, the Final Approach Spacing Tool (FAST), has achieved a series of milestones over the past year. A new approach for sequencing and assigning runways for arrival traffic that is based on examination and deconfliction of aircraft trajectories was designed and implemented. This trajectory-based sequencing and runway allocation algorithm was evaluated in hundreds of hours of real-time simulation by Dallas/Fort Worth controllers.

The simulations received highly favorable evaluations and resulted in a deployment of the sequencing and runway allocation functionalities at Dallas/Fort Worth in a shadow mode. Preparations are under way for training-room activities in which the system will be tested by an expanded team of controllers.

Future development and evaluation plans for the FAST system include an eventual limited operational assessment of the sequencing and runway allocation advisories at the Dallas/Fort Worth TRACON (terminal radar approach control facility). This activity will commence at the conclusion of training-room activities currently being planned. In addition, there will be further development and simulation evaluation of the speed and heading advisories in FAST, followed by an eventual operational test. The FAST system is being adapted for use in another operational evaluation at the new Denver International Airport.

Ames-Moffett contact: T. Davis

(415) 604-5438

Headquarters program office: OA

Civil Tiltrotor Terminal Area Operations

William A. Decker

Tiltrotor aircraft offer considerable potential as civil transports. Realization of that potential requires development of appropriate aircraft design features, certification standards, vertiport designs, and operating procedures tailored to take advantage of the tiltrotor's capabilities. Tiltrotor aircraft features that have particular impact on terminal area operations include thrust vectoring independent of body pitch attitude, and good low-speed control. Whereas the tiltrotor shares flight characteristics with both fixed-wing airplanes and helicopters, it must convert between those flight modes, typically within the context of precise terminal operations.

A series of piloted simulation experiments has been conducted on NASA Ames Research Center's

Vertical Motion Simulator (VMS) to investigate the influence of tiltrotor cockpit design features on developing certification and operating criteria for civil tiltrotor transports. This joint NASA-Federal Aviation Administration (FAA) effort includes participation by the British Civil Aeronautics Authority, U.S. rotorcraft manufacturers, and potential pilots. Previous simulation experiments in the series investigated issues of (1) where, during an instrument approach, to conduct the conversion from airplane mode to helicopter mode and (2) guidance and display requirements for steep approaches.

An initial terminal-area operating procedure was developed in a fixed-base simulation for a 9-degree

glideslope, suitable for current-generation tiltrotor aircraft. This procedure was formally evaluated during a motion-base simulation on the VMS in November and December 1994 and in subsequent coordinated simulation work at Bell Helicopter Textron and Boeing Helicopters. Desired performance was achieved with the initial terminal-area



Fig. 1. Pilot's view from VMS cockpit during approach to a conceptual vertiport along the Oakland, California, waterfront.

operating procedure when appropriate cockpit display guidance and control features were included. A NASA-developed integrated configuration control (automatic flap and pilot-initiated nacelle angle movement) was further evaluated and received satisfactory pilot handling-qualities ratings for conversion operations.

Operations were conducted into conceptual urban-area vertiports atop parking structures (see figure). Terminal procedure development and evaluation were enhanced by placing vertiports at potential sites within a San Francisco Bay Area visual scene. The natural and man-made obstructions in this operating area helped focus procedure development within typical real-world constraints. The figure shows the pilot's view from 1,000 feet altitude on final approach to a site located near Oakland's Jack London Square. Significant recommendations were collected on the vertiport design, marking, and lighting and have been incorporated in FAA vertiport design projects.

**Ames-Moffett contact: W. Decker
(415) 604-5362**

Headquarters program office: OA

Rotorcraft Modeling Using Flight Test Data

Jay W. Fletcher, Mark B. Tischler

The derivation of mathematical models of system dynamics from measured input and output signals is called system identification. It is an extremely valuable tool because it closes the design loop by verifying (or refuting) the accuracy of analytical dynamic modeling. Valid analytical models of rotorcraft dynamics are needed for flight control system design and analysis as well as for ground based and in-flight simulation. System identification is being used to identify models of the UH-60 flight dynamics for use in simulation model validation and design of flight control laws for the RASCAL UH-60 in-flight simulator.

An Ames-developed system identification package called Comprehensive Identification from Frequency Responses (CIFER) is being used for the linear model identification. Linear parametric models of the aircraft dynamics are identified through the matching of model input/output frequency responses to those calculated from flight data. A robust model-structure determination process ensures that a minimally parameterized model is achieved. An important CIFER milestone was achieved this year with the release of version 2.2 software and the conversion of the package to run under UNIX.

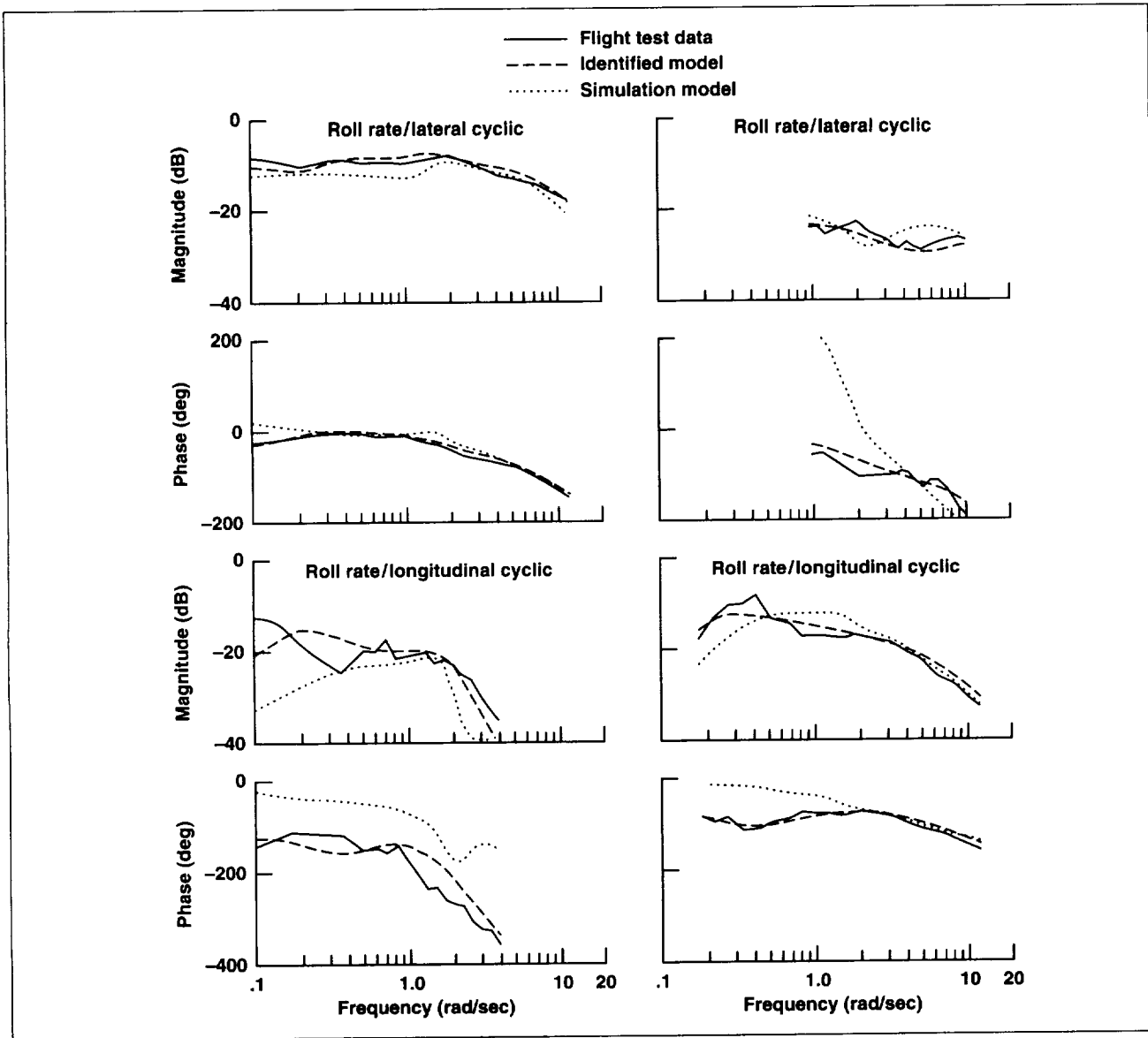


Fig. 1. Comparisons of model and flight data frequency response.

A linear parametric model of the UH-60 flight dynamics at 80 knots has been identified from flight test data collected at Ames Research Center. Flight test measurements from both of the UH-60 research aircraft operated at Ames, the Rotorcraft Aircrew Systems Concepts Airborne Laboratory (RASCAL) and the Air Loads UH-60, were used in this process. Measurements of the rotor blade flapping motions on the Air Loads UH-60 made possible the determination of a more complex flapping dynamics section of the model which includes unsteady aerodynamic effects.

The identified model predicts the dynamic response of the aircraft to control inputs with much greater fidelity than current UH-60 simulation models do. This can be seen in the first figure where the pitch and roll rate frequency responses to longitudinal and lateral cyclic inputs of the identified model and a flight dynamics simulation model are compared with those calculated directly from flight test measurements. Vastly improved prediction of the coupled or "off-axis" responses with the identified model are evident. Correct prediction of these responses is

essential for the model to be used successfully in the design of a control system that will “decouple” the response of the aircraft.

Further improvements in rotorcraft modeling, particularly in the frequency range of 2–5 hertz, are anticipated from further increases in the complexity of identified rotor dynamics models. These will be made possible by the availability of high-quality blade flap, lead–lag, and pitch measurements from the newly installed laser blade motion measurement system on the RASCAL UH-60. Measurement of blade root flap and lead–lag motions relative to the UH-60 main rotor hub arm with laser distance sensors is shown in the second figure. Real-time monitoring of these sensors will also be used for maneuver-envelope cueing and rotor-system health monitoring.

Ames-Moffett contact: J. Fletcher
(415) 604-6115
Headquarters program office: OA



Fig. 2. Laser distance transducers mounted on UH-60 hub arm.

V/STOL Systems Research Aircraft

John D. Foster, Ernesto Moralez III, Delamar M. Watson

In partnership with the U.S. Marines, the U.S. Navy, and the Advanced Research Projects Agency (ARPA), NASA Ames Research Center has developed and completed flight checkout of an integrated attitude and thrust vector, digital fly-by-wire control system and head-up display for the V/STOL Systems Research Aircraft (VSRA) (see photograph). This program was undertaken to provide flight validation of integrated controls and display concepts for adverse weather operations of short takeoff and vertical landing (STOVL) aircraft. The principal contribution of results from VSRA flight experiments is to the ARPA advanced STOVL aircraft technology program and to U.S. industry participants in that effort. Results will have broader applicability to other military and commercial V/STOL programs, particularly to that of the tiltrotor transport.

The integrated control system provides a hierarchy of control modes, including (1) pitch and



Fig. 1. VSTOL Systems Research Aircraft.

roll rate and attitude command, (2) flightpath and longitudinal acceleration command, and (3) longitudinal, lateral, and vertical velocity translational rate command as candidates for pilot evaluation to assess improvements in flying qualities and operational capability in instrument flight conditions. Head-up display presentations, derived from an inertial

measurement unit and global positioning system, are also integrated with the control mode to provide guidance information for these operations. Extensive flight tests during the past year have proven these systems to be fully functional and, through appropriate system monitoring, to operate safely in the event of component or software malfunction.

An extensive flight experiment program is now under way to evaluate these control and display modes during transition from cruise flight to hover and vertical landing. The program is being carried

out at Ames' Crows Landing Flight Facility which offers capability for flight test control, precision navigation and tracking, and telemetry data acquisition. In addition to Ames pilots, participants in the program include pilots and engineers from the Naval Air Warfare Center, McDonnell Douglas, Boeing, Lockheed, and the British Defence Research Agency.

Ames-Moffett contact: J. Foster

(415) 604-6686

Headquarters program office: OA

ASTOVL Lift Fan Simulation

James A. Franklin, William W. Y. Chung, Paul F. Borchers

NASA Ames Research Center is participating in technology development for advanced short takeoff and vertical landing (ASTOVL) fighter aircraft as a member of the Advanced Research Projects Agency program team. NASA's role is to participate in developing design guidelines for integrated flight/propulsion controls, to support technology development for a demonstrator aircraft, and to provide consultation on integrated control design to industry participants. Ames developed a simulation model of a lift fan configuration that represents a prospective ASTOVL concept. Design and performance of a lift-fan-configured ASTOVL aircraft during powered-lift operations are critically dependent on performance and dynamic response of the lift-fan/lift-cruise engine system. An experiment was conducted on the Ames Vertical Motion Simulator to examine the model's flying qualities over the low-speed flight envelope, including transition from conventional to vertical flight, hover, and vertical landing.

The simulation model accounts for subsonic, power-off aerodynamics and jet-induced aerodynamics in hover and forward flight, including ground effects. Propulsion system components modeled include a remote lift fan and a lift cruise engine. Their static performance and dynamic response are represented by the model. The flight/propulsion control system includes modes for several response types

which are coupled to the aircraft's aerodynamic and propulsion system effectors through a control selector tailored to the lift-fan propulsion system.

Objectives of the experiment were (1) to assess the effects of lift-fan propulsion system design features on aircraft control during transition and vertical flight, including integration of lift-fan/lift-cruise engine/aerodynamic controls and lift-fan/lift-cruise engine dynamic response; (2) to evaluate pilot-vehicle interface with the control system and head-up display including control modes for low-speed operational tasks and control-mode/display integration; and (3) to conduct operational evaluations of this configuration during takeoff, transition, and landing similar to those carried out previously by the Ames team for the mixed-flow vectored thrust and augmentor-ejector concepts.

Based on results of the simulation, preliminary assessments of acceptable and borderline lift-fan and lift-cruise engine thrust response characteristics were made. Maximum pitch, roll, and yaw control power used during transition, hover, and vertical landing were documented. Control- and display-mode options were assessed for their compatibility with a range of land-based and shipboard operations from takeoff to cruise, through transition, and back to hover and vertical landing. Flying qualities were

established for candidate control modes and displays for instrument approaches and vertical landings aboard an LPH assault ship and a DD963 destroyer. Test-pilot and engineer teams from the Naval Air Warfare Center, Boeing, Lockheed, McDonnell

Douglas, and the British Defence Research Agency participated in the program.

**Ames-Moffett contact: J. Franklin
(415) 604-6004**

Headquarters program office: OA

Preliminary Field/Flight Testing of Descent Advisor (DA) at Denver

Steven Green

The Center/TRACON Automation System (CTAS) was developed to support increasing demands for greater capacity and efficiency in the National Airspace System. The Descent Advisor (DA) tool, one of three CTAS elements, is designed to assist controllers at the Air Route Traffic Control Center in the efficient sequencing and separation of arrival and overflight traffic. The DA tool computes fuel-conservative, conflict-free trajectories for aircraft (both conventional aircraft and those equipped with a flight management system (FMS)) and translates those trajectories into appropriate air traffic control (ATC) clearance advisories.

The objective is to develop DA and deploy the system for field testing at Denver in a phased approach. The testing will be simple at first and then the functional, procedural, and traffic complexity will be slowly increased until fully operational conditions are achieved. A new air traffic clearance was developed to support the optimum DA descents. The performance objective of DA is to predict complex descent trajectories 20 minutes in advance of arrival with arrival-time errors of less than 20 seconds.

Starting in May 1994, a prototype of DA was implemented in the new CTAS software architecture. Assisted by researchers at NASA Langley, Ames completed extensive validation of the trajectory prediction algorithms in early September. The DA system was deployed to the Denver Center Field Site and operated in a field test for three weeks, ending September 30. The test setup is illustrated in the figure. The test was a highly successful collaborative effort involving the Air Traffic Management and Flight

Human Factors Branches at Ames; Langley Research Center; the Federal Aviation Administration; United Airlines; and the National Center for Atmospheric Research. This was the first time that an active CTAS advisory was issued to a commercial aircraft as an ATC clearance. A total of 108 flights received DA clearances (77 commercial flights and 31 descents flown by Langley's Transport Systems Research Vehicle (TSRV) Boeing 737). The study focused on trajectory prediction accuracy as well as procedural and clearance phraseology issues.

Detailed trajectory analysis is under way, and preliminary results indicate an excellent arrival-time accuracy. For the TSRV cases, the mean arrival-time error was 8 seconds late, with a standard deviation of 16 seconds. When only conventional cockpit techniques were used on board the TSRV, the mean error was 16 seconds, whereas when FMS techniques were used, the mean error was reduced to 3 seconds. The United flights had similar results. None of the FMS cases employed Required Time of Arrival capability. The improvement in the FMS cases results from the superior course-tracking accuracy and altitude control capability of the FMS. In addition, preliminary analysis indicates that DA trajectory predictions were comparable in accuracy to (sometimes more accurate than) those of the FMS. The DA was also able to routinely predict each aircraft's altitude along its path with an average error of less than 300–500 feet—an accuracy requirement to support conflict-free trajectory planning. Overall, controller and pilot response to the DA was favorable.

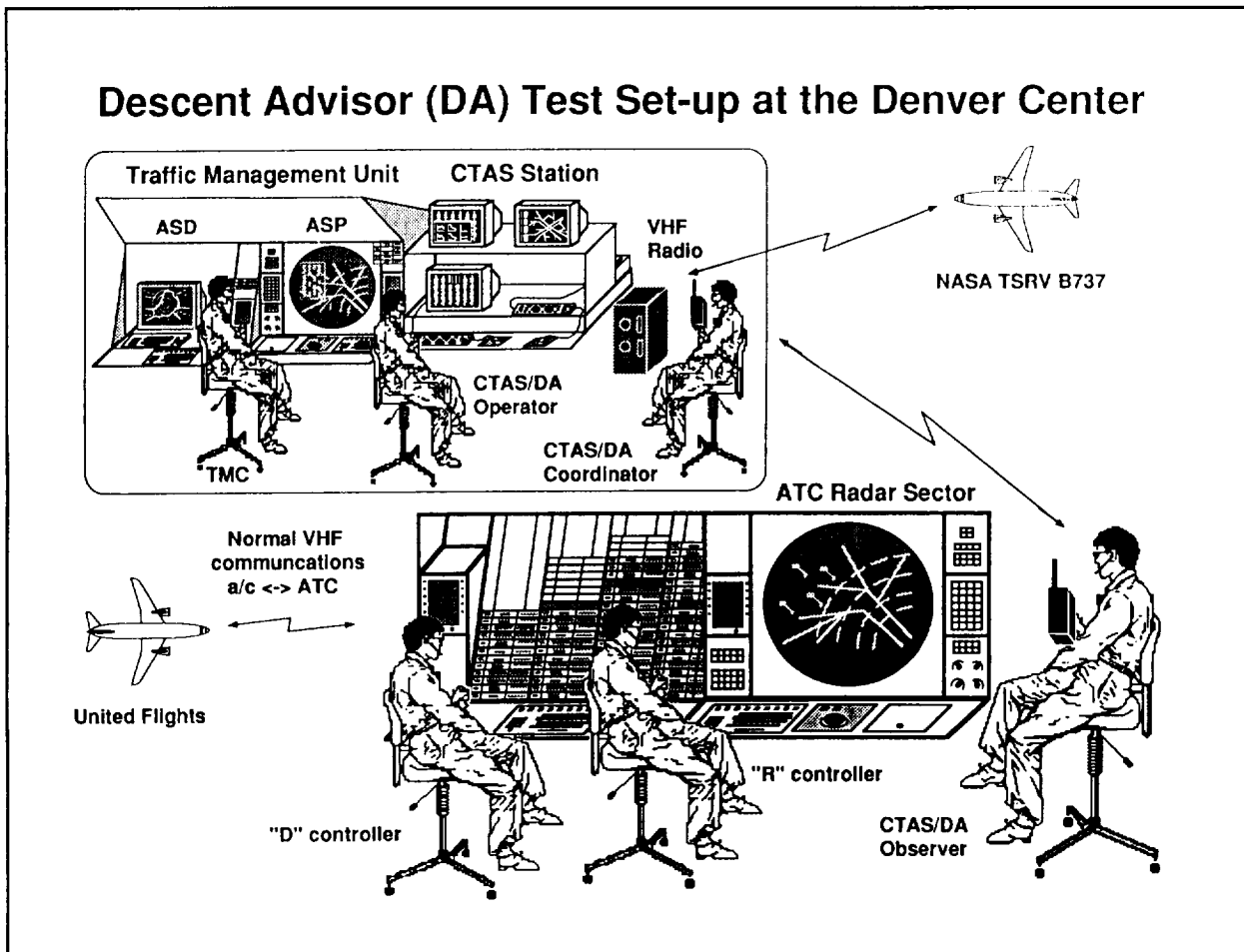


Fig. 1. Descent Advisor test configuration at Denver Center.

Future plans include the development and evaluation of a DA auxiliary display and interface (to operate side by side with existing ATC displays). The DA air traffic clearance and associated procedures will be improved based on results of this test. A more complex field test is scheduled for May 1995 at Denver (two months after the scheduled opening of the new Denver airport). DA software development will continue in the areas of metering advisories,

conflict detection and resolution, and advanced graphical interfaces. A series of real-time simulations with the FAA's System Design Team will prepare the DA system for further field testing in 1996.

Ames-Moffett contact: S. Green
(415) 604-5431
Headquarters program office: OA

RASCAL Noise-Abatement Flight Tests

William S. Hindson, Robert T. N. Chen

Community noise is one of the considerations impacting the further use of rotorcraft in an integrated air transportation system. One of the most significant sources of the noise generated by a passing, overflying, or approaching helicopter occurs when each rotor blade encounters the vortex shed by the preceding blade. The phenomenon is known as blade-vortex interaction (BVI). It is characterized by an impulsive noise, sometimes called blade slap, that can be particularly objectionable during the descent to landing. The usual approach to BVI noise alleviation involves fundamental improvements in rotor system design. However, special flight techniques that avoid operation in conditions that are particularly conducive to BVI are also employed. Conditions during approach and landing that should be avoided are shown conceptually in the figure, along with recommendations for decelerating and descending flightpaths that would avoid them.

In the summer of 1994, flight tests were conducted with the NASA/Army Rotorcraft Aircrew Systems Concepts Airborne Laboratory (RASCAL) UH60A Black Hawk helicopter to assess the potential for operational techniques and specially tailored multisegment glidepaths to contribute to the reduction of BVI during the landing approach.

These operational techniques are well known among helicopter pilots, but the procedures are difficult to follow with the necessary precision even in visual flight conditions. Furthermore, there is presently no capability to tailor approach operations for noise reduction in instrument flight conditions. Even if these operational procedures are proven effective for noise reduction, no support for their use can be envisaged without the means to accurately and repeatably fly these approach profiles in both visual and instrument conditions.

The rapidly developing application of the Global Positioning System (GPS) to civilian uses can provide the means to obtain official support for these procedures, thus opening the way to greater integration of rotorcraft into the urban transportation infrastructure. In the RASCAL flight tests, differential GPS

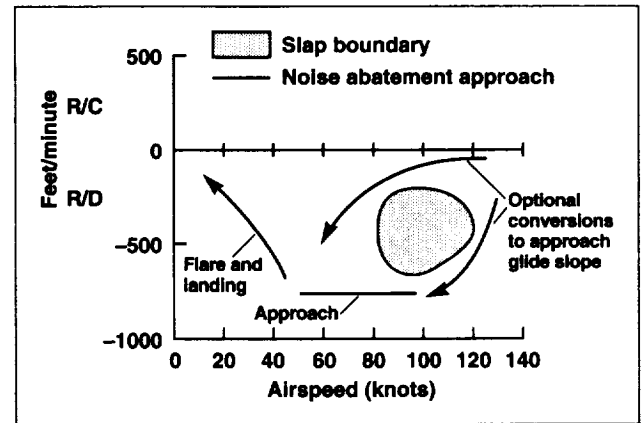


Fig. 1. Noise-abatement flight technique for light helicopters.

navigation was used to obtain the precision three-dimensional positioning needed for flying multi-segment decelerating approach glidepaths. A total of four different approach profiles were evaluated. An on-board computer generated guidance errors in the flightpath, and conventional cockpit displays were used to convey this information to the pilot. Many additional operational factors had to be considered when the approach profiles were constructed. Among them were obstacle clearance planes, clearway to the landing zone, minimum IFR (instrument-flight-rules) airspeeds, engine-out performance for continued approach or go-around, approved minimum altitudes in instrument flight conditions, maximum scheduled rates of descent, and passenger acceptance considerations.

Pilots from the FAA, industry, and NASA evaluated the feasibility of these approaches. Valuable flight test data were collected, including data pertaining to the tracking accuracies that were achieved and the navigational accuracy of the differential GPS as determined by a separate ground-based laser tracking facility. In addition, pilot opinion data in the form of Cooper-Harper pilot ratings were

obtained. The ease and accuracy with which these approaches could be flown offer encouragement for pursuing this method of noise reduction. Together with aeroacoustic improvements in rotor system design, there appears to be a possibility of reducing

helicopter noise to levels that will result in significantly greater community acceptance.

**Ames-Moffett contact: W. Hindson/R. Chen
(415) 604-1106/5008
Headquarters program office: OA**

Enhancing Situation Displays

James C. Johnston

A critical ingredient for many NASA missions is a human being working together with a machine system, with the workload shared between them. One of the key factors limiting the performance of such hybrid systems is the difficulty of getting large amounts of information from the machine to the human operator. One important strategy is to bypass higher cognitive processes that are slow and error prone, and present information through higher-bandwidth perceptual processes.

Present Air Traffic Control (ATC) situation displays provide visual/graphical representation of only a tiny portion of the information needed by controllers (principally an X-Y map of aircraft positions). Other information—e.g., altitude, altitude change, track vector—is not displayed graphically. It is typically available only in an alphanumeric data block. To be used, each field must be fixated, identified, and then cognitively interpreted. It should be possible to use pictorial displays to convey much of this information rapidly (data blocks can be retained for redundant coding of exact values), especially since very-high-resolution color monitors will be available in future ATC equipment suites.

Our initial focus was on designing and testing alternative coding systems for representing aircraft

altitude. We have designed a number of different systems that code altitude either continuously or in discrete bands, and that rely on either chromatic or achromatic (black and white) properties. We have tested these coding schemes in laboratory part-task experiments in which altitude processing plays a key role. Continuous color coding has been found to produce the best performance. We have recently completed an experiment showing that continuous color coding of altitude allows people to find future airspace conflicts in three-dimensional space many seconds faster than present displays.

Another principle that is helpful is that humans can more rapidly take in several properties of one object than one property from each of several objects. We have designed an integrated aircraft icon that augments data blocks with integrated perceptual coding of position, altitude, altitude change, track vector, and speed.

**Ames-Moffett contact: J. Johnston
(415) 604-5686
Headquarters program office: OA**

Dynamic Eye-Point Displays

Mary K. Kaiser

For an increasing number of vehicles, out-the-window displays are being replaced or augmented by synthetic systems. Usually, these systems display imagery from video cameras, imaging sensors, or computer databases to simulate the perspective views pilots are accustomed to using for vehicular control. Numerous efforts are focused on ensuring

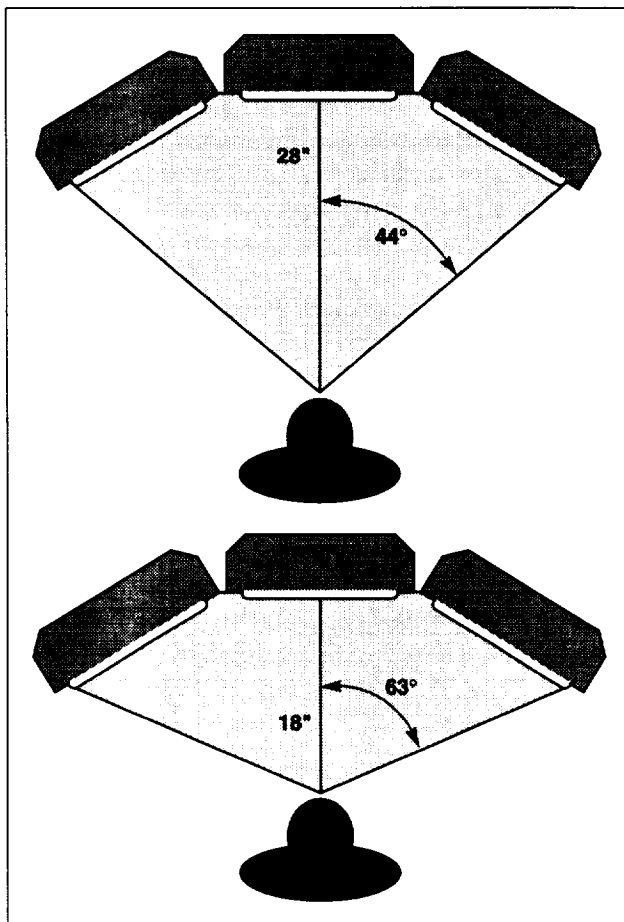


Fig. 1. Dynamic eye-point displays alter the graphical viewing volume (field of view, center of field) appropriate to the viewer's current eye position. Here, the field of view increases from 88 to 126 degrees as the viewer moves closer to the displays.

that the synthetic imagery contains sufficient image quality (e.g., resolution, contrast range) and content (e.g., level of detail) to substitute for out-the-window displays.

However, there is another important difference between optical windows and panel displays which has critical implications for user interaction. Windows are apertures; movement of the pilot's eyes relative to the aperture changes the pilot's viewing volume (i.e., field of view, center of field) through the window. Panel displays, on the other hand, show the same image regardless of the pilot's vantage point. Thus, even if a display panel has the same field of view as a cockpit window when measured at a given design eye point, it will not provide the same field of regard; the window affords the pilot a much greater "look around" capability.

In our laboratory, we are developing a "virtual window" system suitable for flight deck environments. This system uses an unobtrusive sensor to monitor the pilot's eye position in three-dimensional space. The eye-point coordinates are passed to the computer image generator, which renders three perspective scenes appropriate for the three screens of the display. As shown in the figure, the field of view of the display changes dynamically as a function of the viewing distance. Likewise, the center of projection will change appropriately if the viewer moves off the center axis. Such dynamic, real-time modification of the graphical eye point gives the rendered scene the same viewing geometry transformations that occur when the pilot looks through optical windows.

The current system is configured for computer-generated imagery. In principle, the system can be adapted to video and sensor systems; in these cases, the head position data would be used to drive the camera/sensor servo-mount positions and lens focal length settings. Again, the coupling of camera/sensor position and eye point relative to the display panel

would provide the synthetic display with the natural look-around capability of optical windows.

In addition to increasing field-of-regard capabilities in synthetic vision systems, this technology can be used to enhance the fidelity of aircraft simulators

by allowing simulated contact displays to behave more veridically.

Ames-Moffett contact: M. Kaiser
(415) 604-4448
Headquarters program office: OA

Effects of Automation on Crew Communication and Coordination

Barbara G. Kanki, Elizabeth Veinott, Cheryl Irwin, Kimberly Jobe

In principle, advances made in today's automated aircraft are assumed to yield rewarding payoffs for flight operations, but we are concerned about the unanticipated hidden costs that the crew may be paying. Crew Factors researchers are investigating the behaviors and strategies shown by crewmembers as they perform their tasks in automated versus more traditional aircraft. For example, in one study, we have contrasted crew behaviors at two levels of flight deck automation (DC-9 and MD-88), using videotape data obtained from a full-mission simulation study. Although no performance differences between crews of the two aircraft were found, communication and coordination of workload between crewmembers were quite different. In the more automated aircraft (the MD-88), for instance, crews used significantly more communications to accomplish the same performance level. Differences were often (1) speaker role specific (captain vs. first officer), (2) greatly accentuated during high-workload conditions, and (3) associated with specific types of speech acts (questions and commands) and not others (acknowledgments, dysfluencies).

A more detailed examination of questions yielded the following results: compared to DC-9 crews, MD-88 crews (1) asked more information-seeking questions (no differences with respect to verification questions), (2) asked more questions on navigation and system topics (no differences on procedure questions), and (3) left more questions unanswered (no difference with respect to confirm/disconfirm answers). Finally, most of the differences were stronger during the abnormal phase of the simulated flight. These results lead us to question

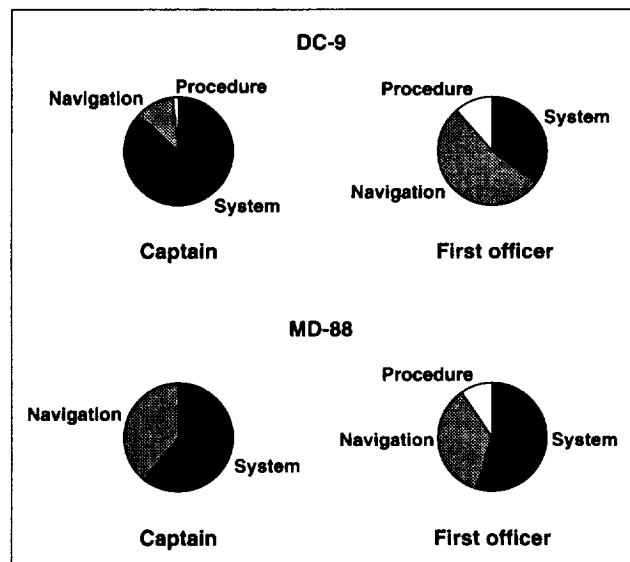


Fig. 1. Distribution of nonverbal control actions for crewmembers in the DC-9 and MD-88 aircraft.

whether automation is creating a workplace in which information access (on both navigation and systems topics) is less direct or less clear than in standard cockpits.

A follow-up study focusing on nonverbal activities was also conducted. Because results were generally stronger during the abnormal phase, nonverbal control actions were coded during the 10 minutes of highest workload only. Three kinds of behaviors were coded: navigation actions, systems actions, and procedure actions. Results from these

analyses revealed that traditional asymmetric work roles were maintained by the DC-9 crews. Specifically, the captain exhibited primarily systems actions, whereas the first officer exhibited primarily navigation actions. However, the MD-88 crews showed very different patterns. As shown in the figure, the captain and first officer showed more equally distributed systems actions, and the captain showed more navigation actions than the first officer in spite of the fact that the captain was also the pilot flying. Thus, in addition to the information access issue, automation appears to affect the work management structure,

resulting in a shift away from traditional work roles. In a variety of subtle ways, automation in the cockpit may be substantially altering crew communication and coordination requirements. This may be a constructive shift (resulting in successful crew strategies), but any changes in practices should be thoroughly understood so that training and procedures can be made compatible.

Ames-Moffett contact: B. Kanki
(415) 604-5785
Headquarters program office: UL/FAA

New Metric for Domain Analysis

Michael W. McGreevy

Designers rely on domain analysis—the analysis of specialized areas of human activity—in order to organize computer programs and systems that gather and manipulate information that is important in human activities, and that provide this information to participants in such forms as online documents, electronic displays, and virtual environments. To improve the process of designing these specialized programs and systems, a new relational metric for domain analysis has been developed. The metric provides developers with models relating the important tangible and conceptual objects, object attributes, attribute values, and actions of the domain in a form that is useful for design. The models produced by the relational metric method are also useful for understanding the domains themselves. They can, for example, be interpreted as models of presence in the domain.

Verbal data are a useful source of information about specialized domains of human activity, and these data are increasingly available in digital form. The ability to automatically, objectively, and quantitatively model important patterns in these data would be useful in domain analysis. Of particular interest are verbal records created by those who are themselves participants in the domain. Such records include incident reports, answers to interview

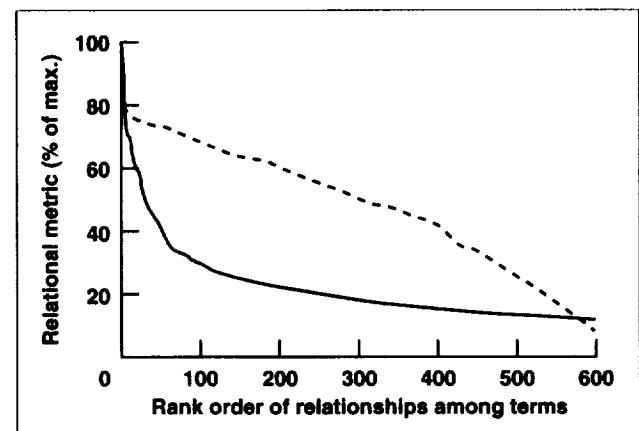


Fig. 1. Comparison of relational metric values. Solid line = new relational metric; dashed line = paired comparisons method.

questions, reports of domain activities, and other similar reports. These can be processed using the new metric in order to obtain insights into how the domain appears to be structured from the point of view of the participants. To test the method, it was applied in fiscal year 1994 to a document describing a remote-sensing project within the scope of the Earth Observing System (EOS). Results

of the analysis include a network model of the domain and an object-oriented relational analysis report which describes the nodes and relationships in the network model. Other products include a data base of relationships in the domain, and an interactive concordance.

The core of the new analysis method is a proximity-weighted frequency of co-occurrence. This metric is applied to relations between terms (words or multiword entities) that occur most frequently in the domain text, and the terms found within the contexts of these terms. Contextual scope is selectable. That is, the context around a term of interest can be varied in size from one to any number of words. Because of the discrimination power of the metric, data reduction from the association matrix to the network is simple. The initial results indicate that this method provides greater discrimination among verbal terms than that obtainable by typically used

methods such as paired comparisons, sorting tasks, and logging of sequential selections. The figure shows that the new relational metric (solid line) clearly distinguishes the relationships among the verbal terms, whereas the paired comparisons method (dashed line), which produces the best of the typical metrics, is less discriminating. A detailed review of the evidence supports the reliability and validity of the method, and additional validation can be achieved.

Currently, this new relational metric method of domain analysis is being applied to the full narratives of 300 mode-related incident reports from the Aviation Safety Reporting System. The results will aid in further evaluation of this new method.

**Ames-Moffett contact: M. McGreevy
(415) 604-5784
Headquarters program office: UL**

Aeronautical Team Decision Making

Forty-seven percent of fatal air transport accidents between 1983 and 1987 involved failures in crew decision making, planning, or communication. The goal of our research is to support crews in making the safest and best decisions possible under stress, through training, decision aids, and procedures. Decision making is a component of most crew resource-management training courses given by major airlines. However, little scientific research has been available until recently to support training. We are only now beginning to understand what constitutes effective decision making and what should be taught. The objectives of our work are (1) to examine the relationships between (a) crew communication, problem solving, and decision making and (b) overall levels of crew performance, especially in abnormal or emergency situations; (2) to investigate the effect of cockpit automation on crew behavior; and (3) to analyze the characteristics and bottlenecks of flight

Judith Orasanu, Ute Fischer, Michelle Rodvold

decision making that involve the cockpit crew and ground personnel, as shown in the figure.

Our approach to cockpit decision making emphasizes both situational demands and crew behavior in different problem situations. Analyses of incident and accident reports suggest that there are six different types of decision events in the cockpit. These fall into two subgroups that differ primarily in whether or not a rule exists that defines a response appropriate to a given situation. These differences should translate into differences in cognitive work required to make the safest and most efficient decision. Research is currently under way to test this hypothesis.

Flexible strategy use in response to different decision events was observed in our analyses of crew behavior during simulated flight. In particular, crews with few operational errors adapted their

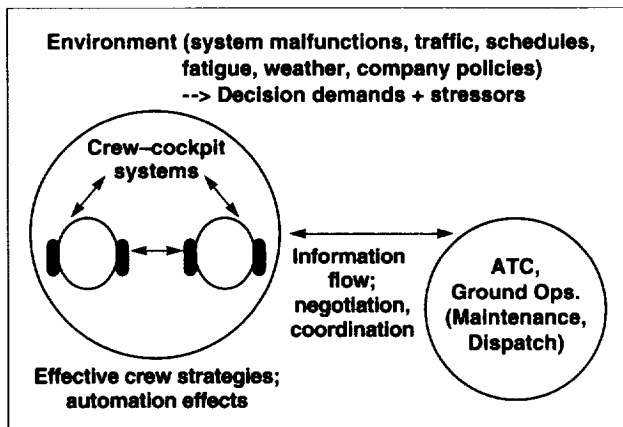


Fig. 1. Components of aeronautical team decision making.

decision-making strategies to the demands of a particular problem situation. One situational variable that research on crew decision making has not yet addressed is cockpit automation. One of our current projects analyzes how different levels of cockpit automation affect decision-making strategies.

The importance of situational features in aeronautical decision making has been validated in a recent study that investigated pilots' perception of hypothetical problem situations. Our findings indicate that pilots with different aviation experience frame situations differently. Captains were particularly concerned about risk, time pressure, and choices. Except for time pressure, first officers and flight engineers showed other priorities. First officers were sensitive to situational complexity and guidelines for decision making. Flight engineers, in

contrast, were concerned with the nature of the problem and its effect on the flight plan.

Communication is both a medium through which crews accomplish their tasks and a reflection of the cognitive processes of individual crewmembers. Early studies led to several general conclusions about the relationship between crew communication and performance: crews that made fewer operational errors talked more overall, and made more commands, observations, and acknowledgments. Several new analyses confirm and elaborate on the original conclusions. Higher-performing crews were more effective in allocating and structuring tasks. They also stated more plans and strategies and were more responsive to each other's contributions. Strategies in dealing with communication problems were found to be related to problem type: ambiguities were mainly resolved by speakers; errors were corrected by those addressed.

To date, work on aeronautical decision making has focused primarily on crews operating face to face in a shared environment. It is important to understand this working situation, but we also need to understand how the broader operational context affects pilot decision making. We are currently expanding our analyses to include decision-making situations that involve participants who are physically remote and who have different areas of expertise, such as pilots, dispatchers, and air traffic controllers.

**Ames-Moffett contact: J. Orasanu/U. Fischer
(415) 604-3404/0018**

Headquarters program office: OA/FAA

Computational Modeling of Team Communications Demands

Roger W. Remington

Information technology has only recently begun to address issues of cooperative work. This area of study has particular relevance for NASA since many critical operations are done by highly coordinated teams of engineers. Coordinated teams are involved in shuttle launch control, mission control, satellite monitoring, and science operations on shuttle missions. Effective teamwork requires an efficient division of labor and an effective set of procedures to ensure timely communication of information. It has taken years to hone communications and procedures for launch control and mission control. Shuttle science missions, however, are often given only a few months in which to build a team and develop operating procedures. Past experience can guide development, but often unique mission characteristics dominate.

We tested the feasibility of discrete-event modeling and simulation as an aid to procedure development, especially communications. Our goal was to develop a model of the Jet Propulsion Laboratory operations team responsible for data collection for the SIR-C/X-SAR shuttle mission. We reviewed draft procedures, observed mission simulations, and interviewed team members. Three questions emerged that were of concern to the Operations Director: (1) Did the communications specified for each task satisfy the goal of informing all relevant team members? (2) Did the procedures distribute the workload, including communicating, in a reasonable manner among the team members? and (3) How should the access to the communications channels be handled to reduce communication workload?

The model we developed treats each team member as a separate "agent" that passes information to (i.e., communicates with) other agents (team members). The real situation dictated that communication be asynchronous and constrained to occur over a fixed set of communications channels. The procedures for each task are specific to an agent's role and serve to specify its behavior. Upon receiving a message, the agent interprets the message in terms of the current context to determine its response. A simple model with a minimal agent structure was sufficient to check completeness of communications. A more sophisticated treatment of human mental processing was needed to account for communication load. Each agent had to embody a model of human cognition to enable the agent to respond like a human operator would to increased message frequency, task difficulty, and interruptions. We developed a simple model of mental processing that assumes that each human team member can buffer incoming auditory information, but can only respond to one message at a time. Preliminary testing suggests that this crude model shows promise for simulating many aspects of human behavior. We are hopeful that future testing will show that this model can approximate human behavior in various team environments.

Ames-Moffett contact: R. Remington

(415) 604-6243

Headquarters program office: OA

High-Speed Research Piloted Simulations

Jeffery A. Schroeder, Shawn A. Engelland, Dan W. Dorr, Charles S. Hynes

NASA Ames leads the Guidance and Control technology element of NASA's High-Speed Research program. As part of this program, two piloted simulations of a high-speed civil transport (HSCT) were conducted last year on the Ames Vertical Motion Simulator. One simulation was a joint effort between NASA and McDonnell Douglas; the other was a joint effort between NASA and Boeing.

In contrast to typical commercial transports in the fleet, the HSCT is expected to operate on the back side of the power-required curve. The purpose of the NASA/McDonnell Douglas simulation was to determine how far on the back side of the power-required curve a transport vehicle could be before excessive pilot workload is required. Several methods may be imposed to compensate for operating on the back side of the power curve. One method is to require the pilot to use a different technique to manage the vehicle's speed and flightpath: to use throttle to manage flightpath and stick to manage airspeed rather than vice versa, as in conventional transports. The drawback with this method is that it places additional training requirements on the airlines.

Another method is to employ an autothrottle that must not fail. This approach allows a pilot to use the conventional transport flying technique. The drawback with this method is that current autothrottle designs do not meet stringent reliability requirements, and developing one that does would be expensive.

A third method is to use a head-up display that provides the pilot with information sufficient to perform the autothrottle task. If speed errors are displayed in an intuitive manner, then the pilot can manipulate the throttle to null the speed error without a significant increase in pilot workload. While this method requires a head-up display, the associated expense may be less than that of developing a more reliable autothrottle system. The NASA/McDonnell Douglas simulation investigated this method.

The second simulation, conducted jointly by NASA and Boeing, had several objectives. First,

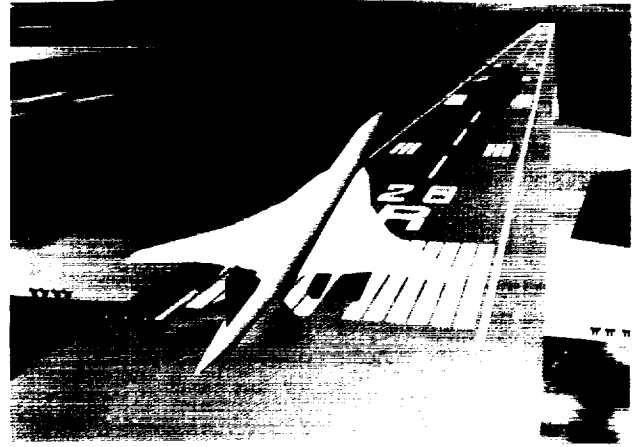


Fig. 1. High-speed civil transport aircraft.

several advanced control system concepts had been developed by both NASA and Boeing, and the simulation allowed these systems to be evaluated by a broad range of pilots to determine system acceptability. A second objective was to determine whether extremely low visibility landings can be made satisfactorily by a pilot if given a head-up display and one of the advanced control systems. If the latter objective can be accomplished, a potential exists for using the control and display combination as a viable alternative to the automatic landing systems that must be used today to achieve landings in the conditions tested.

The attached figure shows a visual database representation of the HSCT vehicle that was tested in both of the above simulations.

**Ames-Moffett contact: J. Schroeder
(415) 604-4037**

Headquarters program office: OA

Precision Approaches to Closely Spaced Parallel Runways

Rhonda Slattery

The Center/TRACON Automation System (CTAS) has been developed for use in the air traffic control environment. As part of the Terminal Area Productivity Air Traffic Management program, research has begun on expanding CTAS to apply to aircraft with advanced guidance capabilities. Through the next decade, an increasing number of aircraft will be equipped with advanced navigation systems. To examine the implications of this situation, we are studying airports with closely spaced parallel runways. Many airports have parallel runways that are too close together for simultaneous instrument landing system (ILS) landings. The runways are so close that aircraft will lose separation if the landing routes are not followed precisely. Proposed advanced navigation systems, such as the Global Positioning System, have much smaller navigation errors than conventional systems and could effectively allow aircraft to follow closer routes while maintaining separation. The figure shows the experimental setup developed for this project. It consists of two parallel runways at the Dallas–Fort Worth airport—runway 18R, equipped for normal ILS landings, and runway 18L, equipped for advanced-navigation approaches. The advanced-navigation aircraft follow a route parallel to both the ILS route and runway 18L until they are about 3 nautical miles from the runway threshold. Then the aircraft change to visual flight rules and perform a sidestep maneuver to the runway threshold.

The objectives of this project are to find out how air traffic controllers deal with various combinations of equipped and unequipped aircraft in the absence of CTAS, and to examine the requirements for air traffic control automation.

A simulation was performed to evaluate controller procedures for landing aircraft on closely spaced parallel runways using staggered approaches and simultaneous approaches. A staggered procedure requires aircraft on the ILS approach to be separated by at least 2 nautical miles from aircraft on the

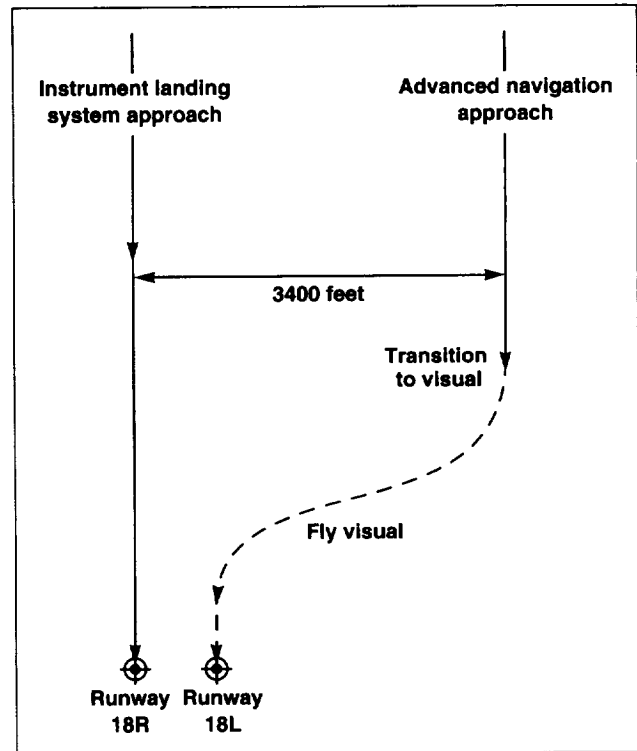


Fig. 1. Parallel runway experimental setup.

advanced-navigation approach. For a simultaneous approach the two runways are independent. The number of equipped aircraft was varied between 33% and 100% of all the aircraft, and there were two different numbers of aircraft per hour released into the simulation. The simulation was performed without CTAS advisories, and results will be compared with those from a simulation with CTAS planned for the next fiscal year. The simulation showed that both types of approaches could be managed even without automation if traffic load is sufficiently light. With heavy traffic, however, the workload and aircraft delays increase dramatically, demonstrating a need for CTAS-type advisories.

During the next year, we will examine the effectiveness of air traffic control automation in alleviating the problems found in manual control. We will also investigate the adaptations to CTAS required for situations with closely spaced parallel runways. Taking advantage of the Flight Management Systems available on aircraft, together with advanced

navigation systems, we will test the ability of aircraft to follow more complicated advisories.

**Ames-Moffett contact: R. Slattery
(415) 604-5435**

Headquarters program office: OA

Real-Time Passive Ranging

The detection of obstacles in the flightpath of a vehicle has both military and civilian applications. We have developed algorithms that can detect and find range to objects in the field of view of a passive electro-optical video or infrared sensor mounted on a vehicle. The figure shows stereo cameras mounted on the NASA UH-60 RASCAL helicopter. The computer vision algorithms use feature-based correlation techniques, vehicle motion information, and Kalman-filter estimation techniques. These algorithms have been tested using video images acquired in flight. The ranging algorithms are computationally intensive and may require a system capable of approximately 2 gigaFLOPS.

The vision algorithm was parallelized for multiple-instruction, multiple-data (MIMD) parallel computers. The algorithm was refined using Sun and Silicon Graphics workstations and has been successfully ported to a modified 32-processor Mercury-Computer-based passive ranging system under a Phase 2 Small Business Innovative Research (SBIR) contract with Innovative Configurations, Inc. (ICI). Two innovative features of this system are the ability of the parallel computer to accept video and aircraft parameters and its ability to display computed ranges on the original image. The system can compute up to 500 features at 15 frames per second. The ICI system has the additional capability of being programmable in higher-level languages and it

Banavar Sridhar, Ray Suorsa



Fig. 1. Stereo cameras mounted on the NASA UH-60 RASCAL helicopter.

can be used to investigate other approaches for obstacle detection.

The ICI system is being tested in the laboratory using stored imagery from previous flight tests. After thorough evaluation and preparation of the computer hardware, the system will be flight tested on the RASCAL helicopter.

**Ames-Moffett contact: B. Sridhar
(415) 604-5450**

Headquarters program office: OA

Traffic Management Advisor Adaptation for Denver International Airport

Harry N. Swenson, Laurie Engle

The Denver Air Route Traffic Control Center and terminal radar control facilities (TRACON) have been used as the primary development and evaluation site for NASA's Center/TRACON Automation System (CTAS). The CTAS tool known as the Traffic Management Advisor (TMA) currently assists the Denver Center and TRACON in managing air traffic flow into Denver Stapleton Airport. Denver International Airport, designated to replace Denver Stapleton, has different airway structures and will begin operations using Miles-In-Trail flow-control algorithms for traffic management, in place of metering. The objective of this effort was to develop the Miles-In-Trail-based algorithms to support efficient traffic management decisions and to adapt the TMA to the new Denver airport.

The TMA was adapted from the four Standard Arrival Routes (STARS) supporting 44 runway configurations at Denver Stapleton for use on the eight STARS supporting 14 runway configurations at Denver International. The TMA scheduler was

modified to dynamically support Miles-In-Trail flow control for Denver International. Several successful simulation evaluations were conducted at NASA Ames with air traffic controllers from the Denver Center and TRACON. The simulation also included Federal Aviation Administration (FAA) controllers from Chicago's O'Hare Airport which was selected by the FAA as one of the sites for the early national deployment of the TMA. The simulations resulted in several design recommendations for the human interface to the TMA and the new Miles-In-Trail advisory tools.

Future plans include refinement of the Miles-In-Trail interface based on operational evaluations in order to aid traffic management decisions and provide a transition to eventual time-based metering.

**Ames-Moffett contact: H. Swenson
(415) 604-5469**

Headquarters program office: OA

Advanced Rotorcraft Flight Control Design

Marc D. Takahashi, Mark B. Tischler

Systematic approaches to designing four-axis high-bandwidth control laws for rotorcraft operating in degraded visual environments and adverse weather conditions have been developed that use dynamic decoupling surrounded by high-gain loops for each axis of control (roll, pitch, directional, and vertical). The dynamic decoupling reduces the cross coupling between each axis of control, and the high-gain loops provide the feedback to improve

disturbance rejection, stability, and tracking performance. These laws were analyzed using linear and nonlinear helicopter simulation models, which include the flap and lag rotor degrees of freedom, inflow states, nonlinear lead-lag damper, component-level engine model, sensor delays, and nonlinear actuator dynamics. The figure shows the pitch response of the simulation model with the

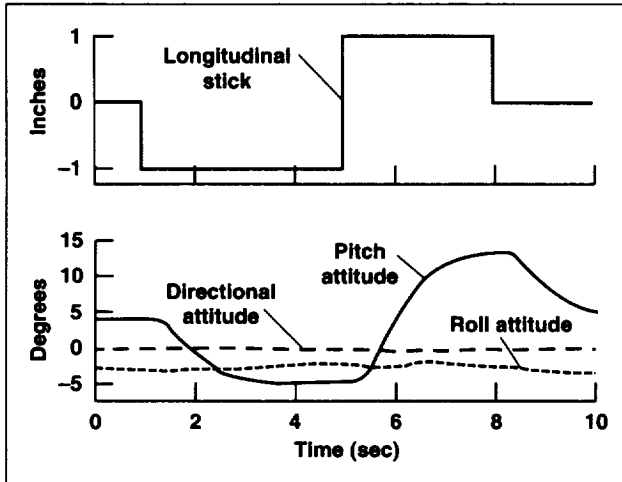


Fig. 1. Closed-loop pitch response to a longitudinal doublet.

previously mentioned control law engaged. The graphs show a well-damped response to the pitch doublet input and good decoupling from the roll and directional axes. More advanced laws using body measurements and rotor state measurements will also be investigated to further increase the gain of the feedback. Other methods to design the feedback and the dynamic decoupling, such as Riccati solution-based methods and quantitative feedback theory, will be investigated and flight demonstrated.

Ames-Moffett contact: M. Takahashi
 (415) 604-5271
 Headquarters program office: OA

Real-Time Facility for Safety Monitor Concept Evaluation

Marc D. Takahashi, Mohammadreza H. Mansur

The U.S. Army and NASA are currently developing the Rotorcraft Aircrew Systems Concepts Airborne Laboratory (RASCAL) at Ames Research Center. The RASCAL is a UH-60 that is being modified in a phased development program to incorporate a research flight control system (RFCS) and an advanced navigation research platform. Monitors are a critical safety feature on the RASCAL and are necessary to detect RFCS failures. These monitors must detect failures quickly to allow time for the system to disengage the RFCS and transfer control to the safety pilot. As part of the contract to develop the RFCS, the prime contractor, Boeing Helicopters, developed several monitor concepts to detect failures of control laws programmed into the flight control computer. These monitor concepts were jointly evaluated at Ames by Boeing and NASA/Army engineers, using a real-time facility developed for this purpose. The figure shows a monitor concept

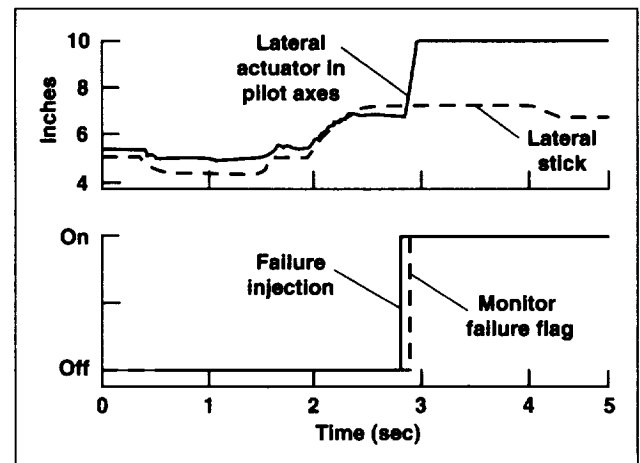


Fig. 1. Monitor detecting a failure during a lateral maneuver.

detecting a failure that occurred while the pilot was performing a lateral maneuver. The failure resulted in a sudden change in the actuator motion. This motion was detected by the monitor, which issued the failure flag.

The real-time facility consisted of a Silicon Graphics Onyx workstation interfaced with a B&G Flybox, giving the pilot an out-the-window visual scene and a set of controls to simulate the flying tasks. The model, which was driven by the pilot controls and which drove the visual scene, consisted of a previously existing blade-element model of a UH-60 (GenHel) integrated within a scene-generation program (HelSim). The simulation model was heavily modified to simulate the RASCAL helicopter

by modeling the safety-pilot and evaluation-pilot paths to the RFCS actuators, safety monitors, RFCS actuators, safety pilot backdrive, RFCS engage/disengage logic, and simulated RFCS failures. A representative four-axis flight control law was also modeled to represent the type of control law that will be tested on RASCAL as part of its research function. In addition to the model modifications, ancillary software was developed to support data input to the model, record output signals, and play back pilot inputs to the model.

Ames-Moffett contact: M. Takahashi
(415) 604-5271
Headquarters program office: OA

Limited Operational Assessment of the Traffic Management Advisor

Leonard Tobias

A limited operational assessment of the Traffic Management Advisor (TMA) was conducted at the Denver Air Route Traffic Control Center in February 1994. The TMA is a sequencing and scheduling tool, one of the main tools of the Center/TRACON Automation System (CTAS).

The assessment was a critical step toward replacing the existing metering system with the TMA. In today's operation at Denver, when delays for arrival aircraft reach 3–4 minutes, metering is put into effect. This means that lists of aircraft, metering fix times, and delays are displayed at the appropriate arrival sectors, and the radar controllers are required to have aircraft pass through their metering fix at the posted times. During the assessment, TMA-generated times and delays were sent to the radar positions in place of the existing metering data during periods of 1–2-minute delays. This was the first CTAS field site where CTAS-generated data was transmitted back to the existing Federal Aviation Administration (FAA) computer system.

This was also the first time that clearances were given by the radar controllers to commercial airline flights in order to meet the TMA-generated times. Since these times were displayed when metering was

not actually in effect, the use of the time-planning data had to be coordinated with the airlines whose flights might be impacted. The airlines were supportive and, in fact, provided blanket approval for participation of flights in the tests. In general, TMA estimated times of arrival (ETAs) were observed to be stable and to accurately reflect the path of the aircraft. The TMA sequences, which were based in part on a reference ETA order, appeared to be consistent with the controller's preference in the majority of cases. In addition, the TMA scheduled times of arrival were observed to be reasonable for the traffic conditions encountered, and the controllers appeared to be able to meet the scheduled times to within a 1-minute accuracy.

Follow-on testing to be conducted in fiscal year 1995 will use the TMA during actual metering periods, typically 45 minutes to 1 hour long. If the TMA is successful during these live traffic operations, it will soon become the primary arrival traffic tool at several FAA-designated sites.

Ames-Moffett contact: L. Tobias
(415) 604-5430
Headquarters program office: OA

Characterizing the Human Visual Motion Filter

Andrew B. Watson, Kathleen Turano

An understanding of the human visual system provides rich payoffs in diverse applications such as visual interface design, image compression, and robotic vision. Human vision is exquisitely sensitive to image motion, and this sensitivity underlies our capacities for object detection, visually guided locomotion, tracking, and grasping. In earlier work we proposed a basic filter model to describe the motion-sensing mechanisms at the earliest stages of human vision. Each motion filter selectively extracts the image components corresponding to image motion in one direction, and discards all others. Whereas this model is now the de facto standard, the finer characteristics of the motion filter, particularly its three-dimensional (3-D) frequency passband, are still in dispute.

In this research we used a novel technique to estimate the 3-D frequency passband of the human motion filter. A mathematical argument can be made that the motion stimulus with least "contrast energy" identifies the shape of the motion filter. In effect, we

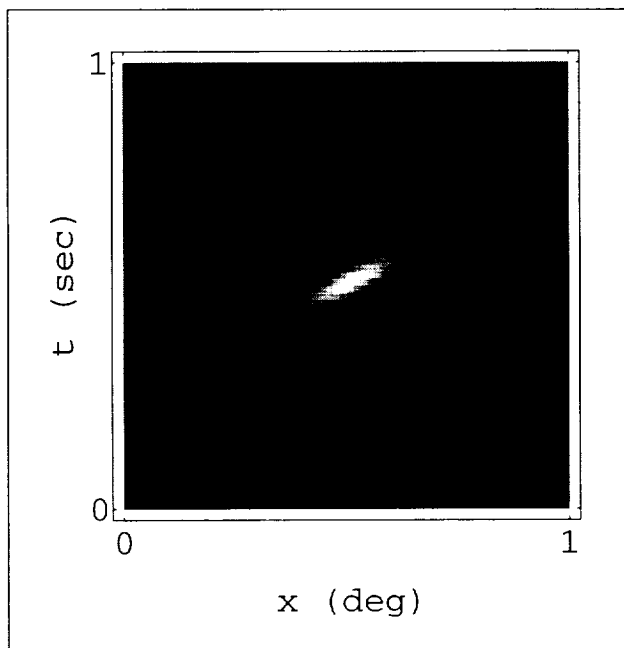


Fig. 1. The space-time image of the optimal motion stimulus.

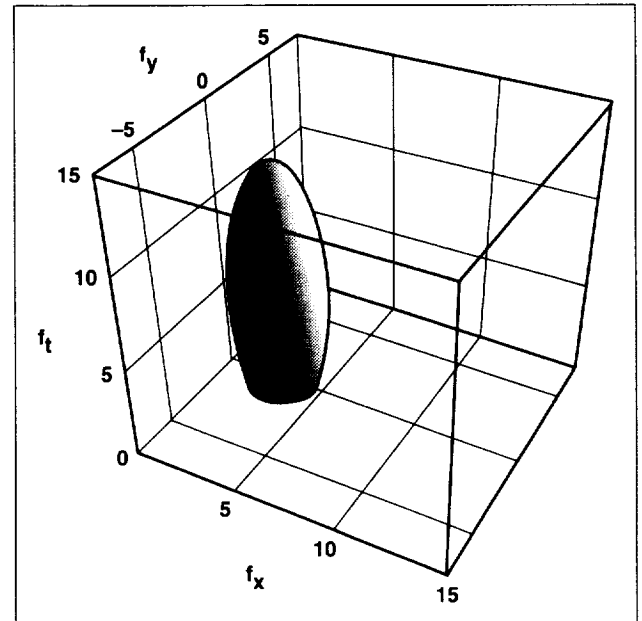


Fig. 2. The three-dimensional frequency spectrum of the human visual motion sensor (f_x = horizontal spatial frequency; f_y = vertical spatial frequency; f_t = temporal frequency).

look for the "key" that most efficiently unlocks the motion sensor; just as the shape of a key must match that of the lock, so our optimal stimulus must match the filter.

To search for the optimal motion stimulus, we used drifting sinusoidal luminance perturbations multiplied by an aperture that was Gaussian in space and time. We call these perturbations generalized Gabor stimuli (since they are 3-D generalizations of the 1-D functions developed in communications theory by Dennis Gabor). For each stimulus examined, we determined the contrast energy required for a human observer to identify the direction of stimulus motion (left or right).

The results are summarized in the figures, which show the space-time image of the optimal motion stimulus (first figure), and the band of spatiotemporal image frequencies that are selected by the human

motion filter (second figure). Important features of this passband are that it is broad in temporal frequency, narrow in spatial frequency, and oriented parallel to the Cartesian axes.

These results will enhance our fundamental understanding of human vision, and will be directly incorporated in our computational models of human

visual processing. They will also assist in the design of optimized video image compression schemes and robotic motion estimation algorithms.

Ames-Moffett contact: A. Watson
(415) 604-5419
Headquarters program office: OA

Perceptual Consequences of Engineering Compromises During Spatial Sound Synthesis

Elizabeth M. Wenzel

In implementing a real-time spatial auditory display, many engineering compromises must be made in order to achieve a practical system. One such system, the Convolvotron, simulates three-dimensional sound over headphones using a very-high-speed digital signal processor. Spatial cues are imposed on any incoming sound in real time by digitally filtering the sound with filters that are based on head-related transfer functions (HRTFs) measured in the ear canals of individual persons for many different source locations. Sound sources can then be placed at fixed locations in virtual space by using a head-tracking device to select the appropriate HRTF-based filters with which to spatialize the incoming sound. Since it is not practical to measure HRTFs at all possible locations, the moving sounds and locations between known locations are simulated by computing a linear weighted average of the four measured filters nearest the desired location. Interpolation is also useful because memory limitations in such devices make it advantageous to reduce the number of filters that must be stored.

Whereas simple linear interpolation seems to be a reasonable approach, comparisons of the acoustical features of interpolated and noninterpolated HRTFs reveal obvious differences, particularly in the temporal (phase) properties of the filters. During informal listening, the spatialized sounds simulated by the Convolvotron are not obviously distorted when inputs such as music are used. However, with signals like white noise, there is an unnatural comb-filtering effect (incorrect frequency and loudness changes

over time) when the listener and/or the source is in motion. One suggested technique for minimizing interpolation errors is to use what is called a minimum-phase approximation of the HRTFs. Such errors may also be lessened by using relatively small interpolation intervals (currently 15 degrees azimuth and 18 degrees elevation in the Convolvotron).

The perceptual consequences of interpolation can only be assessed by behavioral studies. Listeners' judgments of apparent location tend to show two kinds of errors—relatively small errors of about 5 to 20 degrees and a special class of errors known as confusions (front positions heard in the rear, down locations heard as up, etc.). Confusion rates are usually low for real sound sources but may greatly increase for virtual sources. One recent study compared listeners' estimates of location for non-interpolated vs. interpolated stimuli synthesized from the participants' own HRTFs. In general, localization accuracy for stimuli based on minimum-phase interpolations at small interpolation intervals (15 degrees azimuth and 12 degrees elevation) was comparable to the accuracy in noninterpolated conditions. Interpolations of normal HRTFs, on the other hand, resulted in decreased accuracy (primarily increased front-back confusions) for even the smallest interpolation intervals. However, as is the case for most virtual acoustic displays, this study did not investigate simulations based on nonpersonalized HRTFs.

The present study compared localization judgments for interpolated and noninterpolated sounds synthesized from the HRTFs of a female subject (SDO), a “good localizer,” whose HRTFs constitute one of the data sets provided with the Convolvotron. Interpolation intervals were varied in both azimuth and elevation for both normal and minimum-phase HRTFs. The pattern of the data was remarkably similar across all synthesis conditions, the most obvious differences occurring in confusion rates. The overall level of confusions was quite high, showing a predominance of front-to-back reversals. However, one participant (like SDO, a relatively small female) showed lower overall rates, with the minimum-phase HRTFs producing the fewest confusions.

In contrast to the study that used personalized HRTFs, these data suggest that localization accuracy is largely unaffected by interpolation of either normal or minimum-phase HRTFs, even for the largest

interpolation intervals (e.g., 60 degrees azimuth and 36 degrees elevation). The data are similar to those from another study in which participants’ real-source localization was compared to localization of virtual sources synthesized from SDO’s noninterpolated HRTFs. It appears that the perceptual effect of interpolation is relatively small compared to the impact of using nonpersonalized HRTFs. Thus, it may be that several sets of HRTFs from participants with different physical (and therefore acoustical) characteristics should be made available with a virtual acoustic display so that the best match possible can be made between listeners and the data sets. The fact that the participant who was physically most similar to SDO had the lowest overall confusion rates supports this view.

**Ames-Moffett contact: E. Wenzel
(415) 604-6290
Headquarters program office: OA**

New Dynamic Planner for CTAS

Gregory Wong, Heinz Erzberger

A new Dynamic Planner, the scheduler element of the Center/TRACON Automation System (CTAS), has been designed using object-oriented techniques in order to enhance robustness, modularity, and expandability of the software. The new design incorporates previously available functionalities as well as new functionalities motivated by experience gained from field tests and deployments. In addition, the Dynamic Planner will be an essential component in the CTAS operational system which will be deployed in air traffic control centers nationwide.

The Dynamic Planner calculates arrival schedules that ensure a smooth flow of traffic into the terminal area. It uses a first-come, first-served scheduling algorithm to compute arrival times at the feeder gates and runways while observing constraints entered by the controllers. The Dynamic Planner will integrate with the Traffic Management Advisor, the Descent Advisor, and the Final Approach Spacing

Tool to form the suite of automation tools that make up CTAS.

The Dynamic Planner separates the scheduling process into two phases which are performed sequentially. These phases are shown in the figure. The first phase schedules aircraft to the feeder gates which are about 35 nautical miles from the airport. This phase ensures that the aircraft are properly separated at each feeder gate and that the total traffic flow from all feeder gates does not exceed the acceptance rate for the airport.

The second phase assigns aircraft to the landing runways and schedules them from the feeder gates to the runway thresholds. This phase incorporates all important safety constraints such as the proper wake vortex separation. The two-phase scheduling process meets a multiplicity of operationally important constraints and still achieves high computational

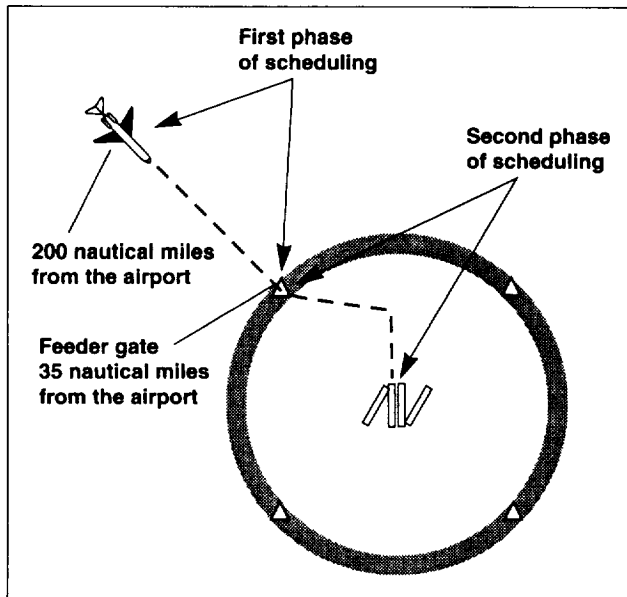


Fig. 1. The dynamic planner's two phases of scheduling.

efficiency. Furthermore, the two phases are integrated into a complete scheduling system from any initial point to touchdown.

After a critical review of the previous design as well as interviews with air traffic controllers and

researchers, a new design concept emerged and a set of requirements for the Dynamic Planner was drafted in April 1994. Object-oriented analysis and design techniques were applied to the requirements, and preliminary and detailed object-oriented designs were completed in July 1994. Implementation of the first phase was completed in October 1994.

Delivery of software for the first phase of the new Dynamic Planner is scheduled for November 1994. It will be deployed at the Denver Center and Fort Worth Center for field development and assessment with end users in an operational environment. Delivery to the field of software for the second phase will take place in February 1995. Optimization of the scheduling algorithm will continue in 1995, and a limited operational assessment of the Dynamic Planner is scheduled for mid-1995.

Implementation of the new Dynamic Planner has validated the design objective of greater modularity and computational efficiency than the previous design. Its flexibility will enable it to serve the needs of air traffic controllers and researchers far into the future.

Ames-Moffett contact: G. Wong

(415) 604-1439

Headquarters program office: OA

Helicopter Guidance System with Obstacle Avoidance Capability

Rick Zelenka

NASA Ames and the U.S. Army Command/Control and Systems Integration Directorate, Fort Monmouth, New Jersey, have developed a guidance system to aid pilots during low-altitude flight. The baseline NASA/Army low-altitude system employs a digital terrain elevation map and radar altimeter to allow VFR (visual flight rules) terrain-following/terrain-avoidance (TF/TA) flight at 150 feet altitude and 80 knots airspeed, using a helmet-mounted display. This system has been flying for over 2 years. During June and July 1994, the guidance system was integrated and flight tested with a recently developed U.S. Army/Northrop Obstacle Avoidance

System (OASYS) laser radar sensor. The figure shows the Army STAR UH-60 helicopter with the OASYS sensor.

The OASYS-enhanced TF/TA guidance system adds an obstacle detection and avoidance capability and allows flight in reduced visibility at even lower altitudes. Flights at 50 feet altitude and 80 knots airspeed were flown through the rugged terrain near Carlisle, Pennsylvania, aboard a UH-60 Blackhawk helicopter. The OASYS laser radar sensor was found capable of detecting wires, towers, and terrain, thereby extending the flight envelope of the



Fig. 1. Army STAR UH-60 helicopter with the OASYS sensor.

NASA/Army low-altitude guidance system. Flight data collected during this phase of testing will be studied prior to further flight testing in November 1994. Personnel from Northrop and the Army Night Vision and Electronic Sensors Directorate, Fort Belvoir, Virginia, also participated in the flight testing.

The baseline NASA/Army low-altitude guidance system and the OASYS-enhanced system have received much interest from the major helicopter manufacturers and some aerospace systems companies. Potential markets targeted by these groups include the military special operations community, day and night helicopter firefighting, and emergency medical services.

Ames-Moffett contact: R. Zelenka
(415) 604-5433
Headquarters program office: OA

Takeoff Trajectory Optimization for Category-A Helicopters

Yiyuan Zhao, Robert T. N. Chen, William S. Hindson

Engine failure represents a major safety concern in helicopter operations. Because of this, the FAA certifies helicopters according to their ability to continue operations after engine failures. Federal Aviation Regulation Part 29 specifies that transport helicopters must be certified as either category A or category B. Category-B helicopters must be able to land safely in the case of failure of one or all engines. There is no requirement, however, for continued flight capability. In contrast, category-A certification, which applies to multiengine helicopters with independent engine systems, requires that helicopters continue the flight with one engine inoperative (OEI). Therefore, category-A helicopters are capable of operating from sites such as rooftops and oil rigs, and flying to areas where no emergency landing sites are available. Specifically, in a takeoff flight (first figure), the pilot must continue the flight if one engine fails after the helicopter has passed the takeoff decision point (TDP), and should land, or reject the takeoff, if the engine failure occurs before reaching

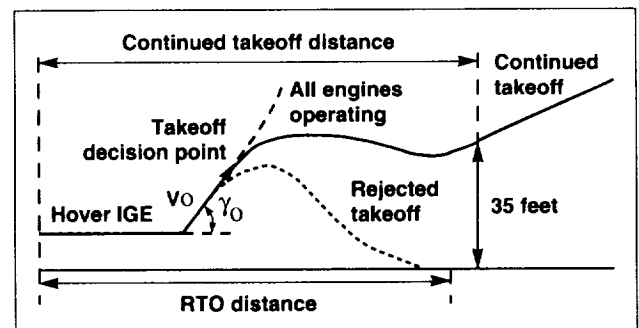


Fig. 1. Category-A takeoff from a clear heliport.

the TDP. Although there is no maximum weight limit, category-A helicopters must be able to satisfy OEI operation requirements within the available runway field.

To date, category-A flight procedures have been determined from flight tests, which can be dangerous

and time consuming. Flight-manual instructions based on flight tests provide the pilot with very conservative recommendations with regard to maximum takeoff weight or required runway length. For example, the pilot cannot trade reduced takeoff weight or favorable ambient conditions for a shorter runway. Furthermore, there are limited theoretical studies on this subject. An analytical study was therefore undertaken to investigate optimal takeoff trajectories of a twin-engine helicopter operating in a clear heliport in the event of failure of one engine. To initiate the effort, a point-mass model representative of the UH-60A helicopter was employed to address the three important issues concerning category-A helicopter operations: safety, payload capability, and runway requirement. Two optimal control problems were formulated for both continued takeoff and rejected takeoff after failure of a single engine. Subject to specified safety conditions, the first formulation minimizes the runway length required for a given takeoff weight, whereas the second maximizes the takeoff weight for a given runway length in continued takeoff and for an unspecified runway length in rejected takeoff. Constraints on rotor speed, thrust inclination angle, and available thrust range were included in the extensive optimization study. For the continued takeoff, an optimal speed for takeoff safety was found to be approximately 10 knots above the initial airspeed at engine failure (second figure). The runway length required for OEI continued takeoff flight depends on the helicopter airspeed, flightpath angle, and altitude at engine failure. The maximum takeoff weight is dictated by the remaining power available after one engine failure if the runway length is sufficient, and is otherwise determined by the available runway length. The runway required for OEI rejected takeoff flight depends on the all-engine-operating (AEO) climb speed. A higher airspeed results in a longer landing distance. Both the required runway length and the helicopter payload capability show little sensitivity to other conditions at time of engine failure. In some key characteristics, these

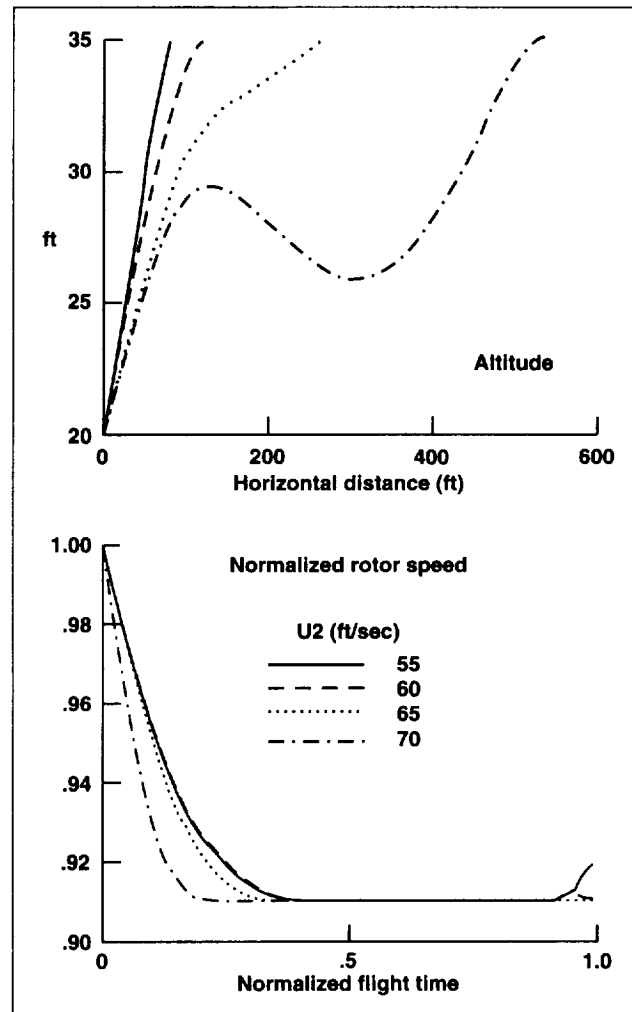


Fig. 2. Minimum runway length for continued takeoff.

results replicate those from flight tests documented in the literature. Finally, by combining the minimum runway lengths for continued takeoff and rejected takeoff, takeoff decision point conditions that result in overall minimum runway lengths can be determined.

Ames-Moffett contact: R. Chen
(415) 604-5008
Headquarters program office: OA

Variable-Complexity Genetic Algorithm for Topological Design

Peter Gage, Ilan Kroo, Hirokazu Miura

Standard optimization methods operate on the values of a fixed set of parameters, but for many optimization tasks the best set of parameters is not known a priori. Hence, an algorithm that can vary the parameter set during optimization has been developed. This variable-complexity algorithm is particularly appropriate for design studies, in which it is common to start with a simple representation and progress to more detailed descriptions that use more design variables. A number of tasks that are not easily solved by gradient-based optimization have been successfully handled by the new "genetic" method.

Genetic algorithms are designed to mimic evolutionary selection. A population of candidate designs is evaluated at each iteration, and the candidates compete to contribute to the production of new designs. Each individual is represented by a

genetic string—a coded listing of the values of the design variables. The entire string is analogous to a chromosome, with genes for the various features (or variables). When individuals are selected to be parents for offspring designs, their genetic strings are recombined in a crossover operation, so that the new designs have elements of two earlier designs. (The variable-complexity algorithm allows crossover to occur at different points in each parent, so that offspring have genetic strings of varying length.) A mutation operation also allows modification of elements of the new individual so that it may include new features that were not present in either parent.

The effectiveness of genetic algorithms depends on useful correlations between parts of the genetic string (genotype) and the performance of the individual it represents (phenotype). Substrings, or

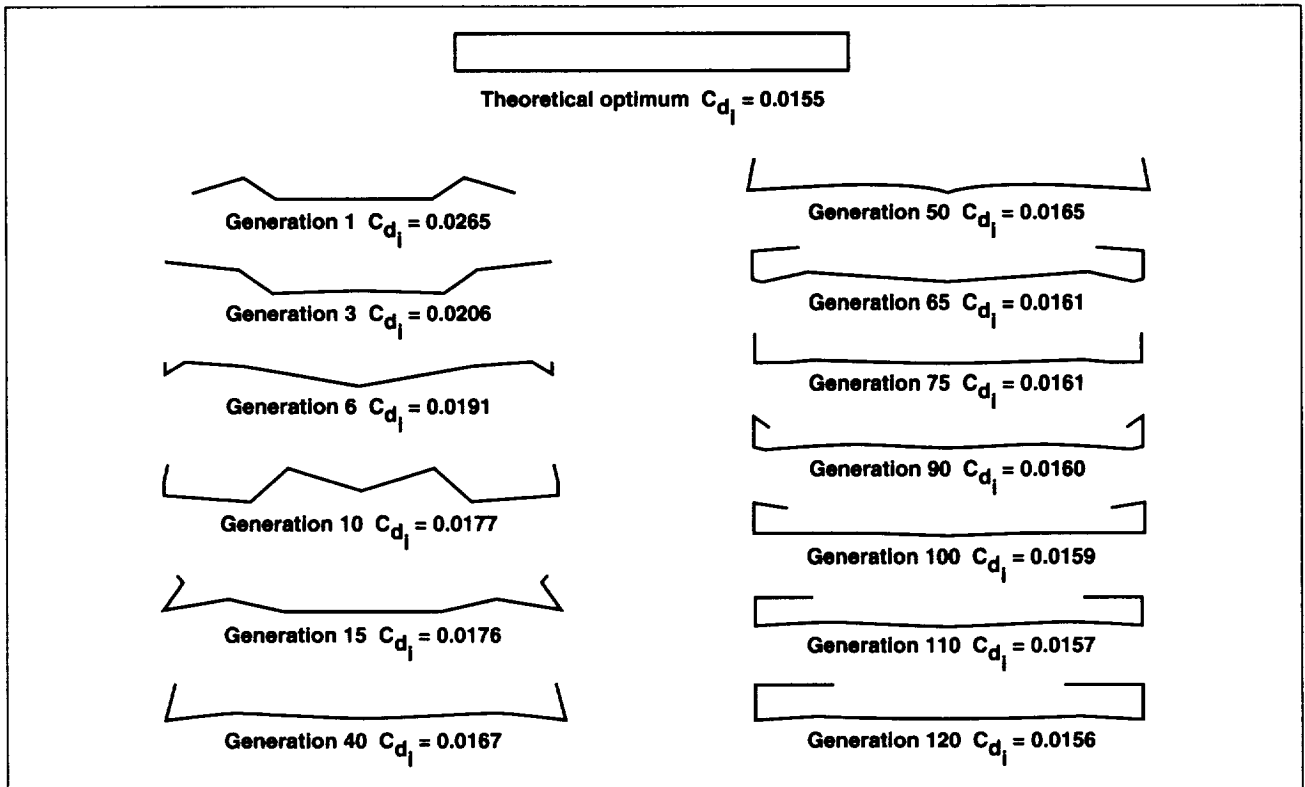


Fig. 1. Evolution of wing design during optimization.

building blocks, that appear in the description of above-average phenotypes are likely to survive into the next generation, even if the genotype is broken up by the action of crossover and mutation. Short, low-order building blocks are retained and combined to form higher-order building blocks, with the process repeating over many generations until the best design is found. Promising features of different candidates can be recombined to produce improvements in complete designs. The variable-length encoding aids in the identification and retention of superior building blocks.

The figure shows the evolution of a wing that minimizes induced drag while satisfying span and height constraints. Gradient-based optimizers and standard genetic algorithms, which use a fixed number of design variables throughout the optimization process, typically get stuck at local minima that satisfy the geometric constraints by folding the wing. The new algorithm initially satisfies the constraints by

using only a few variables. When these simple wings are refined, it is possible to introduce more elements and discover more complex designs. Winglets are added only after the wing has maximum span. Horizontal winglet extensions appear and grow in span when the main wing is flat and winglets are vertical. The performance of the final solution is almost identical to the theoretical optimum. When parasite drag is included in the problem formulation, a simple analytic result is no longer available, but the genetic algorithm still correctly identifies the optimal wing shape.

Peter Gage and Ilan Kroo are in the Aeronautics and Astronautics Department at Stanford University. This work was funded in part by grant NAG2-640 from Ames Research Center.

**Ames-Moffett contact: H. Miura
(415) 604-5888**

Headquarters program office: OA

Conceptual Aircraft Geometry Modeling Program

James R. Gloude-mans, Paul Gelhausen

A new, highly interactive, parameter-based conceptual aircraft modeler has been developed and tested. This program, called RAM (Rapid Aircraft Modeler), is a three-dimensional (3-D) computer-aided design system specifically designed to generate complete aircraft geometry models. The first figure shows the wide variety of configurations that have been modeled using RAM.

The actual parameters used to evaluate the design are also used to control the shape of the geometry. Instead of curves and/or surfaces, the model is defined and stored in terms familiar to the aircraft designer. For example, the planform of a wing can be defined by span, aspect ratio, taper ratio, and sweep. This manner of definition leads to a quick and intuitive method of generating aircraft components. The second figure shows the main

screen and the control panels used to modify the parameters describing a wing. This figure also shows a scanned 2-D drawing of the aircraft placed in the background of the modeling area to aid the user in creating the 3-D model.

RAM was written in C++ using object-oriented design methods which have helped reduce development time and have enhanced maintainability. For example, inheritance was used to create the specific geometry objects. The wing and fuselage classes were derived from a basic component class that contains general functions, such as rotate and scale. This type of code reuse, coupled with the use of some general class libraries, has greatly reduced development time.

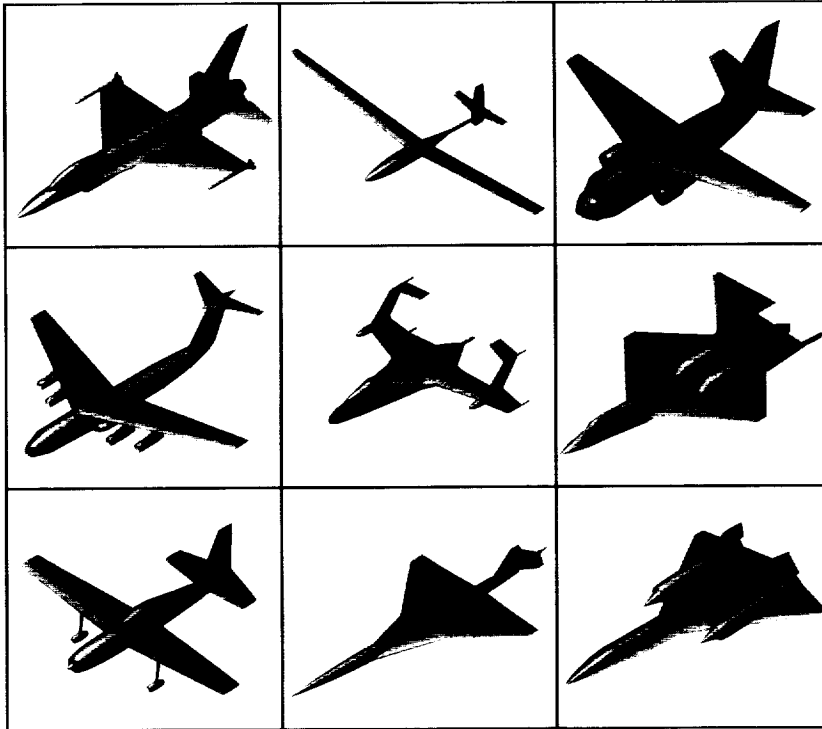


Fig. 1. Aircraft configurations that have been modeled using RAM.

The models created in RAM are used to improve the aerodynamic and weight calculations in conceptual aircraft design synthesis codes such as ACSYNT. The models can also be used as input for more detailed aerodynamic codes. Currently there are file output options for Vorview/Vorlax (a vortex lattice code) and an unstructured volume gridding program called Felisa.

Future plans include integrating RAM with ACSYNT to allow design optimization using the improved geometry and user interface in RAM. Other planned improvements include user definable links between parameters and new component types.

Ames-Moffett contact: J. Gludemans
(415) 604-1223
Headquarters program office: OA

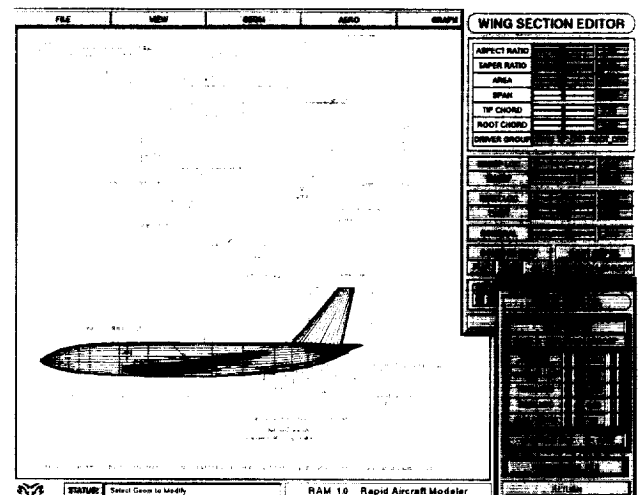


Fig. 2. Main screen of the RAM aircraft modeling program.

Oblique All-Wing Aircraft First Flight

Tom Gregory

The oblique wing has been studied at Ames for over 30 years because it is the lowest-drag shape for supersonic cruising flight. Several wing-plus-body shapes have been studied, wind tunnel tested, and even flown. However, a study of the oblique all-wing system showed this aircraft to be extremely efficient when it is large enough to contain passengers inside the wing. A remaining question was whether this unstable shape could fly efficiently with computer assistance. Other questions remained about the details of the best type of control surfaces and their relationship to the flight control computer.

A model of the oblique all-wing aircraft made its first flight (see figure) from the Ames Research Center, Moffett Field runway on 10 May 1994. The electronically stabilized, unpiloted aircraft completed two circuits within the Field and made a landing on the runway centerline. The aerodynamically unstable aircraft is 20 feet in span, weighs approximately 80 pounds, and is powered by two ducted fan engines. The onboard electronic stabilization system controls 10 trailing-edge segments along the span and two rudders on the downstream wing. This unique aircraft has no fuselage and is all wing except for the engine nacelles, vertical fins, and four landing gear. The variable-sweep airplane was flown at a sweep angle of 40 to 50 degrees on this flight. Data from the flight were recorded with an on-board computer and downloaded after the landing. The research program to simulate, build, and fly the aircraft was conducted by Stanford University under a grant from NASA Ames. The Stanford design was influenced by engineers from NASA Ames, Boeing, and McDonnell Douglas. The data are being used to

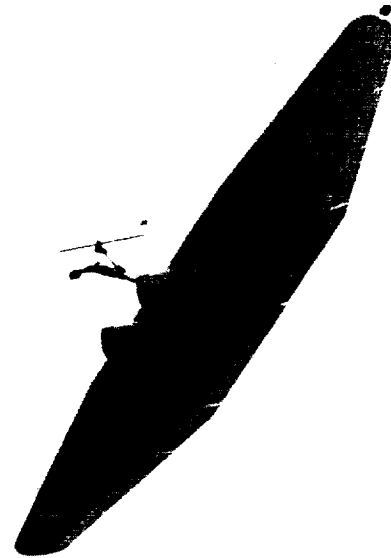


Fig. 1. Unpiloted oblique all-wing aircraft in flight.

understand the stability and control of oblique all-wing aircraft, and to formulate improved designs.

Future plans include investigation of optimal flight control algorithms and aircraft shapes, as well as integration of on-board electronic navigation using the global positioning system.

Ames-Moffett contact: T. Gregory

(415) 604-5978

Headquarters program office: OA

Aircraft Concepts for High-Altitude Remotely Piloted Vehicle Missions

Andrew S. Hahn

Two series of conceptual aircraft were designed as baseline remotely piloted vehicles (RPVs) that could be used in assessing technology alternatives and mission requirements for the Environmental Research Aircraft and Sensor Technology (ERAST) program.

The first series of RPVs was designed to meet an existing mission requirement that the RPVs be able to carry a 100-pound payload to 82,000 feet altitude and have an endurance of 35 minutes. The first figure shows the basic layout of the aircraft. Three propulsion concepts were examined: a recirculated exhaust cycle, a bi-propellant piston expander cycle, and a triple-turbocharged, spark-ignited internal combustion cycle. The assumptions and basic airframe layouts were kept as similar as possible in an attempt to identify the propulsion-specific technology issues. The results, shown in the top graph of the second figure, indicate that with a similar airframe both the turbocharged and expander cycles yield vehicles that are lighter by more than 300 pounds than a vehicle with the recirculated exhaust cycle engine.

A second series of aircraft was designed to meet a proposed requirement that it carry a 200-pound payload to 90,000 feet altitude and have an endurance of 240 minutes. The same three propulsion concepts were designed in much the same way as the first series. Results were significantly different from those for the previous series, primarily because of the longer duration. In this series, the recirculated exhaust and expander cycles were unable to meet the



Fig. 1. Basic airframe layout.

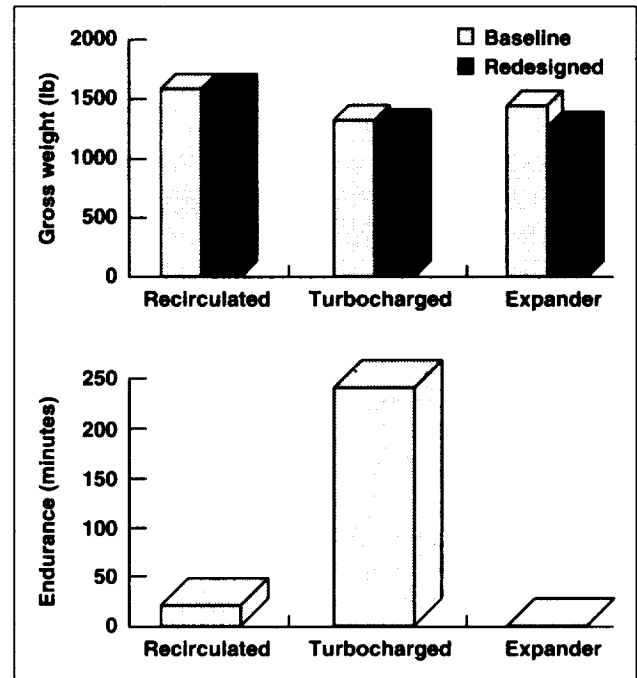


Fig. 2. Analysis results. Top: series 1, gross weight comparison; bottom: series 2, endurance comparison.

requirements because of their high fuel consumption. This finding led to a different comparison being made. Since the turbocharged cycle was fully compliant at a gross weight of 2,782 pounds, it was decided to use this approximate weight as a baseline and perform a simple reduction in endurance until a viable design was obtained for the other two cycles at the same weight. This showed that the recirculated exhaust cycle had an endurance of 20 minutes, whereas the expander cycle had an endurance of only 1 minute. These results are shown in the bottom graph of the second figure. Because of the problem with having unconverged, uncompliant baseline designs, these airframes could not be redesigned to improve performance as was done with the previous series. We plan to rectify this problem by fixing the gross weight of all three concepts and then optimizing the airframe to maximize endurance.

After examining the turbocharged aircraft, it was noted that the wing weight was 23% of the gross weight, an unusually high percentage. A sensitivity analysis was performed with a higher airfoil-thickness-to-chord ratio at the wing root, and results indicate that either an additional 100 pounds of payload could be carried or 500 pounds of gross

weight could be saved. These results show that for the turbocharged cycle, the wing structure is critical.

Ames-Moffett contact: A. Hahn
(415) 604-0968
Headquarters program office: OA

Internal Layout Module for ACSYNT

Shahab Hasan

The objective of this research was to enhance the ability of the aircraft designer to arrange, modify, view, and analyze the internal components of an airplane during the conceptual design phase. To accomplish this, new software called the Internal Layout Module has been added to the aircraft synthesis program ACSYNT.

Before the new module is invoked, ACSYNT is used to create a geometric model of an airplane. The module is then launched from within ACSYNT and transfers the aircraft geometry into a new graphical user interface. This interface allows the user to partition the aircraft cabin into sections in which the internal components are arranged. The program incorporates algorithms that determine the minimum required dimensions of the fuselage to adequately carry the desired internal components. The user communicates the requirements to the program through parameters such as seat pitch, seat and aisle width, seat configuration, and cargo container dimensions. The modified fuselage geometry is then sent back to ACSYNT for analysis of aerodynamics, weights, and other specifications.

New fully parametric, three-dimensional, surfaced aircraft internal components, including seats, lavatories, galleys, and various cargo containers, have been successfully created using core ACSYNT geometric modeling techniques. The Internal Layout Module is written in the C++ programming language under the object-oriented programming paradigm and is fully integrated with the procedural FORTRAN code of ACSYNT. A new graphical user interface has been designed and implemented that includes a top



Fig. 1. Typical output produced by the Internal Layout Module.

view and a cross-sectional view of the aircraft and a large menu with the various parameters used to arrange the internal layout. The figure shows how the module appears on the computer screen.

The new module has been successfully used to lay out the passenger cabin of various subsonic and supersonic transport airplanes. It has been effective in identifying situations in which there is insufficient or

extra cabin volume and has allowed the engineer to more efficiently shape the fuselage. Future design studies will be facilitated because the designer is able to consider the internal layout concurrently with the external shape and size of new airplane concepts. Results from the Internal Layout Module will also be used to more accurately estimate the mass properties of future aircraft.

This new module of ACSYNT will be included in the next release of the program, version 3.0. Near-term plans include the incorporation of code to determine the center of gravity and balance data for

the airplane. Future plans include a rewrite of the graphics to utilize a combination of OpenGL for the three-dimensional geometry and OSF/Motif for the graphical user interface. Other planned features include a flexible library of components such as electrical/avionics boxes, landing gear, and cockpit equipment.

**Ames-Moffett contact: S. Hasan
(415) 604-1014**

Headquarters program office: OA

Detailed Aerodynamic Information from Conceptual Aircraft Geometry

A new methodology has been developed to predict the aerodynamics of complete aircraft configurations with higher accuracy than was previously possible. Confidence in the design of future concepts has been greatly increased by the availability of more accurate aerodynamic predictions.

The acceptance of computational fluid dynamics (CFD) in the conceptual stages of aircraft design has been slow. This lack of acceptance is largely due to the setup time involved to develop a usable CFD model. The labor-intensive tasks of geometry definition and grid generation continue to hinder the recognition of CFD as a true design tool. The present methodology attempts to address these problems by developing or acquiring the tools required to generate detailed aerodynamic information from conceptual aircraft geometry.

To simplify the geometry definition task, a new interactive, parameter-based Rapid Aircraft Modeler (RAM) was developed. The design engineer can quickly model complex aircraft configurations in real time using standard aircraft design parameters. The

David Kinney, James R. Gloude-mans, Paul Gelhausen

parameter-based geometry is then intersected and trimmed using a new recursive bounding-box intersection algorithm to provide the necessary information for the generation of the unstructured surface and volume grids. The unstructured frontal grid-generation package FELISA is used to generate the triangulated surface and tetrahedral volume grids.

Solutions on the unstructured tetrahedral grids are obtained with the new unstructured full-potential solver FPS-3D. FPS-3D solves the conservative full-potential equation using a second-order-accurate, limited upwind flux formulation. The discrete equations are solved using an implicit, preconditioned stabilized-conjugate-gradient-squared algorithm embedded in an inexact Newton method. Local grid refinement is used to improve the solution quality in regions of large solution error.

Pressure coefficient results for the ONERA M6 wing at a Mach number of 0.839 and 3.06 degrees angle of attack are shown in the first figure. The grid contains 344,400 points; 59,676 triangles; and

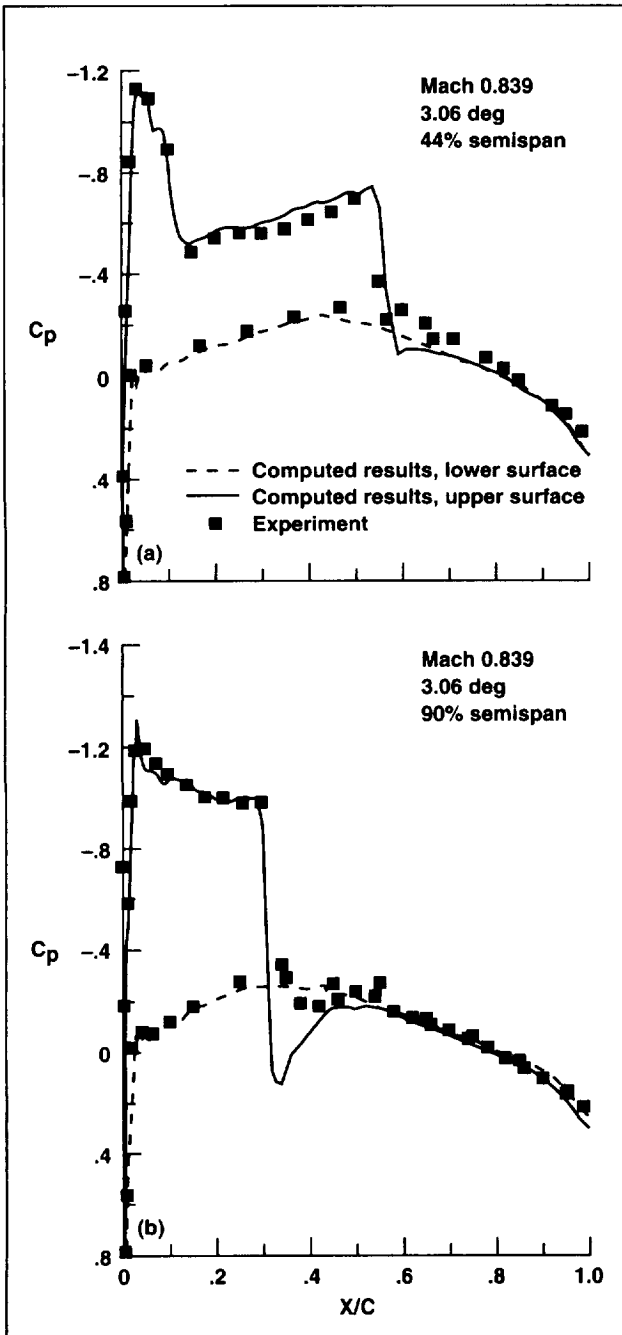


Fig. 1. ONERA M6 wing pressure coefficient (C_p) at (a) 44% semispan and (b) 90% semispan.

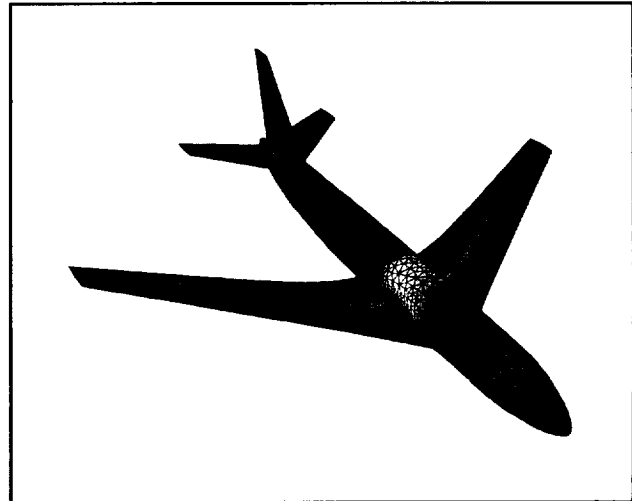


Fig. 2. Generic subsonic transport; Mach 0.8, 6 degrees angle of attack.

1,946,390 tetrahedra. The grid is the result of two levels of automatic grid refinement starting with an initial grid of 34,574 points. Preliminary results for a generic subsonic transport configuration at Mach 0.8 and 6 degrees angle of attack are shown in the second figure. The transport grid contains 93,929 points; 14,418 triangles; and 496,391 tetrahedra.

Ames-Moffett contact: P. Gelhausen
 (415) 604-5701
 Headquarters program office: OA

New Approximation of Frequency Responses for Structural Optimization

Hirokazu Miura, Mladen Chargin

A new approximation of frequency responses was developed to make it feasible to carry out structural optimization involving frequency responses computed by the direct method. When structural design parameters are perturbed, the natural vibration frequencies may shift. With a lightly damped structure and an excitation frequency near one of the natural frequencies, even a very small shift in natural frequencies will result in large changes in vibration characteristics. Therefore, the relationship between design variables and frequency responses could involve highly nonlinear implicit functions. For this reason, the various techniques developed to handle static responses were found to be inadequate for building an efficient optimization capability. Although recent efforts have addressed development of a high-quality approximation of frequency responses computed by the modal method, no adequate approach is known that is applicable to frequency responses computed by the direct method. Since the modal method itself is an approximate technique, it is desirable to develop a capability that is based on the direct method, because increasingly large problems can be solved by the direct method as the available data processing speed increases.

The approach used in this new formulation is an extension of the algorithm developed by Larsson and Sas for system parameter identification. Assume that the number of displacement degrees of freedom, M , directly affecting the design process is small compared to the total number of structural system degrees of freedom, N ($N \gg M$). The exact system of equilibrium equations of the reduced M was derived, and an efficient and convenient process to calculate the sensitivity of the reduced impedance matrix was found. Recognizing that the components of the impedance matrix are often linear or at least smooth functions of the design parameters, a linear approximation of the reduced impedance matrix is used to obtain an approximate model that allows estimation of approximate frequency responses by solving small systems of linear equations.

The figure shows a typical case at near resonant conditions. When the design parameter deviates from

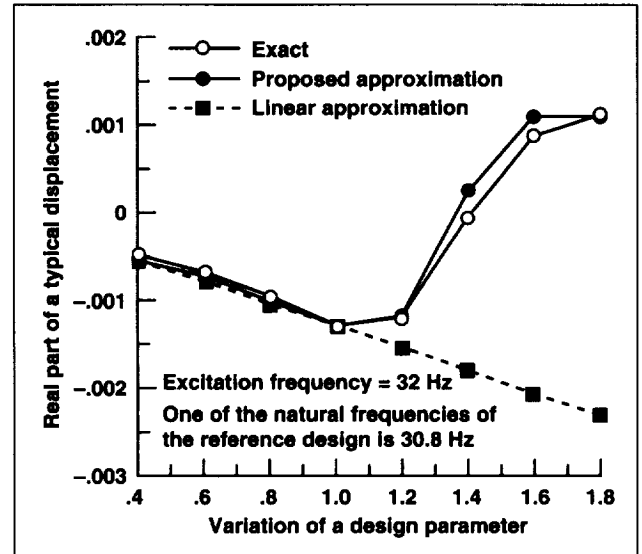


Fig. 1. Typical performance of the proposed approximation near resonant conditions.

the reference design 1.0, exact displacement shows highly nonlinear variations; thus a linear approximation is applicable only in the immediate neighborhood of the reference design. The proposed new approximation, however, is capable of following the strong nonlinearity over a wide range of design variable variations. In the design optimization, this feature permits the use of relatively large move limits and in turn results in efficient and stable convergence characteristics.

The proposed approximation is not an explicit function of design parameters. Hence, this is a departure from the traditional approximation concept in structural optimization. Computational burden increases for this type of implicit form of approximation, but the improved performance will justify the use of implicit approximations as affordable high-speed computational resources become available.

**Ames-Moffett contact: H. Miura
(415) 604-5888**

Headquarters program office: OA

Minimum-Weight Structural Design of an Axisymmetric Inlet

Shari-Beth Nadell

A project is currently being completed to improve the ability to predict the weight of high-speed inlets through the development of minimum-structural-weight design methods. Improved accuracy of weight estimation during conceptual and preliminary design will increase the fidelity of propulsion and vehicle design studies performed to support projects such as the High-Speed Civil Transport. Weight-versus-cost studies similarly have greater accuracy and allow designers to assess competing concepts with more confidence. The methods developed also produce an initial structural design of the inlet, which can be used for performing finite element analyses earlier in the design phase.

The initial inlet model is developed using information that is available from inlet conceptual design tools. The model includes the inlet flowpath, gross external geometry, internal normal and hammer shock pressures, and aerodynamic external pressures. A parametric cubic curve is fitted to the gross inlet geometry to provide a smoother surface for mass properties integration. The inlet centerbody, internal cowl, and external cowl (see figure) are designed independently. Each is assumed to be based on a stiffened shell concept consisting of panels, longitudinal stiffeners, and ring frames. Nine different variations of this concept, including Z-stiffened and

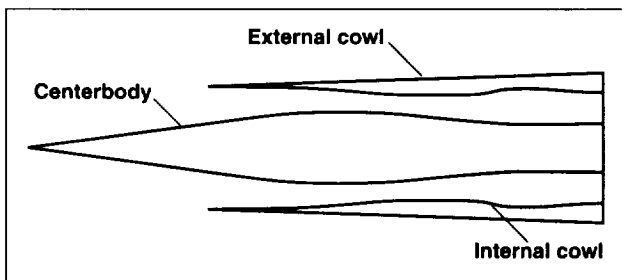


Fig. 1. Axisymmetric inlet geometry.

truss core, are included in the method. Stress analysis is performed at several stations along the length of the inlet. The minimum structural thicknesses required for both shell and frame structures to resist the maximum loads produced by various load conditions are then determined. The analysis is performed with the assumptions that the structure behaves in a manner similar to a beam for asymmetric load requirements and like a cylindrical shell for axisymmetric load requirements. Additional weight for non-optimum structure and inlet systems (e.g., bleed, bypass) is added to the computed structural weight to give an estimate of the total weight of the inlet. Preliminary results indicate that inlet hammer shock pressures are a critical design load condition for much of the inlet. Failure of the inlet centerbody is generally caused by radial buckling or compression; failure of the inlet cowl is generally caused by compression. The failure mechanism varies with the structural concept used for the design. Minimum gage requirements for foreign object damage determine the design of the cowl lip and forward portion of the centerbody spike. For both centerbody and cowl structures, internal pressure loads are more critical in the structural design than the inertial loads of the structure itself.

The minimum-weight design method will be verified with study inlets and finite-element analysis. Future plans include extending the analysis to the design of two-dimensional inlets and variable-geometry inlets. Improved integration with conceptual aircraft and propulsion-system design codes will also be addressed.

Ames-Moffett contact: S. Nadell

(415) 604-5020

Headquarters program office: OA

Oblique All-Wing Control Surface Design

James D. Phillips

The goal of the oblique all-wing wind tunnel test was to measure the lift-to-drag ratio of a realistic configuration. Part of this process involves designing the control surfaces so that the full-scale aircraft can be trimmed in all expected flight conditions, including emergencies.

The full-scale layout is shown in the figure. There are a total of 24 wing control surfaces and two vertical fins: one on top and one below. The large number of control surfaces are coordinated to trim the aircraft in pitch, roll, and yaw. The upper drawing shows the wing control surfaces with a silhouette of the fins in the takeoff and cruise position. The center drawing shows the fins in side view. With a minimum roll clearance of 5 degrees, the lower fin must

be folded when the aircraft is on the ground. The lower drawing shows the large folding tips that allow the aircraft to meet projected span limitations for large aircraft during takeoff.

The control surfaces were sized by two flight conditions: one engine out during takeoff, unswept; and cruise at Mach 1.6, at a sweep angle of 68 degrees. It was decided that takeoff be unswept with tips folded in order to meet an FAA requirement that passengers be seated within 17 degrees of the flight direction and to avoid having to skew the seating arrangement. This decision also allowed the engines to be located inboard of the cabin ends and not interfere with the landing gear until they are retracted. The engines were located inboard

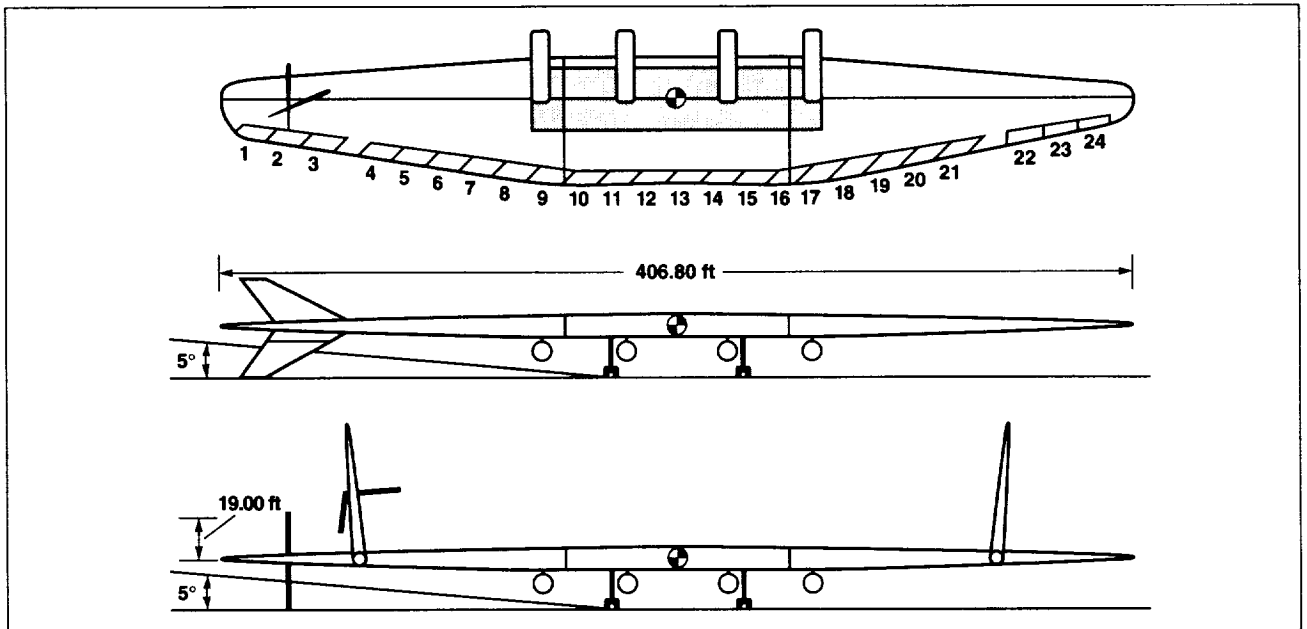


Fig. 1. Oblique all-wing. Top: plan view; middle: front view, showing fin planform; bottom: front view, showing folding wingtips.

spanwise to avoid a yawing moment that could not be trimmed with reasonably sized control surfaces. When the engines are yawed with their pivots ahead of the center of gravity, a large unbalanced yawing moment is created by offsets of the thrust lines. This yawing moment could not be overcome by fins or spoilers if the engines were too far outboard.

At low sweep angles, drag devices are more effective yaw moment controls than fins. It was calculated that at least surfaces 4 and 5 and 20 and 21 need to be spoilers to control the yaw moment created by an engine failure during takeoff. The remaining engines can easily overcome the drag of the spoilers and meet FAA climb requirements because of the very high aerodynamic efficiency of the oblique all-wing at low speeds unswept.

The fins were sized by the yaw trim required in cruise. Unlike symmetric aircraft, the oblique all-wing with elliptic loading in cruise generates a large yawing moment which tends to unsweep the wing. This yawing moment occurs because rearward airfoil surfaces must generate lift in the presence of downwash from forward airfoil surfaces. This means that rear surfaces have greater induced drag for the same lift than forward surfaces. This asymmetric induced-drag distribution causes the yawing moment

that must be trimmed by the fins. Calculations show that this aerodynamic yawing moment is larger than that caused by a single engine failure or thrust line offsets that result from engines yawed about pivot points ahead of the center of gravity chordwise.

The wing control surfaces are sized to trim the aircraft in pitch and roll. The edges of each control surface are swept at 45 degrees to the span line, except for surfaces 22, 23, and 24. The swept edges ensure that the flaps will be within the Mach cone at cruise. The wing taper causes the control surfaces on the forward wing to be more swept than the span line and those on the rear wing to be less swept than the span line. Calculations of effectiveness determined by a panel code showed that surfaces 22, 23, and 24 were ineffective at 68 degrees sweep and therefore should be locked and faired in cruise. They can therefore be unswept since they are only used at subsonic speeds.

**Ames-Moffett contact: J. Phillips
(415) 604-5789**

Headquarters program office: OA

Validation and Application of a Conical Viscous Flow Solver

David R. Schleicher

The three-dimensional (3-D) high-speed flow over simple conical geometries can be analyzed using an assumption that the flow is approximately conically self-similar. This conical approximation reduces the 3-D flow to a 2-D flow problem to be solved at a given cross-sectional Cartesian plane. Theory supports the exact use of this approximation in the case of inviscid flow, but its extension to viscous flow is not as straightforward. The figure shows characteristic viscous particle streamlines.

In this project, the numerical solution of the conical Navier–Stokes equations was attempted for a number of viscous flow problems using a conical flow code developed by Von Karman Institute (VKI). The first part of the project involved validating the VKI conical code using a number of well known one- and two-dimensional flow test cases chosen from past theoretical, numerical, and experimental studies. Once validated, the conical code was applied to two problems of interest: a 3-D shock wave/laminar boundary layer interaction and a hypersonic delta wing/fuselage interference problem.

Extensive use of the conical code for viscous applications reveals the fact that conical solutions are useful for the prediction of high-speed viscous flow quantities, but care must be taken in their application. For viscous flows, the inviscid pressure field will be reliably calculated regardless of the geometry investigated, but the reliability of the values of more detailed flow characteristics (i.e., skin friction, heat transfer) will be geometry dependent.

**Ames-Moffett contact: D. Schleicher
(415) 604-5020
Headquarters program office: OA**

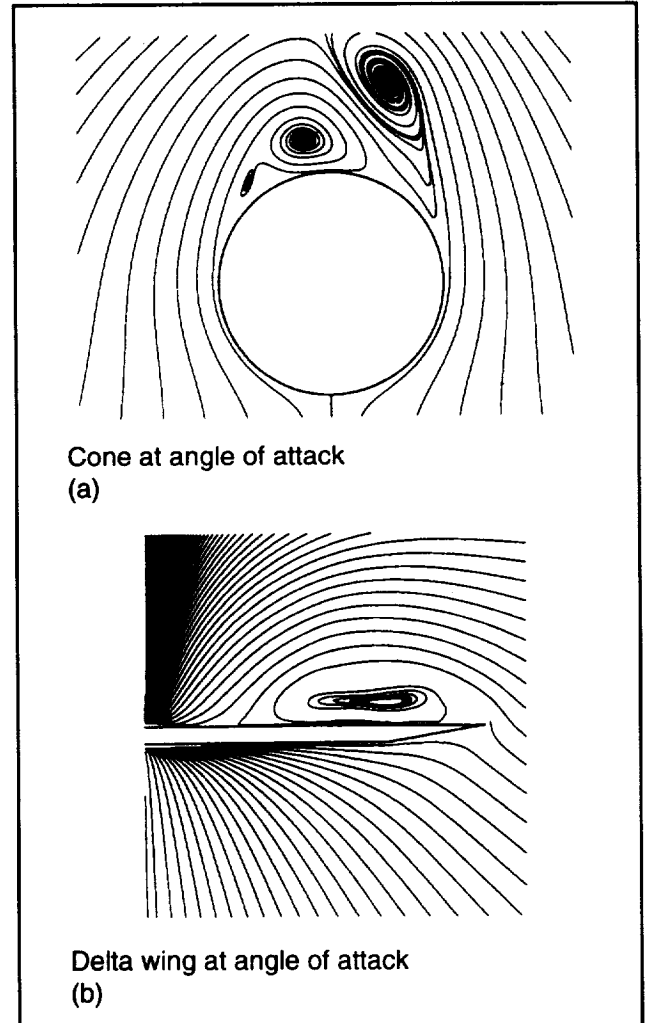


Fig. 1. Viscous conical flow particle streamlines. (a) Cone at angle of attack, (b) delta wing at angle of attack.

Portable Computer Technology Project

Rick Alena

Two major areas undertaken by the Portable Computer Technology (PCT) project in 1994 were the design and development of a second-generation Advanced Portable Workstation (APW-II) and the initiation of the PCT wireless network testbed. The APW-II is an Intel Pentium-based computer featuring high performance, a wide range of peripheral interfaces, and modular packaging suitable for use aboard aerospace vehicles. The PCT wireless network testbed will be used to perform feasibility testing of a radio frequency local area network (LAN) using the APW-II as a wireless network server.

The APW-II, developed under a contract with Scientific Applications International Corporation, features a new low-power Pentium processor, a PCI local bus for video graphics, network and disk access, a 1,024- by 768-pixel color flat-panel display, and a video input interface for television display and frame capture. Several industry-standard interfaces are provided (SCSI-II, PCMCIA, serial, parallel, and SVGA) for connection of peripheral devices. The modular packaging scheme provides the greatest

flexibility in mounting and using the computer aboard aircraft and spacecraft. The modules include processor, display, keyboard, and battery pack. The display and keyboard can be mounted up to 10 feet away from the processor, allowing crewmember access in restricted areas such as airplane cockpits. The processor can be used alone as a network server in an alternate configuration.

The PCT wireless network testbed is used to perform the system development work for the Mir Wireless Network Experiment. This experiment is planned for the STS-74 shuttle flight to be launched for docking with the Russian Mir space station in October 1995. The testbed setup duplicates the experiment by setting up a wireless LAN of personal digital assistants and notebook computers for measuring network performance and coverage. The figure shows the experiment configuration.

Ames-Moffett contact: R. Alena

(415) 604-0262

Headquarters program office: ARPA

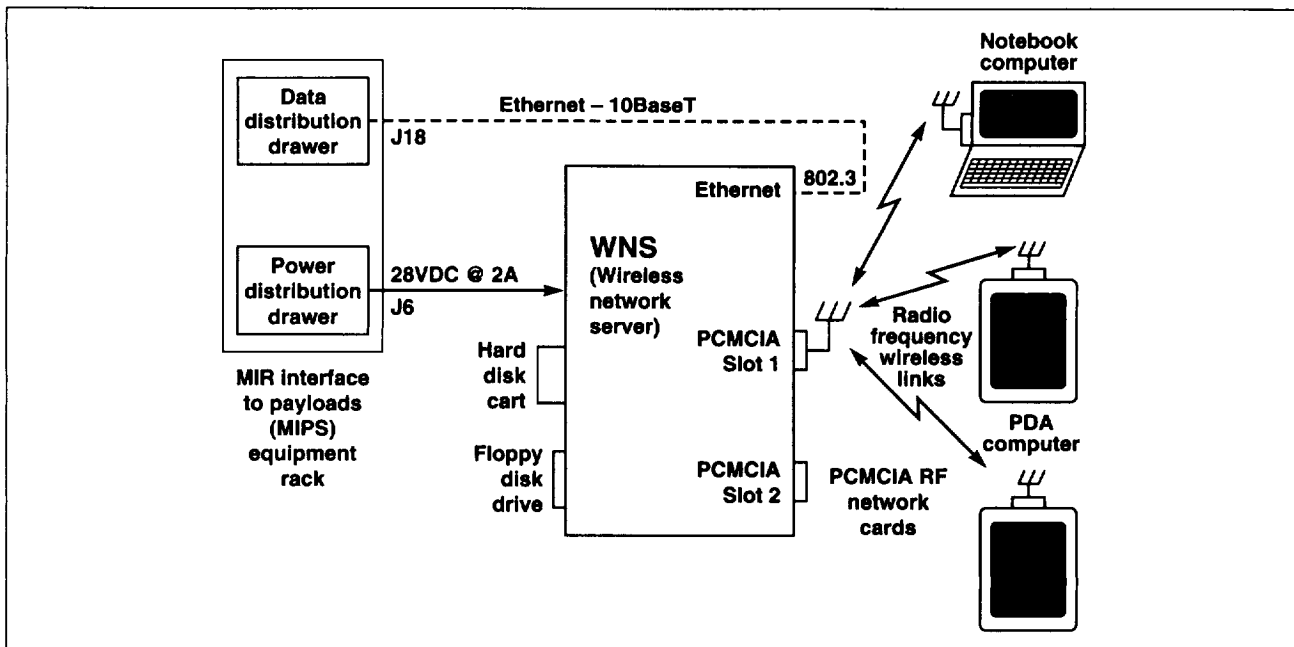


Fig. 1. PCT wireless network testbed.

Super-Resolution Imaging from Multiple Images

Peter Cheeseman, Bob Kanefsky, Richard Kraft

A Bayesian inference research team is developing the theory and practice of super-resolution modeling through multiple-image data combination. The initial application generates super-resolved images, using multiple images taken from similar locations and under similar lighting conditions. Slight differences in instrument position and orientation ensure that such images contain similar—but not identical—information. When pixel grids from multiple images are projected back to the imaged surface, one finds that no two pixels have imaged exactly the same surface patch. Differences in these imaged patches are recorded as pixel differences, which can be used to infer original surface differences over subpatch areas. Resolution is then limited by the largest open areas remaining in the composite of all the projected image grids, rather than the projection of a single grid.

Prototype software that uses a simple two-dimensional (2-D) albedo model has been applied to images from the Viking Orbiter missions. Remarkable super-resolution has been obtained from multiple images originally made for movie sequences of cloud movements. Less dramatic, but appreciable, super-resolution is possible with overlapping regions from the Mars mapping images. In cooperation with the Ames Space Sciences Division, the latter have been used to make maximum-resolution images of candidate landing sites, particularly Gusev crater, for future exobiology missions to Mars. These applications have proven the concepts behind 2-D super-resolution, and thus extended the design space for high-resolution imaging techniques.

Our long-term, and much more difficult, goal is the construction of super-resolved 3-D surface/texture/color models using image sets obtained with different instruments, instrument locations, and lighting conditions. This requires inverting the 3-D graphics-rendering problem. A rendering system takes a 3-D surface/texture/color model and specified lighting sources and predicts what a specified camera would record from any given location and orientation. We have the recorded images, the instrument locations and orientations, and the lighting conditions, and could, in principle, “back-project” to get the model. Unfortunately, we need extremely precise back projection, to sub-pixel accuracy, in order to exploit sub-pixel differences—and we never know the projection parameters well enough to do so directly. Thus we have the inference problem of determining both the model and the projection parameters that would most probably have produced the images actually obtained, given the uncertainties in exactly how they were obtained. We have developed a mathematical model for images of 3-D surfaces viewed with multiple instrument positions and illumination directions, and are developing code to implement this model.

**Ames-Moffett contact: P. Cheeseman
(415) 604-4946**

Headquarters program office: OSAT

Anechoic Chamber Evaluation of Fiber-Optic Aeroacoustic Transducers

Young C. Cho, Maria Bualat

Acoustic measurements in wind tunnels are subject to certain interference effects including wind noise, flow-sensor interaction noise, and flow-induced sensor vibration. Currently existing acoustic sensor techniques are not adequate to cope with these problems. In an attempt to overcome these difficulties, Ames Research Center embarked on a program to develop new advanced acoustic sensors. The main element of this program involves fiber-optic interferometric sensors. The technology of these sensors utilizes the fact that the light propagating through the optical fiber undergoes phase modulation when the fiber is exposed to external fields. This phase modulation is interferometrically retrieved and processed to determine the external fields. Fiber-optic sensors offer a number of advantages, including high sensitivity, wide dynamic range, compact sensor package, light weight, geometric versatility, great telemetry capability, and immunity to electromagnetic interference.

NASA's first fiber-optic microphone was developed and fabricated in breadboard form in 1990. This transducer consists of three main components: a laser, fiber-optic sensor heads, and an optical detector with signal processors. These components are integrated using optical fibers as transmission lines. Extensive anechoic chamber tests demonstrated the microphone's potential for aeroacoustic measurements in wind tunnels. The recent test results show that the noise floor is lower than 20 decibels with a

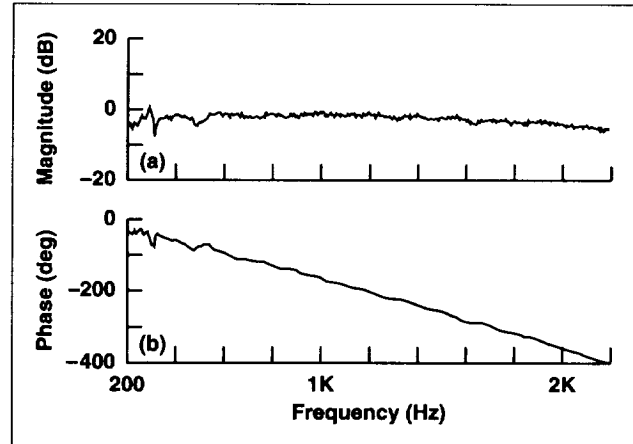


Fig. 1. Frequency response function of fiber-optic microphone. (a) Magnitude, (b) phase.

reference pressure of 20 micropascals for frequencies above 200 hertz. Such a noise floor is far below the requirement for aeroacoustic measurements. The measured frequency response function, which is stable and repeatable, demonstrates adequate performance of this fiber-optic microphone (see figure).

Ames-Moffett contact: Y. Cho
(415) 604-4139

Headquarters program office: OSAT

Prototype Electronic Purchase Request System

Michael Compton, Shawn Wolfe

For the past several years, the Information Sciences Division at Ames has been investigating the applicability of artificial intelligence and other advanced automation techniques to the streamlining of various business processes. The first system in which these techniques have been applied, the Prototype Electronic Purchase Request (PEPR) system, was put into use in 1994.

The PEPR system combines a commercial electronic forms package with a knowledge-based system that ensures that the submitted purchase requests (PRs) and other related forms are correct and complete. If they are, the PEPR system then generates an "electronic routing slip" that is based on the content of various fields on the form. This electronic routing slip contains information about which offices and individuals must approve the PR, and is used by the electronic mail system to send the form to the proper people. The system also utilizes digital signatures both to verify the sender's identity and to ensure the integrity of the data on the PR.

During 1994, the PEPR system was used by several different groups within the Aerospace Systems Directorate at Ames to process a particular class of PRs—those that apply to the funding of external research at colleges and universities. Initial results indicated that the system could dramatically reduce

the time required to originate and process PRs and their supporting paperwork by ensuring that PRs entering the system are error-free and automatically routing them to the proper individuals. The system also provides a tracking capability by which the originator of a PR can query the system about the status of a particular PR and find out exactly where it is in the approval process.

In addition to providing PR validation and routing capability, the PEPR team at Ames collaborated with researchers in the Electrical Engineering and Computer Science Department at Washington State University (WSU) on applying machine learning techniques to the form-completion process. The WSU researchers designed, implemented, and evaluated a functioning form-completion apprentice program that was used to process 269 leave report forms. The operational prototype is fully functional with respect to form-completion, learning, prediction, and printing. Overall, the system achieved an 87% savings in keystrokes and provided correct default values 89% of the time.

**Ames-Moffett contact: M. Compton
(415) 604-6776**

Headquarters program office: OSAT

Bacteriorhodopsin Films for Optical Processing and Sensing Applications

John Downie

Bacteriorhodopsin (BR) is a protein found within the cell membrane of a naturally occurring bacterium. Thin films made from polymer suspensions of the isolated material show promise for a nonlinear optical device that is well suited to the requirements and architectures of optical information processing systems and optical sensing and measurement systems. Some advantages of BR films are: (1) real-time writing and erasing; (2) durability, allowing millions of write/erase cycles without degradation; (3) very high spatial resolution—2,000–5,000 line pairs/millimeter; (4) good light sensitivity, of approximately 10 millijoules per square centimeter; (5) the encoding of both amplitude and phase patterns; and (6) the use of visible light for writing and reading. The composition of the films can be altered by chemical means to control the optical characteristics, and the BR molecules themselves can be mutagenically changed for performance optimization.

In the past year, several experiments with BR films have been successfully completed. We first demonstrated the applicability of BR to the problem of imaging through a phase aberration by encoding a real-time hologram in the film to effectively cancel the aberration and reconstruct a high-quality image.

This technique is especially suited for imaging through time-varying aberrations. The second application experiment exploited the photochromic property of BR to perform parallel optical image processing by means of logarithmic transformation of images with multiplicative noise such as speckle. This transformation process allows optical filtering of the noise and is potentially useful for all-optical processing systems such as optical correlators for pattern recognition. The third major application area studied involved using BR to write real-time images in a focusing schlieren system for refractive index visualization in an optical testing or a fluid flow density measurement. By writing the image with blue light and reading with green, we effectively encode the negative image, which is central to the schlieren application. In this experiment we successfully demonstrated the proof of concept while determining current limitations of the films and possible solutions to enable practical working systems.

Ames-Moffett contact: J. Downie

(415) 604-3588

Headquarters program office: OSAT

Efficient Scheduling of Automatic Telescopes

Mark E. Drummond

This project is defining and implementing a new paradigm for automatic telescope operations. The goal of the new paradigm is to achieve extremely low operating costs while maintaining high efficiency and high scientific productivity.

In this new operations paradigm, astronomers submit requests for telescope observing time as programs written in a language called the Automatic Telescope Instruction Set. These requests are submitted using electronic mail and World-Wide Web infrastructure. The observing-time requests are collected in a database that is managed by a human principal astronomer (PA). The PA is responsible for defining the rules by which telescope time is allocated. The actual allocation of time is carried out automatically, by software known as the Associate Principal Astronomer, or APA.

The APA examines the database of observing-time requests and allocates time over many months into the future. It also allocates time for each request to be processed during the night to come. Before each night of processing, the APA initiates communication with the remotely located automatic telescope and sends a schedule that shows the allocations it has made. During the night, the APA monitors schedule execution at the telescope, dynamically rescheduling as events require. In the morning, it sends an electronic mail message to the astronomers for whom new data have been obtained. These astronomers obtain their new data via the World-Wide Web, in

much the same manner as they submitted their original requests.

Preliminary results suggest that this operations system has a number of significant advantages over previous manual telescope operations. Working with scientists at Tennessee State University, we have determined that one astronomer using two automatic telescopes is able to obtain a lifetime of data in a single year of operation. Furthermore, the cost per observation has been reduced by a factor of 40. The APA is also expected to increase the quality of the data obtained using automatic telescopes. Currently, the scheduling mechanism employed by these telescopes tends to make observations at very high airmass. That is, the telescope tends to make observations near the horizon, just after a star (or other object) has risen or when it is about to set. With more advanced scheduling methods, the APA is capable of making observations at much lower airmass. The APA's scheduler uses methods for solving constrained optimization problems—in which a multiattribute objective function is provided that characterizes the various factors involved in scheduling observations, and the relative importance of these factors.

**Ames-Moffett contact: M. Drummond
(415) 604-4710
Headquarters program office: OSAT**

Optical Matrix Processors for Structural Control and Plume Analysis

Charles Gary, Maria Bualat

An optical matrix processor is a simple computer that uses light rather than electricity to perform its calculations. The advantages of an optical processor over an electronic digital computer are greater speed (measured in operations per second), smaller size, and lower power consumption. The limited accuracy of the analog optical processor is a disadvantage.

The figure shows the basic architecture of an optical matrix-vector processor. The optical processor performs a matrix vector multiplication in five basic steps. First, the intensities of a row of independent light sources represent the values of the input vector. Second, the light from these sources is spread so that each input point exposes a column of the matrix. The transmittance of each pixel of the matrix is proportional to the value of the corresponding point in the mathematical matrix. As the light passes through the matrix, at each pixel, the transmitted amplitude is the product of the input intensity from one point of the vector and the transmittance of one point of the matrix. Thus, in this third step, the individual products that compose the matrix vector product are formed. The fourth step focuses the transmitted light from each row to a point, thus adding along the rows to form the inner products of the matrix vector product. Last, the light from each point of the resulting column must be detected and converted to a useful form to read the result.

This year we completed a prototype optical matrix processor, the Ames 64-M, capable of 64 million operations per second. This processor was constructed using an array of acousto-optic spatial light modulators for the vector input and a liquid-crystal spatial light modulator for the matrix information. The detector used an array of avalanche photodiodes.

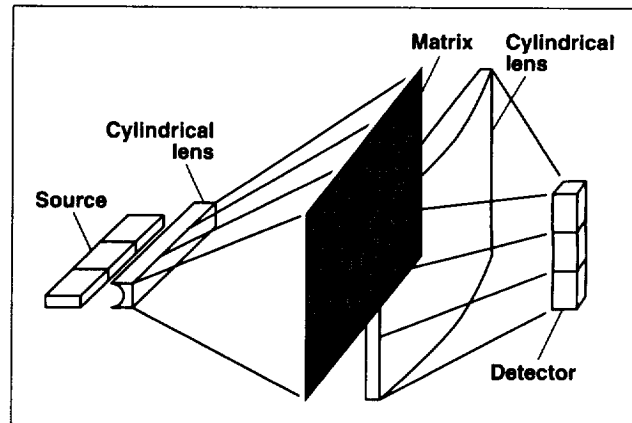


Fig. 1. Essential components of an optical matrix-vector processor.

Currently, optical matrix processors are being developed for two applications: (1) the analysis of spectral plume data from the Space Shuttle main engine and (2) feedback calculation for damping vibrating truss structures. The Ames 64-M processor calculated real-time compositions of the plume elements with an accuracy of within 5% for the elements present in test runs at the demonstration test facility at Stennis Space Center. The Ames 64-M processor also successfully calculated the feedback for real-time damping of a ten-bay truss structure on loan from the Control Structures Integration Laboratory at Langley Research Center.

**Ames-Moffett contact: C. Gary
(415) 604-3590**

Headquarters program office: OSAT/OACT

Payload Data Systems Engineering and Analysis

Terry L. Grant

The Real-Time Data Systems group at Ames has provided a variety of systems engineering and analysis services to develop the data management system architecture for future life science payloads on the International Space Station Alpha. This project included four interrelated tasks: (1) requirements analysis and a point-design study for the data systems on the Centrifuge Facility Project (CFP); (2) analysis and critique of requirements and design issues for the Standard Interface Rack in the Gravitational Biology Facility (GBF); (3) participation in an inter-center coordination team for defining payload data system issues to the Space Station developers; and (4) development of a video testbed for exploring the unique imaging requirements of the GBF BioCulture System.

The data systems engineering and analysis task for the CFP included delivery of a hypertext database with over 100 cross-classified requirements, and two technical reports which highlight various design drivers and provide a point design of system-level hardware and software. The effort has provided an in-depth understanding of the data system which is critical to low-risk development. One of the potentially most valuable results has been the identification of an opportunity to reduce software-development and maintenance costs by using a standard database and commercial software for user interfaces, and the distributed processing environment.

The task for the GBF has provided the challenge of cross-project and cross-center communications with Johnson Space Center to identify common requirements for interface services from the International Space Station Alpha. The task has helped to build valuable technical liaisons between the life science projects at the two centers, and a common language based on shared lessons learned in data system development. A significant side issue was the evaluation of the maturity of various bus and network standards that are candidates for the payload's Standard Interface Rack. The evaluations are summarized in the final report on the data system development.

The video testbed was developed as scheduled, along with a final report. It provides a full-scale, working apparatus that delivers high-resolution, magnified-color, remote-video views of biological cells as they appear within various cell growth chambers. The apparatus will be used to evaluate proposed system specifications, perform imaging tests, and demonstrate representative image quality to future Space Station experimenters.

**Ames-Moffett contact: T. Grant
(415) 604-4200**

Headquarters program office: OLMSA

Principal Investigator in a Box

Nick Groleau

The Principal-Investigator-in-a-Box project improves the scientific return of experiments performed in space by providing astronaut experimenters with an "intelligent assistant" that encapsulates much of the domain- and experiment-related knowledge mastered by the principal investigator (PI) on the ground. Expert Systems technology and flight-qualified personal computers are used to encode the requisite knowledge and make it available to astronauts as they conduct experiments in space. The PI-in-a-Box system performs four major functions: diagnosis and troubleshooting of experiment apparatus, data collection and quality monitoring, detection of "interesting" data, and protocol management. The system software is based on three commercial off-the-shelf software packages.

The first experiment to include PI-in-a-Box automation measures human adaptation to weightlessness in the context of the neurovestibular system. The figure shows the astronauts using the PI-in-a-Box portable computer on the SLS-2 shuttle mission in October 1993. Extensive postflight analysis of the scientific data and the use of PI-in-a-Box proves the system's success. In several instances, the system quickly alerted the astronauts to decreasing data quality. The astronauts fixed the problems in seconds rather than minutes. The system also made modifications to experiment schedules as the astronauts added an additional subject to each session. These changes saved valuable experiment setup time by optimizing the ordering of protocols. Finally, PI-in-a-Box saved all of the data that was lost in shuttle-to-ground data communications.

We are now in the process of expanding the scope and sophistication of the system to allow increased use (with many experiments) during the Neurolab shuttle mission scheduled for 1998. The Neurolab effort includes developing new scientific and engineering experiment partners. The technology will be applied in key situations to leverage the investment in PI-in-a-Box. Examples include "smart"

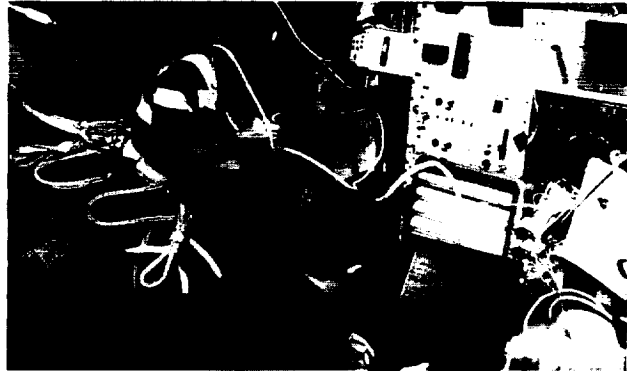


Fig. 1. PI-in-a-Box being used by astronaut David Wolf on board the shuttle Columbia.

electronic procedures (as opposed to static paper procedures), complex hardware monitoring and troubleshooting, and tracking consumables stowage.

The PI-in-a-Box was the first application developed by the Automation Support System for Expert Telescience (ASSET). Work is under way to expand this technology to other domains of interest to NASA and the nation:

1. In cooperation with the Office of Commercial Technology, we are developing a portable evaluation system for neuromotor evaluation of brain damaged patients. The system integrates ASSET technology as the Intelligent Computer Assistant.
2. In cooperation with Kennedy Space Center's Plant Space Biology Laboratory, development of an ASSET system for plants in space is being considered.
3. Development is under way of a semi-autonomous ground station for a proposed Earth ionosphere tomography satellite based on the PI-in-a-Box flight-software experience.

Ames-Moffett contact: N. Groleau

(415) 604-0611

Headquarters program office: OSAT

Dante II at Mt. Spurr, Alaska

Butler Hine

The Carnegie–Mellon University Field Robotics Center (FRC) developed Dante II, a tethered walking robot, to explore the Mt. Spurr volcano in Alaska's Aleutian Range in July 1994. High-temperature fumarole gas samples are prized in volcanic science, yet their acquisition poses significant challenges. In 1993, eight volcanologists were killed in two separate events while sampling and monitoring volcanoes. The use of robotic explorers such as Dante II opens a new era in field techniques by enabling scientists to conduct research and exploration remotely.

Using its tether cable anchored at the crater rim, Dante II is able to rappel down sheer crater walls to gather and analyze high-temperature gases from the crater floor. In addition to contributing to volcanic science, a primary objective of the Dante II program is to demonstrate the capabilities of robotic exploration of extreme (i.e., harsh, barren, steep) terrains such as those found on planetary surfaces.

The Intelligent Mechanisms Group (IMG) in the Computational Sciences Division at Ames has been developing advanced telepresence- and virtual-environment-based operator interfaces since 1991. These advanced interfaces are important for terrestrial science and exploration applications, and are critical for planetary surface missions. The IMG provided the Dante II project with virtual environment and visual simulation tools. These tools provided vehicle

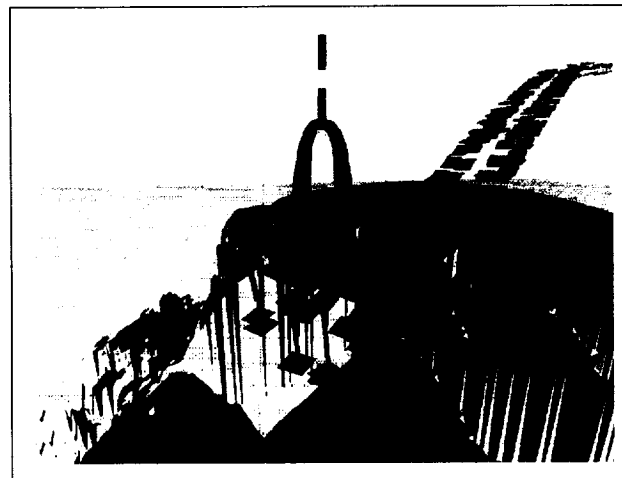


Fig. 1. Virtual Dante.

configurations and terrain visualization to operators and scientific observers. In addition, the IMG provided its teleoperations expertise for implementing live stereo video on Dante II and for enabling the interaction of multiple observation sites in the continental United States during the July 1994 mission.

Ames-Moffett contact: B. Hine
(415) 604-4379

Headquarters program office: OSAT

Application of Neural-Network Technology to Wind Tunnel Testing

Charles Jorgensen, James Ross

Neural networks were demonstrated to increase productivity and reduce costs in wind tunnel operations by "learning" to predict the performance of aircraft models undergoing wind tunnel testing. A significant amount of time in wind tunnel testing is spent measuring the aerodynamic effects of a large number of geometric variations. Such variations include flap and slat positions and deflection angles, elevator and rudder deflections, and power settings. If a neural network could be trained to accurately predict the effects of these various parameters on the aerodynamic coefficients (lift, drag, side force, pitching moment, yawing moment, and rolling moment) while using a smaller subset of the test matrix than would normally be required to generate an adequate database, significant savings in test time and associated costs could be realized.

In 1994, data collected during scheduled tests were simultaneously used to train a multilayer neural network. As more and more test data were acquired, the network learned to produce highly accurate estimates of test results for new, unseen conditions if given only the aircraft test configurations. The network eventually learned a complete static model of the aircraft which, along with a set of developed software analysis tools, was used to predict the results of the next session's tests and to identify points of major interest such as maximum lift.

The procedure is highly adaptable to different test data and conditions and has been applied to

previously collected data from the T-39 and the High-Speed Civil Transport scale model. In December it was used in tests of the Super-High-Alpha Research Concept aircraft (SHARC). The method proved to be very fast compared to approaches that use completely mathematical simulation of flows; a model of the entire aircraft was learned in under 30 seconds, with an error level of well under 1%. The need for much smaller amounts of test data than are required using current methods was also demonstrated. In wind tunnel tests of the SHARC, the learning of an adequate predictive model was shown with approximately 40% fewer data. This reduction translates into marked savings in facilities operations costs, through a reduction in the number of wind tunnel hours required for testing of a new aircraft. Long-term benefits of the method include faster development of new aircraft prototypes through more rapid simulation of aircraft flight performance and possibly less need for small-scale model development for estimating aircraft flight characteristics. The method has been delivered to the wind tunnel as a software package, and a patent application has been filed.

Ames-Moffett contact: C. Jorgensen/J. Ross

(415) 604-6725/6722

Headquarters program office: OSAT

Intelligent Aircraft Control System

Charles Jorgensen, James Urness

The objective of this program is to develop and flight demonstrate a revolutionary control concept that can efficiently identify aircraft stability and control characteristics using neural networks. The work is being performed under a 4-year advanced-concepts initiative involving two NASA centers, Ames-Moffett and Ames-Dryden, in cooperation with McDonnell Douglas Aerospace Corporation, St. Louis. The program emphasizes techniques for reducing the costs of control-system software for new aircraft designs and for flight systems that can accommodate sudden major changes in aircraft stability and control behavior which might result from failures in flight control actuation or damage to aircraft control surfaces.

In 1994, this program demonstrated the ability of a multilayer perceptron to learn the rate and control equation parameters of an F-15 aircraft. This was done in the Six-Degree-of-Freedom Simulator and in McDonnell Douglas aircraft in St. Louis by comparing the network performance to online performance

of the actual controller during simulated flight maneuvers. In parallel with this development, the ACTIVE test aircraft at Ames-Dryden was modified to accept neural network control commands. Work also began in exploring a second-generation neural control method designed to perform real-time, online reconfiguration control. Three network types were coded at Ames, including infolding nets, CMAC variations, and modified Levenberg Marquardt neural algorithms. Work began on a virtual-reality ACTIVE simulation testbed to permit pilot assessment of neural network performance. In 1995, the ACTIVE aircraft at Dryden will be flight tested using the initial neural controllers. Work will continue on improving network performance and increasing the accuracy of the off-line models and analysis tools prior to flight testing.

**Ames-Moffett contact: C. Jorgensen
(415) 604-6725
Headquarters program office: OA**

Mars Atlas on the World-Wide Web

Bob Kanefsky, John Stutz

The recent explosive growth of the World-Wide Web (WWW) has made it possible to provide interactive graphical tools to assist scientists in obtaining Viking Orbiter images of any desired region of Mars, using standard browser software on their personal computers or workstations. Many images have been available on CD-ROM for the past few years, and some have even been available online. But images are identified by orbit number and frame number, not by latitude, longitude, or altitude, and this had made it tedious to find all the adjacent images of a given region at desired viewing angles and wavelengths. A graphical interface can show the footprints of the available images, superimposed on a

map of the area. Once located, if an image is online it can be displayed immediately, even if images are scattered between a dozen institutions.

An online Mars Atlas was created in 1994. It displays USGS map tiles, re-projected so that they fit together almost seamlessly (in some browsers), and can be scrolled in any compass direction in 5-degree steps. Locations can be selected from a list of feature names, or chosen by pointing and clicking at a global map, zooming in on a 15- by 15-degree area. After locating a desired area, centered on a 5- by 5-degree tile, the user can either display the tile's 256-pixel/degree digital image map or view a Viking Orbiter

coverage map. The coverage map shows footprints of all known overlapping images as colored outlines superimposed against the map, at a scale chosen to clearly display the image outlines. This information was previously available only on printed coverage maps or in tabular form by database query. An additional click of the mouse on an image outline displays a thumbnail rendition of the raw image, and another displays the full image, if it is on one of the online CD-ROMs. In addition to the comprehensive coverage, special sections have been manually prepared to show detailed information on the Mars Pathfinder landing site and on Gusev crater.

This work is a spinoff of the image-finding tools written for locating datasets for a super-resolution multiple-image processing algorithm, now under development in the Computational Sciences Division. When the super-resolution algorithm was ready to be applied to sites of scientific interest, we found that planetary scientists rarely possessed good tools

for locating raw digital images, and were often working with much-lower-resolution maps. Clearly, before offering super-resolution processing, it was important to provide our colleagues with the best existing images. The widespread availability of WWW tools made an easy-delivery vehicle possible.

The Mars Atlas also serves as a public outreach and an educational resource. More than 12,000 different machines (and presumably about the same number of users) accessed it in its first 6 months. Several Ames scientists have used it extensively for image finding, and there appear to be a handful of regular users outside of NASA. The atlas is found at <http://ic-www.arc.nasa.gov/ic/projects/bayes-group/Atlas/Mars/>.

**Ames-Moffett contact: B. Kanefsky
(415) 604-3514**

Headquarters program office: OSAT

Human Exploration Demonstration Project (HEDP)

David J. Korsmeyer

The Human Exploration Demonstration Project (HEDP) was a multi-Division effort that addressed the advanced technology requirements for a planetary surface habitat. The HEDP project began in the fall of 1991. The goal was to integrate the specific technologies under development by the Information Sciences Division, the Aerospace Human Factors Division, the Life Science Division, and the Advanced Life Support Division at Ames. All of the technologies are necessary for an integrated working and living environment.

Four basic achievements of the HEDP were that it (1) enhanced the technology development and evaluation process through synergistic cooperation of multiple divisions at Ames; (2) provided a simulator for evaluation of technology in an integrated system setting; (3) created a realistic environment for introduction of new technology; and (4) identified promising technology concepts for NASA operations centers, for new and existing projects.

The project developed an integrated demonstration environment consisting of (1) a habitat structure and life support system testbed, (2) a human-powered centrifuge and a physiological monitoring system for the crew, (3) a virtual-environment workstation for robotic operations, and (4) centralized data-acquisition and habitat systems health monitoring. Several robotic systems external to the habitat performed activities to provide representative work loads of the crew.

The figure shows the basic components of the HEDP. The HEDP consisted of a working environment contained in a living environment. The living environment consisted of the Controlled Environment Research Chamber (CERC), which housed the human-powered centrifuge on its lower floor. The working environment was made up of advanced workstations in the upper floor of the CERC that controlled and remotely operated systems on the

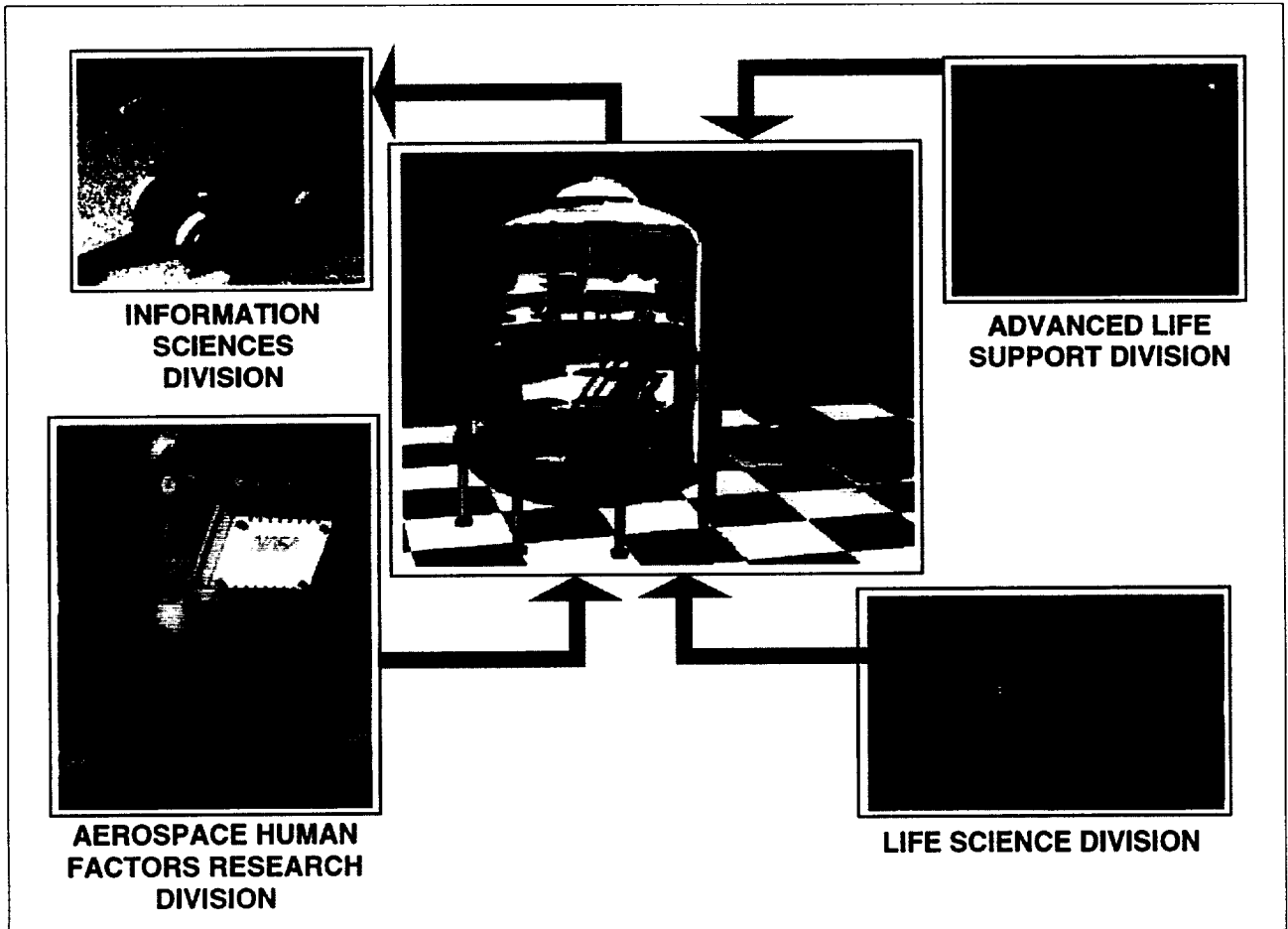


Fig. 1. Components of the HEDP.

simulated planetary landscape. The HEDP tried to create realistic operational scenarios equivalent to those anticipated on the lunar surface and to develop the robotic controls systems and technologies required. The two environments were coupled through an underlying data network that includes a common set of services and provides a medium for overall system integration. Many of these services utilized artificial intelligence technologies to maximize autonomy and minimize crew work loads.

At the end of August 1994, the HEDP had finished all four phases of development and the demonstration phase. Demonstrations and an analysis of the completed project are planned to begin in April 1995.

**Ames-Moffett contact: D. Korsmeyer
(415) 604-3114
Headquarters program office: DDF**

Pattern Recognition Tool Kit for Mission Control

Philip Laird

For more than 20 years, NASA Space Shuttle flights have been controlled from the Flight Control Room (FCR) at the Johnson Space Flight Center, but now a new Space Operations Control Room (SOCR) is in the final stages of construction at Johnson. The new facility will control both Shuttle flights and Space Station Freedom operations, beginning in October 1995. Modern Unix(c) workstations replace the obsolete display equipment in the older facility.

The pen-and-ink strip chart recorders now used by controllers in the FCR to track sensor values are being replaced in the SOCR by graphical displays. But instead of simply substituting an electronic display for the strip chart, the new Pattern Recognition Toolkit provides controllers with intelligent interpretation of the data. The result is an improvement in the controllers' ability to make critical decisions accurately and rapidly during flights.

The tool kit, a collaboration between the Ames and Johnson centers, is designed to make the design, implementation, and certification of new pattern recognition applications as inexpensive as possible. It focuses on three important classes of problems:

1. Signature recognition—finding, recognizing, and reporting events in sensor data (e.g., a device being turned on);
2. Anomaly detection—detecting a change in the normal pattern of sensor data and alerting controllers; and
3. Trend analysis—predicting the future values of a set of sensors and notifying controllers if these values may exceed acceptable limits.

All these problems entail learning: to recognize and label signals, to identify normal behavior, and to extrapolate stationary time series. A broad set of tools applicable to these tasks has been assembled, drawing both from classical methods (Bayesian classifiers, Kalman filters) and from more recent techniques (neural networks, genetic algorithms).

An object-oriented language for defining and configuring a system, from modules and a client-server interface to control-center data streams, makes the construction of applications efficient. The time required to generate an application has been reduced from several months to about 1 week. And since the applications are built from common modules, certification costs will be greatly reduced. Finally, a graphical builder tool that will enable controllers to generate the applications themselves is expected to be completed in 1995. Once all these tools are available, the primary bottleneck will be the collection and labeling of flight data so that the pattern recognizers can be trained.

Three applications are now running in the SOCR during flights: an electrical power system; a system to anticipate failures in the auxiliary power units during launch and descent; and a guidance, navigation, and control system to identify faults in the inertial measurement units. The electrical power system is undergoing flight certification.

Ames-Moffett contact: P. Laird

(415) 604-3362

Headquarters program office: OSAT

Amphion: Real-World Automatic Programming

Michael Lowry, Andrew Philpot, Thomas Pressburger

For the past two years, the Information Sciences Division at NASA Ames has been investigating the applicability of artificial intelligence and formal methods for radically improving the software engineering process. A generic system called Amphion has been developed and applied to several different NASA domains. In 1994, the most advanced of these applications was installed at the Jet Propulsion Laboratory (JPL) and was put in use to generate real-world programs. Amphion is suitable for application domains for which a mature software component library has been developed.

The objective of Amphion is to enable users familiar with the basic concepts of an application domain to program at the level of abstract domain-oriented problem specifications rather than at the level of detailed component calls. End users often do not make effective use of component libraries. Sometimes this happens because a component library is developed without following good conventional software engineering practices. The results include inadequate documentation, untrustworthy code, and a lack of coherence in the various functions performed by the individual components. In addition, the effort to acquire the knowledge to effectively use a component library is often perceived as being greater than that required to develop the code from scratch.

Amphion is an effective solution to this knowledge barrier. Three Amphion applications have thus far been developed: Amphion/NAIF (solar system geometry), Amphion/CFD (computational fluid dynamics), and Amphion/TOT (space shuttle navigation). The Amphion/NAIF application is the most mature of these three and was the main focus of work in 1994.

Amphion/NAIF generates programs consisting of calls to JPL's Spicelib subroutine library, developed by the NAIF group at JPL. Spicelib provides a well engineered, well documented tool kit for planetary scientists to use in constructing programs analyzing the geometry of scientific observations for interplanetary missions. Typical problems include eclipses, occultations, moon shadows, and illumination angles.

Amphion consists of a program synthesis component and a graphical user interface front end. The program synthesis component takes as input a specification written in logical notation. The output of program synthesis is a program in the target language, e.g., FORTRAN for the NAIF application and C++ for the space shuttle flight-planning application. Amphion generates a program by a technique called deductive synthesis, which concurrently generates a program and proves that the program implements a correct computational solution to the specification. Thus a program generated by Amphion is guaranteed to be correct.

Writing a problem specification in logical notation is difficult for most users. Amphion therefore has a graphical user interface front end that enables users to enter a specification graphically through a menu-guided interface. These specification diagrams consist of icons and links that represent intuitive concepts in an application domain. The Amphion interface translates completed specification diagrams into the logical notation used by the program synthesis component. The Amphion user interface is particularly well adapted to modifying and reusing previously developed specifications.

In qualitative tests, space scientists were able to generate programs an order of magnitude faster using Amphion than they could by manually coding a program. Furthermore, Amphion is easy to learn to use: scientists were able to develop their own specifications after a 1-hour tutorial. Amphion is currently moving beyond the in-house testing phase, and has recently been applied to generate programs used in a Cassini science scheduler (Cassini is an upcoming mission to Saturn), programs for visualizing and analyzing the 1995 Saturn ring crossing (when Saturn's rings will appear edge-on from the viewpoint of the Hubble Space Telescope), and programs in a system called CCGS that will be used to plan imaging sequences for interplanetary missions.

**Ames-Moffett contact: M. Lowry
(415) 604-3369
Headquarters program office: OSAT**

Advanced Interactive Media

Nathalie Mathé, Joshua Rabinowitz, James Chen

Our objective is to facilitate access to electronic information via the development of intelligent tools integrating hypertext, multimedia, and knowledge-based systems capabilities. Particular needs for solutions were identified at NASA Johnson Space Center (JSC), and the result was an effort to support production, storage, distribution, and use of documents in an electronic format, both for Mission Control operations and for use in the office environment.

As the amount of available electronic information is increasing dramatically, rapid and effective access to information is becoming critical. Access to information is facilitated if the specific, relevant information needed by a user can be automatically supplied. Current information retrieval and hypermedia tools offer only limited mechanisms (e.g., annotation and bookmark facilities) for users to add subjective relevance information to their documents. Our approach provides a way to refine existing information access methods with subjective relevance learned from user feedback.

We developed a new model for interactive learning of subjective relevance during information access, and incremental adaptation of retrieved information to individual user profiles. The model learns, over time, from its interaction with users, and automatically retrieves and ranks the information according to its subjective relevance. The model was implemented in C++, and simulation results showed that the model was able to memorize relevance information with 100% recall (proportion of relevant materials retrieved) and 94.8% precision (proportion of retrieved materials that are relevant). Query response was immediate.

The model was applied in the JSC Electronic Documentation Project (EDP) to support operations at the Combined Control Center (CCC) for Space Shuttle and Space Station. The goal of the EDP project is to support production, storage, distribution, and use of Mission Control documents in an electronic format, both for the CCC and for use in the

office environment. In December 1993, after flight controllers' needs were identified and the document viewer requirements were defined, the Hyperman system, under development in the JSC Software Technology Branch, was chosen as the EDP hypertext document viewer. Hyperman was successfully demonstrated in July 1994 in an office environment. Hyperman 2.0, including online hyperlinked timelines, was then successfully tested with flight controllers in the CCC environment in November 1994.

We worked closely with JSC to integrate a capability for viewing timelines generated with the Flight Planning System (FPS) into Hyperman. The FPS is used daily by Shuttle Operations to edit and revise mission timelines. FPS-generated timelines are used as control documents to coordinate activities of flight controllers and astronauts: each task on a timeline is labeled according to the procedures and documents associated with this task. We developed the online version of the timelines, in which each task is automatically hyperlinked to the associated procedures in the appropriate document to provide immediate access to the correct information. After the recent Hubble repair mission, flight controllers reported that this flight would not have been successful without FPS.

In a separate collaboration with the Boeing Commercial Airplane Group and Apple Computer, a prototype support system for airplane maintenance, developed with a new Apple multimedia authoring tool, was demonstrated in September 1994. In 1995, we will develop techniques for merging technical documentation and training material and for creating sharable and reusable training material, according to emerging platform-independent multimedia document standards.

**Ames-Moffett contact: N. Mathé
(415) 604-3515**

Headquarters program office: OSAT

Science Planning and Sequencing for Space-Based Observatories

Nicola Muscettola, Sunil Mohan

In a scientific space mission, a spacecraft carries one or more instruments in order to gather scientific information that is not accessible from Earth. Science planning and sequencing is the process of gathering observation requests from the scientific community, allocating time to observations that will use the spacecraft instruments, and producing sequences of commands that the spacecraft will execute to achieve the planned observations. Planning and sequencing involves as many as 100 people for large observatories like Voyager and Galileo, and greatly impacts mission operations costs.

We are developing software tools to reduce the personnel needed for science planning and sequencing and ultimately to completely automate the process. We have developed a constraint-based domain description language that accounts for the most crucial constraints to be satisfied by a spacecraft sequence: timing of critical operations, avoidance of dangerous pointing directions (such as pointing an instrument directly at the sun), and operation of the spacecraft within its resource limits (such as power and data storage capacity). A temporal object-oriented database has also been developed in which specific scheduling decisions can be stored and assembled into a complete science plan. Decisions posted in the database are automatically checked with respect to constraints specific to the spacecraft. This allows early detection of problems and guarantees that a generated sequence is correct without the need of a long, costly sequence validation process.

A major complicating factor in science planning is the fact that scientific goals can require several additional engineering activities. For example, making an observation with an instrument might require putting the spacecraft in a specific mode and reorienting the spacecraft so that the target is in the instrument's field of view. We have developed a planning algorithm that recursively checks the decisions posted in the database, determines the need for auxiliary engineering activities, and adds them to the database as additional decisions. A user of the science planning system can therefore communicate more abstract goals to the system, leaving the determination of further details to the system.

We have been working in close collaboration with two science planning teams: the Extreme Ultraviolet Explorer (EUVE) science planning team at UC Berkeley and the Cassini Saturn rings science working group at Ames. Constraint models have been built for both missions. We have implemented a manual science planning procedure and a graphical user interface that allows easy browsing and inspection of the science plan while it is being developed. The capabilities of the system were demonstrated in the construction of a science plan for an entire revolution of the Cassini Saturn orbiter mission.

**Ames-Moffett contact: N. Muscettola
(415) 604-4744**

Headquarters program office: OSAT

DMS Advanced Monitoring and Diagnosis Application (DMS AMDA)

Ann Patterson-Hine, David Iverson

A prototype of a new application for the Space Station Freedom Data Management System (DMS) was delivered to the Control Center Complex (CCC) at Johnson Space Center in April 1994. The DMS Augmented Monitoring and Diagnosis Application (DMS AMDA) is intended to enhance baseline monitoring and diagnosing capabilities of the DMS console in the CCC. It will ease the console operator's task by managing and displaying information by means of a direct-manipulation graphical user interface. The central component of DMS AMDA is this "status at a glance" (SAAG) capability. The capability allows a console operator to quickly and easily determine whether all DMS components are operating correctly. If there are anomalies, the SAAG allows the operator to quickly determine which components need adjustment, and provides quick access to more information.

The DMS AMDA project demonstrates advanced automation capabilities for the CCC. DMS AMDA's operation is intended to integrate as seamlessly as possible into the baseline fault detection and management functions. In addition to traditional limit sensing and fault detection, DMS AMDA provides advanced diagnostic capabilities to CCC users. It is a proof-of-concept application for utilizing and augmenting traditional engineering strategies for online diagnostics, integrating conventional fault detection algorithms with automated diagnostic techniques.

**Ames-Moffett contact: A. Patterson-Hine
(415) 604-4178**

Headquarters program office: OSAT

Phased-Array Microphone for Noise Measurement in Wind Tunnels

Michael Watts, Paul Soderman

FAA restrictions on noise levels during takeoffs and landings at airports are becoming increasingly stringent and could preclude fully loaded operation of large aircraft. New airframes and engines under development by American industry are being designed for low noise production in order to be able to compete with quieter Airbus products. The Ames 40- by 80-Foot Subsonic Wind Tunnel is being acoustically lined in order to measure the noise produced by new aircraft. Utilization of this facility will require sensitive, directional acoustic sensors—sensors that are not currently available.

The background noise measured by a single microphone in the wind tunnel can be at the same level or even louder than that from the aeroacoustic sources that researchers currently want to measure. The figure shows an example in which the background sound pressure level is about the same as that from the aeroacoustic source. The acoustic level measured by a single microphone contains a small hump. Without more information, the small hump could be interpreted as part of the scatter in the spectrum or as the result of a low-level noise source. The lower line shows the same measurement made with a microphone array. The noise from the aeroacoustic source stands out well above the background level, and the level measured is more accurate.

Phased-array technology was developed in 1994 by a joint team formed by the Computational Sciences and Applied Aerodynamics Divisions at Ames. A 15-element microphone array was demonstrated in the 40- by 80-Foot Wind Tunnel during

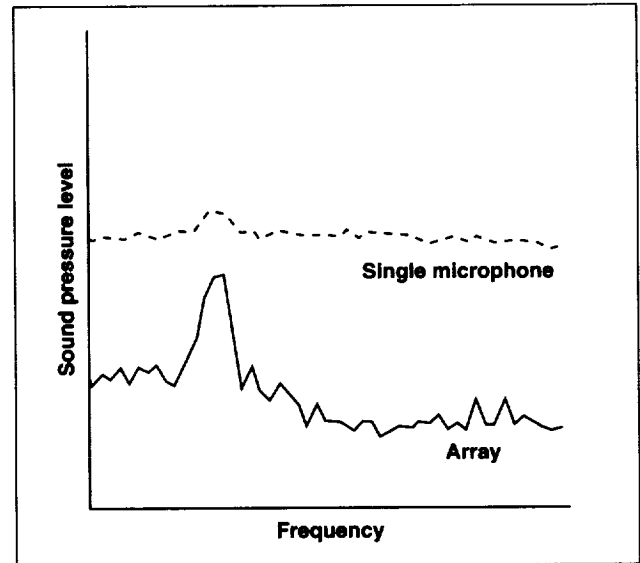


Fig. 1. Spectrum of aircraft model noise in the 40- by 80-Foot Wind Tunnel measured by a single microphone and by a 15-element microphone array.

tests of a NASA/Boeing/General Electric engine model and a NASA/Boeing high-speed civil transport aircraft model. This technique enables researchers to measure noise previously masked by the wind tunnel background noise and to accurately locate the noise sources on models.

**Ames-Moffett contact: M. Watts
(415) 604-6574**

Headquarters program office: OA

Solid State PhotoMultiplier (SSPM)

John H. Goebel

The Solid State PhotoMultiplier (SSPM) is an infrared detection technology capable of detecting individual infrared photons. It represents the ultimate in sensitivity available in the infrared wavelength range of 2 to 40 microns. In the low-flux limit, it increases the sensitivity of infrared detection by a factor approaching 1,000 compared with other currently available infrared detector technologies. Since the SSPM is produced by photolithographic manufacturing procedures, it has a very low cross section for cosmic ray impacts. The blocked impurity band structure it uses rejects signals produced by interactions with energetic particles.

Research has been conducted at Ames to evaluate the performance of the SSPM, which is manufactured by Rockwell, under a variety of operating conditions that could be expected in future space missions that utilize infrared detector technology. The purpose is to determine the suitability of this technology for implementation in instruments involved in the collection of astronomical data. Such

instruments include photometers, spectrometers, and imaging cameras. The laboratory measurements are conducted in a specially designed cold and dark environment into which controlled amounts of photons can be admitted from a calibrated blackbody radiation source.

The dominant influence on detector performance is operating temperature. This temperature strongly affects the dark count rate generated within the SSPM silicon chip, and the quantum efficiency of the detection mechanism. As the temperature falls below about 11 kelvin, the dark count rate drops exponentially, while the quantum efficiency declines slowly. We have found that typically there is an optimum temperature, around 6 kelvin, at which the quantum efficiency is high and the dark count rate is sufficiently low.

**Ames-Moffett contact: J. Goebel
(415) 604-3188**

Headquarters program office: OSAT

Multiline Si(Li) Gamma-Ray Spectrometer

G. Scott Hubbard, Robert E. McMurray, Jr., Robert G. Keller, Paul F. Wercinski

We have previously reported laboratory experimental data and Monte Carlo analysis results for a lithium-drifted silicon (Si(Li)) gamma-ray detector stack. This detector configuration has been developed primarily for space science applications (e.g., orbiting platforms and Mars surface operations). That work established that 662-kiloelectronvolt (keV) gamma rays (cesium-137) could be detected with good resolution (full width at half maximum (FWHM) ≤ 10 keV) at temperatures up to 230 kelvin, and that Compton-scattered background could be suppressed for a single photopeak in a 2-centimeter stack using a "split-stack" coincidence technique.

The current work addresses the multiline spectroscopic performance of an Si(Li) stack at elevated temperature. Barium-133 spectra from 300 keV to 450 keV (line spacing approximately 20–30 keV) and silver-110 peaks up to 1 mega-electronvolt (MeV) are obtained using a variety of techniques to enhance the peak-to-background ratio.

The first figure shows the multiline barium-133 resolution of the Si(Li) stack at 172 kelvin compared to the performance of a 10%-efficient high-purity germanium (HPGe) detector and a 1-inch sodium iodide (NaI) scintillator detector. As can be seen,

the Si(Li) stack clearly distinguishes the principal barium-133 photopeaks. FWHM resolution at 355 keV is 4.86 keV, only about a factor of two worse than HPGe, and an order of magnitude better than NaI. Peak symmetry is excellent with a FWHM to tenth maximum ratio of 1:1.87. The adjacent peak at 383 keV is a factor of about seven less intense yet is also clearly resolved, with good peak shape. It was found that at energies on the order of 300 keV, most of the full-energy photopeaks were collected in the thicker (2-centimeter) bottom pair. The split stack technique was found to be unnecessary for this energy range and thus it was not employed.

In order to evaluate the effectiveness of the split-stack technique in a multiline environment, we collected data using a silver-110 source. This isotope produces a series of lines from about 650 keV to greater than 1 MeV. In this energy range, Compton scattering is by far the dominant charge-production mechanism. The summed stack data yields almost no full-energy photopeaks. The higher-energy photons (approximately 1 MeV) produce sufficient Compton scattering to mask the principal photopeak at 657 keV, resulting in a spectrum that is dominated by the Compton edges, with little other structure.

The second figure shows that using the split-stack anticoincidence technique, the principal full-energy photopeaks are clearly resolved. FWHM resolution of the 657-keV peak is 10.1 keV at 186 kelvin, meeting the basic performance requirement of resolution of approximately 10 keV in the region of interest. In addition, the principal photopeaks at 885 keV and 937 keV are also clearly observed, with resolution (FWHM) of approximately 9 keV.

In summary, the Si(Li) stack exhibits the desired spectrometer performance over the temperature range of interest. For closely spaced barium-133 peaks at 355 and 383 keV, we have observed an FWHM of less than 6 keV for temperatures up to 200 kelvin and less than 10 keV for up to 230 kelvin. An optimized peak shape was obtained using longer shaping time as device temperature increased.

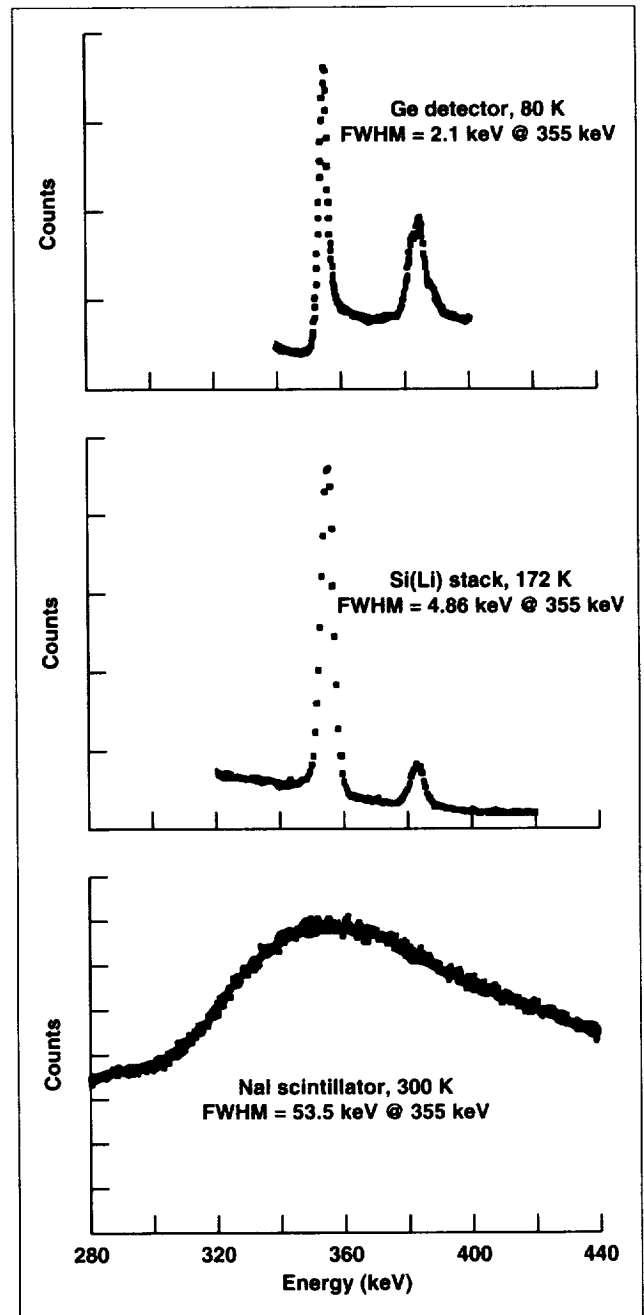


Fig. 1. Comparison of resolution of Si(Li) stack with that of HPGe and NaI detectors.

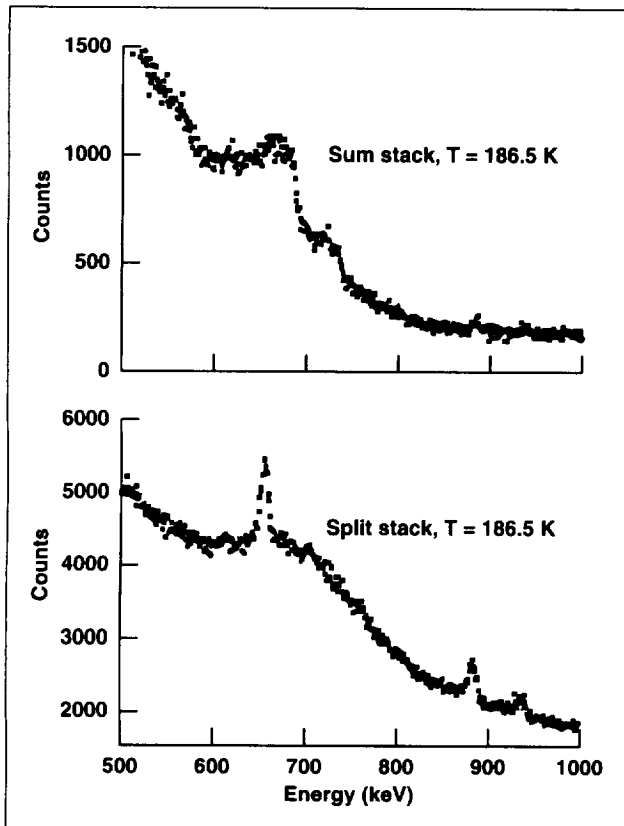


Fig. 2. Silver isotope (^{110m}Ag) spectra from the sum of the detectors and the split detector stack at 186.5 kelvin.

Further measurements using a silver-110 source have shown that the 2.7-centimeter Si(Li) stack can effectively resolve peaks up to 1 MeV in the presence of a significant Compton-scattered background. This is an important result, considering that to fully absorb 1-MeV photons requires on the order of 7 centimeters of silicon. This paper presents the first results that clearly show that the Si(Li) stack approach can be used in a realistic spectroscopic setting, where closely spaced peaks and/or peaks that exist in a significant background can be properly resolved at elevated temperature.

In conclusion, we believe that this Si(Li) gamma-ray detector stack represents a method for achieving good-resolution spectrometer performance across a wide range of temperatures and thus is a technique that should be seriously considered for a number of applications, especially resource-limited space missions.

Ames-Moffett contact: G. Hubbard
(415) 604-5697
Headquarters program office: OSS

2-Kelvin Magnetic Cooler

An adiabatic demagnetization refrigerator (ADR) operating between 2 and 10 kelvin has been developed and successfully tested (see figure). The ADR is capable of providing 30 milliwatts of cooling at 1.85 kelvin for 150 seconds. The cycle period is 750 seconds, with a peak magnetic field of 6.5 tesla. The experimental efficiency of the ADR relative to ideal (Carnot) efficiency is 25%.

The refrigerant for the ADR is gadolinium gallium garnet (GGG). Slices of single-crystal GGG are sandwiched together with strips of high-purity

copper. Indium foil is used at all the interfaces to improve the thermal conductance between the GGG and the copper. The sandwich is held under compression by Kevlar strands which are tensioned by a draw-bar mechanism. The copper strips are used to transfer heat between the GGG and the 2-kelvin and 10-kelvin heat switches. The heat switches employed in the ADR have no moving parts, which increases their reliability.

Ali Kashani, Ben Helvensteijn

Both heat switches are made of copper configured as two matching surfaces separated by a narrow gap. A switch is on when its gap is filled with helium and off when the gap is emptied. This filling and emptying is accomplished by an activated-carbon pump. The carbon adsorbs helium when cooled and desorbs it when heated. The 2-kelvin heat switch is a liquid-gap heat switch to reduce the required heat transfer surface area, taking advantage of the high thermal conductivity of superfluid helium. The 10-kelvin heat switch is a gas-gap heat switch since the thermal conductivity of gaseous helium is sufficiently high at 10 kelvin. The thermal conductance of the gas-gap heat switch in the on state is 8,000 times higher than its conductance in the off state. This switch turns on in 30 seconds and off in about 60 seconds. The on-state conductance of the liquid-gap heat switch is 6,900 times its conductance in the off state. This switch turns on in less than 1 minute; however, its turn-off time is more than 3 minutes.

The magnet used in the tests is a 10-henry superconducting magnet that is rated to 7 tesla at 4 kelvin. The field homogeneity is within 5% over the entire length of the copper/GGG sandwich.

The temperature gradients developed during the ADR cycle reduce the efficiency of the system. When 30 milliwatts is applied to the ADR, the temperature gradient across the 2-kelvin heat source and the GGG is 0.15 kelvin.

A computer model that simulates the ADR cycle has been developed. The model predicts a 31% efficiency for the ADR relative to Carnot (the standard reference). These developments are encouraging for ultimate application in zero-gravity space science missions which require 2-kelvin cooling.

Ames-Moffett contact: A. Kashani
(415) 604-6534
Headquarters program office: OSAT

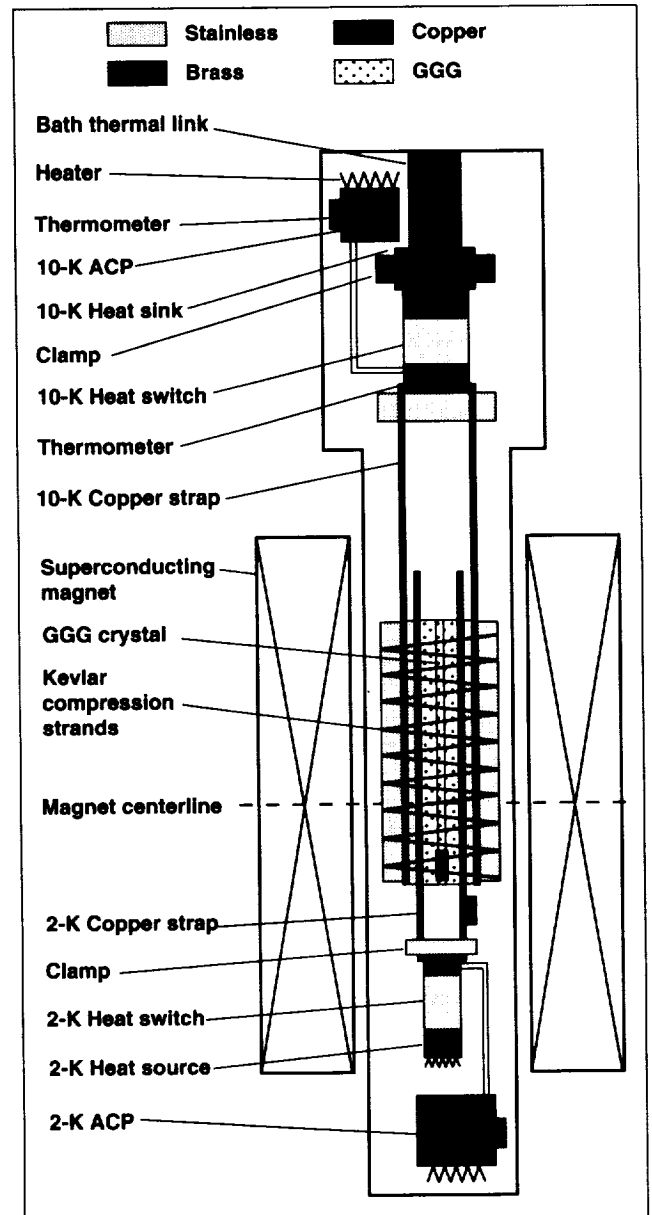


Fig. 1. Schematic of the adiabatic demagnetization refrigerator.

Steady mass flow circulation resulting from the steady Reynolds stresses is also calculated and compared to experimental results. The Reynolds stresses are shear-stress forces that are quadratic in time and are therefore nonvanishing when time averaged. These time-averaged forces result in steady mass circulation with a length scale on the order of the tube length. This is shown in the second figure.

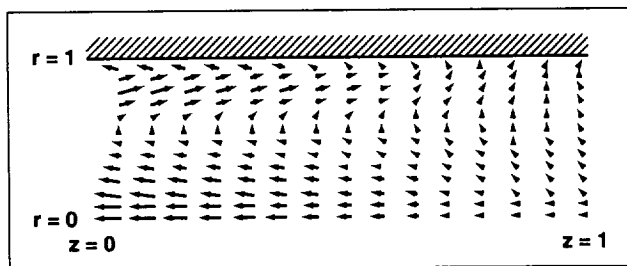


Fig. 2. Steady velocity field within the open tube of a pulse tube refrigerator.

Mass flow circulation is a loss mechanism because it allows a direct convection of enthalpy between the hot and cold ends of the tube. Steady mass circulation, which has been visually confirmed through smoke flow experiments, is predicted by the model in direction and magnitude.

The early success of the two-dimensional transport model is encouraging. Further modeling will include temperature gradients of order one and minimization of the loss mechanisms. The fundamental equations will also be applied to the regenerator and heat exchanger components, which will eventually lead to a complete design package for pulse tube refrigerators.

**Ames-Moffett contact: J. Lee/P. Kittel
(415) 604-5693
Headquarters program office: OSAT**

Detectors for IR Astronomy

Mark McKelvey, Robert E. McMurray, Jr., Craig R. McCreight

The development of focal-plane detector array technology that will allow reliable background-limited operation in the radiation environment found in Earth orbit is a key requirement for successful infrared (IR) astronomy from space-based platforms such as the Space Infrared Telescope Facility (SIRTF). A team at Ames Research Center is evaluating the performance of a number of detector and readout-device technologies to determine their suitability in space-infrared (IR) astronomy applications.

Impurity band conduction (IBC) focal plane detector arrays produced by several manufacturers are under evaluation for applications in the 5- to 30-micrometer wavelength range. IBC detectors rely on a thin, highly doped IR-active layer to provide

high quantum efficiency from a small detector volume, minimizing the ionization cross section for cosmic ray events. A high-purity blocking layer prevents the high doping levels in the IR-active layer from causing excessive dark current. IBC arrays also exhibit wider spectral response than alternative photoconductor (PC) architectures, without many of the anomalies associated with PC devices. IBC architectures are well suited to modern epitaxial fabrication methods, and the technology has progressed to the point where large-format hybrid focal plane arrays (FPAs) that are sensitive to IR wavelengths as long as 40 micrometers can be reliably produced.

Work in fiscal year 1994 was concentrated on a project aimed at the development of readout circuitry optimized for operation at cryogenic temperatures. Present metal-oxide semiconductor (MOS) transistors suffer degraded noise performance at temperatures below roughly 20 kelvin. A contract with Hughes Aircraft Company to develop devices that overcome the increased noise commonly seen at deep cryogenic temperatures has just been completed. The chief objective has been the manufacture of 1- by 32-element, 1.5-kelvin, multiplexed readout circuits and smaller test structures, optimized for use with long-wavelength IR detectors in the University of Arizona's Multiband Imaging Photometer for SIRTf (MIPS). Devices from a number of process splits were analyzed, with each representing a unique variant of the baseline design. Evaluations of the performance of devices from each split have been conducted at Ames and in the laboratory of Dr. Erick Young at the University of Arizona.

The performance of devices built under the Hughes contract represents a significant advance. Read noise levels as low as 25 electrons have been demonstrated on an input capacitance of 1 picofarad, with excellent stability. Testing at Ames included nondestructive-read sampling schemes, and derivation of mathematical expressions for the transfer function of various sampling algorithms.

This program has provided important technical evidence that present technology can be modified to produce readout devices whose sensitivity is limited by the fundamental physical constraint imposed by background flux, even in the difficult low-background regime of space-based astronomy.

Recent efforts have turned to measurements of optical crosstalk and persistent image problems in large-format IBC IR detector arrays. A spot-scanning optical system has been constructed and is being used to measure spatial resolution limits in observations of simulated point-source objects. Software development continues, with the aim of providing improved test flexibility, automation, and repeatability.

Further experimentation and optimization of both full-hybrid focal plane arrays and elemental electronic devices will continue in the next year, with emphasis on maturing IBC technology and improved readouts to enhance overall IR focal plane performance in NASA space-based and airborne astronomy applications.

**Ames-Moffett contact: M. McKelvey
(415) 604-3196**

Headquarters program office: OSAT

Boreal Ecosystem–Atmosphere Study (BOREAS) Aircraft Data Processing

Gary Angelici, Lidia Popovici, Steve Klooster

The Boreal Ecosystem–Atmosphere Study (BOREAS) is an international, interdisciplinary scientific study which has the goal of improving our understanding of the interactions between the boreal forest biome and the atmosphere in order to clarify their roles in global change. Hundreds of investigators and staff have been involved in deploying a wide range of sophisticated instruments and aircraft in the boreal forest of Canada during several 20-day periods in 1993 and 1994. Selected investigators in the Earth System Science Division are performing research with BOREAS. This effort involves the generation of several high-precision data products from the imagery returned by the MODIS Airborne Simulator (MAS) and NS001 sensors flying on NASA's C-130.

NS001 image data received from several aircraft overflights of BOREAS study areas will be screened for problems and logged. Navigational data will be used to geometrically correct the aircraft imagery, which is distorted by aircraft perturbations such as pitch and roll. The imagery will then be registered to a map base. Optical thickness data and atmospheric radiance models will be used to atmospherically correct visible and near-infrared channels of both NS001 and MAS data. In addition to image products, corrected reflectance and temperature statistics will be generated from these calculations. These numbers

will be loaded into the BOREAS Information System (BORIS) and applied by BOREAS scientists in ecosystem models and in various research investigations. After the project, the images and statistics will be published on CD-ROM for use by investigators and others for years to come.

In 1994, software to geometrically and atmospherically correct the data and create Earth Observing System (EOS) Level-2 data products was written and tested. Atmospheric models such as Modtran and 6S were applied to BOREAS radiosonde, sunphotometer, and other data to derive parameters necessary to atmospherically correct both visible and thermal channels of the sensors. The objective of this work is to create the first software system capable, in a single execution, of making large quantities of geometrically distorted and atmospherically uncorrected aircraft data useful not only for scientific studies such as BOREAS, but also for geographic information system applications which can utilize the remotely sensed information provided by aircraft sensors.

**Ames-Moffett contact: G. Angelici
(415) 604-5947**

Headquarters program office: OSS

Grapevine Remote-Sensing Analysis of Phylloxera Early Stress (GRAPES) Project

Cindy Bell, Kathleen Dammann, Liane Guild, Christine Hlavka, Lee Johnson, Brad Lobitz, Joan Salute

Ames investigators continue a collaboration with industry and university partners to develop and transfer the use of remote sensing and geographic information system (GIS) technology as a vineyard management tool. The technology is intended to provide timely information on the extent of phylloxera (root-louse) infestation in the Napa Valley, to assess factors affecting its spread, and to evaluate land use patterns over large regions. Research results, data, and analysis methods are being made available to interested grape growers, commercial remote-sensing product vendors, and the broader agricultural community.

Airborne remote-sensing systems were used to evaluate the phylloxera-related decline in Napa Valley vineyards during the 1994 growing season. Image data from two sensors, an electro-optic camera developed at Ames Research Center and the Digital Multi-Spectral Video (SpecTerra Systems Ltd.) were compared with data acquired over the same region in the 1993 growing season. All data were transformed to a normalized difference vegetation index ($[(\text{infrared} - \text{red})/(\text{infrared} + \text{red})]$), which is sensitive to vegetation vigor, and categorized into six levels of vigor. In 1993, 42% of the 11-acre intensive-study site was classified as highly vigorous. In 1994, this proportion had declined to 30%, with over 70% of the site declining by at least one level between years. The ability to make objective, quantitative determinations of this sort is an improvement over conventional vineyard management tools.

A GIS database is being developed to support assessment of factors affecting the spread of phylloxera decline in vineyards. The aircraft data were co-registered with the GIS to allow further evaluation in light of other factors known or suspected to be associated with phylloxera spread: rootstock, soil type, soil moisture, and vine spacing. The GIS is also being used to further our understanding of the introduction and spread of phylloxera in the Napa Valley. Vineyards first damaged by phylloxera in the late 1970s and early 1980s are being identified and

integrated into the GIS database, along with associated attribute information including vineyard owner and manager and related environmental data including soil type, hydrology, and transportation networks.

The Airborne Infrared Disaster Assessment System (AIRDAS) scanner, developed at Ames, was flown over most of the Napa Valley at the beginning and end of the 1994 growing season. Of primary interest was the AIRDAS thermal channel, which was used to measure the temperature of the grapevine canopy. Generally warmer temperatures were observed in areas of phylloxera infestation relative to uninfested areas. The warmer temperatures were primarily due to the greater amount of relatively warm exposed soil in the more sparsely covered infested areas. In addition, ground-based measurements showed both mildly and severely infested vines to be approximately 1°C warmer than uninfested vines, as a result of water stress and stomatal closure.

Satellite imagery is being used to develop a multiyear land cover classification for the Napa Valley and the neighboring Carneros region. A semi-automated image classification was performed on Landsat Thematic Mapper data (collected July 1993) to identify and develop acreage estimates for the following categories: low-leaf-area plant canopy, primarily vineyard (37% of image, or 28,000 acres); high-leaf-area canopy (again, primarily vineyard) (17%); urban (18%); trees/shrubs (5%); bare soil (15%); and "other" (8%). Similar classifications will be performed for the years 1983–1991 to track changes in vineyard acreage resulting from pressures of phylloxera infestation and urbanization.

Together with collaborators from the University of California, Davis, and California State University, Chico, research is being conducted at the leaf and vine level in support of the remote sensing and GIS efforts. Analysis of 1993 data showed that reflectance of leaves collected from mildly infested vines was significantly different from that of uninfested and

severely infested vines throughout the growing season. During 1994, the number of study plots was increased from 9 (in 1993) to 19, with each plot containing between 20 and 40 vines. Adding to a data base initiated in 1993, measurements were made of individual leaf reflectance and concentrations of chlorophyll, nitrogen, potassium, and

phosphorus. Potassium deficiency, which has been previously hypothesized to be a symptom of phylloxera-induced decline, has not been observed.

Ames-Moffett contact: L. Johnson
(415) 604-3331
Headquarters program office: OSAT

Satellite Sensing of Fires and Estimation of Resultant Emissions in Brazil

James A. Brass, Christine A. Hlavka, Robert B. Chatfield, Liane S. Guild, Susan Alexander

Biomass burning is a common human activity in much of the developing tropical world, where it has wide-ranging environmental impacts.

In Brazil, much of the burning occurs in the cerrado, or Brazilian savanna, which occupies approximately 1,800,000 square kilometers, primarily on the great plateau in Central Brazil. Wildland and agricultural fires are sources of regional air pollution in Central Brazil; they release trace gases, including greenhouse gases and other chemically active species. Knowledge of trace gas emissions from biomass burning in Brazil is limited by a number of factors, most notably the lack of relative emission factors for gases from specific fire types and fuels, and accurate estimates of temporal and spatial distribution and extent of fire activity.

The goal of this research is the estimation of fire extent and resultant seasonal fluxes of trace gases produced by biomass combustion in the Brazilian Cerrado. We are developing and testing methods for estimating the extent of area burned and resultant trace gas emissions using remote sensing and geographic information system (GIS) technology. Emissions by cerrado vegetation class are estimated by combining emission factors from combustion experiments in the cerrado (reported in the literature) with data on fuel characteristics and area burned. Particular trace gas species measured include carbon monoxide, methane, ethane, ethylene, acetylene, propane, propylene, aldehydes, acetone, benzene, methyl bromide, methyl chloride, other aromatics, nitrogen oxide, ammonia, and nitrate.

Fire behavior and emissions vary as functions of ecosystem and environmental characteristics. Therefore, it is necessary to stratify land areas into unique, functionally different ecological classes and specific vegetation classes having characteristic and predictable fire dynamics and trace gas emissions. To define cerrado classes by fuel characteristics, we used the digitized version of the 1988 Instituto Brasileiro de Geografia e Estatística (IBGE) vegetation map of Brazil. In addition to the IBGE map, a number of digital databases of vegetation, soil, terrain, land use, and climate were evaluated for use in characterizing the spatial distribution of the cerrado vegetation or fuel types. The collection of GIS layers for the project became known as the Fire Information System (FIS) and is currently being integrated into our collaborator's GIS at Instituto Brasileiro do Meio Ambiente e Dos Recursos Naturais Renováveis (IBAMA—Brazil's Natural Resource and Fire Research Agency).

We have been exploring detection of fire activity and scars with National Oceanic and Atmospheric Administration (NOAA) Advanced Very-High-Resolution Radiometer (AVHRR) and Landsat imagery. We acquired AVHRR data from daily passes of NOAA-11 over Brazil in September 1990 and Landsat Thematic Mapper quarter-scenes of two areas, Brasília and Emas National Park, for three dates in 1990 from Instituto Nacional de Pesquisas Espaciais (INPE—the Brazilian space agency). In addition, AVHRR data from overpasses of NOAA-11

in September 1992, and 1992 Landsat Multispectral Scanner (MSS) scenes of six areas, were acquired from Eros Data Center. Methods of detecting areas with fire fronts and of mapping large fire scars were tested. A preliminary estimate of fire scars and bare soils derived from 1990 AVHRR data was distributed to collaborators in Brazil.

We estimated trace gas emissions from fires in the Brazilian Cerrado during three weeks of September 1992 that incorporated vegetation information, pyrogenic emission factors calculated from ground and aircraft missions, and INPE fire

information derived from AVHRR data. The data analysis indicated that burns in the Cerrado totaled 27,054 square kilometers. Most of the burning occurred in natural areas of mixed shrubs and grasses or in areas used as pasture. Estimates for 17 types of gaseous emissions resulting from combustion of plant carbon and nitrogen were reported.

Ames-Moffett contact: J. Brass

(415) 604-5232

Headquarters program office: OMTPE

ER-2 Meteorological Measurement System

K. Roland Chan, T. Paul Bui, Stuart W. Bowen, Leonhard Pfister

The NASA ER-2 aircraft are used as a platform for high-altitude atmospheric missions. The ER-2 Meteorological Measurement System (MMS) was designed specifically for atmospheric research to provide accurate and fast-response measurements of pressure (± 0.3 millibar), temperature (± 0.3 kelvin), and the three-dimensional wind vector (± 1 meter per second). The objectives of the MMS are to provide atmospheric state variables to investigators on a timely basis, to study mesoscale and small-scale dynamical phenomena, and to conduct collaborative research in atmospheric chemistry and dynamics.

Operational since 1986, the MMS participated in the 1987 Stratospheric-Tropospheric Exchange Project (STEP), the 1987 Airborne Antarctic Ozone Experiment (AAOE), the 1989 Airborne Arctic Stratospheric Expedition (AASE), the 1991-1992 AASE-II, the 1992-1993 Stratospheric Photochemistry, Aerosols, and Dynamics Experiment (SPADE), and the 1994 combined mission of the Airborne Southern Hemispheric Ozone Experiment (ASHOE) and Measurements for Assessing the Effects of Stratospheric Aircraft (MAESA).

The MMS consists of three major systems:

(1) an air motion sensing system to measure the velocity of the air with respect to the aircraft, (2) a high-resolution inertial navigation system (INS) to measure the velocity of the aircraft with respect to the

Earth, and (3) a lightweight data acquisition system to sample, store, process, and compute the measured and meteorological parameters. The system sampling rate is 65 times per second, and the data output rate is 5 times per second. MMS calibration processes involve the determination of (1) the static accuracy of individual sensors, (2) transient responses of sensors and subsystems, (3) dynamic characteristics and accuracy of the INS, (4) parameter constants through the iteration process and inflight aircraft maneuvers, and (5) data quality by spectral analysis.

During 1992 and 1993, all major systems of the MMS instrumentation were modified: (1) the radome differential pressure system for airflow-angle measurement was redesigned and relocated in order to accommodate a new instrument in the ER-2 nose; (2) a new INS (a Litton LTN-92 with the capability of updating information from the Global Positioning System) was integrated into the MMS configuration in order to reduce science payload weight by more than 120 pounds; and (3) a new data acquisition system was developed in order to enhance the computational capability and reduce operational labor.

Ames-Moffett contact: K. Chan

(415) 604-6263

Headquarters program office: OSS

Simulating the Lower-Atmosphere Ozone Buildup

Robert B. Chatfield, John A. Vastano

Ozone (O_3) is a greenhouse gas, but it also destroys the tissues of wild and agricultural crops, even at the low concentrations found below the main ozone layer in the troposphere. We are attempting to explain the buildup of ozone and other trace constituents high above the central Atlantic Ocean, thousands of kilometers away from possible source areas over Africa and South America, which has been observed by surface, satellite, aircraft, and balloon-borne sensors. This requires, essentially, an accurate model of smog chemistry, but over vast intercontinental distances and to the top of the troposphere (15 kilometers). The smog model must describe in detail the origin, transport, and reactions of carbon monoxide (CO), the nitrogen oxides, and roughly a hundred other compounds. All of these compounds have an effect on the Earth's ozone oxidizing capacity, as they mix and react over large intercontinental regions.

A chemistry "event simulator," the Global Regional Atmospheric Event Simulator (GRACES), can be used with detailed actual observations of weather and chemical composition. This composition information can be inferred from aircraft-borne sensors and remote-sensing instruments in intensive observation campaigns. We also seek to understand whether the current laboratory knowledge of chemical processes is adequate to explain existing ozone levels. Use of event simulators is necessary to determine if global climate and chemistry models are adequate to predict the future, or if they show merely fortuitous general agreement with the state of today's atmosphere. Such fortuitous agreement can happen if several processes are misrepresented.

Our simulations show how the burning of tropical plant matter in Brazil and Africa is the main source of the ozone buildup. Burning for pastures and agriculture is the main source of the nitrogen oxides that spur ozone creation. The lifting of emissions from strongly heated tropical dry-region

boundary layers over the cooler marine and rain forest boundary layers provides an important insulation mechanism, isolating ozone and its precursors and helping to explain why the highest ozone level is found over the ocean. This mechanism is thought to work in cooperation with the deep-cloud venting mechanism that we have previously described. It provides quantitative estimates for the ratios of CO, nitrogen oxides, and ozone as they are modified by chemistry and absorption by the Earth's surfaces. The results have been compared to the aircraft measurements of West African biomass burning plumes made in the French-German TROPOZ campaign and NASA's CITE-3 (Chemical Instrumentation Test and Evaluation) campaign. Current work is extending this to NASA's TRACE-A (tropical atmospheric chemistry experiment-Atlantic) mission. The general comparison is good: we simulate plumes very like those observed. However, comparison of certain details strongly suggests that more field work to measure the biomass that is burned, and also more laboratory studies to explain the anomalous prevalence of active forms of nitrogen oxides (NO and NO_2 , rather than HNO_3) are necessary. The observations show more ozone far downstream than our models can predict on the basis of a tracer of burning like CO.

Data on emissions from biomass burning, properties of the land surface, and initial and boundary conditions are important to the working of the model. The assumed diurnal variation of fires has a strong effect on results. These are specified and controlled with a generalized, easily readable data-file/control-file program. Assumptions and changes are easily documented in place, and the history of model improvement can be tracked.

**Ames-Moffett contact: R. Chatfield
(415) 604-5490**

Headquarters program office: OMTPE

Spectral Reflectance and Leaf Chemistry

Jennifer Dungan, Lee Johnson, Vern Vanderbilt

New remote sensing instruments called imaging spectrometers allow the measurement of virtually continuous spectral information in the visible and infrared regions. Studies have suggested that it may be possible to monitor canopy biochemical contents using imaging spectrometers, but few experiments have been accomplished under controlled conditions. If such monitoring were possible, the status of forests in many parts of the world could be determined, adding to the scientific community's understanding of forest ecosystem processes.

An experiment was designed to test the possibility that these high-spectral-resolution spectroradiometers can provide information about the biochemical make-up of vegetation. Small Douglas fir seedlings were fed three different fertilization solutions (high, medium, and low concentrations) to alter the biochemistry of their needles. Typically, tree foliage will respond to such fertilization treatments with different chlorophyll, nitrogen, and amino acid concentrations. Since these chemicals absorb light at specific wavelengths, the absorption features may allow the chemicals to be quantified.

The fir foliage was measured at two different scales. First, canopies composed of seedlings for each treatment were measured by two field spectroradiometers in natural sunlight. Then needle samples were measured in the laboratory by a bench spectrometer. Approximately 1,000 spectra were collected with the field instruments and 180 spectra with the lab instrument. The measurements from this experiment were analyzed in 1994.

Needle and canopy reflectances showed large differences among fertilization treatments in the visible region, most likely caused by the large

variation in chlorophyll achieved by the treatments. In the infrared, the canopy spectra showed large magnitude differences that were not seen in the needle spectra. The needle spectra showed more subtle effects in narrow wavebands, many of which coincided with known protein absorption features. Despite the strong similarity of needle and canopy bidirectional reflectances, the narrow-band features present in the needle infrared spectra appear to be absent in the canopy data. The absence of these features is most likely due to the low signal-to-noise characteristics of the field spectroradiometer relative to the laboratory instrument, since canopy geometry effects were averaged out in the experimental design.

The data set is one of the few available in which needle and canopy reflectance measurements were acquired from the same trees. These data, and the accompanying data on chlorophyll and nitrogen concentrations, tree shape, and structural variables, have the potential to be used to parameterize current canopy reflectance models that use leaf optical properties as a basis. The data were made available to the research community over the Internet.

This work was part of a team effort by a group of researchers funded by NASA under the Accelerated Canopy Chemistry Program. The team had their final meeting in August and made a summary report of their findings available to a committee charged with deciding future instruments for NASA's Earth Observing System.

**Ames-Moffett contact: J. Dungan
(415) 604-3618**

Headquarters program office: OSS

Human-Induced Land Transformations

Leonard Gaydos, William Acevedo, Cindy Bell

As populations increase worldwide, humans are transforming landscapes—with important consequences. Some of the most profound, yet little studied, changes are occurring near the world's great cities. With support from the U.S. Geological Survey, Ames scientists are documenting past land use changes, building models of the urbanization process, and making data, visualizations, and maps available to other scientists, policymakers, and the public for a variety of applications.

The goal of the Human-Induced Land Transformations project is to map patterns and rates of major land use changes at the regional scale for the last 200 years, and to make projections for the next 200 years. The San Francisco Bay Area has served as an initial study site.

Using historic topographic maps, land use maps, and Landsat data, a geodynamic-mapping data base is being completed to document land use change in the San Francisco Bay Area since the Gold Rush.

Seven historic eras have been mapped, and the maps have been used to construct an animation that shows the extent and pace of urbanization in the region. Starting with initial settlement of the core cities of San Francisco, Sacramento, Oakland, and San Jose, the animation shows how the area grew slowly in the early years and then explosively after World War II (see figure). We are currently refining the data for publication on CD-ROM, adding information on transportation development.

A computer model of urbanization, developed by collaborators at Hunter College in New York City, is being calibrated with the historical data. This computer model employs cellular models to determine whether grid cells become urbanized in each iteration, according to a set of parameters related to existing state and neighborhood properties. Once calibrated, the model will be used to predict several scenarios of future growth.

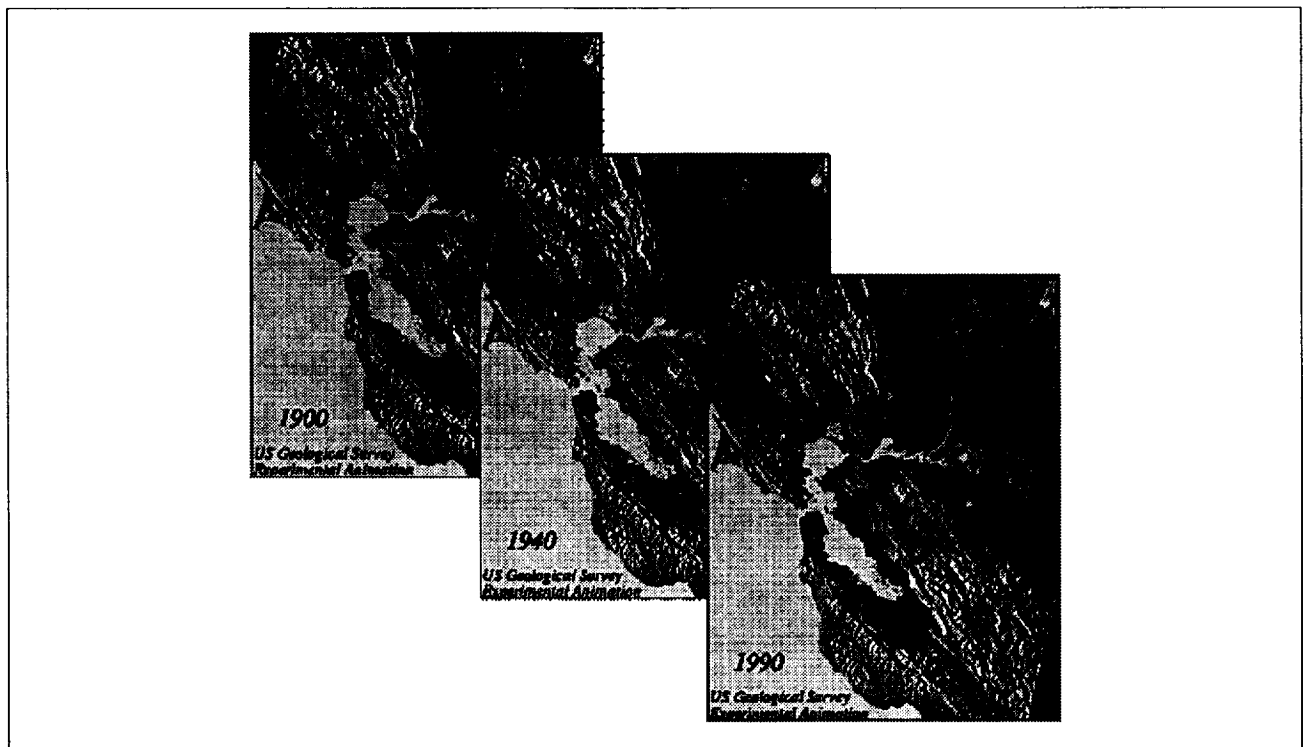


Fig. 1. Change in urban land use (black patches on the maps) in the San Francisco Bay Area.

Several applications of the work are being pursued. U.S. Geological Survey hydrologists have seen correlations between urbanization trends and increased heavy metal concentrations in San Francisco Bay. U.S. Forest Service scientists are interested in the impact of further urbanization on forest land in the Sierra Nevada. Urban planners

and conservationists have used the data to focus attention on alternatives to urban sprawl.

Ames-Moffett contact: L. Gaydos

(415) 604-6368

Headquarters program office: (USGS)

Terrestrial Remote Sensing Using Imaging Interferometry

Philip D. Hammer, David L. Peterson, William H. Smith

Scientific observations that provide simultaneous spatial (image) and spectral (wavelength dependence) information are a powerful means for studying the Earth's environment. Remote sensing of the Earth's radiative fields at visible and infrared wavelengths is an important way to explore the structure and processes of the surface and the atmosphere. Understanding complex and variable environmental phenomena such as light interaction within plant canopies or through clouds in the atmosphere requires spatial, spectral, and temporal observations that are both extensive and detailed. Thus there is considerable motivation for designing simple, versatile, and cost effective imaging spectrometers for Earth remote sensing applications.

We have been developing a new technique to make remote measurements. The instrumental concept is called Digital Array Scanned Interferometry (DASI). Recent advances in imaging technology have made it possible to use this new approach for a variety of scientific studies. DASI instruments have advantages over grating- or prism-based instruments with regard to compactness, device simplicity, and performance. DASI instruments have many of the positive characteristics associated with Fourier transform spectrometers (which have been used for several decades for making nonimaging spectral observations), with the additional capability of spatial imaging.

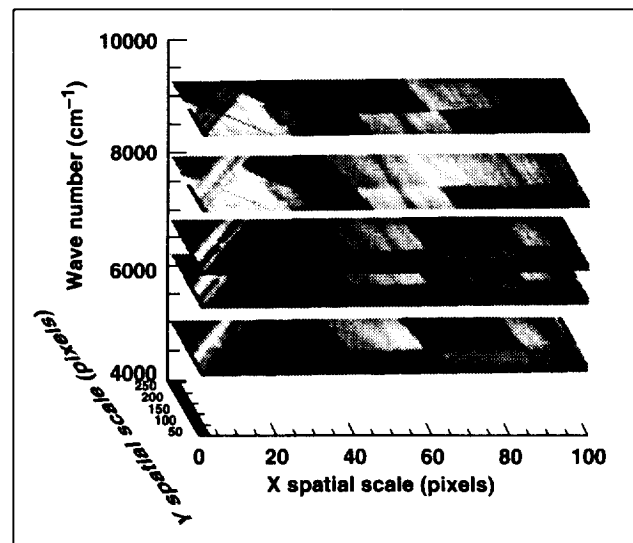


Fig. 1. Spectral image of the San Joaquin Valley from DASI/C-130 measurement, March 1994. This aircraft-based observation was made using a DASI instrument equipped with a short-wavelength infrared detector array. The image is shown at five selected wave-number values. The diagonal strips at the left are part of a runway. A variety of agricultural fields constitutes most of the other features. Spatial resolution was 31 meters long track (x axis) and 2.4 meters cross track (y axis). The scene dimensions are 3.1 kilometers long track and 0.61 kilometers cross track. Spectral resolution was 266 inverse centimeters, corresponding to 17 effective bands within the spectral range of sensitivity.

This year, we have published an analysis of cloud measurements made from the ground using DASI. These measurements were compared with model results to obtain information about the properties of the clouds. In addition, we have made first-time airborne observations of the Earth's surface using a downward-looking DASI instrument on the

NASA C-130 aircraft. The figure shows a selected spectral image derived from these observations.

**Ames-Moffett contact: P. Hammer
(415) 604-3383**

Headquarters program office: OMTPE

Stratospheric Dehydration by Thin Cirrus Clouds

Eric J. Jensen, Owen B. Toon, Leonhard Pfister, Henry B. Selkirk

The extreme dryness of the stratosphere is believed to be caused by freeze-drying of the air as it enters the stratosphere through the cold tropical tropopause. As part of the Stratosphere-Troposphere Exchange Project, aircraft campaigns were undertaken in the tropics to evaluate the roles of mixing and precipitation in the anvils of deep convective systems. However, ice crystals formed near the tropopause may also play an important role in the stratospheric water budget. Recent observations have shown the presence of a persistent thin cirrus cloud layer near the tropical tropopause that is apparently not associated with deep convective systems. Satellite, lidar, and aircraft measurements show that this cloud layer occurs primarily over the tropical western Pacific. The cirrus layer appears to be present as much as 80 percent of the time in this region.

Sedimentation of ice crystals in the thin cirrus layer may provide a significant downward flux of water vapor. It has also been suggested recently that gravity waves generated by convection may drive the formation of ice clouds in the lower stratosphere and that precipitation of crystals in these clouds may serve as a stratospheric dehydration mechanism. We have used a detailed ice cloud process model to evaluate the potential dehydration of the tropical tropopause region by in situ formation and precipitation of ice crystals. We simulate the life cycle of a thin cirrus cloud formed in the cold trough of a wave near the tropopause. Time scales corresponding to

both short-period gravity waves (1–2 hours) and long-period synoptic-scale motions (12–24 hours) are assumed in the simulations.

Calculations of ice nucleation by spontaneous freezing of sulfuric acid aerosol suggest that large numbers of ice crystals will probably form, especially in gravity waves with short time scales and rapid cooling. As a result, the crystals will not grow larger than about 10 micrometers, and crystal fall speeds will be less than about a few centimeters per second. Simulations using the detailed cloud model suggest that ice clouds formed in typical gravity waves (wave periods of 1–2 hours) result in little or no precipitation or water vapor depletion. However, ice clouds formed by large-scale vertical motions (with periods of a day or more) should have fewer crystals and more time for crystal sedimentation to occur, resulting in water vapor depletions of as much as 1 part per million just below the tropopause.

The results for a thin tropopause cirrus cloud simulation under ideal conditions for dehydration are shown in the figure. The cloud formation in this simulation was driven by a 24-hour oscillation in the vertical wind speed with an amplitude of 1 centimeter per second in the region near 17 kilometers. We limited the number of ice nuclei available such that very few ice crystals were formed. The upward motion near 17 kilometers drives cooling, supersaturation, and ice crystal formation. The crystals grow

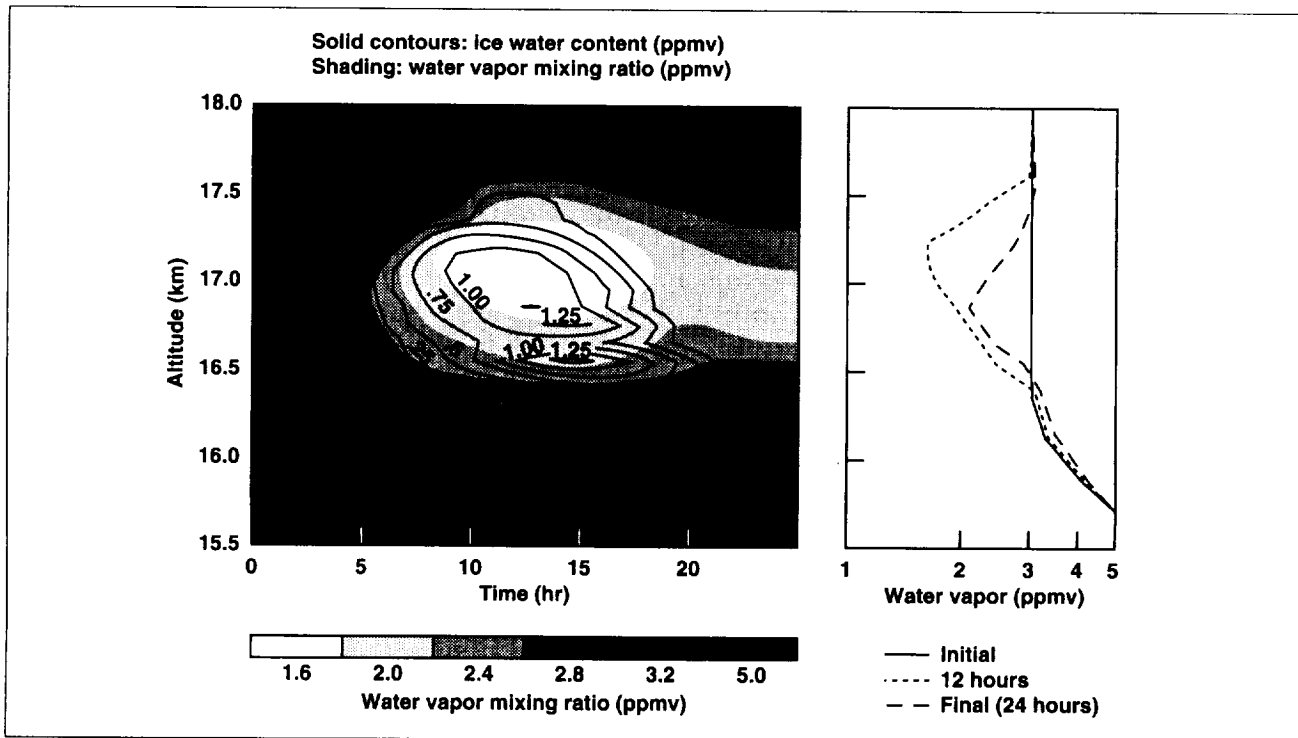


Fig. 1. Ice water content and water vapor mixing ratio versus time and altitude for a simulation of thin cirrus formation at the tropical tropopause. The water vapor altitude profiles (right panel) show the depletion of water vapor in the 16.5- to 17.5-km region as a result of growth and sedimentation of ice crystals.

rapidly and fall out of the region near the tropopause. The water vapor is effectively removed from the region and carried down to lower altitudes. The downward motion during the last 12 hours of the simulation drives heating and sublimation of the crystals. At the end of the 24-hour period, the water vapor mixing ratio near 17 kilometers has been reduced by 0.92 parts per million.

Our calculations suggest that dehydration by thin cirrus clouds formed in the lower stratosphere will only be effective if the motions driving the cloud formation are relatively slow and only if very few ice nuclei are available. We have also shown that

formation of widespread thin cirri in slowly lifting air over the western Pacific may limit the flux of water vapor into the stratosphere and limit the water vapor mixing ratio at the tropopause. These results suggest that the thin tropopause cirrus clouds may play an important role in maintaining the low water vapor mixing ratios in the tropical lower stratosphere.

**Ames-Moffett contact: E. Jensen
(415) 604-4392**

Headquarters program office: OMTPE

ERS-1 SAR Investigations of High-Latitude Wetlands

Leslie A. Morrissey, Gerald P. Livingston

The predominance of methane-producing wetlands in the tundra and taiga (boreal forest) makes these ecosystems important contributors to the global methane budget. European Remote Sensing (ERS-1) satellite synthetic aperture radar (SAR), launched in July 1991, provides the first spaceborne SAR system for multiyear, multitemporal assessment of high-latitude ecosystems. Analysis of ERS-1 C-band SAR data is under way to determine the type and extent of wetlands (methane source areas), the extent and timing of inundation (anaerobic substrates are required for methane production), and vegetation community type and amount (vegetation is the methane transport pathway). This research is being conducted in collaboration with the Jet Propulsion Laboratory and the NASA Ames Research Center methane project, with funding from NASA's Ecological Processes and Modeling Program.

Project activities have focused on the acquisition and analysis of ERS-1 SAR data from Barrow, Prudhoe Bay, and Minto, Alaska, during the annual cycles of 1991 through 1993. Results from ERS-1 data collected over northern Alaska have shown that methane emissions are positively related to the position of the local water table relative to the ground surface and

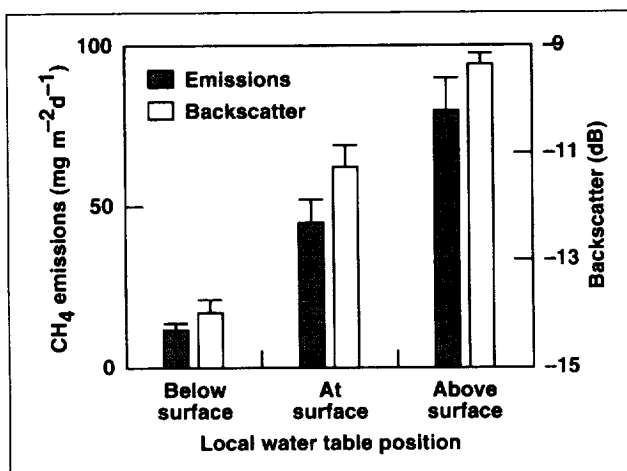


Fig. 1. Methane emissions and ERS-1 SAR backscatter related to the position of the local water table for herbaceous tundra sites (mean \pm standard error).

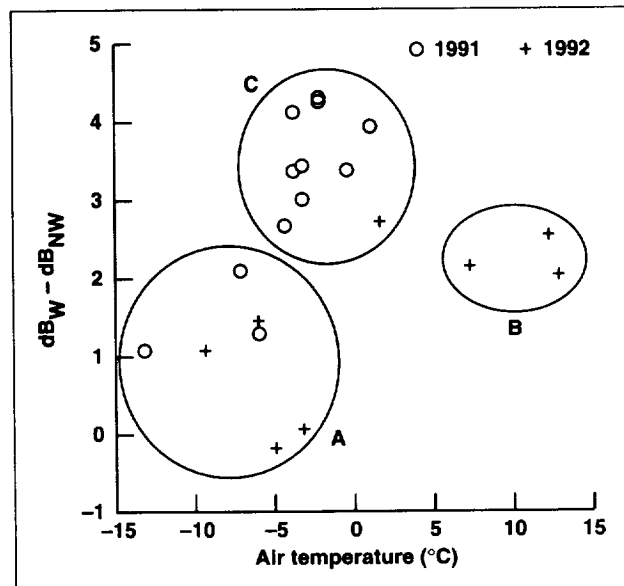


Fig. 2. Differentiation of backscatter between wetlands (dB_W) and nonwetlands (dB_{NW}) in relation to air temperature at the time of the SAR data acquisition.

radar backscatter. As shown in the first figure, rates of methane emissions from the Arctic tundra are highest for inundated sites, decreasing dramatically for comparable sites where the water table is either at the surface or 5 centimeters or more below the surface. Similarly, ERS-1 SAR backscatter is directly related to the position of the local water table; the strongest return is from herbaceous sites with standing water.

Differentiation of methane source areas (wetlands) and sink areas (nonwetlands) with ERS-1 SAR data was highly dependent on hydrology and air temperature at the time of data acquisition. Differential freezing of surface materials on daily to seasonal time scales greatly enhanced the separability of sources and sinks with SAR data as a result of changes in the dielectric constant (a key determinant of radar backscatter) of plant and surface materials with phase change during freezing. As shown in the second figure, the separability between sources and sinks is greatest when the air temperature during satellite acquisition is near freezing

(group C). The lowest differentiation between the two classes occurs in the winter, when there is extended freezing (group A). Intermediate separability is observed when air temperatures are above freezing. Optimal selection of SAR data to differentiate sources and sinks is best when the data is collected during a

nighttime overpass, when air temperatures are likely to be near freezing.

Ames-Moffett contact: L. Morrissey

(415) 604-3617

Headquarters program office: OMTPE

NASA Science User Networks Working Group

Leslie A. Morrissey

The NASA Science User Networks (NSUN) at Ames Research Center, as part of the Earth Observing System Data and Information System (EOSDIS), was initiated in 1993 to facilitate scientific research requiring high data rate transfer and computationally intensive modeling efforts. Initial activities of the

NSUN working group (NSUNWG) include video conferencing, international connectivity, and end-to-end high data rate transfer. It was established to ensure that science user requirements are the primary basis for the design, development, and operation of

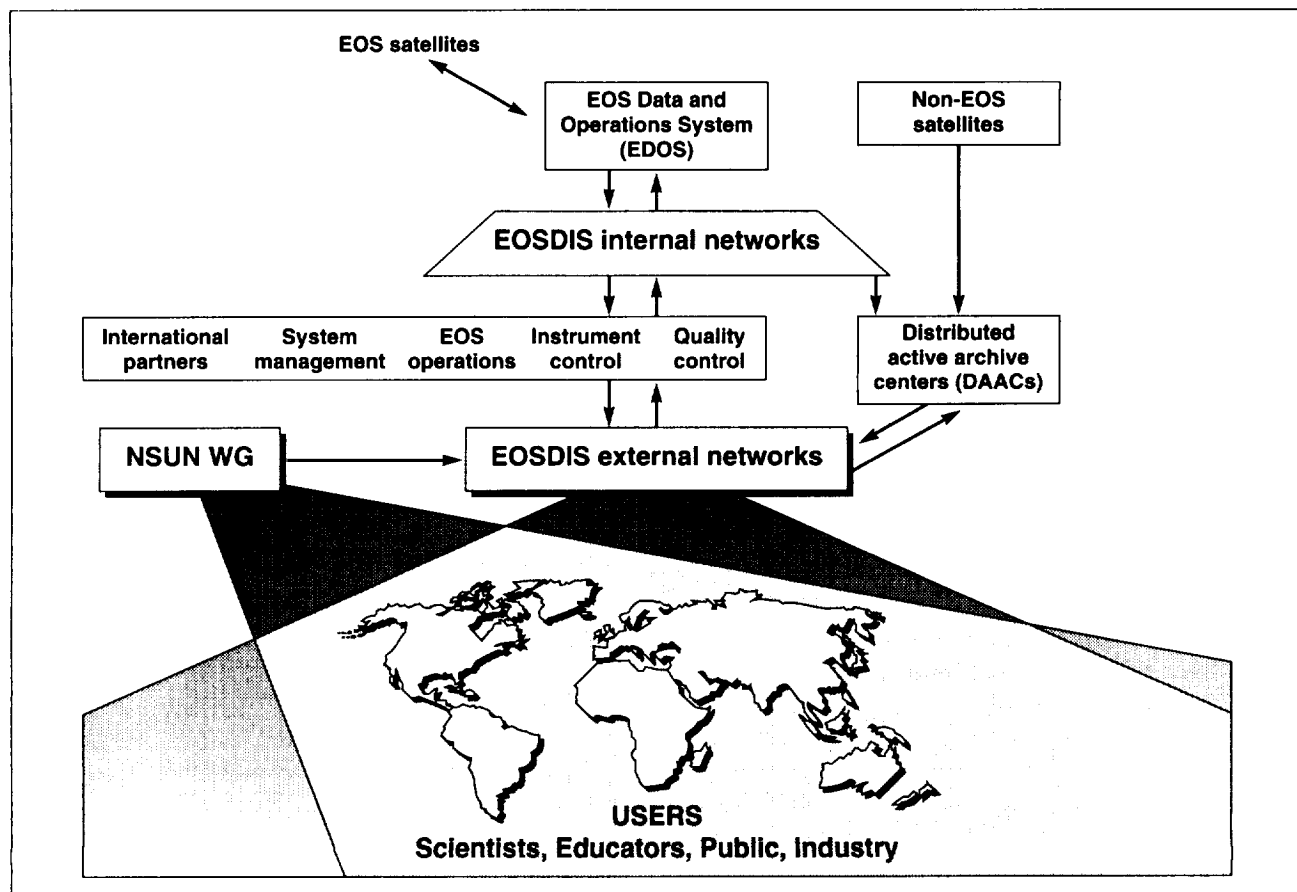


Fig. 1. As representatives of the EOS scientific community, NSUNWG members oversee activities of the external networks, the "front door" for EOSDIS.

EOSDIS external networks. As the "front door" to EOSDIS, the external networks provide the key interface between the scientific community of EOS users and EOSDIS (see figure). If the external networks fail, EOSDIS fails. The NSUNWG oversees activities on the external networks (see figure) so that

EOSDIS is accessible to all users with the launch of EOS in 1998.

**Ames-Moffett contact: L. Morrissey
(415) 604-3617**

Headquarters program office: OMTPE

Polar Stratospheric Cloud Detection Using Advanced Very-High-Resolution Radiometer Satellite Imagery

Kathy L. Pagan, R. Stephen Hipskind, Steven E. Gaines

Polar stratospheric clouds (PSCs) are a crucial component in the ozone depletion process over the polar regions. PSCs occur during the polar winter when temperatures in the stratosphere fall to levels low enough to saturate the air with nitric acid and/or water. The timing of onset and duration of PSCs, as well as their geographic extent, are not well understood. To date, no extensive or detailed climatology of PSCs has been assembled.

Our goal is to assemble a climatology of PSC events over Antarctica using Advanced Very-High-Resolution Radiometer (AVHRR) satellite data. The AVHRR sensors aboard the National Oceanic and Atmospheric Administration (NOAA) polar-orbiting satellites have been collecting data over the polar regions since 1979. These satellites provide excellent spatial and temporal coverage of the polar regions, allowing the construction of a long-term climatology if a reliable means of PSC detection could be developed.

Two problems exist which make the use of AVHRR data for PSC detection difficult. First, PSCs occur during the polar winter and early spring when little or no sunlight is present, thus rendering the AVHRR visible channels useless. Second, many PSCs are optically thin and appear against a cold background. Therefore, in thermal imagery there is often little contrast between the clouds and the cold Antarctic surface. However, recent research has shown that the use of multispectral data (for example, from AVHRR channels 3 and 5) and various pattern-recognition algorithms based on both spectral and textural features can be used to identify a variety of clouds over ice and snow surfaces.

Fundamental to the establishment of a long-term climatology is the development of automated methods for detecting and monitoring PSCs. We are currently working on a rule-based classification method for PSC detection. The first stage of this rule-based method involves image segmentation, in which various geographic regions that differ by surface temperature and composition are studied separately. We began with an investigation of the Weddell Sea region, where the thermal contrast between PSCs and the surface is the greatest and the detection of optically thick PSCs the easiest. We have processed AVHRR channel 5 data from the McMurdo and Palmer stations in Antarctica for the 1992 winter and spring, and are compiling a time series of optically thick PSC events that occurred over the Weddell Sea during that period. These PSC events are being verified with stratospheric temperature and aerosol extinction coefficient data from the cryogenic limb array etalon spectrometer (CLAES) aboard the Upper Atmosphere Research Satellite, along with other ancillary data sets.

In order to automate the detection of these optically thick PSCs, we have developed various thresholding algorithms to identify clouds in the PSC temperature range. Our next step is to develop algorithms that can detect optically thin PSCs over the Weddell Sea. We have tried various multispectral techniques for the detection of these PSCs (for example, the use of AVHRR channel 3 and 5 data, and channel 4 and 5 data), along with several textural filters. These methods have proved promising, and we will continue to develop other algorithms

based on these techniques. Our final step will be to develop algorithms to detect both optically thick and optically thin PSCs that occur over other regions of Antarctica, such as the cold interior where little thermal contrast between clouds and surface exists.

Once we have developed algorithms for PSC detection based on the 1992 data and verified with various ancillary data sets such as CLAES, we will combine these algorithms into a rule-based classification system that can be used on the entire record of AVHRR data in order to assemble a long-term climatology of PSC events over Antarctica. Such a PSC climatology will be extremely useful to a variety of researchers in the study of ozone depletion and the formation of the ozone "hole" over Antarctica.

We are also investigating an alternate method of automated PSC detection using a neural network trained with a back-propagation learning algorithm. Various studies have shown that by combining two or more artificial intelligence (AI) strategies for image classification (such as rule-based classification systems and neural networks), the overall classification error can be reduced. By combining the information from both AI systems, we hope to improve the accuracy of our PSC climatology.

Project participants include Patricia G. Foschi and Oswaldo Garcia at San Francisco State University.

Ames-Moffett contact: K. Pagan
(415) 604-0713
Headquarters program office: OSS

Ozone Power Spectra and Deposition

Richard Pearson, Jr.

Fast-response ozone (O_3) measurements have been used to obtain experimental measurements of O_3 deposition which the State of California Air Resources Board has incorporated into a regional air-quality regulatory model. A special-purpose instrument was designed and built for this work. It measures changes in ozone mixing ratio (or concentration) with a bandwidth of 20 Hz, and has a sensitivity exceeding 0.1 part per billion by volume. The same set of data has enabled us to obtain what may be the first measurements of the power spectra of O_3 in the surface layer of the atmosphere. Tropospheric O_3 , unlike its counterpart in the stratosphere, is largely the byproduct of photochemical oxidation of hydrocarbons in the presence of oxides of nitrogen, which serve as catalysts. This is particularly true during periods of air stagnation which result in so called pollution episodes. A major removal mechanism, or sink, for O_3 is dry deposition. Dry deposition occurs when O_3 reaches a reactive surface and is removed permanently from the atmosphere.

Accurate measurements of O_3 deposition are difficult to make. Until this work, the only models

available to regulators with actual deposition measurements were based either on data from the eastern U.S., which has very different surface characteristics and meteorology from the western and mountain states, or a totally unrealistic model of the atmosphere without time dependence.

The figure shows some of the unique characteristics of the O_3 measurements obtained in this work. Frequency-weighted power spectra are shown for temperature, humidity, and O_3 as functions of frequency, n . The data were obtained near noon at a height of 5 meters above a field of actively growing cotton. The measurements have been normalized by micrometeorological surface-layer scaling, and are dimensionless. Throughout most of the range of frequencies the three spectra are very similar. The increase in O_3 values at the right side of the graph is due to noise intrinsic to the measurement process. Steven Oncley and Anthony Delany of the National Center for Atmospheric Science provided the meteorological data used in this study.

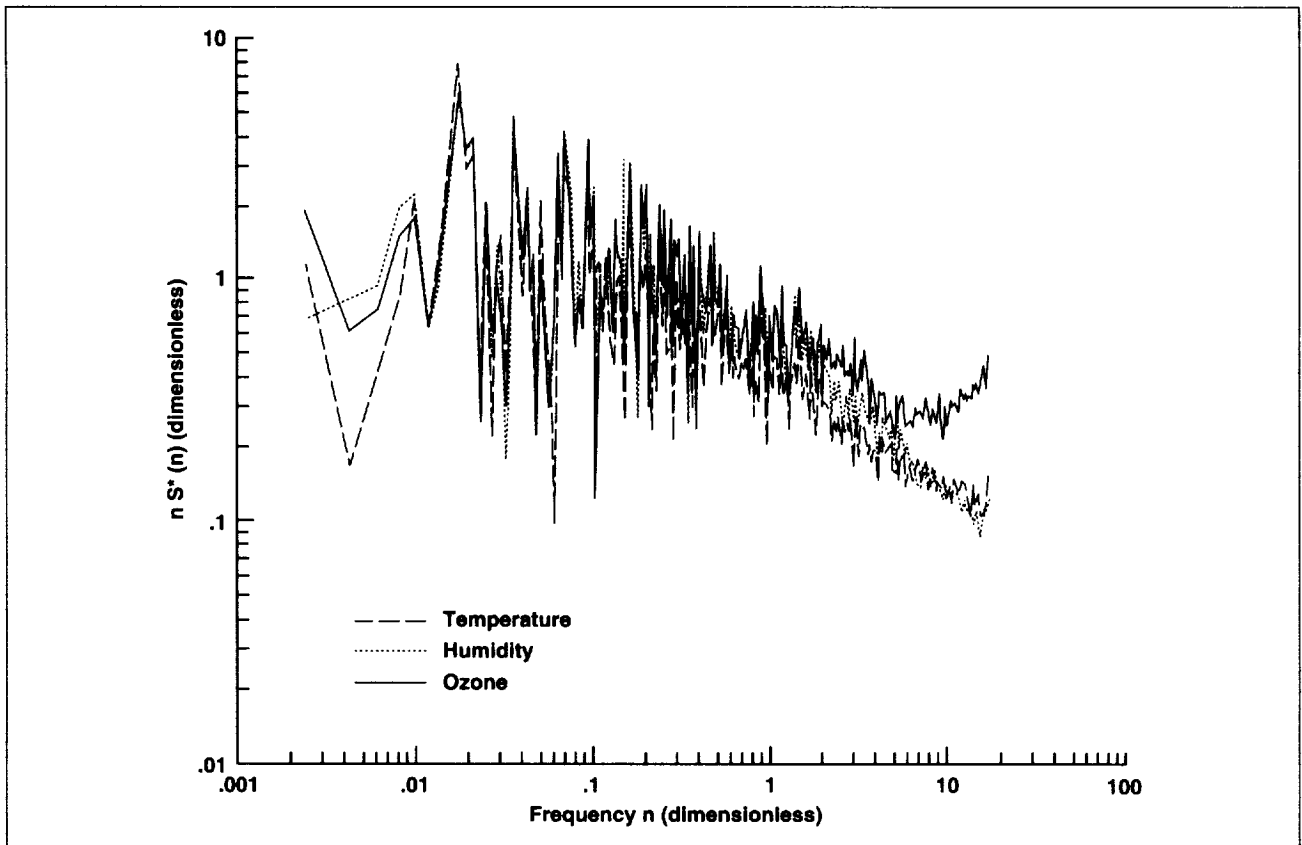


Fig. 1. Frequency-weighted power spectra (S) for temperature, humidity, and ozone.

Studies of spectra such as these may yield information on the similarities and differences of these properties of the atmosphere which have implications for the sampling requirements needed to make valid air quality measurements. The instrument used to measure O_3 has potential new applications in harsh environments such as solid rocket motor exhaust plumes in the stratosphere, where other kinds

of instruments are strongly affected by interference from the chemicals or particles present.

**Ames-Moffett contact: R. Pearson
(415) 604-4388**

Headquarters program office: OMTPE

Analysis of Stratosphere–Troposphere Exchange

Leonhard Pfister, Henry B. Selkirk

Our task is to develop an understanding of mesoscale transport processes in the lower stratosphere and at the tropopause. Among the specific scientific problems of interest are (1) gravity and inertia-gravity waves excited by convection, (2) inertia-gravity waves in midlatitude jets, (3) turbulent and convective transport mechanisms near the tropical tropopause, (4) the stratospheric water budget as affected by the cold tropical tropopause, (5) radiative and microphysical processes near the tropical tropopause, (6) small and mesoscale motions in the arctic and antarctic polar vortex, and (7) horizontal transport mechanisms within the lower stratosphere and between stratosphere and troposphere. The approach combines the analysis of aircraft measurements from several major field projects (the Stratosphere–Troposphere Exchange Project (STEP); the first and second Airborne Arctic Stratosphere Expeditions (AASE 1 and 2); the Stratospheric Photochemistry, Aerosols, and Dynamics Experiment (SPADE); and the Airborne Southern Hemisphere Ozone Experiment/Measurements for the Assessment of the Effects of Stratospheric Aircraft (ASHOE/MAESA)), mechanistic modeling using linear gravity wave models, and air parcel trajectory calculations.

Among the results of this work are (1) the first estimates of the net irreversible effect of convectively generated gravity waves on the tropical upper

stratosphere; (2) evaluation of upward fluxes of horizontal momentum due to gravity waves in the midlatitude and arctic stratosphere; (3) extensive measurements of turbulence in the tropical, midlatitude, and arctic stratosphere; (4) estimation of the stratospheric dehydration potential of the Australian monsoon circulation; and (5) demonstration that a leaky barrier to horizontal lower-stratospheric transport exists in the subtropics, and that this barrier is related to structures in the local wind field. Future problems of interest include (1) examination of midlatitude convection in the southern hemisphere as a source for stratospheric gravity waves; (2) establishing the mechanisms for generating observed turbulence in the tropical, midlatitude, and polar stratosphere; (3) evaluating the contributions of convectively generated gravity waves to the momentum budget of the tropical stratosphere; (4) evaluating the annual cycle of water injection into the tropical stratosphere; and (5) assessing the ability of global models to represent stratosphere–troposphere exchange by comparing the results of model-based trajectory analyses with aircraft measurements.

**Ames-Moffett contact: L. Pfister
(415) 604-3183**

Headquarters program office: OMTPE

Satellite Weather Data for Stratospheric Science

Leonhard Pfister, Henry B. Selkirk, Steven Hipskind, Steven Gaines

The purpose of this project is to provide real-time satellite weather data for use in aircraft field missions for NASA's Upper Atmosphere Research and Atmospheric Effects of Aircraft programs. The data is then archived for use in scientific analysis of aircraft data, such as evaluations of (1) cloud reflectivities, to examine their effect on stratospheric photochemistry; (2) the relationship between convective activity and gravity waves/turbulence observed by overflying aircraft; and (3) the relationship between tropopause height and structures in the 6-micron "water vapor channel" imagery. Geostationary satellite imagery from GMS-4 (western Pacific) and GOES-7 (western U.S.) are supplied by other researchers through the Internet as well as by the Ames satellite ground station and are composited to provide a mercator (or other projection) image over more than half the globe (see figure). This data is routinely available within about an hour of capture by satellite. It is assembled into animation loops covering any area of interest, providing guidance for flight planning. Future plans include (1) including GOES-8 imagery, thereby extending the longitude range of coverage to 80 degrees east through 10 degrees west, and (2) developing an ability to seamlessly display meteorological data on the satellite imagery.

Visible imagery is used to evaluate reflectivities. These are important for understanding the nitrogen chemistry in the stratosphere, and, under some conditions, the chemistry of the hydroxyl radical as well. Infrared imagery indicates the extent and intensity of mesoscale convective and synoptic storm activity. Relationships of infrared imagery to aircraft observations of gravity and inertia-gravity waves can ultimately be used to evaluate global momentum fluxes caused by storm and convective activity. Previous studies have shown that variations in



Fig. 1. Composite of 11-micron infrared imagery at 0 hours universal time on 14 September 1994 from two geostationary satellites, GMS-4 (located at the equator and 140 degrees east), and GOES-7 (located at the equator and 112 degrees west). Colored regions indicate cloud-top temperatures less than -35°C . The coldest temperature (red near 160 degrees east and 11 degrees north) is about -85°C . (See color plate 12 in Appendix)

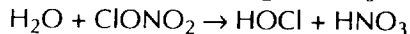
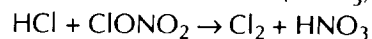
tropo-pause height are related to the 6-micron infrared imagery available on GOES-7 and GOES-8. We will use this imagery to plan flights near the midlatitude tropopause whose purpose is to examine stratosphere-troposphere exchange mechanisms.

**Ames-Moffett contact: L. Pfister
(415) 604-3183**

Headquarters program office: OMTPE and OA

Stratospheric Ice

Aerosol surfaces in the atmosphere permit chemical reactions to occur that would otherwise be kinetically unfavorable. In the stratosphere, catalysis of nitrate transformations on or in polar stratospheric cloud particles is now proven to be capable of inverting the standard relationships between chlorine reservoirs and reactive radicals in the polar regions. A direct consequence has been massive Antarctic ozone depletion. In the cold Antarctic stratosphere, particles of nitric acid n-hydrate (type I polar stratospheric clouds) first condense at about 195 kelvin; water ice particles (type II clouds) form when the temperature falls to about 188 kelvin. These polar stratospheric clouds provide surfaces for reactions that are the key to the Antarctic ozone hole. The heterogeneous reactions convert inert hydrogen chloride (HCl) and chlorine nitrate (ClONO₂) to reactive molecular chlorine (Cl₂) and hypochlorous acid (HOCl), and inert nitric acid (HNO₃):

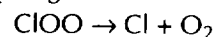
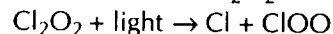
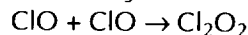
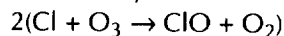


The molecular chlorine and hypochlorous acid are gases that can be photolyzed by solar radiation to form chlorine radicals that can catalyze ozone destruction.

In contrast, the HNO₃ produced by those heterogeneous reactions remains condensed on the

cloud particles. This condensation ties up the nitrogen compounds that, were they in the gaseous phase, would react with active chlorine to re-form inert ClONO₂. During the winter, some of the relatively large type II (ice) particles have settling velocities large enough to transport the HNO₃ to lower altitudes. This process of denitrification physically separates HNO₃ from ozone-reactive chlorine radicals, thereby extending the lifetime of ozone-destructive chlorine.

By polar spring, when the sun reappears, photons dissociate Cl₂ into chlorine atoms (Cl) that attack ozone, yielding molecular oxygen and chlorine monoxide (ClO), which forms a dimer that also is photolyzed to Cl to destroy more ozone:



We measure type I and type II polar stratospheric cloud particles by collecting them on wire impactors that are exposed to stratospheric air outside the left wingtip of the ER-2 research aircraft. When the temperatures are forecast to be low enough to form ice, some of the wires are replaced by quartz rods which are coated with Formvar, a resin that is liquid when exposed to specific solvents. Ice particles deposited on the Formvar-coated rods are encased by it. The resin hardens after the solvent has evaporated, leaving replicas of ice particles. The samples are brought back to the laboratory where substance-specific reactions detect nitric acid aerosols, and morphological analyses using optical and electron microscopes distinguish ice particles. The figure shows an example of a replicated columnar ice particle, the left portion of which is covered by nitric acid. The ringlike structure above the columnar ice particle is the replica of a plate, another habit that is typical of ice.

Ames-Moffett contact: R. Pueschel

(415) 604-5254

Headquarters program office: OSS



Fig. 1. Ice crystal with nitron-nitrate reaction: Airborne Southern Hemisphere Ozone Experiment (ASHOE) (28 July 1994).

Aerosols and Their Radiative/Climatic Effects: Space, Air, and Ground Measurements and Analyses

Philip B. Russell, Rudolf F. Pueschel

As a part of Science Team activities for the spacecraft sensors SAM II (Stratospheric Aerosol Measurement) and SAGE, SAGE II, and SAGE III (Stratospheric Aerosol and Gas Experiments), Ames has designed, participated in, and analyzed measurements by aircraft, balloons, and ground-based remote sensors to validate and complement the spacecraft measurements. Recent and ongoing activities include ER-2 and DC-8 campaigns to measure particle size distribution, composition, and optical depth spectra before and after the Pinatubo eruption (in coordination with SAGE II measurements), developing the data validation plan for the SAGE III sensor (to fly on the Earth Observing System (EOS)), and designing several autotracking sunphotometers to fly on a variety of occupied and unoccupied aerial vehicles as components of multidisciplinary studies of aerosol climatic effects.

A SAGE II Science Team data analysis objective is to bring together experimental evidence required to build realistic models of the global evolution of physical, chemical, and optical properties of the aerosol resulting from the 1991 Pinatubo volcanic eruption. Such models are needed to compute the effects of the aerosol on atmospheric chemistry, dynamics, radiation, and temperature. Whereas there is now a large and growing body of post-Pinatubo measurements by a variety of techniques, some results are in conflict; a self-consistent, unified picture is needed, along with an assessment of remaining uncertainties. This task is to examine data from photometers, radiometers, impactors, optical counter/sizers, and lidars operated on the ground and from aircraft, balloons, and spacecraft. Example data sources include

- tracking sunphotometers and lidars at Mauna Loa Observatory (MLO) and on the DC-8
- particle spectrometers and wire impactors on the ER-2 and DC-8
- dustsondes (particle counters/sizers on balloons)
- SAGE II, SAM II, AVHRR, CLAES, and ISAMS sensors on a variety of satellites

The SAGE II Science Team will assess the mutual consistency of these disparate data sets and derive "consensus" properties and uncertainties in the process of developing a composite data set.

Related efforts have developed scientific strategies for measuring tropospheric aerosol properties and radiative/climatic effects, and for testing the mutual consistency of these measurements and the model calculations that link them. These strategies are described in the plans for the Tropospheric Aerosol Radiative Forcing Observational Experiment (TARFOX) and the Aerosol Characterization Experiment (ACE), field studies planned for 1995–1997. These experiments will combine space, air, and Earth-surface measurements to improve scientific understanding of aerosol effects on climate.

Project participants include John M. Livingston of SRI International and Patrick Hamill, Shari Brooks, Jill Baumann Hughes, and Robert Bergstrom of San Jose State University.

**Ames-Moffett contact: P. Russell
(415) 604-5404**

Headquarters program office: OMTPE

Airborne Autotracking Sunphotometry

Philip B. Russell, Robert Wrigley, David Bergner, Damon Ried, Danelle Ketner, Rudolf F. Pueschel

The Ames Airborne Autotracking Sunphotometer measures the attenuation of sunlight by aerosols, clouds, and certain absorbing gases (e.g., water vapor). It does this by tracking the sun and measuring the (relative) intensity of the solar beam in six spectral channels. Each channel consists of a multibaffled entrance tube, an interference filter, a photodiode detector, and an integral preamplifier. The entrance baffles define a detector field of view (FOV) with measured half-angle $Y_D = 2.2^\circ$. The six filter/detector/preamp sets are mounted in a common heat sink maintained at $45 \pm 1^\circ\text{C}$. Filters are currently centered at wavelengths 382, 451, 526, 861, 940, and 1020 nanometers. Filter full widths at half-maximum (FWHM) are about 5 nanometers. Solar tracking is achieved by azimuth and elevation motors driven by error signals derived from a differential-shadowing sun sensor. Data are digitized and recorded every 2 to 10 seconds. The science data set includes the six detector signals, detector temperature, sun tracker azimuth and elevation angles, tracking errors, and time. Aerosol and cloud attenuation data are analyzed and expressed in terms of their optical depth spectrum. A laptop-PC-based control and data system developed in 1994 provides a variety of scientific analysis and display products in real time in the field, as well as instrument control and data storage functions.

The sunphotometer has flown on a variety of aircraft (e.g., the NASA DC-8, C-130, and CV-990, the University of Washington C-131, and the Department of Energy Twin Otter) and has been used to study background and volcanic stratospheric aerosols, smokes from oil and forest fires, and the impact of tropospheric aerosols on remote imaging of the Earth's surface.

The instrument was particularly active in 1992–1994. In January–March 1992 it flew on the NASA DC-8 in the second Airborne Arctic Stratospheric Expedition (AASE II), measuring the impact of the Pinatubo volcanic aerosol on stratospheric processes, including its potential to affect ozone chemistry and temperatures both in the stratosphere and at the Earth's surface. In May 1992 it flew again

on the DC-8 as part of a northern-to-southern-hemisphere experiment to validate the SAGE II satellite sensor. In September–October 1992 it flew on the NASA C-130 in the Hydrologic Atmospheric Pilot Experiment in the Sahel (HAPEX-Sahel) to measure the impact that desert haze has on the satellite imagery used to study hydrology in Africa. In May–September 1993 it flew on the NASA DC-8 over Alaska, Central and South America, Australia, and the Pacific to measure the Pinatubo volcanic decay in conjunction with the SAGE II satellite sensors and lidars. In April 1994 it participated in an instrument intercomparison at the University of Arizona's Mt. Lemmon Observatory as part of preparations for the Boreal Ecosystem–Atmosphere Study (BOREAS). In May–September 1994 it flew on the NASA C-130 in three BOREAS Intensive Field Campaigns (IFCs) in Canada. And in September 1994 it made measurements under Space Shuttle flight STS-64 to provide correlative data for the Lidar In-Space Technology Experiment (LITE). The latter measurements were made both on the C-130 in Canada and on the ground in Southern and Central California. The results of these expeditions have been published in a series of journal articles and conference presentations, and further publications and presentations are in progress.

Future plans include participation in the Tropospheric Aerosol Radiative Forcing Observational Experiment (TARFOX) and the first and second Aerosol Characterization Experiments (ACE-1 and ACE-2) field studies planned for 1995–1997. Options include flights on a variety of occupied and unoccupied aerial vehicles (UAVs). Preparations have included several designs of sunphotometers optimized for flight on UAVs.

Project participants include John M. Livingston of SRI International, Ronald Guzman of Sverdrup Technologies, and Jill Baumann Hughes of San Jose State University.

**Ames-Moffett contact: P. Russell
(415) 604-5404**

Headquarters program office: OMTPE

Environmental Research Aircraft and Sensor Technology

Philip B. Russell, Steven Wegener

Platform aircraft, including NASA's ER-2s, C-130, and DC-8, have made major contributions to our current understanding of earth science, through missions such as the 1987 Airborne Antarctic Ozone Experiment (AAOE), the 1989 and 1991–1992 Airborne Arctic Stratospheric Expedition (AASE I and II), the 1994 Boreal Ecosystem–Atmosphere Study (BOREAS), and many others. The aircraft measurements have proven to be an indispensable complement to measurements from space, ground, and balloons. Many of the characteristics of aircraft measurements (e.g., variety of measured constituents, spatial and temporal resolution and range, duration over a given site, controllability of trajectory, quick response to geophysical events) cannot be achieved by other techniques and are especially powerful in revealing the processes by which natural and manmade global change occurs.

The many scientific successes of the current earth science aircraft fleet (at NASA and other agencies), coupled with today's critical scientific questions, have caused many groups to cite the need for aircraft with more capabilities than today's fleet—e.g., higher ceiling, longer range and/or duration, heavier payloads and/or the ability to fly over inhospitable terrain. In response to this need, Ames established an Earth Science Advanced Aircraft (ESAA) Team in September 1990 with the following goals:

- Identify the best ways of applying NASA aeronautical capabilities to the advanced-aircraft needs of the broad earth science community
- Foster NASA's continuing leadership role in multi-investigator earth science aircraft missions
- Interact with ESAA teams at other agencies and institutions
- Develop funded projects to achieve the above goals.

The ESAA initiative was instrumental in the formation of the Small High-Altitude Science Aircraft (SHASA) Project to develop and test-fly the Perseus-A unoccupied scientific research aircraft. Perseus A's goal is to advance stratospheric research by carrying scientific payloads of at least 75 kilograms to

altitudes of at least 25 kilometers. (For reference, the corresponding ER-2 capabilities are 1,400 kilograms and 21 kilometers.)

The broad need for unoccupied aerial vehicles (UAVs) both within and outside the earth science community, coupled with the potential economic benefits of fostering a robust U.S. civil UAV industry, led NASA to establish the agency-wide Environmental Research Aircraft and Sensor Technology (ERAST) Program in 1994. ERAST's goals are to

- Advance the state of the art of UAV capabilities and sensor technologies such that, when they are used in combination as an integrated science platform, the data collection requirements of the science community are achieved.
- Assist in the formation of an economically viable U.S. UAV industry through active cooperation and effective technology transfer between government, industry, and academia.

ERAST's primary objectives are to (1) conduct major flight demonstrations of advanced UAV technologies to demonstrate their viable application to a broad spectrum of scientific, government, and private uses; and (2) focus on the miniaturization/optimization of UAV-class airborne atmospheric instruments and their integration into advanced UAVs, culminating in a series of science mission demonstrations.

The ERAST program includes components at NASA's Ames-Moffett, Ames-Dryden, Langley, and Lewis Research Centers. The Sensor Technology component of ERAST is managed by Steven Wegener of Ames-Moffett. NASA is implementing ERAST through a Joint Sponsored Research Agreement (JSRA) that includes four companies: Aerovironment, Aurora Flight Sciences, General Atomics, and Scaled Composites. One activity subsumed in the JSRA is continued flight testing and demonstration of Perseus A, initiated in the ESAA SHASA Project. Other JSRA plans call for technology investigations and demonstrations, including science missions, using a wide range of other UAVs such as an upgraded Gnat-750,

a Raptor Demonstrator, a Raptor Pathfinder, and Perseus B, as well as UAV simulators (human-occupied aircraft that demonstrate or simulate UAV functions). Activities of the Sensor Technology component of ERAST include development and demonstration of a variety of science instruments in

support of the Assessments of the Effects of Aviation Program (AEAP).

**Ames-Moffett contact: P. Russell
(415) 604-5404**

Headquarters program office: OA

Composition of the Atmosphere over the Pacific

Hanwant B. Singh

The Pacific troposphere is a large region of the northern hemisphere that is relatively free of direct influences from man-made pollution. Tremendous industrial growth in Asia and North America in recent decades has the potential to impact this pristine region significantly. The Pacific Exploratory Mission (PEM) is a series of NASA-led experiments to study the composition and chemistry of the perturbed and the unperturbed atmosphere over the Pacific Ocean. The PEM aims to elucidate mechanisms by which ozone in the troposphere is formed, destroyed, transported, and otherwise impacted by human sources. To achieve this aim, a comprehensive set of airborne field measurements (0–12-kilometer altitude) have been undertaken that involve the study of nitrogen, carbon, sulfur, and chemical tracer species. Highly sensitive measurements of reactive nitrogen species, oxygenated hydrocarbons, and chemical tracers were performed by NASA Ames by deploying an instrument called PANAK. Although analysis is continuing, some preliminary findings follow.

High concentrations of chlorine atoms (approximately 10^5 molecules per cubic centimeter) have been inferred to be present in the marine boundary layer of the tropical Pacific Ocean. In this region, photochemistry destroys ozone because of extremely low concentrations of nitrogen oxides (NO_x). Low NO_x , chlorine atoms, and low entrainment rates collectively have been found to be responsible for the extremely low ozone concentrations (2–10 parts per billion) encountered in this region.

The distribution of reactive nitrogen, its partitioning into chemical constituents, and its sources have been studied in detail. Shortcomings in measurement methods and theory have been identified. Known reactive nitrogen species that were measured could account for less than half of the total measured reactive nitrogen (NO_y). In the upper troposphere the sources of NO_x are only roughly quantifiable. We calculate that only a small fraction (approximately 20%) of the surface source of NO_x actually impacts the upper troposphere and the remainder is either removed or quickly converted into relatively inert NO_y species. It is further found that these NO_y species can be transported long distances and can slowly release NO_x and constitute an important source of global NO_x . Lightning is an important but poorly quantified source of NO_x . Global models have been tested and are beginning to provide descriptions that agree with actual observations. These results have direct bearing on new NASA initiatives designed to obtain an understanding of the role of subsonic aircraft in modifying the atmosphere.

Further analysis of these extensive measurements is ongoing.

**Ames-Moffett contact: H. Singh
(415) 604-6769**

Headquarters program office: OMTPE

Improved Measurement of Terrestrial (Infrared) Radiation

Francisco P. J. Valero, Anthony W. Strawa, Warren J. Y. Gore

One of the primary goals of the Radiation Group in the Atmospheric Physics Branch is to study the effects that natural and man-made changes to the environment have on the Earth's atmosphere and climate. The accurate and precise measurement of radiative parameters associated with the interaction of the atmosphere with radiation is essential to this goal. Ames is involved in two projects whose purpose is to improve measurement of terrestrial (infrared) atmospheric optical radiation.

The first project is the development of a state-of-the-art ground-based instrument capable of measuring terrestrial radiative fluxes and spectral radiances. The instrument has a design similar to that of the group's flight instruments which have proven to be accurate and reliable on many past field missions. The instrument must be able to function in a wide range of climatic conditions, from desert to Arctic, and provide measurement of fluxes and radiances with an absolute accuracy within 1%. A prototype of the instrument has been tested at the Southern Great Plains Cloud and Radiation Testbed site in Oklahoma in support of the Unmanned Aerospace Vehicle and the Radiation and Cloud Study Intensive Operating Period held in April 1994.

The second project is participation in an international intercomparison of hemispherical field-of-view infrared radiometers organized by the World Meteorological Organization Baseline Surface Radiation Network. The aim of the intercomparison is to establish state-of-the-art instrumentation, calibration, and measurement procedures to reduce the level of uncertainty currently experienced with this type of measurement. Improvements in these measurements will be valuable in the validation of predictive models of the Earth's climate.

The organizations participating in the comparison include NASA Ames Research Center, Scripps Institute, and the National Oceanic and Atmospheric Administration in the USA; the Atmospheric Environment Service in Canada; the German Weather Service; the Geographisches Institute in Switzerland; the Meteorological Research Institute in Japan; and the Meteorological Research Flight in Great Britain.

**Ames-Moffett contact: A. Strawa
(415) 604-3437**

Headquarters program office: DOE

Measurement of Atmospheric Radiation Using an Unmanned Airborne Vehicle

Francisco P. J. Valero, Warren J. Y. Gore, Shelly K. Pope, Larry Pezzolo, Neil Heather

The Department of Energy's Atmospheric Radiation Measurement (ARM) program is directed toward improving our understanding of Earth's atmospheric radiation budget and the role of clouds. An extension of this program involves using unoccupied airborne vehicles (UAVs) as instrument platforms for making key measurements of atmospheric properties. UAVs offer a cost-effective means of making direct measurements at high altitudes over time periods as long as several diurnal cycles.

The ARM-UAV program included a demonstration phase consisting of a series of UAV flights over an ARM test site (a cloud and radiation testbed (CART)) where a suite of ground-based instruments was collecting atmospheric data. The radiometers of the Atmospheric Physics Branch Radiation Group were selected as the primary scientific instruments to fly in the UAV payload for the demonstration and interim phases of the ARM-UAV program. A pair of broadband radiometers, one solar and one infrared, is upward-looking and another pair is downward-looking. Also, a multispectral-channel total-diffuse-direct radiometer, upward-looking, is on board. The UAVs are "stepped" through altitude to obtain radiative flux profiles. Data from the radiometers are telemetered to the ground station throughout the 6-hour flight. The first figure is a photograph of the General Atomics Gnat, the UAV used in the demonstration phase.

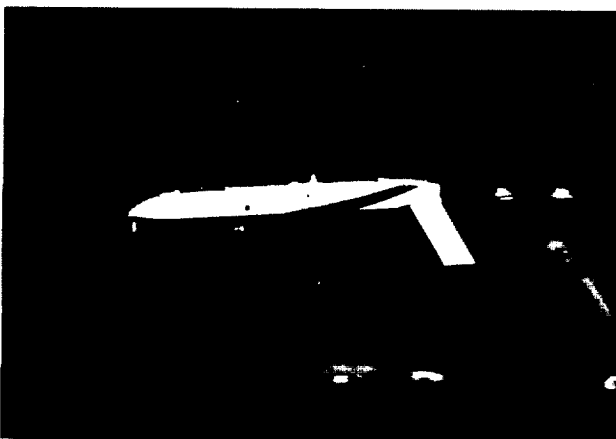


Fig. 1. The Gnat UAV with radiometers installed.

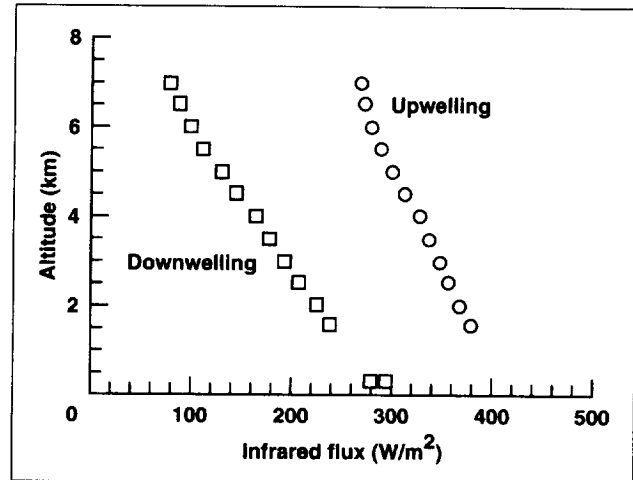


Fig. 2. Infrared fluxes measured on 19 April 1994 at the CART site in Oklahoma. The flux, in watts per meter squared, is plotted as a function of altitude in kilometers.

The objectives of the demonstration phase were (1) to obtain meaningful data relevant to ARM issues, (2) to gain operational experience with UAVs used for atmospheric research in conjunction with an ARM CART site, and (3) to exercise a prototype UAV-CART data system. These objectives were successfully met with the completion of six science flights over a 3-week period in April 1994. The second figure shows radiative-flux data from one of the flights. Data points from the group's ground-based infrared radiometer, measuring downwelling infrared flux during the flight, are also plotted.

The program is proceeding with the interim phase of operations, using two UAVs flying in a stacked formation over the CART site. The instrumentation for the interim phase will consist, as before, of upward- and downward-looking broadband hemispherical flux radiometers and an upward-looking total-diffuse-direct radiometer (a complete set will fly on each UAV). The basic mission will be to measure the radiation flux profiles and divergences.

Ames-Moffett contact: W. Gore
(415) 604-5533

Headquarters program office: DOE

Cloud Modeling for the Study of Climate Change

Douglas L. Westphal, Eric J. Jensen, Stefan A. Kinne, Annette L. Walker

Our goal is to develop theoretically based parameterizations of ice clouds (cirri) that are accurate, yet practical, for use in state-of-the-art climate models. We are meeting this goal through a combination of approaches. We are evaluating the theoretical basis of ice microphysical parameterizations currently in use and are updating them according to new theory and measurements. Validation is done by comparing the model results with satellite, aircraft, and surface-based observations. We have found that the ice production parameterizations used in current cloud models invoke various assumptions about particle size and shape that are inappropriate for cirrus clouds. The choice of size and shape is important since the calculations of mass, fall velocity, mass flux, radiative heat transfer, and other properties are dependent upon these two factors. For example, we note that the current cloud models assume a hexagonal-plate particle shape for ice, whereas columns and bullet rosettes are more frequently observed. We also find that the assumed snow-particle size distribution is inappropriate for cirrus clouds since it includes too many large particles. The use of the wrong particle shape and size distribution leads to mass fluxes that are too large by a factor of four. We have developed and are testing a corrected distribution that, when combined with accurate fall speed equations, yields a realistic mass flux.

We have also explored the ability of our regional-scale weather forecast model to simulate the multidimensional complexities of the water vapor, cloud, and radiation fields associated with cirrus clouds. We have conducted simulations and

sensitivity tests over several periods during NASA's FIRE (First International Satellite Cloud Climatology Program (ISCCP) Regional Experiment) Program centered over Kansas in November and December 1991. In particular, the November 26, 1991, case study has been used as a testbed for our improvements in microphysical parameterizations because a good variety of cloud types was sampled by aircraft that day. A comparison with the measurements shows that the model adequately captures the time of formation, the cloud boundaries, and ice water concentrations of the cirrus clouds observed between 1600 and 2100 hours universal time on November 26 over Kansas. However, our inclusion of a 44-band radiative transfer model in the regional model allows a more rigorous verification of the cirrus cloud simulations since we not only verify the cirrus cloud properties such as ice water content and cloud boundaries, but we also verify climatologically important fields such as outgoing infrared flux, solar albedo, and other satellite-inferred quantities. For example, in the case mentioned above, we find that further research is necessary because a comparison of the measured and simulated fields of albedo and outgoing infrared flux reveal discrepancies that may be due either to the modeled particle sizes or to optical properties.

**Ames-Moffett contact: D. Westphal
(415) 604-3522**

Headquarters program office: OMTPE

Global Monitoring and Human Health

Byron Wood, Louisa Beck, Sheri Dister, Mike Spanner

The Global Monitoring and Human Health (GMHH) program comprises four activities: the Malaria Project, Outreach, the initiation of the Center for Health Applications of Aerospace Related Technologies (CHAART), and Technology Development. The focus of the Malaria Project is to develop a landscape epidemiologic approach to identify malaria risk according to the environmental factors that determine the temporal and spatial distribution of both the vector and the disease. This research is being conducted on *Anopheles albimanus* along the Pacific coastal plain of Chiapas, Mexico. The landscape approach integrates remote sensing (RS) and geographic information system (GIS) capabilities to successfully discriminate between villages that are at high risk and those that are at low risk for malaria transmission, as defined by *A. albimanus* abundance. Landsat Thematic Mapper (TM) data acquired during the wet and dry seasons were digitally processed to generate a map of 12 landscape elements. A GIS was then used to determine the proportion of each of these remotely sensed elements surrounding 40 randomly selected villages. Only landscape elements that occurred within 1 kilometer of a village boundary were included, because this distance is the typical flight range of the female mosquito. Mosquito abundance data were collected in the 40 villages during the middle to late wet season. The relationship between mosquito abundance and landscape composition was then investigated using stepwise discriminant analysis and stepwise linear regression. Both analyses indicated that the key landscape elements that determined mosquito abundance were the proportions of transitional swamp and unmanaged pasture in the land surrounding a village. Discriminant functions generated for these elements were able to correctly distinguish between villages with high and low mosquito abundance, with an overall accuracy of 90%. This approach is currently being tested in another area in Chiapas.

The major goal of Outreach is to promote the use of RS/GIS in monitoring and predicting the spatial patterns of human diseases. As part of this task, several collaborative studies are currently under way.

In one study, Ames is working with researchers from the New York Medical College (NYMC) to develop a predictive model of Lyme disease transmission risk in suburban New York. Recent research efforts have focused on relating tick abundances on residential properties, collected by NYMC investigators in two communities of Westchester County, to TM-derived spectral indices, topographic data, and soil type for these properties. Because over 65% of the tick bites in this county are acquired on residential properties, these spectral indices could provide an efficient means of mapping high-risk residences over large areas. Ames scientists are also exploring the use of RS/GIS for studying yellow fever risk in Kenya and cholera dynamics in the Bay of Bengal. Ames investigators have initiated a collaboration with researchers at U.C. Berkeley to study schistosomiasis in China. As part of Outreach, a Visiting Scientist Program was initiated during the 1994 fiscal year. Under this program, an Egyptian medical entomologist from Ain Shams University in Cairo is spending a year at Ames learning RS and GIS technology and how to use these tools to further his research on filariasis in the Nile Delta.

An activity related to Outreach was the initiation of CHAART at Ames, in order to promote the application of RS/GIS and related technologies to issues of human health and to maintain ongoing collaborations with investigators from universities, research/control agencies, and private industry. The objectives are to assist health investigators through the use of CHAART facilities to achieve the objectives of their research; to initiate innovative, collaborative, interdisciplinary research relating the patterns of health to environmental parameters using aerospace-related technologies; to expand the use of these technologies by the human-health community through training, education, application projects, and direct transfer of proven technologies and knowledge to research/control agencies and universities; and to evaluate existing and planned aerospace-related technologies for use in human-health research.

The goal of Technology Development is to formulate design criteria for an RS system dedicated to disease surveillance, and to prepare a strategy for identifying, equipping, and training people in developing countries to use RS technology for disease surveillance. In 1994, the University of Texas, El Paso, received a grant from NASA's Office of Minority Programs to support research on sensor fusion, which can be applied to the processing,

analysis, and modeling of large multispectral data sets. The GMHH scientists also reviewed a proposal from the Daedalus Corporation that was approved for funding in fiscal year 1995.

Ames-Moffett contact: B. Wood
(415) 604-4187
Headquarters program office: OLMSA

Aerosol Measurements for the Boreal Ecosystem-Atmosphere Study (BOREAS)

Robert Wrigley, Philip Russell, John Livingston, Brad Lobitz

Automated tracking sun photometers were deployed by NASA Ames Research Center aboard the NASA C-130 aircraft and at a ground site for all three intensive field campaigns (IFCs) of the Boreal Ecosystem-Atmosphere Study (BOREAS) in central Saskatchewan, Canada, during the summer of 1994. BOREAS is a large multinational, multidisciplinary study of the interaction of boreal landscape with the atmosphere in the context of global change. The sun photometer data were used to derive aerosol optical depths for the total atmospheric column above each instrument. The airborne tracking sun photometer obtained data in both the southern and northern study areas (1) at the surface prior to takeoff, (2) along low-altitude runs near the ground tracking sun photometer, (3) during ascents to 6-8 kilometers mean sea level along remote sensing flightlines at altitude, (4) during descents to the surface, and (5) at the surface after landing. The ground sun photometer obtained data from the shore of Candle Lake in the southern areas for all cloud-free times.

During the first IFC in May and June, ascents and descents of the airborne tracking sun photometer indicated that the aerosol optical depths decreased steadily from the surface to 3.5 kilometers, where they leveled out at approximately 0.05 (at 525 nanometers), well below levels caused by the eruption of Mt. Pinatubo for the last 2 years. On a very clear day, 31 May, surface optical depths

measured by either the airborne or ground sun photometers approached those levels (0.06-0.08 at 525 nanometers), but surface optical depths were often several times higher. On 4 June they increased from 0.12 in the morning to 0.20 in the afternoon with some evidence of brief episodes of pollen bursts. During the second IFC, surface aerosol optical depths were extremely variable as a result of smoke from large western forest fires. On 20 July the aerosol optical depth at 525 nanometers decreased from 0.5 in the morning to 0.2 in the afternoon. They decreased still further the next day to 0.05 and remained consistently low throughout the day to provide excellent conditions for several remote-sensing missions flown that day. Smoke was heavy in the early morning of 24 July but cleared partially by 1030 local time and cleared fully by 1130. Heavy smoke characterized the rest of the IFC in both study areas.

These and other aerosol optical depth measurements will be used to provide quantitative corrections for atmospheric effects in satellite and aircraft image data acquired in the BOREAS study areas.

Ames-Moffett contact: R. Wrigley
(415) 604-6060
Headquarters program office: OSS

Calcium Balance in a Spaceflight Model

Sara B. Arnaud, Meena Navidi

Negative calcium balance is a well recognized consequence of spaceflight that was well documented in nine astronauts during the Skylab missions. In calcium balance studies carried out by D. Whedon and his colleagues at the National Institutes of Health, greater amounts of calcium were found in the excretions (urine and feces) of the astronauts than in their diets at the time. The major explanation for this negative calcium balance (according to tracer studies carried out by V. Schneider and A. LeBlanc at Johnson Space Center in the human bedrest model for spaceflight) is reduced intestinal absorption of calcium. Calcium losses from intestinal fluids excreted in the feces and from the active pool of total body calcium excreted in urine also contributed to negative calcium balance, to a lesser degree.

It is uncertain whether negative calcium balance during spaceflight represents a regulated physiologic adaptive process, as illustrated in the figure, or an uncontrolled leak related to bone loss. Decreases in circulating vitamin D hormone, which facilitates the absorption of calcium in the intestine, suggest that negative calcium balances are a reflection of regulated physiologic processes geared to the supply of mineral for bone. When mineral is in demand for bone formation (lower panel of figure), calcium absorption is more efficient and balances are positive; when less is needed, as in the upper panel, absorption is reduced, and balances are negative relative to normal, which can be considered zero.

To evaluate the impact of increases in urinary calcium excretion on calcium balance, we used mature 450-gram male rats for metabolic studies carried out in cages tailored specifically for the rat model with unloaded hindlimbs (i.e., tail suspended) developed by Emily Holton at Ames. High-sodium diets were used to increase the excretion of urinary calcium. Mature animals fed normal-calcium, 8% salt diets showed increases in calcium excretion of about 12% of their dietary calcium. In spite of this apparent loss, calcium balances were more positive in both ambulatory and unloaded rats on the high-sodium diet. This proved to be due to the higher rate of

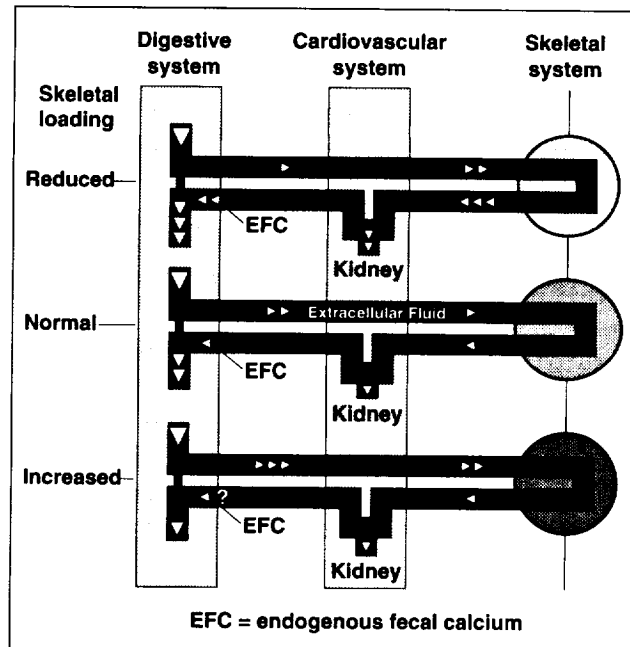


Fig. 1. The regulated flow of calcium, indicated by triangles, through intestine, bone, and kidney—the target organs of calcium metabolism—in response to skeletal loading.

intestinal absorption that occurred with the high-sodium diet in both the control and the unloaded animals. However, in the spaceflight model, calcium balances were consistently about 20% lower than in the ambulatory controls. We concluded from these experiments that high-salt diets are associated not only with calciuria, but also with increased calcium absorption and positive calcium balances. The capacity of the spaceflight model to increase intestinal calcium absorption was limited and calcium balances were consistently less than in normal controls.

The implication from these basic animal studies is that negative calcium balance is the appropriate response to reduced bone loading and the need for bone mineral. Theoretically, negative calcium

balance will normalize with regimens that provide adequate bone loading. The evidence for the regulated nature of calcium balance in spaceflight models also provides support for the view that total body calcium deficits resulting from prolonged periods of negative calcium balance will be difficult to quantify in individuals who embark on spaceflight with relatively high levels of total body calcium. In fact,

changes in total body calcium have not been recorded in cosmonauts after 6 or more months in space in spite of regional losses in the weight-bearing skeleton.

**Ames-Moffett contact: S. Arnaud
(415) 604-6561
Headquarters program office: OSS**

Noninvasive Test of Bone Strength

Sara B. Arnaud, Teresa Hutchinson

A means has been developed for measuring the strength of the long bones in the upper and lower extremities after spaceflight. The technique, originated by D. Young at Ames Research Center and C. Steele at Stanford University, has been used in a spaceflight experiment in animals, and also has been applied in research on medical problems of humans on Earth. The measurement technique uses an instrument designed and manufactured by Gait Scan, Inc., in New Jersey with the support of a grant from NASA. A low-frequency vibration is applied with a probe that rests on the skin surface at the center of a resting long bone. The response of the bone is detected at the same site and analyzed using the relation $K_b = 48EI/L^3$, where EI is the cross-sectional bending stiffness (E is the elastic modulus, I is the cross-sectional moment of inertia) and L is the bone length. Bending stiffness determined noninvasively with the new instrument (called the MRTA) agreed with that measured by standard three-point bending tests of the same bones ($R^2 = 0.95$, $p < 0.0001$).

Using the Ames-developed technique, S. Smith and A. Burshell of the Ochsner Clinic in Louisiana tested the long bones of the arms in a group of patients with osteogenesis imperfecta (an inherited disease characterized by fragile bones). Mineral density in the bones of the 10 patients, who had suffered more than 13 fractures in the upper extremities, was the same as in those of the 9 age-matched

unaffected relatives who had a history of less than one fracture. The EI, however, determined by the MRTA, was 30% lower in the patients than in the controls and clearly identified the affected individuals. This study illustrates the importance of evaluating the biomechanical properties of bone to estimate their function rather than the mineral content alone—a major, but not the sole, source of bone strength.

Preliminary results from Gail Dalsky's laboratory at the University of Connecticut, where patients with postmenopausal osteoporosis are being evaluated, reveal consistent agreement of low EI and low mineral density values in the ulnas of small groups of patients. The use of the MRTA to monitor treatment programs in osteoporosis is currently under way.

The system is the only method available that provides a direct measure of bone biomechanical properties in a noninvasive manner. It promises to be useful in the management of patients with bone disease because of the simplicity of the testing procedure, its sensitivity and precision, and the absence of radiation exposure.

**Ames-Moffett contact: S. Arnaud
(415) 604-6561
Headquarters program office: OSS**

Intramuscular Pressure During Treadmill Walking

Richard E. Ballard, Donald E. Watenpaugh, Gregory A. Breit, Gita Murthy,
Robert T. Whalen, Alan R. Hargens

Currently, there is no direct, practical method for measuring the forces produced by individual skeletal muscles during locomotion in humans. Information on these forces is important for understanding muscle physiology, musculoskeletal mechanics, neurophysiology, and motor control. Such information will also aid in the development of exercise hardware and protocols for spaceflight, rehabilitation, and training. Electromyography (EMG, the measurement of electrical activity in muscle) has been used for many years to assess muscle activation patterns during various activities. However, attempts to use EMG magnitudes for predicting individual muscle forces during dynamic muscle actions have been largely unsuccessful.

Intramuscular pressure (IMP) is the fluid pressure in a muscle, which changes as the muscle contracts within its fascial compartment. In a recent investigation, we demonstrated that IMPs in the soleus and tibialis anterior correlate linearly with ankle joint torque during all three major types of isokinetic muscle activity (concentric, eccentric, isometric). This IMP/force relationship is independent of contraction velocity (first figure). Intramuscular pressure may therefore be used to estimate the contribution of individual muscles to overall force output during dynamic exercise.

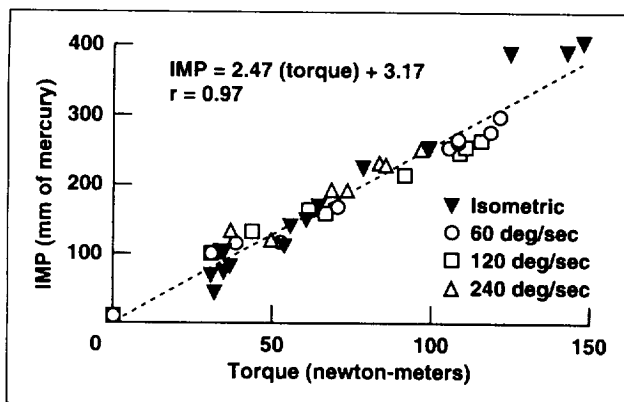


Fig. 1. Soleus intramuscular pressure and ankle joint torque during isometric and concentric contractions in one subject. The linear IMP/torque relationship is independent of contraction velocity.

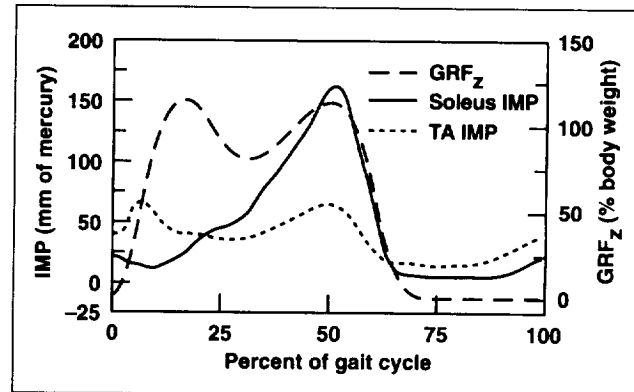


Fig. 2. Soleus and tibialis anterior IMP during treadmill walking ($N = 9$). GRF_z is the vertical ground reaction force.

To assess the efficacy of IMP measurement for studying muscle function during locomotion, IMP was recorded in the tibialis anterior (a dorsiflexor) and soleus (a plantarflexor) muscles of nine volunteers (eight males, one female) during treadmill walking. IMP was measured using Millar transducer-tipped catheters, and ground reaction force was measured with an insole force sensor. The second figure shows the intramuscular pressure and ground reaction force data averaged over all nine subjects. Soleus IMP exhibited a single peak (176 ± 71 millimeters of mercury (mean \pm standard deviation)) during the push-off phase of the gait cycle ($53\% \pm 2\%$ of gait cycle, referenced to 0% at heel strike). Soleus IMP closely paralleled footward force during push-off. IMP patterns in the tibialis anterior were somewhat more variable, but consistently showed a biphasic response. The first peak (76 ± 43 millimeters of mercury) occurred near heel strike ($5\% \pm 3\%$), and the second peak, generally smaller in amplitude (67 ± 28 millimeters of mercury), occurred near push-off ($49\% \pm 2\%$).

The observed IMP patterns associated with gait were consistent among the subjects. Furthermore, these patterns closely parallel the expected patterns of muscle activation obtained from biomechanical

and mathematical models and measurements of direct Achilles tendon force during walking. Peak IMP magnitudes were also consistent between cycles within each subject, in spite of the known variability between different subjects. These pressure magnitudes can be converted to quantitative torque estimates using a calibration curve similar to that in the first figure. Accurate conversion, however, requires separate calibration curves for each subject since the IMP/force relationship varies between subjects.

Although this technique is invasive, intramuscular pressure measurement provides direct, practical estimates of individual muscle force production during locomotion in humans. This procedure will greatly aid development of exercise protocols and hardware for spaceflight.

**Ames-Moffett contact: R. Ballard/A. Hargens
(415) 604-5747/5746
Headquarters program office: OLMSA**

Cardiovascular Responses to Real and Artificial Gravity

**Gregory A. Breit, Donald E. Watenpaugh, Theresa M. Buckley, Richard E. Ballard,
Gita Murthy, Alan R. Hargens**

Assumption of upright posture establishes a linear gravitational pressure gradient along the length of the body. Increased pressure in the lower body creates a propensity for venous pooling of blood which, if left unchecked, can result in decreased central blood pressure and eventual fainting. To prevent this, peripheral arterioles generally constrict during standing to maintain central blood pressure and facilitate blood flow to the brain. The magnitude of this peripheral vascular response varies along the length of the body because of the interaction of central controls with regional responses to local blood pressure: arterioles and venules constrict reflexively when local blood pressure increases. Thus the cardiovascular response depends on the distribution of blood pressure along the length of the body; this distribution is induced by the specific real or artificial gravitational stress.

Artificial-gravity-like stresses, such as G_z centrifugation and lower-body negative pressure (LBNP), generate cardiovascular responses that are qualitatively similar to upright standing. However, the body-length distribution of blood pressure created by these procedures may differ markedly from that experienced during standing. Unlike Earth's gravity, the centripetal acceleration imparted by centrifugation is not constant along the length of the body and results in a nonlinear blood pressure gradient from head to foot. LBNP applies no direct

stress in the upper body, but causes an abrupt and uniform change in pressure across blood vessels from the waist down. Given the importance of local blood pressure distributions in the cardiovascular response to gravity, we hypothesized that the peripheral vascular response to artificial gravity stresses differs from the response to whole-body tilting in a manner consistent with their respective blood pressure distributions.

Regional microvascular blood flow in the skin was measured by three laser Doppler flowmeters placed at the neck, thigh, and lower leg of 15 normal volunteers (8 male, 7 female). These instruments use a low-power laser to provide a linear but uncalibrated measure of microvascular flow in a small volume of tissue. Subjects underwent stepwise head-up tilt (HUT), and short- and long-arm centrifugation protocols from supine control ($0 G_z$) to 0.2, 0.4, 0.6, 0.8, 1.0, 0.8, 0.6, 0.4, 0.2, and $0 G_z$ at the feet, for 30-second periods with 10-second transitions between levels. The same subjects went through a supine LBNP protocol with stress levels at foot level corresponding to the HUT and centrifugation protocols (up to 100 millimeters of mercury (mmHg) in 20-mmHg increments and back to zero pressure). Heart rate and arterial blood pressure were measured continuously throughout each procedure.

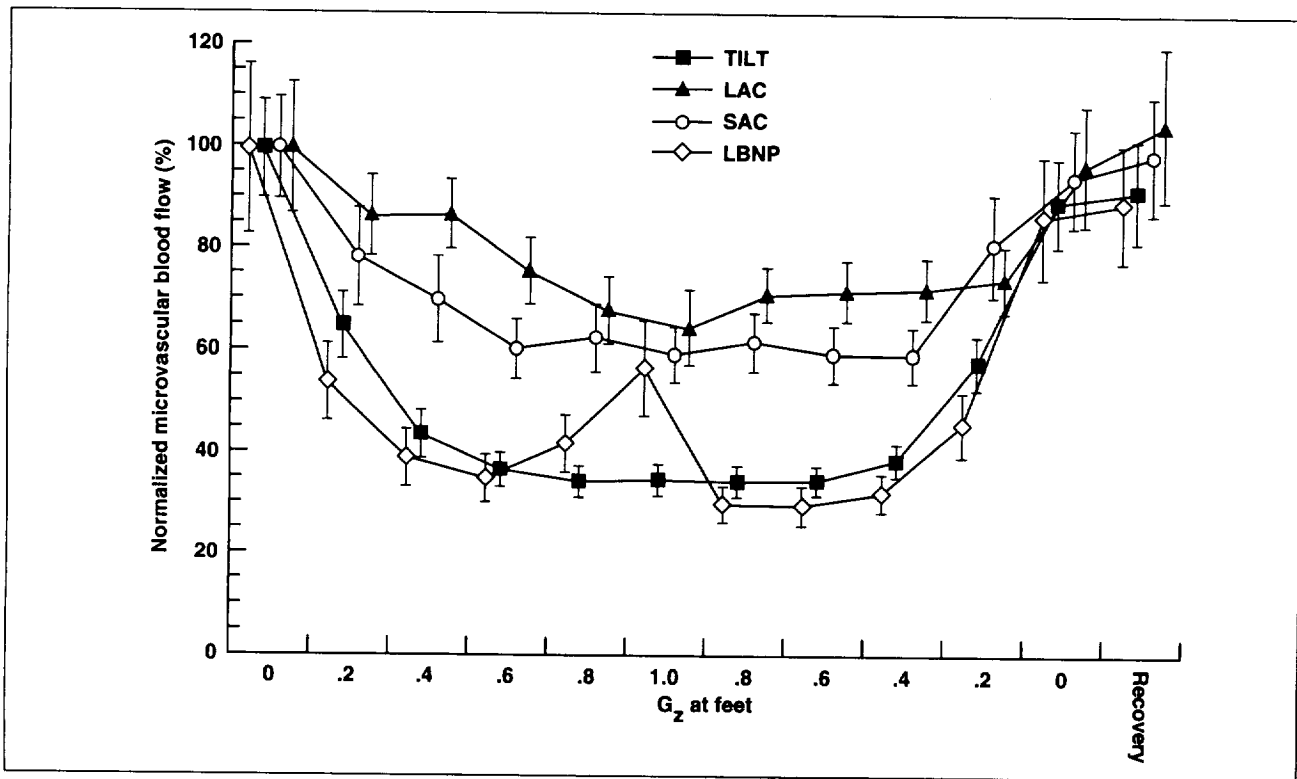


Fig. 1. Microvascular flow (normalized to the mean baseline level across subjects) at the leg during tilting, LBNP, and long-arm (LAC) and short-arm (SAC) centrifugation in male and female subjects. Error bars denote standard errors of the mean.

The first figure summarizes changes in local blood flow observed in the lower leg during the four forms of stress. In general, application of progressively higher gravitational stress resulted in successively greater flow reductions in the lower body, probably because of local vasoconstriction. The exception was LBNP, which showed a minimum microvascular flow at approximately 60 mmHg, and a subsequent paradoxical climb in flow as negative pressure was increased to 100 mmHg. In general, blood flow did not decrease with centrifugation to the degree observed with tilting and LBNP. Responses at the thigh were similar, but were less profound than those at the lower leg. Blood flow at the neck tended to increase with increasing gravitational stresses.

To interpret our blood flow results in terms of local arterial pressure increases as stimuli for vasoconstriction, local pressure at each measurement site for each gravitational stress type was modeled mathematically for each subject, based on heart-level

arterial blood pressure measured during the experiments. Observed changes in local blood flow are plotted against these calculated local blood pressures in the second figure. Although, as seen in the first figure, the four forms of stress generate disparate blood flow responses, the analysis suggests that these differences can be attributed largely to the body-length arterial pressure distributions generated by each stressor, as evidenced by the generally strong agreement between the flow change/pressure change relationship across stress types and measurement sites. The obvious outliers in this relationship are those experimental points representing the lower-leg flow response to centrifugation (filled triangles). Not only is average leg microvascular flow higher during centrifugation than during either tilting or LBNP, across subjects, but the centrifugation responses are much less consistent, as evidenced by the relatively large standard errors.

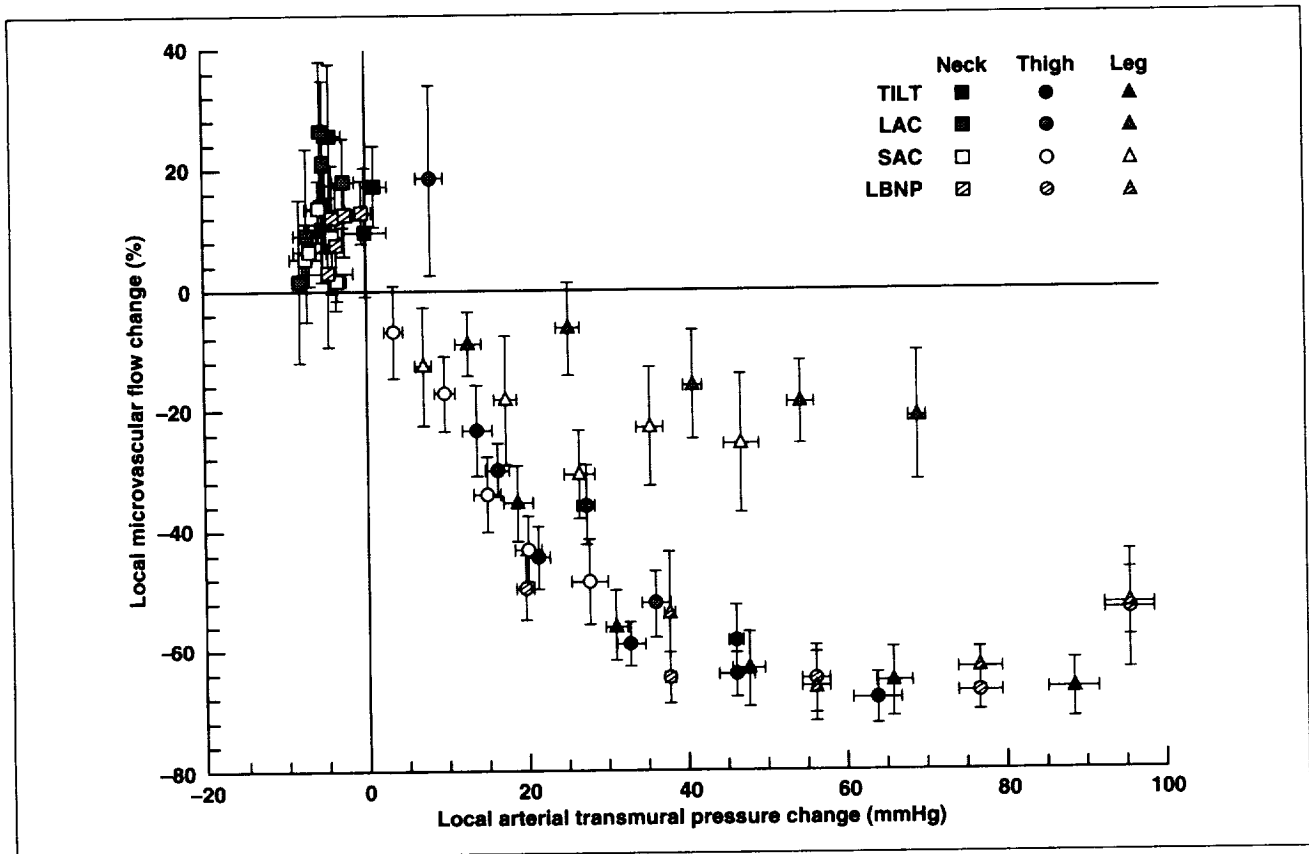


Fig. 2. Percent changes in microvascular flow plotted against calculated local arterial transmural pressure in male subjects. Averages are grouped by stress type and measurement site for each increasing level of stress. Bars denote standard errors of the mean. Variability in pressure (horizontal error bars) is due to inter-subject variability in body dimension and heart-level arterial blood pressure responses to the stresses.

Our data suggest that there are significant differences in peripheral vascular response to the four gravitational stresses, and that these differences are related to the distribution of local vascular transmural blood pressures generated by the stresses. The resulting distinctions are potentially crucial when LBNP and centrifugation are considered

as countermeasures against the cardiovascular deconditioning associated with prolonged exposure to microgravity.

Ames-Moffett contact: A. Hargens
(415) 604-5746
Headquarters program office: OLMSA

Cyclic Skeletal Forces During Daily Activity

Gregory A. Breit, Robert T. Whalen

Theoretical models and experimental studies of bone remodeling indicate that bone density and structure are influenced by local cyclic skeletal tissue stresses and strains, such as those that occur during walking and running in humans. Estimation of long-term habitual loading histories in humans is usually achieved by assessment of physical activity level by questionnaires, logbooks, and portable step counters. These methods provide some indication of the mechanical loading history, but fail to consider the true magnitude of the lower-limb skeletal forces generated by various daily activities. These techniques cannot account for individual gait characteristics, gait speed, and unpredictable high-loading events that may influence bone mass significantly.

We have developed a portable system for long-term monitoring and recording of foot ground reaction forces (GRF). The system consists of an insole force sensor, placed in one shoe, that connects to a compact (5 × 2.5 × 1.5 inches) battery-powered digital data logger worn on a belt around the waist. Every 0.01 second, the GRF from the insole sensor is recorded and analyzed. Using a sophisticated filtering algorithm to extract only significant maxima and minima of the GRF, up to two weeks of cyclic loading data can be stored on the logger's 2-megabyte memory card.

We recently formulated an alternative approach to logging cyclic GRF loads during human gait that overcomes limitations resulting from nonlinearity and fatigue in the force sensors. During walking or running, the principal determinant of peak GRF, from cycle to cycle, is the gait velocity. In general, an increase in gait speed results in higher peak GRF, as well as a concomitant decrease in the amount of time the foot is in contact with the ground. Consequently, we hypothesized that during gait, contact times are reliable indicators of peak GRF and can be used in lieu of direct force measurements to determine cyclic loading histories during daily activity.

For an individual subject, an empirical GRF-contact-time relationship (first figure) was established in the laboratory using an instrumented force plate connected to a microcomputer-based

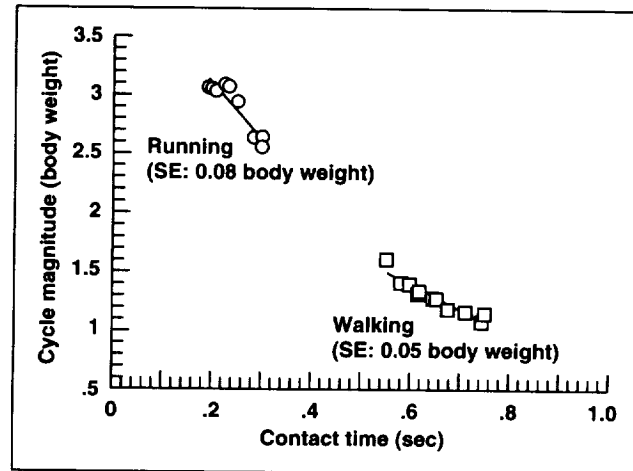


Fig. 1. Empirical relationship between GRF cycle magnitude and foot-ground contact time for walking and running, determined by linear regression of individual cycles over a range of speeds. Regression standard errors (SE) account for typical step-to-step variability in GRF.

data acquisition system. The subject was instructed to walk and run over the plate at a variety of speeds. Gait speed was determined by measurement of transit time between two points of known separation. Because of the disparity between typical contact times for walking (0.5–0.8 seconds) and running (0.1–0.35 seconds), these two types of gait are easily distinguishable on this basis alone. Linear regression equations for peak GRF versus contact time were calculated separately for running and walking. The regression standard error (SE) was noted to account for the normal step-to-step variability of peak GRF.

Subsequently, we used our portable system to record GRF data while the subject walked and jogged outdoors for 40 minutes. A history of the zero-offset cyclic loads (i.e., those cycles that start at zero force, reach a peak, and return to zero) was determined from the data. Furthermore, a step-by-step contact time history was generated by noting all time intervals between upward and downward crossings of a critical GRF level (≥ 0.2 body weight). Each interval

was identified as either walking or running on the basis of its duration, and was converted to an estimated peak GRF by the appropriate regression equation. To simulate the variability of these forces, a Gaussian random number of variance SE^2 was added to each estimated GRF. The true and estimated cyclic loading histograms are shown in the second figure. Discrepancies in step counts between the two are attributed to errors in mapping of histogram bins. An electronic step counter worn during data collection indicated that 2,390 steps were taken; this number differs by 1% from the total of 2,366 found by counting cycles.

With regard to instrumentation, estimation of GRF cycles by means of contact times is an attractive alternative to direct force measurement. The sensor, signal conditioner, and A/D converter in our current system could be replaced by a simple binary switch connected to a single digital input on the microprocessor. As seen in the second figure, the cyclic loading history estimated from contact times matches closely that determined directly from GRF measurements—the distribution means differ by less than the histogram resolution (0.1 body weight). This approach has limitations, however. The technique does not measure static loading, such as that experienced during upright standing. Furthermore, force/contact time calibration data are collected on level ground and may be inappropriate for situations such as stair climbing or walking on inclined surfaces. Nevertheless, the loads believed to have the greatest influence on bone occur during gait over level ground, which minimizes the significance of these limitations.

Current models of bone remodeling identify cyclic loading as a crucial determinant in skeletal adaptation. Accurate determination of long-term GRF histories may be essential to our understanding

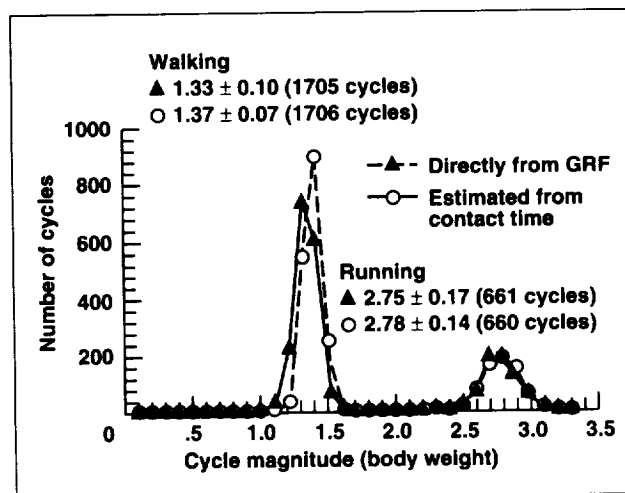


Fig. 2. True and estimated histograms of GRF cycle magnitude for data recorded during 40 minutes of outdoor walking and jogging. Mean \pm standard deviation (in body weights) is given for each phase of each distribution (split at 1.8 body weight).

of the relationship between mechanical loads and bone remodeling and may be a useful approach for examining activity decline with age and its influence on bone density. Our system is able to quantify normal daily standing and walking and to detect the few non-normal walking loading cycles that may contribute to the bone-maintenance stimulus. Monitoring daily GRF histories may also be used to evaluate exercise activities in space to establish loading histories equivalent to Earth activity levels.

Ames-Moffett contact: R. Whalen
(415) 604-3280
Headquarters program office: OSS

Spaceflight and Hindlimb Suspension Affect the Posture and Gait of Rats

Meryl L. Corcoran, Robert A. Fox, Nancy G. Daunton, Emily Morey-Holton

The instability of posture and gait seen in astronauts after spaceflight is thought to result from both (1) atrophy of antigravity muscles induced by unloading of these muscles in microgravity and (2) alterations in neural processing in brain areas involved in control of posture and locomotion, produced during adaptation to the microgravity conditions. To increase our understanding of the neural and molecular processes underlying these effects of microgravity exposure, studies using an animal model with unloading produced by hindlimb suspension (HLS) as well as spaceflight were conducted. To begin this process, the posture and gait of rats were examined after exposure to either spaceflight or HLS, and during recovery from these conditions.

Rats were exposed to spaceflight (STS-58) or to HLS for 14 days. Typical changes in posture induced by exposure to these two different conditions are shown in the first figure. In the first locomotion test conducted after spaceflight (6 hours after touchdown) flight rats walked very slowly with their backs dorsiflexed, their hindlimbs more flexed than in controls, their hindquarters carried significantly lower than normal (all, $p < 0.01$), and their tails dragging. The ankles were extremely dorsiflexed (plantar-extended), producing foot placements characteristic of 10-day-old rather than adult rats. After 2 days of recovery, however, flight animals walked with hindlimbs more extended, rather than more flexed, than control animals, and they now held their hindquarters higher than normal (all, $p < 0.01$). Similar measures obtained after HLS showed that immediately after 14 days of hindlimb unloading, these animals, like the flight rats, walked more slowly than normal animals; however, in contrast to flight rats, HLS rats walked with the back straight or

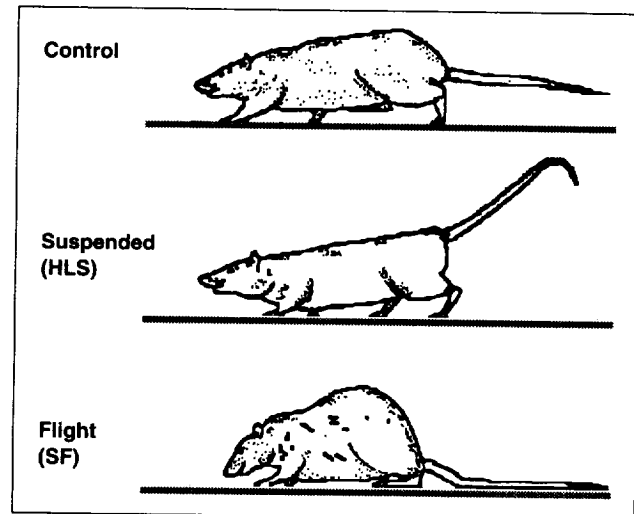


Fig. 1. Typical postures observed in rats immediately after exposure to either spaceflight or unloading of the hindlimbs.

ventroflexed. Immediately after removal from suspension, HLS rats exhibited a posture similar to that of recovering flight animals in that they held their hindquarters higher than normal and they extended their hindlimbs more than control rats did ($p < 0.005$). Both flight and HLS rats walked with a pronounced sinusoidal, vertical oscillation of the pelvic region, a characteristic seldom seen in normal animals. The second figure shows the effects of spaceflight and HLS on one measure of posture during walking (elevation of the hindquarters) obtained shortly after removal from HLS or spaceflight (recovery day 0) as well as during the process of readaptation to normal gravity or loading (recovery days 2–14).

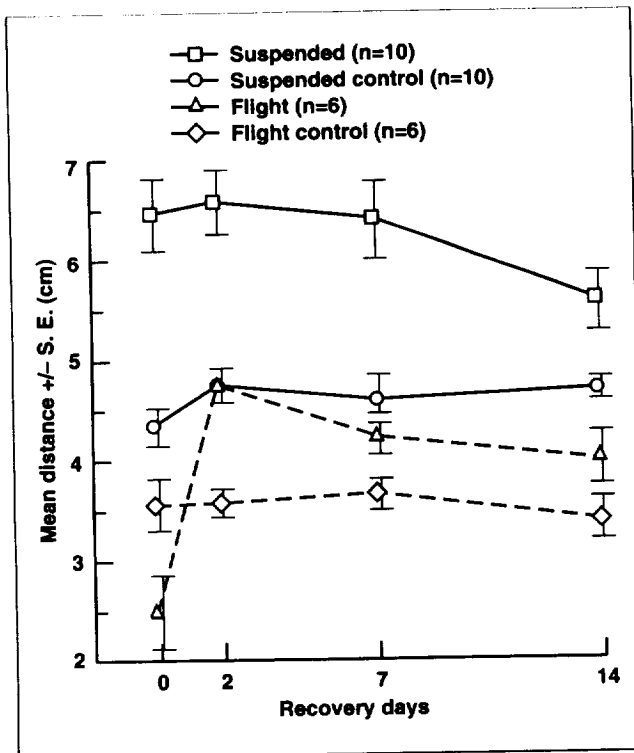


Fig. 2. Elevation of the hindquarters of rats during spontaneous locomotion, measured as the distance from the base of the tail to the surface of the walkway.

The increased elevation of the hindquarters, dorsiflexion of the ankle, and vertical oscillation of the pelvic region observed in rats after flight and HLS may result from an altered balance between flexor and extensor muscles produced by conditions in which the "mechanical use" of weight-bearing muscles is decreased. It has been reported that the atrophic effects observed in flight and suspended rats are muscle specific, with slow extensors (antigravity muscles) most affected, fast extensors moderately affected, and flexors least affected, thus creating the imbalance between flexors and extensors. Some of the documented changes that occur in muscle after spaceflight, including protein changes, may also result in the relative dominance of flexors over extensors. This flexor dominance could produce the alterations in the dynamics of flexion and extension during movements of the hindlimbs that were identified in this study of posture and gait after spaceflight and hindlimb suspension.

Ames-Moffett contact: R. Fox/N. Daunton
(415) 604-4819/4818
Headquarters program office: OSS

Effects of Autonomic Conditioning on Motion Sickness and Physiology

Patricia S. Cowings, William B. Toscano, Neal E. Miller, S. Sekiguchi

More than half of all astronauts suffer from the symptoms of space motion sickness (SMS) during their first few days in space. In recent years, a physiological training procedure, autogenic-feedback training (AFT), has been tested in space as an alternative to anti-motion-sickness medication. The present study shows the effects of AFT on the motion tolerance of five astronauts—three men and two women—with associated changes in physiological responses to stress. In this study, astronauts were to receive 6 hours of AFT within 1 year prior to their space launch. However, because the launch date slipped by 1 year, these crewmembers received an additional 6 hours of training (a total of 12 hours of AFT). Subjects were given four rotating-chair motion

sickness tests separated by 1-week intervals in the first year. The criterion for successful learning was that they be able to tolerate this test for longer periods of time and at higher rotational speeds. The first test was used to determine their initial susceptibility to motion sickness. Training was administered in twelve 30-minute sessions with a total of 2 hours before the second, third, and fourth motion sickness tests. One year later, three additional rotating-chair motion sickness tests were administered to determine how much control of symptoms they had remembered and their rate of "relearning." In the second year, subjects received 2 hours of training before the fifth, sixth, and seventh rotating chair tests.

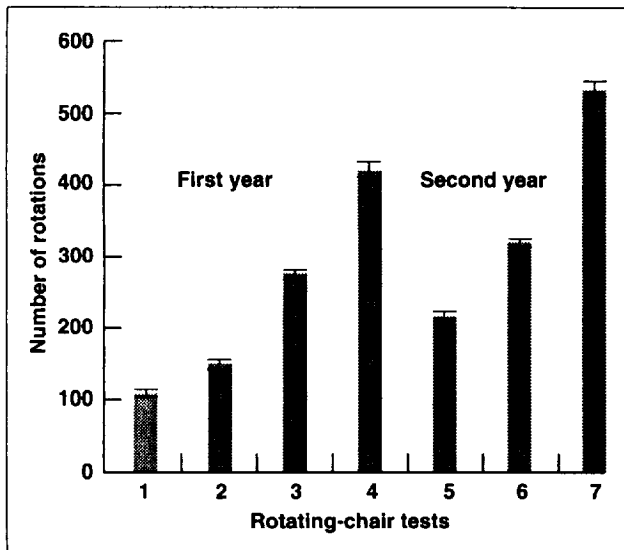


Fig. 1. Average changes in motion sickness tolerance before and after training.

The first figure shows the average number of rotations the crewmembers could tolerate on each rotating chair test (N = 5). The subjects' tolerance improved with training (test 1 versus 4, $p < 0.004$). Even though tolerance was initially lower after a 1-year interval (test 5), subjects were able to relearn control quickly, and had even higher motion tolerance by test 7 than at test 4.

The second figure shows physiological responses of one subject during his first rotating-chair test and after 6 and 12 hours of AFT. The physiological responses measured were blood volume in the hands (blood volume pulse (BVP)), respiration rate (RR), heart rate (HR), and sweating (skin conductance level (SCL)). On each chart, a z score of 0 is the subject's resting response level. Before training, responses change suddenly from baseline at the start of the test (minute 10), but as AFT proceeds, the subject keeps

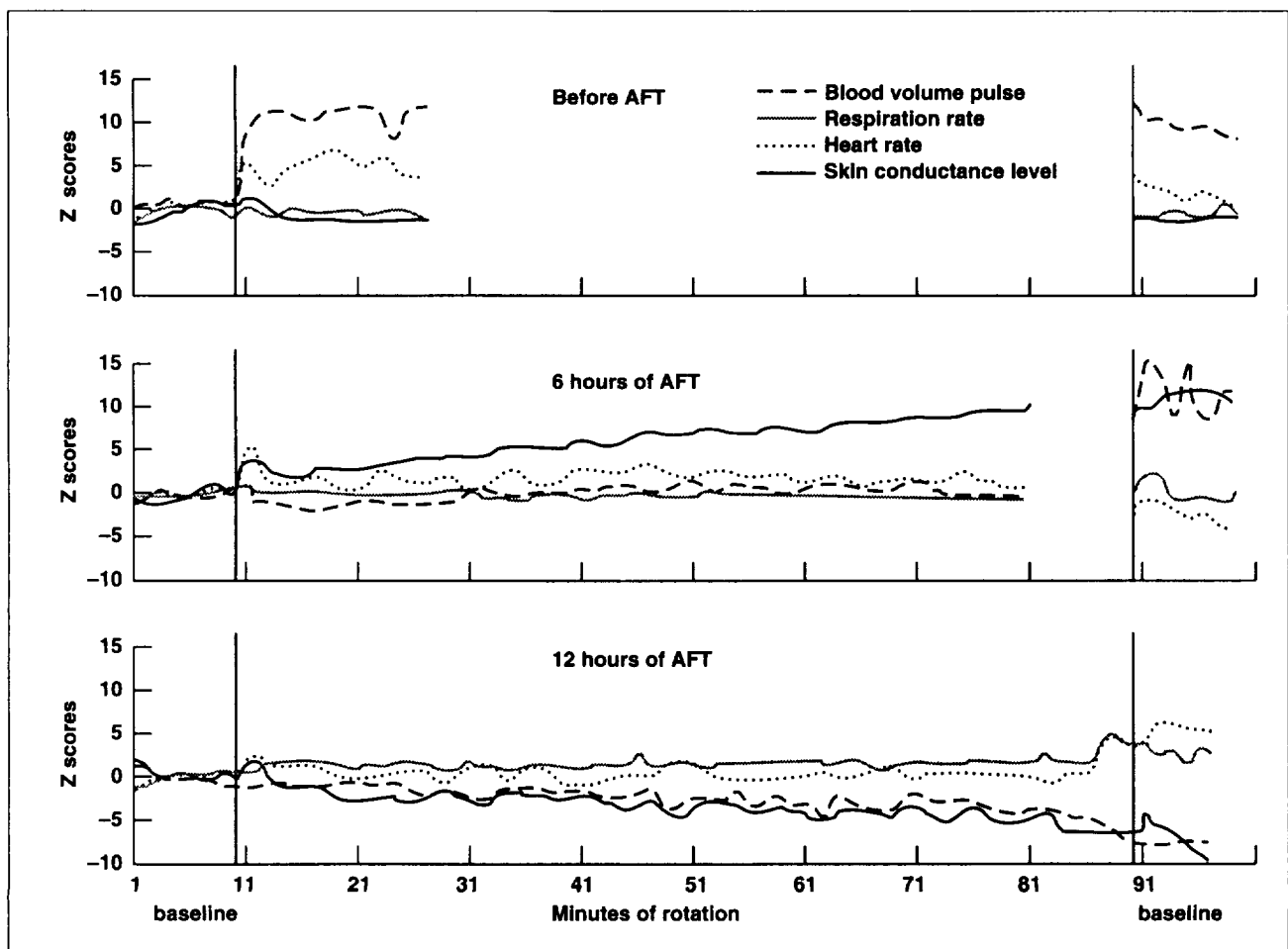


Fig. 2. Physiological responses of one subject during rotating-chair test and after autogenic-feedback training.

levels closer to his or her own baseline for longer periods of time and at higher chair speeds.

These results show that training to control symptoms of motion sickness can be "remembered" for up to 1 year and is rapidly relearned, making this a practical and effective preflight program for astronauts. Furthermore, data from this experiment demonstrate that the greater the ability of the subjects to control their own physiological responses (i.e., maintain them at or near their own optimal baseline), the more effective will be their ability to suppress their own motion sickness symptoms.

Other Earth-based applications of AFT include (1) prevention of airsickness in high-performance

military aircraft; (2) alleviation of low blood pressure and associated fainting in paralyzed patients, diabetics, and others; (3) improvement of crew coordination and communication in multicrew aircraft, leading to reduced risk of human-error accidents; and (4) possible use as a means of suppressing nausea resulting from radiation or chemotherapy in cancer patients.

**Ames-Moffett contact: W. Toscano
(415) 604-5724**

Headquarters program office: OSS

Effects of Promethazine on Performance, Motion Sickness, and Physiology

**Patricia S. Cowings, Cynthia S. Stout, William B. Toscano, Samuel M. Reynoso,
Charles W. DeRoshia, Neal E. Miller**

This study examined the mechanisms by which pharmacological treatments improve motion sickness and space motion sickness tolerance and the impact of these treatments on cognitive function. Twelve men, ages 30 to 40 years, participated in this study. All subjects participated in four 1-day experiments separated by 1-week intervals. The first day was a "training" day (no injection). On the second, third, and fourth experiment days, subjects received a 25- or 50-milligram intramuscular injection of promethazine or a placebo injection. During each daily session, subjects were given four repetitions of three batteries of cognitive tasks. On the training day (day 1), baseline data were collected and subjects were trained to a performance plateau on each task. For the remaining days of the study, the order of drug or placebo injections was counterbalanced; a double-blind procedure was used. Heart rate, respiration rate, skin conductance level, finger pulse volume, and hand temperature were continuously recorded in ambulatory subjects throughout each day (approximately 8 hours). Samples of blood and saliva were also collected. Approximately 4 hours after the injection, a rotating-chair motion sickness test was administered. The first figure shows the group

average scores on two of the performance measures, the Critical Tracking Task and Reaction Time. Performance levels of subjects before the injections (baseline) and after injections at 1 hour, 4 hours, and 6 hours after the rotating-chair motion sickness test ("post-CSSI"), are shown. After injection with either dose of promethazine, the subjects' scores on the tracking task decreased significantly and their reaction time (in milliseconds) was much longer.

Statistically significant reductions in performance were observed for most cognitive and psychomotor tasks after subjects were given 25- or 50-milligram injections of promethazine ($p < 0.01$ compared to placebo). Analyses revealed no significant differences in performance effects between the two doses of promethazine. Regression equations indicated that performance decrements were equivalent to those associated with blood alcohol levels (BAL) of 0.08% for 25 milligrams of promethazine and 0.13% for 50 milligrams. The second figure shows the average motion tolerance of all subjects across days. A significant increase in tolerance to rotating-chair motion sickness tests was found at both doses ($p < 0.03$).

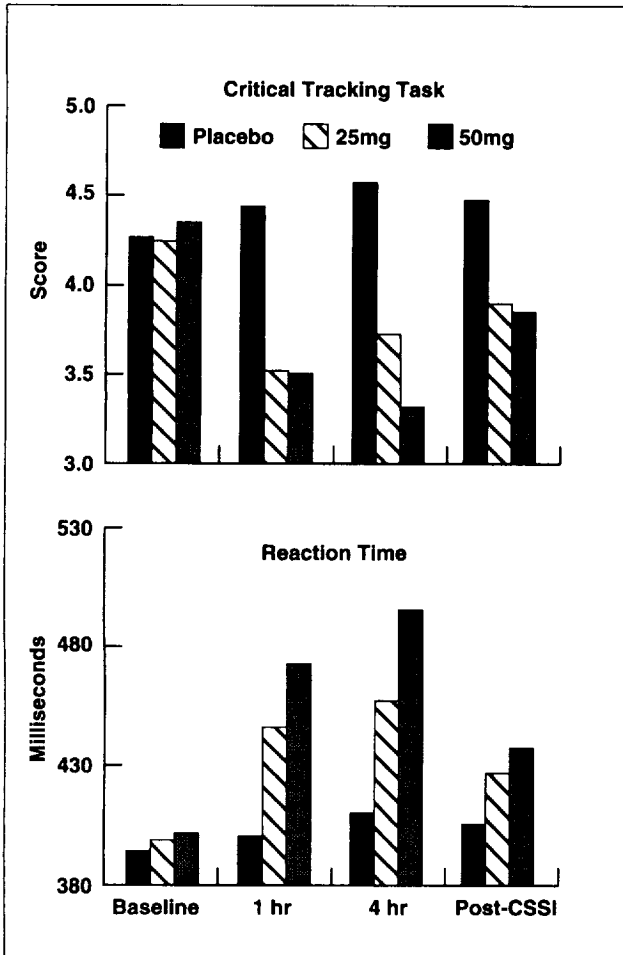


Fig. 1. Effects of promethazine on two cognitive performance tasks.

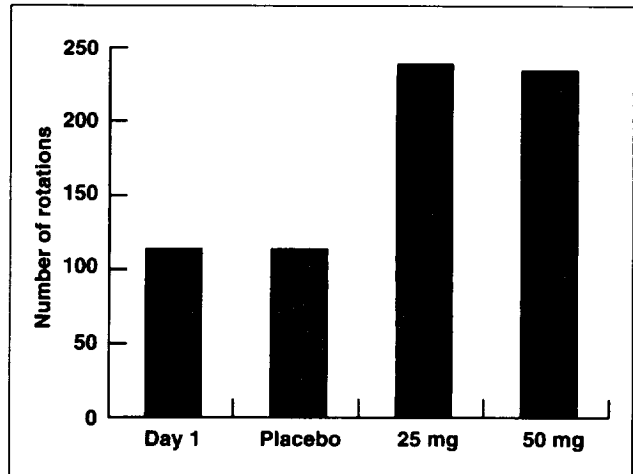


Fig. 2. Effect of promethazine on motion sickness tolerance.

Decreases in motion sickness after medication with promethazine were associated with lower autonomic response levels (e.g., a significant decrease in skin conductance level). Physiological data may be used to identify the subjects most responsive to medication. This work may contribute to the assessment of individual differences in effectiveness of promethazine as a countermeasure for space motion sickness. Our data suggest that doses of promethazine currently used to counteract space motion sickness in crewmembers may significantly impair their operational performance.

Ames-Moffett contact: W. Toscano/C. Stout
 (415) 604-5724/6848
 Headquarters program office: OSS

Potential Treatment for Postflight Low Blood Pressure in Astronauts: Autogenic-Feedback Training

Patricia S. Cowings, William B. Toscano, Neal E. Miller, Thomas G. Pickering, David Shapiro, David Robertson

Postflight orthostatic intolerance (low blood pressure when standing up) has been identified as a serious biomedical problem associated with long-duration exposure to microgravity in space. High priority has been given to the development of countermeasures for this disorder that are both effective and practical. Clinical research has demonstrated that people can be taught to increase their own blood pressure voluntarily and that this is an effective treatment for chronic orthostatic intolerance



Fig. 2. Subject lying on tilt table used to study effects of gravity on blood flow.

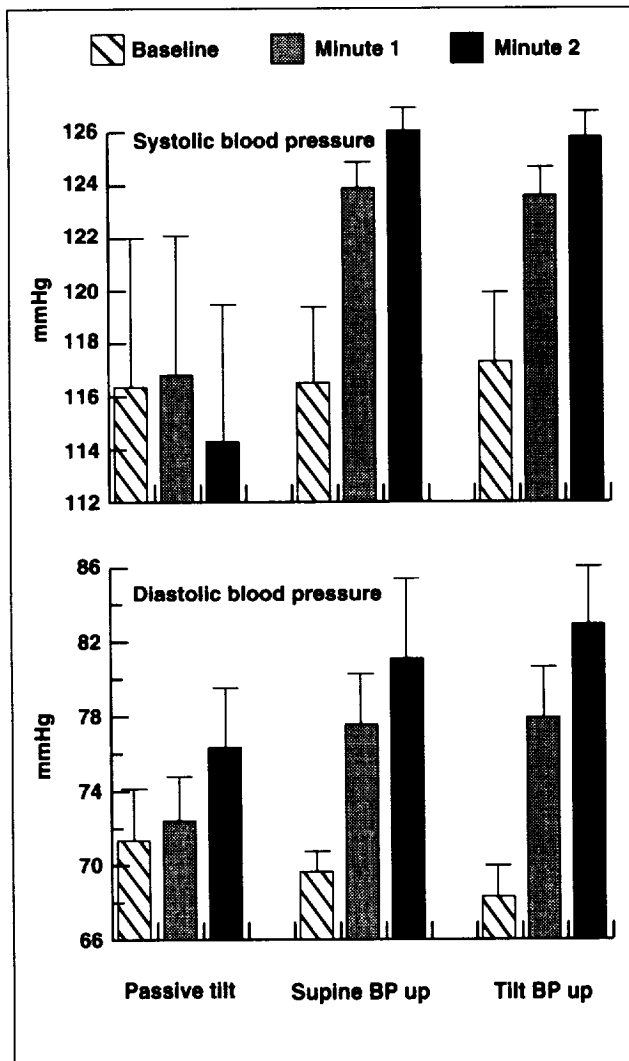


Fig. 1. Effect of autogenic-feedback training on subjects' ability to modify their own blood pressure.

in paralyzed patients. The present pilot study examined the feasibility of adding training in the control of blood pressure to an existing preflight training program designed to facilitate astronauts' adaptation to microgravity. Using an operant-conditioning procedure, autogenic-feedback training (AFT), three men and two women participated in four to nine 15- to 30-minute training sessions. At the end of training, the average increase in systolic and diastolic blood pressure as well as mean arterial pressures that the subjects achieved ranged between 20 and 50 millimeters of mercury under both supine and 45-degree head-up tilt conditions.

The first figure shows the average changes in blood pressure (in millimeters of mercury (mmHg)) achieved by subjects during this study. The bars for baseline are subjects' average blood pressure while lying flat for one minute. When an untrained subject is tilted head-up at a 45-degree angle, the normal response is to show a slight drop in systolic blood pressure (three bars at left in top graph) and a rise in diastolic blood pressure (bottom left set of three bars). After training, subjects can voluntarily raise both systolic and diastolic blood pressure while lying flat on their backs (Supine-AFT) or while

being tilted head-up on the tilt table (Tilt-AFT). Their blood pressure continues to increase over a 2-minute period.

Studies are planned that examine the physiological mechanisms by which learned control of blood pressure is achieved. Noninvasive measures of cardiovascular dynamics (cardiac output, stroke volume, total peripheral resistance) will be added to the measures now used. Optimum training protocols will be developed to implement AFT for orthostatic intolerance into regular astronaut training.

These findings suggest that AFT may be a useful alternative treatment or supplement to existing approaches for preventing postflight orthostatic intolerance. The use of operant-conditioning methods for training cardiovascular responses may contribute to the general understanding of the mechanisms of orthostatic intolerance.

**Ames-Moffett contact: W. Toscano/C. Stout
(415) 604-5724/6848**

Headquarters program office: OSS

Technology Transfer from Spaceflight Research

Philip Davies

The Clinton administration and NASA have repeatedly emphasized the need to identify benefits of space-related research for life on Earth. The Space Life Sciences Payloads Office team at Ames has worked to develop flight technologies, tools, and methodologies that have dual-use functions. The number of spin-off technologies and capabilities generated from spaceflight research has grown steadily, and currently includes commercial, clinical medicine, education, and nonprofit research and development applications.

Spaceflight research in muscle physiology has led to the development of a new nerve staining technique that allows surgeons to more accurately reconnect the nerves in severed limbs. The technique was developed by Danny Riley of the Medical College of Wisconsin during a Spacelab-3 flight investigation on muscle atrophy in rats. The procedure involves the application of enzyme-specific stains to distinguish between sensory and motor nerves. Accurate nerve mapping allows nerve reconnection in a manner that ensures maximum restoration of movement and feeling to reattached limbs. The new process has been patented and will be marketed as a nerve identification kit. In addition to its benefits in limb reattachment, the technique can be used as a diagnostic aid for organ transplants and to correct problems in previous injury repairs.

The diagnostic function is applicable to injuries that may occur in space; it will enable a more accurate assessment of the extent of damage and the urgency for repair.

Another benefit to clinical medicine has been generated by spaceflight research on immune function. Studies with rats have shown that immune system activity is depressed in space. Commercially sponsored payloads have been implemented to test new drugs that stimulate the immune system. The results of several recent secondary payload experiments may lead to the development of a new treatment for use on Earth to bolster a malfunctioning immune system.

The Frog Embryology Experiment on Spacelab-J in 1992 has provided a model for space science education for a range of academic levels. Principles of space science, space biology, and general biology are taught to students nationwide through a combination of lectures, demonstrations, and video media. A CD ROM has been developed and distributed that combines animated simulations, video, and graphics in an interactive framework for use in the classroom; this CD ROM is commercially available. Using the program, students are able to replicate the frog experiment and gain a better understanding about the scientific process, from hypothesis formulation to laboratory operations.

Similarly, the Jellyfish Experiment on SLS-1 is the foundation for one segment (entitled *From Under Sea to Outer Space*) of a three-part video created by Johnson Space Center to stimulate interest in space research and science in general. The video will be available to the public through the Teacher Resource Centers in January 1995.

As a result of work on a biological calorimeter project funded by NASA, H. F. Poppendiek, in association with a research and development organization, has made improvements in direct calorimetry for the measurement of metabolic heat release in animals and humans. Computer programs have been developed to improve the reductions in measurements of the calorimeter systems. Some of these improvements have been commercialized.

A study of swimming behavior of tadpoles returning from spaceflight on Spacelab-J has led to the development of new software for automated events recording. Richard Wassersug and Scott Pronych of Dalhousie University created a three-channel event recorder program, the StopWatch Event Recorder (SER), for optokinetic and other behavioral data collection. Events are recorded by depressing particular keys on a computer keyboard which are assigned to specific activities of the organism. The SER tracks the cumulative time each activity consumes and, upon completion of a trial, calculates the percentage of time partitioned to each activity. SER can export data to other programs to enable statistical analyses and graphic representations of the results. The software is currently available commercially to the behavioral research community.

In 1987, with the support of NASA and the French space agency, CNES, primate scientists at

Georgia State University developed the Psychomotor Test System (PTS). The PTS is a 386-based computer used to generate stimuli displayed on a color monitor which elicit trained responses from a subject through manipulation of a joystick. Automated versions of the classic paradigms used in cognitive psychology, human factors research, and comparative physiology make up some of the varied task demands.

Originally developed as a methodology for collecting spaceflight data on various aspects of behavior and performance, and for providing a source of enrichment for captive primates, the PTS has generated spin-off applications that are being put to use on Earth. The PTS is being used in studies of basic comparative cognition. In this application, the PTS has been successfully used with a variety of primates, including humans, at more than 30 laboratories worldwide, and has been cited in more than 50 peer-reviewed science publications. In addition, the PTS has been used to benefit mentally or verbally handicapped children. The computer-facilitated nonverbal tasks have proved effective in examining capabilities in perceptual-motor, cognitive learning, and neuropsychological function. The creators of the PTS have shown that school-aged children with some cognitive dysfunction can learn to perform the tasks independently.

**Ames-Moffett contact: P. Davies/K. Souza
(415) 604-3608/5736**

Headquarters program office: OLMSA

Hyperhydration Fluids for Astronauts

John E. Greenleaf, R. Looft-Wilson, C. D. Jensen, James H. Whittam

Astronauts exposed to microgravity incur chronic reduction of body water (hypohydration) from their cellular and extracellular (interstitial and plasma) fluid compartments. This hypohydration may compromise astronauts' performance during reentry and contribute to the "reentry syndrome" which includes fatigue and dizziness or disorientation when an astronaut tries to stand immediately after landing. One countermeasure for the reentry syndrome is to provide fluid/electrolyte drinks to hyperhydrate astronauts a few hours before reentry. Formulations consumed inflight include fruit drinks, salt (NaCl) tablets and water, and various other saline solutions, including bouillon.

This study of four new fluid formulations (see table) was designed to test the hypothesis that drink composition is more important than drink osmolality for maintaining and increasing plasma volume at rest and during exercise.

Each of six men (22–39 years old) underwent six treatment regimens during which they sat for 90 minutes with an oxygen uptake of 0.4 liters per minute and then performed 70 minutes of sitting cycle ergometer exercise with an oxygen uptake of 2.1 liters per minute (70% of maximal oxygen uptake (see figure)). Fluid formulations were consumed intermittently during "rest" (the first 90 minutes) (768 milliliters) and during exercise (768 milliliters). No fluid (0) was consumed during rest with treatments 5 and 6. The performance 1 formulation (P1) was consumed during exercise with treatments 1–5; no fluid was consumed in treatment 6.

Percent change in plasma volume at rest (left half of figure) increased significantly only with P1 (by 5%) and HyperAde (HA) (by 7%). Plasma volume decreased with onset of exercise with all treatments and then increased toward baseline as

Table 1. Composition of Fluid Formulations

Formulation	Sodium, mEq/L	Osmolality, mOsm/kg HO	Glycerol, mg/dL	Glucose, mg/dL	Citrate, mg/dL
Performance 1 (P1)	55	365	2	2,049	416
Performance 2 (P2)	97	791	4	3,579	753
Performance 2G (P2G)	113	1,382	2,916	3,543	731
HyperAde (HA)	164	253	1	1	854

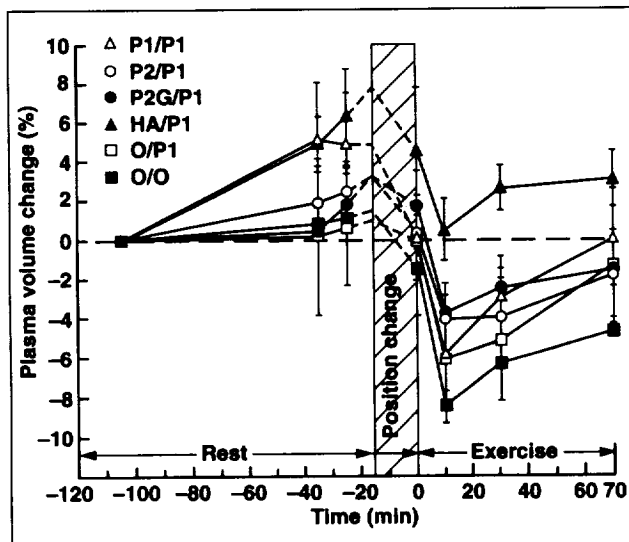


Fig. 1. Percent change in plasma volume (mean \pm standard error) during rest and exercise for the six treatment regimens.

exercise progressed (right half of figure). Plasma volume decreased most with O/P1 and O/O, and increased most with HA/P1. Thus, formulation HA, with 164 milliequivalents per liter sodium and the lowest osmolality (253 milliosmoles), maintained plasma volume best at rest and during exercise, whereas the other formulations, with lower sodium (55–113 milliequivalents per liter) and higher osmolality (365–1,382 milliosmoles) did not respond as well. It appears that sodium content of a drink is more important than its total osmotic content for increasing plasma volume at rest and maintaining it during exercise. This study was supported by NASA Grant 199-18-12-07 and Shaklee Grant JSRA-7.

Ames-Moffett contact: J. Greenleaf
 (415) 604-6604
 Headquarters program office: OLMSA

Force and Mammalian Cells

Rosalind A. Grymes

The Cellular and Molecular Biology Laboratory at Ames Research Center studies the physical forces (including gravity) that affect specific mammalian cell behaviors. A cell interacts with the extracellular matrix through transmembrane integrins, and contacts neighboring cells through transmembrane cadherins. Membrane connections between the cell and its environment are tethered to internal cytoskeletal filament systems which supply structural integrity and mediate the dynamic intracellular force balance. Physical interconnectivity creates meta-level tissue and organ architectures from the building blocks of cellular structures. The architectures of living systems, composed of cells and extracellular matrix molecules, experience both compression and contraction strains. Dermal (skin) fibroblasts undergo both stretch and flexure; endothelial (blood-vessel lining) cells are exposed to strong blood flow pulses;

osteoblasts (bone cells) are sensitive to both structural and load-bearing forces; and muscle cells provide both contraction and support strength. Research in the domains of extracellular matrix biology, tissue engineering, and signal transduction has demonstrated the importance of cell shape and intra- and extracellular tension balance in the determination and regulation of cell behavior.

We have previously demonstrated that dermal fibroblasts act as finely tuned force sensors when grown on flexible disks and subjected to mechanical strain. The resultant force vector lines can be calculated and represented diagrammatically (first figure, part (a)). Over roughly 70% of the flexible disk, the pattern observed is symmetric and radially distributed. At the edges of the disk, the pattern is turbulent and circular. Cultured dermal fibroblasts position

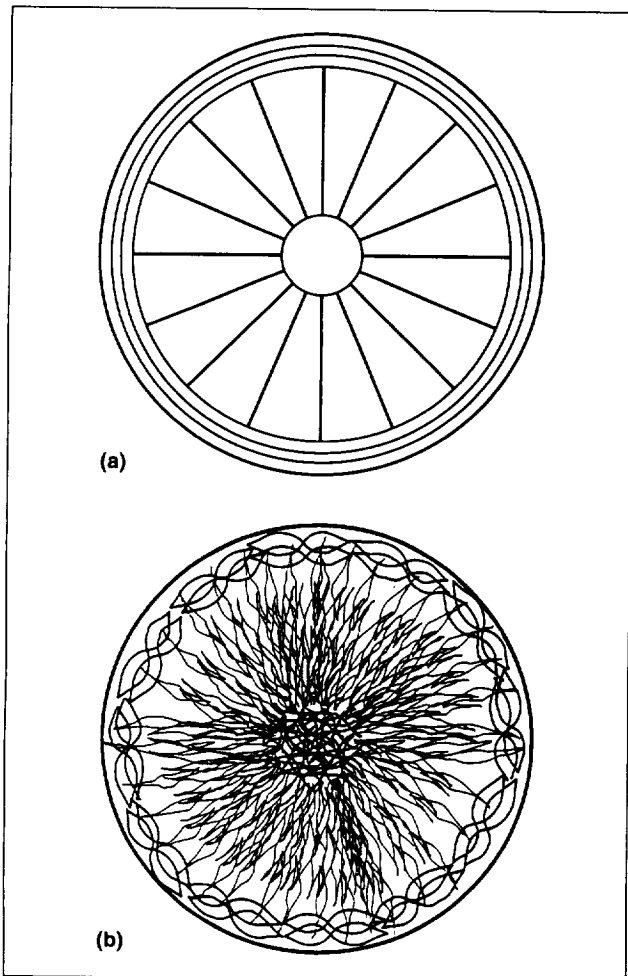


Fig. 1. Force alignment diagrams. (a) Force vector lines occasioned by the application of a mechanical stretch to the flexible disk. The force is applied by pulling down from the center of the disk, which leads to a biaxial stretch that creates a gradient of strain along the radial lines indicated, and circumferential strain at the edges of the disk. At the center of the disk, strain is minimal. (b) The characteristic response of cells cultured on the stretch disk.

themselves exactly in accord with these vectors, demonstrating exquisite sensitivity in interpolating and responding to applied force (first figure, part (b)). To evaluate the factors affecting this behavior, it is necessary to add quantitative measurement to these striking visual observations. The theory behind our method for quantifying morphological changes is explained in part (a) of the second figure, and the

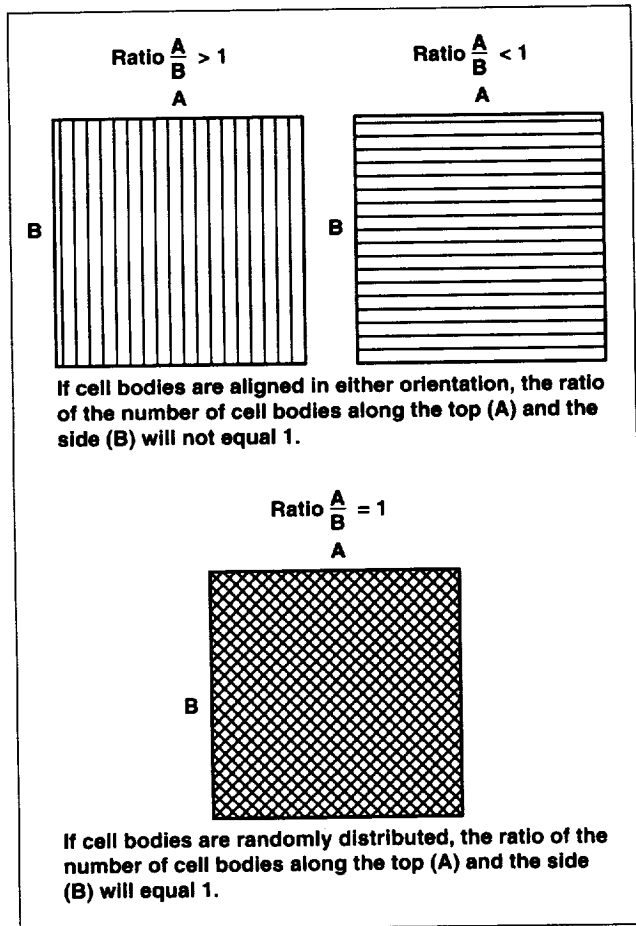
results of quantifying an alignment study are shown in part (b). Comparison of the integers assigned to unstretched control cultures and symmetrically arranged stretched cultures shows a significant difference ($P < 0.05$, Student's t-test).

We have studied the role of the actin cytoskeletal network in cellular realignment, and have extended these studies to include the intermediate filament and microtubule structural networks. These systems can be disrupted using polymerization inhibitors, and then the ability of treated cultures to realign in response to applied mechanical force can be evaluated. Intermediate filaments are also involved in the cellular response to force, whereas microtubules appear not to play a role. Thus, microtubules are compression resistance elements, and intermediate filaments and actin microfilaments distribute tensional stress.

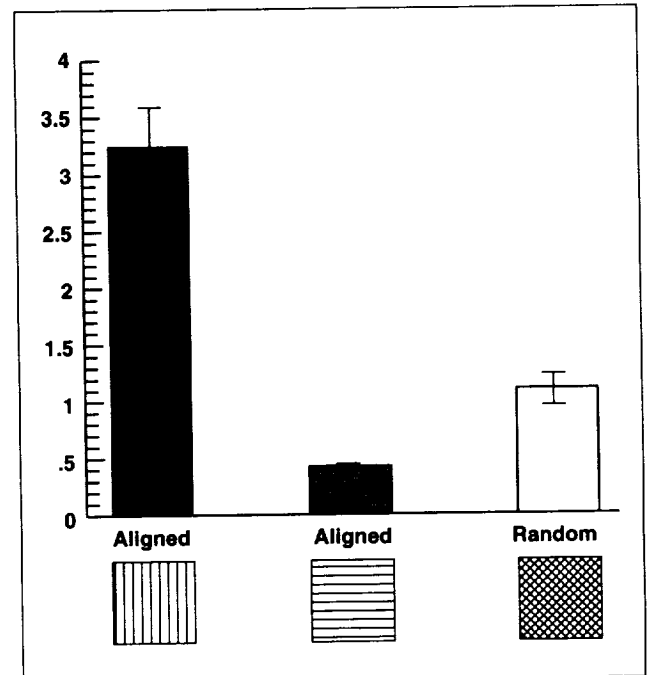
We are also investigating the role of extracellular matrix (ECM) connectivity by cultivating cells on flexible disks coated with individual ECM molecules, including synthetic versions that contain specific repeated binding sites. Preliminary work indicates that the aligned cells produce their own matrix, which contains "tracks" of alignment that can be used by freshly added cells. Some of the directional information, then, is provided by the trail produced by stretched cells.

Our collaborator Andrew O. Martinez of the University of Texas (San Antonio) discovered a new research direction for his collection of normal, mutant, and transformed cells while resident in our laboratory. We were able to identify transformed and mutant cells that had lost the ability to align in response to applied mechanical stretch, and to correlate this behavior with their pattern of expression of cell surface markers. Among the characteristics of tumor cells are the ability to form spheroids and abnormal solid masses and the ability to dissociate from normal architectures and metastasize. We are investigating the relationship between the loss of normal force perception and alignment response and the acquisition of the transformed phenotype.

Our collaborator Barbara Johnson-Wint of the University of Northern Illinois examined the hypothesis that fibroblasts respond to external force by exerting their own force on the ECM molecule collagen type I, either directly through



(a)



(b)

Fig. 2. Quantitation of alignment. (a) Possible outcomes of the extreme cases of cell alignment, and the case of random cell distribution. We have applied counting grids to photomicrographs of experimental and control cultures, and counted the number of cell bodies crossing sides A and B of the grid. By counting six independent grid areas per photograph, we are able to determine a ratio A/B and an accompanying standard deviation. (b) Results of such a quantification study (significant at $P < 0.05$ (Student's *t*-test)).

integrin-actin-myosin connections or by cell-cell attachments involving cadherins. She made use of our facilities for the application of vectorially averaged gravitational, rotational, and hypergravitational forces. Using chemical agents that disrupt polymerization of cytoskeletal networks and binding site blockers for integrins and cadherins, she demonstrated combinatorial roles for cytoskeletal and

transmembrane components in the active contraction of collagen by cells.

**Ames-Moffett contact: R. Grymes
(415) 604-3239
Headquarters program office: OSS**

Small Payloads Flown on Space Shuttle Missions

Joellen Jarvi

In fiscal year 1994, NASA Ames Research Center managed three life sciences secondary-payload missions. These included National Institutes of Health.Cells.1 (NIH.C1) on STS-59, IMMUNE.-1 on STS-60, and the Physiological Systems Experiment (PSE).04 on STS-62.

NIH.C1

NIH.C1, formerly known as Space Tissue Loss-4 (STL-4), was part of an 11-day mission launched 9 April 1994. It was the first in a series of experiments jointly selected and supported by NASA and the National Institutes of Health (NIH). This payload was the first of three involving the Institute of Arthritis and Musculoskeletal Diseases. The objectives of this series were to determine if muscle or bone cells in culture are influenced by gravity and, if so, to determine the functional aspects of exposure to microgravity.

The NIH.C1 payload comprised three experiments, which shared the STL hardware developed by Walter Reed Army Institute of Research. This was the fourth flight of the STL hardware, a completely automated cell culture facility that fits inside a single middeck locker. The unit has four rails (compartments), each housing four to six hollow fiber bioreactor cell cartridges. The STL hardware provides a typical cell incubator environment and, although not used on this mission, automated inflight media exchange or injection of fixatives.

The individual objectives of the three investigations on NIH.C1 were (1) to investigate where and how the observed defect in bone mineralization and architecture occur by comparing the maturation rates and the mineralization process of the cells in flight and on the ground; (2) to examine whether gene expression is altered by spaceflight as evidenced by a previous finding that space-flown myoblasts do not fuse after return to Earth gravity; and (3) in support of the objective of the first experiment, to investigate bone maturation rates at two different cell culture ages to help elucidate the point at which the defect in bone occurs.

The mission had varying degrees of success. Because of mechanical problems, some of the cultures did not yield viable cells upon return to Earth. Preliminary results for the successful cultures indicate that primary rat osteoblasts exposed to spaceflight may be metabolically less active than ground controls; less glucose is consumed and less lactic acid is produced by flight cultures than by control cultures. In addition, morphological differences are evident. Exposure to spaceflight appears to reduce the amount of rough endoplasmic reticulum and causes the formation of numerous ill defined vacuoles. These samples are undergoing further analysis.

IMMUNE-1

IMMUNE-1, launched 3 February 1994, was an experiment sponsored by BioServe Space Technologies, a NASA Center for the Commercial Development of Space. The commercial partner in the investigation was the Chiron Corporation. The goal of the 8-day experiment was to reduce or prevent changes seen in the immune system of rats after exposure to spaceflight, through drug administration. A drug compound similar to the commercially available Interleukin-2, commonly used as an immune system stimulant, was administered to six rats housed in an Animal Enclosure Module (AEM). (A second AEM contained an equal number of rats given a placebo.) The treatment compound was polyethylene-glycol-modified recombinant human interleukin-2, (or PEG-IL-2), a longer-lasting immune stimulant than Interleukin-2 (which must be injected up to three times daily in standard treatment protocols with humans). It was hoped that PEG-IL-2 would reduce or prevent the suppression of the immune system previously documented in space-flown rats.

The results are being analyzed and will be published shortly. If found effective, PEG-IL-2 may become part of a standard treatment protocol for aging people who show decreased levels of natural interleukin-2. This new form of recombinant human

interleukin-2 could be used along with flu shots to amplify the immune system.

PSE.04

A related study was carried out on PSE.04, the fourth payload sponsored by the Center for Cell Research at Pennsylvania State University. This class of missions was designed to evaluate pharmaceutical, agricultural, or biotechnological products. The goal for the 8-day mission was to study the sophisticated and complex relationship between the immune and skeletal systems during exposure to microgravity.

The results of previous PSE flights have shown that musculoskeletal and immune system functions are impaired soon after exposure to spaceflight. This dual impairment occurs in certain disease conditions on Earth as well, suggesting that the physiological controls are interconnected. PSE.04 was designed to test this hypothesis by application of a specific pharmaceutical capable of modulating both bone

and immune systems simultaneously. The compound was administered to 6 of 12 adult rats before they were loaded into two flight AEMs. An equal number of control animals was treated similarly and placed into two AEMs on the ground, after a 24-hour delay. This delayed synchronization of flight and ground operations ensured that the ground animals were exposed to the same environmental variations seen by flight animals.

The results of this investigation can not yet be publicly disclosed due to the proprietary nature of the PSE series of experiments. The results of this experiment could aid in the treatment of Earth-based disorders of the musculoskeletal system.

Ames-Moffett contact: J. Jarvi

(415) 604-5682

Headquarters program office: OLMSA

Evaluation of Structural and Material Properties of Long Bones

A noninvasive method of determining three-dimensional structural properties of long bones may be useful to model the growth and loading history. Such a technique could effectively monitor effects of disuse, as in spaceflight or after spinal cord injury, or overuse in intensive exercise. It could be useful in clinical assessment of fracture risk in paraplegics, quadriplegics, and people with osteoporosis. The objective of our research is to assess whether a noninvasive determination of cross-sectional areal properties of long bones, using only the mineral component of bone, accurately predicts the true structural properties. In this study, section properties of pairs of embalmed human tibiae were compared using two methods: (1) special analysis of bone densitometry data and (2) experimental determination of flexural rigidities from bone surface strain measurements during controlled loading.

Noninvasive bone densitometry scans of each tibia were taken using a Hologic QDR-1000/W densitometer. Three scans were taken of the entire

BethAnn Katz, Tammy M. Cleek, Robert T. Whalen

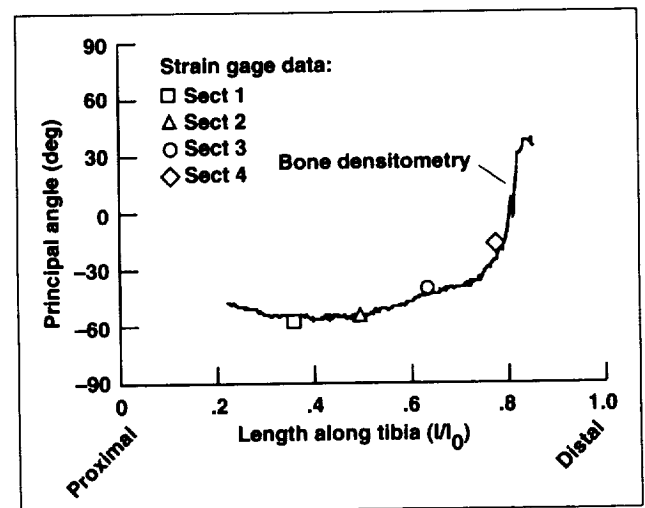


Fig. 1. Correlation of (1) principal major axis orientation (in degrees) at four cross sections from strain measurements with (2) trace of principal major axis orientation along the length of the tibia calculated from densitometry.

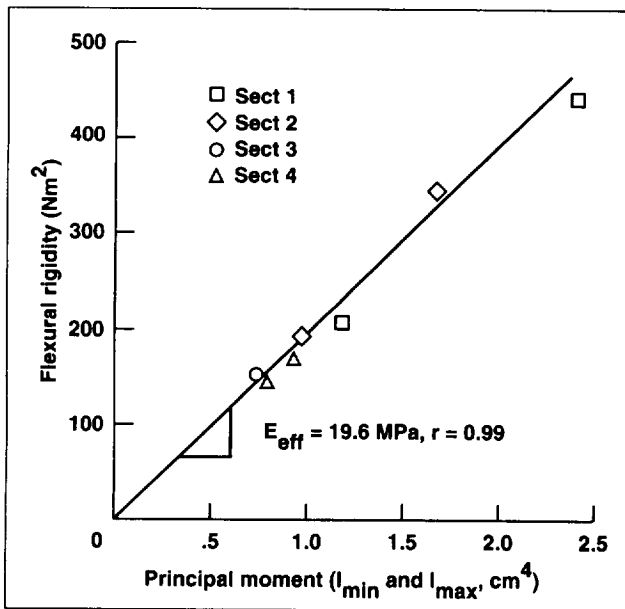


Fig. 2. Principal flexural rigidities (in newton-meters squared) from strain gage measurements versus minimum and maximum principal moments of inertia (in centimeters to the fourth power) from densitometry. Slope E_{eff} (effective elastic modulus, in megapascals) is calibrated to aluminum.

tibia at rotations of 0, 45, and -45 degrees about the bone's long axis. Pixel attenuation data from the high-energy beam were converted to equivalent aluminum thicknesses using an aluminum calibration wedge and the converted data were used to compute section properties, line by line, for each of the scans. Cross-sectional area, centroid, and the second moment of area of the mineralized tissue in the plane of the x-ray beam were computed by integrating pixel bone mineral content (or equivalent aluminum thickness) across the scan. The principal area moments of inertia and orientation of the principal major axis at each line, i.e., bone section, were determined by combining the areal properties obtained from the independent analyses of the three noncoplanar scans. Section properties from

individual cross sections of the bone were then combined to form a whole-bone structural model.

After the scanning, four single-element strain gages, aligned along the long axis of the tibia, were bonded uniformly around the circumference at each of four cross sections. A known load producing a known bending moment at each cross section was hung vertically from the distal end of each tibia. Strain data were recorded from all strain gages as the bone was rotated through 360 degrees in 45-degree increments. To compute principal flexural rigidities, curvatures were computed from strain data, then the section centroid was calculated from curvatures and strains, and section principal flexural rigidities about the centroid were derived from simultaneous solution of equations using the known curvatures and known bending moments.

In our preliminary results, the agreement between the two methods was excellent. The principal major axis orientation computed from bone densitometry agreed well with that from surface strain measurements, as shown in the first figure. The second figure indicates that the principal area moments of inertia of bone mineral were linearly related to the principal flexural rigidities, indicating a good correlation between the two methods and a reasonably consistent measure of the flexural modulus between each of the four sections and between the two bones. The isotropy indices (the ratio of minimum to maximum principal moments and principal flexural rigidities) were also very similar at each of the four bone sections. We conclude that a noninvasive bone densitometry approach, analyzing only the mineral component of bone, may be a highly accurate and effective way to measure changes in bone mineral distribution related to aging, disuse, spinal cord injury, exercise, or spaceflight.

**Ames-Moffett contact: R. Whalen
(415) 604-3280
Headquarters program office: OSS**

Cardiovascular Responses of Snakes to Hypergravity

Harvey B. Lillywhite, Richard E. Ballard, Alan R. Hargens

During exposure of humans to microgravity, all hydrostatic blood pressure gradients are lost, tissues of the legs become dehydrated while those of the head and neck become swollen, and plasma volume decreases. After return to normal gravity, blood shifts to the lower extremities, which may cause fainting (orthostatic intolerance). Despite widespread recognition of cardiovascular changes in altered gravitational environments, these changes are not well understood. They are a concern for current short-duration Shuttle missions and pose significant problems for future, longer-duration spaceflights. To address these problems, attention must be given to understanding cardiovascular changes and their underlying mechanisms in a sensitive animal model.

Snakes are good animal models for investigations of cardiovascular adaptation because of their elongate body form and diverse behavioral ecology. William Harvey first recognized the utility of snakes in cardiovascular studies more than 3 centuries ago. Snakes are unique in the extent and range of their cardiovascular adaptations to gravity. Regulatory responses of climbing snakes to upright posture resemble those of humans to upright standing, and the gravitational problems experienced by nonclimbing species of snakes resemble problems of humans after cardiovascular deconditioning during microgravity or bed rest. Cardiovascular adaptation to gravity is an integral part of the responses of these animals to changes in gravitational environment, and therefore invites further study.

The purpose of this study was to evaluate cardiovascular adjustments of yellow rat snakes to hypergravity. We hypothesized that acclimation to hypergravity increases cardiovascular performance and tolerance to gravity in a semiarboreal snake. Yellow rat snakes were exposed to a $+1.5 G_z$ (1.5 times the force of gravity in the head-to-tail direction) centrifugal force on a 2.4-meter-diameter centrifuge for 30 minutes, three times a day, for a period of 3 months. Control animals were acclimated to normal horizontal posture.

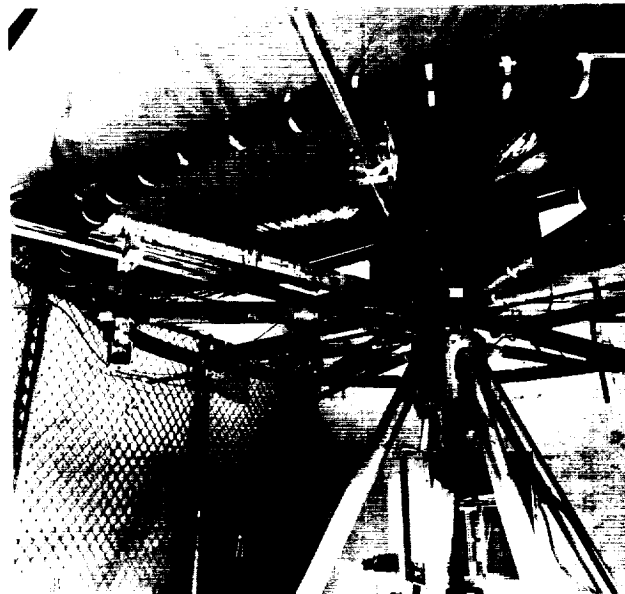


Fig. 1. Yellow rat snakes on the NASA Ames 8-foot-diameter centrifuge.

After the 3-month acclimation period, both control and acclimated snakes tolerated acute exposure to acceleration forces exceeding $+3.0 G_z$. Tolerance to increased gravity was quantified as the equivalent gravitational force at which headward blood flow ceased. Acclimated snakes showed higher G_z tolerance, greater increases of heart rate in response to head-up tilt and acceleration, greater increase of blood pressure in response to circulating norepinephrine, lower plasma and whole blood volumes, and greater levels of circulating substances that control blood pressure and flow. The adjusted mean G_z tolerances for control and acclimated snakes were 2.37 and 2.84, respectively, which correspond to the 0.5-G difference between chronic centrifugation stress ($+1.5 G_z$) and Earth gravity.

As in other vertebrates, G_z tolerance in snakes is enhanced by acclimation, short body length, high arterial pressure, and large blood volume. Body

movements are also important for promoting headward blood flow at the higher levels of G_z stress. The description of cardiovascular function presented here provides a clear example of compensatory physiological adjustments to hypergravity. These studies in snakes are significant because of the sensitivity of these animals to the effects of gravity on blood

pressure and circulation, and the potential application of these models to human spaceflight.

**Ames-Moffett contact: R. Ballard/A. Hargens
(415) 604-5747/5746**

Headquarters program office: OLMSA

International Microgravity Laboratory-2 Mission

Chris Maese

The International Microgravity Laboratory-2 (IML-2) was an international cooperative program that enabled scientists from around the world to investigate various phenomena in the microgravity and life sciences research areas. It was the second Spacelab mission carrying life sciences experiments managed by NASA Ames Research Center during fiscal year 1994. The flight of IML-2, launched 8 July 1994 on STS-65, was the longest Shuttle mission so far, with a duration of nearly 15 days in space. The two Ames-managed experiments involved the study of gravity receptor development in newts and jellyfish.

Embryos of the Japanese red-bellied newt were used to study how gravity-sensing organs located in the middle ear develop in microgravity. Groups of newt eggs laid at various intervals prior to launch were attached to special trays and placed in three cassettes (48 eggs each) in the Aquatic Animal Experiment Unit (AAEU) developed by the Japanese Space Agency, NASDA. As its name indicates, the AAEU provides life support for aquatic or semi-aquatic organisms within Spacelab. It consists of two independent systems: four individual enclosures for animals—in this case, newts; and a water tank for fish. The crew can observe and videotape the animals through a window, and can access the animals through a separate port on each enclosure.

Once in flight, the 144 eggs, which occupied the same cassettes as the adult newts, were observed at various times to determine their developmental status. After only a short time in flight, one of the adults died and the chamber holding the still viable

eggs was removed from the unit to avoid possible contamination of the other cassettes. These 48 eggs were lost. A second adult newt died later in the flight, but in this instance the crew was instructed to remove the dead animal and replace the cassette still containing 48 viable eggs in the AAEU. In the case of the third cassette, the experiment proceeded without incident. Some casualties occurred in the remaining 96 eggs, leaving a total of 62 live newts available for the postflight analyses. Most of the larvae were preserved at various postflight intervals for histological analyses of otoconia development; a few were kept alive as a reserve.

Initial examination of the surviving flight larvae showed no apparent differences from ground control specimens in the rate of overall development. In the flight larvae, the hind limbs appeared to be farther along in development than the forelimbs. The gills of flight larvae appeared to be slightly stunted compared to those of the controls. These results are based upon preliminary observation and can only be confirmed after careful examination of the fixed tissues is completed.

The German built NIZEMI Slow Rotating Centrifuge Microscope was the key hardware used to carry out the objectives of the Jellyfish experiment. Using the NIZEMI, scientists can observe both living and nonliving matter exposed to levels of gravity ranging from 10^{-3} to 1.5 gravitational unit.

The two-stage *Aurelia* jellyfish was used to determine gravity thresholds both in ground-developed ephyrae (the free-swimming stage) and in

ephyrae metamorphosed from polyps (the sedentary stage) while in flight. The gravity-sensing organs were removed from subsamples of the ground-developed ephyrae, used for the flight and control studies, in order to compare their behavioral response to varying gravitational forces with the behavior of those having gravity sensors intact. Some specimens were fixed in flight, others were returned alive.

Analysis of the in-flight videos taken at various gravitational levels and the histological examinations

of the gravity receptor organs are proceeding. It is hoped that the results of this experiment will help to clarify the effects of microgravity on developmental processes of animals and the role of gravity in the behavioral and developmental responses of organisms on Earth.

Ames-Moffett contact: C. Maese

(415) 604-6633

Headquarters program office: OLMSA

From Neurons to Robots

Muriel D. Ross

A major challenge in the development of expert systems and intelligent robots is the application of knowledge of the neuronal circuitry used by human brains in problem solving and in discovery, to improve system design. Workers in the field of artificial neural networks have made admirable progress in producing systems that, for example, can identify faces or navigate robots over steep terrain. However, these systems currently lack the creativity that lends versatility to human behavior or the decision-making capability that improves the possibility of survival in unfamiliar environments.

A relevant topic under study in the Biocomputation Center at Ames is gravity-sensor neuronal circuitry. Mammalian gravity sensors represent the simplest form of the complex circuitry that characterizes higher neural centers such as the retina of the eye and the outer surface (the cortex) of the brain. Gaining knowledge of this circuitry and its functions has many useful applications: in space exploration, to better understand the implications of space adaptation syndrome; in clinical medicine, to better understand disease; and in the field of expert system design, to make the systems more versatile and autonomous.

Our present knowledge of gravity sensor circuitry is the product of space research focused on understanding gravity sensor capacity for change in an altered gravitational environment. Each gravity sensor (humans have a total of four, two on each side of the

head) is a linear bioaccelerometer and is designed much like the accelerometers designed by engineers. Each sensor consists of a test mass of tiny crystallites that is loosely connected to an underlying patch of neuronal detectors which, in turn, is attached by connective tissue to the temporal bone of the skull. During head acceleration, whether from gravity or as a result of linear motion such as is experienced in an elevator, the neuronal detectors move with the skull but the crystallites lag behind. This difference in motion of the two parts stimulates the detecting units and indicates the direction and magnitude of linear acceleration at any moment in time. It is the function of the neuronal circuits to decode this input and then to recode it as useful information for transmission to the central nervous system. There, the information is used to help maintain posture and balance.

To carry out their functions, gravity sensors have two kinds of circuits. The circuits process information in parallel, but their outputs are intertwined so that neither circuit alone is responsible for providing information to the central nervous system. This is an important point. In the "direct" circuit, the detectors (type I neurons) communicate only with the expanded nerve fiber terminal (calyx) that nearly surrounds them (see figure). In the "local" circuit, the detectors (type II neurons) distribute their output to several nearby terminals (calyces or branches of calyces or nerve fibers). Communication from the

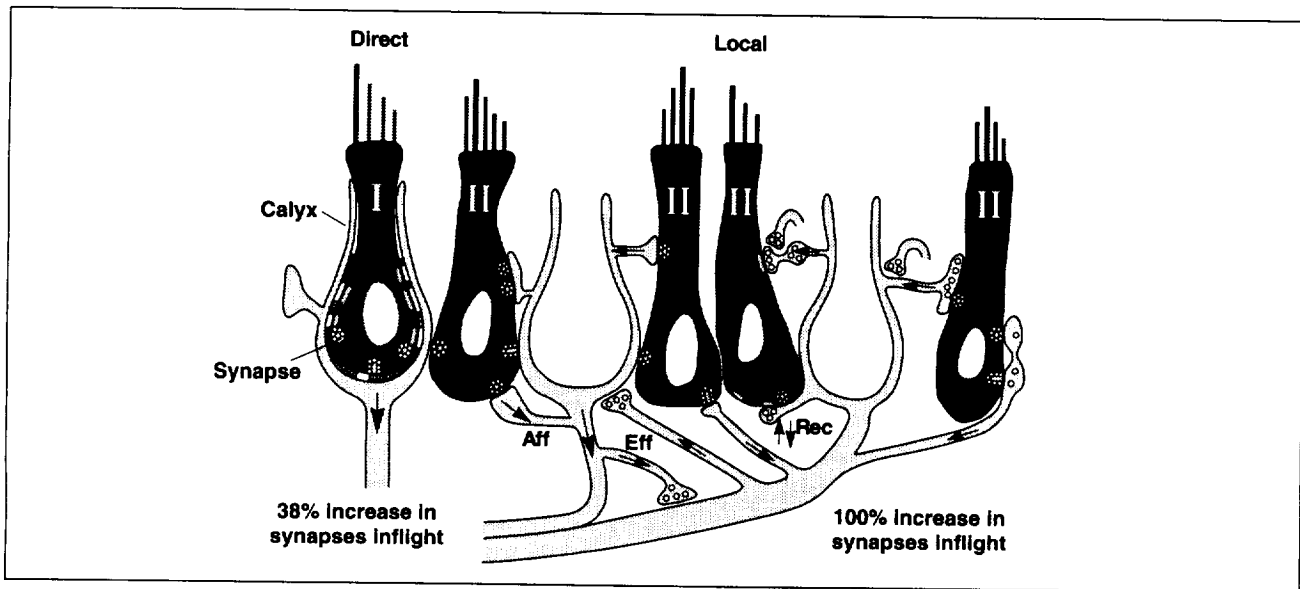


Fig. 1. Basic organization of a gravity sensor into direct and local circuits. *Aff* = afferent or feedforward connection; *eff* = efferent or feedback connection; *rec* = reciprocal connection—both feedforward and feedback synapses at the same site. The arrows indicate the direction of information flow in the circuitry.

detecting neurons to the nerve fiber terminals is called "feedforward." However, some of the nerve fiber terminals bring information back to the type II cells to modify their output (this is "feedback"). Feedforward–feedback loops and local circuit modification of the final output characterize all neuronal systems in mammals, including the human brain. The fundamental organization is the same.

Space research has provided insight into some of the functions of the circuits. It was proposed more than 20 years ago that local circuits of higher neuronal systems would be those most subject to change in an altered environment, and could be involved in memory and learning. Space research has verified this hypothesis. Sites of communication between neurons (synapses) increase in number in the microgravity of space, particularly in the local

circuits. This finding, incorporated into computer simulations of a functioning gravity sensor, is beginning to shed light on the interactions between the two circuits. Studies of simple neuronal systems such as gravity sensors will provide us with insight into the normal activities and integrative functions of direct and local neuronal circuits. This information should enhance the development of more intelligent, autonomous robots for the scientific exploration of space and for the study of hostile environments on Earth.

Ames-Moffett contact: M. Ross
(415) 604-4804
Headquarters program office: OSS

Space Life Sciences-2 Mission

Paul D. Savage

Space Life Sciences-2 (SLS-2), a 14-day mission that was launched 18 October 1993 on STS-58, was one of two successful life sciences Spacelab missions managed by Ames Research Center in fiscal year 1994. Under a Biospecimen Sharing Plan (BSP), rat biosamples were made available to scientists around the world: the final payload complement consisted of the 6 primary U.S. investigators and 26 BSP investigators (15 Russian, 7 French, and 4 Japanese) who represented 39 separate scientific studies.

A key feature of SLS-2 was the new capability to carry out in-flight dissection and fixation of tissues. Until the SLS-2 mission, flight rats had to be returned alive to the investigators before they could be euthanized and their tissues extracted and preserved for analysis. This procedure made it difficult to isolate the effects of microgravity from those of reentry, landing, and reexposure to Earth gravity; sometimes several hours elapsed before analyses could begin. In addition to the in-flight tissue samples requested by the primary investigators, samples were made available to the BSP scientists.

A total of 48 rats were housed in two Research Animal Holding Facilities. A General Purpose Work Station provided an enclosed, laminar-flow workbench for two crewpersons to jointly carry out the in-flight operations on the animals. Dissections of six rats were carried out just before the end of the mission on flight day 13. Tissues were preserved in the manner requested by the investigators.

Four mammalian physiological systems were represented in the experiments aboard SLS-2: vestibular, skeletal, muscular, and hematological. A description of the main goals of the primary studies follows.

The in-flight dissections were critical in the examination of the impact of microgravity on the vestibular apparatus. Because of the adaptive elasticity of the vestibular system, spaceflight-induced physiological changes are rapidly reversed upon reexposure to Earth gravity. It is hoped that results of the histological examinations of the vestibular tissues obtained during flight will provide information

regarding structural changes and associated expression of space motion sickness seen in astronauts.

Studies of spaceflight-related changes in bone mineralization and resorption processes were aided by the administration of nonradioactive calcium isotope to a subgroup of rats soon after their exposure to microgravity. The results of these investigations may help clarify when, how, and where changes occur to bone, and how quickly and to what extent bone recovers after return to Earth.

Two studies focused on the nature and progression of spaceflight-induced atrophy of muscle and the associated functional aspects. The results may reveal the cellular and metabolic bases for the observed deterioration in muscle structure and endurance in microgravity. The knowledge gained from these studies should help in determining the appropriate combination of countermeasures (e.g., weight-bearing exercise and hormone therapy) necessary to maintain normal muscle mass and strength in microgravity, and to minimize the deleterious effects of return to Earth gravity. The studies also have applications on Earth in the treatment of muscle atrophy and functional disorders related to disuse.

The fourth area of the primary investigations was the hematological response to spaceflight. Two investigations were designed to accomplish two basic goals. The first was to quantify the changes in the various aspects of erythropoiesis and blood volume that have been observed on previous missions. The second goal was to determine the suitability of the rat model for studying the changes in erythropoiesis that occur in humans in space. The results of these studies should reveal the sequence and degree of changes to red blood cell kinetics and production rates that occur in space and whether these changes persist postflight.

Ames-Moffett contact: P. Savage

(415) 604-5940

Headquarters program office: OLMSA

Effective Presentation of Motion Information in Aerospace Display Systems

Leland S. Stone, Preeti Verghese

Advanced display systems, such as those used by air traffic controllers or shuttle flight controllers, are being designed to present greater quantities of information to human operators with the assumption that all the information is usable. However, human visual capacity is not unlimited, and the information presented is not necessarily absorbed. In order to design more effective display systems, one needs a greater quantitative understanding of how well humans can process multiple pieces of visual information presented simultaneously.

In collaboration with the Vision Group of the Aerospace Human Factors Division at Ames, we have measured the ability of humans to combine information from multiple moving display icons. We measured human ability to discriminate differences in speed between groups of moving icons presented in two temporal intervals. Within each interval all of the icons moved at the same speed. Subjects were asked to judge in which interval the icons moved more quickly. The figure is a plot of performance data (normalized threshold) of four subjects as a function of the number of icons (N) in the group. The idea is that, although the multiple icons in this special case provide redundant information, if all the information is absorbed and used optimally, thresholds should improve by the square root of N by simple averaging. The graph shows that when the number of icons was increased, mean performance did indeed improve—i.e., discrimination thresholds were reduced. When the multiple moving icons are presented simultaneously at different locations in a display, humans combine this information to improve their performance (squares). However, comparison of the human data with simulations of the optimal model (long dashes) shows that the improvement in performance is less than optimal. We have proposed an alternate model (short dashes) that combines the information non-optimally and that has been used previously to successfully predict human detection ability. This

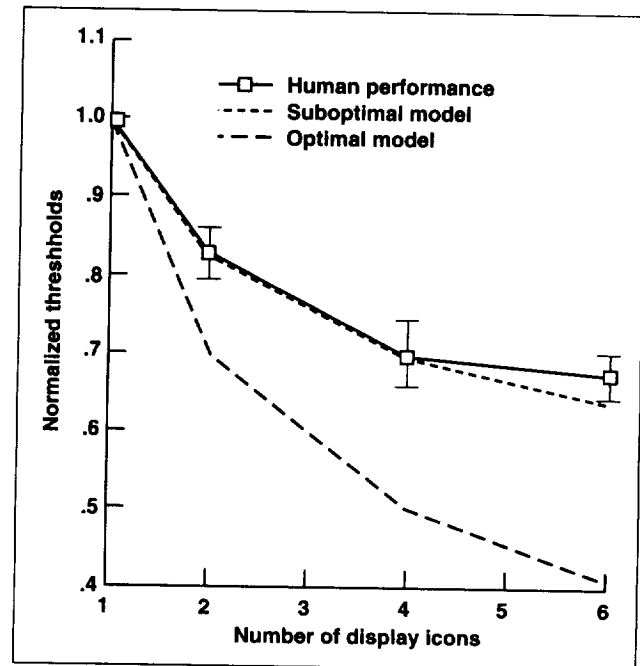


Fig. 1. Performance of human subjects in a task to discriminate differences in speed of moving icons on a visual display.

suboptimal model better explains performance in our speed discrimination task; we are in the process of examining this promising model in other paradigms.

The development of quantitative models of human visual information processing is critical for the design of effective and efficient display systems. The displaying of unusable information is potentially dangerous because critical information may not be processed, and is wasteful because displaying unusable information squanders resources.

**Ames-Moffett contact: L. Stone
(415) 604-3240**

Headquarters program office: OSS

Noninvasive Measurement of Human Eye Movements

Leland S. Stone, Brent R. Beutter, Philippe A. Stassart

Microgravity causes an adaptation of the neural responses to visual-vestibular stimuli. Because adaptation is associated with diminished performance and potentially dangerous performance errors, a number of flight experiments have examined visually and vestibularly driven eye movements preflight, in flight, and postflight. However, the resolution has been less than optimal and NASA's mission to understand the effect of gravity on visual-vestibular interactions would benefit greatly from the availability of a high-resolution yet inexpensive and noninvasive human eye tracker.

In collaboration with the Vision Group of the Aerospace Human Factors Division at Ames, we obtained a commercially available infrared 60-hertz video-based tracker system and, through careful calibration and optical magnification, set up the system so that the stated optimal spatial resolution of less than 0.2 degree is readily achievable. Furthermore, in collaboration with ISCAN, Inc., and JC Labs, Inc., we are refining the system to provide 240-hertz temporal sampling which will allow for the full bandwidth of human eye movements. We are now examining smooth-pursuit eye movement responses to visual motion. The figure shows the eye movement response to a pattern that moved briefly downward and to the left beginning at time = 100 milliseconds. After a delay, a small (less than 2-degree amplitude) smooth-pursuit response is initiated. The raw data traces illustrate that we can measure the direction of pursuit with an angular resolution of a few degrees, even for small eye movements, without averaging. We have also developed software that automatically detects saccades (small, jerky movements of the eyes as they jump from one fixation point to another). The vertical line in the figure indicates where this algorithm reported the onset of a saccade. We can use this marker to analyze the saccade and smooth-pursuit responses separately without resorting to the standard subjective techniques. This enhanced

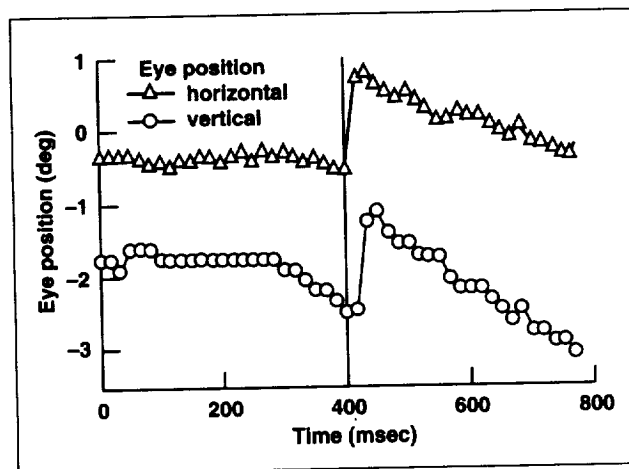


Fig. 1. Eye movement response to a moving pattern.

tracker system and its associated calibration and analysis software will allow us to address scientific questions with nearly the same spatial and temporal resolution as that obtained using expensive, bulky, invasive eye-tracker systems.

Human eye movement responses have long been used to examine the underlying neural processing of visual and/or vestibular signals. More precise measurements of the effect of altered gravity on eye movements will give a better understanding of neural adaptation to spaceflight. Our specific aim is to provide noninvasive eye-tracker technology with adequate resolution for state-of-the-art scientific measurements, suitable for transition to flight hardware. The ultimate goal is the reduction of performance errors through the design of more effective countermeasures, including scientifically based training paradigms or compensatory display systems.

**Ames-Moffett contact: L. Stone
(415) 604-3240**

Headquarters program office: OSS

Spinal Lengthening in Simulated Microgravity

Jorma R. Styf, Richard E. Ballard, Donald E. Watenpaugh, Klaus P. Fechner, Alan R. Hargens

Astronauts experience total-body height increases of 4 to 7 centimeters in microgravity. Thus, stretching of the spinal cord, nerve roots, and muscle and connective tissues may be responsible for the lower back pain commonly associated with life in microgravity. Whereas 6-degree head-down tilt (HDT) is a common model for simulating cardiovascular effects of spaceflight, axial compression (foot to head) of the spine makes HDT alone unsuitable for simulating spinal acclimation to microgravity. Axial compression can be counteracted by balanced traction consisting of 10% body weight ($\sin 6^\circ = 10\%$) applied to the legs. The purpose of this study was to evaluate the effects of 6-degree HDT with balanced traction on spinal elongation and back pain.

Six healthy male subjects (aged 33–43 years, height 175–188 centimeters, weight 69.5–99.1 kilograms) underwent 3 days each of 6-degree HDT with balanced traction and horizontal bed rest (HBR) with a 2-week recovery period between treatments (crossover design). Total-body and spine length, lumbar disc height, and back pain were measured before, during, and after each treatment. Total-body (head to feet) and spine (seventh cervical vertebra to

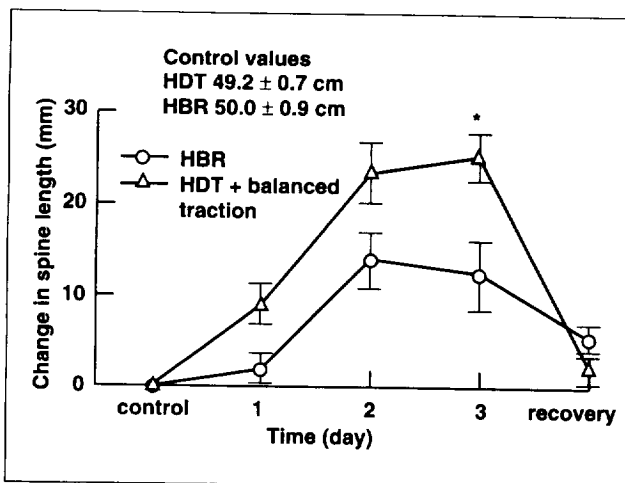


Fig. 1. Spine length increased more during head-down tilt (HDT) with balanced traction than during horizontal bed rest (HBR). * = greater than corresponding HBR value.

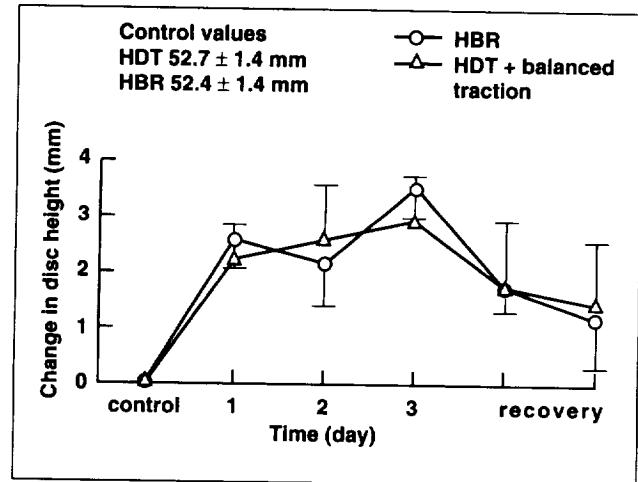


Fig. 2. Lumbar disc height increased significantly from baseline values, but there was no difference between treatments.

sacrum) lengths were measured with a tape measure. Lumbar intervertebral disc height (sum of two discs) was measured with ultrasonography. Back pain intensity was measured on a visual analog scale.

The first figure shows that spine length increased significantly more during HDT with balanced traction (25 ± 2 millimeters, mean \pm standard error) than during HBR (12 ± 4 millimeters). Total-body length also increased more during HDT with balanced traction than during HBR. The second figure shows that lumbar intervertebral disc height increased significantly in both treatments to the same degree (2.9 ± 0.8 millimeters, HDT with balanced traction; 3.3 ± 0.6 millimeters, HBR). Subjects experienced significantly greater back pain during HDT with balanced traction than during HBR.

Whereas neither model increased height to the magnitude observed in microgravity, HDT with balanced traction more closely simulated the spinal elongation and back pain reported by astronauts in microgravity. Spinal elongation can occur through either an increase in disc height or a decrease in spinal curvature. The observation that total-body and

spinal lengths increased more with HDT with traction than with HBR, whereas disc height increases were similar between the two forms of bed rest, suggests that greater spinal flattening (loss of curvature) occurred during HDT with traction than during HBR. Therefore, loss of spinal curvature may contribute to the relatively greater back pain intensity experienced during HDT with traction, and may also be important

in generation of back pain in microgravity. (Richard Ballard received honorable mention for this research in the annual student competition of the American Society for Gravitational and Space Biology.)

**Ames-Moffett contact: R. Ballard/A. Hargens
(415) 604-5747/5746
Headquarters program office: OLMSA**

Autonomic Responses to Microgravity

In space, the absence of gravity alone causes unique physiological stress. This paper describes a biomedical monitoring system designed to measure astronaut physiological responses in space and to investigate individual differences in adaptation to this unique environment. The objectives of this study were (1) to study the effects of microgravity on human autonomic nervous system (ANS) responses; (2) to compare ANS responses in flight to data collected during ground-based mission simulations; and (3) to examine the ANS characteristics of early adaptation to space.

The first figure shows a crewmember wearing an ambulatory physiological monitoring system, the Autogenic Feedback System-2 (AFS-2). This self-contained, battery-operated system allowed crewmembers to record and display (on a wrist display unit) their own heart rate, respiration rate, sweating responses (skin conductance level (SCL)), and blood flow to their hands (skin temperature and blood volume pulse (BVP)), continuously during waking hours in space (approximately 12 hours per day).

William B. Toscano, Patricia S. Cowings, Neal E. Miller

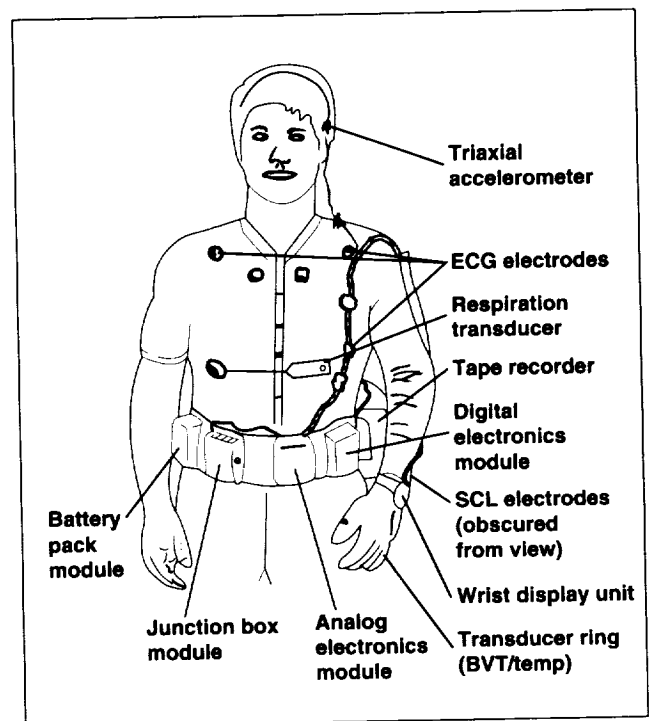


Fig. 1. The Autogenic Feedback System-2 (AFS-2).

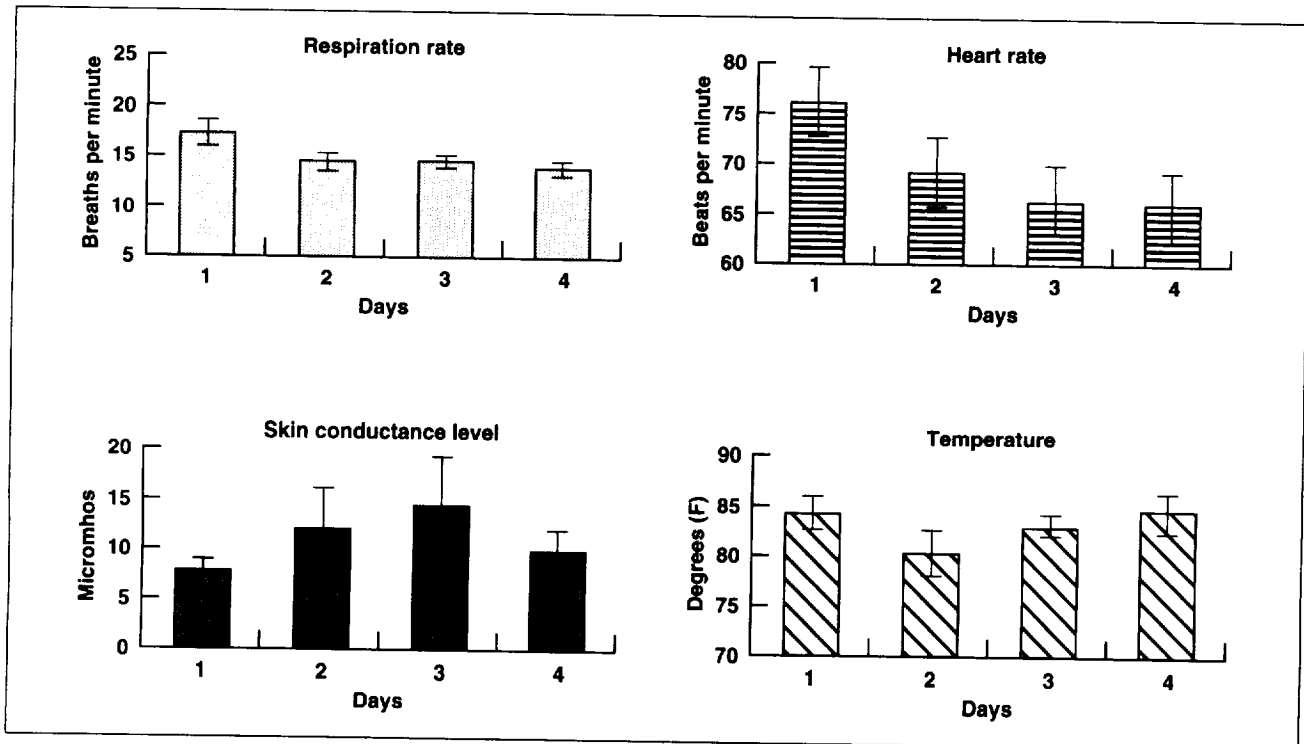


Fig. 2. Average physiological response levels during 4 days in space ($N = 6$).

The second figure shows the daily average levels of physiological responses recorded by these crewmembers in space. Both heart rate and respiration rate decreased significantly from day to day ($p < 0.05$). When these responses were compared to ground-based data collected during a simulation of mission day 2, heart rate was found to be significantly lower in space than on Earth ($p < 0.007$). Changes in all response levels of individual subjects were found to reflect episodes of space motion sickness as well as individual differences in the rate of adaptation to space over days.

It was concluded that the AFS-2 provides an effective means of studying ANS responses to the unique environment in space and that these data can be used to determine the effectiveness of behavioral (e.g., exercise) and pharmacological

(e.g., anti-motion-sickness drugs) treatments aimed at facilitating adaptation of astronauts to microgravity and their readaptation to Earth.

Other Earth-based uses of the AFS-2 include (1) long-term ambulatory monitoring of patients to enable better diagnosis (e.g., of cancer patients); (2) monitoring operator responses in aircraft and ground vehicles; and (3) recording and assessing the effects of environmental stressors, workload, and fatigue on human performance (e.g., in air traffic controllers).

**Ames-Moffett contact: P. Cowings/W. Toscano
(415) 604-5724**

Headquarters program office: OSS

Heart Rate Variability During Early Adaptation to Space

William B. Toscano, Patricia S. Cowings, Neal E. Miller

Approximately half of all astronauts suffer from symptoms of space motion sickness (SMS) ranging from mild discomfort to repeated vomiting. A wide range of autonomic nervous system (ANS) responses to laboratory induced motion sickness have been reported in animals and humans. These include a variety of vasomotor, cardiac, gastrointestinal and respiratory reactions. However, it is not known whether these autonomic perturbations are also characteristic of SMS.

In a recent study, prominent low-frequency (<0.03 hertz) heart rate oscillations were observed in two astronauts during periods of severe SMS. This observation led to the hypothesis that there may be individual differences in neurologic control of such responses as heart rate variability in space. These individual differences may be useful in determining if a person is likely to adapt well to space and which countermeasures (such as autonomic feedback training (AFT) or medications designed to facilitate adaptation) are most effective.

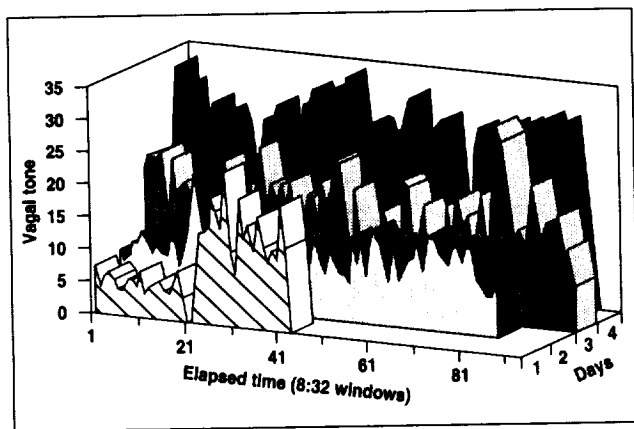


Fig. 1. Cardiac vagal tone during spaceflight. Daily electrocardiograph recordings were divided into contiguous "windows," each covering a period of 8 minutes 32 seconds; estimates of vagal tone were derived for each window.

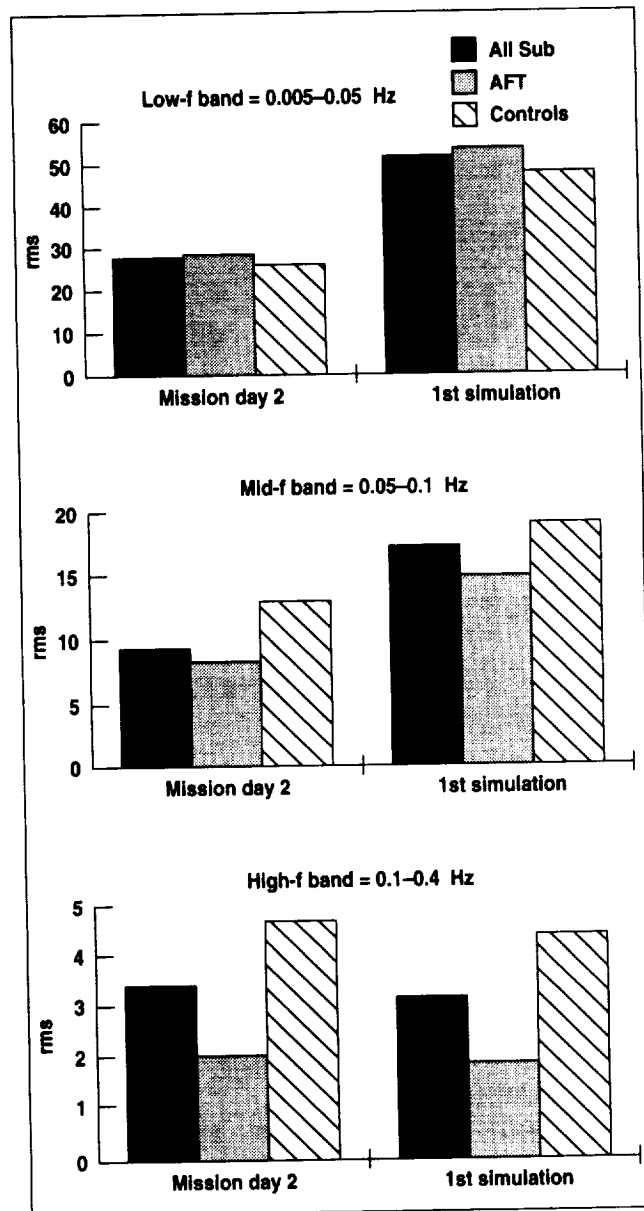


Fig. 2. Average heart rate variability in space compared to that during Earth-based simulation.

This report describes the preliminary results of a Shuttle flight experiment in which AFT, a physiological conditioning method, was tested as a treatment for space motion sickness. The objectives of this study were (1) to investigate changes in patterns of heart rate variance (e.g., low-frequency oscillations) during early adaptation to space (i.e., when subjects are symptomatic and after recovery from sickness); (2) to compare heart rate variability in space with data collected on Earth during mission simulations; and (3) to examine the effects of behavioral (e.g., AFT) and pharmacological treatments on heart rate variability and space motion sickness.

The first figure shows changes in cardiac vagal tone of one astronaut over 4 days of spaceflight. In this crewmember (who suffered only mild symptoms, on day 1, in space) vagal tone increased steadily over the days.

The second figure shows heart rate variability in all subjects (N = 6) and compares the AFT (N = 3)

and control (N = 3) subjects. The average root-mean-square power of each frequency band collected on mission day two in space is compared to that of a simulation of mission day two performed by crewmembers in a mock shuttle prior to the actual flight. Clearly, in the low- and mid-frequency bands the magnitude of these responses is reduced in space compared to their magnitude on Earth. Although there is not enough data (only six subjects) to determine if there are statistically significant differences between the AFT and control subjects, the trend of the data indicates that this is the case. AFT given for control of heart rate, respiration, and other ANS activity influenced both the vagal control measures and the SMS symptoms experienced.

**Ames-Moffett contact: W. Toscano
(415) 604-5724**

Headquarters program office: OSS

Gravity Simulation and Redistribution of Body Fluids

Donald E. Watenpugh, Gregory A. Breit, Richard E. Ballard, Gita Murthy, Alan R. Hargens

Gravity creates blood pressure gradients that cause a tendency of blood to pool in the legs and feet during upright posture. Therefore, anatomic and physiologic mechanisms have been evolved to maintain cerebral perfusion by preventing excessive blood accumulation in the lower body. Microgravity (lack of gravitational stimulation) "deconditions" some of these mechanisms: human space travelers often experience an inability to stand after spaceflight. Centrifugation and lower-body negative pressure (LBNP) have been proposed for simulating the effects of gravity during long-term existence in microgravity, and thus preventing microgravity-induced deconditioning. Based upon a theoretical analysis of relative gravitational stress, we hypothesized that the magnitude of upper-to-lower-body fluid redistribution and tachycardia would be increased by gravitational stressors in the following

order: short-arm centrifugation (SAC), long-arm centrifugation (LAC), head-up tilt (HUT, normal gravity), and LBNP.

For comparison, the various stimuli were standardized to produce a peak of 1 gravitational unit (G_z) of force at the level of the feet. For each gravitational stimulus, 0 to 1 G_z was produced in human volunteers in 30-second, 0.2- G_z steps, with 10-second transitions between steps. Supine 100-millimeter-of-mercury (mmHg) LBNP generates footward force and produces blood pressures in the foot approximately equal to 1 G_z (90-degree HUT), so 20-mmHg-LBNP steps were employed to reach the peak level of 100 mmHg. Fifteen subjects gave informed consent to participate (8 males, 7 females; aged 23 to 49 years (median = 31 years); weight 66.6 ± 10.2 kilograms (mean \pm standard deviation);

height 171 ± 8 centimeters. We employed liquid metal-in-rubber strain gauges to measure volume changes of the neck, thigh, and calf during exposure to the various gravitational stimuli. Heart rate was measured by cardiometry. Finger arterial blood pressure at heart level was measured with a Finapres device (Ohmeda, Inc.). Control measurements were made while subjects were supine.

All gravitational stimuli reduced neck volume and increased leg volume. The first figure shows that SAC and LAC elicited similar increases in thigh volume at $1 G_z$ ($2.3\% \pm 0.4\%$ and $2.1\% \pm 0.1\%$, respectively (mean \pm standard error), whereas LBNP consistently increased thigh volume more than other gravitational stimuli at similar levels. A paradoxical 0.6% reduction in thigh volume occurred between 0.8 and $1.0 G_z$ HUT. There was no reduction in thigh volume with increasing G_z in any of the other conditions. Responses at the calf were similar to, although less definitive than, those seen at the thigh. Neck volume decreased less during HUT than during the other stimuli. The second figure shows that heart rate increased similarly during HUT (18 ± 2 beats per minute) and LAC (12 ± 2 beats per minute), and exhibited still greater elevation during LBNP (29 ± 4 beats per minute), yet did not increase during SAC. HUT at $1 G_z$ increased central arterial blood

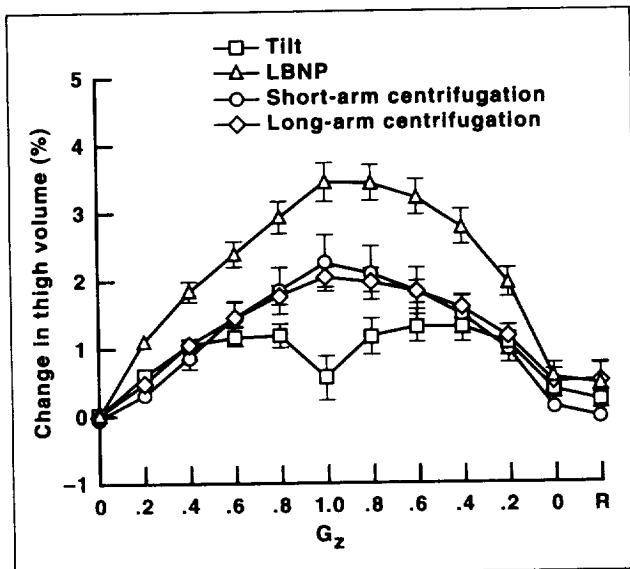


Fig. 1. Thigh volume responses to various gravitational stimuli.

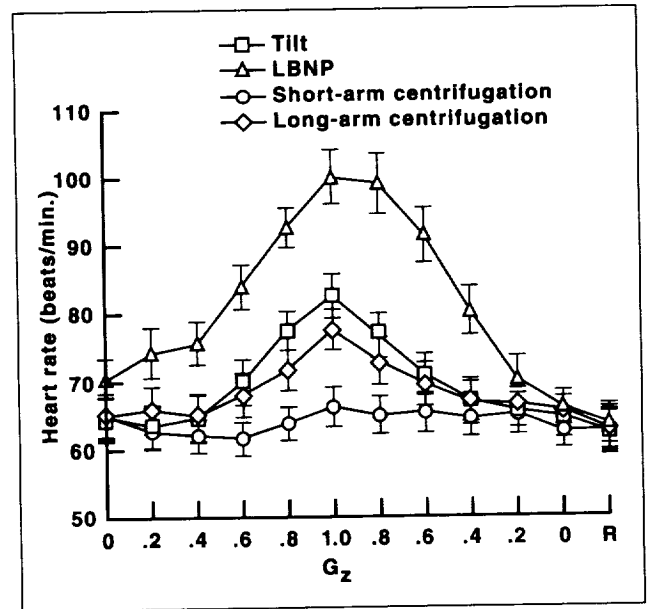


Fig. 2. Heart rate responses to various gravitational stimuli.

pressure, whereas blood pressure was constant during the other treatments.

At $1 G_z$, HUT elicited less footward fluid redistribution than the other stimuli. These results suggest that upright posture activates mechanisms that counteract footward fluid redistribution that are not activated during supine applications of simulated gravity. To generate an Earth-like cardiovascular stress at the systemic level, SAC in microgravity probably requires rotation rates that generate greater than $1 G_z$ at the feet. As expected, LAC more closely approximated the influence of normal gravity (HUT) than LBNP, which produced greater thigh and calf volume and heart rate increments than all other treatments. Therefore, when LBNP is being considered for simulating gravity, the cardiovascular stress imposed by LBNP should be reduced, while preserving its gravity-like footward force. (Donald Watenpugh received first place for this research in the annual student competition of the American Society for Gravitational and Space Biology.)

Ames-Moffett contact: D. Watenpugh/A. Hargens
(415) 604-5747/5746

Headquarters program office: OLMSA

Outer Heliosphere and Termination Shock

Aaron Barnes

In earlier work we developed a number of self-consistent one-dimensional models of the response of the heliospheric termination shock to upstream variations in the solar wind, in order to estimate the speed of the shock as it moves back and forth. We found that, for typically observed variations in solar wind density, the shock speed would be approximately 50 to 200 kilometers per second, and a typical inward or outward excursion would be on the order of 1 to 10 astronomical units. However, for models allowing energetic-particle acceleration to be an important dynamical process at the shock, the motion of the disturbed shock would be substantially slower than in the gas dynamic case.

In 1994 we applied these concepts to the global heliosphere, in the context of the high-latitude Ulysses mission. We expect the mean distance of the heliospheric termination shock to be greater or smaller at polar latitudes than at equatorial latitudes, depending on whether the mean dynamic pressure of the solar wind is greater or smaller at high latitudes. The heliospheric termination shock is expected to move in response to variation in upstream solar wind conditions, so that at any particular instant the termination shock will resemble a distorted asymmetric balloon with some parts moving inward and others moving outward. If the shock is a gas dynamic or magnetohydrodynamic shock, the results of the analysis depend only very weakly on the nature of the upstream disturbance. Typical speeds of the

disturbed shock are 100 to 200 kilometers per second. In the absence of a significant latitude gradient for the typical magnitude of solar wind disturbances, typical motions of the disturbed shock at polar latitudes would be about twice as fast, because of the higher speed of the high-latitude wind. If the dynamics of the termination shock are dominated by acceleration of the anomalous component of the cosmic rays, the motion of the shock in response to a given disturbance is substantially slower than in the gas dynamic case. Conceivably, particle acceleration might be a less important effect at higher latitudes; we envision the possibility of a termination shock that is dominated by particle acceleration at lower latitudes and is a magneto-hydrodynamic shock at high latitudes. In this event, high-latitude solar wind disturbances would produce substantially larger inward and outward motions of the shock in the polar regions.

Outside collaborators in various aspects of this activity are A. Lazarus, Massachusetts Institute of Technology; F. McDonald, University of Maryland; J. Simpson, University of Chicago; E. Smith, Jet Propulsion Laboratory; and J. Van Allen, University of Iowa.

Ames-Moffett contact: A. Barnes

(415) 604-5506

Headquarters program office: OSS

Production of Organic Molecules in Cometary and Interstellar Ice Analogs

Max P. Bernstein, Scott A. Sandford, Louis J. Allamandola, Sherwood Chang

Now that support is growing for the notion that comets may have brought organic materials to the Earth that were crucial to the development of life, there is great interest in characterizing the chemicals of which comets are composed, and modeling the reactions that are expected to occur under astrophysical conditions. The identification of astrophysical organic molecules may profoundly affect our understanding of how life on this planet developed. Most of our knowledge about cometary (and interstellar) ices derives from the assignment of bands in the astronomical spectra of distant objects, rather than from direct measurement. Laboratory simulations to determine what molecules may occur under conditions similar to astronomical environments are essential for the identification of organic species in comets and interstellar ice grains.

Interstellar ice grains reside in environments with such low temperatures (<40 kelvin) that essentially anything hitting the grains, with the exception of

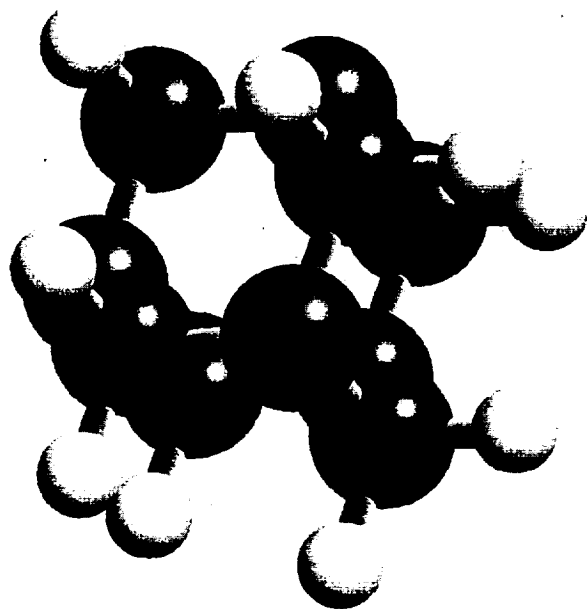


Fig. 1. Molecular structure of hexamethylenetetramine (HMT; $C_6H_{12}N_4$): the black spheres are carbon atoms, the red spheres are nitrogen atoms, and the small white spheres are hydrogen atoms. (See color plate 13 in Appendix)

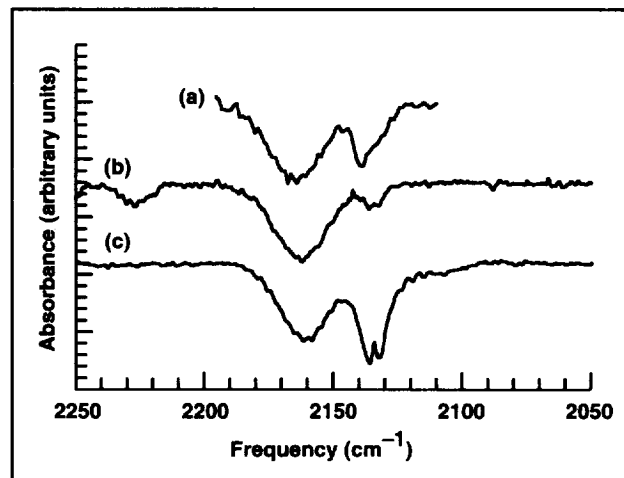


Fig. 2. The $2,250\text{--}2,050\text{ cm}^{-1}$ (4.444–4.878 micrometer) infrared spectrum of (a) W33A, a protostar deeply embedded in an interstellar cloud of dust, gas, and ice; (b) HMT photolyzed in H_2O at 12 kelvin and subsequently warmed to 150 kelvin; and (c) an astrophysical dust analog consisting of an $H_2O:CH_3OH:CO:NH_3 = 20:10:2:2$ ice photolyzed at 12 kelvin and subsequently warmed to 150 kelvin. In all three cases, the broad band at $2,165\text{ cm}^{-1}$ is attributed to the mysterious X-CN.

helium, sticks. As material accretes on the surface of the grains it is exposed to ambient ultraviolet (UV) radiation and cosmic rays. When this radiation impinges on the ice, chemical bonds are broken, molecules are destroyed, and radicals and other molecular fragments are formed. A thermal event (such as the passage of a shock wave, collisions between grains, or entry into a stellar system) then causes the ice to warm to the point at which molecular fragments begin to move, react, and form new molecular species. Thus the compounds found in interstellar and cometary ices are the products of radiation and heat. When the temperature exceeds 200 kelvin, the ice sublimates away, leaving an organic residue. Until recently, the identity of the molecules that make up these residues was a mystery.

The study of these organic residues has been a major research effort in the Astrochemistry Laboratory at Ames Research Center for several years. To synthesize an astronomical residue in the laboratory, water, methanol, carbon monoxide, and ammonia (simple materials known to make up interstellar ices) were frozen together under vacuum, in proportions consistent with astronomical data, and exposed to UV radiation. These irradiated ices were then heated to room temperature, and the resulting organic residue was studied using infrared spectroscopy, nuclear magnetic resonance spectroscopy, and gas chromatography–mass spectrometry. The results of our laboratory simulations of interstellar and cometary ices indicate that hexamethylenetetramine (HMT; $C_6H_{12}N_4$) (first figure) may be one of the most abundant molecules in the organic crust on the surface of comets and ice grains.

The presence of significant amounts of HMT on the surface of comets and interstellar ice grains would be significant for a number of reasons. Exposure of HMT to UV radiation produces cyanide (CN) compounds, including “XCN,” the mysterious interstellar cyanide compound that has been observed in dense molecular clouds in the direction of protostars (second figure). Exposure of cometary HMT to solar radiation could be a source of the formaldehyde and cyanide seen in the comae of comets. Solutions of HMT in acidic water produce amino acids; thus HMT may have been a source of amino acids delivered to the early Earth by meteorites.

**Ames-Moffett contact: S. Sandford
(415) 604-6849
Headquarters program office: OSS**

New Structural Forms of Water Ice and Their Possible Role in the Processing and Delivery of Prebiotic Organic Materials to Early Earth

David Blake, Peter Jenniskens

The Earth is a warm planet, where water sometimes freezes but almost always in one particular form: hexagonal crystalline ice. The hexagonal symmetry is revealed in the shape of snowflakes and is a consequence of the way water molecules are arranged in the icy solid. In outer space, many other water ice structures are possible, in part because of the extremely low temperatures under which the ice is formed. New research has revealed that structural changes in these other forms of water ice may have controlled how and what prebiotic organic material was delivered to early Earth.

In cold molecular clouds, which are the birthplace of stars and planetary nebulae, water is frozen from the vacuum of space onto tiny silicate grains (0.1 micrometer, or 1/1,000 the diameter of a human hair) at temperatures of 10–20 kelvin. These icy grain mantles act as hosts for small molecules which are frozen down along with the water. This solid assemblage of water, carbon monoxide, methane, carbon dioxide, etc. represents the first association of the

biogenic elements (those elements essential for life as we know it, including hydrogen, carbon, oxygen, and nitrogen). Within cold molecular clouds, icy grain mantles are processed and modified by ultraviolet radiation (UV) and temperature fluctuations in the range 10–70 kelvin. Irradiation by UV photons breaks chemical bonds in the ice and creates radicals and free hydrogen. The radicals remain trapped within the ice until such time as they are made mobile enough to react with each other, yielding prebiotic organic material. From laboratory experiments, it is known that many of the radical reactions in these interstellar ices occur in the temperature range 30–70 kelvin, a surprisingly low temperature, at which the water matrix was thought to inhibit radical diffusion. It was thought that radical recombination and volatile release from the grains occurred at higher temperatures, coinciding with the crystallization and evaporation of the original amorphous (structureless) ice.

In research results published in 1994, the underlying physical processes that control radical recombination, mobility of molecules within astro-physical ice analogs, and volatile release have been described for the first time. When water vapor freezes onto the interstellar grains, the result is a glassy film rather than a crystalline solid. This glassy or amorphous ice has the same basic structure as liquid water, in which the water molecules are connected to each other by four strong hydrogen bonds in a continuous network. The result is an open cage-like structure. At very low temperatures (less than 40 kelvin (-387°F)), some water molecules are trapped in the cages of this structure during freezing. By simulating the freezing process in the laboratory and observing the structure of the ice by electron diffraction using a transmission electron microscope, it was found that water at less than 30 kelvin has a unique structure in which the molecules are trapped in the cages (this process is called "self-enclathration"), resulting in a "high-density amorphous structure." As the temperature of the ice is raised from 15 to 65 kelvin, the ice is gradually transformed to a lower-density structure in which water molecules are no longer in the cages (first figure). A complete restructuring of the ice structure occurs in this temperature range. During this process, radicals created by UV photolysis are able to recombine, resulting in prebiotic organic compounds trapped in the still amorphous ice (second figure). UV photons are able to transform the ice back into the high-density form and create new radicals, thus allowing a continuous cycling of the ice at relatively low temperatures. The result is a high efficiency of prebiotic organic molecule formation.

It is believed that much of the biogenic element and volatile inventory of the Earth resulted from the bombardment of the inner solar system by icy planetesimals (i.e., comets) more than 4 billion years ago. Comets, which are made up of more than 40% water ice, are thought to be composed of interstellar grains from part of the cold molecular cloud that collapsed to form the early solar nebula. The biogenic element and volatile content of a comet is a function of the original structure of the water ice and the detailed processing history, both within the

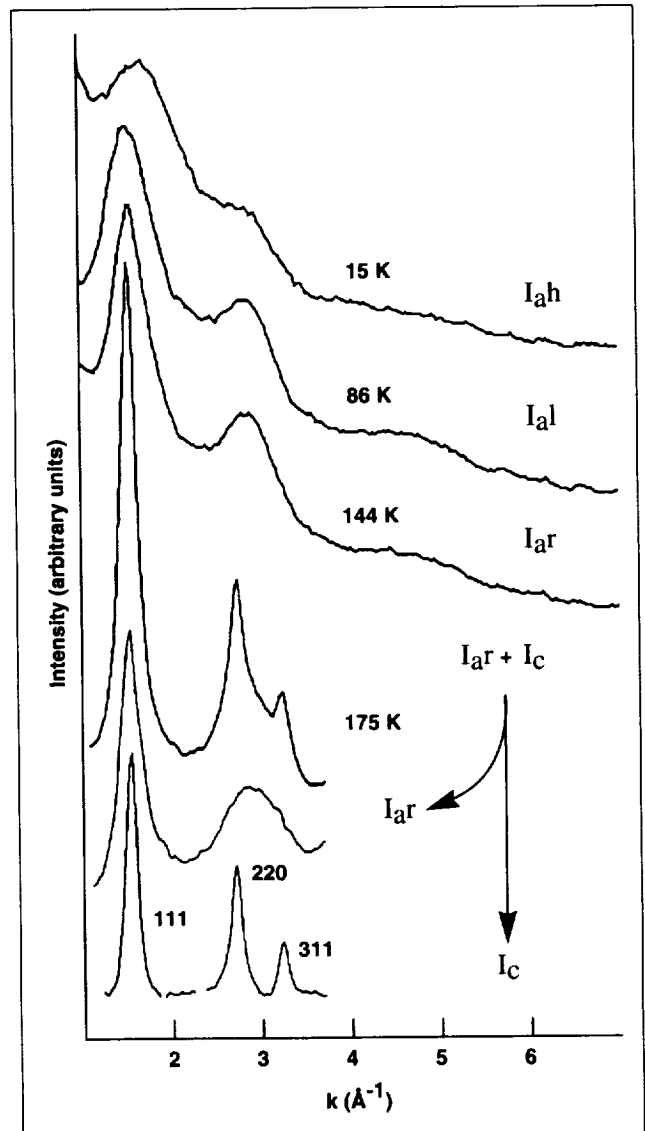
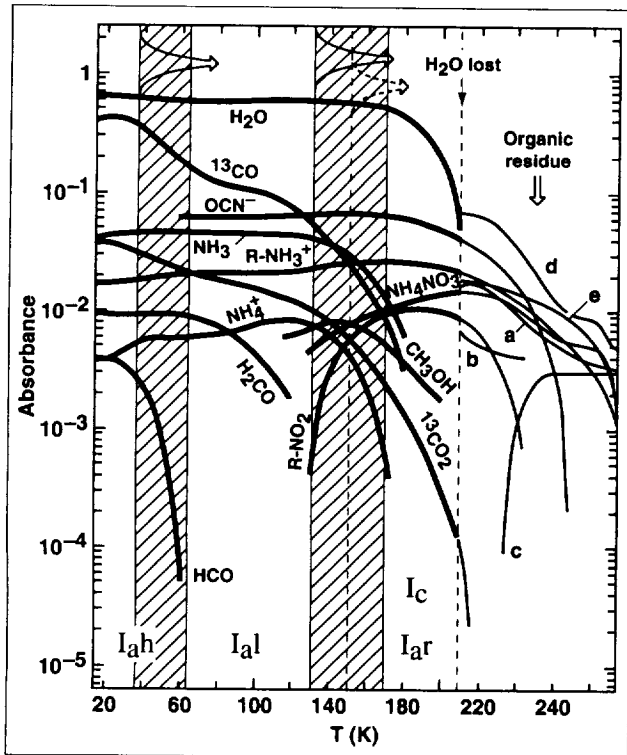


Fig. 1. Electron diffraction patterns of the different forms of vapor-deposited water ice. The forms encountered are high-density amorphous ice (I_{ah}), low-density amorphous ice (I_{al}), restrained amorphous ice (I_{ar}) (while transforming from I_{al}), and a composite of restrained amorphous I_{ar} and cubic crystalline ice (I_c). The latter can be separated into two components by subtraction of a standard cubic pattern as indicated, which allows one to follow changes in the amorphous component after the onset of cubic crystallization.



original cold molecular cloud and when it was an icy planetesimal in the outer solar system. Many of these processes can be understood through an understanding of the structural transitions and physical processes of the host water matrix.

Ames-Moffett contact: D. Blake

(415) 604-4816

Headquarters program office: OSS

Fig. 2. A laboratory simulation of the formation of reduced organic matter ("organic residue") from a UV-photolyzed ice mixture $H_2O:CO:NH_3$ (0.63:0.25:0.12) deposited at 15 kelvin (data from W. A. Schutte (1988)). This figure shows the intensity of a number of infrared absorption bands that were monitored during warm-up at about 1 kelvin per minute; the band assignment to functional groups is that of Schutte. The structural transitions marked on the figure are clearly seen in the changes in the infrared absorption spectra during warm-up.

Spectral Imaging from the Kuiper Airborne Observatory

Jesse D. Bregman

Using an infrared camera equipped with a circular variable filter and a 128×128 gallium-doped silicon array, we (David Rank and Pasquale Temi from Lick Observatory; Bregman and David Harker from Ames) observed emission from polycyclic aromatic hydrocarbons (PAHs) at 6.21 and 7.8 microns, and also searched for an emission line of nickel II in external galaxies. We had previously imaged several objects from ground-based telescopes in two PAH emission bands that are caused by C-H bonds. The 6.21- and 7.8-micrometer bands are attributed to C-C modes. With these new observations, we could provide a good test of fluorescent-excitation PAH models. Analysis of the data shows good agreement with the models, and indicates that the PAH molecules have a range of sizes.

We took images of the starburst galaxy M82 at the wavelength of the nickel II emission line at 6.63 microns. From spectra we had obtained

previously of the supernova SN1987A, we knew that the nickel line in supernovae would be very strong for 1-2 years after the explosion. Also, there are no other objects that exhibit a strong nickel emission line. If we could find nickel emission, we were almost certain that we had located a recent supernova. Our goal was to find supernovae hidden within starburst galaxies. Since starburst galaxies are producing lots of new stars, they are good places to look for supernovae. However, they are also dusty, and thus the visible light from a supernova could easily be hidden. We did find one possible supernova, but at a brightness level far above what we had projected. Further study is required to determine exactly what causes this bright nickel II emission.

Ames-Moffett contact: J. Bregman

(415) 604-6136

Headquarters program office: OSS

Significance of Fullerenes in Nature

Ted Bunch, Luann Becker

Fullerenes (Buckyballs, Buckminsterfullerenes) are mostly of C_{60} structure with a small amount of C_{70} . C_{60} (the more stable form) has carbon atoms arranged in the cage shape of a soccer ball, 20 hexagons and 12 pentagons. Fullerenes are the rarest form of carbon in nature; diamond and graphite are the other forms. Each of these forms has a specific mode of formation and stability environment and can be used to “fingerprint” a specific rock-forming or energetic event. For example, diamonds on the Earth are formed at great depths under extreme pressures and temperatures, and graphite is formed in rocks over long periods of time under low pressure and moderate temperature. Synthetic fullerenes have been made by high-energy synthesizing techniques (laser ablation, ion beams, carbon arcs, and combustion). Diamonds and fullerenes also form during shock (impact events): diamonds during the high-pressure/high-temperature phase and fullerenes during the low-pressure/high-temperature phase after shock, i.e., in the hot plasma.

We (with J. Bada, University of California, Davis; R. Winans, Argonne National Labs; F. Radicati and R. Fleming, Charles Evans & Associates; B. French, NASA Headquarters) initiated a systematic search for fullerenes in nature. The first discovery was made in a chondritic (meteoritic or cometary) carbonaceous residue of a tiny (0.14-millimeter-diameter) impact crater on the Long Duration Exposure Facility (LDEF). These fullerenes probably formed from a carbon precursor on impact. Fullerenes are also associated with the K-T impact event that caused the extinction of the dinosaurs 65 million years ago. In this case, fullerenes formed as the result of intense global fire storms that were initiated by the huge impact and/or from impact shock. Interestingly, diamonds are also found in the K-T boundary deposits.

We have also discovered fullerenes in impact deposits of a 1.85-billion-year-old, 200-kilometer-diameter impact crater in Canada. The Sudbury crater is the second largest proven crater on Earth. Only the Chicxulub Crater in the Yucatan is larger, and its

creation is the event that may be responsible for the extirpation of the dinosaurs 65 million years ago. In the case of the Sudbury cratering event, the large amount of carbon (approximately 1.0% by weight) contained in the impact deposits (the Onaping Formation, which is 1 kilometer thick and encompasses hundreds of cubic kilometers) implies that the carbon came from the impacting body (the impactor) and not the target rocks, as these rocks contain little or no carbon. Some carbon may have also come from impact-driven thermal dissociation of CO_2 in the atmosphere when CO_2 was much more abundant than it is in the present atmosphere. Fullerenes were probably synthesized during the impact from other carbon forms or organic compounds contained in the impactor. This is very significant in that, for the first time, we can say that most of this carbon is extraterrestrial. Other investigators have recently suggested that much of the carbon that was involved in the evolution of life on the early Earth may have been delivered to Earth by meteorites, comets, and dust, although until now little direct evidence has been available. Moreover, by making some general assumptions about the impactor size (approximately 15 kilometers in diameter) and calculating the total amount of carbon in the impact deposits, we conclude that the impactor originally contained 20%–30% carbon which means that the impactor was probably a comet—only comets have that much carbon. For comparison, the size of the impacting body that made the Sudbury Crater was much greater (radius = 7.5 kilometers) than the total mass of the approximately 21 comet fragments (radius = 1–2 kilometers) that recently struck Jupiter in spectacular fashion. Thus, the Sudbury impact energy was orders of magnitude greater than that of the Comet P/Shoemaker-Levy 9 combined impacts.

**Ames-Moffett contact: T. Bunch
(415) 604-5909**

Headquarters program office: OSS

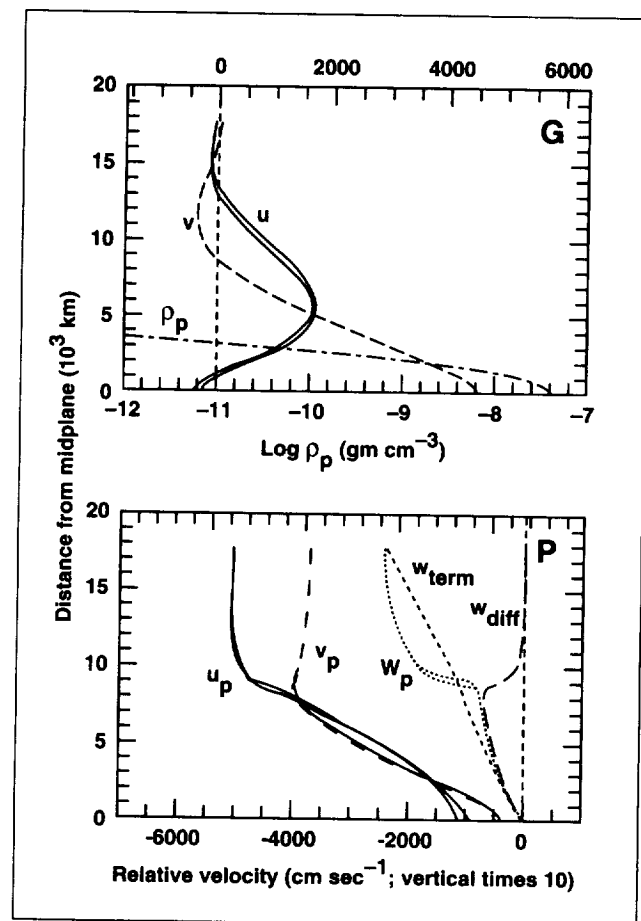
Particle-Gas Dynamics in the Protoplanetary Nebula

Jeffrey Cuzzi

Our emphasis here is on the stage of planetary formation during which growing particles become large enough to evolve independently of the mass-dominant gas. Interesting coupling and feedback effects are seen over four to six orders of magnitude of particle radius. Many of the modeling results have direct connections with the earliest actual record of conditions in this preplanetary stage. The primitive meteorites called "chondrites" have long been known to provide strong evidence for aerodynamic size sorting. That is, the sizes and densities of the particles are correlated such that their aerodynamic stopping time, or time to reach terminal velocity in a continuously moving gas, is rather narrowly defined within

a particular meteorite class. This has never been understood. Some past hypotheses have suggested settling toward the nebula midplane under the net vertical acceleration of the sun's gravity; immediate gravitational instabilities in this settled midplane were then advanced as a way of aggregating these collections of particles. This gravitational instability hypothesis now appears untenable for several reasons (see first figure), and we propose a different scenario. We believe that concentration of narrowly sized particles

Fig. 1. Results from our nebula midplane model for 60-cm-radius particles. Upper panel: vertical profiles of particle density (ρ_p), and gas radial and orbital velocity (u, v). The peak particle density is about 40 times the gas density. The velocities are relative to a velocity that is slightly smaller than Keplerian as a result of outward gas pressure forces. Lower panel: Particle radial, orbital, and vertical velocities (u_p, v_p, w_p) relative to Keplerian. Away from the midplane, the particles experience a headwind, orbit more slowly than Keplerian, and drift inward. In the dense midplane, the gas is driven by the particles and the headwind and radial drift are smaller. Turbulent viscosity driven by vertical wind shear diffuses the particle layer and prevents settling into a sufficiently high density for gravitational instability to occur. That is, there is an upward diffusion velocity w_{diff} that offsets the downward settling velocity w_{p} leaving the particle layer in a steady state. The particle terminal velocity is w_{term} .



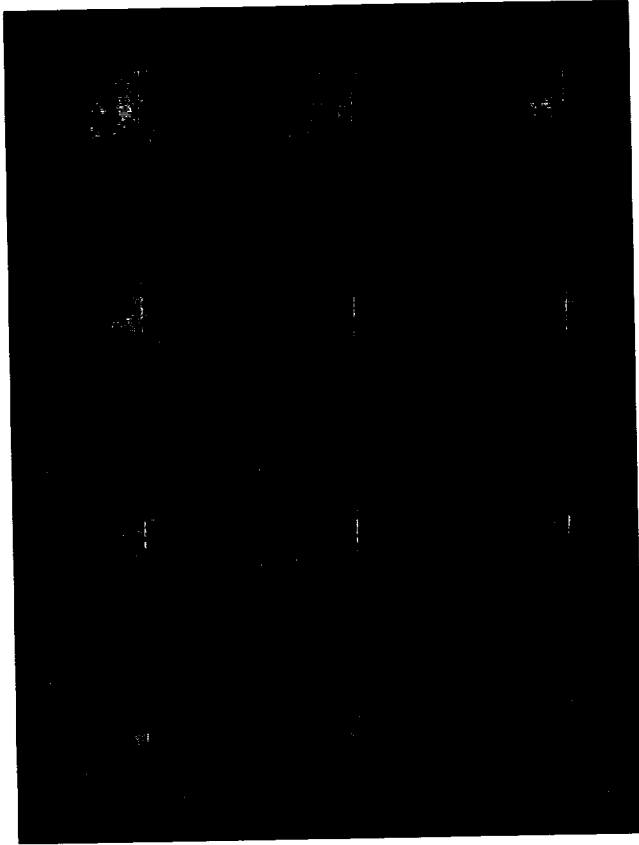


Fig. 2. A series of frames from a time evolution of particles of the optimally concentrated size. Clumps are identified at three different times; the particles in each are identified and assigned a color. The entire time sequence is then played so that the time evolution of particles into and out of clumps can be studied. Particles converge to a clump slowly and from remotely separated regions; they pass through the clump and are dispersed along streamers. Presumably, the sequence is repeated, with particles finding different clumps in the next cycle. Our hypothesis is that after a certain number of such "transient" clumping events, the statistical distribution of clump densities that we are now studying provides particles with an unusually dense clump to encounter, in which collisions or other nonlinear effects prevent subsequent dispersion. (See color plate 14 in Appendix)

occurs in nebula turbulence, with particles spending most of their time in a series of dense "nodes" or clumps with scales comparable to the smallest scale of the turbulence (the Kolmogorov scale). A series of frames from a time evolution of particles of the optimally concentrated size is shown in the second figure. From turbulent scaling laws, one can relate the physical size of the concentrated particles to the energetics of the turbulence (its Reynolds number). Remarkably, the most optimally concentrated particle in nebula turbulence, for currently accepted levels of turbulence, is about a millimeter in diameter—in excellent agreement with the sizes of "chondrules" in these primitive meteorites. The concentration factors can be several orders of magnitude.

Once a sufficiently dense clump forms, particle collisions, turbulence damping, or perhaps gravitational binding energy allows the particles in it to become permanently associated—they become a rubble pile which can settle into a denser midplane region, where an entire subsequent process of slow growth and compression leads to planetesimal-sized objects with the granular properties of the earliest constituents. We also showed that even small "seeds" can grow rapidly to planetesimal-sized objects in a particle-rich midplane.

Our fluid dynamics group (Cuzzi, A. Dobrovolskis of University of California, Santa Cruz, and J. Dacles-Mariani of the University of California, Davis) interacts closely with Ames Astrophysics and Meteorite experts P. Cassen and T. Bunch.

**Ames-Moffett contact: J. Cuzzi
(415) 604-6343
Headquarters program office: OSS**

Planetary Ring Dynamics and Morphology

Jeffrey Cuzzi

Planetary ring and moon systems are slowly revealing new insights into their structures and the processes that create them. These processes were also important in the formation of the planets.

During this year, we completed projects that characterize the spatial variation of two different structural properties of Saturn's virtually unexplored B ring. Our color ratio work has revealed that the spatial variation of color (and thus composition) in Saturn's main rings changes character at the same location where the spatial scales change magnitude. Both of these shifts in properties correlate with an abrupt change in the optical depth, or matter density, in the rings. These changes are the manifestation of currently unknown local variations in ring properties—composition, surface graininess, or perhaps even volume density, with stirring and thus porosity increased, perhaps, by proximity to a massive fragment of the primordial satellite or satellites from which the rings derived. The figure is a false-color image demonstrating compositional variations in the main rings. In a related numerical modeling study of ejecta transport and associated structural and compositional changes, we have shown how the ring composition evolves as primitive, absorbing interplanetary material falls onto them. The observed radial profile of the ring albedo and color is in good agreement with the properties seen in our model results. These correspondences lead one to infer an age for the rings that is significantly less than the age of the solar system. Our collaborator Mark Showalter, who manages the Planetary Rings Discipline Node, has also demonstrated that the clump structure in Saturn's "kinky" F ring changed dramatically between the two Voyager encounters. These results and others support our earlier idea that a veritable asteroid belt of moonlets surrounds the F ring and its companion

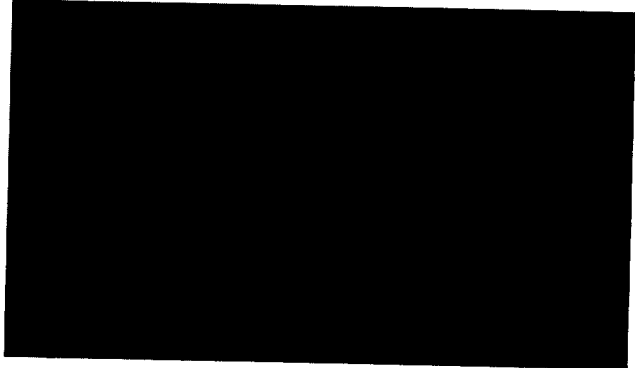


Fig. 1. Artificial color version of Saturn's rings, created by taking ratios of three radial brightness profiles obtained in different Voyager filter bands. Different colors in this representation manifest distinct radial variations in the spectral shape of the ring reflectivity; that is, different materials lie at different radii. The left (bluish) side is the inner edge of the C ring; the central (reddish) region is the nearly opaque B ring; the next region outward (bluish) is the nearly transparent Cassini Division, which has color and reflectivity comparable to the C ring. The outer or A ring has an unusual composition at its inner edge, as seen in the greenish band, but appears similar in composition to the B ring elsewhere. (See color plate 15 in Appendix)

ringmoons. This work involves a group that includes P. Estrada (Cornell), M. Showalter (Stanford), R. Hogan (Synernet), L. Horn (Jet Propulsion Laboratory), and others.

**Ames-Moffett contact: J. Cuzzi
(415) 604-6343**

Headquarters program office: OSS

Earth's Atmospheric Oxygen Supply is Linked to the Evolution of Its Crust

David J. Des Marais

Free oxygen was once not abundant in our atmosphere; its concentration thus has increased during the Earth's history. Oxygen-producing organisms were needed to sustain this large increase, but they evolved long before oxygen concentrations attained their modern levels. Factors such as declining volcanism and the stabilization of the continental crust played important roles in oxygen's ascendancy to prominence in our atmosphere.

Almost all of the organic matter and oxygen produced during photosynthesis are soon destroyed by biological respiration. However, some organic matter escapes in sediments deposited in river deltas, estuaries, and swamps. This burial allows some of the photosynthetic oxygen to accumulate in the atmosphere. If we could estimate how much photosynthetic organic matter was buried in crustal sediments during the history of the Earth, we could deduce how rapidly oxygen and other oxidized species accumulated. Measurements of stable carbon isotopes in carbonates and organic matter indicate that the crustal inventory of organic carbon increased between 3.0 and 0.5 billion years ago, consistent with the apparent increase in atmospheric oxygen.

The inventory of organic matter in the Earth's crust apparently rose most dramatically at discrete time intervals during global-scale episodes of collision and stabilization of continental crust. These collision events enhanced the rates of erosion and sedimentation. Such circumstances are known to sustain relatively rapid rates of organic burial in modern environments. But the buried organic matter still could have been decomposed by the thermal

alteration of crustal sediments. This destruction was pervasive prior to the formation of extensive, stable tracts of continental crust.

Increases in atmospheric oxygen have been recorded in ancient, preserved soils as an increase in the amount of oxidized iron retained during soil formation. The increases in oxygen correlate with time intervals in which there was a greater degree of preservation of sedimentary rocks, and these time intervals in turn correlate with global-scale events of stabilization of continental crust. Large, stable continental tracts emerged episodically between 3.0 and 1.8 billion years ago and created environments in which the heating and destruction of organic matter in sediments was less pervasive, allowing organic matter to accumulate.

Thus several kinds of independently acquired data indicate that increases in free oxygen are correlated with increases in crustal organic matter, and both of these are correlated with episodes of stabilization and emergence of large continental platforms. To the extent that changes in atmospheric composition have influenced the evolution of life, our biosphere's development has been linked to the geological evolution of the Earth.

**Ames-Moffett contact: D. Des Marais
(415) 604-3220**

Headquarters program office: OSS

Refinement of Planetary Protection Policy for Mars Missions

Donald L. DeVincenzi, Pericles D. Stabekis, Jack Barengoltz

Under existing international policy adopted by the Committee on Space Research (COSPAR) in 1984, missions to Mars (landers, probes, and some orbiters) are designated as Category IV missions for the purpose of arriving at cleanliness standards for spacecraft assembly. In this category, the procedures for implementing planetary protection requirements could include trajectory biasing, cleanroom assembly, bioload reduction, sterilization of hardware, and bioshields; i. e., requirements could be similar to those used on the 1976 Viking missions to Mars.

In 1992, however, a U.S. National Academy of Sciences study recommended that controls on forward contamination of Mars be tied to specific mission objectives. The report recommended that Mars landers with life detection instruments be subject to at least Viking-level sterilization procedures for bioload reduction, and that spacecraft (including orbiters) without life detection instruments be subject to at least Viking-level pre-sterilization procedures for bioload reduction but need not be sterilized.

In light of these recommendations, it was proposed that the current policy's Category IV missions and their planetary protection requirements be divided into two subcategories: Category IV A, for missions comprising landers and probes without life detection experiments and some orbiters, which will meet a specified bioburden limit for exposed surfaces; and Category IV B, for landers and probes with life detection experiments, which will require complete system sterilization. In addition, Category III orbiter mission specifications were expanded to be consistent with these recommendations. The existing COSPAR policy was modified to reflect these changes, and they are now incorporated into international policy.

**Ames-Moffett contact: D. DeVincenzi
(415) 604-5251
Headquarters program office: OSS**

Airborne Astronomy

Edward W. Dunham, Edwin F. Erickson, Jacqueline A. Davidson

The twentieth year of operation of the Gerard P. Kuiper Airborne Observatory (KAO) was 1994. The anniversary was marked in July by an Airborne Astronomy Symposium involving 150 astronomers from many institutions, both domestic and foreign. At the same time, the KAO staff was preparing for a major deployment to Australia to observe the impact of Comet P/Shoemaker-Levy 9 on Jupiter. This deployment capitalized on the KAO's ability to study water vapor in extraterrestrial environments from its operating altitude of 41,000 feet; its ability to deploy to locations around the world; and the dedication,

resourcefulness, and stamina of its staff. The campaign to observe the comet's impact was highly productive; seven 9-hour flights and two instrument changes were successfully carried out in 9 days. The data are still being analyzed, but detection of hot water vapor at the impact sites, apparently from the comet rather than from Jupiter's atmosphere, has already been announced.

During 74 flights from Moffett Field, Brazil, New Zealand, Hawaii, and Australia, astronomers used the KAO to make observations of water in

star-forming regions; to measure calibration objects for the European Infrared Space Observatory (ISO); to determine abundance gradients in the Galaxy; to find signs of supernovae in distant galaxies; and to observe an occultation of a star by Chiron, a large comet orbiting in the outer solar system. The Chiron occultation required a deployment to Brazil on short notice just before a scheduled deployment to New Zealand. This was made possible by means of an intricate plan to travel directly from Brazil to New Zealand via Easter Island, thus avoiding additional ferry flights to and from Ames. The total number of flights this year was somewhat low because of the major maintenance program required every 5 years for C-141 aircraft.

The KAO is under continuous technical development to improve its reliability and scientific performance. Major activities this year included work on the telescope's pointing and tracking systems, including development of a simple image motion compensation system. Work is continuing on a new tracking system that will be portable to the Stratospheric Observatory for Infrared Astronomy (SOFIA). Many other new developments have been postponed pending a decision on whether SOFIA will start in 1996, since the SOFIA development plan calls for shutting down the KAO at the start of the SOFIA development period.

During its 20 years of operation, the KAO has continually improved in sensitivity as new detectors and instruments have become available. Although further improvements are possible, the instruments have now reached a stage where major improvement in sensitivity can only be reached with a larger telescope that is capable of observations of fainter objects and observations with significantly better angular resolution. This need will be filled by SOFIA, the next step in the airborne astronomy program. SOFIA will carry a 2.5-meter telescope in a Boeing 747 aircraft, and will achieve about ten times better sensitivity and three times better angular resolution than the KAO. Questions that airborne astronomers using SOFIA will address include: What

is the structure, composition, and chemistry of planetary atmospheres? How do protoplanetary disks form and evolve? How are bipolar outflows and disk formation involved in star birth processes? Is there a black hole at our galactic center? How do stars form in different types of galaxies? and What fuels star bursts and active galactic nuclei? The National Research Council's (NRC) report on priorities in Astronomy and Astrophysics in the 1990s, the Bahcall report, places SOFIA as the highest-priority new NASA initiative in the moderate cost category. An additional review this year by another NRC-sponsored panel confirmed this recommendation.

Much of the radiation in the universe is found at infrared wavelengths which are not observable from ground-based telescopes; SOFIA's ready and frequent access to these wavelengths will provide a capability critical to an understanding of many important astronomical phenomena. The U.S. has established world leadership in infrared science through detector technology, the KAO, the Infrared Astronomy Satellite (IRAS), and the Cosmic Background Explorer (COBE). If developed as planned, SOFIA will continue this tradition, with operations beginning just after the turn of the century.

Historically, SOFIA has been planned as a collaborative venture, with the U.S. providing the aircraft and associated systems and Germany providing the telescope. After several years of uncertainty, Germany's participation once again appears certain. This year, workers at Ames and in U.S. industry carried out studies of critical-path technology items, and a wind tunnel test of the aft-mounted telescope configuration was completed using both 747-SP and 747-200 models. The cost of the project has been further reduced by use of an innovative hangar design.

**Ames-Moffett contact: E. Dunham/E. Erickson
(415) 604-5523/5508**

Headquarters program office: OSS

Stellar Occultation Study of Chiron

Edward W. Dunham

Chiron is one of a large number of icy objects that normally orbit the Sun beyond the orbits of Neptune and Pluto. These Kuiper-belt objects are analogous to the familiar asteroids located at the edge of the inner solar system; they are thought to be relatively undisturbed planetesimals left over after the formation of the outer solar system. Chiron's orbit has apparently been perturbed, and it now orbits between Saturn and Uranus. It is the largest known and nearest Kuiper-belt object.

Even the most basic properties of Chiron, its size and surface brightness, were previously unknown but could be determined by means of a stellar occultation. Chiron possesses a tenuous and time-variable "atmosphere," or coma, that is created by evaporating ice which blows dust grains away from certain regions on its surface. This surface activity may also give rise to dust "jets" similar to those seen in many nearby comets. The opacity of the coma and the structure of possible dust jets could also be elucidated by a stellar occultation observation. We were fortunate this year to have two Chiron occultation opportunities, one in November 1993 and the other in March 1994.

The first event involved a relatively faint star, Ch02, and was successfully observed with portable charged-coupled-device (CCD) occultation photometers using fixed and portable ground-based telescopes. Many observers from Ames, the University of Arizona, Lowell Observatory, MIT, and the SETI Institute participated in this observation. One of our stations witnessed an occultation by Chiron itself, while the others observed what appeared to be a dust jet extending for hundreds of kilometers from Chiron's nucleus. The length of the single chord across Chiron and the apparent miss at the next nearest observing station implies that Chiron's radius must be 166 kilometers or more, and that its surface reflects no more than 11% of incident light.

The second event involved a much brighter star, Ch08, and was observed with the Ames portable CCD system and an infrared array camera from Lick Observatory on the Kuiper Airborne Observatory (KAO), which was deployed to Brazil for the observation. Many other observers attempted ground-based

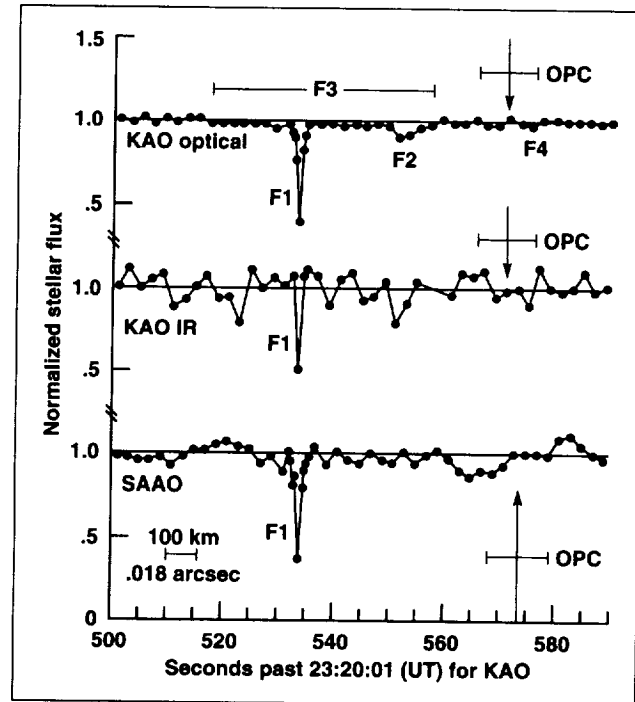


Fig. 1. As Chiron passed by the star Ch08, the starlight was dimmed by its passage through Chiron's dusty coma. These lightcurves show the structure of Chiron's coma with a resolution of about 10 kilometers. The simultaneous optical and infrared lightcurves constrain the size of the dust grains.

observations from Brazil, but were thwarted by bad weather. One ground-based observation was successfully made by D. Kurtz from the South African Astronomical Observatory (SAAO). The KAO team included J. L. Elliot and C. B. Olkin (Lowell Observatory); E. W. Dunham (NASA Ames); C. H. Ford (SETI Institute); D. K. Gilmore, P. Temi, and D. M. Rank (University of California, Santa Cruz/Lick Observatory); and D. Lazzaro (Observatório Nacional, Brazil). As seen from both the KAO and the SAAO, Chiron appeared to pass very close to the star, but the nucleus missed the star by about 20 kilometers. All of the observations show a short sharp drop in the star's brightness, labeled F1 in the figure, which is most

likely due to occultation by a dust jet. The simultaneous infrared and optical KAO observations imply that the size of the dust grains in the jet must be larger than 0.7 micrometer. In the KAO optical data, the star appeared to be dimmed a small amount by dust in the coma (F3 in the figure, with a local concentration at F2). Finally, there is tentative evidence of additional extinction where light from the star crossed Chiron's orbital plane (F4, near OPC, in the figure).

These observations have given us our best look at a comet nucleus since the spacecraft flyby missions to comet Halley, and our first close look at a Kuiper-

belt object. The results will elucidate the composition of this primitive object, and provide a glimpse of the conditions prevalent during the formation of the solar system. We will attempt to observe Chiron occultations in the future, as opportunities arise. We would like to obtain two occultation chords across Chiron's nucleus to measure its diameter accurately, and to observe the behavior of its coma as it reaches and then recedes from perihelion over the next decade.

**Ames-Moffett contact: E. Dunham
(415) 604-5523
Headquarters program office: OSS**

Exploring for an Ancient Martian Biosphere

Jack D. Farmer, David J. Des Marais

Of the other planets in our solar system, Mars holds the greatest potential for having developed extraterrestrial life. There is compelling evidence that the climate of early Mars was more Earth-like, with a denser, warmer atmosphere and abundant liquid water. Life arose very quickly on the Earth (after the formation of the crust about 4.1 billion years ago, but some time before the oldest fossils, 3.5 billion years ago). This was during the critical interval in Martian history when liquid water was seemingly abundant there. Could life have also developed on Mars, gradually dying out in surface environments as the planet lost its atmosphere and began to cool? If life was present on Mars, it is very likely to have left behind a fossil record. Since Viking missions, the focus of Mars exobiology studies has been broadened to include the search for a Martian fossil record. This shift in our thinking has led to the emergence of a new area of exobiological research we call "exopaleontology." At this early stage, our focus is on developing a strategy to explore Martian surface environments for a fossil record, and on applying this strategy to selecting targets for high-resolution orbital imaging and landing sites for future surface missions.

Because the development of a biosphere on Mars is likely to have been arrested early, at least in surface environments, we believe that the early fossil record on Earth provides a reasonable proxy for a Martian fossil record. In refining an exploration strategy for Mars exopaleontology, we have drawn on experience with the interval of geologic history called the Precambrian. The Precambrian fossil record consists of three basic types of information: chemical fossils (e.g., biomarker compounds indicative of particular life processes), permineralized cells of microorganisms (actual organic remains that were quickly replaced by stable minerals prior to decay), and stromatolites (layered sedimentary structures formed by stratified microbial communities called "mats"). Key questions include What factors control fossilization and long-term preservation? and What environments are most likely to show a fossil record on Mars, and how do we recognize them from orbit?

According to the Precambrian record, the key factor in the long-term preservation of organic materials and biomolecules is the rapid entombment of living organisms by stable mineral phases like

silica, phosphate, or carbonate. This concept of rapid, early mineralization is central to our search strategy for Mars. Through Earth-based analog studies we have identified four major aqueous (water-rich) environments where rapid mineralization frequently interacts with high biological productivity to enhance microbial fossilization. These environments include mineralizing springs (both thermal and cool springs), "evaporite" basins (where salts precipitate from brines), hard-pan soils, and biomediated weathering surfaces (e.g., rock varnish). Over the past year we have been studying these and related environments to better understand how biological information is incorporated into mineral deposits and preserved for the long term. Through collaborations with Malcolm Walter (Macquarie University, Sydney, Australia) and Donald Lowe (Stanford University), we are studying modern and ancient thermal springs as environments for early life. With David Agresti (University of Alabama) we are assessing the potential of Mossbauer spectroscopy for identifying iron springs on Mars. Through collaborations with David Blake and Sherry Cadi (Ames Research Center), we have been adapting methods of analytical transmission electron microscopy (ATEM) to extract more biological information from ancient rocks. With James Brass (Ames Research Center), we are learning how to identify key mineral deposits from orbit using remote sensing analog studies and instruments similar to those that will be flown to Mars during upcoming

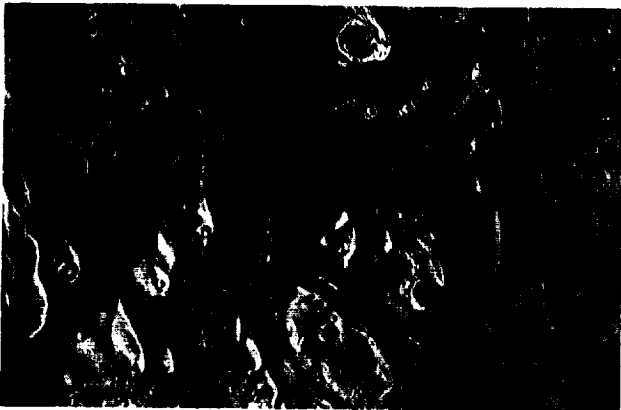


Fig. 1. Distal reaches of Ares and Tui Valles outflow channels at the southern edge of Chryse Planitia, Mars.

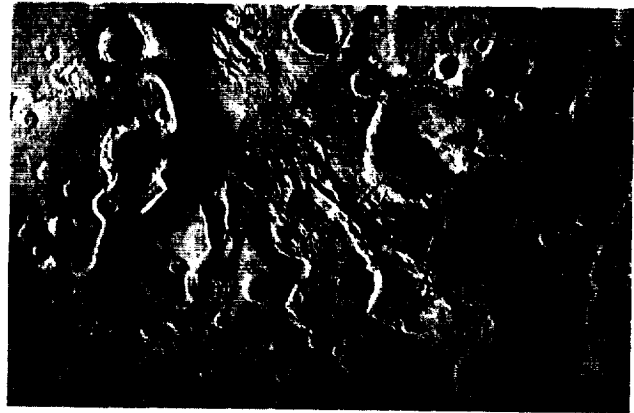


Fig. 2. Ares and Tui Valles channels originate in "chaos" terranes that probably formed by subsurface heating and melting of ground ice.

orbital missions. In addition, our participation in field trials of the Russian Marsokhod rover have provided a basis for assessing the instrumentation requirements for future robotic missions for exopaleontology.

Our research also requires a strong interface with Mars site selection activities involving collaborations with Ronald Greeley (Arizona State University). Using Viking data, we have been targeting key Exobiology sites on Mars for high-resolution imaging during the future orbital missions. Our site recommendations proved influential in 1994 in helping to select the primary landing site for the Mars Pathfinder mission, scheduled for launch in 1996. The Pathfinder site is located where large outflow channels of Ares and Tui Valles systems debouch onto Chryse Planitia. Outflows from these areas originate in probable hydrothermal areas (chaotic terranes) and could have carried fossiliferous spring minerals down the channels, depositing them at the Pathfinder landing site. Working with the Pathfinder team we hope to get a first glimpse of aqueous mineral deposits on Mars in 1997.

**Ames-Moffett contact: J. Farmer/D. Des Marais
(415) 604-5748/3220**

Headquarters program office: OSS

Carbonaceous Components in Comet Halley Dust

Marina N. Fomenkova, Sherwood Chang

Comets are believed to be the most primitive objects in the solar system. They were born far out in the presolar nebula and, because of their small size, have not experienced heating or alteration. Thus, cometary nuclei are likely to retain some preserved interstellar material as well as volatile chemicals from cold regions of the protosolar nebula. Comets are also possible sources of water and organic matter on the prebiotic Earth. Determining the nature and abundances of cometary components containing the biogenic elements—carbon (C), hydrogen (H), oxygen (O), and nitrogen (N)—is a prerequisite to understanding the organic chemical evolution of the early solar system and assessing the role that comets may have played in the origin of life on Earth.

Cometary grains containing large amounts of carbon and/or organic matter were discovered by *in situ* measurements of comet Halley dust composition during flyby missions VEGA and GIOTTO to comet Halley in 1986. Dust-impact time-of-flight mass spectrometers on board the spacecraft established that a substantial fraction of the cometary dust contains the bulk of carbon, probably bonded to hydrogen, oxygen, and nitrogen in organic chemicals. Yet our knowledge of the nature of these grains is limited.

Particles composed predominantly or exclusively of one or more of the biogenic elements were called “CHON particles.” Hierarchical cluster analysis has been applied to the spectra of 515 CHON particles to reveal possible groupings according to chemical composition. Additional knowledge about the population (i.e., chemical models, observations of other primitive solar system samples) is needed to make sense of the observed clusters. So far, the chemistry of biogenic elements and organic matter in carbonaceous meteorites has been much better characterized than that in comets. The view that these meteorites and comets both accreted components in varying proportions from common interstellar and solar nebular source regions suggests that knowledge of the chemistry of one type of object may shed light on that of the other.

Abundant evidence exists for the derivation of meteoritic carbonaceous phases from interstellar

sources. These components or their precursors should also occur in cometary dust, which is supposed to be more primitive than carbonaceous chondrites and to preserve relatively unprocessed interstellar grains.

The attempt to classify comet Halley organic dust grains by means of cluster analysis reveals more than two dozen compositional types. Many of these compositions are similar to those of classes of components observed in interstellar medium and in carbonaceous meteorites. Implicit in the analysis is the notion that distinct clusters represent specific components, yet in a few cases we have explicitly suggested multicomponent mixtures. At present we cannot exclude the strong possibility that most, if not all, CHON particles are mixtures of various carbons and organic components rather than a single component. At least, elemental carbon grains, hydrocarbons, and probably polymers of cyanopolyynes and multicarbon monoxides appear to be distinct contributors to the particle population.

The chemical heterogeneity among clusters presumably reflects differences in composition of precursor dust in the protonebular molecular cloud from which the solar system originated. Maintenance of this heterogeneity indicates that physical and chemical processes that occurred before and during accretion of comet Halley did not result in chemical homogenization at the submicron grain size level. Origin of all the observed types of organic components in the same environment at the same time is incompatible with their chemical properties. Apparently, comet Halley inherited material from a protosolar molecular cloud in which organic matter was either produced in different spatial domains or experienced different histories, or both.

In future work, cluster analysis will be applied to comet Halley dust grains that are composed of mixtures of CHON elements and inorganic minerals.

Ames-Moffett contact: S. Chang

(415) 604-5733

Headquarters program office: OSS

Mars Soil Oxidant—A Science Puzzle

Minoru M. Freund, John J. Plombon, Steven J. Butow, Friedemann Freund

Over twenty years ago the Viking Mission's Life Detection Experiments did not find life on Mars, but demonstrated that the Martian soil is extraordinarily oxidizing. Oxygen gas (O_2) evolved when the soil was exposed to water vapor (H_2O), and carbon dioxide (CO_2) evolved upon the addition of an aqueous solution with organic nutrients, intended to stimulate the growth of Martian living organisms. These reactions characterize the Mars Soil Oxidant—a reagent so strong that it might have wiped out traces of life on Mars. The physical and chemical nature of this powerful oxidant is therefore of great interest to NASA's Exobiology Program and to any forthcoming missions in search of extant or extinct life on Mars.

How did the Mars Soil Oxidant form? It's possible that, in the thin, cold Martian atmosphere, photochemical reactions occurred between traces of H_2O and the ultraviolet (UV) radiation from the Sun, leading to hydrogen peroxide (H_2O_2) which in turn condensed onto the soil grains. Such an H_2O_2 frost would indeed be highly oxidizing upon thawing, capable of destroying organics, as observed during the Viking missions.

Our laboratory experiments are based on a distinctly different line of thought, without the need to invoke an H_2O_2 frost. We have studied the physical and chemical properties of terrestrial magmatic minerals that crystallize in H_2O -laden magmas, which are analogs for minerals in the Martian soil. Their surfaces become strongly oxidizing as the result of a series of solid state reactions, starting with the dissolution of H_2O during crystallization. Structurally dissolved H_2O commonly occurs as pairs of hydroxyl groups, OH^- . Many OH^- pairs undergo a redox conversion, splitting into molecular hydrogen (H_2) and peroxy- (O_2^{2-}). The H_2 molecules are mobile and diffuse out. The lattice-bound O_2^{2-} molecules dissociate, either thermally or upon UV irradiation, generating O^- radicals. Inside the mineral structure, these O^- radicals behave as electronic defects, similar to the "holes" known to semiconductor physics. They move as electronic

charge carriers through the crystal structure. Because they carry a positive charge and repel each other in the bulk, they are pushed toward the surface. At the surface the O^- radicals reveal their radical, highly oxidizing nature. They can strip an H atom from methane (CH_4), the most stable of all hydrocarbons, causing the formation of methyl radicals, $\bullet CH_3$. The reaction between surface O^- and CH_4 is of prime importance to the petrochemical industry for the conversion of methane into liquefiable hydrocarbons.

Because O^- radicals are omnipresent in terrestrial magmatic minerals, they will also exist in the corresponding minerals on Mars. This suggests that the Mars soil oxidant has a similar origin, also consisting of O^- surface radicals derived from peroxy- within the mineral grains.

To study O^- in natural and synthetic materials we developed a new technique called charge density analysis (CDA). CDA has received an endorsement by the National Institute of Standards and Technology as "a new technique to measure previously unmeasurable fundamental properties of materials." It measures the dielectric polarization in an electric field gradient and determines surface charges as they appear or disappear during heating or cooling or after illumination. With support from the Department of Energy's Energy-Related Innovative Research Program, CDA is currently under development for applications in the petrochemical industry. CDA is a technique of choice to identify the nature of the Martian soil oxidant.

We have proposed a charge density probe (CDP), a miniaturized, lightweight, low-power-consumption version of CDA. It is currently in the design stage as a candidate flight instrument for deployment on a Martian lander or robot. The concept drawing in part (a) of the figure shows a CDP that utilizes state-of-the-art atomic force microscope technology developed at the AT&T Bell Laboratories. The CDP sensor is contained in a vacuum chamber with a robotic arm running along its center. The arm will grab a sample of Martian soil and position it underneath the CDP tip

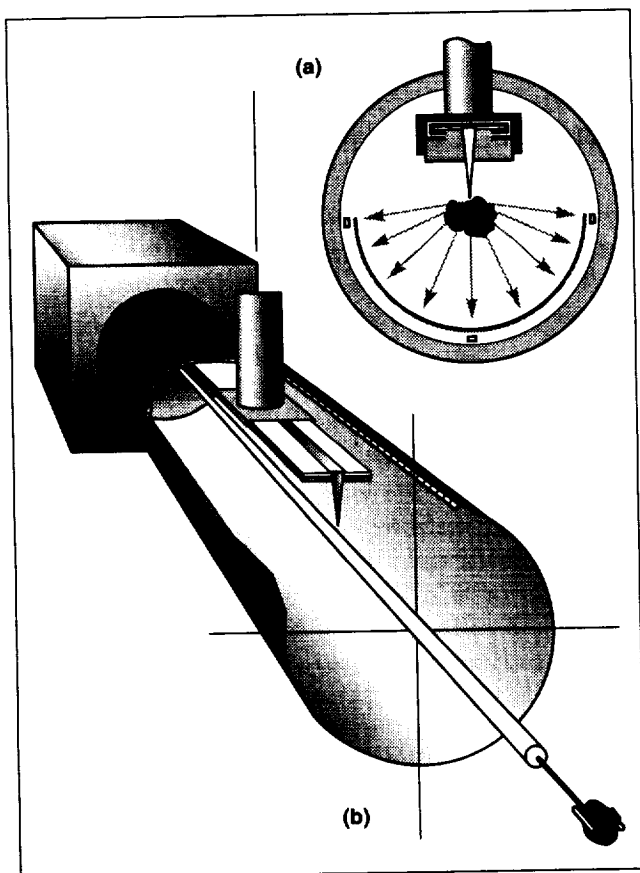


Fig. 1. (a) Perspective view of the charge density probe (CDP) sensor with the robotic arm holding a soil grain; (b) cross section showing the CDP tip protruding downward toward the ground electrode.

which forms one side of an asymmetrical capacitor. Part (b) of the figure shows a cross section through the tip, the sample, and the hemispherical ground electrode. During measurement, a series of voltages with positive and negative polarity will be applied across the capacitor. If the oxidant consists of O^- radicals on the grain surfaces, these surfaces will carry a positive charge. In addition, the CDP will allow the Martian soil grain to be heated radiatively and illuminated with UV flashes. Peroxy- in the bulk will then dissociate, generating O^- . The O^- will diffuse to the surface, forming a distinct positive surface charge. By contrast, an H_2O_2 frost, condensed from the Martian atmosphere onto the grain surfaces, will not cause such a surface charge. A CDP instrument on Mars can therefore unambiguously distinguish between an O^- -generated surface charge layer and a surface veneer of neutral H_2O_2 molecules on soil grains.

Ames-Moffett contact: F. Freund
(415) 604-5183
Headquarters program office: OSS

Accurate Evaluation of Quantum Integrals

David C. Galant, David Goorvitch

Accurate eigenvalues are seldom needed in spectroscopy because the actual values are directly observable. The eigenvalues are usually used to construct the potential function that is used in Schroedinger's equation to obtain the eigenfunctions, i.e., wavefunctions. The only need for the wavefunctions is for the evaluation of expectation values of operators, such as the dipole moment function to obtain intensities, or the overlap integrals to obtain Franck-Condon factors. Thus what we really need is a relatively quick, accurate numerical method to evaluate integrals involving wavefunctions. The method should have a reasonably good a posteriori error estimate. Such a method is obtained by combining the method of calculating wavefunctions as the eigenvectors of a symmetric matrix with the trapezoidal rule for numerical quadrature.

Combining an appropriate finite difference method with Richardson's extrapolation results in a simple, highly accurate numerical method for solving Schroedinger's equation. Important results are (1) that error estimates are provided, and (2) that one can extrapolate expectation values rather than the wavefunctions to obtain highly accurate expectation values. We discuss the eigenvalues, and the error growth in repeated Richardson's extrapolations of

those values, and show that the expectation values calculated on a crude mesh can be extrapolated to obtain expectation values of high accuracy.

In a series of papers we presented the results of applying Richardson's extrapolation to zero mesh width to finite difference approximations of the eigenvalues and corresponding wavefunctions of Schroedinger's equation for some problems that have been difficult to solve by traditional methods. The method is limited to computing bound-bound transitions for the potential. As an example of extrapolating integrals we have calculated the expectation value of x^2 for the harmonic oscillator. The exact values are $n + 1/2$, where $n = 0, 1, 2, \dots$. We see that the final extrapolated values agree to better than 3 parts in 100,000 with the exact result. For the lowest number of mesh points, the expectation value of x^2 at high vibrational number is quite far from the exact value.

**Ames-Moffett contact: D. Galant
(415) 604-4851**

Headquarters program office: OSS

Halite Crystals as an Exobiological Resource

Lawrence I. Hochstein, Harold Morowitz

Surface features suggest that Mars may have had a considerable aqueous component at one time. One such feature is what appears to have been a lake basin (about 3.5 billion years ago). While the chemical composition of this site is unknown, the high albedo is suggestive of evaporites composed of magnesium and sodium chlorides. If Mars did have an aqueous history, and conditions were propitious for the origin and evolution of life, one can imagine an evolution that terminated once conditions on the surface of the planet precluded the existence of liquid water. The transition from an aqueous to an arid planet would have been accompanied by environments where the concentration of ionic species would approach saturation and ultimately result in their deposition, possibly as halite crystals. Evidence for a putative chemical and/or biological evolution on Mars would be sequestered within crystals constituting these sedimentary deposits. This reasoning provides a rational search strategy for any program whose purpose is to search for past or present life. The presence of organisms (or their remains) in ancient halites represents an untapped pool of evolutionary information about life as it was at the time of entrapment. In a sense, this material provides a snapshot into evolutionary history. Finally, evidence that a putative Martian biota or material indicative of an earlier chemical and/or biological evolution may occur in halites would affect how standards related to planetary quarantine are viewed.

Viable bacteria have been isolated from a variety of fossil materials, including salt deposits whose age is on the order of 200 or more millions of years. The age of these organisms is uncertain because the possibility that they were of exogenous origin was not adequately excluded. Proteins and DNA have also been isolated from a variety of fossil materials but, again, the possibility that these compounds are of more recent origin than the material in which they

are found has not been eliminated. It should be pointed out that all claims to having isolated putatively ancient organisms from ancient sources suffer from the same uncertainty.

These and other issues were addressed at a workshop organized in collaboration with Harold Morowitz, Robinson Professor at George Mason University. The attendees concluded that the possibility should not be ignored that sedimentary deposits, particularly those containing halites, may contain materials contemporary with the deposits. A consensus was developed concerning the issues to be addressed in order to investigate such materials. These include age dating the materials within the halite crystals; developing methodologies for isolating the contents within halite crystals in order to prevent external contamination; applying, or developing as necessary, methods for isolating and analyzing small quantities of sample material, particularly proteins and nucleic acids; and ascertaining how the methods of molecular biology can be applied to characterize the materials within halite crystals. The fluid phase within a halite crystal consists of a saturated solution of a variety of salts. It is not clear to what extent such conditions favor the integrity of biological materials. It was therefore suggested that the survival of bacteria, biopolymers, and their constituent monomers be studied, with the aim of providing phenomenological information and a theoretical basis for the behavior of materials in the halite crystals. Resolving the issues associated with halite crystals requires an integrated intradisciplinary work group, and research support in this area is encouraged.

**Ames-Moffett contact: L. Hochstein
(415) 604-5938**

Headquarters program office: OSS

Center for Star Formation Studies

David J. Hollenbach, Patrick M. Cassen

The Center for Star Formation Studies, a consortium of scientists from the Space Science Division at Ames and the Astronomy Departments of the University of California at Berkeley and Santa Cruz, conducts a coordinated program of theoretical research on star and planet formation. The Center, under the directorship of D. Hollenbach at Ames, supports postdoctoral fellows, senior visitors, and students. The group meets regularly at Ames to exchange ideas and to present informal seminars on current research, hosts visits of outside scientists, and conducts a week-long workshop on selected aspects of star formation each summer.

The Star Formation Summer Workshop in 1994 was held on the campus of the University of California at Santa Cruz. It included, in addition to the Center scientists, about 100 astrophysicists from around the world. The topics discussed included the fragmentation of molecular clouds, the gravitational collapse of these fragments to form stars and protoplanetary disks, and the formation of binary stars and multiple star systems.

The main focus of work in 1994 was the formation of clouds in the interstellar medium, the collapse of dense clouds to form a protostar with a protoplanetary disk, the coagulation of dust particles in the disk to form comets and the precursors of planets, the thermal instabilities in these disks which may lead to bursts of accretion of disk material onto the protostar, and the later evolution of comets' orbits. M. Wolfire, D. Hollenbach, A. Tielens, and C. McKee (University of California at Berkeley) showed how the heating of interstellar gas by the photoejection of energetic electrons from dust grains produced a two-phase neutral medium. The two phases are a warm, low-density component at a temperature of 10,000 kelvin in pressure equilibrium with denser cold clouds with temperatures of about 70 kelvin. These clouds merge and cool further to form even denser clouds which collapse to form stars. Hollenbach, Tielens, and C. Ceccarelli (Frascati Observatory) modeled the expected temperature and

chemistry in a collapsing cloud and showed that infrared emission from carbon monoxide and water molecules, as well as oxygen atoms, dominate the emergent spectrum. J. Tsai at Ames showed how the heating generated by the collapse, or the winds from the young protostar, could slow or even eventually halt the collapse. T. Dobrovolskis and J. Cuzzi modeled the turbulence in the protoplanetary disk, quantitatively demonstrating how small dust particles coagulate and grow to form larger objects such as comets. R. Bell and D. Lin (University of California at Santa Cruz) showed how thermal instabilities in the disk would lead to intermittent periods of extremely high accretion of disk material onto the central protostar. This high accretion induces a huge increase in the luminosity of the protostar, and explains why young protostars are observed to have large outbursts of luminosity. L. Dones (University of California at Santa Cruz) has used a computer code to follow the evolution of the orbits of comets over tens of millions of years to calculate, for example, the probability of their colliding with planets such as Jupiter and Earth. These studies are of great current interest given the impact of Comet P/Shoemaker-Levy 9 with Jupiter in July 1994.

These theoretical models have been used to interpret observational data from such NASA facilities as the Infrared Telescope Facility (IRTF), the Kuiper Airborne Observatory (KAO), and the Infrared Astronomical Observatory (IRAS), as well as from numerous ground-based radio and optical telescopes. In addition, they have been used to determine requirements of future proposed missions such as the Stratospheric Observatory for Infrared Astronomy (SOFIA) and the Space Infrared Telescope Facility (SIRTF).

**Ames-Moffett contact: D. Hollenbach
(415) 604-4164**

Headquarters program office: OSS

Simulations of the Martian Water Cycle

Howard C. Houben, Robert M. Haberle, Aaron P. Zent

Water on Mars has been a subject of interest ever since Percival Lowell speculated at the turn of the century that the planet was crisscrossed with canals constructed by a dying civilization. Of course, we now know that Mars has no canals, but it does have water. Though temperatures and pressures on Mars are too low for water to exist in liquid form, water can exist as vapor in the atmosphere, ice on the surface, and adsorbate in the soil. The Viking spacecraft measured atmospheric water vapor and found that it changed significantly with season and latitude. This implies that Mars has an active hydrological cycle in which water is exchanged between the surface and the atmosphere. Questions to be answered include What is the nature of the surface reservoirs? and Are these reservoirs growing or shrinking with time?

To answer these questions, we have constructed a model of the Martian water cycle that contains (1) a complete description of the seasonally varying global atmospheric circulation system; (2) a precipitation/evaporation scheme that allows water to condense in the atmosphere or sublime from ice on the surface; and (3) a shallow subsurface reservoir (the regolith, approximately 10 centimeters deep) that allows water to condense onto soil grains (a process called adsorption). The water contained in the regolith is allowed to diffuse into the atmosphere on a daily time scale, or into the "deep" soil below it on a monthly time scale. We also assume that an extensive ice deposit exists at the north pole that serves as a source for water during summer as indicated in the Viking observations.

In our first simulation we found that without a regolith the results did not resemble the Viking observations. After several years the atmosphere saturated and ice deposits formed everywhere. In our

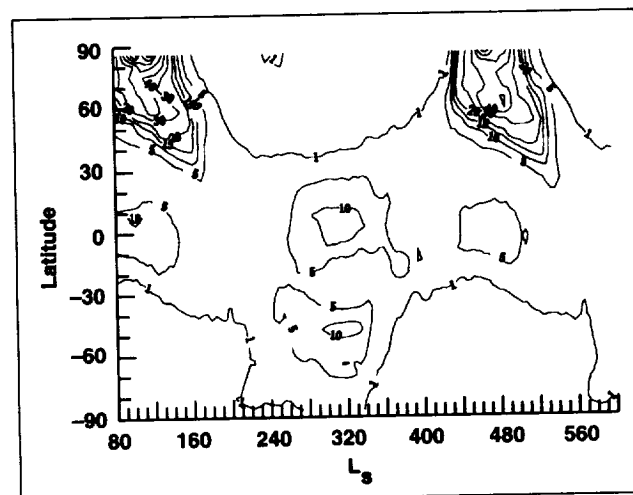


Fig. 1. Water vapor in the Martian atmosphere as simulated by our model. Units are precipitable microns. L_s is an angular measure of season on Mars referenced to northern spring. This water vapor behavior is similar to that observed by the Viking spacecraft.

second simulation we found that with a regolith the atmosphere was too dry—water subliming from the north cap was quickly soaked up by the regolith as it moved to lower latitudes. Only when we started with a globally charged regolith were we able to reproduce the observed behavior. The results of that successful simulation are shown in the figure. Thus, the Martian water cycle appears to be strongly buffered by the regolith.

Ames-Moffett contact: H. Houben
(415) 604-3381
Headquarters program office: OSS

Evolution of Bacterial Symbiosis at Deep-Sea Methane Vents

Linda L. Jahnke

Virtually all life on Earth is dependent on the capture of the Sun's energy by photosynthetic organisms. However, far below the ocean's photic zone, in the permanently dark environment of the deep sea, other types of ecosystems have been discovered that are driven by energy from the bacterial oxidation of reduced chemical compounds (chemosynthesis). Along tectonic ridges on the ocean floor, fissures allow the extraction of reduced gases by the circulation of seawater deep into mantle basalts and ancient organic sediments. In hydrothermal vent systems, effluents have high concentrations of hydrogen sulfide. Sulfur-oxidizing bacteria break down this gas metabolically, releasing energy in the process. The clusters of mussels, clams, and tube worms found in these deep-sea hot spring environments are in fact fueled by such microbial reactions, by forming symbiotic associations with the bacteria.

The vast majority of chemosynthetic symbioses described so far rely on reduced sulfur for energy. However, other cold-seep vents with fluids rich in methane have been shown to support animal life. The "methane mussels" of the Louisiana slope inhabit regions of the Gulf of Mexico where natural gas, composed primarily of methane, seeps through the sediments to the oxygenated bottom water. The gills of these mussels contain intracellular methane-oxidizing bacteria. These methanotrophic bacteria biochemically convert methane to cellular constituents and actually grow within the host cells where they are gradually consumed by the mussel as its source of food. Working with an organic geochemist, Roger Summons (Australian Geological Survey Organization), and with methane mussel tissues provided by Charles Fisher (Pennsylvania State University), we initiated a study of the metabolic relationship between the host mussel and the symbiotic, methanotrophic bacteria.

Two stable carbon isotopes occur naturally, carbon-12 (^{12}C) and carbon-13 (^{13}C). During the microbial oxidation of methane, biochemical molecules are synthesized that are depleted in ^{13}C relative to ^{12}C . This fact allowed us to analyze various mussel tissues for specific compounds

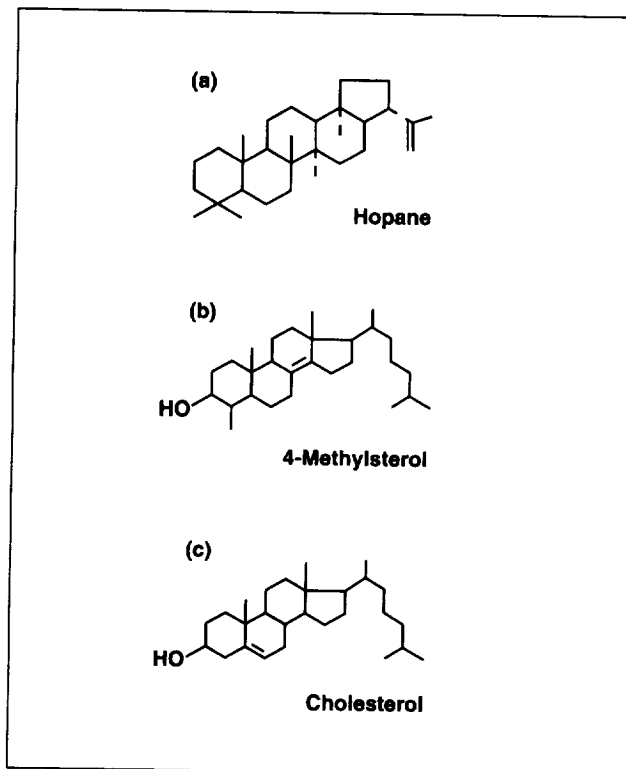


Fig. 1. Biomarker molecules.

characteristic of animal or bacterial constituents (biomarker molecules), and to use the biomarker's carbon isotopic composition in order to understand the biosynthetic flow of carbon from bacterium to host. The gill tissue, known site of the intracellular symbiont, contained large amounts of methanotrophic biomarkers such as hopanoids (part (a) of the figure) and methylsterols (part (b)). Only small amounts of these methanotrophic molecules were recovered from the other portions of the mussel. Tissues poor in methanotrophic biomarkers, such as the mantle and foot, were instead rich in cholesterol (part (c) of the figure) and several other cholesterol-like sterol molecules considered to be biomarkers for animal tissues. All of the biomarkers—hopanoids, methylsterols, and cholesterol—were highly depleted in ^{13}C , indicating synthesis of both bacterial and

animal constituents from methane-derived carbon. It was also clear from the intramolecular positions of the unsaturated carbon bonds found in the various methylsterols and cholesterol-like sterols that these compounds were biosynthetic intermediates and that the bacterial sterols were being directly converted to cholesterol for use by the animal.

Although the biosynthesis of hopanoids and methylsterols in methanotrophic bacteria has been viewed as a primitive, evolutionary analogue to the synthesis of cholesterol in more highly evolved

eukaryotic organisms (nucleated cells), little information has been available about the nature of the biochemical transitions that must have occurred to span the gap from synthesis in a primitive bacterium to synthesis in eukaryotic tissues. The study of this unique methanotroph–mussel symbiosis provides an evolutionary insight into this process.

Ames-Moffett contact: L. Jahnke
(415) 604-3221
Headquarters program office: OSS

Exobiology Science Strategy for Mars Exploration

Harold P. Klein, Donald L. DeVincenzi

Of the other planets in the solar system, Mars is the most promising for further elucidation of current concepts about chemical evolution and the origin of life. Exobiological objectives for Mars exploration include (1) determining the abundance and distribution of the biogenic elements and organic compounds, (2) detecting evidence of an ancient biota on Mars, and (3) determining whether indigenous organisms exist anywhere on the planet. Both approved and planned missions to Mars were evaluated for their potential to contribute to the understanding of these three exobiology science objectives, and an exploration strategy was developed for each objective.

Each strategy examines how the complement of scientific instruments on the currently approved missions will lay the groundwork for understanding the most important exobiology questions posed for the three objectives. In addition, missions and science payloads, beyond those already approved, were evaluated for their suitability for conducting sophisticated experiments critical for a complete understanding of the exobiological questions. This analysis produced a preferred sequence of missions and payloads designed to achieve each of the three major exobiology objectives.

The three strategies are quite similar and, in fact, share the same sequence of five phases. In the first phase, each requires global reconnaissance and remote sensing by orbiters of selected sites of interest for detailed in situ analyses. In the second phase, lander missions are conducted to characterize the chemical and physical properties of the selected sites. The third phase involves conducting critical experiments at sites whose properties make them particularly attractive for exobiology. These critical experiments include, for example, identification of organics, detection of fossils, and detection of extant life. The fourth phase is the detailed analysis of samples returned from these sites in Earth-based laboratories to confirm and extend previous discoveries. Finally, in the fifth phase, human exploration is needed to establish the geological settings for the earlier findings or to discover and explore sites that are not accessible to robotic spacecraft.

Ames-Moffett contact: H. Klein
(415) 604-4223
Headquarters program office: OSS

FOSTER: The Flight Opportunities for Science Teacher Enrichment Project

David G. Koch, Garth Hull, Carl Gillespie

The nation, NASA, and Ames Research Center are continuing to place considerable emphasis on the relevance of research to our nation and the important role to be played by researchers in educational outreach. The new Office of Space Science Strategic Plan for 1995–2000 states, "Because of its mobility and the fact that nonspecialists can fly on a SOFIA [Stratospheric Observatory for Infrared Astronomy] mission, [the Flight Opportunities for Science Teacher Enrichment (FOSTER) project] will be the only NASA program in which educators can actively participate as flight members with scientists and engineers. This will build on the highly successful, beneficial experience that many K–12 teachers have had on the KAO." The FOSTER project at Ames continues to grow and develop as a unique educational outreach tool.

The FOSTER project has expanded this year to include more teachers from more areas of the country. FOSTER began with teachers only from the San Francisco Bay Area, and then included teachers from Hawaii, where the Kuiper Airborne Observatory (KAO) is deployed a few times per year. This year, the project included teachers from the home communities of the scientists that fly on the KAO—specifically, from Arizona, Massachusetts, and Wisconsin. The plan for the project calls for continuation of this expansion by next including teachers from any of the 11 Western states served by the Ames Educational Programs Office.

The workshop for the teachers this summer was held 19–24 June and included 22 teachers of grades 6–12. It consisted of presentations by NASA scientists and engineers and by KAO mission staff and pilots, demonstrations of classroom activities that students and teachers can perform, provision of an abundance of curriculum and resource materials, training on the use of the Internet, tours of facilities and of the Lick Observatory, and orientation for the flight on a

research mission of the KAO. In addition to flying teachers from Moffett Field and Hawaii, accommodations were made for one of the teachers to fly on the Comet P/Shoemaker-Levy 9 flights from Australia with financial support for the teacher coming from his school district. The teachers have found both the workshops and the flights to be an enriching experience whereby they have been able to better understand and personally witness the excitement, hardships, challenges, discoveries, teamwork, social relevance, and educational value associated with carrying out scientific research. They have been able to use this experience in teaching their students the usefulness of science.

Other accomplishments by the FOSTER project staff included production of a half-hour educational video, "Kuiper: Window on the Universe"; a Saturday Internet training workshop for FOSTER alumni teachers; production of an Electronic Picturebook hypercard stack of the Orion Nebula by a FOSTER alumnus as a summer IISME project (Industry Initiatives for Science and Math Education/Lawrence Hall of Science), working with scientists in the Space Science Division; and creation of the FOSTER On-Line project ("Ask a Scientist . . ." from anywhere on Internet), in collaboration with the National Research and Education Network project at Ames.

The staff for FOSTER consists of individuals from many diverse organizations, working together to provide a unique opportunity for science teacher enrichment. Contributions come from the Space Science Division, the Science and Applications Aircraft Division, the Educational Programs Office, and the SETI Institute (NASA grant NAGW-3291).

**Ames-Moffett contact: D. Koch
(415) 604-6548**

Headquarters program office: OSS

Light Transmission and Reflection in Perennially Ice-Covered Lakes on Earth and on Mars

Christopher P. McKay

The dry valleys of Antarctica are the environment on Earth that is the most similar to the environment on Mars. The mean temperatures are -20°C and the precipitation is extremely low; there is no apparent life in these frozen deserts. Surprisingly, there are a series of lakes on the floors of the valleys. The lakes maintain a thick cover of ice all year, but beneath the ice is liquid water up to 50 meters deep, in which microbial life is found. This life derives its energy from the small amount of sunlight that propagates through the ice cover. We have investigated the transmission and reflection of light from one of these lakes, Lake Hoare. Our data base consists of year-round measurements of the photosynthetically active radiation (400–700 nanometers) under the ice, measurements of the spatial variation of the under-ice light in midsummer, and spectrally resolved measurements of the albedo and transmission of the ice cover in early summer (November) and in midsummer (January). The spectrally resolved measurements from 400 to 700 nanometers show that about 2% to 5% of the incident light in this spectral region penetrates the 3.5-meter-thick ice cover. We have analyzed the spectral data using a two-stream scattering solution to the radiative transfer equation with three vertical layers in the ice cover. The figure shows the data and the results of the model that gives the best fit to the data. A surficial glaze of scattering ice 1 centimeter thick overlies a layer of sandy, bubbly ice about 1 meter thick, and below this is a thick layer of sand-free ice with bubbles. We find that the ice cover is virtually opaque at wavelengths longer than 800 nanometers. The net transmission of solar energy is about 2%. Significant changes in the thickness of the ice cover have been reported at Lake Hoare. These are due primarily to changes in the thickness of the bottom layer only. Because this layer is relatively clear, the effect on the transmission through the ice cover from these changes is less than would be predicted assuming a homogeneous ice cover.

These results have interesting applications to the question of whether ice-covered lakes existed on

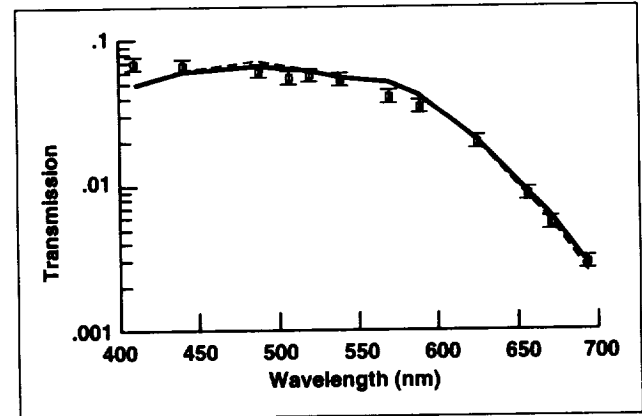


Fig. 1. Spectral transmission of the ice cover on Lake Hoare in the austral summer, during which the ice thickness was 3.5 meters. Standard errors of 10% are shown. The solid line is the computed transmission using a two-stream radiative transfer model.

early Mars. On Mars, the temperatures would have become even colder than those in the Antarctic dry valleys. Thus, the ice cover on any Martian lakes would have been thicker than that in the dry valleys. However, the amount of light (essential for photosynthesis) would be greater than one might expect, because the bottom layer of ice is much clearer than the top layers. Most of the extinction of light in the Antarctic dry-valley lakes is due to these top layers. On Mars it is the bottom layer that would become much thicker, and thus there would be only a small reduction in light levels below the ice cover. We conclude that sufficient light would have penetrated perennial ice covers on early Mars to allow life to exist.

Ames-Moffett contact: C. McKay
(415) 604-6864
Headquarters program office: OSS

Extragalactic, Galactic, and Solar System Organics

Yvonne J. Pendleton

Until relatively recently, the presence of organic molecules on interstellar dust grains was inferred from the infrared absorption spectra of hydrocarbons along only one line of sight through our galaxy—that toward the heavily extinguished galactic center. In order to know whether this organic material is widespread throughout our galaxy, researchers at NASA Ames (Pendleton, L. Allamandola, S. Sandford, A. Tielens) began a vigorous observation program to detect the hydrocarbon absorption signature (near 3.4 micrometers) along different sightlines through our galaxy. The feature that so clearly reveals the presence of organic material has now been detected along a dozen different sightlines through our galaxy,

and most recently has also been detected in other galaxies (by Pendleton and University of Hawaii coworkers A. Bridger, T. Geballe, and G. Wright). Such widespread distribution supports the assertion that the organic component of the interstellar dust is available for incorporation into newly forming planetary systems. With the support of a strong laboratory astrophysics program (Allamandola and Sandford) at NASA Ames, the telescopically observed features are being compared to the chemically processed interstellar ice analogs produced in the laboratory to investigate the physical processes involved in the production of the interstellar organics in dense molecular clouds. Although laboratory

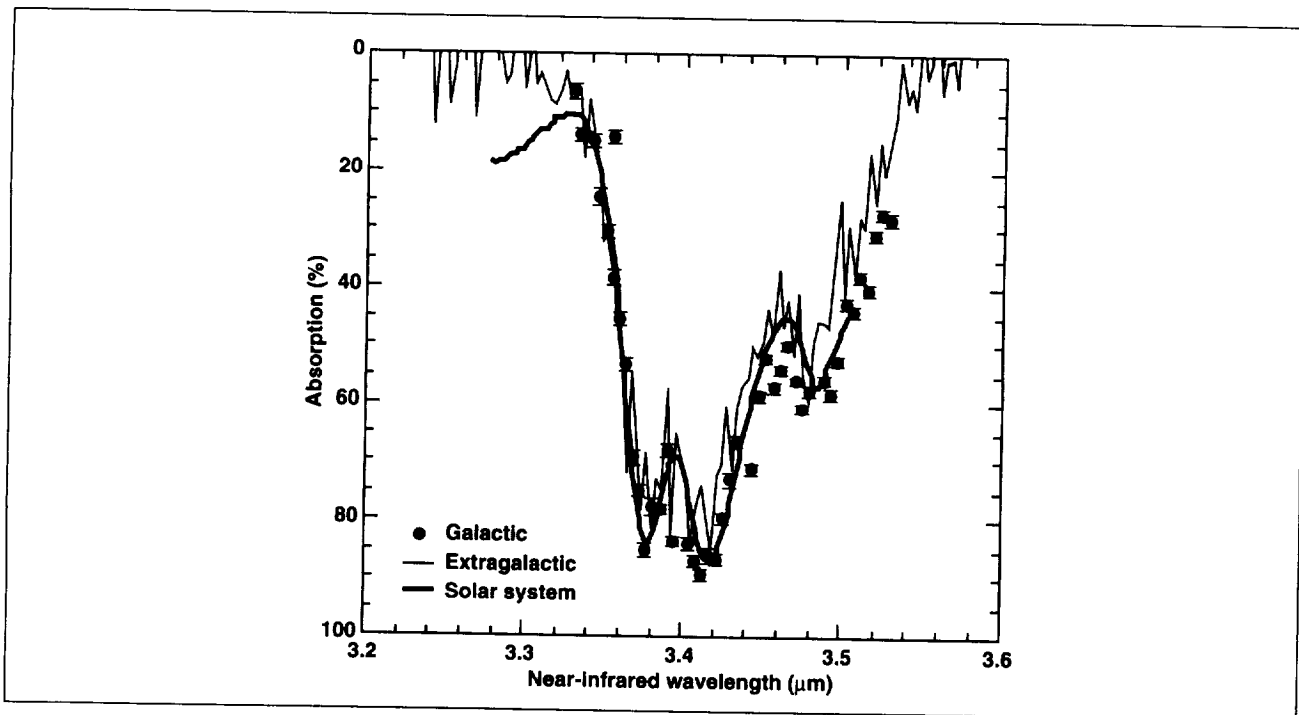


Fig. 1. A comparison of the 3.4-micrometer absorption feature seen toward a luminous IRAS galaxy (thin line), the galactic center (solid points), and the organic residue from the Murchison meteorite. The extragalactic data have been corrected for redshift so that the wavelength positions can be compared. Galactic center data have been normalized to the extragalactic data at 3.4 micrometers. (Galactic center data were obtained at the NASA Infrared telescope facility; external galaxy data were taken at the United Kingdom Infrared Telescope Facility and were provided by Gillian Wright (Univ. of Hawaii); meteoritic data were provided by Sherwood Chang at NASA Ames.)

experiments are helping to reveal the composition of the organic material (i.e., the recipe for chain-like hydrocarbons that give rise to the absorption features near 3.4 micrometers), the best match to the interstellar data continues to be one provided by nature, from the Murchison meteorite which fell to the Earth in 1969. The figure shows a comparison of the organic material seen in an external galaxy, in our own galaxy, and in the organic residue from the Murchison meteorite. The Murchison meteorite is a carbonaceous chondrite that contains isotopic anomalies that cannot be explained other than by origination from interstellar material. The remarkable similarity of the interstellar dust spectra to the

Murchison meteoritic spectrum suggests the possibility that the organic component of the carbonaceous meteorites may be, in part, remnants of the interstellar dust. It is intriguing that the widespread organic material that we see in our own galaxy and in distant galaxies is so similar to that found in a meteorite on Earth, because the delivery of the organic material to the Earth could have played a role in the origin of life.

**Ames-Moffett contact: Y. Pendleton
(415) 604-4391**

Headquarters program office: OSS

Mechanism of Unassisted Ion Transport Across Membranes

Andrew Pohorille, Michael A. Wilson

Ions play an essential role in a wide variety of processes in contemporary cells, including bioenergetics, signaling, and catalysis of chemical reactions. They are also needed to maintain the biologically active structures of biopolymers. Considering their widespread importance in the biology of present-day cells, ions must have been important chemical constituents in the emergence of life.

To enter cells, ions must permeate the lipid membranes that form cell walls. A large activation energy is required for the process of transferring ions from the polar aqueous environment to the nonpolar interior of the membrane. In contemporary cells, ion transport is aided by ion channels, carriers, and pumps located in membranes, which serve to lower the activation energy. However, at the earliest stage of cellular evolution ion transport must have proceeded without assistance from these highly evolved molecules.

The permeability of membranes to the unassisted transport of ions can be estimated from a standard model in which the membrane is represented as a structure of fixed width, which is poorly penetrable by water. These estimates lead to the conclusion that membranes are practically impermeable to ions.

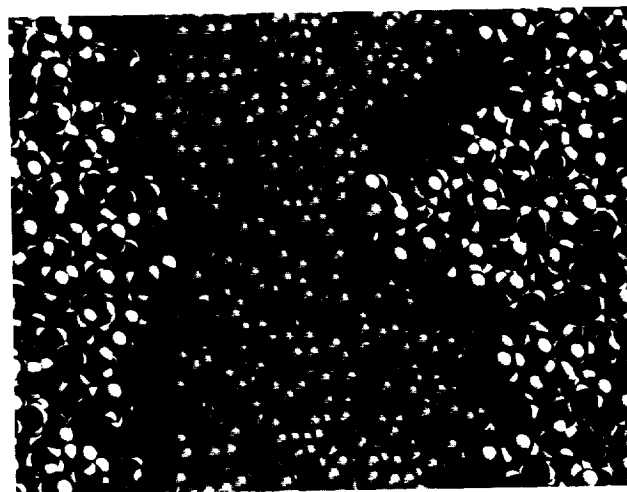


Fig. 1. A representative configuration of sodium ion (Na^+) in the membrane obtained from computer simulations. The ion is yellow, the lipid head groups are magenta, and the lipid tails forming the nonpolar membrane interior are blue. The oxygen and hydrogen atoms of water molecules surrounding the membrane are red and white, respectively. (See color plate 16 in Appendix)

These results are in conflict with experimentally measured permeabilities of model membranes, which are 13 to 15 orders of magnitude higher. The discrepancy indicates that the standard model ignores some essential features of the transfer process which lower the ionic permeabilities considerably.

To identify these features we performed large-scale computer simulations of unassisted transport of two biologically essential ions, sodium (Na^+) and chloride (Cl^-), across the membrane. We found that an ion creates a local deformation in the membrane as it moves into the interior. This defect results from the tendency of water molecules and the polar head groups of the membrane-forming lipid molecules, which are normally restricted to the surface of the membrane, to follow the ion into the nonpolar interior (see figure). As the ion crosses the center of the membrane the deformation changes

sides; the initial defect slowly relaxes and a new defect forms in the outgoing side of the membrane. During the whole process of transfer, the ions remained well solvated by both water and polar lipid head groups. Membrane defects and ion solvation considerably lower the activation energy to unassisted ion transport, making this process feasible.

The results of this study offer valuable insights into a broad range of chemical and biochemical processes, such as assisted ion transport, charge stabilization inside membranes, time-controlled drug delivery, and ion transport between two immiscible liquids, a fundamental process in electrochemistry.

Ames-Moffett contact: A. Pohorille
(415) 604-5759

Headquarters program office: OSS

Isotopic Ratios of Carbon and Oxygen

Examination of the isotopic ratios of various elements, including carbon (C) and oxygen (O), in soil samples can yield important information. Variations in isotopic ratios of $^{12}\text{C}/^{13}\text{C}$ and $^{16}\text{O}/^{18}\text{O}$ in Martian soil samples could be important clues to the planet's geologic and biologic history. Such variations would be expected to be generated in a sample by any process of elemental transfer whose rate limiting step is diffusion controlled. This category of processes could include past or present volcanism, freeze-thaw cycles, incorporation of carbon dioxide into the soil from the Martian atmosphere, enzymatic reactions, or respiration. Isotopic variability could also be caused in a sample by its having been mixed with other reservoirs of carbon or oxygen. We are developing a Stable Isotope Laser Spectrometer (SILS) that employs high-resolution tunable diode lasers to measure the ratios of the stable isotopes of carbon and oxygen, $^{13}\text{C}/^{12}\text{C}$, $^{18}\text{O}/^{16}\text{O}$, and $^{17}\text{O}/^{18}\text{O}$, contained in the carbon dioxide released during the heating of a rock or soil sample. Modern high-temperature diode laser systems are rugged, light-

Todd B. Sauke, Joseph F. Becker, Clayton G. Bratton

weight, and low power, and operate at temperatures above 200 kelvin, and therefore are well suited for use in flight hardware applications. In addition, laser spectroscopy offers important advantages over conventional mass spectrometry for measurements on a planet's surface. Because of the high spectral resolution of the laser spectrometer, the detailed and complex sample preparation and purification required for reliable mass spectrometry is unnecessary—contaminant gases do not interfere with the measurement. The goal is to develop an instrument for laser spectroscopic isotope analysis of planetary soils and ices on possible near-term Mars missions such as the Mars Polar Pathfinder and the Mars Rover with Sample Return missions.

This past year a new level of accuracy and precision has been achieved with $^{12}\text{C}/^{13}\text{C}$ isotopic ratios being measured to better than 0.1% and $^{16}\text{O}/^{18}\text{O}$ isotopic ratios measured to about 0.2%. Recent full integration of a pyrolysis oven and gas separation system now allow investigation not only

of total isotopic ratio in a solid sample but also of thermal differentiation of isotopic ratio as the sample is decomposed. This feature allows discrimination of the source of the carbon dioxide released from soil samples (e.g., organic residues versus inorganic calcite deposits).

Improved accuracy and thermal control provide the SILS with capabilities that are applicable and important to NASA planetary exploration missions designed to provide information to geologists, biologists, and planetary scientists. Future plans include measurement of isotopic ratios in real soil

and mineral samples in order to further demonstrate the instrument capabilities, and developing the capability to measure $^{15}\text{N}/^{14}\text{N}$ and $^{34}\text{S}/^{32}\text{S}$ in rock and soil samples. The design and development of a new miniaturized compact instrument is planned in an effort to prepare a flight-ready instrument for a Mars mission.

**Ames-Moffett contact: T. Sauke
(415) 604-3213
Headquarters program office: OSS**

Star Formation in Colliding Galaxies

Bruce F. Smith, Richard A. Gerber

The importance of galaxy interactions in clusters of galaxies and the effect of these interactions on the evolution of galaxies is a subject of considerable interest. Many processes need to be understood individually. Observable consequences within a galaxy that are directly traceable to environmental effects are difficult to sort out. Differences between galaxies within and outside clusters might reflect differences at the time of formation or changes induced by the cluster environment. Conditions during formation and subsequent changes doubtless both contribute.

The connection between disturbed galactic morphology and the presence of a nearby galaxy has long been observed. Collisions between galaxies do more than induce morphological changes; any gas present in a galaxy will be affected in ways that can lead to a number of observable phenomena. Observations at many wavelengths have confirmed that enhanced star formation appears to be taking place in many, but not all, morphologically disturbed pairs of galaxies. The most striking observational evidence for increased star formation comes from infrared studies. Infrared selected samples of galaxies tend overwhelmingly to pick out interacting systems. A sample

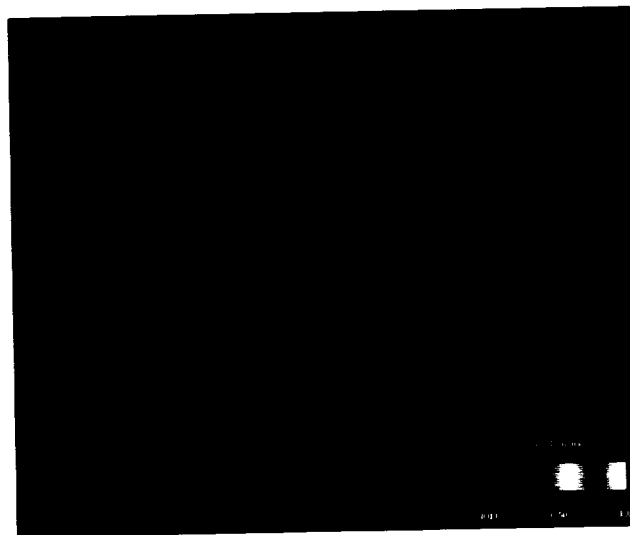


Fig. 1. Computer model of the distribution of gas in a galactic disk after a central collision with a smaller "intruder" galaxy. A dense ring of gas propagates outward after the encounter, triggering the formation of dense "knots" in the outer ring and sheared radial "spokes." The dense regions in the ring are the sites of unusually vigorous star formation.

of optically selected disturbed pairs have a factor-of-two increase in infrared luminosity, on average, over that of a sample of normal spiral galaxies. The most strongly interacting systems show the most extreme values of infrared excess. Whereas a link between galactic interactions and bursts of star formation seems clear, the mechanism by which star formation occurs is poorly understood at best.

When galaxies collide, one possible outcome is the formation of a ring galaxy. Because of the near-circular nature of these galaxies, studying them can provide a wealth of information about the nature of the disks in spiral galaxies and how star formation is triggered by galactic interactions. Using supercomputers at the Numerical Aerodynamic Simulation (NAS) facility at Ames, we have numerically modeled the formation and evolution of ring galaxies. The

models include a representation of both the stars and the gas in galaxies. Rings form in both the stellar and the gaseous components. A thin ring of shocked, dense gas forms, which coincides with observed regions of enhanced star formation. We have also studied the formation of dense knots and "spokes" observed in some ring galaxies. These features are related to instabilities in the disk of the precollision galaxy. The figure shows the distribution of gas in a perturbed model disk. Dense knots of gas form in the outer ring, and spokes are visible extending toward an inner ring.

**Ames-Moffett contact: B. Smith
(415) 604-5515**

Headquarters program office: OSS

Telepresence for Planetary Exploration

Carol Stoker

The Telepresence Project is a collaboration between scientists in the Space Science Division and engineers in the Information Systems Division. Telepresence and virtual reality are being developed and tested for their application to controlling remote vehicles on the surfaces of other planets. Telepresence is a method for operating a remote vehicle with a very-high-fidelity information interface that gives the operator a strong sense of being present in the remote environment. Virtual reality provides the user with a sense of presence within a graphic model of the remote space which is generated by a computer. Exploration of other planetary surfaces by mobile robots is enabled using these technologies because they provide much greater ease of operation and data interpretation from remote vehicles. Together, these technologies have the potential for expanding the range of mobile robots, and vastly decreasing the cost of mission operations for planetary surface missions. As well as enabling future planetary surface exploration, these technologies

may have an application in dangerous or hostile environments on Earth. In the last year, we have performed a series of field experiments to develop and demonstrate the use of telepresence and virtual reality systems for controlling rover vehicles on planetary surfaces.

In 1993, we developed a telepresence-controlled remotely operated underwater vehicle (TROV) and used it to explore an ice-covered sea environment in Antarctica. The goal of the mission was to perform scientific exploration of an unknown and hostile environment using a remote vehicle with telepresence and virtual reality as a user interface. The vehicle was operated both locally, from above a dive hole in the ice through which it was launched, and remotely over a satellite communications link from a control room at Ames Research Center, for over 2 months. Local control of the vehicle was accomplished using a control box containing joysticks and switches, with the operator viewing stereo video

camera images on a stereo display monitor. Remote control of the vehicle over the satellite link was accomplished using the Virtual Environment Vehicle Interface (VEVI) control software we developed. The remote operator interface included either a stereo display monitor similar to that used locally or a stereo head-mounted, head-tracked display. Stereo video from the vehicle was transmitted to Ames over a satellite channel. Another channel was used to provide a bidirectional Internet link to the vehicle control computer through which the command and telemetry signals traveled, along with a bidirectional telephone service. In addition to the live stereo video from the satellite link, the operator could view a computer-generated graphic representation of the underwater terrain, modeled from the vehicle's sensors. The actual vehicle was driven either from within the virtual environment or through a telepresence interface. All vehicle functions could be controlled remotely over the satellite link.

During the 1993 Antarctic mission, the TROV was operated nearly continuously for over two months both locally and remotely from Ames. The primary scientific objective of the mission was to perform transects of selected areas between 60 and 1,000 feet depth, and produce a video record of benthic organisms. A secondary objective was to collect samples with the manipulator arm. The data from the mission are being analyzed, and will be used to generate a multiresolution terrain model of the area, with the video record overlaid as textures on the terrain elevation data.

The vehicle interface was easy enough for an untrained operator or even a child to use. The operation of the remote vehicle was demonstrated to the public at a special event held at the National Air and Space Museum. The project also supported an educational outreach activity which produced a public broadcast educational program, "Live from Other Worlds," featuring school children remotely operating the vehicle in Antarctica from classrooms across America using home computer technology.

In March 1994, a second field experiment was performed in which the remote control system developed for the Antarctic TROV mission was used to control the Russian Marsokhod rover, an advanced planetary surface rover intended for launch in 1998. Marsokhod consists of a 6-wheeled chassis and is

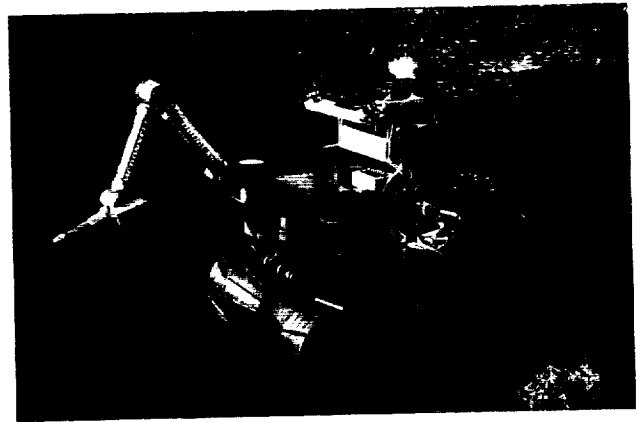


Fig. 1. Marsokhod rover at Amboy, California.

capable of traversing several kilometers of terrain each day (see figure). The rover can be controlled remotely, but is also capable of performing autonomous traverses. It was outfitted with a manipulator arm capable of deploying a small instrument, collecting soil samples, and other tasks. The Marsokhod rover was deployed at Amboy Crater in the Mojave desert, a Mars analog site, and controlled remotely from Los Angeles in two operating modes: (1) a Mars rover mission simulation with long time delay and (2) a Lunar rover mission simulation with live action video. A team of planetary geologists participated in the mission simulation. The scientific goal of the science mission was to determine what could be learned about the geologic context of the site using the capabilities of imaging and mobility provided by the Marsokhod system in these two modes of operation. During the Amboy test, we supported an educational outreach activity to demonstrate the operation of the Marsokhod at the National Science Teachers Association meeting. During this demonstration, the Marsokhod was operated by the NASA Administrator and the Chief Scientist.

The technologies this project has developed are being rapidly incorporated into plans for upcoming planetary surface missions. The project team, in collaboration with McDonnell Douglas and the University of Hawaii, has submitted a proposal to the Discovery Program to explore the Aristarchus region of the Moon with a telepresence-controlled Marsokhod rover. In addition, we are working toward

providing a control system for the Marsokhod rover which will be launched to Mars in 1998 as part of a joint international mission to Mars called "Mars Together." We are continuing to work with the Marsokhod rover to perform field work in a mode that simulates these planetary surface missions to

develop flight qualified control systems for planetary surface exploration.

**Ames-Moffett contact: C. Stoker
(415) 604-6490**

Headquarters program office: OSS

Nitrogen Fixation for the Origins of Life

David P. Summers

A source of fixed nitrogen in a reduced and chemically active state is necessary for life to survive. Such nitrogen is needed for the formation of amino acids, nucleic acids, and other important molecules. Today, such nitrogen comes from nitrogen-fixing organisms in the biosphere. Where did fixed nitrogen come from before such organisms evolved?

In a methane and ammonia atmosphere, shock heating (such as lightning) will lead to the production of amino acids. However, it now seems increasingly likely that the early Earth had an atmosphere of carbon dioxide and elemental nitrogen (a non-reducing atmosphere). In such a system, shock heating only produces nitrogen oxides. One approach to the problem of prebiotic (before life) sources of reduced nitrogen is to focus on the nitrogen oxides that lightning produces. Such oxides would likely end up as ions (nitrate and nitrite) in the ocean. Whereas these ions are too oxidized to be directly important for the origins of life, they are comparatively reactive and provide a way past the relative inertness of elemental nitrogen. What we need now is a way for the nitrate and nitrite to be reduced to form reduced nitrogen compounds such as ammonia.

For the reduction of nitrogen oxides, we look to iron present on the early Earth. Without oxygen around to oxidize it, iron was present as +2 ions (ferrous ions), rather than as +3 ions (ferric ions). The presence of banded layers of sedimentary iron deposited in the early oceans is evidence that such ferrous ions were present, since ferric ions would have been too insoluble to be transported over the

distances involved. In addition, increased volcanic activity on the early Earth, along with iron in the oceans, indicates that iron sulfides were probably more abundant.

Work by David Summers of the SETI Institute, along with Sherwood Chang of the Planetary Biology Branch at Ames, has established that nitrite and nitrate ions are reduced to ammonia by aqueous ferrous ions. (The reduction of nitrite is faster than that of nitrate.) The reaction is fast enough to have provided a significant source of ammonia on the early Earth. Salts (for example, sodium chloride or calcium sulfate) that are likely to have been present in the early oceans do not inhibit the reaction. In fact, the presence of sodium chloride has a beneficial effect. This source of ammonia is favored by an early Earth that was warm and had slightly alkaline oceans. Iron sulfides will also reduce nitrite to ammonia, and will do so under slightly acidic conditions.

Thus we have established a source of reduced nitrogen on the early Earth in the form of ammonia. This is important for an understanding not only of the origins of life, but of many aspects of the geochemistry and evolution of the early Earth. Future work will focus on other sources of reduced nitrogen, and on the fixation and reduction of carbon dioxide under similar conditions.

**Ames-Moffett contact: D. Summers
(415) 604-6206**

Headquarters program office: OSS

Interstellar Dust Destruction

Alexander G. G. M. Tielens, Anthony P. Jones

The extinction of starlight by dust in the interstellar medium (ISM) indicates that a significant proportion of the heavy elements are locked up in this dust (that is, more than 30% of the carbon atoms and more than 90% of the atoms that form silicate minerals, e.g., silicon, magnesium, and iron). Theoretical estimates of the destruction of dust by supernova shock waves indicate that the dust lifetime is of the order of 100 million to 1 billion years. In contrast, the time scale for the formation of new dust by red giants, supernovae, and novae is of order 2.5 billion years. Clearly, the presence of dust in the ISM indicates that the dust must be preserved in some way.

In a collaborative project between Tielens and D. J. Hollenbach at Ames and A. P. Jones and C. F. McKee of the University of California, Berkeley, we have modeled the destruction of dust in steady-state shocks propagating through the medium between the interstellar clouds. The aim of this study is to fully understand all the processes operating on dust in shock waves in the ISM in order to resolve the discrepancy in time scale between formation time and lifetime of interstellar dust.

Dust particles subjected to interstellar shock waves undergo collisional and destructive processing as a result of the differential velocities between the dust particles and between the gas and the dust, and the random thermal motions of the gas-phase species impinging on the dust particle surfaces. Colliding particles may be disrupted, i.e., partially or totally vaporized, shattered, or deformed, with the degree of disruption dependent on the relative velocity and collision geometry. Relative gas/dust velocities result in gas atom/ion impacts on the dust surfaces, and lead to a nonthermal sputtering of those surfaces.

We have calculated the graphite and silicate grain destruction for a range of shocks with initial velocities, V_s , of 50, 100, 150, and 200 kilometers per second, and a range of preshock densities and magnetic fields. The figure shows the silicate dust destruction as a function of shock velocity. Our

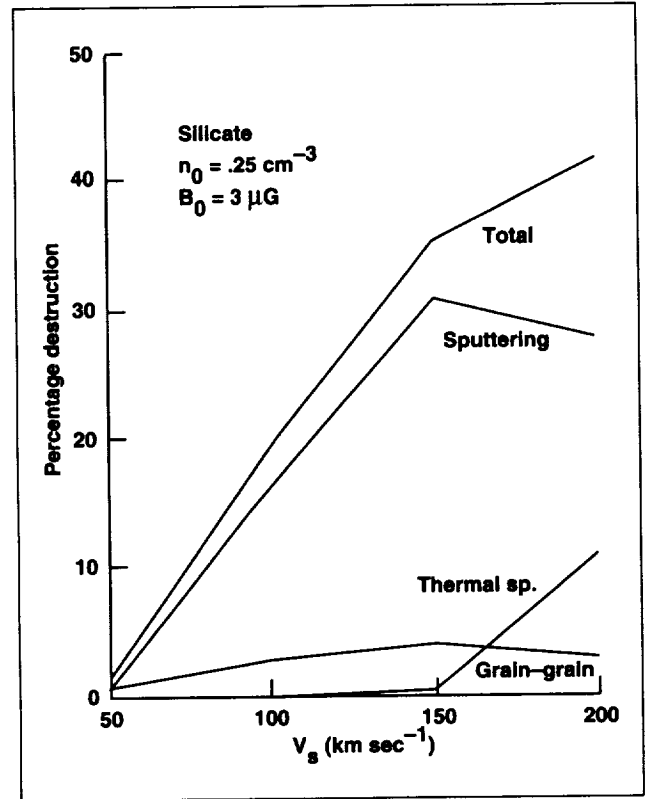


Fig. 1. Postshock silicate dust destruction as a function of shock velocity, V_s , and destructive process for fixed preshock density ($n_0 = 0.25$ hydrogen nuclei per cubic centimeter) and interstellar magnetic field ($B_0 = 3$ micro-Gauss).

calculations use a vaporization scheme that fully accounts for the partial vaporization of dust particles in collisions. This scheme reduces the collisional destruction of the largest grains by a factor of two compared to previous studies.

A major new conclusion of this work is that vaporization in collisions between dust particles is not an important destruction process for dust in interstellar shock waves. We find that dust destruction is dominated by sputtering processes and

conclude that the cores of the particles may be better protected from disruption than has previously been assumed. We calculate dust lifetimes that are somewhat longer than those found in previous studies, but still not long enough to preserve a large fraction of the dust from destruction in shocks in the ISM. Thus we are forced to conclude that the dust must be re-formed in the ISM, that the dust has protective mantles, or that porosity plays a role in mitigating the effects of dust destruction in shock waves.

We are currently investigating the roles of mantles, porosity, and the shattering of dust particles. The shattering of dust in collisions is likely to rapidly destroy the large grains in the ISM and will therefore have a major influence on the interstellar dust size distribution.

**Ames-Moffett contact: D. Hollenbach
(415) 604-4164
Headquarters program office: OSS**

Infrared Spectroscopy of the Impact of Comet P/Shoemaker-Levy 9 on Jupiter

Fred C. Witteborn, Diane H. Wooden

In the early history of the Solar System the impact of large objects onto planetary surfaces and atmospheres was a common phenomenon. Such impacts are evidenced by the cratering of all uneroed surfaces, from the planet Mercury to the satellites of Neptune, and may represent the primary accretion mechanism for planet formation. In recent times, impacts of objects over 1 kilometer in diameter have been rare and certainly have not been subjected to close scientific scrutiny. This situation changed dramatically with the well forecast series of collisions of Comet P/Shoemaker-Levy 9 with Jupiter on 17–22 July 1994. The Kuiper Airborne Observatory (KAO) was one of many major facilities that monitored the impacts, but it was the only one carrying infrared spectrometers to altitudes above 99% of the Earth's water vapor. Of two scientific teams chosen to use the KAO during large fragment impacts, one group, led by Don Hunten and Ann Sprague of the University of Arizona Lunar and Planetary Lab, used the Ames High-Efficiency, Faint Object Grating Spectrometer (HIFOGS). It was operated by Fred Witteborn and Diane Wooden of the Astrophysics Branch at Ames and Richard Kozlowski (Susquehanna University) to monitor the impact zones in the 5–14-micron spectral range during and after the predicted impacts of fragments R and W.

Models of the expected infrared emission of various Jovian and comet gases were calculated by G. Bjoraker of Goddard Space Flight Center.

Spectra were obtained at approximately 3-minute intervals at resolving powers of 130 to 200 (1) in the 5–9-micron band before impact and through most of the very bright aftermath and (2) in the 9–14-micron band before impact and after most of the 5–9-micron observations. The raw spectra were ratioed to raw spectra of the bright infrared standard star, α Boo, whose known flux could then be used to get calibrated spectra of the impact zone. The field of view observed was 10.7 arcseconds in diameter (compared to Jupiter's full 37.8-arcsecond diameter). Despite the fact that the field of view greatly exceeded the expected size of the disturbance, the luminosity increased by an enormous factor (5 to 10 or more) across the 5–9-micron range. Spectra just before and about 10 minutes after impact are shown in the figure. The peaks at 7.4 and 7.7 microns are characteristic of methane heated to a temperature somewhat above Jupiter's normal temperature. The peak at 6.7 microns was eventually identified with steam (water) near 500 kelvin. These emissions decreased rapidly with time and were greatly reduced in 20 minutes. In contrast, a very bright

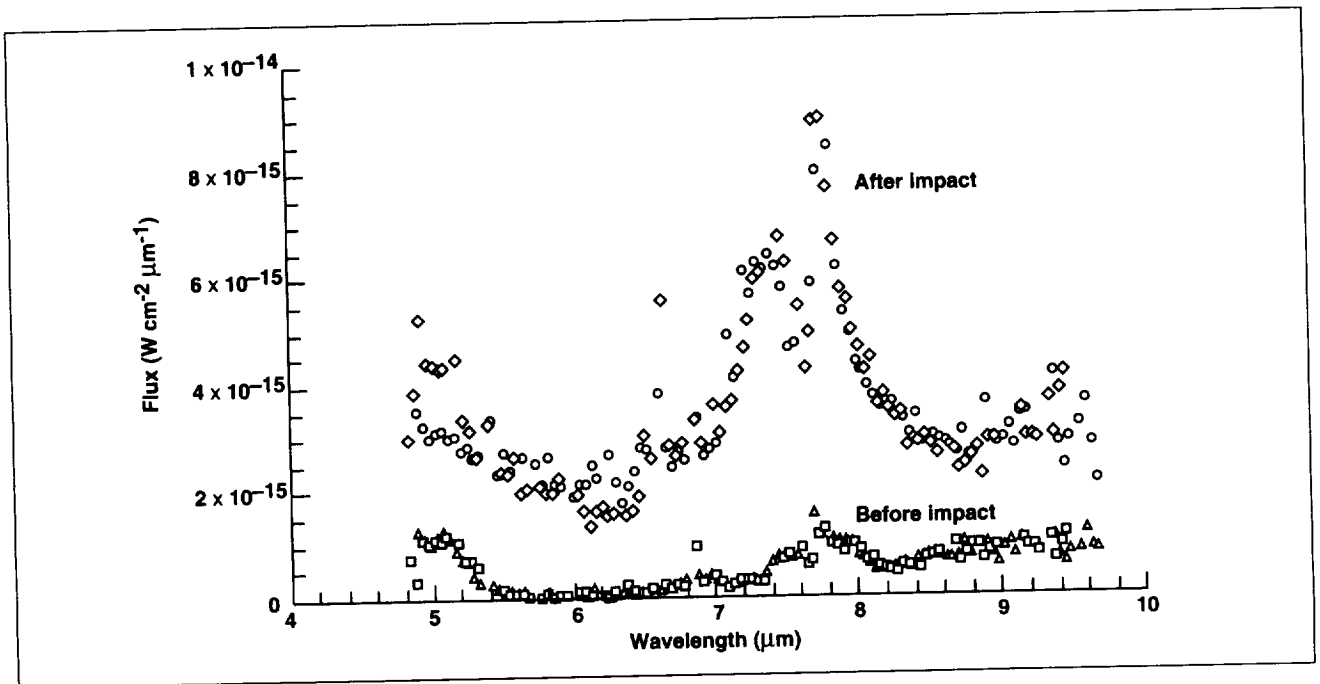


Fig. 1. Jupiter/fragment R impact methane time history (HIFOGS, KAO, 21 July 1994 universal time).

peak attributed to acetylene (at 13.7 microns) appeared to persist longer. Because of its high temperatures, it is believed that the water was from the comet itself. Preliminary results of this work were presented to the Division for Planetary Sciences of the American Astronomical Society meeting in Washington, D.C., in November 1994. Analysis of the decay curves of various portions of the

spectrum will continue in order to identify other molecules and to determine from what altitude the emissions originated.

**Ames-Moffett contact: F. Witteborn
(415) 604-5520
Headquarters program office: OSS**

Simulation of the Mt. Pinatubo Volcanic Aerosol Cloud in the Stratosphere

Richard E. Young, Howard C. Houben, Brian Toon

The 15 June 1991 eruption of Mt. Pinatubo (15°N, 120°E) injected the greatest amount of sulfur dioxide into the stratosphere of any eruption since satellite observations began. Geologic estimates of sulfur dioxide emission suggest that similar or larger eruptions have not occurred since Krakatoa in 1883 or perhaps Santa Maria in 1902. The evolution of the volcanic cloud has been intensively observed from satellites, aircraft, and the ground. We simulate the transport of the volcanic material for the first several months after the eruption using a combined circulation and aerosol transport model, and compare the results to published observations. The principal finding from the computations is that heating of the volcanic aerosols as a result of infrared radiation from the troposphere is a significant factor in producing the observed southward transport of volcanic material across the equator. Although previous numerical simulations have shown that heating by optically thick aerosols could modify stratosphere dynamics, the Pinatubo eruption is the first case in which such modifications may have been observed.

The simulation procedure is to calculate winds in the stratosphere with a three-dimensional global circulation model, and then to input these winds to an aerosol transport model which then computes the transport, accounting for sedimentation, chemistry,

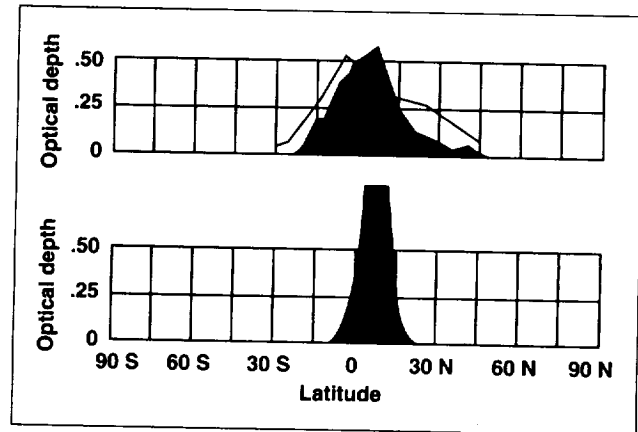


Fig. 1. Comparison of zonal average 0.5-micrometer optical depths for noninteractive and interactive simulations, day 60 (mid-August). Top, interactive; bottom, noninteractive. The noninteractive optical depth has been cropped in the figure; it reaches a maximum value of 1.43. Also plotted with the interactive distribution is the zonal mean 0.5-micrometer optical depth distribution for August as observed by the Advanced Very-High-Resolution Radiometer aboard the NOAA/11 environmental satellite.

and coagulation of aerosol particles. In the interactive mode, the two models work together simultaneously, with the aerosol transport model providing new cloud distribution properties which are then used by the circulation model to determine wind and temperature fields. In the passive tracer mode, there is no feedback allowed from the presence of the volcanic aerosols; the aerosols are simply transported by the winds computed by the circulation model.

Some observed characteristics of the dispersion of the volcanic clouds are fairly well represented using passive tracer simulations. Such observed characteristics as time to circle the globe near the latitude of the eruption (about 3 weeks) and direction of zonal cloud movement (westward) are seen in the simulations, as is the confinement of the cloud to tropical latitudes. However, as the figure illustrates, heating of the Pinatubo volcanic aerosol cloud by infrared radiation from the troposphere is crucial in producing the observed southward movement of the

cloud across the equator. Without the inclusion of the heating, the optical depth distribution is too narrow and confined. With the heating, the optical depth distribution is much more representative of the observations. The simulations have therefore identified an important feedback mechanism between the volcanic aerosols and the atmosphere which produces significant modifications to circulation patterns in the stratosphere.

Future work will consider the dispersion of the El Chichon volcanic cloud, the second largest this century to be observed by satellite, and compare it with that of Mt. Pinatubo. The two volcanic clouds behaved differently, and we want to understand the reasons for the differences.

**Ames-Moffett contact: R. Young
(415) 604-5521**

Headquarters program office: OSS

Collision of Comet P/Shoemaker-Levy 9 with Jupiter

Kevin Zahnle

The pieces of the former Comet P/Shoemaker-Levy 9 struck Jupiter during the week of 16–22 July 1994. The impacts took place on the back side of Jupiter, but the impact sites rotated into Earth's view within minutes. Each explosion produced a plume that reached thousands of kilometers above the clouds, placing the plumes far above Jupiter's limb and into direct view from Earth. The plumes rose and fell over a period of 10 or 20 minutes, governed by the simple laws of ballistics. When the plumes fell back to the atmosphere they were reheated. Embedded dust glowed brightly in the thermal infrared for 10–20 minutes, producing the spectacular infrared events seen on Earth.

The impact sites were directly visible from the Galileo spacecraft. In a typical event, atmospheric entry was followed immediately by an explosion.

The luminosity rose to peak brightness in about 2 seconds. The fireballs expanded adiabatically as they exploded from the atmosphere, cooling and fading in 30–60 seconds. The initial radiating temperature exceeded 7000 kelvin; by 60 seconds the temperature had fallen to 500–700 kelvin. The observed light curve is in good accord with our predictions (first figure). On Earth the hot fireball was detected indirectly through scattered light, and about a minute later the much cooler fireball had risen high enough that it could be directly detected at infrared wavelengths from Earth.

Aerodynamic forces caused the impactors to explode. (Our model was discussed in previous Ames Research and Technology reports.) The apparent altitude of the explosions is consistent with our

analytical model, as verified by our detailed numerical models (this work was done in collaboration with Mordecai-Mark Mac Low of the University of Chicago), and with dynamically based estimates of fragment masses developed by Eric Asphaug (Ames Research Center) and Willi Benz (University of Arizona).

Ultraviolet spectra of an impact site show the presence of large amounts of sulfur, present as S_2 , carbon disulfide (CS_2), and hydrogen sulfide (H_2S). The large quantity of sulfur indicates that the source of the sulfur was shocked Jovian air. Strong shocks occur near the impact site and also where the ejecta plume reenters the atmosphere at high velocity.

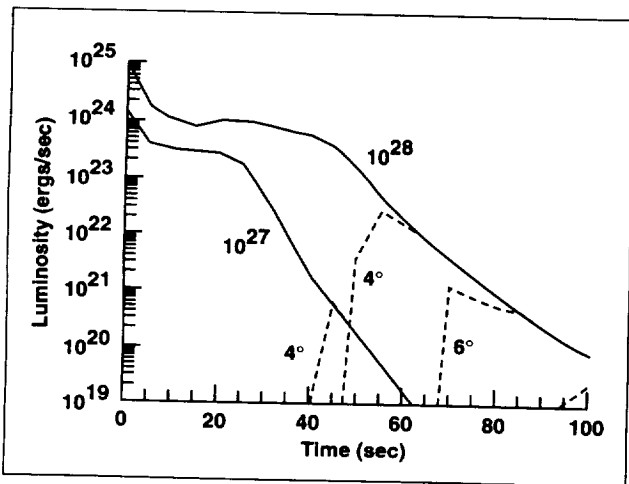


Fig. 1. Predicted luminosity of the entering bolide and the subsequent fireball produced by 0.5- and 1-kilometer-diameter comets striking Jupiter. The solid curves show the view from the Galileo spacecraft. The dotted curves show the direct view from Earth, which allows for the plume rising above the limb. The luminosity peak was detected from Earth by scattered light. Total sunlight reflected by Jupiter is shown for comparison.

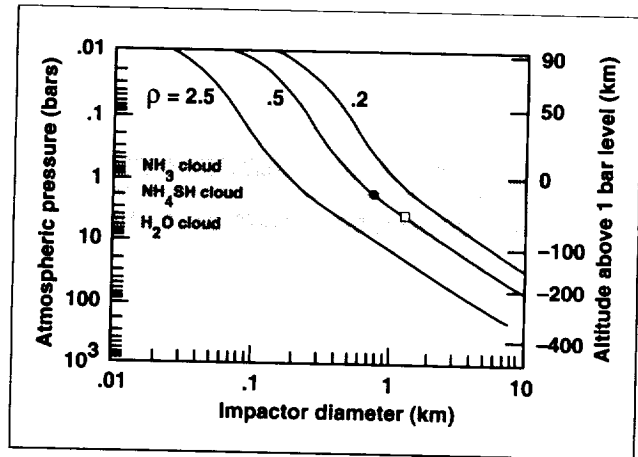


Fig. 2. Airburst altitudes for impactors of different densities, shown as a function of impactor diameter. Altitudes of condensation clouds are marked. The solid circle shows the airburst altitude of an 800-meter-diameter fragment of density 0.5 gram per cubic centimeter. This size and mass were predicted by a model of tidal disruption. Chemical evidence demands that the largest explosions occurred within or below the NH_4SH clouds and above the water clouds. Our preferred impact location is marked with the square.

Conditions in the reentry shock strongly favor the production of S_2 . The chemical composition, especially the presence of the highly reduced species CS_2 and the absence of the oxidized species sulfur monoxide (SO) and sulfur dioxide (SO_2), indicates that there was little or no water present in the shocked air. This places the explosion above the water clouds but below the ammonium hydrosulfide (NH_4SH) clouds, as shown in the second figure.

Ames-Moffett contact: K. Zahnle
 (415) 604-0840
 Headquarters program office: OSS

Spectroscopic Determination of Enthalpy in an Arc-Jet Wind Tunnel

Dikran S. Babikian, Chul Park, George A. Raiche

Arc-jet wind tunnels produce high-enthalpy hypersonic flows which can be used for various purposes such as testing the performance of heat shield materials for reentry vehicles or investigating the combustion phenomena of airbreathing engines operating at hypersonic speeds. The most important parameter in the operation of such a wind tunnel is the enthalpy of the flow at and near the centerline of the produced flow. Previous efforts to determine the enthalpy from velocity and heat transfer rate measurements have not been reliable. Velocity measurements are not very useful because kinetic energy is a relatively small fraction of total energy in this flow regime. Heat transfer rate measurements with the "flow-swallowing" probe runs into difficulty because of high heating rate of the lips of such a probe.

In the present work, an experiment is conducted in the 20-megawatt Aerodynamic Heating Facility in the arc-jet wind tunnel complex at Ames Research Center to determine enthalpy spectroscopically. The experiment is made for air with a small amount of argon. Surface spectral radiation emanating from various distances of a 15-centimeter-diameter flat disk model placed in the test section was observed from a direction normal to the flow. The stagnation pressures for this experiment were 0.028 and 0.01 atmosphere. The main features of the observed spectra were (1) N_2^+ (ionized nitrogen) First Negative system, (2) nitrogen oxide (NO) band systems, and (3) the atomic nitrogen and oxygen lines with background radiation in the red region.

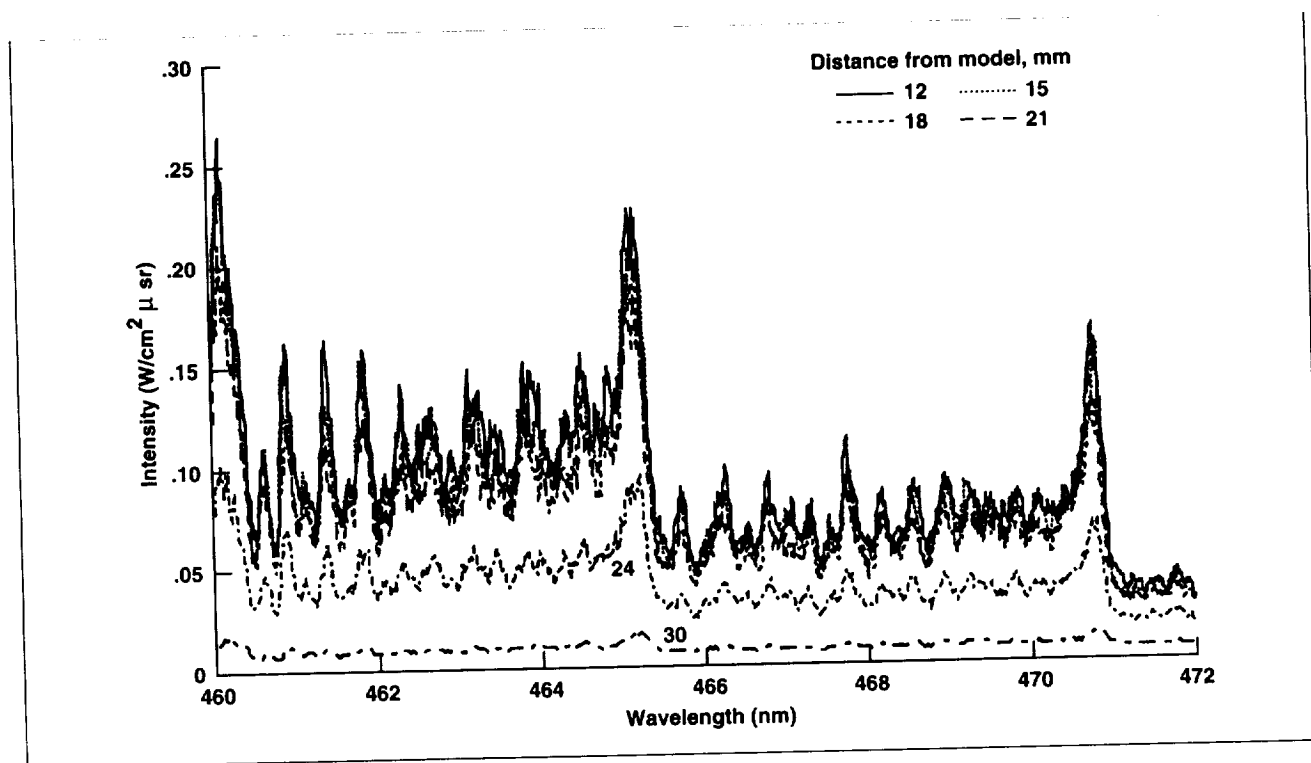


Fig. 1. Spectral intensity of N_2^+ First Negative band system.

The first figure shows the spectral intensities, in units of watts/square centimeter-micron-steradian, from the N_2^+ First Negative band system in the wavelength region between 460 and 472 nanometers. These intensities were obtained at distances of 12, 15, 18, 21, 24, and 30 millimeters from the model surface. At distances shorter than 12 millimeters, the radiation intensity was generally weak. This is believed to be caused by the fact that the region adjacent to the wall surface is within the boundary layer where the gas temperature is generally low. At distances larger than 30 millimeters, radiation was weaker also. The calculated shock standoff distance was about 38 millimeters. Therefore, at distances greater than 30 millimeters, the optical pathlength across the shock layer was diminishing rapidly. The first figure also shows that the variations in absolute intensities and in spectral features are small up to about 18 millimeters from the model surface. This indicates that the radiative properties of the emitting source are the same for these stations, which suggests that the gas may be in equilibrium within this region. A similar trend was also observed in the NO intensity spectra.

The second figure shows a plot of the calculated ratios of the intensity for the station 18 millimeters away from the model surface. The 746.83-nanometer atomic nitrogen line integrated from 746.54 to 747.12 nanometers is ratioed to that of the N_2^+ First Negative system integrated from 465.64 to 471.23 nanometers as a function of total enthalpy. It can be shown that this ratio of intensities depends on the number density of the species and the electronic excitation temperature, which are functions of enthalpy only for a given pressure at thermochemical equilibrium. The second figure also shows the ratio

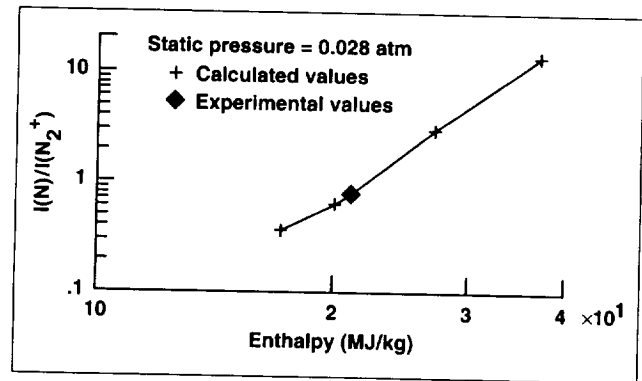


Fig. 2. Sensitivity of intensity ratio to flow enthalpy.

value obtained from the measured spectra that correspond to 21 megajoules/kilogram.

One can summarize the strategy for enthalpy determination as follows. First, using a flat disk, produce a product of pressure (atmospheres) and shock standoff distance (millimeters) greater than about 1 atmosphere-millimeter. Then observe the radiation emanating from the equilibrium region. Take the ratio of intensities of atomic nitrogen or oxygen lines to those of either N_2^+ or NO, or possibly the background radiation in the red region. From those ratios, enthalpy can be determined using an equation that relates the intensity ratio to total enthalpy written for the particular stagnation pressure. The enthalpy determined in this manner for this work was 21 megajoules/kilogram.

**Ames-Moffett contact: D. Babikian
(415) 604-1144
Headquarters program office: OSAT**

Simulations of Collisional–Radiative Nonequilibrium Plasmas

Jean-Luc Cambier

A code is being developed for the simulation of plasmas in thermal and chemical nonequilibrium, with a new level of complexity and capability. The code is intended to probe the physics of the plasma at very short time scales, when deviations from equilibrium can be significant—for example, behind a strong shock wave. In that region, the gas goes through a sequence of relaxation phenomena, which proceed on several time scales. Translational and rotational modes, for example, tend to equilibrate very fast, whereas the chemical (i.e., dissociation) relaxation proceeds at a much slower pace. Generally speaking, the relaxation rate is related to the energy gap of the inelastic collisions. The other important factor is the rate of collisions: free electrons can be very effective in accelerating the relaxation of the various modes of the plasma. The approach underlying most, if not all, simulations of such flows is to assume that the relaxation proceeds through a sequence of near-Boltzmann distributions. For example, the rotational energy levels are described by such a distribution at a temperature T_r , the vibrational levels by another one at T_v , whereas the translational modes are described by a Maxwell–Boltzmann distribution at the temperature T_t . The numerical model therefore only requires us to solve a system of generalized Euler equations, in which the energy density for each internal mode is separately convected. Most codes also assume that some modes are in equilibrium—for example, the vibrational modes, the bound electronic modes, and the free electrons. Although this simplification is appropriate in some cases, it is dangerous to assume that this model can be extended to most flow conditions of interest. Several factors can play a role in breaking down the validity of these assumptions. The strong coupling between free electrons (at a temperature T_e) and the vibrations (T_v) occurs for resonant energy transfers, for example with diatomic nitrogen N_2 . This is not necessarily valid for other molecules. It is clear also that when the number density of molecular species becomes very low, this assumption breaks down. Although the excitation of the bound

electronic modes by inelastic collisions with free electrons is also rapid, these modes may not be populated by a Boltzmann distribution for some time, because the energy gaps between various levels can be quite large and have large variations. The population and depopulation of these levels must also include the radiative mechanisms, which can compete with the collisional effects. Therefore, in order to be able to study the state of the plasma and of its radiation, it is necessary to use more detailed numerical models.

The first step consists of generalizing the model by first eliminating the Boltzmann assumption of the electronic states. Thus each excited state is separately convected and is considered as a separate chemical species. This also implies that the chemistry is generalized to allow for separate reactions, involving each electronic state. A second generalization consists of allowing each molecular state to have its own vibrational temperature. Both of these generalizations considerably enlarge the overall number of fluid equations to be solved. However, this is not the major cost associated with the new model. At this stage, all the rotational modes are lumped together, and are characterized by a Boltzmann distribution with a single temperature T_r . This assumption appears reasonable because the energy gap for rotational excitations is small and nearly the same for most molecular species (except hydrogen). The model may be generalized further at a later stage. This description allows us to include the computation of the competing collisional and radiative processes, whether for line transitions or for bound–free transitions. A simplified radiative model, which computes averages using the distribution of vibrational and rotational levels, is then used in the flow code. The resulting collisional–radiative (CR) model gives us an estimate of the radiative losses and the radiative fluxes. By adding a radiative transport model, we now have a CR nonequilibrium plasma simulation, fully coupled with the radiation.

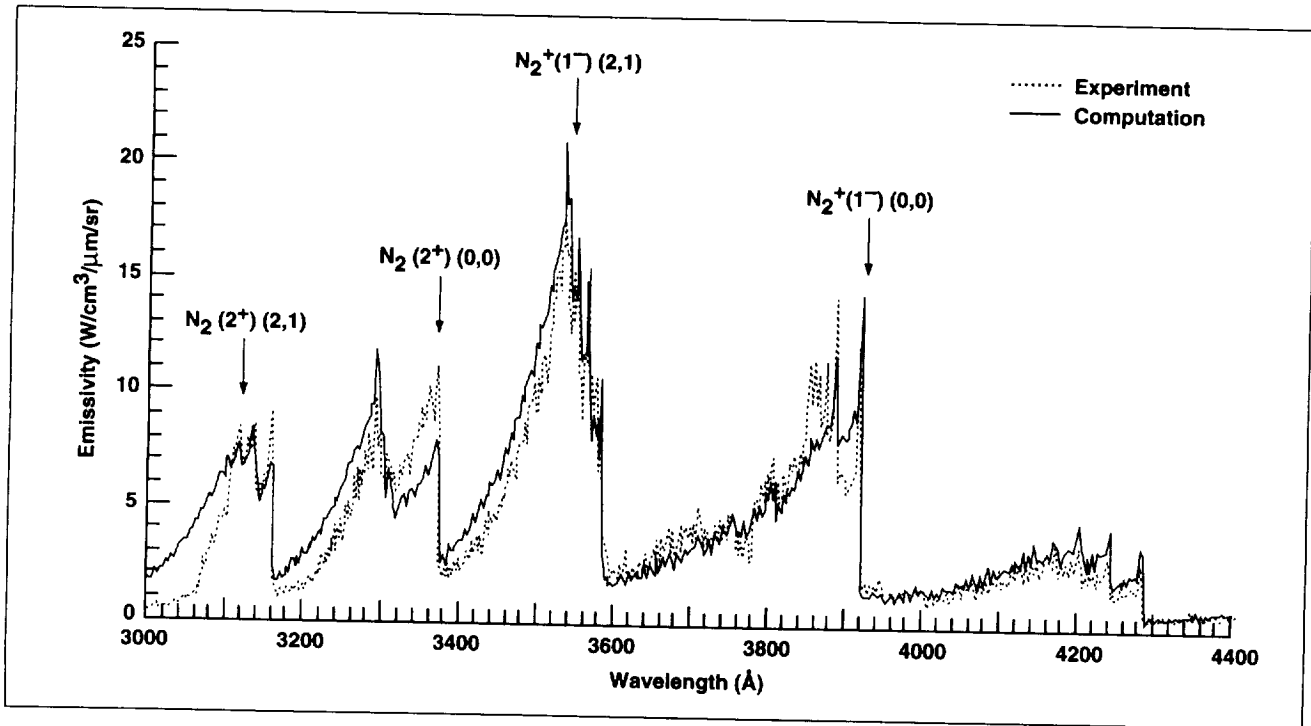


Fig. 1. Shock in nitrogen (N_2): no radiative coupling.

The coupling of the various internal energy modes is the subject of detailed study. The code uses some simple models for elementary processes, then computes averages using the rotational and vibrational distributions. This procedure results in tabulated variables and a function of two or three temperatures. For example, the effect of the rotational and vibrational nonequilibrium on dissociation rates can be formulated in this fashion. Moreover, we can also keep track of the average rotational and vibrational energies removed during the dissociation or replaced during the recombination. A completely coherent chemical nonequilibrium procedure can then be constructed, which has the important property of being able to restore thermal, as well as chemical, equilibrium by itself.

Another important feature of the numerical model is that free electrons have their own temperature and the electron heat conduction is included. Also, the repartition of energy into heavy particle or electron translational modes during some processes, such as the associative ionization and its reverse, is also correctly modeled. This may have the effect of providing an important heating mechanism for the electrons. The code is being tested on a shock

problem in pure nitrogen and the results are being compared with experimental results. The code is capable of running on a workstation with satisfactory turnaround for one-dimensional problems. The current results are encouraging. The figure shows a comparison between the spectra obtained experimentally and the present computation for the test case in nitrogen. Relatively good agreement is obtained in the spectra and also in the location of peak radiation (2 millimeters behind the shock). The most important deviation comes from the nitrogen ($N_2(2^+)$) radiation at low wavelengths, where the band profile seems to indicate some deviations of the rotational and vibrational temperature of that state, $C^3\Pi_u$. The very low number densities associated with that highly excited state make the calculations difficult, and the agreement therefore all the more impressive. Systematic tests are under way. The thermochemical data base will be extended to include all air species.

Ames-Moffett contact: J.-L. Cambier
(415) 604-4283
Headquarters program office: OSAT

Rotational Relaxation Rate Models in Rarefied, Expanding Nitrogen Flows

Lawrence A. Gochberg, Brian L. Haas

Studies of rotational relaxation in rarefied expanding flows generally use the rotational relaxation collision number, Z , to quantify the degree of nonequilibrium in the flow. The Z value can be interpreted as the ratio of the rotational relaxation time to the time between molecular collisions. Previous experiments have shown significant discrepancies in the value of Z for similar free-jet expansions of nitrogen. A computational study was performed to examine the effects of various rotational relaxation rate models, and hence values of Z , on rotational temperature (the energy associated with molecular rotation) profiles in rarefied nitrogen free jets. The computational work was compared to a number of selected experimental results.

The computations were performed by directly integrating the one-dimensional equations of gas dynamics with a linear model for rotational relaxation and appropriate curve fits for viscosity. Three models for the rotational relaxation rate were examined: (1) constant Z , (2) a classically developed temperature-dependent Z (classic Z), and (3) a quantum mechanical modification for the classical Z model at low rotational temperatures (quantum Z). The classic Z model was defined using two parameters, Z_∞ and T^* . In the quantum Z rate model, the rotational transition probabilities were calculated for three different rotational quantum numbers ($J = 4, 5,$ and 6). The first figure shows the different rotational

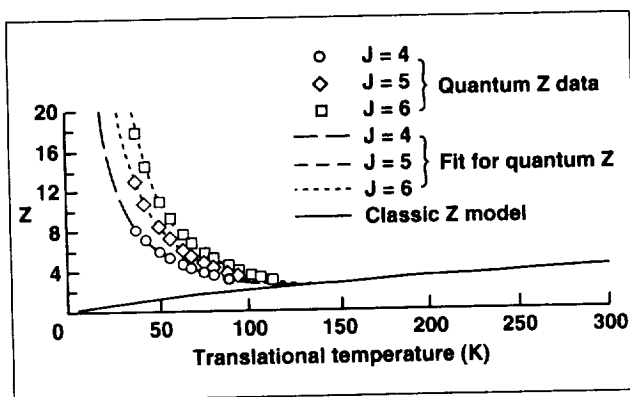


Fig. 1. Classic and quantum Z models versus translational temperature. (J = rotational quantum number.)

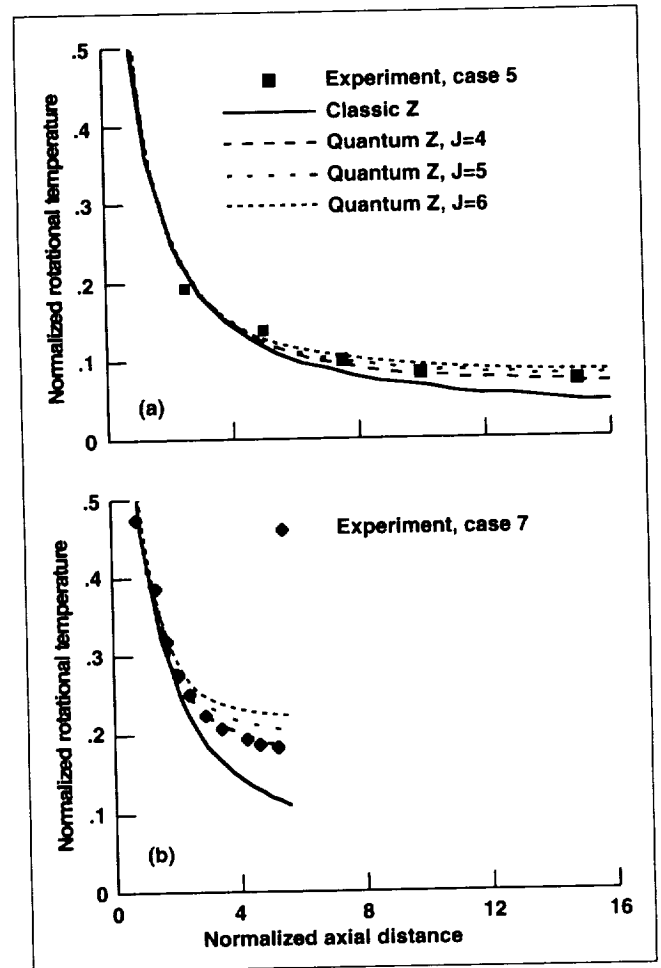


Fig. 2. Two typical rotational temperature profiles.

relaxation rate models used as functions of translational temperature. For each experiment that was simulated, the code calculated an RMS error based on the difference in the computed and experimental rotational temperature at each axial position in the free jet.

Results using the constant Z model showed a scatter in the Z values similar to that seen in the literature data. Parameters for the classic Z model that provided the best fit to experimental rotational temperature profiles also showed large scatter. In

addition, those best-fit Z_{∞} values were far from the values typically quoted in the literature. Thus, neither the constant nor the classic Z models show marked improvement over previous work.

The second figure shows the results from runs using the typical classic Z parameters ($Z_{\infty} = 18$ and $T^* = 91.5$) and runs from the three quantum Z models. The experimental data for the twelve selected cases were chosen because they exhibit little or no effects from translational nonequilibrium, condensation, or background gas penetration into the free-jet core flow. The three quantum Z models exhibit an improved ability to model the rotational relaxation behavior of the experimental data, in most cases. The $J = 4$ case, in particular, exhibits a considerable improvement over the classic Z model results in 11 of the 12 cases examined here.

One limitation in the analysis here is the linear approximation for rotational relaxation. This approximation is widely used in most calculations of rarefied gas dynamic flows. However, its use implies

assumptions of small departures from equilibrium which may not be appropriate for expanding free-jet flows that exhibit considerable nonequilibrium.

Although these results were generated with a one-dimensional computational model, they are also relevant for applications that use multidimensional direct-simulation Monte Carlo (DSMC) methods. Only the classic Z rate model with small modifications has been adapted to those codes thus far. As demonstrated in the present work, an improvement in the ability to compute rotational relaxation in rarefied expanding flows can be achieved by using a quantum model for the rotational relaxation rate. This model should be considered for adaptation to DSMC in cases where low-temperature, expanding flows are examined.

**Ames-Moffett contact: G. Deiwert
(415) 604-6198**

Headquarters program office: OSAT

Simulation of Galileo Probe Aerobraking

Brian L. Haas, Frank S. Milos

Flows along an aerobraking trajectory were computed in support of the Galileo mission to Jupiter. Just before it encounters and begins to orbit the planet in December 1995, the Galileo spacecraft will release a probe that will enter the Jovian atmosphere. During aerobraking at the very highest altitudes prior to peak heating, the probe will encounter the rarefied flow regime that is bounded by the effective free molecule limit at 750 kilometers altitude and the near-continuum limit at 350 kilometers. The Atmosphere Structure Experiment on board the Galileo probe will deduce atmospheric density, pressure, and temperature from deceleration measurements at these altitudes as long as the vehicle drag coefficient is known accurately.

Because of the lack of sufficient experimental data, the objective of the present work was to estimate by computation the Galileo probe drag

coefficient during aerobraking in the rarefied flow regime. At these high altitudes where gas density is low and the mean free path between molecular collisions is large, the flow regime is ill-suited to simulations that are based on the continuum Navier–Stokes equations. Instead, rarefied flows are best computed using direct-simulation Monte Carlo (DSMC) particle methods. In DSMC, gas dynamics are modeled directly by the motion and interaction of millions of discrete particles on a computer. The simulation permits accurate assessment of vehicle aerodynamics, heating, and properties of the flow field at low densities. A measure of the degree of rarefaction is the Knudsen number, Kn , defined as the ratio of the mean free path and a characteristic vehicle dimension. The flows of interest in the present work corresponded to $Kn > 0.05$.

The DSMC method uses simple models for particle collision dynamics and gas-surface interactions. Flows at several trajectory points for Galileo probe aerobraking were simulated by assuming that the surface simply radiates all incident convective energy away. This boundary condition provided an upper bound for the computed surface temperature of the vehicle. However, because of the high entry velocity of the Galileo probe even in the rarefied regime, surface heating will be great enough to cause the carbon phenolic heat shield to pyrolyze—that is, to vaporize the shield material and emit gas from the surface.

Pyrolysis can affect the vehicle aerodynamics significantly. To simulate these effects, the dynamic response of the surface material was calculated by coupling routines from the Charring Material Thermal Response and Ablation (CMA) program directly into the DSMC code. CMA is a finite-difference procedure for computing one-dimensional transient energy transport within a thermal protection material, accounting for transient convective heating, in-depth conduction, radiation, and the flow of pyrolysis gas through the porous material.

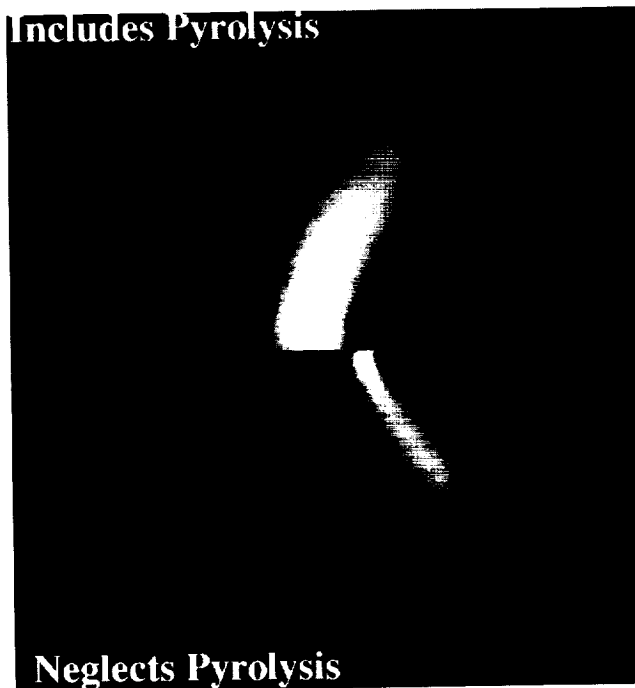


Fig. 1. Flow temperatures about the Galileo Probe during aerobraking at 350 kilometers altitude. (See color plate 17 in Appendix)

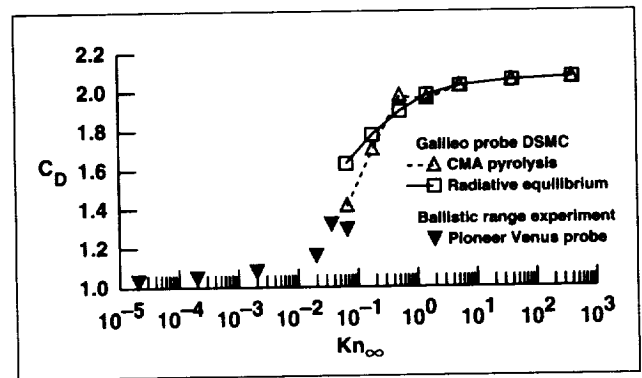


Fig. 2. Drag coefficients for the Galileo Probe during aerobraking.

Using the coupled DSMC/CMA code, the simulations showed that surface pyrolysis will be negligible during the initial atmospheric entry but will become pronounced once the probe drops below 450 kilometers altitude. Indeed, the computed surface emission mass flux was ten times the incident free-stream influx of atmospheric molecules at these conditions. Pyrolysis led to considerably lower convective heat fluxes and surface temperatures at the nose of vehicle. The first figure shows a comparison of profiles for flow field translational temperature computed with and without pyrolysis for the trajectory point at 350 kilometers altitude. Surface pyrolysis had a distinct effect on the flow field, increasing the upstream influence of the body on the incident flow. The second figure shows drag coefficients for the Galileo probe plotted and compared to the experimental ballistic range results for the Pioneer Venus probe. The computed results blend well with the experimental results at the lowest Knudsen numbers. At the higher altitude and Knudsen number, where pyrolysis was significant, the flow was sufficiently rarefied that the pyrolysis gas had very little influence on the incident flow, and the drag coefficient was greater than when pyrolysis was not included in the calculation. Farther along the trajectory, as the altitude and Knudsen number dropped, the flow density and pyrolysis emission increased. The greater frequency of molecular collisions in front of the body caused a marked decrease in the convective heat transfer and the incident momentum flux imparted to the surface. That is, pyrolysis resulted in a lower drag coefficient for the last two trajectory points at the lowest Knudsen numbers simulated.

In general, whether these competing effects of pyrolysis would lead to a net increase or decrease in overall vehicle drag is difficult to predict without performing these simulations. By incorporating material response directly into its surface model, the coupled DSMC/CMA code simulates the entry environment and predicts vehicle aerodynamics

accurately as required for this and other aerobraking missions.

Ames-Moffett contact: B. Haas

(415) 604-1145

Headquarters program office: OSAT

Simulation of Polymer Properties

Richard L. Jaffe

Computational chemistry methods are being applied to high-performance polymers for aerospace applications. Material simulations of the morphological and mechanical properties of polymers have been made more reliable by the use of accurate molecular interaction energies determined in this work. Examples of the high-performance materials studied include poly(perfluoroalkyl ether) lubricants, polyimide resins used in structural composites, and lithium-salt-poly(alkyl ether) electrolytes used in lithium polymer batteries. This research will assist in efforts by NASA and industry to develop new custom-made high-performance polymeric materials with specific properties.

In recent years, materials simulation methods have been developed that permit calculations of structural and mechanical properties for a wide range of polymers, if the intrachain and interchain forces are known. These forces are usually expressed mathematically as a potential energy force field that is made up of (1) stretching, bending, and torsional terms, which represent the molecular vibrations, and (2) pairwise nonbonded terms, which represent van der Waals and electrostatic interactions.

In the present study, ab initio quantum chemistry methods are being used to determine these parameters. Appropriate model molecules are used to represent short segments of the polymer chain. For example, 2,4-diphenyl pentane is used to represent polystyrene, and phthalimide and diphenyl ether are used to represent parts of a typical polyimide repeat unit. The molecular geometry, relative energy, and vibrational frequencies for each conformer are computed. The calculations utilize standard quantum

chemistry methods, but they are formulated to ensure a high degree of accuracy in the resulting force field. This is accomplished through the use of large atomic orbital basis sets with at least two functions for each atomic valence orbital augmented with polarization functions (e.g., d-type orbitals for carbon, oxygen, etc.) and through the use of methods that incorporate the effects of electron correlation in the calculations. For most chemical systems, relative conformer energies are determined to within 0.25 kilocalorie per mole. The unique feature of this research is the use of calculations on molecular complexes in the parameterization of the nonbonded interactions.

These calculations have been used to determine potential energy force fields for the components of most of the polyimides being developed at Langley Research Center. We have also derived force fields for polyalkyl ethers used as electrolytes in lithium polymer batteries, perfluorinated alkanes (e.g., teflon), and perfluorinated polyethers (e.g., Fomblin Z) used as lubricants for jet turbines and computer disks.

Currently, polymer simulations are being carried out for most of these systems using these potential energy force fields. Combining ab initio quantum chemistry methods with molecular dynamics simulation methods is resulting in a major increase in the reliability of polymer simulations.

Ames-Moffett contact: R. Jaffe

(415) 604-6458

Headquarters program office: OA

Durable Flexible Insulation

Demetrius Kourtides

Silica fibrous insulations known as Advanced Flexible Reusable Surface Insulation (AFRSI) are currently used as a thermal protection system (TPS) on the exterior of the Shuttle Orbiter. This and other insulations such as the Composite Flexible Blanket Insulation (CFBI) and the Tailorable Advanced Blanket Insulation (TABI) are subject to physical damage during routine maintenance operations because of the vulnerability of the top ceramic fabric to tearing and breakage. The new Durable Flexible Insulation, described here, is a substantial improvement over these other insulations with regard to durability and resistance to damage. The enhanced durability is attributed to the use of a metal alloy foil rather than ceramic fabrics on the surface.

The Durable Flexible Insulation is useful as a TPS for specific heating environments that contain conductive, convective, and radiative heating components. It is intended for use on the exterior surfaces of future aerospace vehicles such as the proposed Single-Stage-to-Orbit Vehicle (SSTO), where an all-weather, durable, multiuse TPS is required to protect the vehicle from the reentry thermal environment.

The metal alloy foil of the new insulation blanket, shown in the figure is brazed onto a metal alloy screen which is attached to the surface of the blanket. The insulation blanket materials are quilted together with ceramic threads such as Nextel 440. The current version uses a metallic fabric sewn onto the surface of the blanket with the same ceramic thread that is used to quilt the blanket. The foil is subsequently brazed to the metallic fabric at the top surface. The foil also partially covers the blanket on the exposed sides. The metal alloy foils used include nickel-base superalloys such as Inconel 617.

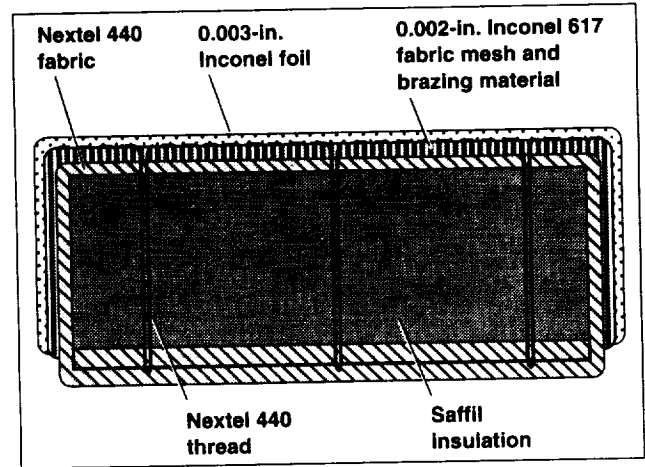


Fig. 1. Durable Flexible Insulation.

The insulation blanket is fabricated by sewing the refractory metal alloy screen at the time the insulation is being sewn together with a ceramic thread. Subsequently, brazing foil strips are placed on top of the insulation and the top foil is brazed onto the metal screen. Since bonding between the braze alloy and the ceramic is not required, conventional (as opposed to active) alloys or pure metals such as copper or nickel are used. Conventional braze alloys do not wet the ceramic surfaces; therefore adverse chemical and physical interactions are minimized. This type of insulation could also be useful in other applications where an insulation with a durable outer surface is required.

Ames-Moffett contact: D. Kourtides
(415) 604-4784
Headquarters program office: OSS

Heating Analysis of a Single-Stage-to-Orbit Vehicle

Grant Palmer, Bill Henline, David Olynick

There is an increasing need for more cost effective launch vehicles that will continue to provide mankind with access to space. One option for the next generation of launch vehicles for delivering payloads to low Earth orbit (LEO) is to replace the shuttle with a fleet of fully reusable single-stage-to-orbit (SSTO) launch vehicles. These vehicles would use advanced technologies to meet the requirements of improved safety and reduced operations cost. The vehicles must accommodate space station resupply and 20,000- to 25,000-pound mass satellite deployment missions.

One of the candidate reusable vehicles is the lifting body. This vehicle is essentially a larger version of the lifting bodies tested during the 1960s. The SSTO lifting body has two small wings extending from the aft section of the fuselage to augment the significant lift generated by the fuselage shape itself. To maximize payload, minimizing the structural weight of the vehicle is critical.

Reacting-gas computational fluid dynamics analysis was performed on the vehicle to determine the thermal environment the vehicle will experience during reentry. This information will be used to size and optimize the thermal protection system. The heat transfer to the body surface is obtained by solving the three-dimensional Navier–Stokes equations over the body including the effects of finite-rate chemical reactions. Realistic surface boundary conditions have been built into the solution algorithm including surface catalysis and a variable temperature wall.

The figure shows temperature contours along the symmetry plane of the vehicle at the 70-kilometer

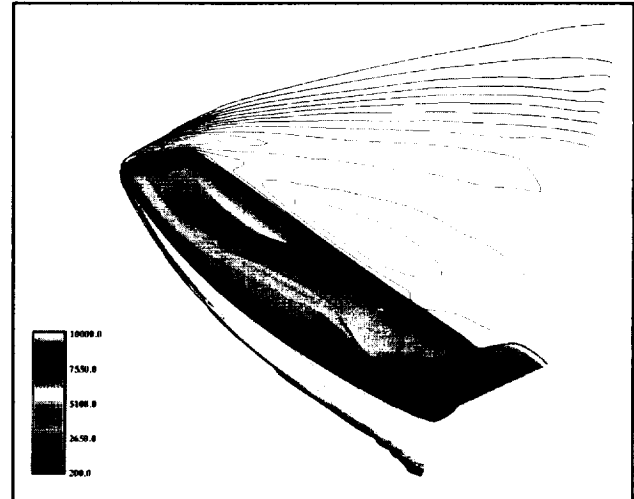


Fig. 1. Temperature contours along the symmetry plane of the lifting body, 70-km trajectory point. (See color plate 18 in Appendix)

trajectory point. The vehicle is reentering the Earth's atmosphere at an angle of attack of 40 degrees. A peak convective heating value of 11.5 watts/square centimeter occurs on the bottom surface of the vehicle near the nose. The heat transfer rate falls off rapidly away from the nose and over most of the body; except at the wing leading edge, the heating rate is less than 10 watts/square centimeter.

**Ames-Moffett contact: G. Palmer
(415) 604-4226**

Headquarters program office: OSAT

Stagnation-Point Vacuum-Ultraviolet-to-Infrared Radiation in an Arc-Jet Wind Tunnel

Giuseppe Palumbo, Chul Park, Roger Craig

Spectral radiation incident on the stagnation point of a blunt body was measured in an arc-jet wind tunnel over the wavelength region from the vacuum ultraviolet (VUV) to the near infrared (IR) at an enthalpy corresponding to a flight speed of about 7.8 kilometers/second. The first figure shows a 15-centimeter-diameter flat-disk model that was placed in the flow produced by a 20-megawatt arc-jet wind tunnel. Radiation incident on the stagnation point was directed into a spectrograph. The optical system admitted the rays incident on the stagnation point at 15 degrees from the stagnation streamline, in order to avoid the strong rays emanating from the nozzle throat. Both photographic and photoelectric methods were used in measuring the spectral intensity. The wind tunnel was operated to produce a stagnation point pressure of 0.011 atmosphere, simulating a flight altitude of about 76 kilometers. The model produced a shock layer thickness equal to that of a sphere with about a 0.6 meter radius. The test gas was an 80%/20% mixture by mass of air and argon.

The sensitivity of the system was determined absolutely using two National Bureau of Standards-calibrated standard lamps: a tungsten ribbon lamp for the wavelength region of 3000 to 9000 angstroms and a deuterium arc lamp for the region of 2000 to 3000 angstroms. For the wavelengths between 1200 and 2000 angstroms, where there are no established standards, calibration was performed (1) by using the sensitivity calibration data supplied by the manufacturer of the photomultiplier tube used and (2) by measuring radiation losses of the individual optical components in the system.

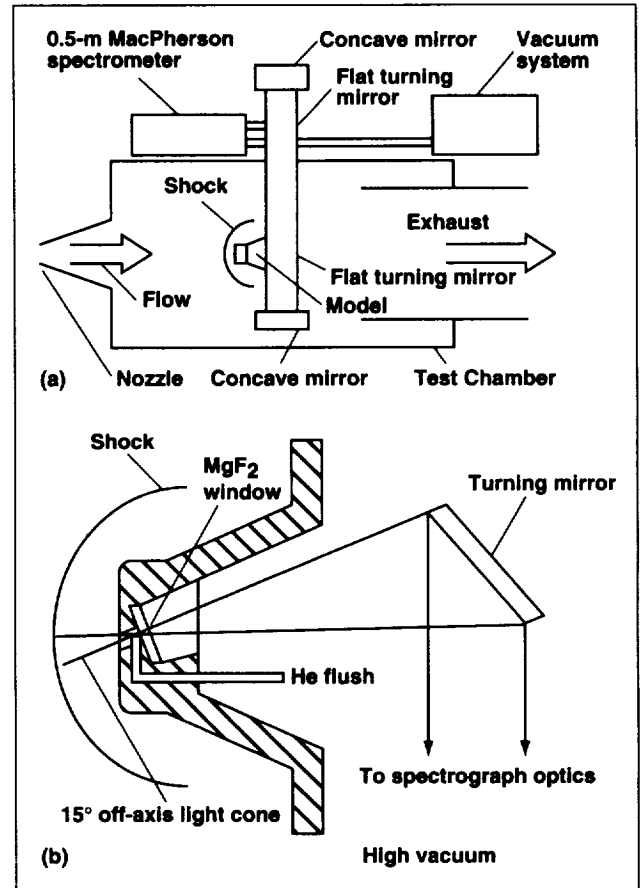


Fig. 1. Mechanical arrangement of the experiment. (a) Wind tunnel test section showing the test chamber and the model; (b) the details of the model with the window, the helium purge, and the direction of view.

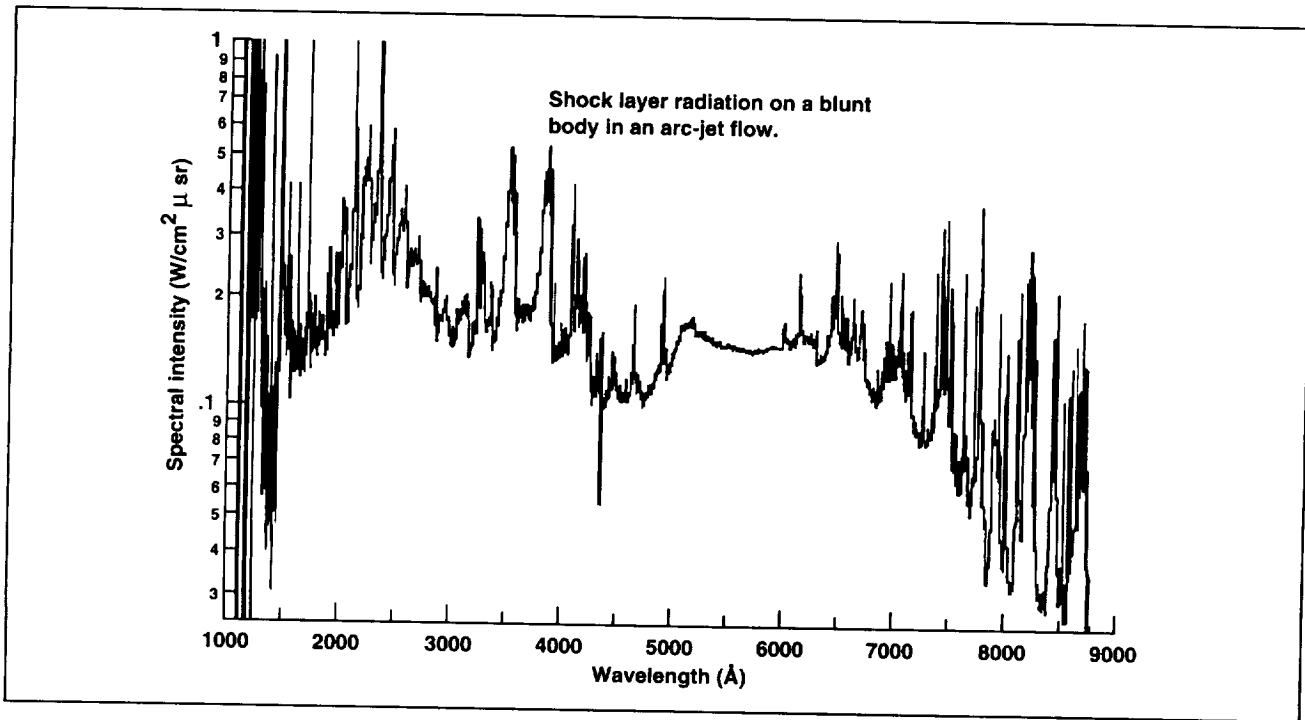


Fig. 2. Spectral intensity of the radiation incident on the stagnation point in an arc-jet wind tunnel at an enthalpy of 30 megajoules/kilogram.

The second figure shows the spectral intensities of the measured radiation. The total radiation observed is 0.092 watt/square centimeter. The figure also shows that the peak intensities of the line radiation in the VUV range are very high. However, the integrated intensities of these VUV lines are only about 9% of the total radiation. This is the result of self-absorption of the VUV lines. If these lines are not self-absorbed, the VUV lines will produce at least

1 watt/square centimeter of radiation. The present measurement confirms recent calculations of this phenomenon.

**Ames-Moffett contact: E. Whiting
(415) 604-3473
Headquarters program office: OSAT**

Computing the Flow about the Venus Composition Descent Module

Periklis Papadopoulos, Paul Wercinski

The Venus Composition Probe (VCP) is an atmospheric entry probe designed to provide observations and measurements of the Venus atmosphere. The probe configuration consists of an aeroshell heat shield and a descent module that contains communications, power, and instrumentation packages. The objective of this work is to calculate the entry and descent trajectories and characterize the flow about the descent module at transonic and subsonic flight conditions.

The atmospheric entry trajectory was calculated using a Venus atmospheric model derived from the Pioneer-Venus missions. Atmospheric entry was defined to occur at an altitude of 200 kilometers. A ballistic trajectory with an entry flightpath angle of -30 degrees was used. The atmospheric entry velocity used was 10,989 meters/second. Based on estimates of the probe mass and heat shield diameter, the entry probe ballistic coefficient used was 167.8 kilograms/square meter. The atmospheric trajectory was calculated for the prescribed entry conditions. The entry and descent sequence of events such as parachute deployment and forebody aeroshell drop-off were also modeled. Flight velocities, deceleration loads, and heating rates were determined along the trajectory as functions of altitude.

After the probe is decelerated aerodynamically to about Mach 0.8, a parachute is deployed. Subsequently, the descent module containing the scientific instruments separates from the aeroshell. After the aeroshell drop-off, the descent module instrumentation package is activated to perform atmospheric measurements. In order to assess the appropriate location of the measuring instruments, it was necessary to understand the flow characteristics about the descent module. The flow field about the VCP terminal decent configuration was computed at three selected flight conditions along the probe's descent trajectory. Note that the flight conditions under

consideration were selected to examine subsonic and transonic flow environments about the VCP descent module. The flow field was computed at the following altitudes: (1) 67.158 kilometers (flight Mach number = 0.8), (2) 66.47 kilometers (flight Mach number = 0.23), and (3) 5 kilometers (flight Mach number = 0.02).

The appropriate VCP descent module geometry was used for numerical simulations. The three-dimensional blunt configuration was approximated using an axially symmetric body. It was therefore only necessary to compute the flow in a plane of symmetry, and thus the computation time requirement was reduced. The axisymmetric "O"-type grid was generated to model the flow about the VCP decent module using both algebraic and hyperbolic grid generators. The flow features, such as the viscous boundary layer and the expansion about the corner of the vehicle were resolved using the appropriate grid refinement. The outer boundary of the grid was extended to 20 body diameters radially from the probe surface to preserve the subsonic inflow boundary conditions.

At the altitude of 67.158 kilometers, the flight velocity corresponds to Mach number 0.8 and the flow is subsonic. In this case the axisymmetric Navier-Stokes equations are solved using the fully conservative, finite-volume General Aerodynamic Simulation Program (GASP). Along the body, a nonslip flow boundary condition is enforced. The vehicle surface temperature was assumed to be fixed at a few degrees higher than the free-stream temperature. The code was set up to implement a real-gas $\text{CO}_2\text{-N}_2$ chemistry model. A time accurate global iteration is performed to capture the subsonic/transonic flow about the probe. Turbulence modeling is applied to capture boundary layer growth along the body. The Baldwin and Lomax algebraic turbulence flow model was used.

To calculate the low-speed subsonic flow environment about the VCP descent module, a more efficient incompressible code was used. The "Incompressible Navier-Stokes" (INS2D) flow solver modified for axisymmetric problems was used to obtain the solution at 66.47 kilometers and 5 kilometers from the surface. The corresponding Mach numbers for these cases were 0.23 and 0.02, respectively. This code solves the incompressible Navier-Stokes equations for steady-state flows. The algorithm is based on the method of artificial compressibility and uses a third-order central difference for the viscous terms. Steady-state solutions were obtained with a line relaxation scheme that allows fast convergence.

In summary, the flow field about the descent body was computed at zero degrees angle of attack for all selected flight conditions. Both the forebody and afterbody flow were calculated. The configuration used was a 45-degree half-angle cone with a nose radius equal to 27 centimeters and a body radius of 50.5 centimeters. The axisymmetric flow about the body was computed using a 137×200 grid.

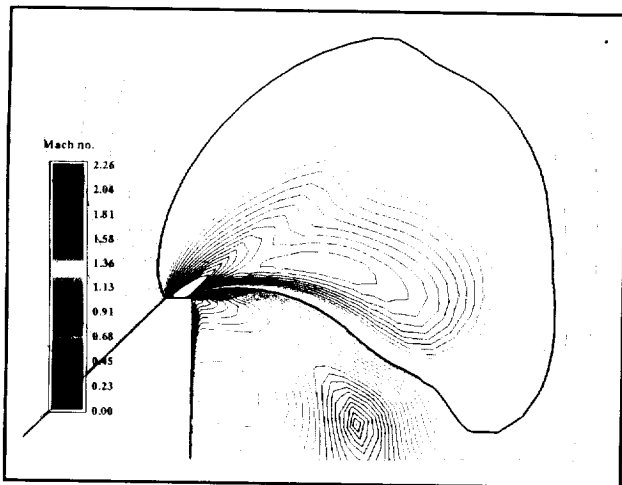


Fig. 1. Mach number contours at an altitude of 67.158 km ($V = 195.4$ m/sec). (See color plate 19 in Appendix)

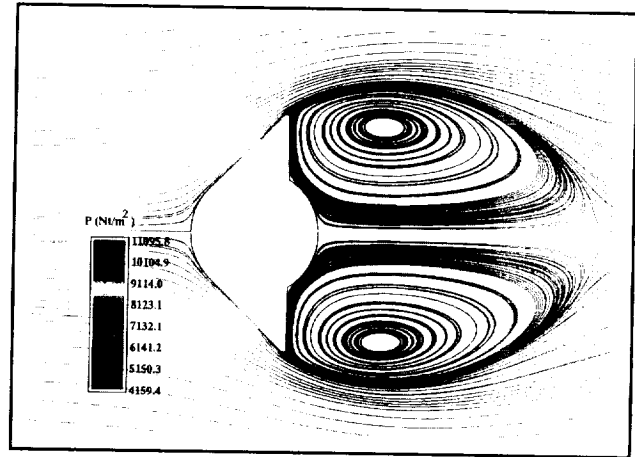


Fig. 2. Flow streamlines at an altitude of 66.47 km ($V = 55.3$ m/sec). (See color plate 20 in Appendix)

For the transonic flight conditions the flow accelerates as it approaches the corner of the vehicle. As a result, the flow near the corner of the vehicle becomes supersonic. The first figure shows an expanded view of the corner flow for condition (a), indicating the supersonic region. As this supersonic region may effect measurements made with an intrusive device, the design of such instrumentation would have to be carefully considered. The second figure shows the condition (b) low-velocity case. As the flow approaches the corner of the vehicle it is accelerated but remains subsonic. Unable to negotiate the sharp turn, the flow separates and forms a small recirculation region. In the afterbody a large vortex of slow-moving gas is formed. Such vortex shading could introduce large variations in the flow field that the probe is measuring. As a result of this analysis, it is evident that sensor instruments located in the flow are needed to consider the different flow features that are described here.

Ames-Moffett contact: P. Papadopoulos

(415) 604-3477

Headquarters program office: OSAT

NASA Ames 16-Inch Shock Tunnel Simulation and Experimental Comparison

Periklis Papadopoulos, S. Tokarcik-Polsky, Ethiraj Venkatapathy, George S. Deiwert

The combustion-driven 16-Inch Shock Tunnel located at NASA Ames Research Center is a unique test facility currently used for hypersonic propulsion testing of near full-scale scramjet combustor test articles in connection with the NASP program. It is the large scale of this shock tunnel that provides a unique capability to simulate the high-pressure, high-enthalpy flows required to study the hypersonic, real-gas environment of an airbreathing ascent vehicle at Mach numbers in the range of 12 to 16.

The facility is 70 meters long and consists of a 47-meter shock tube followed by a 5.8-meter supersonic contoured nozzle segment at the end of the driven tube. The nozzle includes a throat section that allows testing of different flight conditions by changing the area ratio. (The nozzle exit conditions for an area ratio of $A/A^* = 144$ simulates the flow of the inlet of a scramjet flying at Mach 14.) The diameter at the nozzle exit is 1 meter. An open jet test section is located at the end of the nozzle.

The objective of this work is to numerically examine and characterize the nozzle flow field of the Ames 16-Inch Shock Tunnel facility for selected Mach 12, 14 and 16 nozzle contours. The numerical simulation schemes employed here are used to provide code validation against the facility nozzle experimentation and to aid in the understanding of gas dynamic flow characteristics. Consideration was given to nonisentropic flow processes, such as real-gas effects and viscous boundary layer development that take place during the highly expanded nozzle flow.

The general chemical kinetics code NENZF was implemented to obtain preliminary quasi-one-dimensional (1D) nozzle solutions. This code assumes steady, one-dimensional, inviscid flow. For a specified nozzle geometry and stagnation conditions, the program calculates the flow from the reservoir to the nozzle exit accounting for nonequilibrium effects in the flow. Because of its computational efficiency this code was used to study the sensitivity of the nozzle exit pitot pressures to operational parameters such as reservoir pressure and temperature.

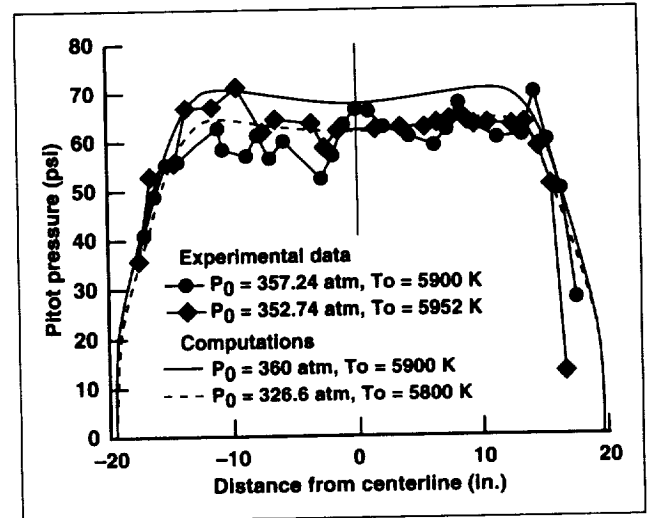


Fig. 1. Pitot pressure (P_0) profile at nozzle exit conditions ($M_\infty = 14$, $A/A^* = 144$).

Although quasi-1D computations are certainly adequate to model the inviscid core flow, assuming uniform velocity, the effect of the boundary layer must be examined using axisymmetric flow computations. Viscous effects are important because they restrict the inviscid core flow region, effectively changing the nozzle contour. In addition, the effective boundary layer thickness reduces the available uniform core flow in the test cabin. An axisymmetric code was implemented to study possible nonuniformities of the nozzle exit plane flow field that enters the test article. To quantify the primary features of the flow, consideration was given to nonisentropic processes such as viscous boundary layer development and real-gas chemistry.

The axisymmetric, Navier–Stokes equations for a gas in thermal and chemical nonequilibrium were solved using the General Aerodynamic Simulation Program (GASP). Along the nozzle wall, a nonslip flow condition was enforced and a fixed wall temperature of 300 kelvin was specified. Real-gas chemistry was implemented using a multiple-species air model including ionization. The following seven

dominant species were considered: N, O, N₂, O₂, NO, NO⁺, and e⁻. The algebraic turbulence flow model by Baldwin and Lomax was implemented near the nozzle wall to capture the boundary layer growth through the nozzle. The viscous boundary layer was resolved using a fine grid stretching at the wall. The figure shows an example of the measured and calculated pitot pressure distribution at the nozzle exit. The experimental pitot pressure data are compared with the axisymmetric numerical calculations. The code captures the boundary layer thickness well.

In summary, the nozzle flow in the 16-Inch Shock Tunnel facility used for hypersonic studies was investigated numerically using 1D and

2D/axisymmetric codes. The flow quantities were determined in the computational domain including both exit conditions and nozzle centerline properties. Three different nozzle contours (Mach 12, 14, and 16) were considered. Results from the Mach 14 case are presented here. It is important to accurately model and understand the physics of the nozzle flow field, since it is the nozzle exit flow properties that determine the flow conditions within the inlet and combustor of the test article.

**Ames-Moffett contact: P. Papadopoulos
(415) 604-3477**

Headquarters program office: OA

Reactive Intermediates in Soot Formation

Stephen P. Walch

Computational chemistry methods have been used to study reactive intermediates and reaction pathways involved in the early stages of soot formation.

The formation of phenyl radical is believed to be the rate limiting step in soot formation. Two different mechanisms for the formation of phenyl radical have been proposed. The first mechanism involves the stepwise addition of acetylenes to give C₄H₃ and phenyl radical. The second mechanism involves reactions of carbenes. This mechanism starts with the CH and CH₂ radicals, which are important under fuel rich conditions. Miller and Melius (Sandia Laboratory, Livermore, California) have proposed that the propargyl radical (CH₂CCH), which can arise from the reaction of CH or CH₂ with acetylene, can dimerize to give benzene (and, with loss of an H atom, phenyl radical).

In the present work, we have studied (1) the reaction of CH(²Π) and singlet methylene with acetylene; (2) the C₄H₄ potential energy surface, especially the reaction of vinylidene (CH₂C) with acetylene; and (3) the ring closure reactions of n-C₄H₃ (CHCHCCH) and iso-C₄H₃ (CH₂CCCH) with acetylene.

The computed potential energy surface for CH(²Π) plus acetylene is found to have low-energy pathways leading to a number of reactive intermediates. These species include iso-CHCHCH, half-benzene, the propargyl radical (all shown in part (a) of the figure), and the open form of C₃H₂ (shown in part (b) of the figure). All of these structures are expected to be very reactive species, and it is found from calculations that iso-CHCHCH, half-benzene, and the open form of C₃H₂ dimerize with no barrier to give benzene, benzene, and para-benzyne, respectively. Half-benzene may also be important in building higher polycyclic aromatic hydrocarbons. Thus, the calculations demonstrate a number of new reactive species as products of the reaction of CH(²Π) with acetylene, which may be important in the carbene mechanism.

The acetylene mechanism starts with the reaction of two acetylenes to give vinylacetylene (CH₂CHCCH). The calculations on this system show that one acetylene must first undergo isomerization to the vinylidene isomer, which is computed to be about 43 kilocalories per mole higher in energy than

acetylene, but that the subsequent reaction to form vinylacetylene is all downhill, other than a small entrance channel barrier. Hydrogen abstraction from vinylacetylene leads to the *n*- and *iso*- isomers of C_4H_3 . The calculations show that *n*- C_4H_3 undergoes cycloaddition with acetylene to give phenyl radical, while *iso*- C_4H_3 undergoes cycloaddition with acetylene to give 1-dehydro-fulvene as the initial addition product.

A pathway was also found for isomerization of 1-dehydro-fulvene to phenyl radical; however, 1-dehydro-fulvene may be important as a reactive intermediate. A mechanism leading from 1-dehydro-fulvene to corannulene by subsequent additions of four half-benzene molecules followed by loss of H or H_2 and a final step of adding acetylene and eliminating an H_2 has been proposed based on these studies. Howard and coworkers have discussed pathways leading from corannulene to the fullerene C_{60} by successive additions of acetylene and elimination of molecular hydrogen. The mechanism discussed here provides the missing pathway to corannulene.

Ames-Moffett contact: S. Walch
(415) 604-6189
Headquarters program office: OA/HSRP

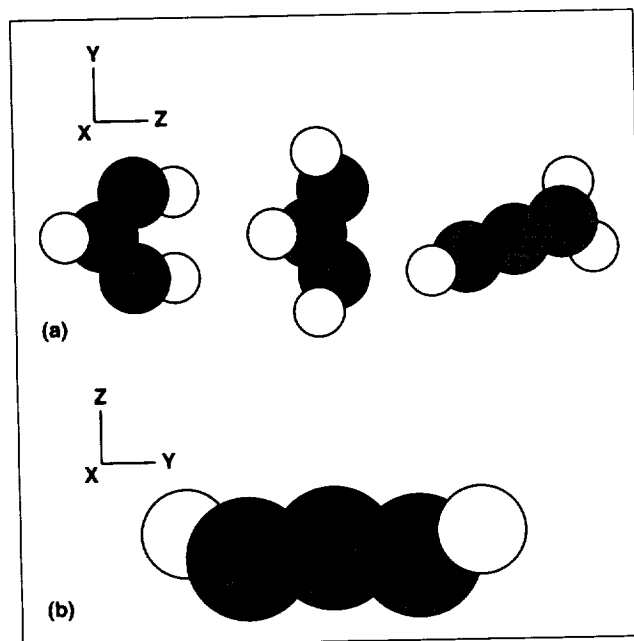
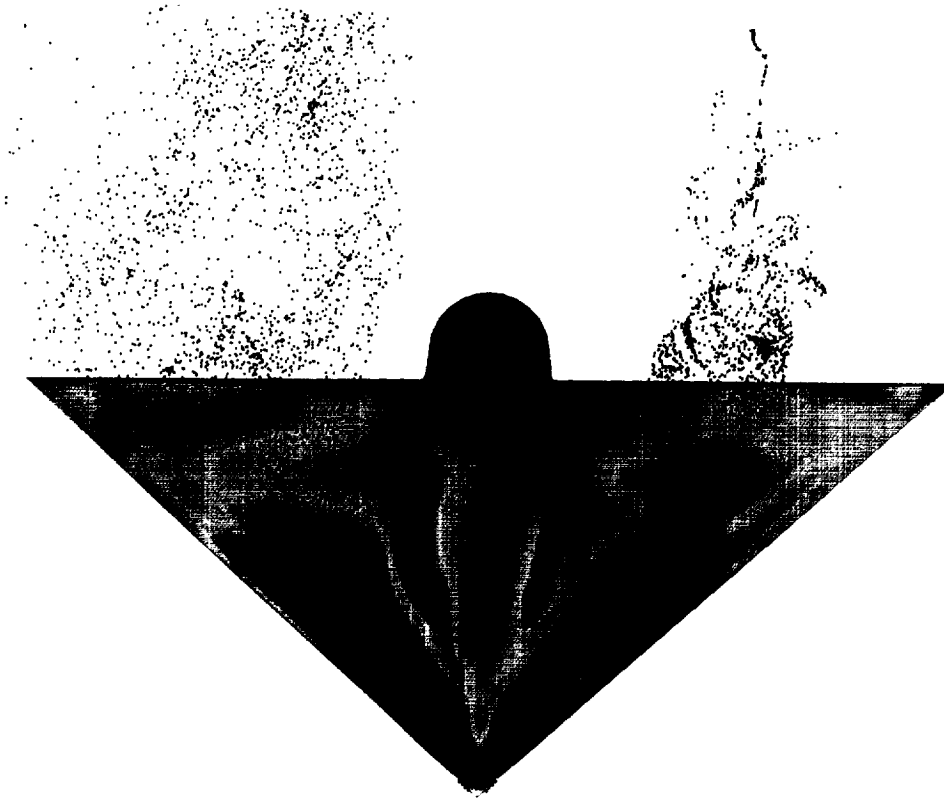


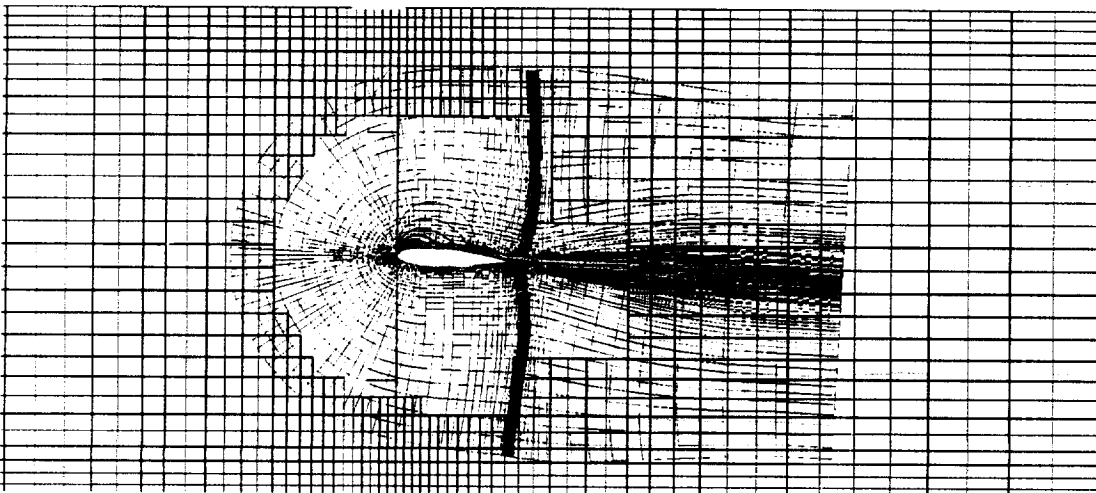
*Fig. 1. Reactive intermediates formed from the reaction of $CH(^2\Pi)$ with acetylene. The structures shown in part (a) are, from left to right, *iso*- $CHCHCH$, half-benzene, and the propargyl radical. Part (b) shows the open form of C_3H_2 .*



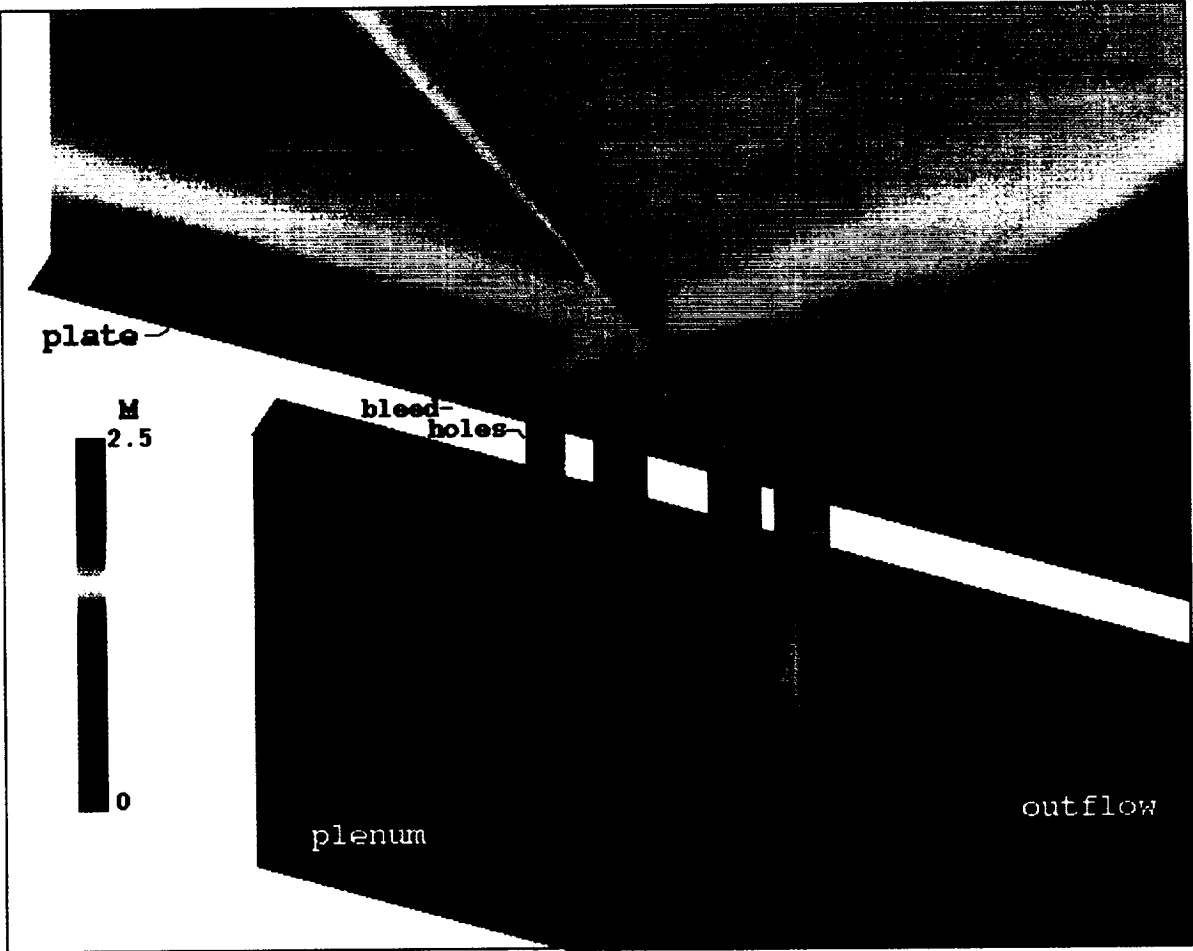
The color plates in this appendix correspond to black and white photographs in the text. Each caption provides the location of the corresponding photograph.



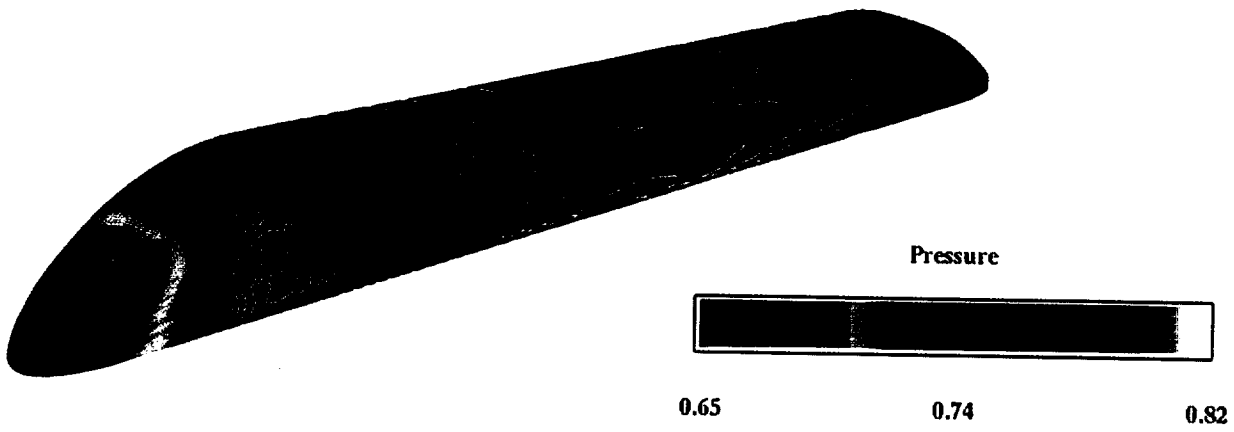
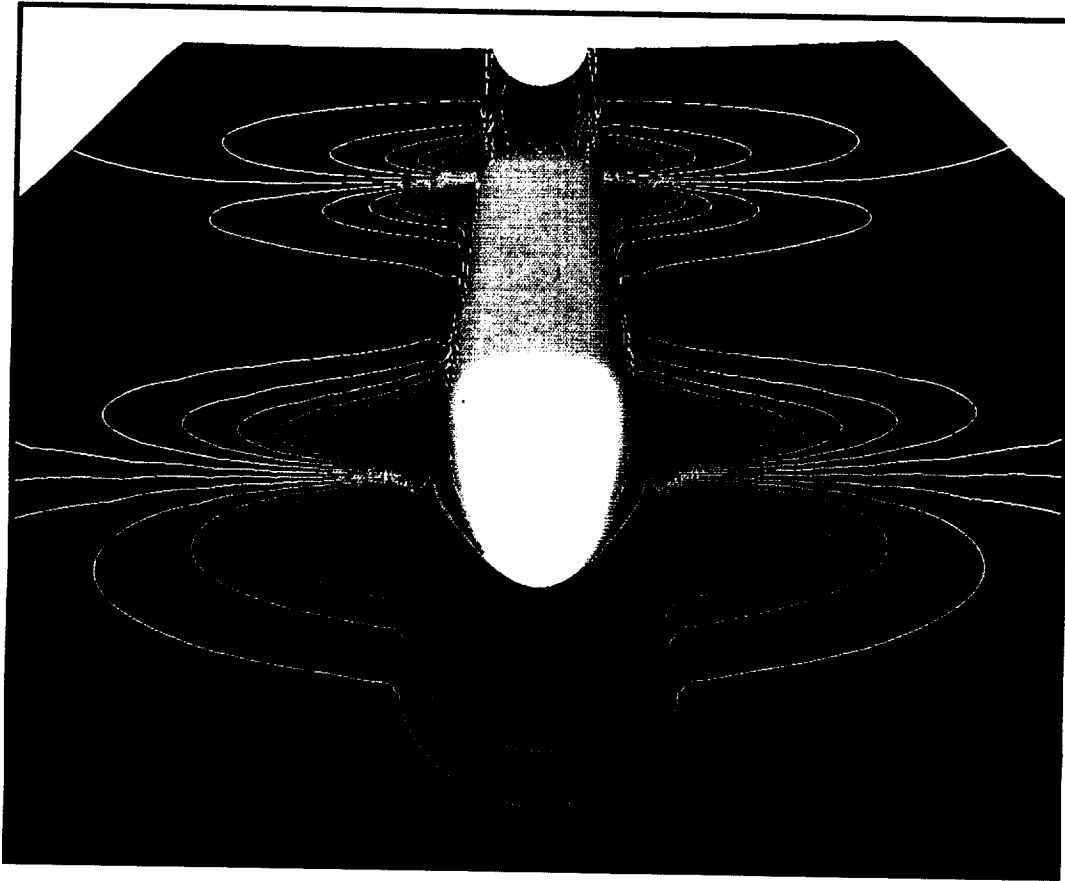
Color Plate 1. Numerical flow visualization of surface pressures and nonsteady leeward-side vortices. (fig. 2, page 2)



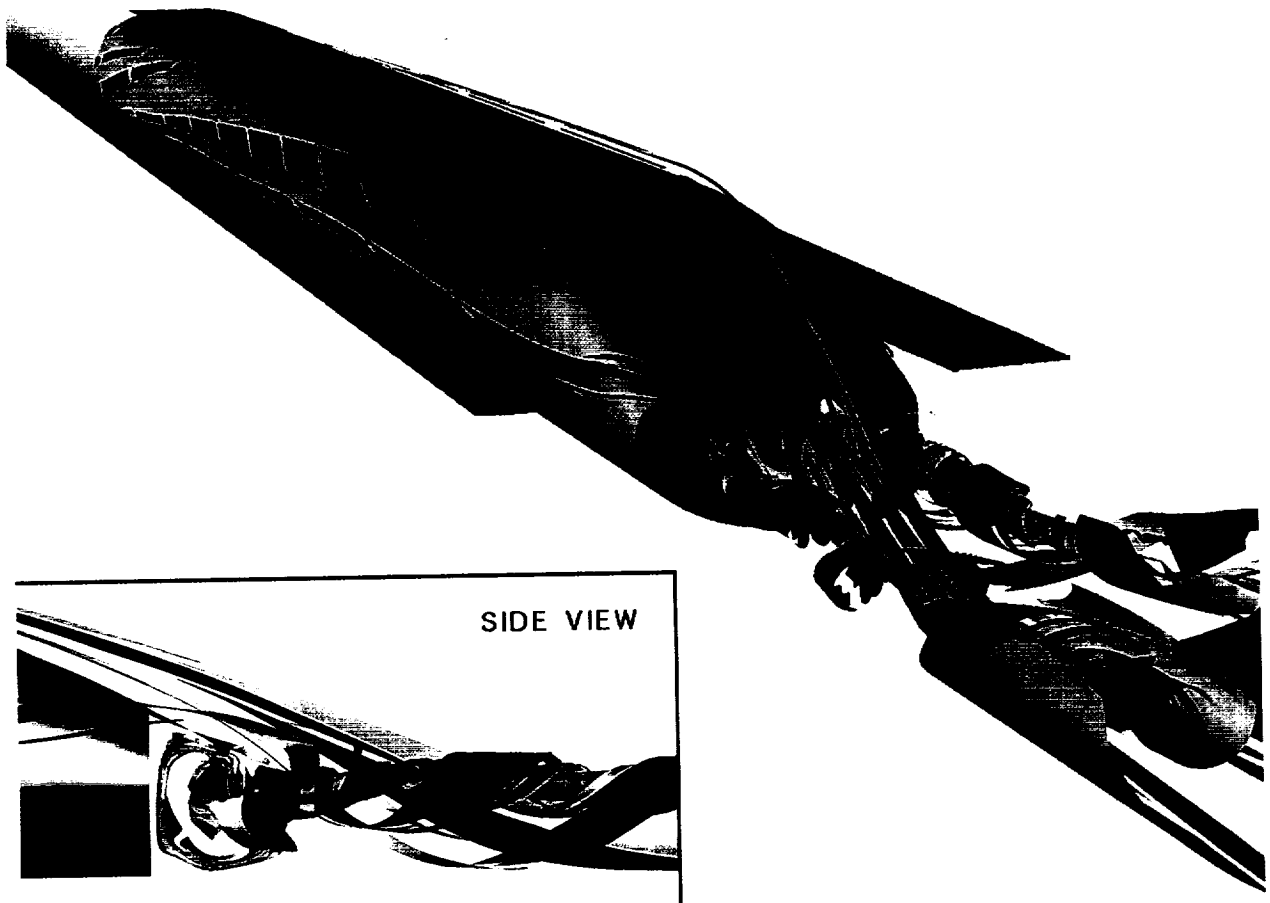
Color Plate 2. Fully parallel, multiple-zone viscous aerodynamic optimization. (fig. 2, page 5)



Color Plate 3. Mach contours of bleed flow field. (fig. 2, page 6)



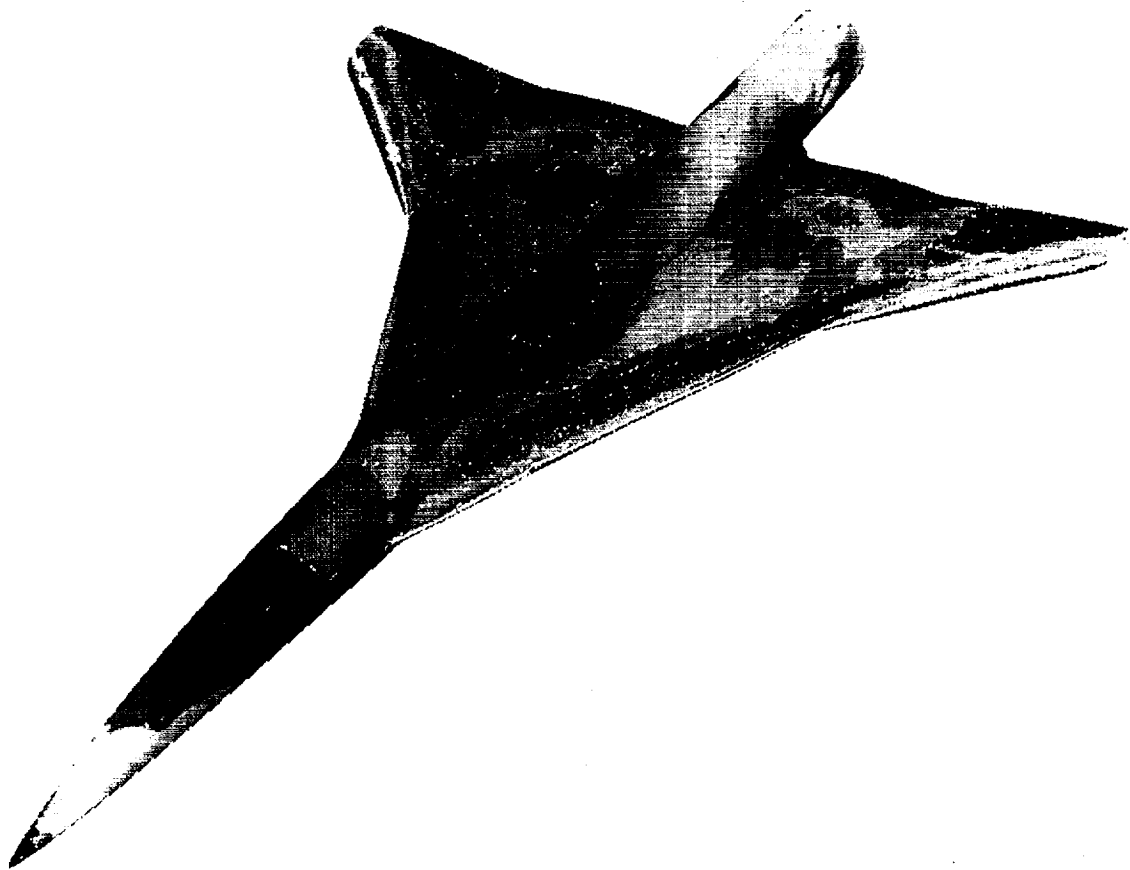
Color Plate 4. Pressure contours on the surfaces of guideway and vehicle. (fig. 1, page 27)



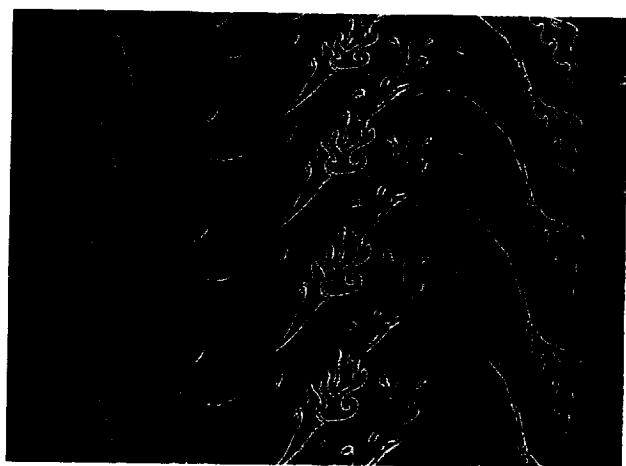
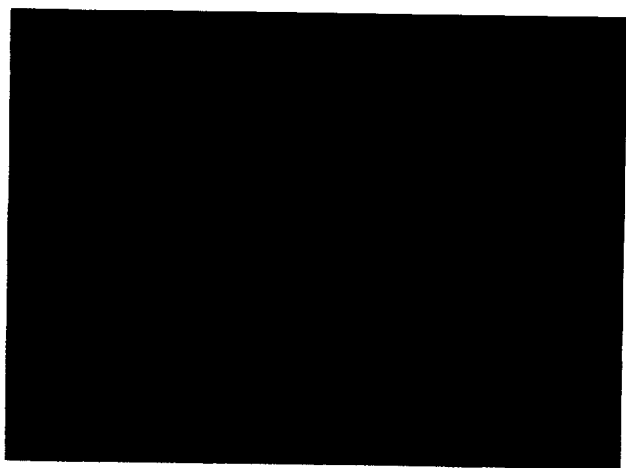
Color Plate 5. Stream surfaces emanating from the nose region manifest large streamwise vortices at the base of the vehicle. (fig. 2, page 27)



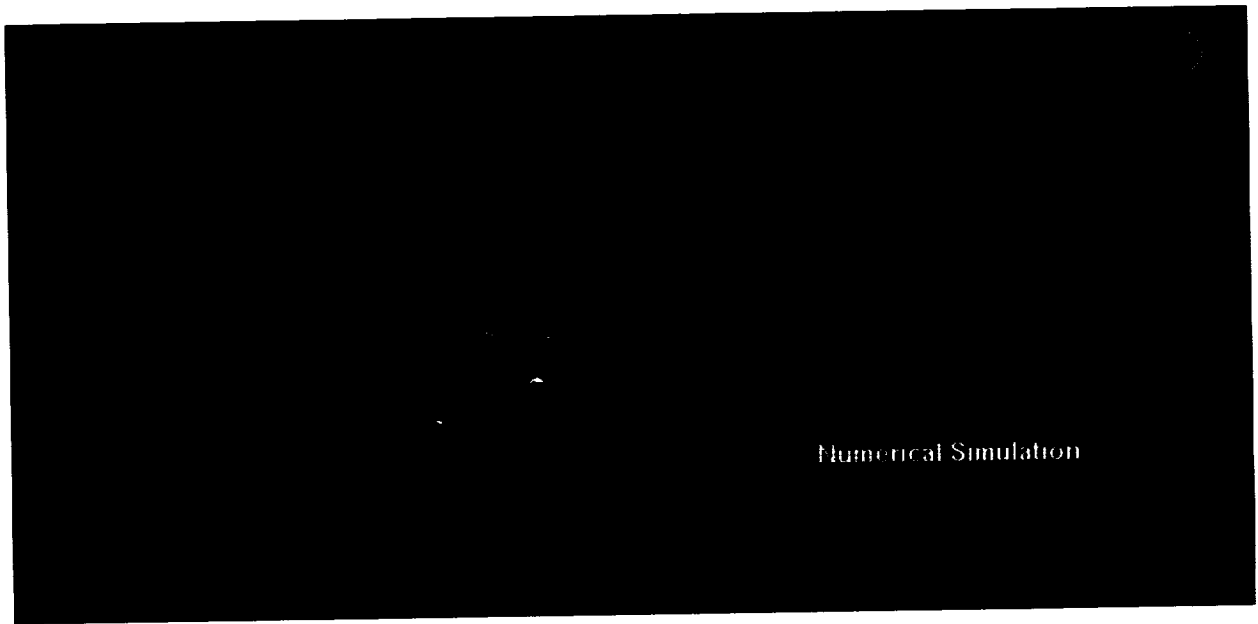
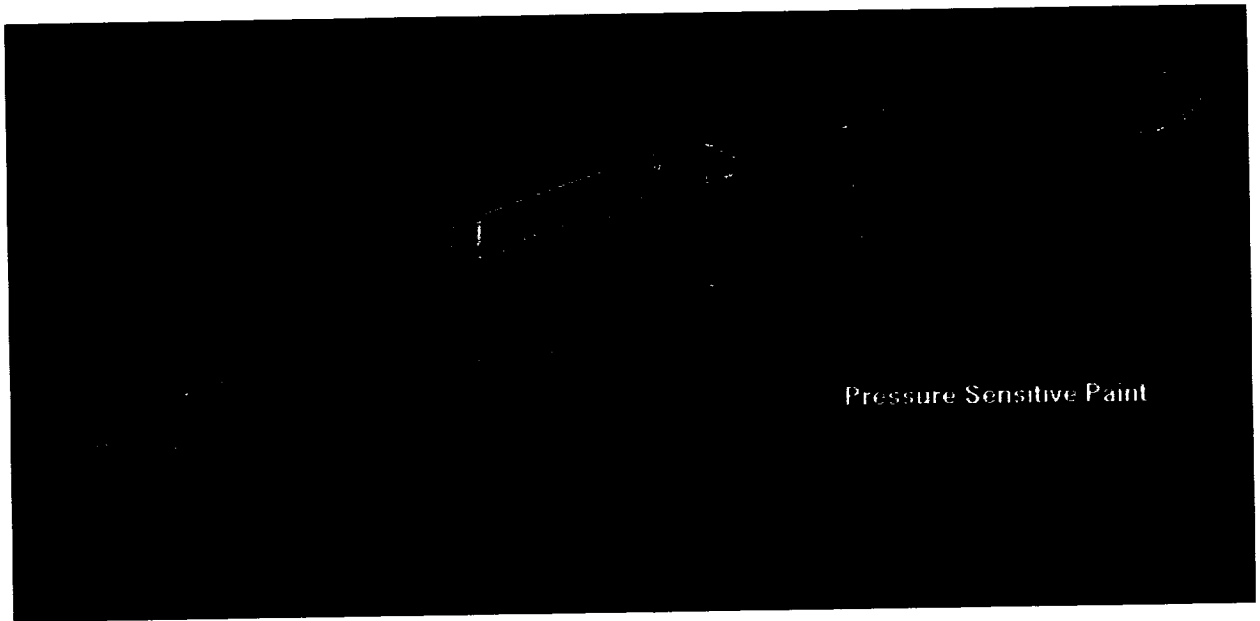
Color Plate 6. Cartesian CFD solution for advanced transonic transport. (fig. 1(a), page 28)



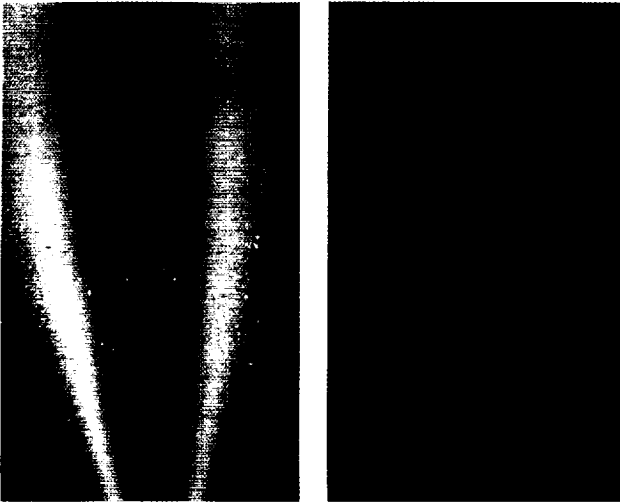
Color Plate 7. Cartesian CFD solution for advanced supersonic transport. (fig. 1(b), page 28)



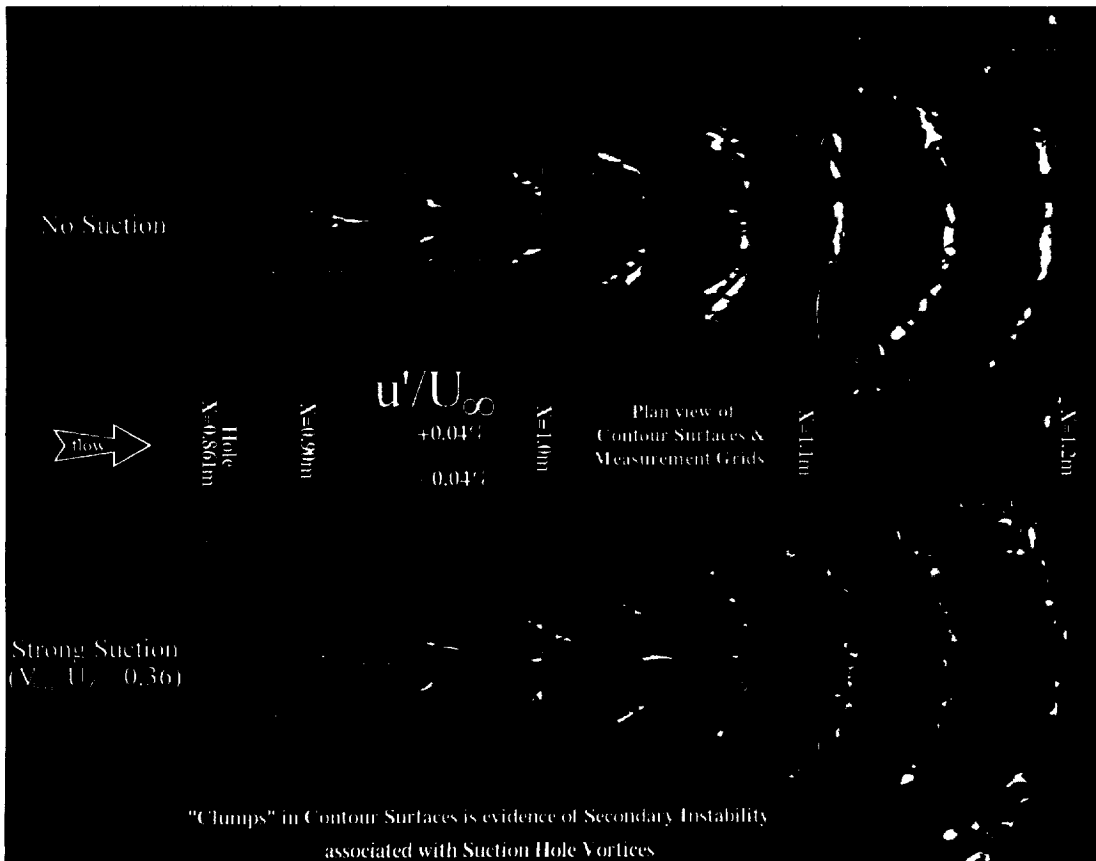
Color Plate 8. The turbine geometry, time-averaged surface pressures, and instantaneous entropy contours within a 1-1/2-stage turbine. (fig. 1, page 45)



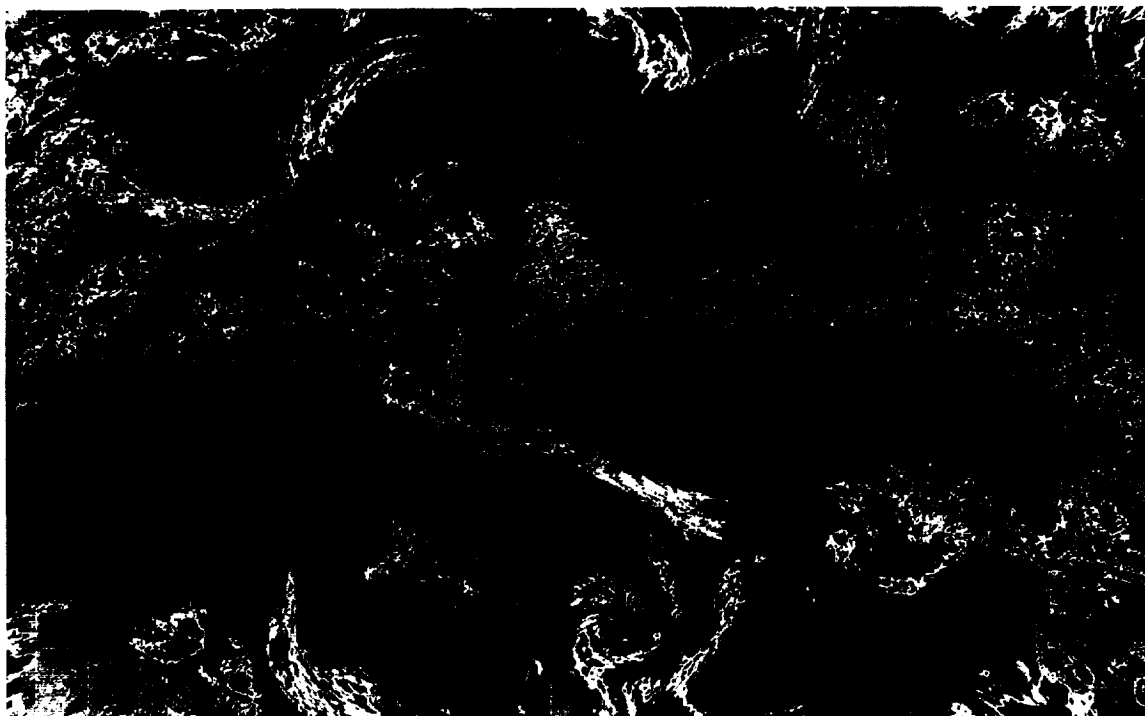
Color Plate 9. Pressure maps of the oblique all-wing. (fig. 1, page 49)



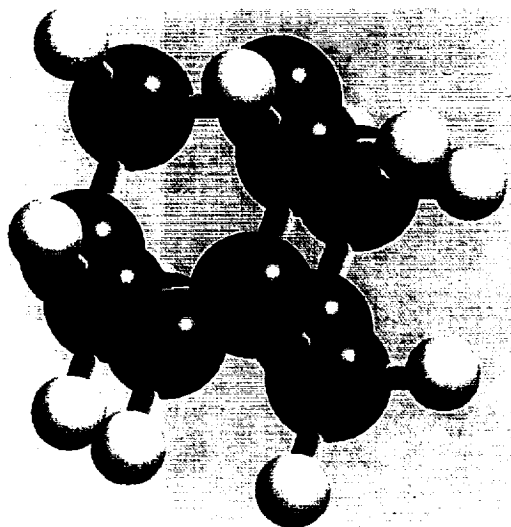
Color Plate 10. Color-change response of liquid crystal coating to tangential jet flow: left-hand side, flow away from camera; right-hand side, flow toward camera. (fig. 1, page 50)



Color Plate 11. A plan view of the 3-D contours under conditions of strong suction and without suction. (fig. 1, page 54)



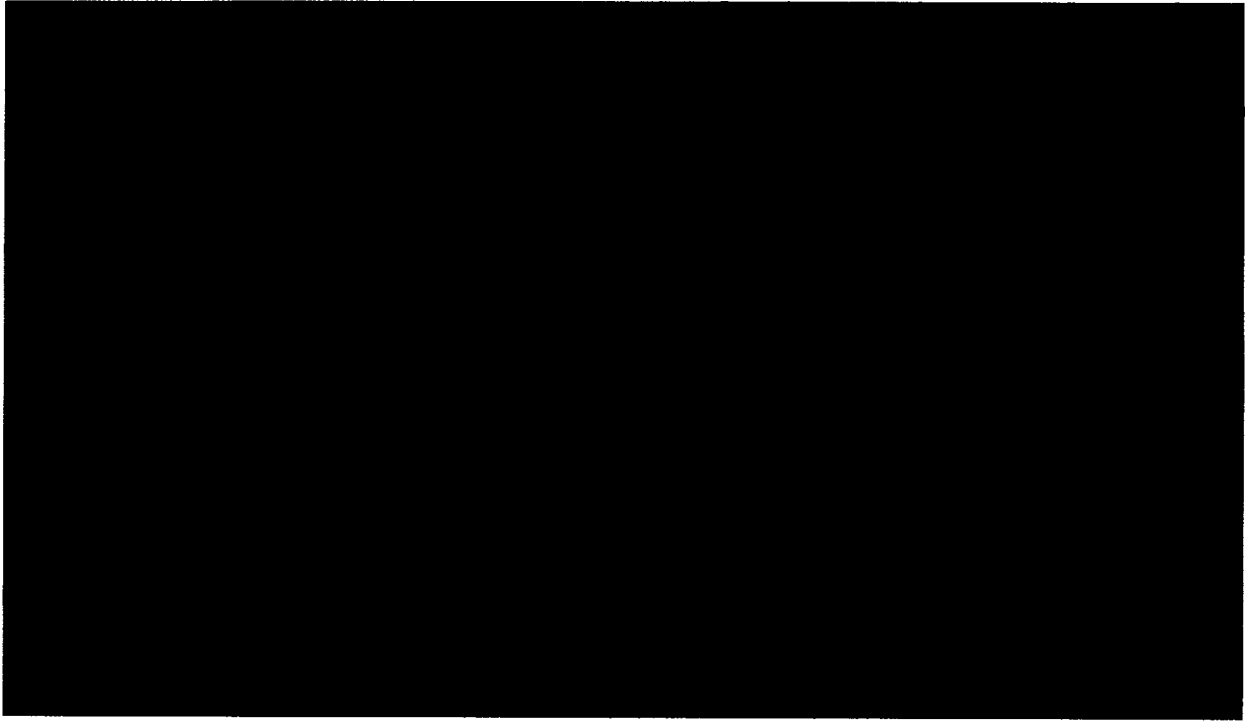
Color Plate 12. Composite of 11-micron infrared imagery at 0 hours universal time on 14 September 1994 from two geostationary satellites, GMS-4 (located at the equator and 140 degrees east), and GOES-7 (located at the equator and 112 degrees west). Colored regions indicate cloud-top temperatures less than -35°C . The coldest temperature (red near 160 degrees east and 11 degrees north) is about -85°C . (fig. 1, page 144)



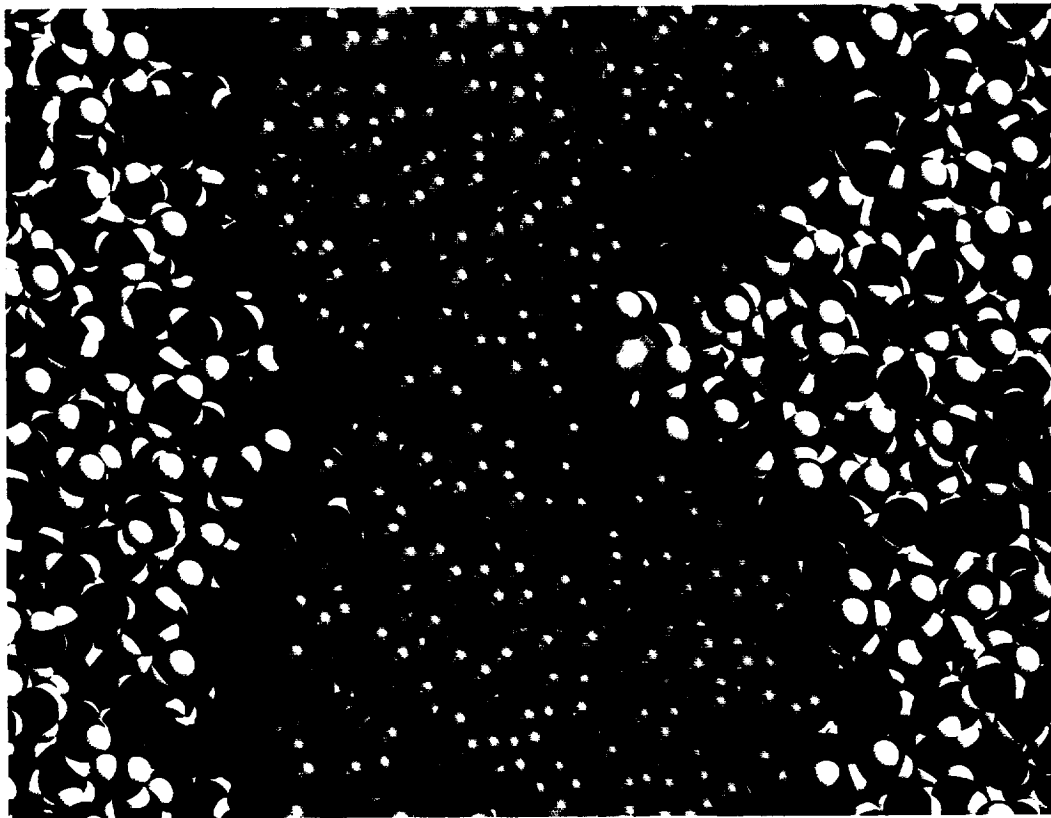
Color Plate 13. Molecular structure of hexamethylenetetramine (HMT; $\text{C}_6\text{H}_{12}\text{N}_4$): the black spheres are carbon atoms, the red spheres are nitrogen atoms, and the small white spheres are hydrogen atoms. (fig. 1, page 192)



Color Plate 14. A series of frames from a time evolution of particles of the optimally concentrated size. Clumps are identified at three different times; the particles in each are identified and assigned a color. The entire time sequence is then played so that the time evolution of particles into and out of clumps can be studied. Particles converge to a clump slowly and from remotely separated regions; they pass through the clump and are dispersed along streamers. Presumably, the sequence is repeated with particles finding different clumps in the next cycle. Our hypothesis is that after a certain number of such "transient" clumping events, the statistical distribution of clump densities that we are now studying provides particles with an unusually dense clump to encounter, in which collisions or other nonlinear effects prevent subsequent dispersion. (fig. 2, page 198)



Color Plate 15. Artificial color version of Saturn's rings, created by taking ratios of three radial brightness profiles obtained in different Voyager filter bands. Different colors in this representation manifest distinct radial variations in the spectral shape of the ring reflectivity; that is, different materials lie at different radii. The left (bluish) side is the inner edge of the C ring; the central (reddish) region is the nearly opaque B ring; the next region outward (bluish) is the nearly transparent Cassini Division, which has color and reflectivity comparable to the C ring. The outer or A ring has an unusual composition at its inner edge, as seen in the greenish band, but appears similar in composition to the B ring elsewhere. (fig. 1, page 199)

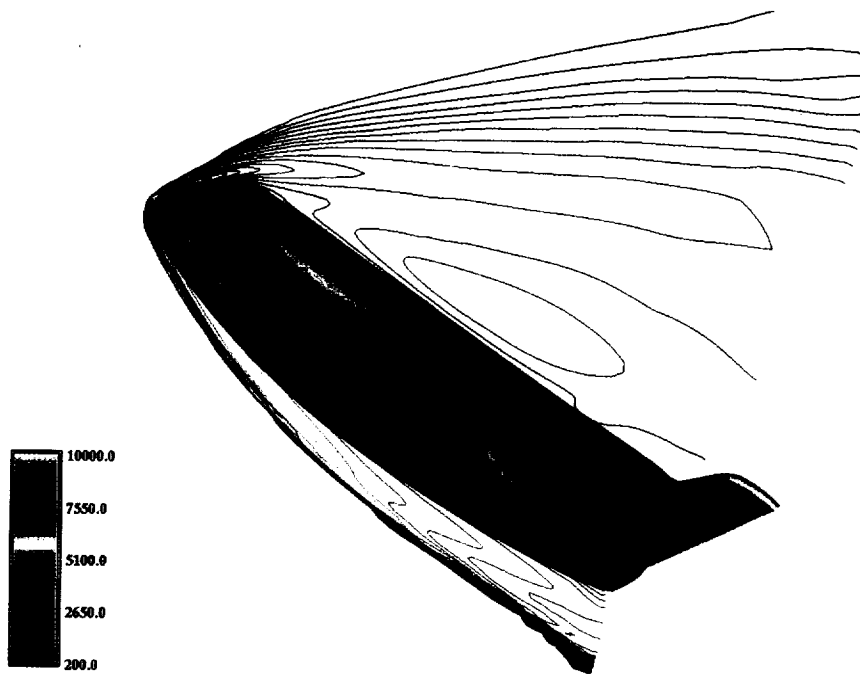


Color Plate 16. A representative configuration of sodium ion (Na^+) in the membrane obtained from computer simulations. The ion is yellow, the lipid head groups are magenta, and the lipid tails forming the nonpolar membrane interior are blue. The oxygen and hydrogen atoms of water molecules surrounding the membrane are red and white, respectively. (fig. 1, page 218)

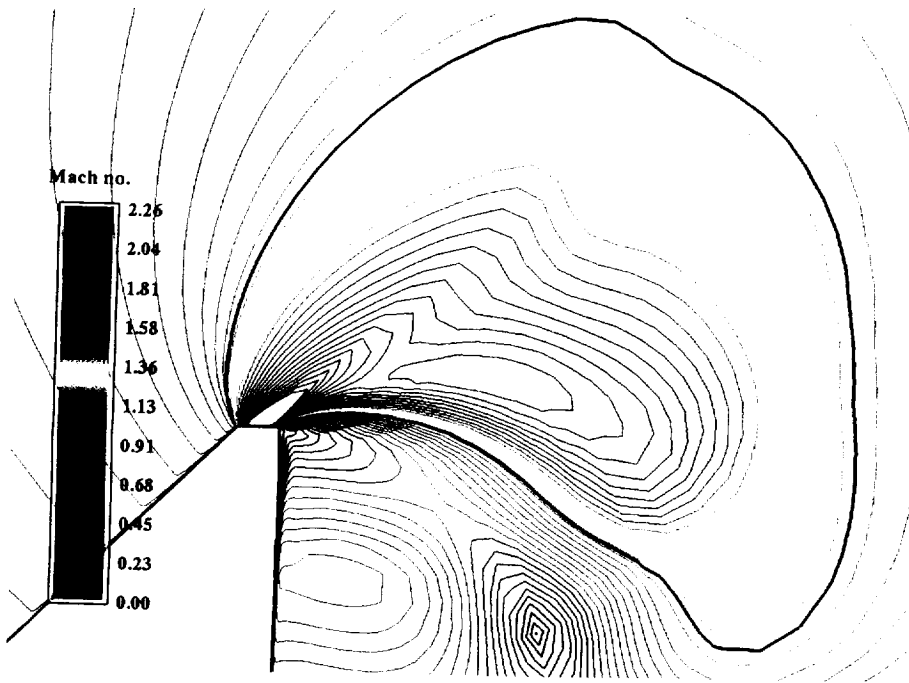
Includes Pyrolysis



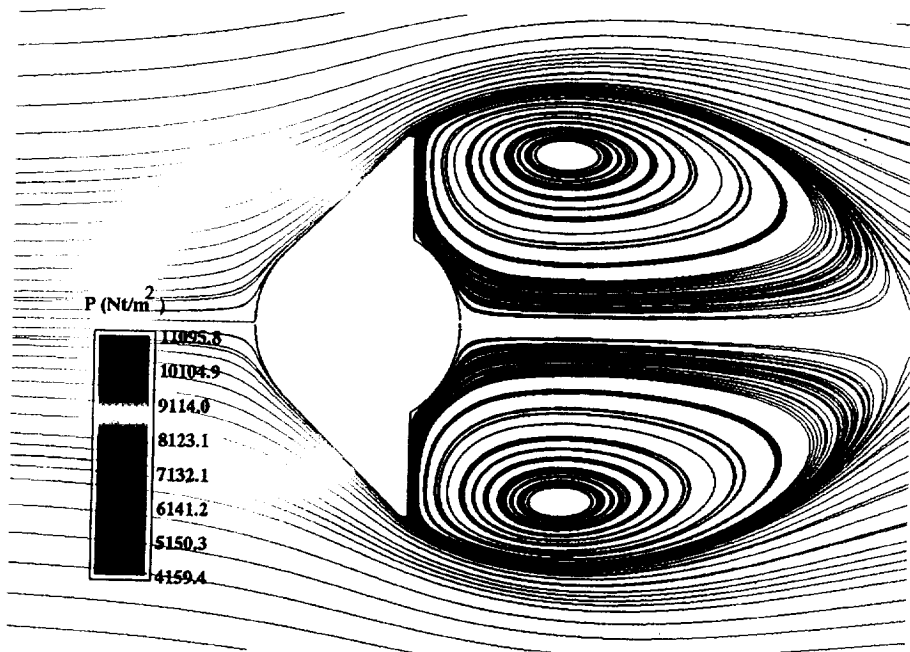
Color Plate 17. Flow temperatures about the Galileo Probe during aerobraking at 350 kilometers altitude. (fig. 1, page 236)



Color Plate 18. Temperature contours along the symmetry plane of the lifting body, 70-km trajectory point. (fig. 1, page 239)



Color Plate 19. Mach number contours at an altitude of 67.158 km ($V = 195.4$ m/sec). (fig. 1, page 243)



Color Plate 20. Flow streamlines at an altitude of 66.47 km ($V = 55.3$ m/sec). (fig. 2, page 243)

REPORT DOCUMENTATION PAGE

Form Approved
OMB No. 0704-0188

Public reporting burden for this collection of information is estimated to average 1 hour per response, including the time for reviewing instructions, searching existing data sources, gathering and maintaining the data needed, and completing and reviewing the collection of information. Send comments regarding this burden estimate or any other aspect of this collection of information, including suggestions for reducing this burden, to Washington Headquarters Services, Directorate for Information Operations and Reports, 1215 Jefferson Davis Highway, Suite 1204, Arlington, VA 22202-4302, and to the Office of Management and Budget, Paperwork Reduction Project (0704-0188), Washington, DC 20503.

1. AGENCY USE ONLY (Leave blank)		2. REPORT DATE September 1995	3. REPORT TYPE AND DATES COVERED Technical Memorandum	
4. TITLE AND SUBTITLE Research and Technology 1994			5. FUNDING NUMBERS	
6. AUTHOR(S) Ames-Moffett Investigators			5. FUNDING NUMBERS	
7. PERFORMING ORGANIZATION NAME(S) AND ADDRESS(ES) Ames Research Center Moffett Field, CA 94035-1000			8. PERFORMING ORGANIZATION REPORT NUMBER A-950019	
9. SPONSORING/MONITORING AGENCY NAME(S) AND ADDRESS(ES) National Aeronautics and Space Administration Washington, DC 20546-0001			10. SPONSORING/MONITORING AGENCY REPORT NUMBER NASA TM-108858	
11. SUPPLEMENTARY NOTES Point of Contact: John T. Howe, Chief Scientist, Ames Research Center, MS 200-16, Moffett Field, CA 94035-1000 (415) 604-5500 or contact person(s) at the end of each article				
12a. DISTRIBUTION/AVAILABILITY STATEMENT Unclassified — Unlimited Subject Category 99			12b. DISTRIBUTION CODE	
13. ABSTRACT (Maximum 200 words) Selected research and technology activities at Ames Research Center are summarized. These activities exemplify the Center's varied and productive research efforts for 1994.				
14. SUBJECT TERMS Aeronautics, Space technology, Space sciences, Earth sciences, Life sciences, Computer science, Research and technology			15. NUMBER OF PAGES 276	
			16. PRICE CODE A13	
17. SECURITY CLASSIFICATION OF REPORT Unclassified	18. SECURITY CLASSIFICATION OF THIS PAGE Unclassified	19. SECURITY CLASSIFICATION OF ABSTRACT	20. LIMITATION OF ABSTRACT	